Sustainable Development for Mass Urbanization

Md. Faruque Hossain

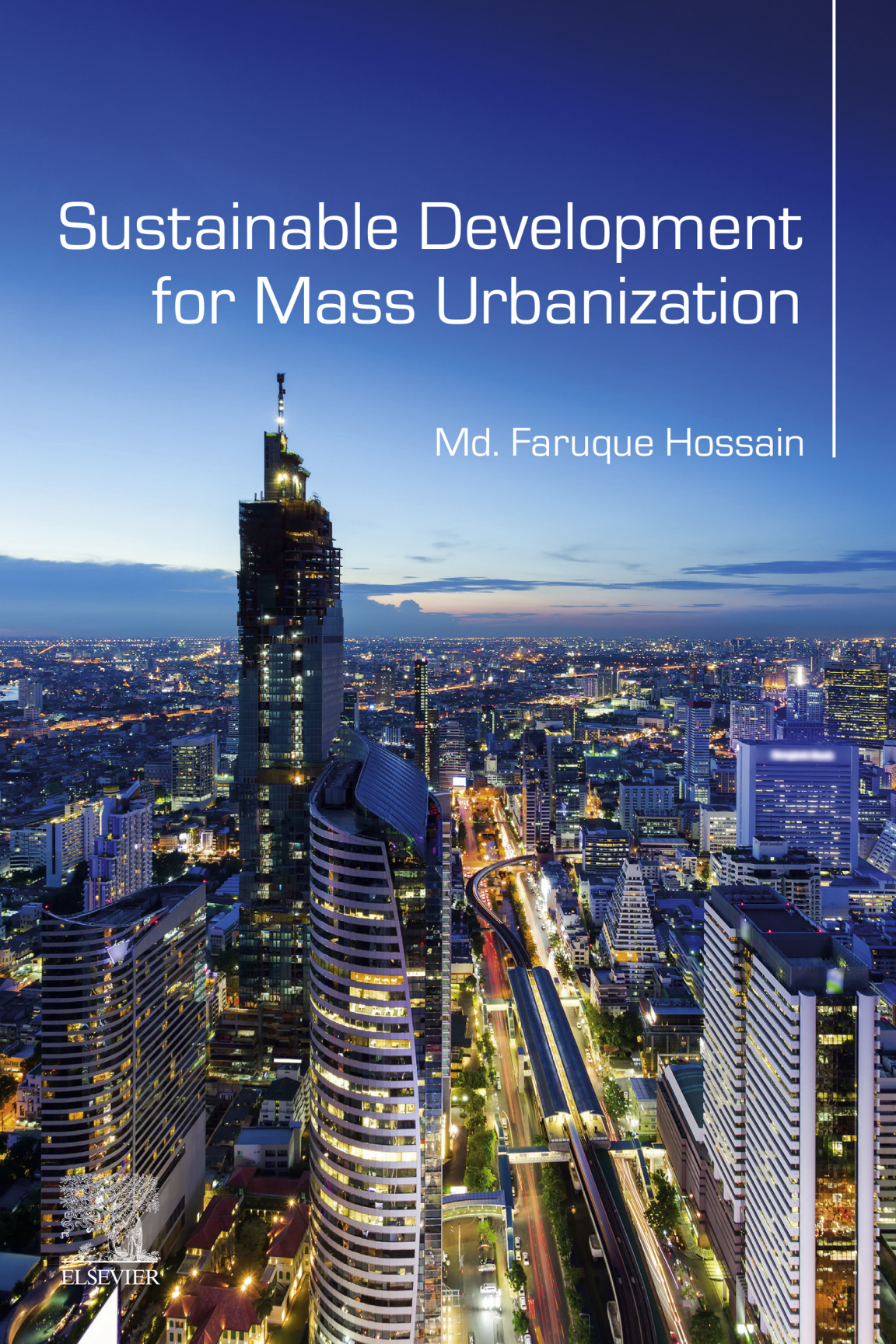

ELSEVIER

SUSTAINABLE DEVELOPMENT FOR MASS URBANIZATION

This page intentionally left blank

This book belongs to Kitab Liaison (ocd1996@gmail.com)

Copyright Elsevier 2023

SUSTAINABLE DEVELOPMENT FOR MASS URBANIZATION

Md. Faruque Hossain

Adjunct Professor, Department of Civil and Urban Engineering, New York University, Brooklyn, NY, United States

and

CEO, Green Globe Technology, Inc., Flushing, NY, United States

ELSEVIER

This book belongs to Kitab Liaison (ocd1996@gmail.com)

Copyright Elsevier 2023

Elsevier
Radarweg 29, PO Box 211, 1000 AE Amsterdam, Netherlands
The Boulevard, Langford Lane, Kidlington, Oxford OX5 1GB, United Kingdom
50 Hampshire Street, 5th Floor, Cambridge, MA 02139, United States

© 2019 Elsevier Inc. All rights reserved.

No part of this publication may be reproduced or transmitted in any form or by any means, electronic or mechanical, including photocopying, recording, or any information storage and retrieval system, without permission in writing from the publisher. Details on how to seek permission, further information about the Publisher's permissions policies and our arrangements with organizations such as the Copyright Clearance Center and the Copyright Licensing Agency, can be found at our website: www.elsevier.com/permissions.

This book and the individual contributions contained in it are protected under copyright by the Publisher (other than as may be noted herein).

Notices

Knowledge and best practice in this field are constantly changing. As new research and experience broaden our understanding, changes in research methods, professional practices, or medical treatment may become necessary.

Practitioners and researchers must always rely on their own experience and knowledge in evaluating and using any information, methods, compounds, or experiments described herein. In using such information or methods they should be mindful of their own safety and the safety of others, including parties for whom they have a professional responsibility.

To the fullest extent of the law, neither the Publisher nor the authors, contributors, or editors, assume any liability for any injury and/or damage to persons or property as a matter of products liability, negligence or otherwise, or from any use or operation of any methods, products, instructions, or ideas contained in the material herein.

Library of Congress Cataloging-in-Publication Data
A catalog record for this book is available from the Library of Congress

British Library Cataloguing-in-Publication Data
A catalogue record for this book is available from the British Library

ISBN: 978-0-12-817690-0

For information on all Elsevier publications
visit our website at https://www.elsevier.com/books-and-journals

Publisher: Mathew Deans
Acquisition Editor: Ken McCombs
Editorial Project Manager: Fernanda A Oliveira
Production Project Manager: Selvaraj Raviraj
Cover Designer: Miles Hitchen

Typeset by SPi Global, India

ELSEVIER Book Aid International Working together to grow libraries in developing countries
www.elsevier.com • www.bookaid.org

This book belongs to Kitab Liaison (ocd1996@gmail.com) Copyright Elsevier 2023

Dedication

Dedicated to Nowshin, Shafin, and Faria.

This book belongs to Kitab Liaison (ocd1996@gmail.com)

Copyright Elsevier 2023

This page intentionally left blank

This book belongs to Kitab Liaison (ocd1996@gmail.com)

Copyright Elsevier 2023

Contents

About the Author *xi*
Preface *xiii*

Part 1 Introduction **1**

1. Building a better urban system **3**

Part 2 Critical infrastructure system **5**

2. Introduction of megacities **7**
Introduction 7
Critical infrastructure system 8
Environmental pollution control 11
Sustainable building 13
Conclusion 14
Acknowledgments 14
References 15

3. Water delivery systems **17**
Introduction 17
Material, methods, and simulation 17
Results and discussion 20
Conclusions 22
Acknowledgment 22
References 22

4. Sanitation and waste disposal systems **25**
Introduction 25
Simulation and method 26
Results and discussion 35
Conclusion 38
Acknowledgments 38
References 39

5. Power systems **41**
Introduction 41
Material and methods 42
Results and discussion 47

This book belongs to Kitab Liaison (ocd1996@gmail.com)
Copyright Elsevier 2023

Conclusions 53
Acknowledgments 53
References 54

6. Sustainable infrastructure systems 57

Introduction 57
Simulations and methods 58
Guideway model 58
Magnetic forces of uplift levitation and lateral guidance 59
Wind energy modeling for the vehicles 61
Wind energy storage in battery system 62
Design of traffic control 62
Results and discussion 64
Construction cost estimate comparison 68
Construction cost estimate comparison 71
Cost of maglev infrastructure 71
Cost of traditional road infrastructure 72
Cost savings 73
Conclusions 74
Acknowledgments 74
References 74

7. Public transportation systems 77

Introduction 77
Methods and simulation 78
Drive train modeling 80
One-mass model 81
Wind energy conversion 83
Control structure 86
Controller design 95
Generator modeling 96
Results and discussion 98
Battery modeling 103
Conclusions 105
Acknowledgments 106
References 106

8. Flying transportation technology 111

Introduction 111
Thoughts and methods 112
Numerical method of solution 113

This book belongs to Kitab Liaison (ocd1996@gmail.com) Copyright Elsevier 2023

Wind energy modeling for flying vehicles 114
Wind energy conversion 116
Generator modeling 116
Battery modeling 118
Optimization and discussion 119
Conclusion 122
Acknowledgments 123
References 123

Part 3 Environmental pollution controls 127

9. Air pollution 129
Urban air pollution impact on global environment 131
Urban air pollution control technology 142
Acknowledgments 148
References 148

10. Water pollution 151
Application of nanotechnology to control urban water pollution 159
Photocatalytic water treatment technology 187
Renewable water engineering 242
Acknowledgments 248
References 248

Part 4 Sustainable buildings 269

11. Green building technology 271
Introduction 271
Simulation and method 272
Design of PV panel 276
Design of bioreactor 279
Results and discussion 281
Conclusion 288
Acknowledgments 288
References 289

12. Green building complexes 291
Introduction 291
Methods and simulation 292
Results and discussion 298
Conclusions 311

This book belongs to Kitab Liaison (ocd1996@gmail.com) Copyright Elsevier 2023

Acknowledgments 313
References 313

13. Applied energy technology 317
Introduction 317
Methods and materials 318
Results and discussion 325
Conclusions 341
Acknowledgments 342
References 342

Part 5 Conclusion 345

14. Sustainable urbanization 347
Urban environmental management 347
Energy management 348
Building management 350
Water management 351
Infrastructure and transportation management 352
General management 353
Conclusion 354
Acknowledgments 355
References 355

Index 359

This book belongs to Kitab Liaison (ocd1996@gmail.com) Copyright Elsevier 2023

About the author

Dr. Md. Faruque Hossain has more than 20 years of industry experience in sustainable designing and building for large-scale urban developments, including advanced research on complex buildings as well as civil, energy, environmental, and critical infrastructure systems to create a better urban system. He has worked and consulted in entities that range from diverse small companies to Fortune listed companies. He has managed sustainable urban development projects that range from those valued at less than a million dollars to those valued at more than a billion dollars. This includes large-scale buildings as well as civil, energy, environmental, and critical infrastructure. Dr. Hossain has also worked for New York city on a senior management team and interacted with government officials from local, state, federal, and international agencies to collaborate on building a sustainable urban system. During his tenure on that team, Dr. Hossain managed a world-class team of scientists, architects, engineers, contractors, and consultants from top-tier engineering firms while maintaining the highest-level professional relationships to conduct sustainability practices on assigned projects. Dr. Hossain received his PhD from Hokkaido University, did postgraduate research in engineering at the University of Sydney, and participated in the executive education in architecture program at Harvard University. He is a LEED-certified professional and editors of several International Journal of Sustainable Urban Design and Build related field. A native of Bangladesh, Dr. Hossain is renowned as an industry leader and notable scientist in the field of sustainable urban research and development. He has dozens of world-class publications in very high-impact journals, and he has written two books (Elsevier) and two book chapters (Francis and Taylor) in the field of sustainable urban designing and building. Currently, he is working as an adjunct professor at the Department of Civil and Urban Engineering at New York University while simultaneously running his own company, Green Globe Technology. His personal motto is, "Practice sustainability for building a cleaner and greener urbanization."

This book belongs to Kitab Liaison (ocd1996@gmail.com)

Copyright Elsevier 2023

This page intentionally left blank

This book belongs to Kitab Liaison (ocd1996@gmail.com)

Copyright Elsevier 2023

Preface

The conventional practice is to develop urban systems by horribly consuming natural resources and causing deadly environmental vulnerabilities for any citizens who plan to comfortably live in urban areas in the near future. Simply put, the total mechanism of a traditional urban system is becoming obsolete and needs to be replaced by utilizing the wise application of sustainable technologies to secure a balanced urban system. The notion of sustainable urban development might be wide, but if we think about a calculative solution for these vulnerabilities, we only need a few innovative technologies to secure an environmentally balanced urban system. Therefore, sustainability research, development, and application must be practiced through the best scholastic approach of science and technology to build a cleaner and greener mass urban system.

Therefore, this book necessarily focuses on the holistic approaches of sustainability applications in all sectors of building, infrastructure, and energy to achieve a best-balanced urban system. Necessarily, this book describes a series of solutions by presenting innovative technologies through research and application for building a sustainable mass urban system. The goal of this book is to define the context of instigation to scientific theories and practical engineering applications to apply sustainable mechanisms to develop mass urbanization through presentation of the following main five themes: Part 1: Introduction (Chapter 1: Building a better urban system), Part 2: Critical infrastructural systems (Chapter 2: Introduction to megacities; Chapter 3: Water delivery systems; Chapter 4: Sanitation and waste disposal systems; Chapter 5: Power systems; Chapter 6: Sustainable infrastructure systems; Chapter 7: Public transport systems; Chapter 8: Flying transportation technology), Part 3: Environmental pollution controls (Chapter 9: Air pollution; Chapter 10: Water pollution), Part 4: Sustainable buildings (Chapter 11: Green building technology; Chapter 12: Green building complexes; Chapter 13: Green building and public housing), and Part 5: Conclusion (Chapter 14: Sustainable urbanization). These are very much interconnected to the total urban infrastructure system. Consequently, the importance of the application of sustainability in all sectors of urban infrastructure, environment, and building has also been discussed, considering the wise application

This book belongs to Kitab Liaison (ocd1996@gmail.com)

Copyright Elsevier 2023

of technologies by trickling down the advanced thoughts, research, and practices to achieve a broader goal to build a better urban system.

Md. Faruque Hossain
Department of Civil and Urban Engineering, New York University,
New York, NY, United States

This book belongs to Kitab Liaison (ocd1996@gmail.com)
Copyright Elsevier 2023

PART 1

Introduction

This book belongs to Kitab Liaison (ocd1996@gmail.com)

Copyright Elsevier 2023

This page intentionally left blank

This book belongs to Kitab Liaison (ocd1996@gmail.com)

Copyright Elsevier 2023

CHAPTER 1

Building a better urban system

Since the 1970s, there has been an expansion in the huge development of mass urbanization, quickening the construction of conventional urban buildings, roads, power stations, and water and sewer systems. This expansion will eventually cause dangerous environmental predicaments for urban citizens. We certainly need the application of advanced technologies to mitigate these malfunctioning urban systems because these traditional urban development technologies are essentially wrecking the total urban systems and their environmental equilibrium. For hundreds of years, architects and engineers have been designing urban buildings, infrastructure, and transportation systems for the betterment of our daily lives. Now, however, those are instantly becoming obsolete because they are causing serious urban environmental vulnerability. Therefore, they are presently required by nature to be "environmentally friendly" in order to protect our urban system and its environment by conforming to sustainable technologies.

Henceforth, the sustainable development of mass urbanization can be illustrated by the commonly accepted definition, developed by the World Commission on Environment and Development in 1987, which described sustainable mass urban development as that "which meets the needs of the present without compromising the ability of future generations to meet their own needs to secure a resilient urban system." Naturally, sustainable strategies must work with climate conditions as well as with environmental factors.

Currently, widespread concern has been raised over the limitations of the urban environment as well as that environment's finite ability to absorb pollutants due to the practice of traditional development of mass urbanization. Therefore, conventional mass urban development needs to be corrected to protect urban resources and the environment by employing much more advanced sustainable technologies in order to keep the urban environment physically, chemically, biologically, and socially balanced. Consequently, this notional term of "resilience" must be implemented for sustainable mass urban development, which would be the "autonomous adaptation," responds to conditions change by the adaptive capacity of modern urban

Sustainable Development for Mass Urbanization
https://doi.org/10.1016/B978-0-12-817690-0.00001-4
© 2019 Elsevier Inc.
All rights reserved.

This book belongs to Kitab Liaison (ocd1996@gmail.com)
Copyright Elsevier 2023

system through applying proper planning and practicing flexible solutions on environmentally friendly technological applications. It will without a doubt make the urban system green and clean as a result of its versatility, adaptability, and manageability, which won't result in maladjustment simultaneously, but the sustainability application for mass urban development.

So, what can we do as the first generation with the tools to see how the urban environmental system is running toward danger due to the practice of traditional mass urbanization? At the same time, we are the last generation with the opportunities to prevent these dangers. Indeed, we can do great work individually and/or collectively by applying these sustainable technologies in every sector of building, energy, infrastructure, transportation, and water development while socially helping to create a total view for implementing these technologies to confirm a cleaner and greener urban system. Moreover, to build such versatile capacity, all technologies for buildings, infrastructure, and environmental engineering systems must be enforced by rules, regulations, and laws to secure a sustainable mass urban system.

This book belongs to Kitab Liaison (ocd1996@gmail.com) Copyright Elsevier 2023

PART 2

Critical infrastructure system

This book belongs to Kitab Liaison (ocd1996@gmail.com)

Copyright Elsevier 2023

This page intentionally left blank

This book belongs to Kitab Liaison (ocd1996@gmail.com)

Copyright Elsevier 2023

CHAPTER 2

Introduction of megacities

Introduction

By 2030, Asia alone will have at least 30 megacities, including Mumbai, India (2015 population of 20.75 million people), Shanghai, China (2015 population of 35.5 million people), Delhi, India (2015 population of 21.8 million people), Tokyo, Japan (2015 population of 38.8 million people), Seoul, South Korea (2015 population of 25.6 million people), and Dhaka, Bangladesh (2015 population of 18.2 million people). The megacities in the Americas will include New York (2015 population of 18.8 million people) and São Paulo, Brazil (2015 population of 18.2 million people). The megacities in Europe and Africa will include Paris, France (11.1 million people), Berlin, Germany (9.2 million people), London, United Kingdom (8.1 million people), Lagos, Nigeria (21.0 million people), and Cairo, Egypt (20.4 million people). The concept of sustainable mass urbanization (SMU) is the application of innovative science and engineering technologies utilized by scientists, consultants, architects, engineers, construction managers, policy makers, and investors to secure a more ecologically balanced urban system. The exercise of SMU is the practical implementation of sustainability tools in all sectors, tools that are environmentally friendly and resource-efficient throughout their life cycle to maximize the achievement of economic value, its net contribution to environmental functions and its social equity to build a resilience community. Necessarily, SMU needs to be practiced by implementing cutting-edge metrics and tools to enhance sustainability throughout the world by primarily focusing on these major sectors [1] critical/green infrastructure systems, [2] environmental pollution control, and [3] sustainable building. SMU can be defined as a combined method to implement and manage green performance for planning, designing, and constructing all sectors of the environment, energy, building, infrastructure, and water. This is accomplished by conducting advanced research and applying environmentally friendly technology to build a better environment on Earth.

Sustainable Development for Mass Urbanization
https://doi.org/10.1016/B978-0-12-817690-0.00002-6
© 2019 Elsevier Inc.
All rights reserved.

This book belongs to Kitab Liaison (ocd1996@gmail.com)
Copyright Elsevier 2023

Critical infrastructure system

Water

Urban environments have been impacted by the conventional urban water cycle by the acceleration of evaporation, which creates a cooling effect on urban areas [4, 5]. The main source of water for urban daily usage is either freshwater or groundwater. This supply of freshwater is constantly replenished through precipitation due to the water cycle. However, for the last several decades groundwater strata have been getting lower by nearly 10 m, scaring the groundwater finite level in the near future [6, 7]. Rising urbanization contaminates freshwater supplies, thereby triggering adverse environmental impacts that eventually scare living beings in an urban area due to the potential shortage of water in the near future. Because water has distinctive features that are important for the proliferation of life to respond in ways that eventually permit replication, it is very important to all living organisms. Water is essential to all living beings for their survival because it has many distinct properties that are critical for the proliferation of life to react in ways that ultimately allow replication. It is, therefore, vital both as a solvent in which many of the body's solutes dissolve and as an essential part of many metabolic (catabolism and anabolism) processes within the living body [5, 8]. In catabolism, water is utilized to break the bonds within large molecules to create smaller molecules, and in anabolism, water is detached from molecules to create larger molecules. These processes of anabolism and catabolism cannot exist without water [9, 10]. In urban forestry, water is the fundamental element for photosynthesis and respiration, where photosynthetic cells use the sun's energy to split off water's hydrogen from oxygen. Afterward, hydrogen is mixed with carbon dioxide (absorbed from the air or water) to form glucose for use as food, and the oxygen is released to balance the ecosystem.

Within the urban economy, water naturally plays a significant role, with almost 70% of the freshwater used by humans going to the agricultural sector, which has a larger contribution to the global economy [11, 12]. For many areas of the planet, fishing in both freshwater and saltwater is a key food source and an important part of the globe's economy that is referred to as the Blue and Brown Economy. In homes and industries, huge amounts of steam, ice, and water are utilized for heating and cooling. For an extensive variety of chemical substances, water is a tremendous solvent, and as result, it is extensively utilized in washing, cooking, and industrial processes.

This book belongs to Kitab Liaison (ocd1996@gmail.com) Copyright Elsevier 2023

Simply, this natural resource is becoming scarcer in urban areas where certain megacities are in a venerable condition such as Mumbai and New Delhi in India. In the developing world, 90% of all urban wastewater still goes untreated into local rivers and streams, which can cause dangerous water environments. In developed countries, the usage of conventional treatment processes causes severe environmental pollution [6, 13]. The strain not only affects surface freshwater bodies such as rivers and lakes, but it also degrades groundwater resources. Currently, about a billion people around the world routinely drink unhealthy water in urban areas, resulting in an estimated five million deaths each year.

Thus, advanced research and development of water resource must need the application of sustainability practice by conducting emerging distributed systems for water supply and water and waste treatment in urban area. Consequently, much more scientifically and technologically advanced research and development must be applied in regard to environmentally friendly (a) physical and chemical treatment processes for water and wastewater, (b) environmental biotechnology for use in water resource management and bioremediation, and to turn wastewater into a useful product, (c) watershed and wetland management to reduce water loss, (d) advanced environmental engineering designs to mitigate groundwater, and (e) sustainable water resource development as a new source of water for urban areas.

Power

The urban atmosphere is now approaching seriously dangerous levels because of the increase of all aspects of the carbon cycle into the atmosphere. This has become a major crisis for sustainable urbanization due to the conventional energy usages [9, 14]. Air toxicity that includes volatile organic compounds, sulfur oxide, and nitrogen oxide as well as airborne pollutants that generate acid rain, photochemical smog, air pollution, and deadly chlorofluorocarbons are having severe effects on the urban atmosphere and environment [15, 16]. Therefore, sustainable energy is an urgent demand to serve the needs of the present without compromising the ability of future generations to meet their needs for sustainable urbanization. Whereas renewable energy refers to energy that is naturally refilled on a human's time scale, sustainable energy is the energy whose usage will not jeopardize the system where it is implemented to the point of exhaustion. Technologies promoting sustainable energy include renewable energy sources such as

This book belongs to Kitab Liaison (ocd1996@gmail.com) Copyright Elsevier 2023

hydroelectricity, solar energy, wind energy, wave power, geothermal energy, bioenergy, and tidal power must be applied as the sustainable technologies to overcome the environmental vulnerability.

The advancement of new technology needs to be carried out in an energy transition from fossil fuels to environmentally sustainable energy systems and, finally, to the point where 100% renewable energy is applied. Therefore, changes that need to be made in today's conventional energy consumption will not only be how energy is supplied, but also how it is used. It is important to reduce the volume of energy needed to deliver different goods and/or services. Stabilizing and decreasing CO_2 emissions requires that energy efficiency and renewable energy remain the twin pillars of environmental sustainability. Based on the current historical examination, the growth rate in energy demand has generally overtaken the enhancement rate in energy efficiency [11, 17, 18]. This is because of the ongoing population and economic growth. Consequently, the aggregate use of energy and correlated emissions of carbon have constantly increased, which ultimately causes deadly climate change in urban areas. In consequence, supplies of renewable and sustainable (clean) energy are an exigent demand to alleviate the urban energy demand and mitigate the urban climate change crisis. Therefore, clean and renewable energy (and energy efficiency) are no longer niche sectors that are promoted only by scientists. They must be promoted by urban authorities by increasing the levels of investment in new technologies for confirming a clean and green urban area. Much focus must be directed toward renewable power system planning, design, and building, and sustainable application of energy within all infrastructure sectors and buildings in urban areas to approve sustainable energy system construction and design, and control to secure a sustainable urban system.

Infrastructure and transportation

Conventional infrastructure is not only causing trillions of dollars every year mainly in urban areas, it also plays a vital role in the loss of land and creates adverse environmental and climate perplexity [6, 19]. As sustainable urban infrastructure is a network providing the ingredients for solving urban infrastructure challenges by building with nature, thus it would be the best option to secure a resilient community. The main components of this approach are roads, highways, bridges, tunnel management to achieve climate adaptation, less heat stress, more biodiversity, food production, better air quality, sustainable energy production, clean water and healthy soils, as well as the more anthropocentric functions such as increased quality of life through recreation

This book belongs to Kitab Liaison (ocd1996@gmail.com) Copyright Elsevier 2023

and providing shade and shelter in and around urban area [20–22]. Subsequently, sustainable infrastructure serves to provide an ecological framework for the social, economic, and environmental health of the surroundings. Thus, sustainable urban infrastructure must be considered as the best engineering practice that would achieve more holistic roads, highways, bridges, tunnels, and management.

On the other hand, traditional transport systems in urban areas have significant impacts on the environment, accounting for nearly 28% of conventional world urban energy consumption. It also is causing proportionally climate change and adverse environmental impact [23–25]. Sustainable transportation refers to the broad subject of transport that should be environmentally benign in the senses of social, environmental, and climate impacts and the ability to indefinitely mitigate environmental pollution. Components for evaluating sustainable urban transport include advanced vehicle technology to be used for road, water, or air transport by using renewable and clean were the infrastructure should be able to accommodate the clean fuel operated transport for roads, railways, airways, waterways, canals and terminals pathways to mitigate energy and traffic jam crisis. Sustainable urban transport systems will make a positive contribution to the environmental, social, and economic sustainability of communities by binding social and economic connections where people can quickly benefit from this sustainable mobility such as zero emission vehicles and flying transportation technology. The promotion of incremental improvements in zero emission fuel vehicles as well as clean and renewable flying transportation vehicles through migration from fossil-based transportation systems would be the best option to measure sustainability and optimization for the development of a resilient urban system.

Therefore, a sustainable urban infrastructure system and advanced transportation vehicles are urgently needed to have better, safer, and faster mobility and less environmental impact compared to traditional infrastructure and conventional vehicles. Therefore, the main research and development efforts must be focused on providing sustainable urban infrastructure development, advanced zero emissions, and advanced technology for flying vehicles to build a cleaner and greener urban development.

Environmental pollution control

Urban environmental pollution is the undesired spread of toxic chemicals into the aquatic and terrestrial habitats. There are many different types of pollution, usually named for the location that has become polluted. The

This book belongs to Kitab Liaison (ocd1996@gmail.com) Copyright Elsevier 2023

burning of coal and wood made the cities the primary sources of pollution. The Industrial Revolution brought an infusion of untreated chemicals and wastes into local streams that served as the water supply. It was the Industrial Revolution that gave birth to environmental pollution as we know it today. Therefore, it is urgent that we control urban environmental pollution in order to develop sustainable mass urbanization. Urban sustainability, within the environmental sector, means that the biological systems must remain productive and diverse for an indefinite period of time. One example of biological systems considered sustainable is a long-lived and healthy ecosystem in an urban system. Generally, urban sustainability can be defined as the durability of processes and systems, including the interrelated domains of culture and politics, economics, and ecology to acquire healthy environments that will support the survival of humans and other creatures [26, 27]. Consequently, in preserving urban environmental resources, sustainability encounters social challenges that involve ethical consumerism, individual and local lifestyles, urban transportation and planning, and national and international laws. Simply environmental pollution for mass urban development must be adopted as the holistic method to acquire a greener and cleaner urban system, by commitment of policymakers, investors, engineers, architects, scientists and authorities to administer and control all environmental pollution to secure a securing resilience urban system [28, 29].

Thus, urban environmental resiliency and sustainability shall be measured by occurrences or junctures where naturally befalling regenerative forces such as biomass, vegetation, atmosphere, soil, water, and solar energy are intermingled with their underlying forces in the environment. Human activities are the major drivers for the destruction of the Earth's systems as well as its biophysical mechanisms [2, 10, 30]. Therefore, the impact of a community on the environment is instigated by a single person or the available population, and this in turn relies on complex ways on exactly what natural resources are being utilized, whether those natural resources are renewable, as well as the human activity scale in comparison to the ecosystems' carrying capacity. Accordingly, the resource consumption pattern within all sectors is generating an adverse effect on biodiversity, conservation biology, and environmental science. Unfortunately, the urban biodiversity loss within the environment, mainly from habitat fragmentation and the loss generated by human land appropriation for agriculture, forestry, and development, as natural capital is rapidly changed all over the globe [3, 31]. As a result, this change in mass urbanization will play a major part in the changes in the urban biosphere in relative magnitudes of urban

This book belongs to Kitab Liaison (ocd1996@gmail.com) Copyright Elsevier 2023

development [3, 14, 32]. To control urban resource consumption, resource productivity, and resource intensity, it is necessary to investigate the pattern of consumption that is associated with urban resources to the economic, social, and environmental effects at the context or scale in order to secure a resilient urbanization.

Sustainable building

Almost all urban buildings have been identified as consumers of very large portions of natural resources, including water and energy. In the present day, the buildings are responsible for 40% of urban CO_2 emissions, which is equal to nine billion carbon dioxide tons yearly. By 2050, these emissions are likely to double [33–35]. It is essential for one to think through the clean building to attain an ecologically friendly building and energy efficiency, which eventually will combine a massive collection of skills, approaches, and practices to cut and finally eliminate the adverse environment impacts. Sustainable building for mass urbanization refers to both a structure and processes that are environmentally responsible and resource-efficient throughout a building's lifecycle from planning to design, construction, operation, maintenance, renovation, and demolition. This requires close cooperation among the contractor, architects, engineers, and client over the entire project lifecycle to achieve the benefits of economy, durability, and comfort. So, sustainable building development has several drives, including social, economic, and environmental benefits. As such, the initiatives of sustainability require a synergistic and incorporated design in both the retrofitting of existing buildings and new construction to support the environment and energy. Considering energy efficiency, toxic waste reduction, maintenance and operations optimization, interior environmental quality improvement, material efficiency, design efficiency, and water efficiency, the technologies or practices applied in sustainable building essentially requires focus so as to generate a larger massed impact.

Making the most of the renewable resources is frequently stressed in sustainable urban buildings. Examples may include utilizing sunlight via photovoltaic equipment, active solar, passive solar, and utilizing trees and planets via rainwater run-off reduction as well as rain gardens and green roofs [36, 37]. In addition, utilizing low-effect construction materials and using permeable concrete or packed gravel rather than asphalt or conventional concrete to improve groundwater replenishment are other approaches that are being used [13, 38]. Moreover, having an appropriate synergistic design

This book belongs to Kitab Liaison (ocd1996@gmail.com) Copyright Elsevier 2023

in place may enable individual green building technologies to join forces to generate increased impact. Clean design or green architecture on the artistic side is the philosophy of planning a construction that is in line with resources near the site and natural features. Designing a clean building involves many key steps: identifying green materials of the building from indigenous sources, reducing loads, optimizing systems, and finally producing onsite renewable energy.

Consequently, it is necessary for all buildings in an urban area to have dynamic clean research and practice for the mass development of urbanization at stages. Essentially, emphasis should be directed to the assessments of project lifecycle, solicitation, preconstruction, design development, project planning, project ecology, site selection, methods and application of construction materials, and proper maintenance to ultimately confirm a sustainable building for all levels of the urban community.

Conclusion

The United Nations Environment Program (UNEP) estimates that each year, 2.4 million people die from environmental pollution, nearly 5 million people die because of urban water pollution, and nearly 10 million people die due to other human-caused environmental factors. The most dangerous and hazardous for health are the emissions of black carbon from urban industrialization, a component of particulate matter that is a known cause of respiratory and carcinogenic diseases as well as being the main contributor to global climate change. Currently, the atmospheric CO_2 is 400 ppm on average for all megacities in the world, and it is increasing at the rate of 2.11% yearly, which running to reach the toxic level of CO_2 concentration of CO_2 into the air of 60,000 ppm when all living being will die in 30 s. If the current level of CO_2 emissions is not stopped, all human races in megacities will be extinct $[\int_{400^{(2.11\%)}}^{60,000}(2017)]$ in 121,017,712 years and thus, it would be the end of human civilization in megacities. Sustainable science and technology implementation is an urgent need in all sectors of the environment, energy, building, infrastructure, transportation, and water for the survival of all living beings in megacities.

Acknowledgments

This research was supported by Green Globe Technology under grant RD-02018-03. Any findings, conclusions, and recommendations expressed in this paper are solely those of the author and do not necessarily reflect those of Green Globe Technology.

This book belongs to Kitab Liaison (ocd1996@gmail.com) Copyright Elsevier 2023

References

[1] N. Arnell, et al., in: R.T. Watson, M.C. Zinyowera, R.H. Moss (Eds.), Climate Change 1995: Impacts, Adaptations, and Mitigation of Climate Change, Cambridge University Press, London, 1996, pp. 325–363.

[2] A.P. Ballantyne, C.B. Alden, J.B. Miller, P.P. Tans, J.W.C. White, Increase in observed net carbon dioxide uptake by land and oceans during the past 50 years, Nature 488 (2012) 70–72.

[3] J.E. Bauer, et al., The changing carbon cycle of the coastal ocean, Nature 504 (2013) 61–70.

[4] R.A. Betts, C.D. Jones, J.R. Knight, R.F. Keeling, J.J. Kennedy, El Nino and a record CO2 rise, Nat. Clim. Chang. 6 (2016) 806–810.

[5] Z. Liu, et al., Reduced carbon emission estimates from fossil fuel combustion and cement production in China, Nature 524 (2015) 335–338.

[6] M.F. Hossain, Application of advanced technology to build a vibrant environment on planet mars, Int. J. Environ. Sci. Technol. 14 (12) (2017) 2709–2720.

[7] Parazoo, et al., Contrasting carbon cycle responses of the tropical continents to the 2015–2016 El Niño, Science 7 (2017) 533–536.

[8] P. Borrelli, D.A. Robinson, L.R. Fleischer, E. Lugato, et al., An assessment of the global impact of 21st century land use change on soil erosion, Nat. Commun. 9 (2017) 38–42.

[9] P. Ciais, C. Sabine, Chapter 6: carbon and other biogeochemical cycles, in: T. Stocker, D. Qin, G.K. Platner (Eds.), Climate Change 2013: The Physical Science Basis, Cambridge University Press, London, 2013.

[10] K.L. Denman, et al., Couplings Between Changes in the Climate System and Biogeochemistry, Cambridge University Press, London, 2007.

[11] J. Fairhead, M. Leach, Misreading the African Landscape: Society and Ecology in a Forest-Savanna Mosaic, Cambridge University Press, Cambridge, 1996.

[12] J. Mason Earles, S. Yeh, K.E. Skog, Timing of carbon emissions from global forest clearance, Nat. Clim. Chang. 2 (2012) 682–685.

[13] S.J. Scherr, Meeting household needs: farmer tree-growing strategies in Western Kenya, in: J.E.M. Arnold, P.A. Dewees (Eds.), Tree Management in Farmer Strategies, Oxford University Press, Oxford, 1995.

[14] J.G. Canadell, et al., Contributions to accelerating atmospheric CO2 growth from economic activity, carbon intensity, and efficiency of natural sinks, Proc. Natl. Acad. Sci. USA 104 (2007) 18866–18870.

[15] S.L. Postel, G.C. Daily, P.R. Ehrlich, Human appropriation of renewable fresh water, Science 271 (1996) 785.

[16] G.R. van der Werf, et al., Climate regulation of fire emissions and deforestation in equatorial Asia, Proc. Natl. Acad. Sci. USA 105 (2008) 20350–20355.

[17] M.F. Hossain, Green science: independent building technology to mitigate energy, environment, and climate change, Renew. Sust. Energ. Rev. 73 (2017) 695–705.

[18] M.F. Hossain, Design and construction of ultra-relativistic collision PV panel and its application into building sector to mitigate total energy demand, J. Build. Eng. 9 (2017) 147–154.

[19] M.F. Hossain, H. Mukai, Importance of nutrients (N, P, and NO3 + NO2) in growth of the surfgrass, Phyllospadix iwatensis Makino, Benthos Res. 55 (2000) 23–35.

[20] M.F. Hossain, Production of clean energy from cyanobacterial biochemical products, Strat. Plann. Energ. Environ. 3 (2016) 6–23.

[21] M.F. Hossain, Theoretical modeling for hybrid renewable energy: an initiative to meet the global power, J. Sustain. Energy Eng. 4 (2016) 5–36.

[22] B.B. Stephens, et al., Weak northern and strong tropical land carbon uptake from vertical profiles of atmospheric CO2 science, Science 316 (2007) 1732.

This book belongs to Kitab Liaison (ocd1996@gmail.com) Copyright Elsevier 2023

[23] M.F. Hossain, In situ geothermal energy technology: an approach for building cleaner and greener environment, J. Ecol. Eng. 77 (2016) 49–55.
[24] M.F. Hossain, Theory of global cooling, Energy Sustain. Soc. 6 (2016) 24.
[25] S. Schwietzke, et al., Upward revision of global fossil fuel methane emissions based on isotope database, Nature 538 (2016) 88–91.
[26] E. Garcia-Robledo, C.C. Padilla, M. Aldunate, F.J. Stewart, O. Ulloa, A. Paulmier, G. Gregori, N.P. Revsbech, Cryptic oxygen cycling in anoxic marine zones, PNAS 114 (31) (2017) 8319–8324.
[27] M.F. Hossain, Invisible transportation infrastructure technology to mitigate energy and environment, Energy Sustain. Soc. 7 (2017) 27.
[28] W. Li, et al., Reducing uncertainties in decadal variability of the global carbon budget with multiple datasets, Proc. Natl. Acad. Sci. USA 113 (2016) 13104–13108.
[29] G. Pickup, G.N. Bastin, V.H. Chewings, Identifying trends in land degradation in non-equilibrium rangelands, J. Appl. Ecol. 35 (1998) 365–377.
[30] R.A. Duce, et al., Impacts of atmospheric anthropogenic nitrogen on the open ocean, Science 320 (2008) 893–897.
[31] K.-H. Erb, et al., Bias in the attribution of forest carbon sinks, Nat. Clim. Chang. 3 (2013) 854–856.
[32] S.J. Davis, K. Caldeira, Consumption-based accounting of CO2 emissions, Proc. Natl. Acad. Sci. USA 107 (2010) 5687–5692.
[33] H. Bao, J. Niggemann, L. Luo, T. Dittmar, S.-J. Kao, Aerosols as a source of dissolved black carbon to the ocean, Nat. Commun. (2017).
[34] M.F. Hossain, Green science: advanced building design technology to mitigate energy and environment, Renew. Sustain. Energy Rev. 81 (2) (2018) 3051–3060.
[35] M.F. Hossain, N. Fara, Integration of wind into running vehicles to meet its total energy demand, Energy Ecol. Environ. 2 (1) (2017) 35–48.
[36] M.F. Hossain, Green science: decoding dark photon structure to produce clean energy. Energy Rep. (2018)https://doi.org/10.1016/j.egyr.2018.01.001.
[37] D. Liverman, E.F. Moran, R.R. Rindfuss, P.C. Stern (Eds.), People and Pixels: Linking Remote Sensing and Social Science, National Academy Press, Washington, DC, 1998.
[38] J. Prietzel, L. Zimmermann, A. Schubert, D. Christophel, Organic matter losses in German Alps forest soils because the 1970s most likely caused by warming, Nat. Geosci. 9 (2016) 543–548.

This book belongs to Kitab Liaison (ocd1996@gmail.com) Copyright Elsevier 2023

CHAPTER 3

Water delivery systems

Introduction

Water is a vital element in our daily lives to run our domestic, industrial, and recreational operations smoothly in urban areas. The tradition water supply from a water reservoir and filtration systems is indeed technologically correct. However, the groundwater level has been getting shorter for the past several decades, which threatens all living beings (8, 12, 23). In this chapter, a detailed strategic investigation of natural water resources is discussed, along with the application of advanced research and technology to conserve and/or recycle water naturally. Thus, a detailed water-capture technology has been proposed to practice sustainable methods of static electricity technology to catch the urban cloud to meet domestic water requirements.

We propose installing a plastic tank that creates static electricity at all houses and buildings to trap the urban cloud by static electricity. Because water has positive and negative charges and the electrons that ended up on the static electrical force have a positive charge, while water molecules have a negative charge on one side, the positive charge of static electric force and negative charges of cloud pull each other closer together, the positive side tug the direction and force the water come down to collect the water in a tank and be treated in site to meet the daily water demand for a modern urban system.

Material, methods, and simulation

Static electric force generation

To capture the urban cloud from the air, a model been proposed to create the *Hossain Static Electric Force (HSEF=ƒ)* by implementing the friction of an insulator into the plastic tank to pull down the urban cloud into the tank [1, 2]. To create the *HSEF* in the plastic tank, I have implemented abelian local symmetry calculations by using MATLAB software, considering the gauge field symmetry and the Goldstone scalar with respect to the longitudinal mode of the vector [3, 4]. Thus, each spontaneously broken particle T^{α} of the local symmetry will correspond to the gauge field of $A_{\mu}^{\alpha}(x)$ where

Sustainable Development for Mass Urbanization
https://doi.org/10.1016/B978-0-12-817690-0.00003-8
© 2019 Elsevier Inc.
All rights reserved.

This book belongs to Kitab Liaison (ocd1996@gmail.com)
Copyright Elsevier 2023

HSEF will start to work at a local U (1) phase symmetry [5, 6]. Therefore, the model will be comprised as a complex scalar field Φ (x) of static electric charge q coupled to the EM field $A^{\mu}(x)$, which is expressed by $\mathcal{L}$:

$$\mathcal{L} = -\frac{1}{4} F_{\mu\nu}F^{\mu\nu} + D_{\mu}\Phi^{*} D^{\mu}\Phi - V(\Phi^{*}\Phi) \tag{3.1}$$

where

$$\begin{aligned} D_{\mu}\Phi(x) &= \partial_{\mu}\Phi(x) + iqA_{\mu}(x)\Phi(x) \\ D_{\mu}\Phi^{*}(x) &= \partial_{\mu}\Phi^{*}(x) - iqA_{\mu}(x)\Phi^{*}(x) \end{aligned} \tag{3.2}$$

And

$$V(\Phi^{*}\Phi) = \frac{\lambda}{2}(\Phi^{*}\Phi)^{2} + m^{2}(\Phi^{*}\Phi) \tag{3.3}$$

Suppose $\lambda > 0$ but $m^{2} < 0$, so that $\Phi = 0$ is a local maximum of the scalar potential while the minima form a degenerate circle $\Phi = \frac{v}{\sqrt{2}} * e^{i\theta}$,

$$v = \sqrt{\frac{-2m^{2}}{\lambda}}, \text{any real}\,\theta \tag{3.4}$$

Consequently, the scalar field Φ develops a nonzero vacuum expectation value $\langle\Phi\rangle \neq 0$, which spontaneously creates the U (1) symmetry of the static electric field. The breakdown would lead to a massless Goldstone scalar stemming from the phase of the complex field Φ (x). But the local U (1) symmetry, the phase of Φ (x)—not just the phase of the expectation value $\langle\Phi\rangle$ but the x-dependent phase of the dynamical Φ (x) field. To analyze this static electricity force mechanism, I have used polar coordinates in the scalar field space, thus

$$\Phi(x) = \frac{1}{\sqrt{2}} \Phi_{r}(x) * e^{i\Theta(x)}, \text{real}\,\Phi_{r}(x) > 0, \text{real}\,\Phi(x) \tag{3.5}$$

This field redefinition is singular when Φ $(x) = 0$, so I never used it for theories with $\langle\Phi\rangle \neq 0$, but it's alright for spontaneously broken theories where I can expect $\Phi\langle x\rangle \neq 0$ almost everywhere. In terms of the real fields $\phi_{r}(x)$ and $\Theta(x)$, the scalar potential depends only on the radial field ϕ_{r},

$$V(\phi) = \frac{\lambda}{8}\left(\phi_{r}^{2} - v^{2}\right)^{2} + \text{const} \tag{3.6}$$

or in terms of the radial field shifted by its VEV, $\Phi_{r}(x) = v + \sigma(x)$,

$$\phi_{r}^{2} - v^{2} = (v + \sigma)^{2} - v^{2} = 2v\sigma + \sigma^{2} \tag{3.7}$$

This book belongs to Kitab Liaison (ocd1996@gmail.com) Copyright Elsevier 2023

$$V = \frac{\lambda}{8}\left(2v\sigma - \sigma^2\right)^2 = \frac{\lambda v^2}{2} * \sigma^2 + \frac{\lambda v}{2} * \sigma^3 + \frac{\lambda}{8} * \sigma^4 \tag{3.8}$$

At the same time, the covariant derivative $D_\mu \phi$ becomes

$$D_\mu \phi = \frac{1}{\sqrt{2}}\left(\partial_\mu\left(\phi_r e^{i\Theta}\right) + iqA_\mu * \phi_r e^{i\Theta}\right) = \frac{e^{i\Theta}}{\sqrt{2}}\left(\partial_\mu \phi_r + \phi_r * i\partial_\mu \Theta + \phi_r * iqA_\mu\right) \tag{3.9}$$

$$\begin{aligned} \left|D_\mu \phi\right|^2 &= \frac{1}{2}\left|\partial_\mu \phi_r + \phi_r * i\partial_\mu \Theta + \phi_r * iqA_\mu\right|^2 \\ &= \frac{1}{2}\left(\partial_\mu \phi_r\right) + \frac{\phi_r^2}{2} * \left(\partial_\mu \Theta qA_\mu\right)^2 \\ &= \frac{1}{2}\left(\partial_\mu \sigma\right)^2 + \frac{(v+\sigma)^2}{2} * \left(\partial_\mu \Theta + qA_\mu\right)^2 \end{aligned} \tag{3.10}$$

Altogether,

$$\mathcal{L} = \frac{1}{2}\left(\partial_\mu \sigma\right)^2 - v(\sigma) - \frac{1}{4} F_{\mu\nu} F^{\mu\nu} + \frac{(v+\sigma)^2}{2} * \left(\partial_\mu \Theta + qA_\mu\right)^2 \tag{3.11}$$

To confirm the creation of this static electric force ($\mathcal{L}_{\text{sef}}$) into the static electric field properties of this *HSEF*, it has been expanded in powers of the fields (and their derivatives) and focuses on the quadratic part describing the free particles,

$$\mathcal{L}_{\text{sef}} = \frac{1}{2}\left(\partial_\mu \sigma\right)^2 - \frac{\lambda v^2}{2} * \sigma^2 - \frac{1}{4} F_{\mu\nu} F^{\mu\nu} + \frac{v^2}{2} * \left(qA_\mu + \partial_\mu \Theta\right)^2 \tag{3.12}$$

Here this *HSEF* ($\mathcal{L}_{\text{free}}$) function obviously will suggest a real scalar particle of positive mass$^2 = \lambda v^2$ involving the $A_\mu(x)$ and $\Theta(x)$ fields to initiate to create a tremendous static electricity force within the electric field of the plastic tank (Fig. 3.1).

In site water treatment

Because the collected water in the plastic tank is just nothing but the liquid form of the urban cloud, thus it will not require any sedimentation, coagulation, or chlorination to clean the water. Only mixing physics (UV application) and filtration will be required to treat the water to meet the US National Primary Drinking Water Standard code [7]. It is the simplest way to treat water by using the *SODIS* system (*SOlar DISinfection*), where a transparent container is filled with water and exposed to full sunlight for several hours. As soon as the water temperature reaches 50°C with a UV

This book belongs to Kitab Liaison (ocd1996@gmail.com) Copyright Elsevier 2023

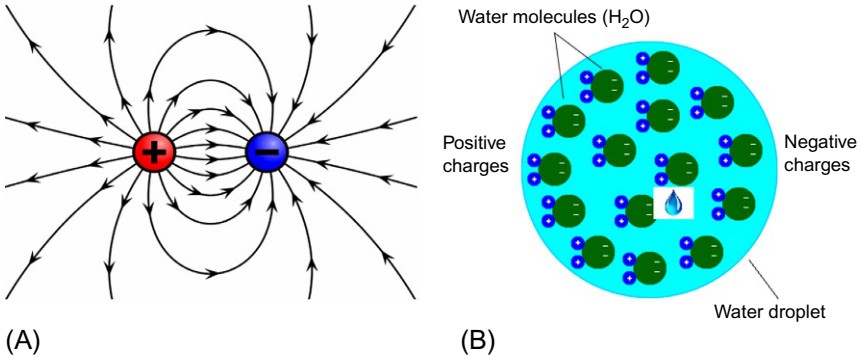

Fig. 3.1 (A) The creation of static electricity force, and (B) its mechanism of conversion of static energy into an electromotive force of positive and negative charges that mobilizes the "static" electricity to tug down the water molecules.

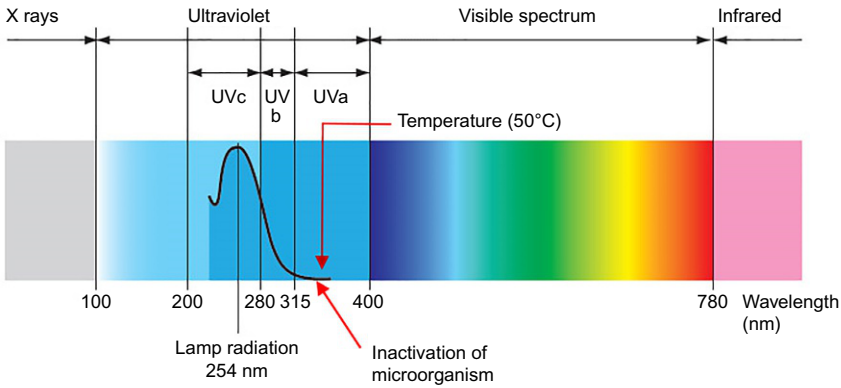

Fig. 3.2 The photo physics radiation application for the purification of water, which shows that once UV radiation of 320 nm is applied to the water, it stars to disinfect all microorganisms immediately once the temperature reaches 50°C.

radiation of 320 nm, the inactivation process will be accelerated in order to lead to complete microbiological disinfection immediately and the treated water shall be used to meet the total domestic water demand (Fig. 3.2).

Results and discussion

Electrostatic force analysis

To mathematically determine the electric static force proliferation around the plastic tank to confirm the water being tugged down at each urban house and building, I have initially solved the dynamic photon proliferation by

This book belongs to Kitab Liaison (ocd1996@gmail.com) Copyright Elsevier 2023

integrating the *HSEF* electric field to create the local U (1) gauge invariant did allow to add a mass-term for the gauge particle under $\varnothing' \rightarrow e^{i\alpha(x)}\varnothing$ to. In detail, it can be explained by a covariant derivative with a special transformation rule for the scalar field expressing by [8, 9]:

$$\partial_\mu \rightarrow D_\mu = \partial_\mu = ieA_\mu \quad [\text{covariant derivatives}]$$

$$A'_\mu = A_\mu + \frac{1}{e}\partial_\mu \alpha \quad [\text{derivatives}] \tag{3.13}$$

Where the local U (1) gauge invariant *HSEF* for a complex scalar field is given by

$$\mathcal{H} = (D^\mu)^\dagger \left(D_\mu \varnothing\right) - \frac{1}{4} F_{\mu\nu}F^{\mu\nu} - V(\varnothing) \tag{3.14}$$

The term $\frac{1}{4} F_{\mu\nu}F^{\mu\nu}$ is the kinetic term for the gauge field (heating photon) and $V(\varnothing)$ is the extra term in the *HSEF* that be: $V(\varnothing^*\varnothing) = \mu^2(\varnothing^*\varnothing) + \lambda(\varnothing^*\varnothing)^2$.

Therefore, the *HSEF* ($\mathcal{H}$) under perturbations into the quantum field has initiated with the massive scalar particles $\phi_1$and ϕ_2 along with a mass μ. In this condition, $\mu^2 < 0$ had an infinite number of quantum, each has been satisfied by $\phi_1^2 + \phi_2^2 = -\mu^2/\lambda = v^2$ and the $\mathcal{H}$ through the covariant derivatives using again the shifted fields η *and* ξ defined the quantum field as $\phi_0 = \frac{1}{\sqrt{2}}\left[(v+\eta) + i\xi\right]$.

$$\begin{aligned} \text{Kinetic term}: \mathcal{H}(\eta, \xi) &= (D^\mu\phi)^\dagger (D^\mu\phi) \\ &= (\partial^\mu + ieA^\mu)\phi^* \left(\partial_\mu - ieA_\mu\right)\phi \end{aligned} \tag{3.15}$$

Thus, this expanding term in the $\mathcal{H}$ associated with the scalar field is suggesting that the *HSEF* electric field is prepared to initiate the proliferation of the static electricity force into its quantum field to tug down the water [10, 11].

To confirm this tug down by the static electricity force, I have implemented the calculation of $\overline{\varphi}[s_0]$ for the confirmation of the expected value of s_0 for capturing water vapor [12, 13]. Thus, the corrective functional asymptotic formulas are being used as follows:

$$\begin{aligned} \overline{\varphi}[s_0] = 2s_0(\ \ln 4s_0 - 2) + \ \ln 4s_0(\ \ln 4s_0 - 2) \\ - \frac{(\pi^2 - 9)}{3} + s_0^{-1}\left(\ \ln 4s_0 + \frac{9}{8}\right) + \cdots (s_0 \gg 1) \end{aligned} \tag{3.16}$$

This book belongs to Kitab Liaison (ocd1996@gmail.com) Copyright Elsevier 2023

$$\overline{\varphi}[s_0] = \left(\frac{2}{3}\right)(S_0 - 1)^{\frac{3}{2}} + \left(\frac{5}{3}\right)(S_0 - 1)^{\frac{5}{2}} - \left(\frac{1507}{420}\right)(S_0 - 1)^{\frac{7}{2}} + \cdots (s_0 - 1 \ll 1) \tag{3.17}$$

The function $\frac{\overline{\varphi}[s_0]}{(s_0-1)}$ is thus described as $1 < s_0 < 10$ for larger s_0, and it contains a natural logarithmic that is s_0 to confirm the tug down of 100% water vapor by the *HSEF* into the plastic tank.

On average, 100 gallons of water are required per day per person in a standard daily life for a four-person family [11, 14]. Thus, it will require a total of (100_{gallons}/day/person $\times$ 4_{persons} $\times$ 365_{days}) 146,000 gallons of water per year for a family of four. Because a standard 1 m^2 plastic tank can trap 40,000 gallons (151,000 L) per year, thus, the tug down of 100% water vapor by HSEF described above will require only two standard 1 m^2 plastic tanks to satisfy the total water demand for a family of four.

Conclusions

The traditional urban water supply is not only problematic, but also causing serous water losses and environmental vulnerabilities. To mitigate these problems, the urban cloud has been proposed to trap and convert it into clean water to meet the total water demand for a sustainable urban area. Not only is this technology an interesting source of water supply for a modern urban system by using electrostatic force to capture this transpiration water vapor and treating onsite by UV application, but it would indeed be a novel, integrated, and innovative field in science to control urban water and the global warming crisis.

Acknowledgment

This research was supported by Green Globe Technology under grant RD-02017-07 for building a better environment. Any findings, predictions, and conclusions described in this article are solely performed by the authors and it is confirmed that there is no conflict of interest for publishing in a suitable journal.

References

[1] R. Andreas, Strongly correlated photons on a chip, Nat. Photonics 6 (2012) 93–96.
[2] M. Tame, S. McEnery, et al., Quantum plasmonics, Nat. Phys. 9 (2013) 329–340.
[3] S. Douglas, H. Habibian, et al., Quantum many-body models with cold atoms coupled to photonic crystals, Nat. Photonics 9 (2015) 326–331.

This book belongs to Kitab Liaison (ocd1996@gmail.com) Copyright Elsevier 2023

[4] Y. Leijing, W. Sheng, Z. Qingsheng, Z. Zhiyong, P. Tian, L. Yan, Efficient photovoltage multiplication in carbon nanotubes, Nat. Photonics 8 (2011) 672–676.
[5] L. Langer, S. Poltavtsev, M. Bayer, Access to long-term optical memories using photon echoes retrieved from semiconductor spins, Nat. Photonics 8 (2014) 851–857.
[6] T. Pregnolato, E. Lee, J. Song, D. Stobbe, P. Lodahl, Single-photon non-linear optics with a quantum dot in a waveguide, Nat. Commun. 6 (8655) (2015).
[7] M. Hossain, Solar energy integration into advanced building design for meeting energy demand and environment problem, Int. J. Energy Res. 40 (2016) 1293–1300.
[8] W. Yuwen, Z. Yongyou, Z. Qingyun, Z. Bingsuo, S. Udo, Dynamics of single photon transport in a one-dimensional waveguide two-point coupled with a Jaynes-Cummings system, Sci. Rep. 6 (2016) 33867.
[9] Q. Li, D. Xu, Recoil effects of a motional scatterer on single-photon scattering in one dimension, Sci. Rep. 8 (2013) 3144.
[10] W. Yan, F. Heng, Single-photon quantum router with multiple output ports, Sci. Rep. 4 (2014) 4820.
[11] F. Hossain, Theory of global cooling, Energy Sustain. Soc. 7 (2016) 6–24.
[12] W. Soto, S. Klein, et al., Improvement and validation of a model for photovoltaic array performance, Sol. Energy 80 (2006) 78–88.
[13] Y. Zhu, H. Xiaoyong, Y. Hong, G. Qihuang, On-chip plasmon-induced transparency based on plasmonic coupled nanocavities, Sci. Rep. 4 (2014) 3752.
[14] T.D. Wheeler, A.D. Stroock, The transpiration of water at negative pressures in a synthetic tree, Nature 455 (2008) 208–212.

This book belongs to Kitab Liaison (ocd1996@gmail.com) Copyright Elsevier 2023

This page intentionally left blank

This book belongs to Kitab Liaison (ocd1996@gmail.com)

Copyright Elsevier 2023

CHAPTER 4

Sanitation and waste disposal systems

Introduction

Global environmental pollution is mostly dependent on the traditional sanitation and waste disposal systems. In fact, these pollutants are having a serious impact on human health and destroying flora and fauna in aquatic environments [1–3]. Due to the development of mass urbanization throughout the world, conventional sanitation and waste disposal systems are increasing rapidly. Therefore, environmental pollution gathering massively on Earth to survive all living being on this planet near future [4, 5]. This environmentally vulnerable condition will continue exponentially until a sustainable sanitation and waste disposal system is developed [6, 7]. It is undoubtedly clear that the sanitation and waste disposal system in modern urban development needs advanced technology to secure a greener, cleaner environment for mass urban development through the deployment of sustainable technology for combatting environmental pollutants. In this paper, thus, a sustainable sanitation and waste disposal system technology has been proposed to recycle urban sanitation and biowaste through the building itself without any outsource connection. Hence, domestic biowaste, including human feces and the wastewater of the building, is to be chosen that can be collected in the solar energy-powered closed detention tank in the cellar. Then, the waste can be separated as (i) wastewater, and (ii) human feces with solid waste into two different chambers. Then, the *methanogenesis* process would be allowed into the closed detention tank to produce bioenergy in context with domestic solid waste and human feces utilization. It is estimated that a person can produce an average of 0.4–0.5 kg/day of feces that can form 0.4 m^3 biogas/day [8, 9]. This amount of biogas (0.4 m^3/day) is good enough to cook three meals for a family of four in a day. On the other hand, treated wastewater *onsite* by applying all primary, secondary, and tertiary processes can be used for gardening and landscaping for a building. Application these sustainable technologies for urban sanitation and waste disposal systems for modern urban development would be an interesting science that is 100% clean and environmentally friendly.

Sustainable Development for Mass Urbanization
https://doi.org/10.1016/B978-0-12-817690-0.00004-X
© 2019 Elsevier Inc.
All rights reserved.

This book belongs to Kitab Liaison (ocd1996@gmail.com)
Copyright Elsevier 2023

Simulation and method

Solar power implemented bioreactor

To implement of solar energy for powering the bioreactor, exterior wall of the curtain wall has been utilized as acting PV panel as a source of self-producing power for the bioreactor. The photovoltaic solar irradiance model that is naturally absorbed by the PV panel is being calculated mathematically, considering the transmission of maximum photon particles into the solar panel [10–12]. It has been necessary to calculate the accuracy of the current-voltage (*I-V*) characteristic parameters by describing the single-diode model of a PV cell circuit [8, 13, 14]. Subsequently, the efficiency of a solar energy conversion rate subject to be raised by the introduced conductive materials into the building walls' exterior skin PV cell. These give it the ability to last for a longer period, among other critical PV panel abilities. Thus, this introduction of the conduction materials aims at creating an advanced PV panel for powering bioreactors to recycle the sanitation and biowaste of urban buildings [15–17]. Hence, the use of the PV array for powering the bioreactor is related to the number of parameters, including transformation rate, voltage proliferation, PVVI curves, and the active solar volt (I_{v+}) that is determined from a single-diode model, as shown in Fig. 4.1.

Another step is the determination of PV current production for the bioreactor through an I_{pv} calculation from a single-model diode, as indicated in Fig. 4.2A, based on the relationship between *I, V,* and *R* in Fig. 4.2B. The photovoltaic array receives the illumination that converts the current from direct current (DC) to alternating current (AC), which is used for voltage current demand for the bioreactor is bring calculated as following equation

$$P_{pv} = \eta_{pvg} A_{pvg} G_t \tag{4.1}$$

where the photovoltaic-generation efficiency is denoted by η_{pvg} while the photovoltaic generator area (m^2) is represented by A_{pvg}. On the other hand, G_t is the titled module plane's (W/m^2) solar radiation. However, η_{pvg} may further be expressed as:

$$\eta_{pvg} = \eta_r \eta_{pc} [1 - \beta (T_c - T_{\text{cref}})] \tag{4.2}$$

where power conditioning efficiency is denoted by η_{pc} (equivalent to 1) upon applying MPPT, whereas β is the temperature coefficient of the bioreactor (0.004–0.006 in every °C). The reference module efficiency is

This book belongs to Kitab Liaison (ocd1996@gmail.com) Copyright Elsevier 2023

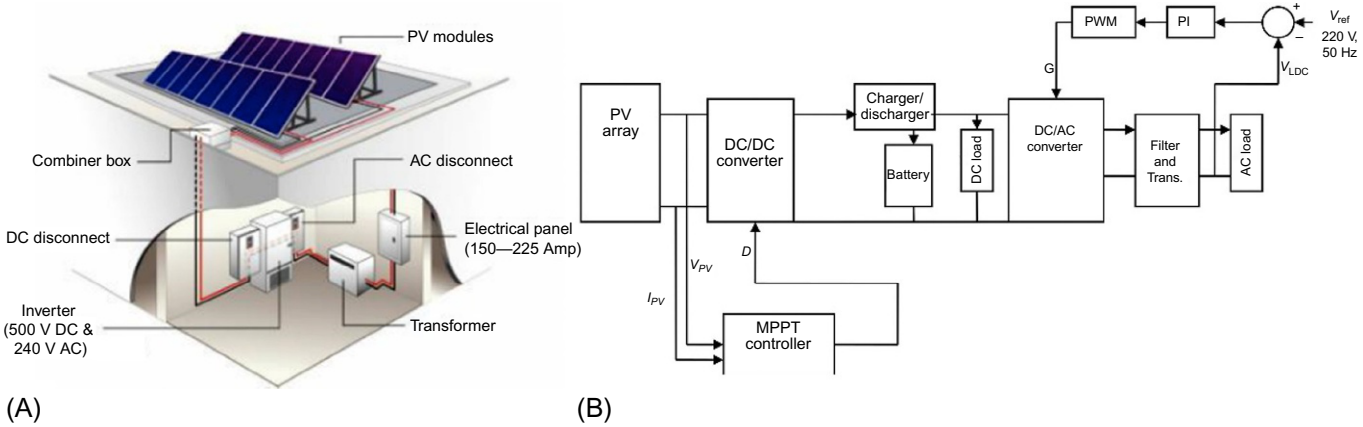

Fig. 4.1 Diagram of PV system model, (A) The module flow chart once photovoltaic solar irradiance is on the PV modules, (B) Simulink block diagram of PV solar array source and the block data of its parameters, respectively.

This book belongs to Kitab Liaison (ocd1996@gmail.com)

Copyright Elsevier 2023

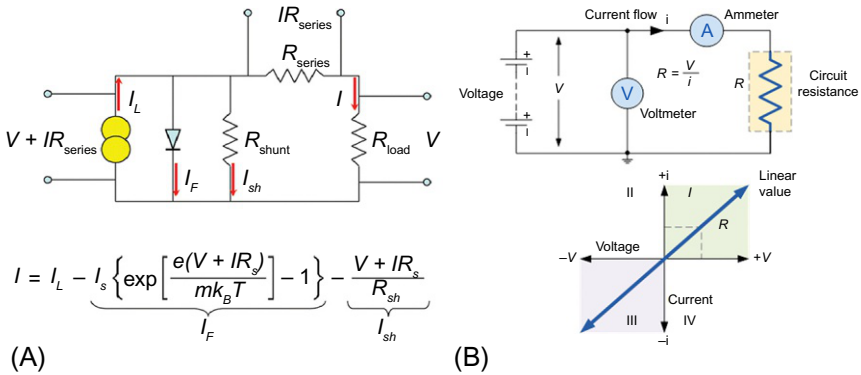

Fig. 4.2 Single-diode circuit of a photovoltaic (PV) cell modeled by MATLAB simulation, (A) the photovoltaic current production, (B) the model with a diode considering the *I-V-R* relationship for the conversion process of DC to AC to power the bioreactor.

represented by η_r while T_{cref} is the temperature of the reference cell (°C), which may be obtained from the following relation:

$$T_c = T_a + \left(\frac{\text{NOCT} - 20}{800}\right) G_t \tag{4.3}$$

From the equation, T_a denotes the ambient temperature (°C) and G_t is the tilted module plane' (W/m^2) solar irradiance. On the other hand, NOCT is the temperature of the standard operating cell (°C). The overall irradiance within the solar cell may be calculated using the following equation, taking into account the diffuse and standard solar irradiance into the bioreactor:

$$I_t = I_b R_b + I_d R_d + (I_b + I_d) R_r \tag{4.4}$$

Electricity is to be produced by the solar cells (P-N junction semiconductor) through the photovoltaic effect, which is interrelated in a parallel-series configuration for the formation of a PV cell [10, 18]. The resulting PV energy efficiency can, however, be integrated into the photovoltaic module for purposes of improvement [12, 19].

The use of a single diode for an N_p parallel-connected to a bioreactor array and the N_s series-connected array cells depends on the relationship between the cell voltage and cell current as:

$$I = N_p \left[I_{ph} - I_{rs} \left[\exp\left(\frac{q(V + IR_s)}{AKTN_s} - 1 \right) \right] \right] \tag{4.5}$$

This book belongs to Kitab Liaison (ocd1996@gmail.com) Copyright Elsevier 2023

where

$$I_{rs} = I_{rr}\left(\frac{T}{T_r}\right)^3 \exp\left[\frac{E_G}{AK}\left(\frac{1}{T_r} - \frac{1}{T}\right)\right] \tag{4.6}$$

T, q, K, and A in Eqs. (4.5), (4.6) denote cell temperature (K), electron charge (1.6×10^{-9} °C), Boltzmann's constant, and the diode idealist factor, respectively. On the other hand, I_{rs}, T_r, E_G, and I_{rr}, represent cell reverse saturation current at temperature (T), cell referred temperature, semiconductor band-gap energy, and reverse saturation current at T_r, respectively. The following equation shows how the radiation and temperature of the cell vary with photo current I_{ph}:

$$I_{ph} = \left[I_{SCR} + k_i(T - T_r)\frac{S}{100}\right] \tag{4.7}$$

where cell short-circuit current at irradiance and reference temperature are denoted by I_{SCR}. On the other hand, S and k_i are the solar irradiance (mW/cm^2) and short-circuit current temperature coefficient, respectively. The I-V PV cell characteristics may be derived through the use of a single-diode model that comprises an additional shunt resistance, which is simultaneous to the model of the optimal shunt diode:

$$I = I_{ph} - I_D \tag{4.8}$$

$$I = I_{ph} - I_0\left[\exp\left(\frac{q(V + R_s I)}{AKT} - 1\right) - \frac{V + R_s I}{R_{sh}}\right] \tag{4.9}$$

where I_{ph}, I_D, I_0, A, q, and K denote the photo current (A), diode current (A), inverse saturation current (A), diode constant, electron charge (1.6×10^{-9} °C), and Boltzmann's constant, respectively. On the other hand, T, R_s, R_{sh}, I, and V represent cell temperature (°C), series resistance (ohm), shunt resistance (ohm), cell current (A), and cell voltage (V), respectively. The photovoltaic cell's output current through the use of a diode model is expressed as the total power supply for a bioreactor:

$$I = I_{PV} - I_{D1} - I_{D2} - \left(\frac{V + IR_s}{R_{sh}}\right) \tag{4.10}$$

From Eq. (4.10):

$$I_{D1} = I_{01}\left[\exp\left(\frac{V + IR_s}{a_1 V_{T1}}\right) - 1\right] \tag{4.11}$$

This book belongs to Kitab Liaison (ocd1996@gmail.com)
Copyright Elsevier 2023

$$I_{D2} = I_{02}\left[\exp\left(\frac{V + IR_s}{a_2 V_{T2}}\right) - 1\right] \tag{4.12}$$

From Eqs. (4.11), (4.12), diodes 1 and 2 reverse saturation currents are also denoted by I_{01} and I_{02}, respectively, while the respective diodes' thermal voltages are represented by V_{T1} and V_{T2} into the bioreactor to supply the power during the advised condition such as cloudy sunlight. Therefore, integrating a_1 and a_2 are the most ideal constants of the diode to simply equations as follows to in order to get energy for the bioreactor steadily and continuously throughout the year:

$$v_{oc} = \frac{V_{oc}}{cK\,T/q} \tag{4.13}$$

$$P_{\max} = \frac{\dfrac{V_{oc}}{cK\,T/q} - \ln\left(\dfrac{V_{oc}}{cK\,T/q} + 0.72\right)}{\left(1 + \dfrac{V_{oc}}{nK\,T/q}\right)}\left(1 - \frac{V_{oc}}{\dfrac{V_{oc}}{I_{SC}}}\right)\left(\frac{V_{oc0}}{1 + \beta \ln \dfrac{G_0}{G}}\right)\left(\frac{T_o}{T}\right)^{\gamma} I_{sc0}\left(\frac{G}{G_o}\right)^{a} \tag{4.14}$$

From the equations, ν_{oc} is the normalized open-circuit voltage value associated with thermal voltage $V_t = nkT/q$ while K, n, T, α, q, γ, and β denote the Boltzmann's constant, idealist factor ($1 < n < 2$), PV module temperature (K), nonlinear effect factor depended upon by the photocurrent, electron charge, nonlinear temperature-voltage effect factor, and a photovoltaic module technology-specific dimensionless coefficient, respectively. The highest single PV module energy output is presented in Eq. (4.14). A valid system contains a number of photovoltaic modules that are connected in parallel and in series. The overall net power output (P_M) equation for the bioreactor is being determined with parallel-connected N_p cells and series-connected N_s cells by the following equation:

$$P_{\text{array}} = N_s N_p P_M \tag{4.15}$$

Finally, to capture the highest amount of sunlight in order to power the bioreactor for a year continuously, the basis of various directional angles is being considered, meaning the Cartesian coordinate system or the spherical coordinate system, as illustrated in Fig. 4.3. Here the x, y, and z represent the horizon conventions, the east-west, and the zenith in order to capture enough sunlight to produce sufficient solar energy to power the bioreactor. The celestial body position in the Cartesian coordinate system can be determined by the azimuth angle. On the other hand, the following protocol is

This book belongs to Kitab Liaison (ocd1996@gmail.com) Copyright Elsevier 2023

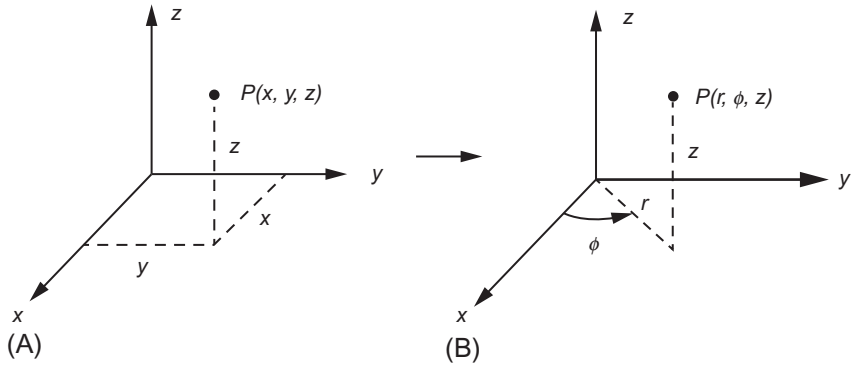

Fig. 4.3 The Cartesian coordinate system. (A) Cartesian coordinate analysis shows the equatorial system and vector control, considering the effect of the placement of solar PV systems, (B) shows the interocular symmetry considering various angles of the right maximum solar irradiance to capture to operate the bioreactor.

used by the equatorial system whereby the z axis points to the North Pole, the y axis and the system horizon are identical, and the x axis is perpendicular to y and z. In addition, ω angle hours and δ decline can help in determining the position. Generally, the analysis results in vector control strategy insertion for regulating reactive and active power with regard to a combination of various controls that can be reproduced and applied in other sophisticated systems [20–22].

The sustainable bioreactor

The load-resistant factor design that basically distributed the sanitation water force load resistance capacity needs to be accounted for consideration the design of a sustainable bioreactor to regularly operate in a high pressure of water force. Thus, the bioreactor should comprise the following capacity to resist the water force load with a velocity of 379 mi/h with the drag coefficient and water pressure of 1.00 per square meter and a standard water density of 1.2 kg/m^3. This helps in ensuring that the bioreactor panel is strongly resistant to the water force. Then, the water stagnation pressure shall be calculated by taking half the water density multiplied by the square of velocity, as shown in Eq. (4.16):

$$p_w = 0.5\rho C_p v_r^2 \tag{4.16}$$

where water pressure (Pa), air density(kg/m^3), water velocity (m/s), and the water pressure coefficient at the height of the bioreactor are denoted

This book belongs to Kitab Liaison (ocd1996@gmail.com) Copyright Elsevier 2023

by p_w, ρ, v_r^2, and C_p. As such, the water pressure may be calculated as $P_w = 0.5 \times 1.2\,\text{kg/m}^3 \times 379^2\,\text{m/s}$, thus giving 86,185 Pa. Thus, net water force (F)= drag coefficient × area × stagnation pressure as shown in the equation below:

$$F = 1\,\text{m}^2 \times 1.0 \times 86,185 = 86,185\,\text{N}\,(8788\,\text{kgf}) = 19,375\,\text{ibf} \qquad (4.17)$$

Once a solar power-assisted, structurally sound bioreactor is developed in the cellar of the building, then it has to be utilized to capture sanitation water and biowaste into its two chambers: (i) the wastewater tank, and (ii) the biowaste, including human feces. During this process, the wastewater needs to be treated by a preliminary treatment, a primary treatment, a secondary treatment, and disinfection. The whole treatment process can remove nearly 100% of the pollutants from the wastewater and disinfect the effluent. Furthermore, the final product can be utilized for local gardening and landscaping (Fig. 4.4).

Apart from the treated wastewater, the resulting sludge is then to be taken into the anaerobic tank, where it is used for the production of bioenergy. This is a transformation process where electrochemically active carbon nanotube filters are used to adsorb and effectively oxidize the contaminant chemicals within the anode [23, 24]. It is a advanced system of waste treatment to combine both adsorption and oxidation at the anode CNT and further oxidation in situ generated hydrogen peroxide (H_2O_2) in the cathode CNT in a small scale. Factors that affect the system's oxidation mechanism and treatment efficiency are systematically studied. This calculation's model indicated that electrode material, flow rate, cathode potential, oxygen dissolved, and pH can affect the hydrogen peroxide flow in order to remove the chemical contaminants [19, 25]. Additionally, phenol is being applied as an aromatic compound model to evaluate the system's odor removal efficiency as well as its rate of oxidation directly correlated with the flow of hydrogen peroxide (Fig. 4.5).

After this step, the product shall be stored in a closed chamber to allow the thermophilic anaerobic codigestion process to thicken. Then, the sludge is to be placed in free oxygen tanks called digesters and heated to at least 95°F for 10–15 days to stabilize the thickened sludge by converting much of the material into methane gas [9, 26]. It will therefore make it a safer environment for the bioreactor when waste is being discharged, which will stimulate the growth of anaerobic bacteria of *Desulfovivrio* and *Methanecoccus*. These consume organic matter in the sludge and thrive in a free anaerobic environment, which is different with bacteria in the aeration tanks.

This book belongs to Kitab Liaison (ocd1996@gmail.com) Copyright Elsevier 2023

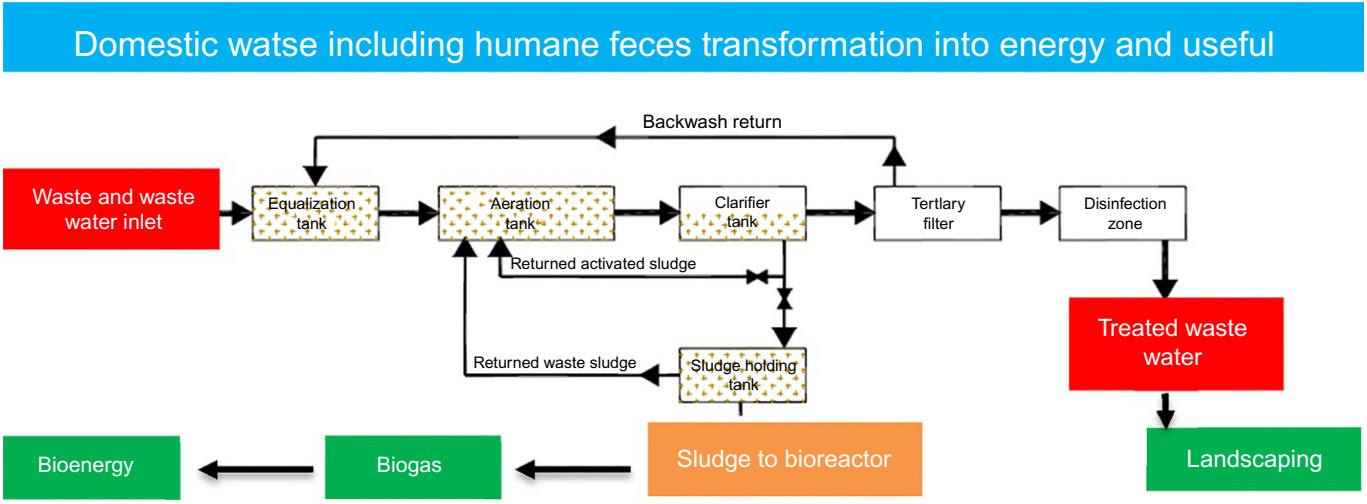

Fig. 4.4 Wastewater treatment process where effluent is used for gardening and the sludge is for a further process to produce biogas.

This book belongs to Kitab Liaison (ocd1996@gmail.com)

Copyright Elsevier 2023

Diagram of *Methanococcus* and *Desulfovivrio* reaction mechanism to produce methane

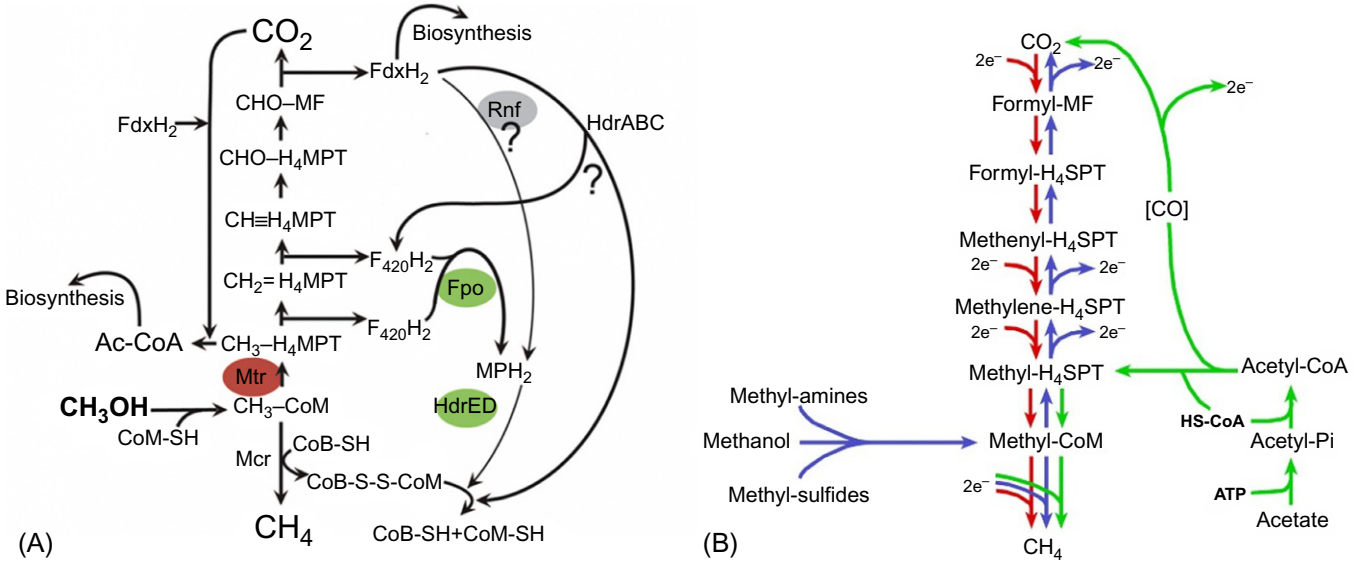

Fig. 4.5 Biochemical path of methanogenesis to a chain reaction for producing methane from domestic waste, including human feces where (A) *Methanococcus* and (B) *Desulfovivrio* bacteria are the main catalysts.

This book belongs to Kitab Liaison (ocd1996@gmail.com)

Copyright Elsevier 2023

Results and discussion

Solar power implemented bioreactor

The implementation of sunlight energy is being taken into consideration due to photon flux movement and electromagnetic waves used in the solar panel for powering the bioreactor. This is because photo-induced charges are related to photophysical charges [1, 27]. As a matter of fact, the first order plays a key role in solar thermal energy application and solar cell antireflective coatings. On the other hand, the second order is essential in solar photochemistry and solar cells. Quantum electrodynamics (a very sophisticated and successful technology in the contemporary fields of physics) represent a combination of both views [28, 29]. Radiation is emitted by all hot bodies. Thus, the highest radiation quantities are emitted by a solar panel at a temperature of about 700°C. As the body color changes to white, orange (dark gray in print version), blue (black in print version), and yellow (light gray in print version), the overlapping load efficiencies are determined within the band gap as well as in the cells and the sun at temperatures of 300 and 6000 K, respectively [12]. The solar radiation energy density is estimated using classical statistical physics based on the frequency of the photon wave, as shown in Fig. 4.6. The highest solar energy formation is modeled using 27.77 MW/m^2 eV of energy based on a photon excitation rate of 1.4 eV, as shown in Fig. 4.6.

Because the solar irradiance intensity is the main energy source for converting solar energy into electricity for powering the bioreactor, thus the amount of light quanta of steady-state irradiance are being measured in respect to the specific polarization type of frequency of energy generation ranging from ν_r to $\nu_r + d\nu_r$ [27, 30]. The highest solar radiation is achieved when the value is 27.77 mW/m^2 eV at 1.4 eV with regard to five hours of mean solar irradiance harvested per day among the range of ν_r [18, 22, 31]. Due to physical principles, there are losses in the conversion of solar energy into DC power and converting direct current into alternating current (AC). This ratio of AC to DC is called the "derating factor," which is typically 0.8 [11, 12, 23]. Thus, the surface texture of a selective solar panel is excellent in energy conversion because the current net conversion by solar panels is 125% higher with an efficiency of 80% [1, 30, 32] of solar panels, which means that $(27{,}770 \times 1.25 \times 0.8) = 27{,}770$ kW/year or 7.6 kW/day. Energy remains equal to the solar initially what is before the introduction to the solar panel. Necessarily, the maximum solar irradiance is depicted as 1.4 eV with an energy value of 27.77 mW/m^2 eV in Fig. 4.6 per year in an average of

This book belongs to Kitab Liaison (ocd1996@gmail.com) Copyright Elsevier 2023

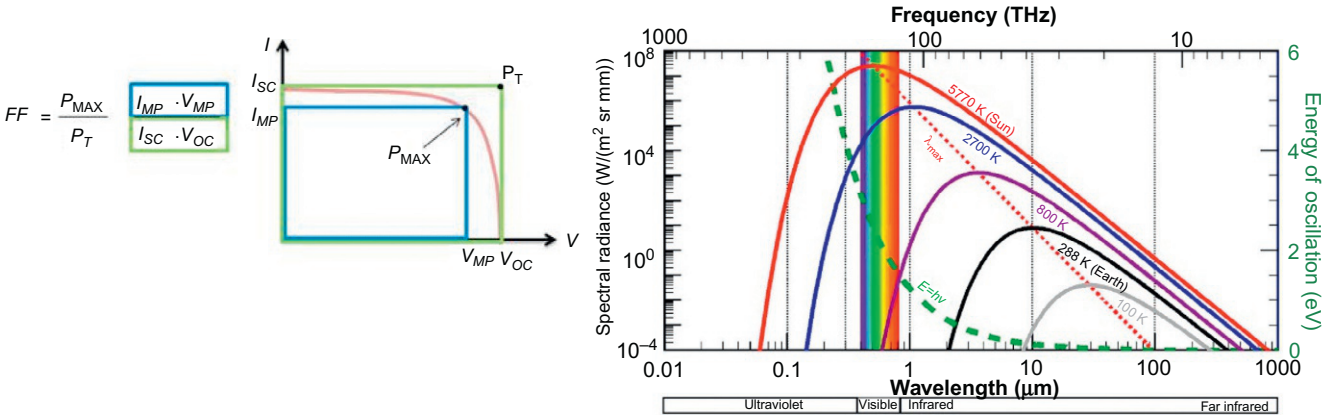

Fig. 4.6 The blackbody radiation in various temperatures at 5770 K power is 6.31 × 107 (W/m^2); Peak E is 1.410 (eV); Peak λ is 0.88 (μm); and Peak μ is 2.81 × 107 (W/m^2 eV).

This book belongs to Kitab Liaison (ocd1996@gmail.com)

Copyright Elsevier 2023

five hours a day maximum levels for 365 days referents by solar panel [18, 31, 33]. A standard residential house requires an average of 6 kW/day [10, 12, 26]. Because the produced energy is equivalent to 27,770 kW/year or 7.6 kW/day, which in fact will meet the energy demand for a standard 5*HP* bioreactor required 6 kW/day by using only one solar panel 1 m^2. In a large scale, the average energy consumption required monthly of a bioreactor of 50 *HP* in order to recycle of a building of 32 m × 31 m with 30 m (10 floors), respectively [29, 34, 35]. In a calculation of a building with an average footprint of 32 m × 31 m with a height of 30 m, the total installed 1 m^2 PV panels require 1195 units (945 + 250) with the capacity of 7.6 kW/unit energy production. This can provide total energy × 1195 = 9082 kW/day to meet the daily energy demand of about 10,000 kW/day for a building to recycle the sanitation and domestic waste.

The sustainable bioreactor

The solar-generated energy should then be introduced to the bioreactor to continuously power it for an entire year in order to recycle sanitation and biowaste where H_2O_2 plays a vital role in this process. The maximum flow H_2O_2 of 1.38 mol/L/m^2 C is being achieved CNT L^{-1} m^{-2} with an applied cathodic potential V −0.4 (vs Ag/AgCl), a pH of 6.46, a rate flow of 1.5 mL/min, and a DO influent flow of 1.95 mol/L/m^2 in order to remove the contaminants from the biowaste. Furthermore, phenol can be used as an aromatic compound model for assessing the removal efficiency of the odor into the system and its oxidation rate correlated with the H_2O_2 flow. H_2O_2 shall react with a phenol anodically activated to itself, which is the reason why the H_2O_2 radical form cannot remove phenol efficiently. In addition, the formation of an electrochemical polymer through chain reaction of phenolic radicals can also contribute to nearly 100% of contaminant removal. A stable removal efficiency of 87.0 ± phenol 1.8% to 4 h of continuous operation can be achieved with an average rate of oxidation of 0.059 ± 0.001 mol/h/m^2 in order to remove the contaminant by nearly 100% [16, 25]. The electrochemical CNT filtering system thus developed with H_2O_2 generated in situ for a new application of filters in this process, where carbon nanotubes are being used as an effective treatment for removing contaminant pollutants nearly 100%.

Then, the process of *methanogenesis* immediately began in the bioreactor once the contaminant pollutant was removed completely from the sludge through the CNT and H_2O_2 treatment because anaerobic *codigestions* started

This book belongs to Kitab Liaison (ocd1996@gmail.com) Copyright Elsevier 2023

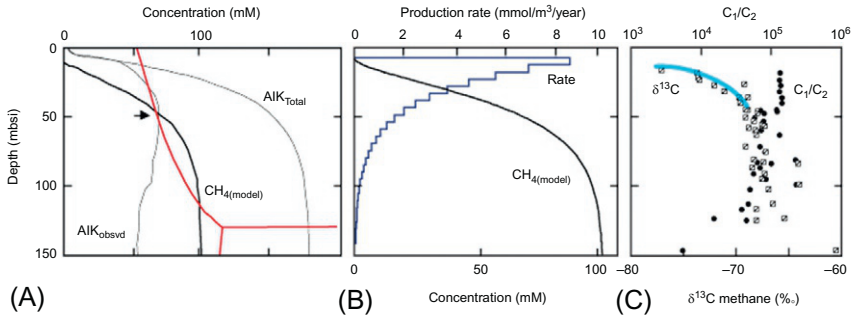

Fig. 4.7 (A) The effects of the depth of biowaste to produce bioenergy (CH_4), (B) the production rate of bioenergy (CH_4) considering the concentration of biowaste, and (C) net biogas production (CH_4) during the continuous anaerobic digestion of the waste.

to work on the sludge immediately in the bioreactor to generate bioenergy (CH_4). The net bioenergy production rate in the bioreactor is being analyzed using a computerized gas chromatograph (Fig. 4.7). Finally, this evolved bioenergy (CH_4) can be stored and utilized for running HVAC and cooking equipment for that building.

Conclusion

The development of mass urbanization around the world has accelerated exponentially over the last few decades. Consequently, urban sanitation and waste management problems are increasing rapidly due to the conventional application of urban sanitation and waste systems. The traditional urban sanitation and waste management system is creating severe environmental pollution, causing damage to human health as well as harm to flora and fauna in the aquatic environment. Here, this innovative technology could be the cutting-edge science to solve the urban sanitation and waste management problems. This innovative technology could mitigate urban sanitation and waste management system problems by recycling the domestic biowaste onsite to produce useful biogas. That would, in fact, be the most innovative technology to develop a sustainable urbanization.

Acknowledgments

This research was supported by Green Globe Technology under grant RD-02018-01 to build a better environment. Any findings, conclusions, and recommendations expressed in this paper are solely those of the author, who confirms that the article has no conflicts of interest for publication in a suitable journal.

This book belongs to Kitab Liaison (ocd1996@gmail.com) Copyright Elsevier 2023

References

[1] A. Diniz, L. Neto, C. Camara, P. Morais, C. Cabral, D. Filho, R. Ravinetti, E. França, D. Cassini, M. Souza, J. Santos, M. Amorim, Review of the photovoltaic energy program in the state of Minas Gerais, Brazil, Renew. Sust. Energ. Rev. 15 (6) (2011) 2696–2706.

[2] M. Hossain, Green science: independent building technology to mitigate energy, environment, and climate change, Renew. Sust. Energ. Rev. 73 (2017) 695–705.

[3] S. Klein, Calculation of flat-plate collector loss coefficients, Sol. Energy 17 (1) (1975) 79–80.

[4] M. Green, Limits on the open-circuit voltage and efficiency of silicon solar cells imposed by intrinsic Auger processes, IEEE Trans. Electron Devices 31 (5) (1984) 671–678.

[5] N. Izadyar, H. Ong, W. Chong, K. Leong, Resource assessment of the renewable energy potential for a remote area: a review, Renew. Sust. Energ. Rev. 62 (2016) 908–923.

[6] J. Rhodes, C. Upshaw, W. Cole, C. Holcomb, M. Webber, A multi-objective assessment of the effect of solar PV array orientation and tilt on energy production and system economics, Sol. Energy 108 (2014) 28–40.

[7] H. Ruiz, A. Martínez, W. Vermerris, Bioenergy potential, energy crops, and biofuel production in Mexico, BioEnergy Res. 9 (4) (2016) 981–984.

[8] B. Bhandari, S. Poudel, K. Lee, S. Ahn, Mathematical modeling of hybrid renewable energy system: a review on small hydro-solar-wind power generation, Int. J. Precis. Eng. Manuf. Green Technol. 1 (2) (2014) 157–173.

[9] S. Diaf, G. Notton, M. Belhamel, M. Haddadi, A. Louche, Design and techno-economical optimization for hybrid PV/wind system under various meteorological conditions, Appl. Energy 85 (10) (2008) 968–987.

[10] I. Gelfand, R. Sahajpal, X. Zhang, R. Izaurralde, K. Gross, G. Robertson, Sustainable bioenergy production from marginal lands in the US Midwest, Nature 493 (7433) (2013) 514–517.

[11] M. Born, E. Wolf, Principles of Optics, seventh ed., Cambridge University Press, Cambridge, 1999. (38).

[12] A.A.B. Mohd Zin, H.A. Mahmoud Pesaran, A.B. Khairuddin, L. Jahanshaloo, O. Shariati, An overview on doubly fed induction generators′ controls and contributions to wind based electricity generation, Renew. Sustain. Energy Rev. 27 (2013) 692–708.

[13] C. Chen, Physics of Solar Energy, John Wiley and Sons, Chichester, 2011, pp. 41–100.

[14] R. Millikan, A direct photoelectric determination of Planck's "h" Phys. Rev. 7 (3) (1916) 355–388.

[15] M. Kane, Small hybrid solar power system, Energy 28 (14) (2003) 1427–1443.

[16] C. Kennedy, H. Price, Progress in development of high-temperature solar-selective coating, in: ASME 2005 International Solar Energy Conference, 2005, pp. 749–755.

[17] J. Zhao, A. Wang, P. Altermatt, S. Wenham, M. Green, 24% efficient PERL silicon solar cell: recent improvements in high efficiency silicon cell research, Sol. Energy Mater. Sol. Cells 41–42 (1996) 87–99.

[18] S. Costa, A. Diniz, L. Kazmerski, Dust and soiling issues and impacts relating to solar energy systems: literature review update for 2012–2015, Renew. Sust. Energ. Rev. 63 (2016) 33–61.

[19] D. Muhsen, T. Khatib, F. Nagi, A review of photovoltaic water pumping system designing methods, control strategies and field performance, Renew. Sust. Energ. Rev. 68 (2017) 70–86.

[20] C. Brabec, N. Sariciftci, J. Hummelen, Plastic solar cells, Adv. Funct. Mater. 11 (1) (2001) 15–26.

This book belongs to Kitab Liaison (ocd1996@gmail.com) Copyright Elsevier 2023

[21] M. Dürr, A. Cruden, S. Gair, J. McDonald, Dynamic model of a lead acid battery for use in a domestic fuel cell system, J. Power Sources 161 (2) (2006) 1400–1411.
[22] A. Gaillard, P. Poure, S. Saadate, M. Machmoum, Variable speed DFIG wind energy system for power generation and harmonic current mitigation, Renew. Energy 34 (6) (2009) 1545–1553.
[23] J.C. Maxwell, A Dynamic Theory of the Electromagnetic Field, Reprinted by Wipf and Stock Publishers, 1864. (32) (1996).
[24] J. Romero-García, A. Sanchez, G. Rendón-Acosta, J. Martínez-Patiño, E. Ruiz, G. Magaña, E. Castro, An olive tree pruning biorefinery for co-producing high value-added bioproducts and biofuels: economic and energy efficiency analysis, BioEnergy Res. 9 (4) (2016) 1070–1086.
[25] D. Rekioua, E. Matagne, Modeling of solar irradiance and cells, in: Optimization of Photovoltaic Power Systems. Green Energy and Technology, Springer, London, 2012.
[26] H. Bethe, Energy production in stars, Phys. Rev. 55 (1) (1939) 103.
[27] B. Liu, R. Jordan, The interrelationship and characteristic distribution of direct, diffuse and total solar radiation, Sol. Energy 4 (3) (1960) 1–19.
[28] M. Hossain, Green science: advanced building design technology to mitigate energy and environment, Renew. Sust. Energ. Rev. 81 (2018) 3051–3060.
[29] M. Hossain, Photonic thermal control to naturally cool and heat the building, Appl. Therm. Eng. 131 (2018) 576–586.
[30] C. Gopal, M. Mohanraj, P. Chandramohan, P. Chandrasekar, Renewable energy source water pumping systems—a literature review, Renew. Sust. Energ. Rev. 25 (2013) 351–370.
[31] E. Madani, S. Assailian, An experiment in linguistic synthesis with a fuzzy logic controller, Int. J. Hum. Comput. Stud. 51 (2) (1999) 135–147.
[32] M. Grätzel, Photoelectrochemical cells, Nature 414 (6861) (2001) 338–344.
[33] L. Duan, S. Sun, L. Yue, W. Qu, J. Bian, Study on different zero CO2 emission IGCC systems with CO2 capture by integrating OTM, Int. J. Energy Res. 40 (10) (2016) 1410–1427.
[34] M. Hossain, Solar energy integration into advanced building design for meeting energy demand and environment problem, Int. J. Energy Res. 40 (9) (2016) 1293–1300.
[35] R. King, D. Law, K. Edmondson, C. Fetzer, G. Kinsey, H. Yoon, R. Sherif, N. Karam, 40% efficient metamorphic GaInP/GaInAs/Ge multijunction solar cells, Appl. Phys. Lett. 90 (18) (2007) 183516.

This book belongs to Kitab Liaison (ocd1996@gmail.com) Copyright Elsevier 2023

CHAPTER 5

Power systems

Introduction

Urban water vapor is the cause of accountable climate change because these water vapor molecules create temporary aerosol in the atmosphere [1–3]. However, the implementation of advanced mechanisms of photoelectrolysis by the application of photophysical reactions can easily split this urban water vapor to create clean energy. Lo et al. and Yang et al. showed that the breakdown of photon energy and its induction into water vapor plays a great role in splitting water molecules into H_2 and O_2 [1, 4, 5]. Therefore, this transpiration water vapor simply can be tugged down by static electricity force in a building and/or house tank, which can be further split by photoelectrolysis to produce clean H_2 energy.

In this research, thus, an innovative mechanism has been clarified to convert urban water vapor into clean energy naturally instead of allowing it to go into the air. Tanks that form static electricity are being installed near buildings and/or houses in order to capture all the water vapor by the force of static electricity created by the tanks [2, 6]. Water vapor contains positive and negative charges and thus, the electrons end up with static electrical force, which contains a positive charge [1, 7]. Because of water molecule has a negative charge on one side, the positive charges of static electric force and the negative charges of water vapor attract each other, the positive charge pull the direction and enforce the water vapor to tug down to come into the tank. The photo-electrochemical-photovoltaic mechanism consists of a photoelectrode semiconductor device to be introduced into the tank to absorb solar light and form the necessary voltage to break water molecules into O_2 and H_2. The highest conversion efficiency for photoelectrolysis is 100%, whereas current photoelectrolysis systems only have 8%–14% efficiency rates [8–10]. Naturally this photoelectrolysis would be the most efficient method of renewable H_2 production, which indeed confirms a meaningful long-term solution for clean energy for mass urbanization because it does not create any greenhouse gases (GHGs) where the byproduct O_2 plays a vital role in balancing the environment. Because fossil energy consumption is expected to reach a finite level in the next 65 years, thus

Sustainable Development for Mass Urbanization
https://doi.org/10.1016/B978-0-12-817690-0.00005-1
© 2019 Elsevier Inc.
All rights reserved.

This book belongs to Kitab Liaison (ocd1996@gmail.com)
Copyright Elsevier 2023

alternative renewable technology is necessary to meet the daily energy demand to mitigate total energy demand for the sustainable urban area [11–13]. Indeed, this innovative technology would be a total solution to meet the urban energy demand as the primary source of power systems that are environmentally friendly.

Material and methods

Electrostatic force generation

To trap the H_2O molecule from the urban air, technology been implemented to form the *Hossain Static Electric Force (HSEF=ℌ)* by creating insulator friction in the tank of a house or home in order to tug down the water vapor into the tank. Therefore, to form this *HSEF* in the tank, an abelian local symmetry is being employed, calculating the gauge-field symmetry and the Goldstone scalar considering the longitude of the vector [14–16]. Therefore, the breakdown of each water particle T^{α} of the local symmetry will correspond to the gauge field of $A_{\mu}^{\alpha}(x)$ where *HSEF* will be commenced to work at local U (1) phase symmetries [17–19]. Necessarily, the mode shall form a complex scalar field $\Phi(x)$ of static electric charge q that is coupled with the EM field $A^{\mu}(x)$, which can be expressed by ℌ [20–22]:

$$\mathcal{H} = -\frac{1}{4} F_{\mu\nu} F^{\mu\nu} + D_{\mu}\Phi^{*} D^{\mu}\Phi - V(\Phi^{*}\Phi) \tag{5.1}$$

where

$$\begin{aligned} D_{\mu}\Phi(x) &= \partial_{\mu}\Phi(x) + iqA_{\mu}(x)\Phi(x) \\ D_{\mu}\Phi^{*}(x) &= \partial_{\mu}\Phi^{*}(x) - iqA_{\mu}(x)\Phi^{*}(x) \end{aligned} \tag{5.2}$$

And

$$V(\Phi^{*}\Phi) = \frac{\lambda}{2}(\Phi^{*}\Phi)^{2} + m^{2}(\Phi^{*}\Phi) \tag{5.3}$$

Suppose $\lambda > 0$ but $m^2 < 0$, so that $\Phi = 0$ is a local maximum of the scalar potential while the minima form a degenerate circle $\Phi = \frac{v}{\sqrt{2}} * e^{i\theta}$,

$$v = \sqrt{\frac{-2m^2}{\lambda}}, \text{any real}\,\theta \tag{5.4}$$

Subsequently, the scalar-field Φ will develop a nonzero particulate expected value $\langle\Phi\rangle \neq 0$, which will spontaneously create the U (1) symmetries into the magnetic field of the tank [5, 23]. These symmetries shall direct a massless Goldstone-scalar stemming by implementing the complex scalar

This book belongs to Kitab Liaison (ocd1996@gmail.com) Copyright Elsevier 2023

field Φ (x). Hence, the local U (1) symmetrical phase of Φ (x) shall confirm the formation of expected value $\langle\Phi\rangle$ while x-consider is the dependent phase of the dynamical Φ (x) field.

To determine this static electricity force formation process, the polar coordinates are being used within the scalar-field space, which can be expressed as,

$$\Phi\,(x) = \frac{1}{\sqrt{2}}\,\Phi_r(x) * e^{i\Theta(x)}, \text{real}\,\Phi_r(x) > 0, \text{real}\,\Phi(x) \tag{5.5}$$

This scalar field represents the active static electricity force Φ $(x) = 0$, thus, it is a mathematical calculation that shall be explained as $\langle\Phi\rangle \neq 0$, where the expected value $\Phi\langle x\rangle \neq 0$ is almost everywhere. Thus, the real static force fields $\phi_r(x)$ and $\Theta(x)$ are the scalar-potential force that depends on the radial field ϕ_r,

$$V(\phi) = \frac{\lambda}{8}\left(\phi_r^2 - \nu^2\right)^2 + \text{const} \tag{5.6}$$

or, in terminology of the radial field transformed by its VEV, $\Phi_r(x) = \nu + \sigma(x)$,

$$\phi_r^2 - \nu^2 = (\nu + \sigma)^2 - \nu^2 = 2\nu\sigma + \sigma^2 \tag{5.7}$$

$$V = \frac{\lambda}{8}\left(2\nu\sigma - \sigma^2\right)^2 = \frac{\lambda\nu^2}{2} * \sigma^2 + \frac{\lambda\nu}{2} * \sigma^3 + \frac{\lambda}{8} * \sigma^4 \tag{5.8}$$

At the same time, the covariant derivative $D_\mu\phi$ becomes

$$D_\mu\phi = \frac{1}{\sqrt{2}}\left(\partial_\mu\left(\phi_r e^{i\Theta}\right) + iqA_\mu * \phi_r e^{i\Theta}\right) = \frac{e^{i\Theta}}{\sqrt{2}}\left(\partial_\mu\phi_r + \phi_r * i\partial_\mu\Theta + \phi_r * iqA_\mu\right) \tag{5.9}$$

$$\begin{aligned} \left|D_\mu\phi\right|^2 &= \frac{1}{2}\left|\partial_\mu\phi_r + \phi_r * i\partial_\mu\Theta + \phi_r * iqA_\mu\right|^2 \\ &= \frac{1}{2}\left(\partial_\mu\phi_r\right) + \frac{\phi_r^2}{2} * \left(\partial_\mu\Theta qA_\mu\right)^2 \\ &= \frac{1}{2}\left(\partial_\mu\,\sigma\right)^2 + \frac{(\nu + \sigma)^2}{2} * \left(\partial_\mu\Theta + qA_\mu\right)^2 \end{aligned} \tag{5.10}$$

All together,

$$\mathcal{L} = \frac{1}{2}\left(\partial_\mu\,\sigma\right)^2 - \nu\,(\sigma) - \frac{1}{4}\,F_{\mu\nu}F^{\mu\nu} + \frac{(\nu + \sigma)^2}{2} * \left(\partial_\mu\Theta + qA_\mu\right)^2 \tag{5.11}$$

This book belongs to Kitab Liaison (ocd1996@gmail.com)
Copyright Elsevier 2023

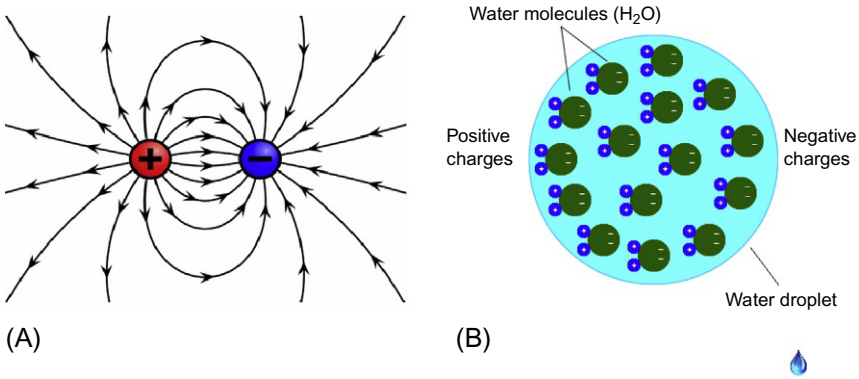

Fig. 5.1 (A) The creating of static force, and (B) its process of the transformation of static energy into electric force charges (ve+ and ve−) to mobilize the static force to pull down the water molecules.

To determine the formation of this static-electric force ($\mathcal{H}_{\text{sef}}$) into the gauge field of this *HSEF*, I have further calculated the expanded power of static force and employed the quadratic force by describing the free particles as follows,

$$\mathcal{H}_{\text{sef}} = \frac{1}{2}\left(\partial_\mu \sigma\right)^2 - \frac{\lambda v^2}{2} * \sigma^2 - \frac{1}{4} F_{\mu\nu} F^{\mu\nu} + \frac{v^2}{2} * \left(qA_\mu + \partial_\mu \Theta\right)^2 \tag{5.12}$$

Here, this *HSEF* ($\mathcal{H}_{\text{free}}$) is a free radical functional force that will form a real scalar field of positive field that is equivalent to mass^2 = λv^2. It will enforce the A_μ (x) and the Θ (x) fields to initiate to create a massive static electric force within the electric field of the plastic tank (Fig. 5.1).

Photo electrolysis/energy formation

Then the collected water in the tank of a building or home shall undergo clean energy production by implementing natural *electrolysis* to convert water into hydrogen energy. Instead of traditional electrolysis, a direct water electrolysis system has been used that is considered as a novel, integrated, monolithic photoelectrochemical (PEC)/PV device (Fig. 5.4) where the contrivance of $GaInP_2$/GaAs p/n, p/n tandem cell are solid consisting of GaAs at lower point connecting to a $GaInP_2$ upper cell via a tunnel diode interconnection [24–26]. At top of p/n $GaInP_2$ junction employing the band gap of 1.83 eV has been proposed to design to absorb the visible part of light spectrum; and the lower part of p/n GaAs junction employing the band gap of 1.42 eV to absorbs the closer-infrared part of the light spectrum

This book belongs to Kitab Liaison (ocd1996@gmail.com) Copyright Elsevier 2023

transmitted via the upper junction to get excited radiant energy to occur electrolysis (Fig. 5.2).

The highest practical light irradiance to electrical efficiency within the presence of the combination of band gaps is to be accounted where the ideal solid form tandem cell occurs at the PEC Schottky junction, implemented at the top of the *p*/*n* junction [27–29]. It is thereafter considered a PEC

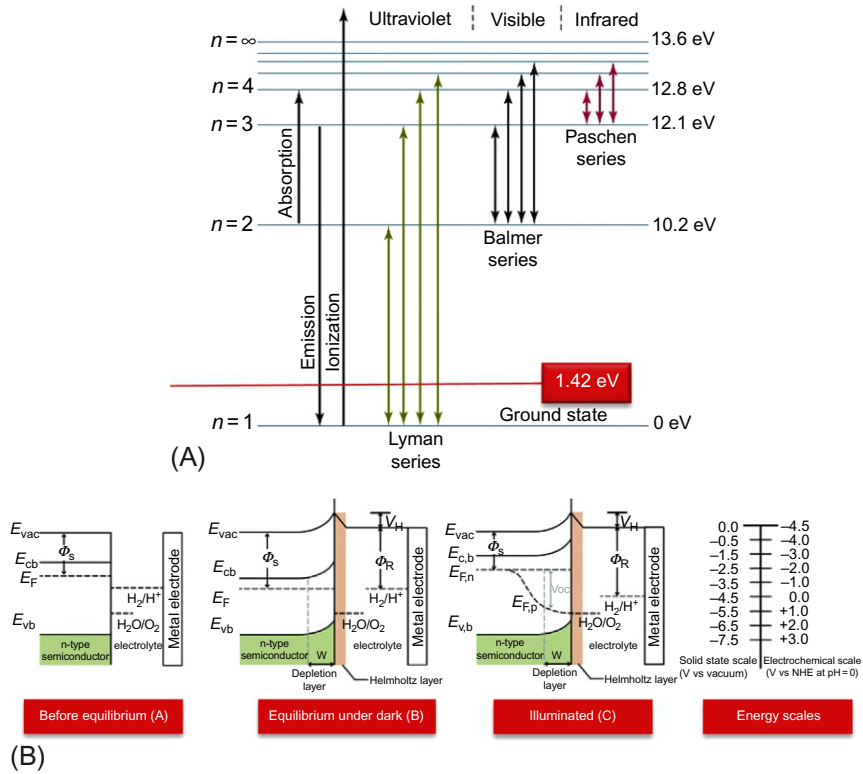

Fig. 5.2 (a) The electron state hydrogen approach by the radiation emission of photon energy (UV light) respectively at the band-gap of 1.42 eV I supporting the conduction of photoelectrolysis under an excited state of hydrogen, (b) The bond formation of the *n*-type semiconduction contact revealing the relationships among the electrolyte redox potential (H_2O/O_2 and H_2/H^+), the Helmholtz power kinetic (V_H), the semiconduction functions (Φ_s), the kinetic function of electrolyte variables (Φ_R), the electrons' quasi-Fermi state ($E_{F,n}$), and the prompt quasi-Fermi state ($E_{F,p}$) within in three functions: (A) Prior to the equilibration within the two phases; (B) Final equilibration into the light state; and (C) in the quasistatic equilibration into the steady-state light energy where the energy generation (V_{OC}) is conducted under the thermal states between the $E_{F,n}$ and the electrochemical faction of the redox potential (H_2O/O_2).

This book belongs to Kitab Liaison (ocd1996@gmail.com)
Copyright Elsevier 2023

maneuver, which is a voltage integrated PV contrivance. Therefore, in the PEC maneuver under solar irradiance, electrons will start to flow to the illuminated area at the ohmic contact to split the water. Because water is being split directly under illumination where solar light is the only energy input into the PEC device, thus, the p-$GaInP_2$/GaAs cells proposed in the research would be most convenient concerning atmospheric pressure equilibrium state electrolysis [25, 30, 31]. Necessarily, the mechanism that consists of an upper surface cell p-$Ga_{0.52}In_{0.48}P$ connecting in a series low-resistivity, cell-in tunnel junction (TJ) toward a GaAs p/n lower part of cell on GaAs to confirm to get the best results of photoelectrolysis [32–34].

To confirm the accurate photoelectrolysis process, the PEC/PV configuration is being implemented with enough GaAs within the bond edges of $GaInP_2$ and H_2O redox potentials (Fig. 5.3). Therefore, the total solar photovoltaic output will approach the thermodynamics of water splitting (1.23 V) naturally by conducting the losses of μ_a and μ_c under the

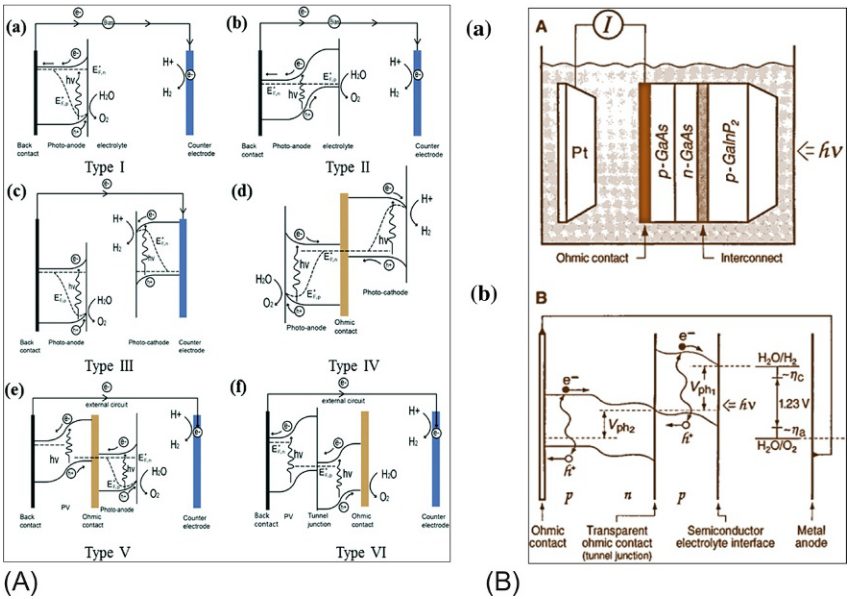

Fig. 5.3 (A) Schematic diagram of various types of PEC/PV water-splitting equipment: (a) type I single irradiance emission device; (b) type II heterojunction photoelectrode; (c) type III wire-connected PEC tandem cells; (d) type IV nonwire PEC tandem cells; (e) type V PV-PEC standard tandem cell; (f) type VI PV electrolyzer cell. (B) detailed diagram of the (a) proposed PEC/PV device and (b) its idealized energy state PEC/PV photoelectrolysis mechanism.

This book belongs to Kitab Liaison (ocd1996@gmail.com) Copyright Elsevier 2023

anode and cathode cell. The standard energy state diagram for photoelectrolysis of H_2O by this device is illustrated (Fig. 5.3), where the solar irradiance attenuation on the PEC/PV configurations initially penetrates the band-gap p-$GaInP_2$ surface to absorb more energy state photons to confirm the electron-hole pair excitation to produce photovoltaic V_{ph1} [7, 35, 36]. Subsequently, the lesser energetic state photons will penetrate via $GaInP_2$, which is to be absorbed by GaAs at the lower part of the p/n junction to generate photovoltaic V_{ph2} (Fig. 5.3). Here, a combination of holes and electrons is being connected at the tunnel junction. Once the resultant photovoltaic $V_{ph} = V_{ph1} + V_{ph2}$ is attained greater than the requirement of photoelectrolysis into the cell configuration, it will force the H_2O to split under the semiconductor electrode and H_2O oxidation under the counter electrode, where only two photons will be required to produce one electron and only four photons shall be required to produce one molecule of H_2, a state of clean energy (Fig. 5.4).

Results and discussion

Electrostatic force

To confirm the formation of static force proliferation into the plastic tank in a building or home in order to tug down the water, I have first calculated the dynamic photon estimation by implementing the *HSEF* electric field. Therefore, the local U (1) gauge field will concede to integrate a mass terminology of the gauge particle $\varnothing' \rightarrow e^{i\alpha(x)}\varnothing$. In detail, it can be described by the functional derivatives with the specific deformation rule fore of the scalar field, which can be expressed by [37, 38]:

$$\begin{gathered} \partial_\mu \rightarrow D_\mu = \partial_\mu = ieA_\mu \left[\text{covariant derivatives}\right] \\ A'_\mu = A_\mu + \frac{1}{e}\partial_\mu \alpha \left[A_\mu \text{ derivatives}\right] \end{gathered} \tag{5.13}$$

Where the local U (1) gauge variable *HSEF* is considered as the complex scalar field by presenting as:

$$\mathcal{L} = \left(D^\mu\right)^\dagger \left(D_\mu \varnothing\right) - \frac{1}{4} F_{\mu\nu}F^{\mu\nu} - V(\varnothing) \tag{5.14}$$

The term $\frac{1}{4} F_{\mu\nu}F^{\mu\nu}$ is the kinetic term for the gauge field (heating photon) and $V(\varnothing)$ is the extra term in the *HSEF* that is: $V(\varnothing^*\varnothing) = \mu^2(\varnothing^*\varnothing) + \lambda\,(\varnothing^*\varnothing)^2$.

This book belongs to Kitab Liaison (ocd1996@gmail.com)
Copyright Elsevier 2023

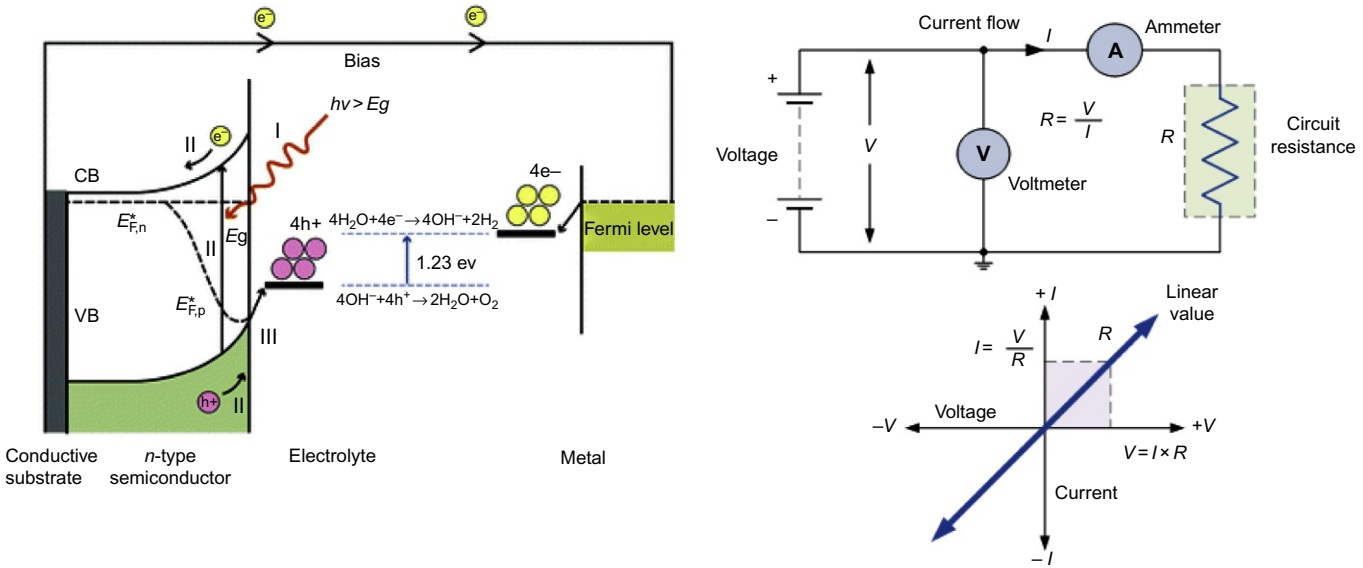

Fig. 5.4 A standard PEC cell designed by considering the *n*-type semiconducting photon that is connected to a metallic countered electrode. On the photoanode, $4OH^- + 4H^+ \rightarrow 2H_2O + O_2$ are being formed where the prime mechanism involved in: (I) light emission captures; (II) charge transporter, and (III) the surface redox potential reactions mechanism.

This book belongs to Kitab Liaison (ocd1996@gmail.com)

Copyright Elsevier 2023

Hence, the *HSEF* ($\mathcal{H}$) into the variable implementation of the quantum field shall initiate the massive scalar particles $\phi_1$and ϕ_2 in accordance of a mass μ. In this model, $\mu^2 < 0$ has an infinite number of quantum that is formed by $\phi_1^2 + \phi_2^2 = -\mu^2/\lambda = v^2$ and the $\mathcal{H}$, which is the functional derivative used by the transformed fields η *and* ξ in order to define the quantum field as $\phi_0 = \frac{1}{\sqrt{2}}\left[(v+\eta) + i\xi\right]$.

$$\begin{aligned}\text{Kinetic term}: \mathcal{H}_{kin}(\eta,\xi) &= (D^\mu\phi)^\dagger (D^\mu\phi) \\ &= (\partial^\mu + ieA^\mu)\phi^* \left(\partial_\mu - ieA_\mu\right)\phi\end{aligned} \tag{5.15}$$

Potential term: $V(\eta,\xi) = \lambda\, v^2\eta^2$, up to second order in the fields and thus, the full *HSEF* can be written as:

$$\begin{aligned}\mathcal{H}_{kin}(\eta,\xi) = &\frac{1}{2}\left(\partial_\mu\eta\right)^2 - \lambda v^2\eta^2 + \frac{1}{2}\left(\partial_\mu\xi\right)^2 - \frac{1}{4}F_{\mu\nu}F^{\mu\nu} + \frac{1}{2}e^2v^2A_\mu^2 \\ &- ev A_\mu(\partial^\mu\xi) + \text{int.terms}\end{aligned} \tag{5.16}$$

Consequently, the massive η, massless ξ, and the formation of the massive quantum and A_μ are determined by the term $\partial_\mu\alpha$ that can be calculated from Eq. (5.14). A_μ and ϕ can be changed simultaneously and thus can be represented as the thermal photon particle produced into the scalar field, which is expressed by [28, 37]:

$$\begin{aligned}\mathcal{H}_{\text{scalar}} &= (D^\mu\phi)^\dagger(D^\mu\phi) - V\left(\phi^\dagger\phi\right) \\ &= (\partial^\mu + ieA^\mu)\frac{1}{\sqrt{2}}(v+h)\left(\partial_\mu - ieA_\mu\right)\frac{1}{\sqrt{2}}(v+h) - V\left(\phi^\dagger\phi\right) \\ &= \frac{1}{2}\left(\partial_\mu h\right)^2 + \frac{1}{2}e^2A_\mu^2(v+h)^2 - \lambda v^2h^2 - \lambda v h^3 - \frac{1}{4}\lambda h^4 + \frac{1}{4}\lambda h^4\end{aligned} \tag{5.17}$$

Therefore, this scalar static electricity force formation term in the $\mathcal{H}$ revealed that the formation of the *HSEF* electric field is ready to initiate the proliferation of static electricity into its quantum field in order to tug down the water.

Photoelectrolysis/energy formation

In this technology, the water-splitting reactions are much easier where H_2 production at the building or home occurs because: (i) H_2 formation requires the least catalyst results in the least voltaic losses, thus allowing the optimized counter electrode for more O_2 formation; and (ii) under solar irradiance, the area semiconductor planes are cathodically protected [4, 39]. A better illustration is shown in Fig. 5.4, where the photocurrent-voltaic

This book belongs to Kitab Liaison (ocd1996@gmail.com) Copyright Elsevier 2023

curves p-$GaInP_2$(Pt) and the p-$GaInP_2$(Pt)/TJ/GaAs electrodes are clarified into the two-electrode configuration. Under illumination, the p-$GaInP_2$ (Pt) electrode shall occur to form H_2 within the voltage 500 mV, which suggests that the solar irradiance and the p-$GaInP_2$ (Pt)/TJ/GaAs electrode will show a very open circuit voltage of ~0.55 V to generate extra photovoltage by the GaAs cell [1, 40]. Naturally, the formation of hydrogen will start soon at 400 mV positive of a short circuit and densities of the photovoltaic current shall be attained of 120 mA/cm^2 at ~0.15 V, where the least saturated photovoltaic current at the p-$GaInP_2$ (Pt)/TJ/GaAs electrode compared to the p-$GaInP_2$ electrode is calculated respectively the p/n GaAs lower part of the cell current-limiting junction (Fig. 5.5).

The production of H_2 energy at the urban home or building by this photoelectrolysis process under solar illumination has been clarified and collected by a mass spectrometer. The efficiency of hydrogen production is to be determined as *Efficiency = (power out)/(power in)* and the calculation revealed that the resultant energy formation is 1190 mW/cm^2 (Fig. 5.5). Naturally resultant energy by assuming 100% photovoltaic current electrolysis efficiency, I have determined the hydrogen formation photovoltaic current of 120 mA/ cm^2 is being multiplied by 1.23 V that is the ideal fuel cell limit to achieve the highest conversion efficiency of H_2 energy from the following calculation $\Delta G = \Delta H - T\Delta S$; $W_{el} = qE = nFE$; $W_{el} = -\Delta G$, therefore the Gibbs free energy is $E_{\text{theo}} = \frac{-\Delta G}{nF} = \frac{237{,}340\,\text{j/mol}}{2x96{,}485\,\text{As/mol}} = 1.23\,\text{V}$.

Conversion of energy into electricity

To use this energy practically, the application of a hydrogen fuel cell consisting of the electrolyte within two electrodes, an anode, and a cathode has been implemented to convert hydrogen into electricity. Because the cell permits the positive charged H^- ions (protons) to travel within the two sides of the fuel cell the anode acts as the catalyst in the fuel to undergo oxidation reactions to generate protons (ve+ hydrogen ions) and electrons. Consequently, the traveling of protons from the anode to the cathode via the electrolyte after the reaction will be conversional production of electricity energy tremendously. Then, the electrons are to be captured from the anode to the cathode via an external circuit to produce direct current electricity by determining the electrical equivalent circuit (Fig. 5.6).

The estimate confirms that a gallon of water has a yield of 0.42 kg of hydrogen. The figure of merit for the used fuel cell is 44.5 kWh/kg-H_2. Therefore, the yields are calculated as 16.7 kWh; a kilowatt hour should

This book belongs to Kitab Liaison (ocd1996@gmail.com) Copyright Elsevier 2023

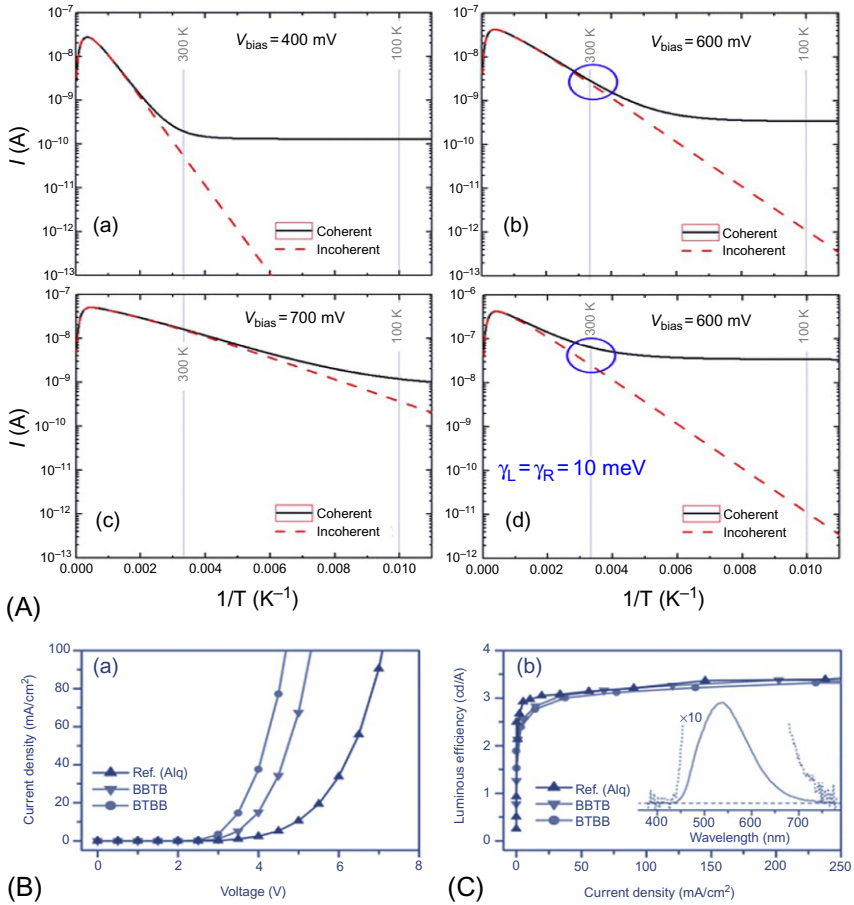

Fig. 5.5 (A) The parameters used in the calculations are $\varepsilon = 0.4$ eV, $\eta = 0.5$, $V_G = 0$, and $\gamma_L = \gamma_R = 1$ meV for (a–c) and $\gamma_L = \gamma_R = 10$ meV for (d), which are typical values in the molecular junctions for this work. (B) shows the current-voltage relationships for p-GaInP2(Pt)/TJ/GaAs (curve 1) and p-GaInP2 (curve 2) electrodes in 3MH 2SO4 at solar irradiance. (C) shows the photovoltaic current time in the short circuit of the PEC/PV tandem cell in3MH 2SO4 with the calculated efficiency of 5120 mA/cm^2 31.23V3100/1190 mW/cm^2 512.4%. CD (current density) [24, 37].

be 3600 kJ, and the enthalpy of formation for hydrogen energy from liquid water at 25°C is −286 kJ/mol has been determined from the following equations.

$$\text{Reduction} - \text{Oxidation reductant} \rightarrow \text{Product} + 4e^-$$

$$\text{Oxidant} + e^- \rightarrow \text{Product} \tag{5.18}$$

This book belongs to Kitab Liaison (ocd1996@gmail.com)
Copyright Elsevier 2023

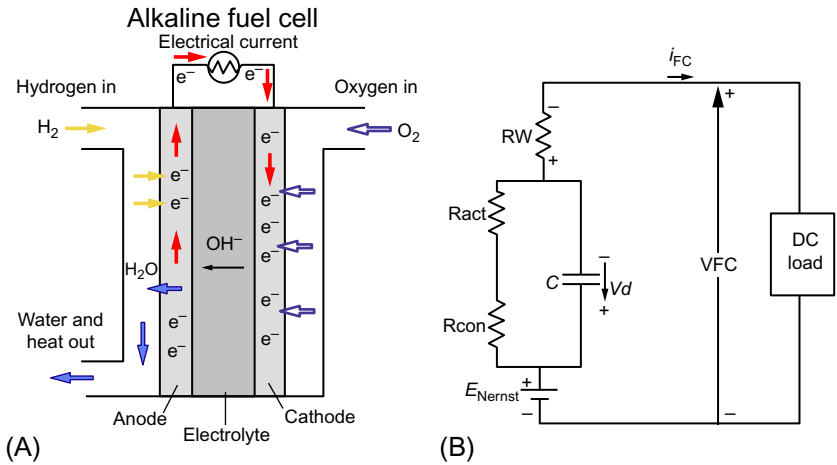

Fig. 5.6 (A) A typical fuel cell, (B) electrical equivalent circuit of the fuel cell. The output voltage from this cell has been determined as $VFC = E_{Nernst} - Ract - VOhmic - Rcon$; where the thermodynamic potential is $E_{Nernst} = 1.229 - 0.85 \times 10^{-3} \times (T - 298.15) + 4.31 \times 10^{-5} \times T \times [\ln(PH2) + 12\ln(PO2)]$, the Activation over potential is $Ract = -[\xi 1 + \xi 2 \times T + \xi 3 \times T \times \ln(CO2) + \xi 4 \times T \times \ln(i_{FC})]$ $Ract = -[\xi 1 + \xi 2 \times T + \xi 3 \times T \times \ln(CO2) + \xi 4 \times T \times \ln(i_{FC})]$, the ohmic over potential is $Vohmic = i_{FC}(RM + RC)$, and concentration over potential represents as $Rcon = -B \times \ln(1 - JJmax)$.

$$\text{Anode half reaction } 2H_2 \rightarrow 4H^+ + 4e^- \tag{5.19}$$

$$\text{Cathod half reaction } O_2 + 4H^+ + 4e^- \rightarrow 2H_2O \tag{5.20}$$

$$2H_2 + O_2 \rightarrow 2H_2O + \text{energy} \tag{5.21}$$

$$H_2 + \frac{1}{2}O_2 \rightarrow H_2O, \Delta H = 286\,\text{kJ/mol} \tag{5.22}$$

Since a gallon of water is 3785 mL, and thus given that water has 18 mL/mol, about 210.3 mol of water and 286 × 210.3/3600 and it gives about 16.7 kWh energy. Because a small family of four shall require on average 30 kWh energy per day where two gallons water vapor per day is satisfactory enough to satisfy the total energy demand for a small family.

In addition to meeting the daily energy demand for urban houses and buildings, this energy technology can also be used for urban transportation systems. Thus, an experimental proof of this hydrogen energy by photolysis of the urban water molecule is thereafter introduced into a car as an experimental tool to use ultimately for all urban transportation systems. The following design of a fuel cell and a hydrogen fuel tank is used to run the vehicle by clean energy that is created from urban water vapor. This new finding

This book belongs to Kitab Liaison (ocd1996@gmail.com) Copyright Elsevier 2023

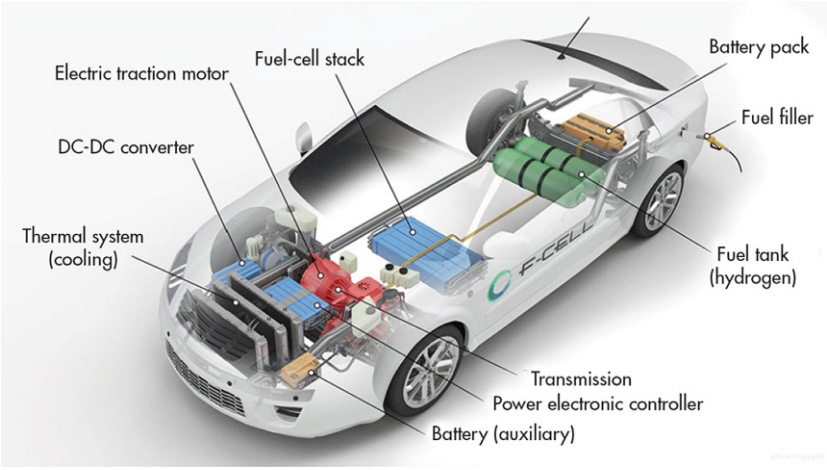

Fig. 5.7 The mechanism of the utilization of hydrogen energy from urban water vapor implemented into a vehicle to run quietly, powerfully, and cleanly.

suggests that the utilization of this new energy by implementing an H_2 fuel cell in vehicles will have zero emissions and run on compressed H_2 fed into a fuel cell stack that produces electricity to power the vehicle to drive quietly, powerfully, and cleanly (Fig. 5.7).

Conclusions

Urban water vapor has been used in photolysis naturally to produce clean energy instead of allowing it to go into the air to create climate change. Thus this research reveals that using the static electricity force and solar irradiance to extract hydrogen energy directly from urban water vapor and purifying it will not only mitigate total energy demand for sustainable urbanization as the primary source of power, but it will also be of great scientific interest in natural science.

Acknowledgments

The research is conducted at the department of research and development of sustainable technology of Green Globe Technology under grant RD-02017-07 for building a better world. Any findings, predictions, and conclusions described in this article are solely performed by the authors and we confirm that there is no conflict of interest for publishing in a suitable journal.

This book belongs to Kitab Liaison (ocd1996@gmail.com) Copyright Elsevier 2023

References

[1] G. Baur, K. Hencken, D. Trautmann, Revisiting unitarity corrections for electromagnetic processes in collisions of relativistic nuclei, Phys. Rep. 453 (2007) 1.
[2] M.F. Hossain, Green science: advanced building design technology to mitigate energy and environment, Renew. Sustain. Energy Rev.. 81 (2) (2018) 3051–3060.
[3] W.-B. Yan, H. Fan, Single-photon quantum router with multiple output ports, Sci. Rep. 4 (2014) 345–349.
[4] L. Yang, S. Wang, Q. Zeng, Z. Zhang, T. Pei, Y. Li, L.-M. Peng, Efficient photovoltage multiplication in carbon nanotubes, Nat. Photonics (2011) 672–676.
[5] P.-Y. Lo, H.-N. Xiong, W.-M. Zhang, Breakdown of Bose-Einstein distribution in photonic, crystals, Sci. Rep. 5 (2015) 9423–9427.
[6] G. Baur, K. Hencken, D. Trautmann, S. Sadovsky, Y. Kharlov, Dense laser-driven electron sheets as relativistic mirrors for coherent production of brilliant X-ray and γ-ray beams, Phys. Rep. 364 (2002) 359.
[7] M.F. Hossain, Transforming dark photon into sustainable energy. Int. J. Energy Environ. Eng. (2018)https://doi.org/10.1007/s40095-017-0257-1.
[8] O. Khaselev, A monolithic photovoltaic-photoelectrochemical device for hydrogen production via water splitting, Science 280 (5362) (1998) 425–427.
[9] J. Masle, S.R. Gilmore, G.D. Farquhar, The ERECTA gene regulates plant transpiration efficiency in Arabidopsis, Nature 436 (2005) 866–870.
[10] T.D. Wheeler, A.D. Stroock, The transpiration of water at negative pressures in a synthetic tree, Nature 455 (2008) 208–212.
[11] M.F. Hossain, Solar energy integration into advanced building design for meeting energy demand, Int. J. Energy Res. 40 (2016) 1293–1300.
[12] J. Eichler, T. Stöhlker, Radiative electron capture in relativistic ion-atom collisions and the photoelectric effect in hydrogen-like high-Z systems, Phys. Rep. 439 (2007) 1.
[13] M.S. Tame, K.R. McEnery, Ş.K. Özdemir, J. Lee, S.A. Maier, M.S. Kim, Quantum plasmonics, Nat. Phys. (2013).
[14] A. Najjari, B. Voitkiv, A. Artemyev, A. Surzhykov, Simultaneous electron capture and bound-free pair production in relativistic collisions of heavy nuclei with atoms, Phys. Rev. A 80 (2009) 012701.
[15] N. Artemyev, U.D. Jentschura, V.G. Serbo, A. Surzhykov, Strong electromagnetic field effects in ultra-relativistic heavy-ion collisions, Eur. Phys. J. C 72 (2012) 1935.
[16] W. De Soto, S.A. Klein, W.A. Beckman, Improvement and validation of a model for photovoltaic array performance, Sol. Energy 80 (1) (2006) 78–88.
[17] M.F. Hossain, Design and construction of ultra-relativistic collision PV panel and its application into building sector to mitigate total energy demand, J. Build. Eng. 9 (2017) 147–154.
[18] M.F. Hossain, Application of advanced technology to build a vibrant environment on planet mars, Int. J. Environ. Sci. Technol. 14 (12) (2017) 2709–2720.
[19] J. Eichler, T. Stöhlker, Radiative electron capture in relativistic ion-atom collisions and the photoelectric effect in hydrogen-like high-Z systems, Phys. Rep. 439 (2007) 1.
[20] M.F. Hossain, Production of clean energy from cyanobacterial biochemical products, Strateg. Plan. Energy Environ. 3 (2016) 6–23.
[21] M.F. Hossain, Theory of global cooling, Energy Sustain. Soc. 6 (2016) 24.
[22] Q. Li, D.Z. Xu, C.Y. Cai, C.P. Sun, Recoil effects of a motional scatterer on single-photon scattering in one dimension, Sci. Rep. 3 (2013) 3144–3146.
[23] M.F. Hossain, Theoretical modeling for hybrid renewable energy: an initiative to meet the global power, J. Sustain. Energy Eng. 4 (2016) 5–36.
[24] A.R. Garrigues, L. Yuan, L. Wang, E.R. Mucciolo, D. Thompon, E. del Barco, C.A. Nijhuis, A single-level tunnel model to account for electrical transport through

This book belongs to Kitab Liaison (ocd1996@gmail.com) Copyright Elsevier 2023

single molecule- and self-assembled monolayer-based junctions, Sci. Rep. 6 (2016) 26517–26519.
[25] T. Pregnolato, E.H. Lee, J.D. Song, S. Stobbe, P. Lodahl, Single-photon non-linear optics with a quantum dot in a waveguide, Nat. Commun. 6 (2015) 8655–8659.
[26] Y.F. Xiao, et al., Asymmetric Fano resonance analysis in indirectly coupled microresonators, Phys. Rev. A 82 (2010) 065804.
[27] U. Becker, N. Grün, W. Scheid, K-shell ionisation in relativistic heavy-ion collisions, J. Phys. B: At. Mol. Phys. 20 (1987) 2075.
[28] W.M. Zhang, P.Y. Lo, H.N. Xiong, M.W.Y. Tu, F. Nori, General non-Markovian dynamics of open quantum systems, Phys. Rev. Lett. 109 (2012) 170402.
[29] S. Jasechko, Z.D. Sharp, P.J. Fawcett, Terrestrial water fluxes dominated by transpiration, Nature 496 (2013) 347–350.
[30] M.W.Y. Tu, W.M. Zhang, Non-Markovian decoherence theory for a double-dot charge qubit, Phys. Rev. B 78 (2008) 235311.
[31] Y. Zhu, X. Hu, H. Yang, Q. Gong, On-chip plasmon-induced transparency based on plasmonic coupled nanocavities, Sci. Rep. 9 (2014) 3455–3459.
[32] M.F. Hossain, Photonic thermal energy control to naturally cool and heat the building, Adv. Therm. Eng. 131 (2018) 576–586.
[33] M.F. Hossain, Green science: independent building technology to mitigate energy, environment, and climate change, Renew. Sust. Energ. Rev. 73 (2017) 695–705.
[34] J. Evaristo, S. Jasechko, J.J. McDonnell, Global separation of plant transpiration from groundwater and streamflow, Nature 525 (2015) 91–94.
[35] M.F. Hossain, Green science: decoding dark photon structure to produce clean energy. Energy Rep. (2018) https://doi.org/10.1016/j.egyr.2018.01.001.
[36] Masujima, Calculus of variations: applications, in: Applied Mathematical Methods in Theoretical Physics, Wiley, London, 2009.
[37] P. Arnold, Photon emission from ultrarelativistic plasmas, J. High Energy Phys. (2001) IOP, London.
[38] R.M. Maxwell, L.E. Condon, Connections between groundwater flow and transpiration partitioning, Science 353 (6297) (2016) 377–380.
[39] L. Langer, S.V. Poltavtsev, I.A. Yugova, M. Salewski, D.R. Yakovlev, G. Karczewski, T. Wojtowicz, I.A. Akimov, M. Bayer, Access to long-term optical memories using photon echoes retrieved from semiconductor spins, Nat. Photonics 8 (2014) 851–857.
[40] A. Reinhard, Strongly correlated photons on a chip, Nat. Photonics 6 (2011) 93–96.

This book belongs to Kitab Liaison (ocd1996@gmail.com) Copyright Elsevier 2023

This page intentionally left blank

This book belongs to Kitab Liaison (ocd1996@gmail.com)

Copyright Elsevier 2023

CHAPTER 6

Sustainable infrastructure systems

Introduction

The urban area massively depends on transportation infrastructure networks, which are primarily constructed with concrete and asphalt. They do not have enough vegetation to absorb the heat caused by this asphalt and concrete [1, 2]. Recent research found that transportation infrastructure on Earth approximately 0.9% of the total planetary surface area of 196.9 million mi^2 which is equivalent to 1.77 million miles square infrastructure on Earth which causing nearly 6% of global warming by reflecting heat (albedo) back to the space [3, 4]. On the other hand, conventional energy utilization for transportation sectors is not only costly, but also causes adverse environmental impacts [5, 6]. Several of studies have been performed to understand long-term climate variations by conventional energy utilization from the transportation sectors that is causing nearly 28% global energy consumption. To mitigate the transportation infrastructure crisis and its adverse environmental impacts, I propose a new technology called a maglev transportation infrastructure system for building a better transportation infrastructure system.

A recent study by Cai and Chen described the dynamic characteristics, magnetic suspension systems, vehicle stability, and suspension control laws of maglev/guideway coupling systems about the maglev transportation system. However, the commercial application of this research modeling, considering the lifecycle cost analysis, technology implementation and infrastructure development, did not show any possibility. Therefore, the approach of this research is to apply the maglev transportation infrastructure commercially for confirming a greener and cleaner transportation infrastructure system where all vehicles shall run just over 2 ft above the Earth's surface at a flying stage by the act of a propulsive and impulsive superconducting force. Because the vehicle will run by electromagnetic force, it will not require any energy while running over the maglev. To mitigate energy consumption when the vehicle needs to run outside the maglev area, additional technology has also been proposed to implement wind energy while the vehicles are in motion as a backup energy source. Thus, detailed

Sustainable Development for Mass Urbanization
https://doi.org/10.1016/B978-0-12-817690-0.00006-3
© 2019 Elsevier Inc.
All rights reserved.

This book belongs to Kitab Liaison (ocd1996@gmail.com)
Copyright Elsevier 2023

mathematical modeling using MATLAB Simulink software has been implemented for this wind energy utilization for the vehicles by performing turbine and drive-train modeling. A series research effort has been performed recently on climate science and found that currently 402 ppm CO_2 presents in atmosphere that causing global warming which required to cut down 300 ppm CO_2 to confirm global cooling at comfortable stage. Once a maglev transportation infrastructure system implemented throughout the world, it will reduce 34% of the CO_2 per year. Thus, it will take only $\{\int_{300}^{402}(1-0.34)dx\} = 67.32$ years to cool the atmosphere, resulting in no more climate change after 68 years. It will be the most innovative technology in modern science to mitigate the cost and decrease global warming dramatically.

Simulations and methods

In order to present maglev transportation infrastructure modeling, I have formulated the following calculation by using MATLAB software in terms of (1) A guideway model system by adopting the Bernoulli-Euler beam equation of series of simply supported beams; and (2) Calculation of magnetic forces for levitation and lateral guidance with allowable levitation and guidance distances, considering the lateral vibration control LQR algorithm, tuning parameters, and maglev dynamics.

Guideway model

To prepare the guideway modeling considering the free body diagram (Fig. 6.1), I have considered multiple magnets with equal intervals (d) that are to be traveling at various levels of speed v, where m = beam weight, c = damping coefficient, EI_y = flexural rigidity in the y direction, EI_z = flexural rigidity in the z direction, l = car length, m_w = lumped mass of magnetic wheel, m_v = distributed mass of the rigid car body, and $\theta_{i=\ x,y,z}$ = midpoint rotation components of the rigid car body. Considering these, I have formulated the equations of motion for the jth guideway girder carrying a moving maglev vehicle suspended by multiple magnetic forces as follows:

$$m\ddot{u}_{y,j} + c_y\dot{u}_{y,j} + EI_y u''''_{y,j} = \sum_{k=1}^{K}\left[G_{y,k}\left(i_k, h_{y,k}\right)\varphi_j(x_k, t)\right] \tag{6.1}$$

$$m\ddot{u}_{z,j} + c_z\dot{u}_{z,j} + EI_z u''''_{z,j} = p_0 - \sum_{k=1}^{K}\left[G_{z,k}\left(i_k, h_{z,k}\right)\varphi_j(x_k, t)\right] \tag{6.2}$$

This book belongs to Kitab Liaison (ocd1996@gmail.com) Copyright Elsevier 2023

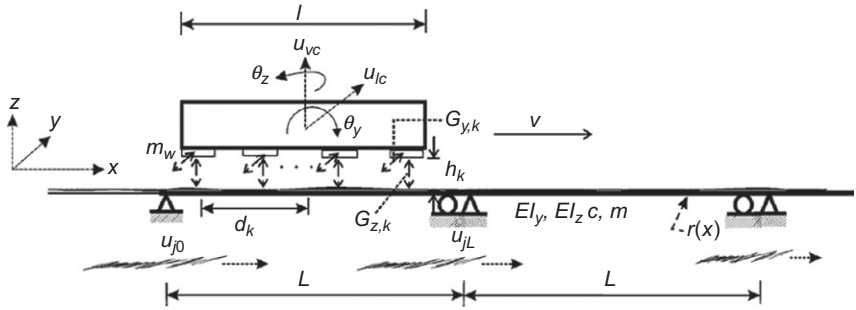

Fig. 6.1 A free body diagram shows the maglev guideway versus the vehicle force, considering the weight and motion where the superconducting guideway is below the vehicle body. It is functioned by a series of equidistant concentrated masses to levitate the vehicle to the superconducting guideway beam; the maglev bar gets stimulated by the lateral multisupport motion, which is induced by the superconducting force to allow traveling in a longitudinal direction.

and

$$\varphi_j(x_k, t) = \delta(x - x_k)\left[H\left(t - t_k - \frac{(j-1)L}{v}\right) - H\left(t - t_k - \frac{jL}{v}\right)\right] \tag{6.3}$$

together with the following boundary conditions with lateral (y-direction) support movements:

$$\begin{aligned} u_{y,j}(0, t) &= u_{yj0}(t),\ u_{y,j}(L, t) = u_{yjL}(t) \\ EI_z u''_{z,j}(0, t) &= EI_z u''_{z,j}(L, t) = 0 \end{aligned} \tag{6.4}$$

$$\begin{aligned} u_{z,j}(0, t) &= u_{z,j}(L, t) = 0 \\ EI_y u''_{y,j}(0, t) &= EI_y u''_{y,j}(L, t) = 0 \end{aligned} \tag{6.5}$$

where $(\alpha)' = \partial(\alpha)/\partial x$, $(\alpha) = \partial(\alpha)/\partial t$, $u_{z,j}(x,t)$ = vertical deflection of the jth span, $u_{y,j}(x,t)$ = lateral deflection of the jth span, L = span length, K = number of magnets attached to the rigid levitation frame, $\delta(\alpha)$= Dirac's delta function, $H(t)$ = unit step function, $k = 1, 2, 3, \ldots, K$th moving magnetic wheel on the beam, $t_k = (k-1)d/v$ = arrival time of the kth magnetic wheel into the beam, x_k = position of the kth magnetic wheel on the guideway, and $(G_{y,k}, G_{z,k})$ = lateral guidance and uplift levitation forces of the kth lumped magnet in the vertical and lateral directions [7, 8].

Magnetic forces of uplift levitation and lateral guidance

Because the maglev vehicle will run over the guideway by a superconducting force with lateral ground motion (as shown in Fig. 6.1), thus guidance

This book belongs to Kitab Liaison (ocd1996@gmail.com) Copyright Elsevier 2023

forces tuned by the maglev system need to control the lateral motion of the moving maglev vehicle. Therefore, this study adopts the lateral guidance force ($G_{y,k}$) and the uplift levitation force ($G_{z,k}$) to keep and guide the k-th magnet of the vehicle; those could be expressed as

$$G_{y,k} = K_0 \left(\frac{i_k(t)}{h_{z,k(t)}} \right)^2 K_{k,z} \tag{6.6}$$

$$G_{y,k} = K_0 \left(\frac{i_k(t)}{h_{z,k(t)}} \right)^2 \left(1 - K_{y,k}\right) \tag{6.7}$$

where $\kappa\ y,k$ and $\kappa\ z,k$ represent induced guidance factors and they are given by

$$K_{y,k} = \frac{\chi_k \times h_{y,k}}{W(1+\chi_k)}, K_{z,k} = \frac{\chi_k \times h_{y,k}}{W(1+\chi_k)} \tag{6.8}$$

In Eqs. (6.6), (6.7), $k_0 = \mu_0 N_0^2 A_0/4 =$ coupling factor, $\chi_k = \pi h_{y,kz,k}/4h$, $W =$ pole width, $\mu =$ vacuum permeability, $N_0 =$ number of turns of the magnet windings, $A_0 =$ pole face area, $i_n\ (t) = i_0 + \iota_n\ (t) =$ electric current, $\iota_n\ (t) =$ deviation of current, and (i_0, h_{y0}, h_{z0}) = desired current and air gaps around a specified nominal operating point of the maglev wheels at *static* equilibrium. And the uplift levitation ($h_{y,k}$) and lateral guidance ($h_{z,k}$) gaps are respectively given by

$$h_{y,k}(t) = h_{y0} + u_{l,k}(t) - u_{y,j}(x_k), u_{l,k}(t) = u_{lc}(t) + d_k\theta_z \tag{6.9}$$

$$h_{z,k}(t) = h_{z0} + u_{v,k}(t) - u_{z,j}(x_k) + r(x_k), u_{v,k}(t) = u_{vc}(t) + d_k\theta_y \tag{6.10}$$

where ($u_{l,k}$, $u_{v,k}$) = displacements of the kth magnetic wheel in the y and z directions, (u_{lc}, u_{vc}) = midpoint displacements of the rigid car, (θ_y,θ_z) = midpoint rotations of the rigid car, $r(x)$ = irregularity of the guideway, and d_k = location of the kth magnetic wheel to the midpoint of the rigid beam. As indicated in Eqs. (6.6)–(6.8), the motion-dependent nature and guidance factors ($\kappa_{y,k}$,$\kappa_{z,k}$) dominate the control forces of the maglev vehicle guideway system. Next, the equations of motion of the 4-DOFs rigid maglev vehicle (see Fig. 6.1) are written as

$$M_0\ddot{u}_{lc} = g(t) + \sum_{k=1}^{K} G_{y,k}, I_T\ddot{\theta}_Z = g(t)\,x\,l + \sum_{k=1}^{K} \left[G_{y,k}d_k\right] \tag{6.11}$$

$$M_0\ddot{u}_{vc} = p_0 + \sum_{k=1}^{K} G_{z,k}, I_T\ddot{\theta}_y = -\sum_{k=1}^{K} \left[G_{z,k}d_k\right] \tag{6.12}$$

This book belongs to Kitab Liaison (ocd1996@gmail.com) Copyright Elsevier 2023

in which $M_0 = m_v l + K m_w$ = lumped mass of the vehicle, $g(t)$ = control force to tune the lateral response of the maglev vehicle, I_T = total mass moment of inertia of the rigid car, and $p_0 = M_0 g$ = lumped weight of the maglev vehicle.

Wind energy modeling for the vehicles

Though the vehicle will run by electromagnetic force, a wind turbine generator is to be used for powering the vehicle as an additional source of energy where the maglev system is not available. Thus, the model is developed by a doubly fed induction generator (DFIG) for producing electricity for transportation vehicles [9–11]. The fundamental equation governing the mechanical power of the wind turbine is

$$P_w = \frac{1}{2} C_p(\lambda, \beta) \rho A V^3 \tag{6.13}$$

where ρ is the air density (kg/m3), C_p is the power coefficient, A is the intercepting area of the rotor blades (m^2), V is the average wind speed (m/s), and λ is the tip speed ratio [12]. The theoretical maximum value of the power coefficient C_p is 0.593; C_p is also known as Betz's coefficient. Mathematically,

$$\lambda = \frac{R\omega}{V} \tag{6.14}$$

R is the radius of the turbine (m), ω is the angular speed (rad/s), and V is the average wind speed (m/s). The energy generated by wind can be obtained by

$$Q_w = P \times (\text{Time})[\text{kWh}] \tag{6.15}$$

It is well known that wind velocity cannot be obtained by a direct measurement from any particular motion [7, 13]. In data taken from any reference, the motion needs to be determined for that particular motion; then, the velocity needs to be measured at a lower motion.

$$v(z)\ \ln\left(\frac{Z_r}{Z_o}\right) = v(Z_r)\ \ln\left(\frac{Z}{Z_0}\right) \tag{6.16}$$

where Z_r is the reference height (m), Z is the height at which the wind speed is to be determined, Z_0 is the measure of surface roughness (0.1–0.25 for crop land), $v(z)$ is wind speed at height z (m/s), and $v(z_r)$ is wind speed at

This book belongs to Kitab Liaison (ocd1996@gmail.com) Copyright Elsevier 2023

the reference height z (m/s). The power output in terms of the wind speed shall be estimated using the following equation:

$$P_w(v) = \begin{cases} \dfrac{v^k - v_C^k}{v_R^k - v_C^k} \cdot P_R & v_C \le v \le v_R \\ P_R & v_R \le v \le v_F \\ 0 & v \le v_C \text{ and } v \ge v_F \end{cases} \tag{6.17}$$

where P_R is rated power, v_C is the cut-in wind speed, v_R is the rated wind speed, v_F is the rated cut-out speed, and k is the Weibull shape factor [14]. When the blade pitch angle is zero, the power coefficient is maximized for an optimal TSR [15]. The optimal rotor speed is to be calculated by

$$\omega_{\text{opt}} = \frac{\lambda_{\text{opt}}}{R} V_{wn} \tag{6.18}$$

which will give

$$V_{wn} = \frac{R\omega_{\text{opt}}}{\lambda_{\text{opt}}} \tag{6.19}$$

where ω_{opt} is the optimal rotor angular speed in rad/s, λ_{opt} is the optimal tip speed ratio, R is the radius of the turbine in meters, and V_{wn} is the wind speed in m/s.

The turbine speed and mechanical powers are depicted in the following graph (Fig. 6.2) with increasing and decreasing rates of wind speed while the vehicle is in motion. When the wind is steady, the persistence forecasts yield good results. When the wind speed is increased rapidly, sudden "ramps" in power output are generated, which is of tremendous benefit for capturing energy.

Wind energy storage in battery system

A standard Simulink/Sim power system has been calculated by using MATLAB-Simulink for the wind energy conversion that is to be stored in the circuit-implemented inverter as a storage buffer. All the electricity is to be supplied through the battery according to Peukert's Law to start the engine and to be used when the vehicle is not in motion.

Design of traffic control

Though an underground maglev system has the capability to allow runs up to 580 kph, the vehicles' high speed shall be calculated based on traffic flow,

This book belongs to Kitab Liaison (ocd1996@gmail.com) Copyright Elsevier 2023

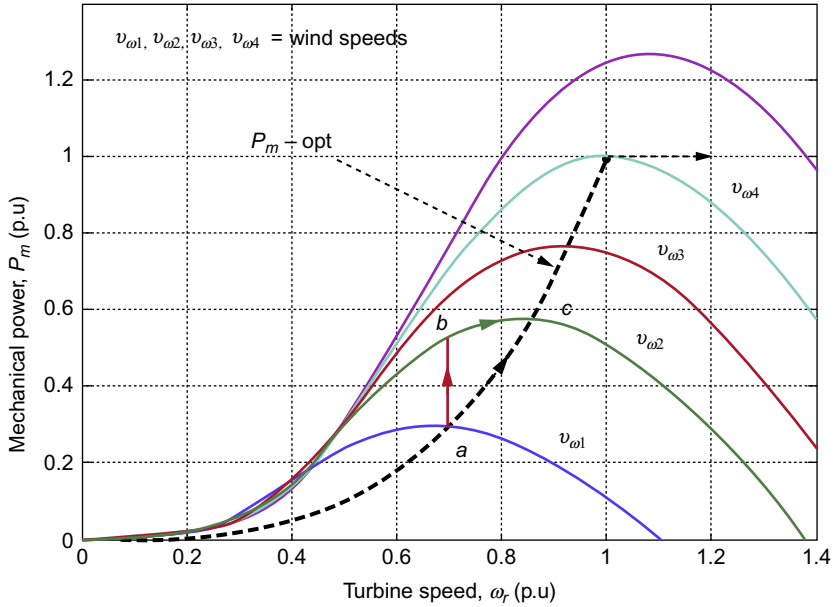

Fig. 6.2 Relationship between mechanical power generation and turbine speeds at different wind speeds for implementation in a car.

composition, volume, the number and location of access points, and the local environment. Also, a sufficient number of lanes will be importantly allotted considering Greenshield's following road and highway capacity analysis (Fig. 6.3).

Since the maglev technology is invisible, thus, to alert drivers and pedestrian, the maglev roads, highways, and exits are to be constructed by landscaping by covering the guideway by herb (green grass) and in between lanes at least 2 ft to be left blank (no landscaping) in order to differentiate the lanes.

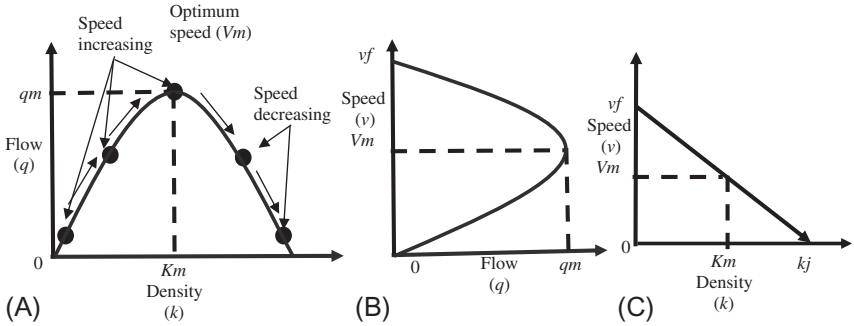

Fig. 6.3 Greenshield's fundamental diagrams (A) speed versus vehicle density, (B) flow versus vehicle density, and (C) speed versus flow analysis.

This book belongs to Kitab Liaison (ocd1996@gmail.com) Copyright Elsevier 2023

Results and discussion

Based on the mathematical modeling described above, I have performed a load resistant factor design (LRFD) calculation considering the following equation and selected a W24 × 84 beam, which is the continuous maglev underground run (metal track guideway) that needs to be structurally sound to carry enough current, load, and levitation force of the vehicles.

$$Fy \propto \frac{nl^2}{h} \tag{6.20}$$

$$Fx \propto \frac{-1}{ktv\varkappa} \; Fx \propto \frac{-nl^2}{h} \tag{6.21}$$

Where Fy is the vehicle weight, n is the total number of coils in the maglev, l is the current on each coil, h is the height of levitation, t is the thickness of the conduction track, and k is the conductivity of the track.

To construct a maglev guideway just 2 ft below the Earth's surface, it will be necessary to have a U-shaped cross-section to fix the pole position. A naturally heavy-duty waterproofing membrane is to be used to protect the maglev underground runs from floods and moisture. It is well researched that the propulsion coils run in elliptical loops along both walls of the guideway, generating a magnetic force when electricity runs through them. So, the levitation and guidance coils will be formed that will create their own magnetic force once the applied superconducting magnets pass on it, where propulsion and levitation are the key factors to run the vehicle. In propulsion, as the direction of the current charges back and forth in the propulsion coils above the wall of the guideway, the north and south poles will reserve repeatedly, shall propelling the vehicle by alternating force of attracting and repulsion (Fig. 6.4). In levitation as the vehicle passes, an electric current is induced in the coil along the guideway and the vehicle will be levitated by the force of attraction, which will pull up on the magnet in the vehicle, as well as by repulsion, which will push up on the magnet [8, 16].

To create levitation and lateral balance in the vehicle, an electromagnetic induction is to be used. To confirm the most efficient and economical way to produce the powerful magnetic field by using the superconducting coils, I have assumed that the permanent currents of about 700,000 amperes go through these superconducting coils [17], hence creating a strong magnetic field of almost 5 teslas, that is, 100,000 times stronger than the Earth's magnetic field, by implementing the following block diagram (Fig. 6.5).

This book belongs to Kitab Liaison (ocd1996@gmail.com) Copyright Elsevier 2023

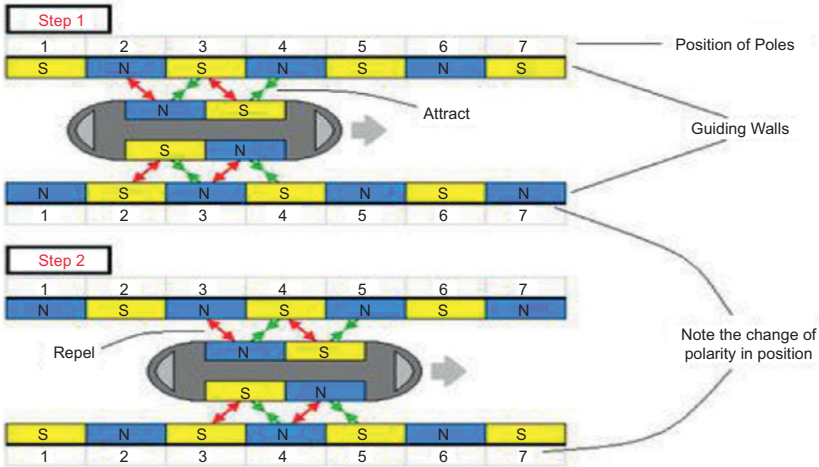

(A)

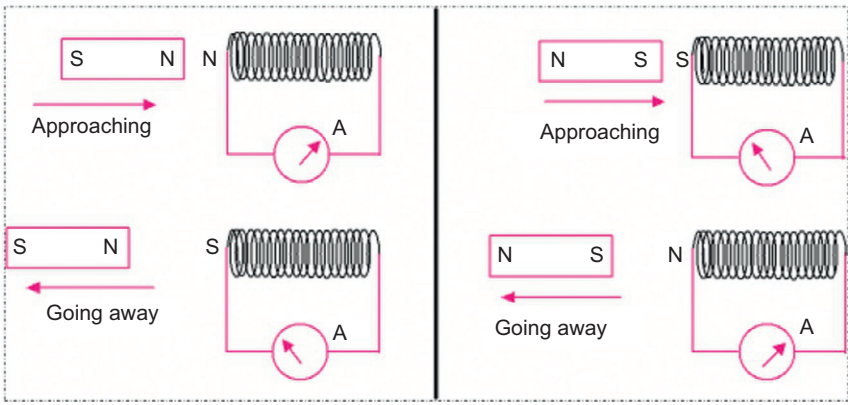

(B)

Fig. 6.4 The polarization of the coil in different cases: (A) Schematic diagram of the director of the running vehicle (must be construction with magnet as shown on this diagram) on maglev propulsion via propulsion coils. (B) Near the receding S-pole, becomes an N-pole to oppose the going away of the bar magnet's S-pole.

It can be explained that when an electric current flows through the propulsion coils, a magnetic field is produced. The forces of attraction and repulsion between the coils and the superconducting magnets on the vehicle propel the vehicle forward in a flying stage up to 4 ft high, where 2 ft shall be considered underground cover and the other 2 ft just over the Earth's surface (Fig. 6.6). The vehicle's speed is to be adjusted by altering the timing of the

This book belongs to Kitab Liaison (ocd1996@gmail.com) Copyright Elsevier 2023

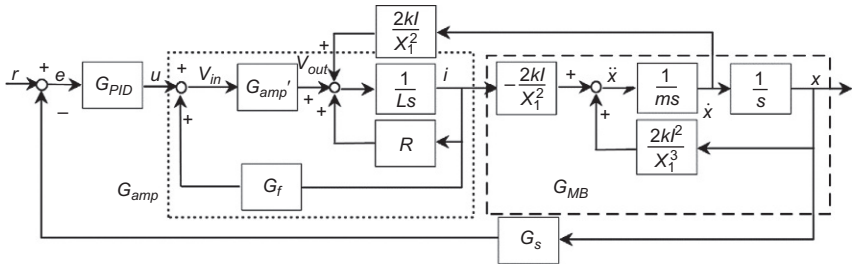

Fig. 6.5 Block diagram to control the mathematically modeled magnetic bearing system, a process to design the driver to operate the electromagnet. Here is the method to determine the peripheral device values of the linear amplifier circuit that has the desired output by applying a generic algorithm and the method to identify the magnetic bearing system.

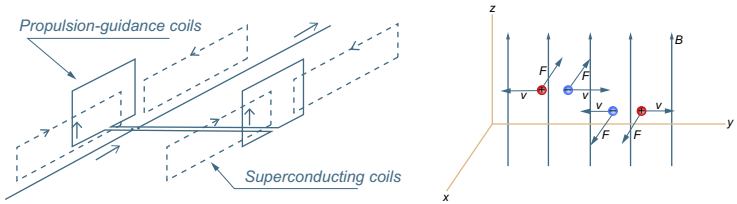

Fig. 6.6 The maglev vehicle's force and directional diagram as shown by propulsion guidance coils and superconducting coils.

polarity shift in the propulsion coils' magnetic field between north and south with the possibility of a maximum speed of 580 kph. As the vehicle passes just 2 ft above the guideway (one foot from the Earth's surface), an electric current is induced in the levitation and guidance coils, creating opposite magnetic poles in the upper and lower loops. The upper loops become the polar opposite of the vehicle's magnets, producing attraction that pulls the vehicle up. The lower loops have the same pole as the magnets. This generates repulsion, which pushes the vehicle in the same direction up. The two forces combine to levitate the vehicle while maintaining its lateral balance between the walls of the guideway.

Subsequently, a niobium-titanium alloy is to be used to create superconducting magnets for the maglev, but to reach superconductivity, they must be kept cold. In order to keep the alloy cool, liquid helium is to be used at a temperature of −269°C because the alloy retains superconductivity at

This book belongs to Kitab Liaison (ocd1996@gmail.com) Copyright Elsevier 2023

temperatures up to minus −263°C, although the maglev system can operate better at 6°C to produce sufficient magnetic force.

In addition to the underground maglev, the wind turbine generation system for the backup energy source is to be implemented by the optimal operation of the whole system. This is based on a robustness test, performed by adding a wind speed signal and power coefficient.

This mechanism permits application of the wind profile is considered to be a wind speed signal with a mean value of 8 m/s and a rated wind speed of 10 m/s; the whole system is tested under standard conditions with a stator voltage of approximately 50% for 0.5 s between 4 and 4.5 s, approximately 25% between 6 and 6.5 s, and 50% between 8 and 8.5 s (Fig. 6.7). Thus, the machine is considered to be functioning in ideal conditions (no perturbations and no parameter variations). Moreover, to guarantee a unity power factor at the stator side, the reference for the reactive power is to be set to zero [18]. As a result of increasing wind speed, the generator shaft speed achieved maximum angular speed by tracking the maximum power point speed. Thus, the wind turbine always works optimally because the pole placement technique is to be used to design the tracking control [4]. Consequently, decoupling among the components of the rotor current was also performed to confirm that the control system worked effectively. The bidirectional active and reactive power transfer between the rotor and power system is exchanged by the generator according to the super synchronous

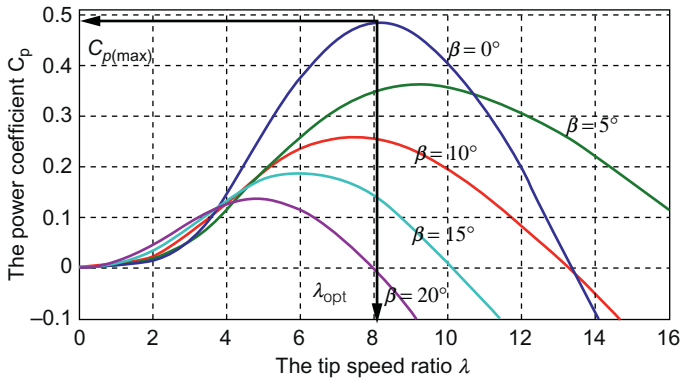

Fig. 6.7 The maximum values of C_p are achieved for the curve associated with $\beta = 2°$. From this curve, the maximum value of C_p ($C_{p,max} = 0.5$) is obtained for $\lambda_{opt} = 0.91$. This value (λ_{opt}) represents the optimal speed ratio.

This book belongs to Kitab Liaison (ocd1996@gmail.com) Copyright Elsevier 2023

operation, achieving the nominal stator power, and the reactive power can be controlled by the load-side converter to obtain the unit's power factor to generate energy for powering vehicles.

Construction cost estimate comparison

An order of magnitude cost estimate was performed by using HCSS (Heavy Bid) software with the standard union rate of New York state locals with a project of 10% general condition, 10% overhead and profit, and 3% contingency over the hard cost of labor, materials, and equipment. A comparison was made between the maglev infrastructure and a traditional infrastructure system for a sample of 100 miles long and 128 ft wide (12 ft wide per four lanes in each directions, a two-sided 10-foot service space, and a six-foot median in the center of the road). In order to determine that the underground guideway (w24 × 84) will last long, I have calculated again the LRFD to provide shoring for both sides for the entire 100 miles in length and 128 ft in width for construction costs. This takes into consideration the standard excavation up to 6 ft, with appropriate shoring with a minimum embedment depth L4 of 5 ft and a standard soil pressure $\Upsilon_s = 120\ \text{lbf/ft}^3$, an angle of pressure $\Phi = 21^0$, and the soil pressure coefficient $c = 800\ \text{lbf/ft}^2$. To prepare the conceptual estimate, we need to determine the length of soldier piles. It has been counted six-foot OC (on center) soldier piles at both sides by illustration, and by using the following LRFD method that the soldier piles must be set at to support the necessary excavation and/or Earth pressure against collapse.

$$\text{Active Earth pressure } K_a = \tan^2\left(45° - \frac{\Phi}{2}\right) \tag{6.22}$$

$$\text{Passive Earth pressure } K_b = \tan^2\left(45° + \frac{\Phi}{2}\right) \tag{6.23}$$

Use Eqs. (6.22), (6.23) to find the lateral Earth pressure the solid piles must support.

$$\begin{aligned} P_{EM} &= \Upsilon_s h\, k_{a,\text{piles}} \\ &= \left(120\frac{\text{lbf}}{\text{ft}^3}\right)(6.0)\tan^2\left(45° - \frac{21°}{2}\right) \\ &= 340.128\,\text{lbf/ft}^2 \end{aligned}$$

To determine the type of steel beams required for the soldier piles, we have taken the bending moments about the tributary area of the piles.

This book belongs to Kitab Liaison (ocd1996@gmail.com) Copyright Elsevier 2023

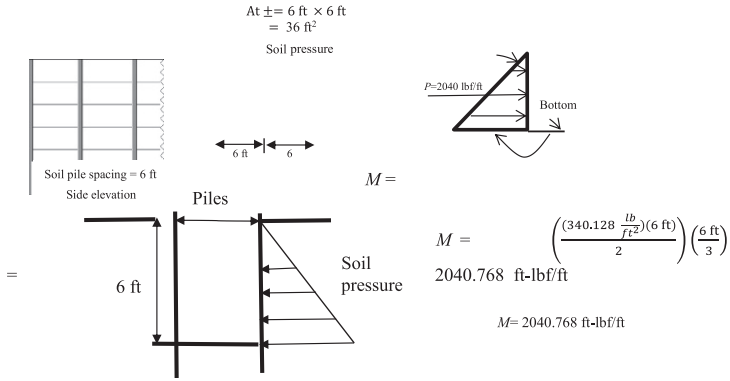

The moment is a distributed moment applied to the base of the tributary area of each soldier pile. Therefore, the moment is 2040.768 ft-lbf per foot. The total moment on the soldier pile (at the base) is

$$
\begin{aligned}
M_0 &= M\,(6\,\text{ft}) \\
&= \left(2040.768\,\frac{\text{ft-lbf}}{\text{ft}}\right)(6\,\text{ft}) \\
&= 12{,}244.61\,\text{ft-lbf}
\end{aligned}
$$

Now,

$$
\begin{aligned}
Z_{\text{req}} = \frac{M_0}{\Phi b\,F\gamma} &= \frac{\left(12\,\dfrac{\text{in}}{\text{ft}}\right)(12{,}244.61\,\text{ft-lbf})}{(0.9)\left(50{,}000\,\dfrac{\text{lbf}}{\text{in}^2}\right)} \\
&= 3.2\,\text{in}^3
\end{aligned}
$$

From the AISC tables, the soldier piles are selected to be W12 × 26, and the perpendicular support w8 × 12 members are 6 ft long.

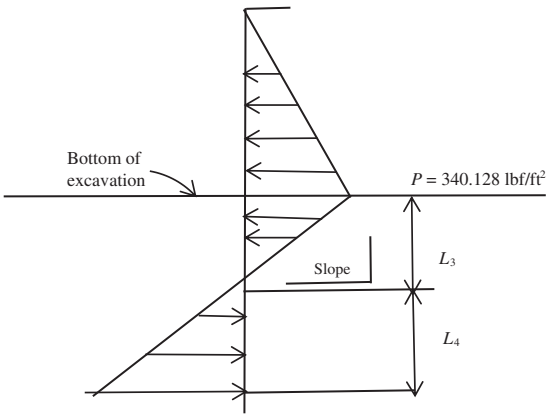

This book belongs to Kitab Liaison (ocd1996@gmail.com)
Copyright Elsevier 2023

Then we have determined the depth required below subgrade by calculating the passive Earth pressure coefficient using Eq. (6.23)

$$K_p = \tan^2\left(45° + \frac{\Phi}{2}\right)$$
$$= \tan^2\left(45° + \frac{21°}{2}\right)$$
$$= 2.12$$

Then we have calculated the active Earth pressure coefficient using Eq. (6.22)

$$K_a = \tan^2\left(45° + \frac{\Phi}{2}\right)$$
$$= \tan^2\left(45° + \frac{21°}{2}\right)$$
$$= 0.4724$$

In order to determine the slopes of the excavation, depth is required because below the bottom of the excavation, both pressures are considered to be passive and have the same slope. The slope of the pressure profile above the reversal point is calculated from the standard equation for the slope, using L_3 as the rise and $\Upsilon h k_a$ as the run (a value equal to the lateral Earth pressure, expressed this way for the purposes of cancelation). Thus, the slope of the pressure profile below the reversal point can be calculated similarly, using L_4 as the rise and the product of $\Upsilon L_4 k_p$ as the run. Because the slopes are the same, the two equations can be equated. Rearranging to solve for L_3,

$$\frac{L_3}{\Upsilon h k_a} = \frac{L_4}{\Upsilon L_4 k_p}$$
$$L_3 = \frac{h k_a}{k_p} = \frac{(6\,\text{ft})(0.4724)}{2.12}$$
$$= 1.337\,\text{ft}$$

The necessary embedment depth is 1.337 ft + 5 ft = 6.337 ft

The total required soldier pile length is = 6.337 ft + 6 ft = 12.337 ft (13 ft assumed)

So, I have determined that the soldier pile (W12 × 26) should be 13 ft long, and the perpendicular support (w8 × 12) should be 6 ft long for structurally sound maglev construction.

This book belongs to Kitab Liaison (ocd1996@gmail.com) Copyright Elsevier 2023

Construction cost estimate comparison

An order of magnitude cost estimate was performed by using HCSS (Heavy Bid) software with the standard union rate of New York state locals with a project of 10% general condition, 10% overhead and profit, and 3% contingency over the hard cost of labor, materials, and equipment. A comparison was made between the maglev infrastructure and a traditional infrastructure system for a sample of 100 miles long and 128 ft wide (12 ft wide per four lanes in each directions, a two-sided 10-foot service space, and a six-foot median in the center of the road). To construct the long-lasting and sophisticated underground maglev, I have performed a load resistant factor design (LRFD) calculation and selected a W24 × 84 beam so that the continuous maglev underground runs (structural beams) are structurally sound. Then I have calculated the required shoring concept for 100 miles long and 128 ft wide construction cost considering standard excavation up to 6 ft, with appropriate shoring with minimum embedment depth $L4$ of 5 ft and standard soil pressure $\Upsilon_s = 120$ lbf/ft^3, angle of pressure $\Phi = 21^0$, and the soil pressure coefficient $c = 800$ lbf/ft^2 in order to determine the length of the soldier piles. So, I have calculated by using LRFD methods again that the soldier pile (W12 × 26) should be 13 ft long, and the perpendicular support (w8 × 12) should be 6 ft long as the support for maglev construction.

Cost of maglev infrastructure

The proposed maglev infrastructure, therefore, requires shoring, excavation, structural steel, and concrete operation. Therefore, I have calculated the estimate considering the following components:

Shoring at 13 ft deep with w24 × 26 steel soldier piles at 6 ft OC both side \$2/lf; top rail w8 × 12 both sides \$2/lf; 6 ft length w8 × 12 perpendicular support 20 OC \$2.lf; and protection board 1,372,800 ft 2 both side at \$4/ft^2 and thus the total cost would be \$23,724,800.

Excavation $(52{,}800'_{\text{length}} \times 128_{\text{width}} \times 6_{\text{deep}} \times 1.3_{\text{fluff factor}})/27$ is 19,524,266.67 yd^3 at \$56/yd^3 cost for digging, stockpiling, and backfilling and the total cost would be \$1,093,358,933.

Cost of materials: A 100-miles maglev system with structural steel (w24 × 84) support for eight lanes is \$354,816,000; 2 × 2 structural concrete strip footing at \$150/yd^3 is \$93,866,666; reinforcement bar at 100 lb/yd^3 and cost is \$62,577,778; concrete form at \$2/ft^2 is \$16,896,000 and thus, the total cost of material is \$528,156,445.

This book belongs to Kitab Liaison (ocd1996@gmail.com) Copyright Elsevier 2023

Cost of labor: 200 iron workers for 2704 working days at \$100/h; 100 concrete cement workers for 2704 working days at \$90/h; 100 laborers for 2704 working days at \$70/h; 50 equipment operators for 2704 working days at \$100/h and thus, the total labor cost is \$886,912,000, considering a standard eight-hour day.

Equipment cost: 10 small tools rented at \$1000/day; 10 small tools rented at \$250/day; 271 concrete pumps at \$2000/each, and thus the total equipment cost is \$34,342,000.

Other costs: Engineering service at \$5/ft^2; survey team at \$4400/day for each working day; and thus the total cost is \$349,817,600. The net construction cost by adding 10% general condition, 10% overhead and profit, and 3% contingency into the excavation, material, labor, equipment, and other costs would be \$3,587,063,487.

Cost of traditional road infrastructure

A typical highway consists of an 8-inch asphalt surface course, a 4-inch binder course, a 4-inch base course, and a 12-inch aggregate with standard wire mesh or framing. Therefore, we have calculated the estimate considering the following components:

Excavation $(5{,}2800_{\text{length}} \times 128_{\text{width}} \times 2.33_{\text{deep}} \times 1.3_{\text{fluff factor}})/27$ is 7,581,924 yd^3 at \$56/yd^3 cost for digging, stockpiling, and backfilling and the total cost would be \$424,587,744.

Cost of materials: \$50/yd^3; 4-foot base course is 834,370 yd^3 at \$50/yd^3; wire mesh or framing is $(528{,}000 \times 128)$ at \$1/ft^2, and 12-inch subbase aggregate is 2,503,111 yd^3 at \$25/yd^3 and thus, the total cost of materials is \$380,472,775.

Cost of labor: 200 asphalt cement workers for 2704 working days at \$100/h; 200 labor foreman for 2704 working days at \$100/h; 200 laborers for 2704 working days at \$70/h; 200 equipment operators for 2704 working days at \$100/h; 100 truck drivers for 2704 working days at \$100/h; 200 small roller engineers for 2704 working days at \$100/h and thus, the total cost is \$2,249,728,000.

Equipment cost: 200 roller rented at \$1000/week; 200 millings rented at \$10,000/week; 100 trucks rented at \$500/week, and thus the total cost is \$502,171,429.

Other costs: Detailing and shop drawing at \$10/ft^2; engineering service at \$5/ft^2; survey team at \$4,400/day for each working day; banking service

This book belongs to Kitab Liaison (ocd1996@gmail.com) Copyright Elsevier 2023

of 301,037 yd^3 at \$1000/yd^3; maiden concrete divider is 106,468 yd^3 at \$818/yd^3, and thus the total cost is \$1,326,694,600. The net construction cost by adding 10% general condition, 10% overhead and profit, and 3% contingency into the excavation, material, labor, equipment, and other costs would be \$6,805,115,863.

Cost savings

In this article, I have calculated cost savings by using a standard 100-mile highway of 128 ft wide (12 ft wide with four lanes in each direction, a two-sided 10-foot service space, and a six-foot median in the center of the road) as an experimental tool to compare construction costs between conventional and maglev infrastructure systems. The total cost estimate for traditional infrastructure is \$6,805,115,863 and the maglev infrastructure system cost is only \$3,587,063,487 for the same 100 miles of highway, for a net cost saving of \$3,218,052,377 (Table 6.1). Consequently, the cost will be reduced by nearly 50% once the maglev infrastructure system is used for the construction of an invisible infrastructure that is also benign to the environment.

Table 6.1 This cost comparison is prepared by using HCSS cost data 2019 for material by utilizing selective manufacturers and labor rates in accordance with international of union wage of each specified trade workers considering US location.

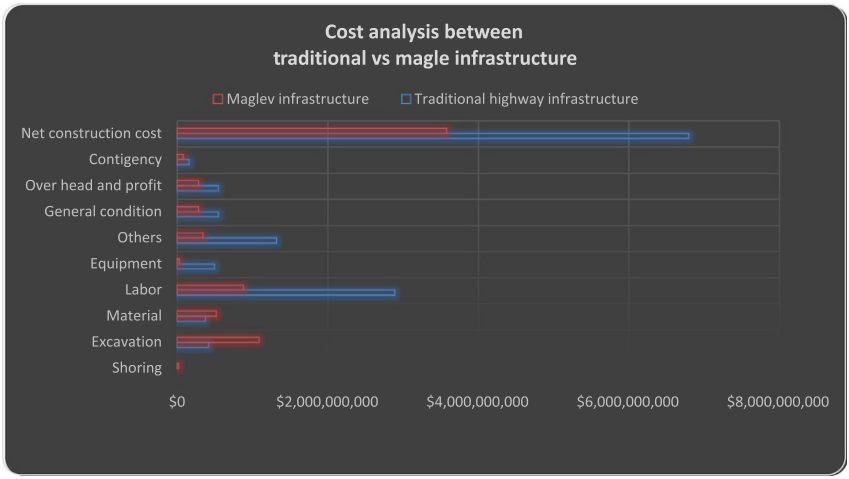

The equipment rental cost is estimated from the current rental market in conjunction with the standard practice of construction.

This book belongs to Kitab Liaison (ocd1996@gmail.com)
Copyright Elsevier 2023

Conclusions

Conventional transportation infrastructure construction and maintenance throughout the world are not only expensive, but also consumes 5.6×10^{20} J/year (560 EJ/year) of fossil fuel each year which indeed dangerous of a cliché when discussing about climate [11, 19]. In order to mitigate this issue, better infrastructure transportation planning needs to be achieved where environmental sustainability and climate adaptation are confirmed to create more resilient and vibrant communities. Interestingly, the *invisible infrastructure transportation* technology proposed in this article for an urban infrastructure transportation system will be the emergent technology in modern science. This is because the technology is cheaper, and it will run by repulsive force and attractive force at the levitating stage while on the maglev system and will run by air (wind energy) while it is in a nonlevitated area without consuming fossil fuel. Indeed, the maglev infrastructure transportation system would be the most innovative technology ever to control the infrastructure, transportation, energy, and global warming crises.

Acknowledgments

This research was supported by Green Globe Technology under support of RD-02017-10. Any findings, conclusions, and recommendations expressed in this paper are solely those of the author and do not necessarily reflect those of Green Globe Technology.

References

[1] K.J. Astrom, T. Hagglund, Automatic Tuning of PID Controllers, Instrument Society of America, Research Triangle Park, NC, 1988.
[2] J.D. Yau, Lateral vibration control of a low-speed maglev vehicle in cross winds, Wind Struct. 15 (3) (2012) 263–283.
[3] R. Chakib, A. Essadki, M. Cherkaoui, Modeling and control of a wind system based on a DFIG by active disturbance rejection control, Int. Rev. Model. Simul. 34 (2014) 55–62.
[4] J.P. Werner, J. Luterbacher, J.E. Smerdon, A pseudoproxy evaluation of bayesian hierarchical modelling and canonical correlation analysis for climate field reconstructions over Europe, J. Clim. 23 (2012) 66–72.
[5] M. Loucif, A. Boumediene, Modeling and direct power control for a DFIG under wind speed variation, in: 2015 3rd International Conference on Control Engineering & Information Technology (CEIT), vol. 45, 2015, pp. 89–94.
[6] M.E. Mann, R.S. Bradley, M.K. Hughes, Global-scale temperature patterns and climate forcing over the past six centuries, Nature 392 (1998) 779–787.
[7] O. El-Anwar, J. Ye, W. Orabi, Efficient optimization of post-disaster reconstruction of transportation networks, J. Comput. Civ. Eng. 11 (2015) 35–43.

This book belongs to Kitab Liaison (ocd1996@gmail.com) Copyright Elsevier 2023

[8] A. Elmansouri, J. El mhamdi, A. Boualouch, Wind energy conversion system using DFIG controlled by back-stepping and RST controller, in: 2016 International Conference on Electrical and Information Technologies (ICEIT), IJRER, New York, 2016.
[9] S.-Y. Jeong, T.H. Nguyen, Q.A. Le, D.-C. Lee, High-performance control of three-phase four-wire DVR systems using feedback linearization, J. Power Electron. 34 (2016) 12–19.
[10] P. He, F. Wen, G. Ledwich, Y. Xue, Small signal stability analysis of power systems with high penetration of wind power, J. Mod. Power Syst. Clean Energy 8 (2013) 91–99.
[11] M.F. Hossain, Theory of global cooling, Energy Sustain. Soc. 13 (2016) 56–63.
[12] X.J. Zheng, J.J. Wu, Y.H. Zhou, Numerical analyses on dynamic control of five-degree-of-freedom maglev vehicle moving on flexible guideways, J. Sound Vib. 235 (1997) 43–61.
[13] Website http://www.supraconductivite.fr/en/index.php?p=applications-trains-maglev-more.
[14] C.F. Zhao, W.M. Zhai, Maglev vehicle/guideway vertical random response and ride quality, Veh. Syst. Dyn. 38 (3) (2002) 185–210.
[15] A. Thomas, M. Pugh, A.R. MacKenzie, J.D. Whyatt, C.N. Hewitt, Effectiveness of green infrastructure for improvement of air quality in urban street canyons, Environ. Sci. Technol. 46 (14) (2012) 7692–7699, https://doi.org/10.1021/es300826w.
[16] H. Lala, S. Karmakar, Continuous wavelet transform and artificial neural network based fault diagnosis in 52 bus hybrid distributed generation system, in: IEEE Students Conference on Engineering and Systems (SCES), 2015, IEEE, New York, 2015.
[17] S. Abdelmalek, L. Barazane, A. Larabi, H. Belmili, Contributions to diagnosis and fault tolerant control based on proportional integral observer: application to a doubly-fed induction generator, in: 4th International Conference on Electrical Engineering (ICEE), 2015, IEEE, New York, 2015.
[18] X.J. Zheng, J.J. Wu, Y.H. Zhou, Effect of spring non-linearity on dynamic stability of a controlled maglev vehicle and its guideway system, J. Sound Vib. 279 (2005) 201–215.
[19] T.T. Soong, Active Structural Control: Theory and Practice, Longman Scientific & Technical, Essex, 1990.

This book belongs to Kitab Liaison (ocd1996@gmail.com) Copyright Elsevier 2023

This page intentionally left blank

This book belongs to Kitab Liaison (ocd1996@gmail.com)

Copyright Elsevier 2023

CHAPTER 7

Public transportation systems

Introduction

Conventional energy utilization for transportation sectors is not only costly but also causes adverse environmental impacts [1–3]. Interestingly, wind power technology can be implemented in all vehicles to meet total energy demand while the vehicles are in motion, which indeed will mitigate the energy and climate change crisis. Thus, wind energy has high potential to produce energy for transportation vehicles once it is utilized by a sophisticated technology. Modern wind turbines are small, simple, and highly sophisticated devices compared with turbines from the mid-20th century. Back then turbines were extremely tall and large with a turbine engine capacity from roughly 5–10 kW; rotors now often exceed 0.25 m in diameter and are positioned on towers exceeding 1 m in height. Thus, modern turbines are indeed much cheaper than previous ones, possibly making them the best tool for vehicle implementation to produce energy naturally. In this article, an innovative theory was analyzed to implement this wind energy into vehicles while the vehicles are in motion. The wind turbine modeling and drive train modeling (by one mass model) were conducted using the MATLAB Simulink software package. The kinetic energy conversion process was divided into two main interacting subsystems, and the detailed process of the conversion procedure was modeled. The results of the energy conversion chain analysis were also analyzed using the MATLAB software. Subsequently, the control structure, design, and generator model were also analyzed using a series of mathematical calculations to prepare a theoretical model for the total process of energy capture by the wind turbine and utilization by running vehicles. Finally, this model was hypothetically applied in a car as an experimental tool, which revealed that wind energy generated transportation vehicles could indeed be a cutting-edge technology to reduce or eliminate the cost of energy for all transportation vehicles.

Sustainable Development for Mass Urbanization
https://doi.org/10.1016/B978-0-12-817690-0.00007-5
© 2019 Elsevier Inc.
All rights reserved.

This book belongs to Kitab Liaison (ocd1996@gmail.com)
Copyright Elsevier 2023

Methods and simulation

A wind turbine generator to power electronic equipment [4, 5] is governed by the operation of variable-speed wind turbines. The reasons for using variable-speed operating wind turbines include possibilities for reducing stress and control of the active and reactive power. The MATLAB Simulink model wind-generation modules that are unique to one of the following with a series of mathematical equations were used for modeling the turbines.

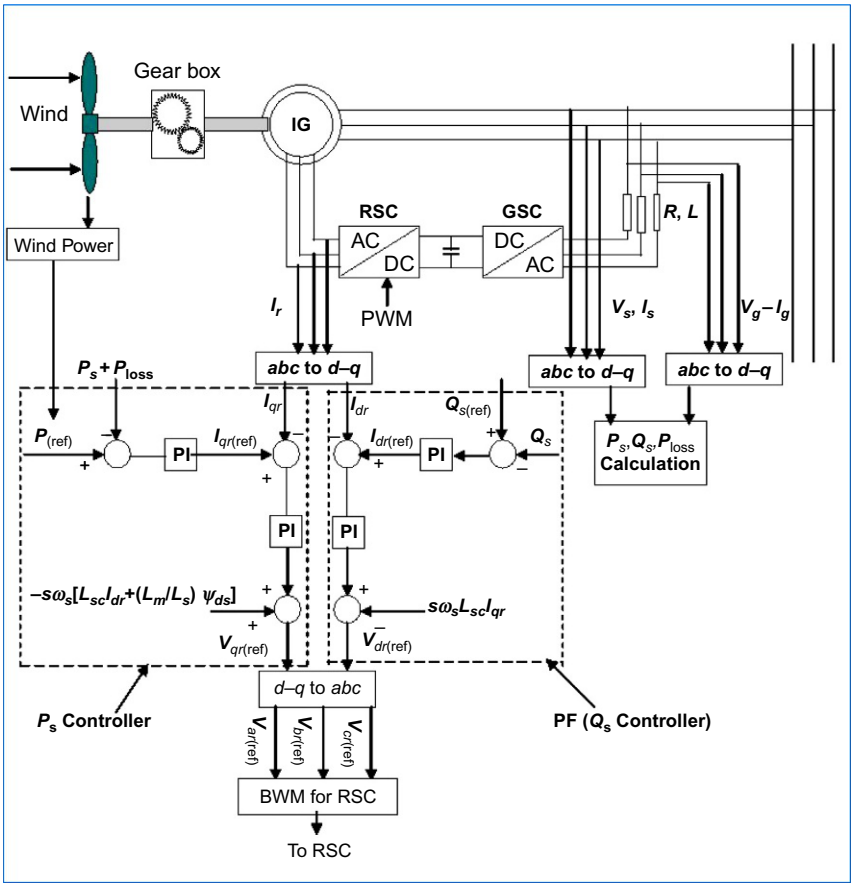

Conceptual Diagram 1. The above sketch illustrates the conceptual MATLAB Simulink model of the wind-generator energy module.

This book belongs to Kitab Liaison (ocd1996@gmail.com) Copyright Elsevier 2023

In this paper, the model that was developed was used to study and simulate the doubly fed induction generator (DFIG) for producing electricity for transportation vehicles. A vector control strategy involving the DFIG order and the power storage box active stator is presented in the following matrix.

$$\frac{d}{dt}\begin{bmatrix}\Delta\omega_t\\ \Delta\omega_r\\ T_g\end{bmatrix}=\begin{bmatrix}\frac{-D_t-D_{tg}}{2H_t} & \frac{D_{tg}}{2H_t} & \frac{-1}{2H_t}\\ \frac{D_{tg}}{2H_g} & \frac{-D_g-D_{tg}}{2H_g} & \frac{1}{2H_g}\\ K_{tg}\omega_e & -K_{tg}\omega_e & 0\end{bmatrix}\begin{bmatrix}\Delta\omega_t\\ \Delta\omega_r\\ T_g\end{bmatrix}+\begin{bmatrix}\frac{T_m}{2H_t}\\ \frac{-T_e}{2H_g}\\ 0\end{bmatrix} \tag{7.1}$$

The fundamental equation governing the mechanical power of the wind turbine is

$$P_w=\frac{1}{2}C_p(\lambda,\beta)\rho A V^3 \tag{7.2}$$

where ρ is the air density (kg/m^3), C_p is the power coefficient, A is the intercepting area of the rotor blades (m^2), V is the average wind speed (m/s), and λ is the tip speed ratio. The theoretical maximum value of the power coefficient C_p is 0.593; C_p is also known as Betz's coefficient [6, 7]. Mathematically,

$$\lambda=\frac{R\omega}{V} \tag{7.3}$$

R is the radius of the turbine (m), ω is the angular speed (rad/s), and V is the average wind speed (m/s). The energy generated by wind can be obtained by

$$Q_w=P\times(\text{Time})[\text{kWh}] \tag{7.4}$$

It is well known that wind velocity cannot be obtained by a direct measurement from any particular motion. In data taken from any reference, the motion needs to be determined for that particular motion; then, the velocity needs to be measured at a lower motion [8, 9].

$$v(z)\ \ln\left(\frac{Z_r}{Z_o}\right)=v(Z_r)\ \ln\left(\frac{Z}{Z_0}\right) \tag{7.5}$$

This book belongs to Kitab Liaison (ocd1996@gmail.com) Copyright Elsevier 2023

where Z_r is the reference height (m), Z is the height at which the wind speed is to be determined, Z_0 is the measure of surface roughness (0.1–0.25 for crop land), $v(z)$ is wind speed at height z (m/s), and $v(z_r)$ is wind speed at the reference height z (m/s). The power output in terms of the wind speed can be estimated using the following equation:

$$P_w(v) = \begin{cases} \dfrac{v^k - v_C^k}{v_R^k - v_C^k} \cdot P_R & v_C \leq v \leq v_R \\ P_R & v_R \leq v \leq v_F \\ 0 & v \leq v_C \text{ and } v \geq v_F \end{cases} \tag{7.6}$$

where P_R is rated power, v_C is the cut-in wind speed, v_R is the rated wind speed, v_F is the rated cut-out speed, and k is the Weibull shape factor. The angular speed of the generator must be changed to extract the maximum power; this process is known as maximum power point tracking (MPPT). When the blade pitch angle is zero, the power coefficient is maximized for an optimal TSR [10–12]. The optimal rotor speed is given by

$$\omega_{\text{opt}} = \frac{\lambda_{\text{opt}}}{R} V_{wn} \tag{7.7}$$

which will give

$$V_{wn} = \frac{R\omega_{\text{opt}}}{\lambda_{\text{opt}}} \tag{7.8}$$

where ω_{opt} is the optimal rotor angular speed in rad/s, λ_{opt} is the optimal tip speed ratio, R is the radius of the turbine in meters, and V_{wn} is the wind speed in m/s.

Drive train modeling

The basic concept is for a drive train to transfer high aerodynamic torque at the rotor to the low-speed shaft of the generator through a gearbox. Because the generator is coupled to the rotor to reduce complexity, a model of the generator is needed and is presented later in this section. Consequently, the drive train can be modeled using a one-mass

This book belongs to Kitab Liaison (ocd1996@gmail.com) Copyright Elsevier 2023

model [13–15] based on the torsional multibody dynamic model per the following matrix:

$$\begin{bmatrix} \dot{\omega}_t \\ \dot{\omega}_g \\ \dot{T}_{ls} \end{bmatrix} = \begin{bmatrix} -\dfrac{K_t}{J_t} & 0 & -\dfrac{1}{J_t} \\ 0 & -\dfrac{K_g}{J_g} & \dfrac{1}{n_g J_g} \\ \left(B_{ls} - \dfrac{K_{ls}K_r}{J_r}\right) & \dfrac{1}{n_g}\left(\dfrac{K_{ls}K_r}{J_g} - B_{ls}\right) & -K_{ls}\left(\dfrac{J_r + n_g^2 J_g}{n_g^2 J_g J_r}\right) \end{bmatrix} \begin{bmatrix} \omega_t \\ \omega_g \\ T_{ls} \end{bmatrix}$$

$$+ \begin{bmatrix} \dfrac{1}{J_r} \\ 0 \\ \dfrac{K_{ls}}{J_r} \end{bmatrix} T_m + \begin{bmatrix} 0 \\ -\dfrac{1}{J_g} \\ \dfrac{K_{ls}}{n_g J_g} \end{bmatrix} T_g \tag{7.9}$$

One-mass model

The turbine inertia can be calculated from the combined weight of the blades and the hub. Therefore, the turbine can be viewed as a large disk with a small thickness. Thus proper data are not available, the simple equation below can be used to estimate the mass moment of inertia of a disk with a small thickness, the turbine can be considered.

$$J_t \dot{\omega}_t = T_a - K_t \omega_t - T_g \tag{7.10}$$

And

$$J_t = J_r + n_g^2 J_g \tag{7.11}$$

$$K_t = K_r + n_g^2 K_g \tag{7.12}$$

$$T_g = n_g T_{em} \tag{7.13}$$

where J_t is the moment of inertia in [kg m^2]; ω_t is the low shaft angular speed in [rad/s]; K_t is the turbine damping coefficient in [Nm/rad/s] that represents the aerodynamic resistance; and K_g is the generator damping coefficient in [Nm/rad/s].

This book belongs to Kitab Liaison (ocd1996@gmail.com) Copyright Elsevier 2023

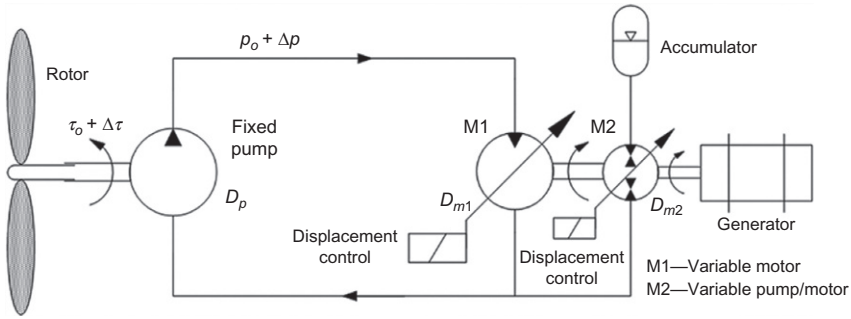

Conceptual Diagram 2. Schematic diagram of a one-mass model of a wind turbine system: a full-scale converter wind turbine with a synchronous machine shows the detailed process of energy accumulation.

Therefore, the maximum power is calculated with the following equation with the one-mass model diagram and series of equations. This shows that the theoretical maximum power extracted from the wind is 0.5925 times its kinetic power.

$$\frac{dP_k}{dV_2} = \frac{1}{4}\rho A V_1^3\left(-3\frac{V_2^2}{V_1^3} - 2\frac{V_2}{V_1^2} + \frac{1}{V_1}\right) = 0 \tag{7.14}$$

$$\Rightarrow \frac{1}{4}\rho A\left(-3V_2^2 - 2V_2V_1 + V_1^2\right) = 0$$

$$\Rightarrow \frac{1}{4}\rho A\left(-3V_2^2 - 3V_2V_1 + V_2V_1 + V_1^2\right) = 0$$

$$\Rightarrow \frac{1}{4}\rho A[-3V_2(V_2 + V_1) + V_1(V_2 + V_1)] = 0$$

$$\Rightarrow \frac{1}{4}\rho A(-3V_2 + V_1)(V_2 + V_1) = 0$$

Here, ρ, A, and $(V_2 + V_1)$ cannot be zero, therefore,

$$(-3V_2 + V_1) = 0 \Rightarrow \frac{V_2}{V_1} = \frac{1}{3}$$

Now, putting this value of V_2/V_1 in Eq. (7.14), we get,

$$P_k = \frac{1}{4}\rho A V_1^3\left(1 - \frac{1}{3^3} - \frac{1}{3^2} + \frac{1}{3}\right)$$
$$\Rightarrow P_k = 0.5925 \times \frac{1}{2}\rho A V_1^3$$

This book belongs to Kitab Liaison (ocd1996@gmail.com) Copyright Elsevier 2023

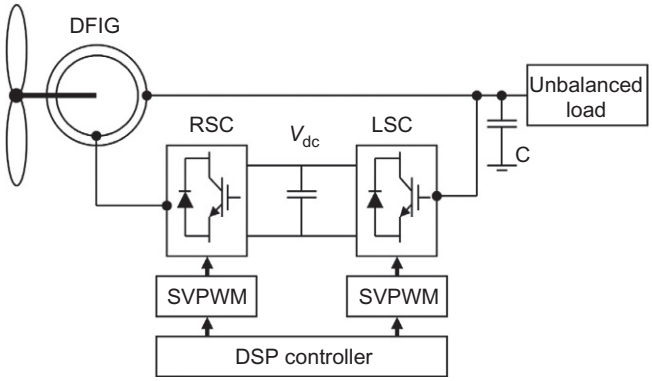

Fig 7.1 Typical wind energy conversion chain.

Wind energy conversion

Given the above conditions, the airflow mass has a certain energy called kinetic energy [16–18]. The kinetic energy is shown in Fig. 7.1, which presents a wind energy conversion system (WECS) that uses a DFIG. These are the aerodynamic subsystem (wind speed, wind turbine, and gearbox) and the electrical subsystem (DFIG).

Aerodynamic subsystem

Signals in the simulations may be to use logs of real speed at the real location of the wind turbine generation system (WTGS).

The choice for the wind speed model is described and proposed in Refs. [19–21]. The deterministic and stochastic parts are added together to obtain the total equivalent wind speed (V), and the expression has the following form:

$$V(t) = V_0 + \sum_{i=1}^{n} A_i \sin(\omega_i t + \varphi_i) \tag{7.15}$$

where V_0 is the mean component and A_i, ω_i, and ψ_i are the magnitude, pulsation, and initial phase of each turbulent mode, respectively. In this article, the turbulence experienced by the rotating wind turbine blades is taken into account. The WTGS converts power from the kinetic energy of the wind and is expressed as C_p, which is called the power coefficient or Betz's factor.

The aerodynamic power is given by [7, 22]

$$P_{aer} = \frac{1}{2} C_p(\lambda, \beta) \rho R \pi^2 V^3 \tag{7.16}$$

This book belongs to Kitab Liaison (ocd1996@gmail.com) Copyright Elsevier 2023

where ρ is the air density, R is the blade length, and V is the wind velocity. The percentage is represented by a coefficient $C_p(\lambda)$, which is a function of the wind speed, turbine speed, and pitch angle of the specific wind turbine blades [10, 23, 24].

Although this equation seems simple, C_p depends on the ratio between the turbine shaft speed Ω_t and the wind speed V. This ratio is called the tip speed ratio:

$$\lambda = \frac{\Omega_T \cdot R}{V} \tag{7.17}$$

Typical C_p versus TSR curves for different values of pitch angle β are shown in Fig. 7.2. In a wind turbine, there is an optimal value for the TSR for which C_p is maximal; thus, this TSR value maximizes the power for a given wind speed. The peak power for each wind speed occurs at the point at which C_p is maximized. To maximize the generated power, it is therefore desirable for the generator to have a power characteristic that follows the maximum $C_{p\max}$ line.

The turbine torque is the ratio of the aerodynamic power to the turbine shaft speed [25]. The turbine is normally coupled to the generator shaft through a gearbox whose gear ratio G is chosen to set the generator shaft speed within a desired speed range. Neglecting the transmission losses,

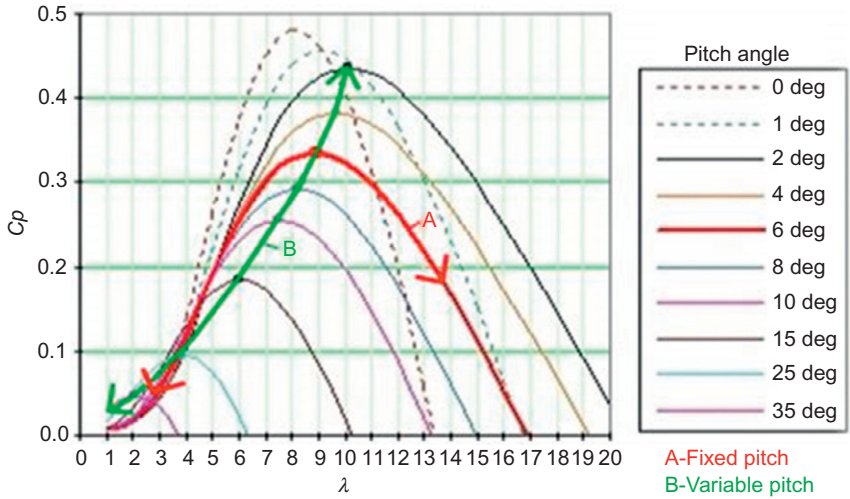

Fig 7.2 Power coefficient variation with TSR and pitch angle.

This book belongs to Kitab Liaison (ocd1996@gmail.com) Copyright Elsevier 2023

the torque and shaft speed of the wind turbine, referred to by the generator side of the gearbox, are given by

$$\begin{cases} T_g = \dfrac{T_{aer}}{G} \\ \Omega_t = \dfrac{\Omega_g}{G} \end{cases} \tag{7.18}$$

where T_g is the driving torque of the generator and Ω_g is the generator shaft speed.

Electrical subsystem

Variable-speed operation is obtained by injecting a controllable voltage into the rotor at the desired slip frequency [26, 27]. The equations for the DFIG are identical to a squirrel-cage induction generator, except that the rotor voltages are not zeros [28–30] and can be expressed as the following [31]:

$$\begin{cases} v_{ds} = \dfrac{d\phi_{ds}}{dt} + \dfrac{R_s}{L_s}\phi_{ds} - \omega_s \cdot \phi_{qs} - M\dfrac{R_s}{L_s}i_{dr} \\ v_{ds} = \dfrac{d\phi_{qs}}{dt} + \dfrac{R_s}{L_s}\phi_{qs} + \omega_s \cdot \phi_{ds} - M\dfrac{R_s}{L_s}i_{qr} \\ \left(v_{dr} - \dfrac{M}{L_s}v_{ds}\right) = \sigma L_r \dfrac{di_{dr}}{dt} - M\dfrac{R_s}{L_s^2}\phi_{ds} + \dfrac{M}{L_s}\omega\phi_{qs} + \left(R_r + \dfrac{M^2}{L_s^2}R_s\right)i_{dr} - \sigma L_r \omega_r i_{qr} \\ \left(v_{qr} - \dfrac{M}{L_s}v_{qs}\right) = \sigma L_r \dfrac{di_{qr}}{dt} - M\dfrac{R_s}{L_s^2}\phi_{qs} - \dfrac{M}{L_s}\omega\phi_{ds} + \left(R_r + \dfrac{M^2}{L_s^2}R_s\right)i_{qr} + \sigma L_r \omega_r i_{dr} \end{cases} \tag{7.19}$$

where
R_s and R_r are the stator and rotor resistances, respectively.
L_s and L_t are the stator and rotor inductances, respectively.
M and σ are the mutual inductance and leakage coefficient, respectively.
$\Omega = p\Omega_g$ is the electrical speed, and p is the pair pole number.
The stator and rotor flux can be expressed as

$$\begin{cases} \phi_{ds} = L_s i_{ds} + M i_{dr} \\ \phi_{sq} = L_s i_{qs} + M i_{qr} \\ \phi_{rd} = L_r i_{dr} + M i_{ds} \\ \phi_{rd} = L_r i_{qr} + M i_{qs} \end{cases} \tag{7.20}$$

This book belongs to Kitab Liaison (ocd1996@gmail.com) Copyright Elsevier 2023

where i_{ds}, i_{qs}, i_{dr}, and i_{qr} are the direct, quadrate, stator, and rotor currents, respectively. The active and reactive powers at the stator, in addition to those provided for the grid, are defined as

$$\begin{cases} P_s = v_{ds} \cdot i_{ds} + v_{qs} \cdot i_{qs} \\ Q_s = v_{qs} \cdot i_{ds} - v_{ds} \cdot i_{qs} \end{cases} \tag{7.21}$$

The electromagnetic torque is expressed as

$$T_{em} = p\left(i_{qs}\phi_{ds} - i_{ds}\phi_{qs}\right) \tag{7.22}$$

Control structure

The wind turbine electric system time responses are much faster than those of the mechanical parts in the WECS. This makes it possible to dissociate the wind turbine and the DFIG control designs and thus describe a cascade control structure based on two subsystem controls:

1. The wind turbine subsystem control concerns the aerodynamic subsystem, which provides the reference inputs for the DFIG subsystem control.
2. The DFIG subsystem control concerns the electric generator via the power converter.

Subsequently, these two control levels will be considered separately, as shown in Fig. 7.3.

It is worth mentioning that there is no need for a reference voltage, torque limiter, or saturation block because of the inherent limits of the references generated at the transients. After obtaining the voltage, pulse width modulation (PWM) is used to generate the gating pulses with a fixed switching frequency for the load-side converter.

Wind turbine subsystem control

Fig. 7.4 shows the four distinct regions in a typical WECS, where $V_{\max}$ is the wind speed at which the maximum allowable rotor speed is reached and $V_{\text{cut-off}}$ is the furling wind speed at which the turbine needs to be shut down for protection.

In practice, there are two possible regions of turbine operation: high- and low-speed regions [32, 33]. High-speed operation (IV) is frequently

This book belongs to Kitab Liaison (ocd1996@gmail.com) Copyright Elsevier 2023

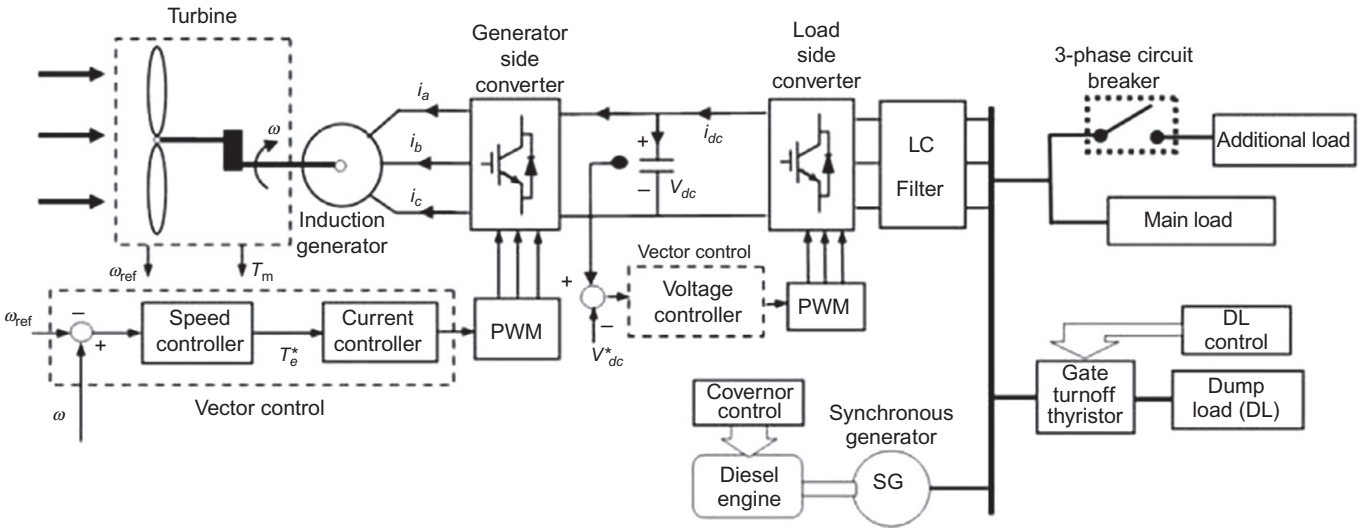

Fig 7.3 The block diagram of the whole system.

This book belongs to Kitab Liaison (ocd1996@gmail.com)

Copyright Elsevier 2023

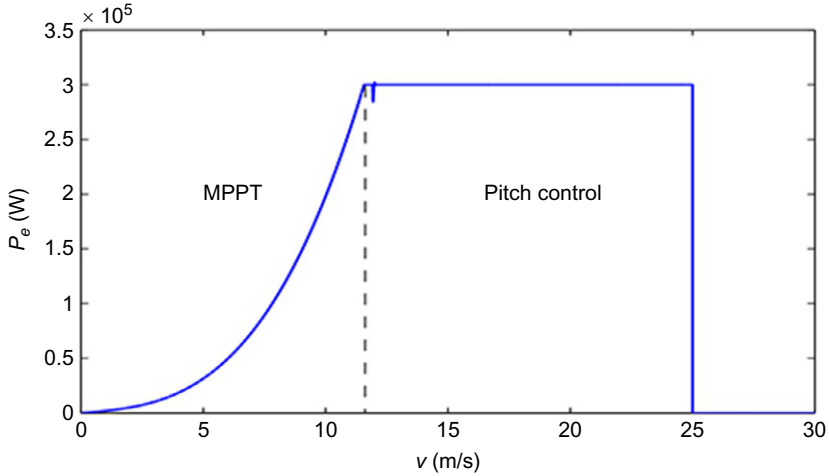

Fig. 7.4 The mechanism of operation and control of WECS considering MPPT and pitch control.

bounded by the speed limit of the machine. Conversely, regulation in the low-speed region (II) is usually not restricted by speed constraints.

However, the system has nonlinear nonminimum phase dynamics in this region. Generally, wind turbine control objectives are functions of the wind speed. For low wind speed, the objective is to optimize the capture of wind power through tracking the optimal rotor speed signals [34, 35]. Once the wind speed increases above its nominal value, the control objective moves to the rated regulating power. Numerous methods for MPPT have been proposed in the literature [36–38].

The method proposed in this paper is simple and is based on the tip speed of the wind turbine. Therefore, an anemometer is required for measuring the wind speed on the wind turbine. Assuming that the optimal value of the TSR λ can be obtained from Fig. 7.2, the optimal speed of the turbine can be determined as follows using Eq. (7.23):

$$\Omega_{t,\mathrm{opt}} = \frac{\lambda_{\mathrm{opt}} \cdot V}{R} \tag{7.23}$$

For this MPPT method, the speed controller continuously adjusts the generator shaft speed to impose the reference electromagnetic torque of the DFIG with the aim of tracking, as shown in Fig. 7.5. The turbine shaft speed is then controlled to obtain a maximum power coefficient.

This book belongs to Kitab Liaison (ocd1996@gmail.com) Copyright Elsevier 2023

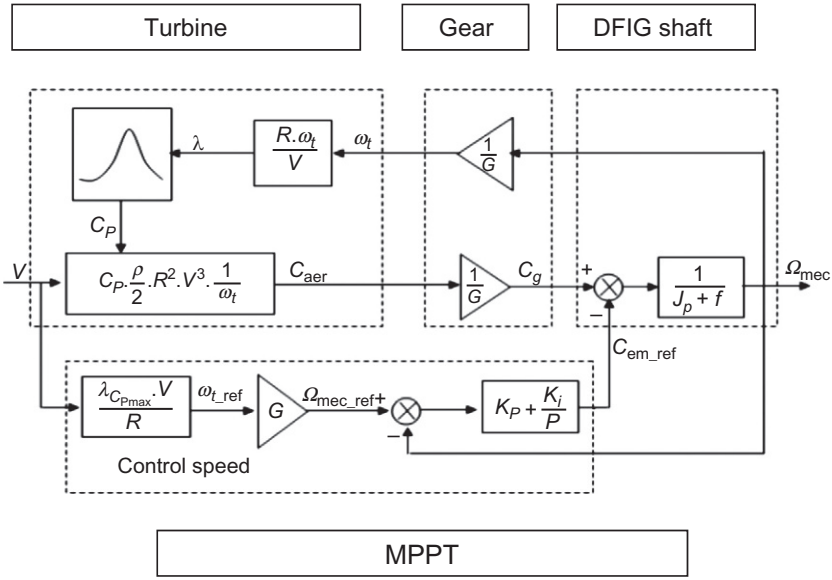

Fig 7.5 The block diagram of the MPPT with enslaved speed.

The MPPT method significantly increases the efficiency of the wind turbine. For each wind speed, there is a certain rotational speed at which the power curve of a given wind turbine has a maximum (C_p reaches its maximum value). Starting the description of the WECS with the aerodynamic subsystem, it should be mentioned that the present work focuses on region II. A block diagram of the MPPT control system for the wind turbine is shown in Fig. 7.5.

This control block diagram of a variable-speed fixed pitch WECS in region II generally aims at regulating the power harvested from wind by modifying the generator speed; in particular, the control objective captures the maximum power efficiency (MPE) of the power rotational speed curves for the 7.8-kW wind turbine that is considered in the present paper under different wind speeds. Connecting all the MPPs from each power curve, the optimal power curve is obtained, and the control system should follow the tracking characteristic curve (TCC) of the wind turbine. Each wind turbine has a TCC similar to the one in Fig. 7.6. When operating in region IV, which occurs above the rated wind speed, the turbine must limit the captured wind power such that safe electrical and mechanical loads are not exceeded.

This book belongs to Kitab Liaison (ocd1996@gmail.com) Copyright Elsevier 2023

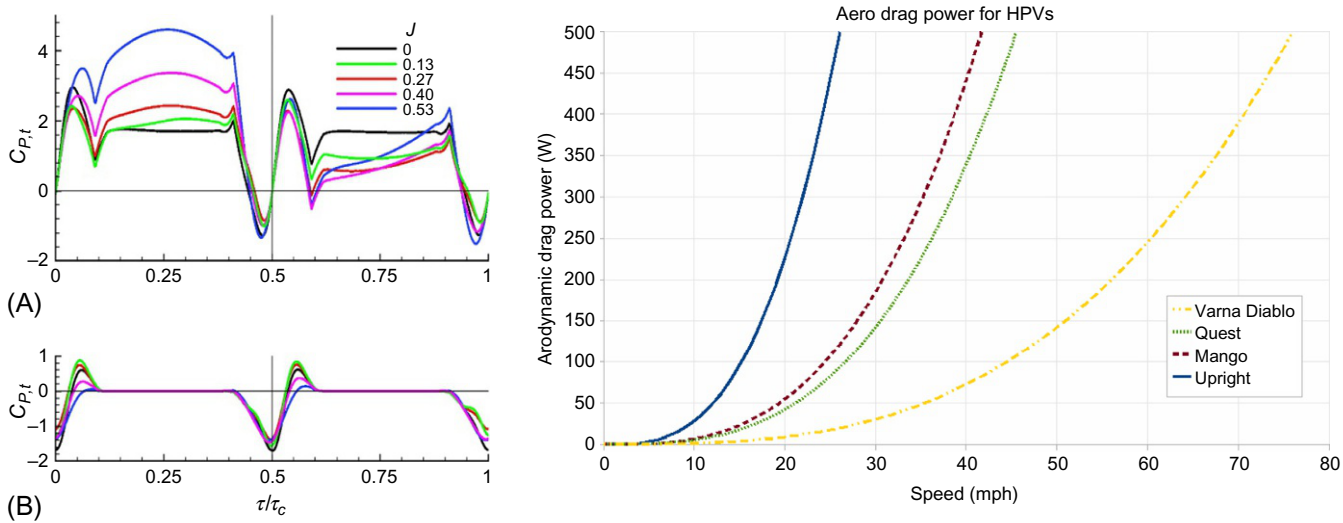

Fig. 7.6 (A) Initiation of aerodynamics at various speeds. (B) Aerodynamic powers at various speed characteristics for different wind speeds with indication of maximum power with tracking curve.

This book belongs to Kitab Liaison (ocd1996@gmail.com)

Copyright Elsevier 2023

DFIG subsystem control

The principle of this method consists of orientating the stator flux in such a manner that the stator flux vector points in the d-axis direction [38, 39]. This approach is realized by setting the quadratic component of the stator flux to the null value:

$$\phi_s = \phi_{ds} \Rightarrow \phi_{qs} = 0 \tag{7.24}$$

In the Park reference frame, this approach is shown in Fig. 7.7. Using the above condition and supposing that the grid system is steady with a single voltage V_s, which leads to a constant flux in the stator ϕ_s, we can easily deduce the voltage as

$$\begin{cases} v_{ds} = 0 \\ v_{qs} = \omega_s \cdot \phi_s = V_s \end{cases} \tag{7.25}$$

The per-phase stator resistance is neglected (the realistic approximation for medium-power machines used in WECS).

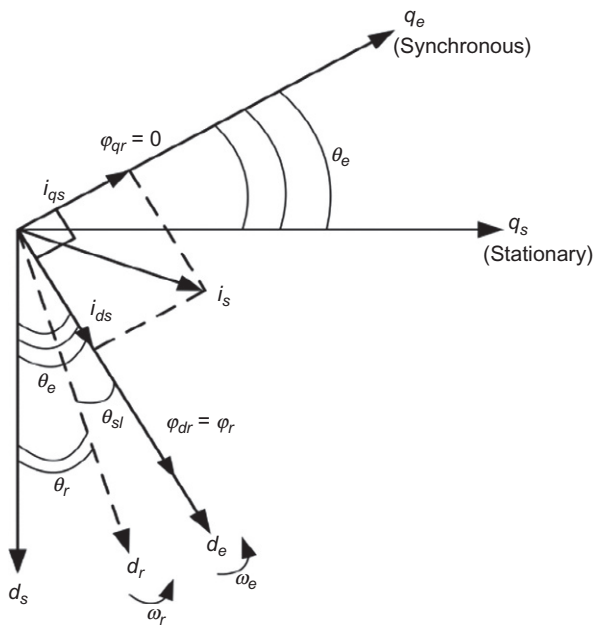

Fig. 7.7 Stator flux orientation determined considering synchronous angles with stationary direction.

This book belongs to Kitab Liaison (ocd1996@gmail.com) Copyright Elsevier 2023

The stator voltage vector is consequently a quadratic advance compared with the stator flux vector. By using Eqs. (7.25), (7.19), we obtain the rotor voltages:

$$\begin{cases} v_{dr} = \sigma L_r \dfrac{di_{dr}}{dt} + R_r i_{dr} - \sigma L_r \omega_r i_{qr} + \dfrac{M}{L_s}\dfrac{d\phi_{ds}}{dt} \\ v_{qr} = \sigma L_r \dfrac{di_{qr}}{dt} + R_r i_{qr} + \sigma L_r \omega_r i_{dr} + g\dfrac{M}{L_s} V_s \end{cases} \tag{7.26}$$

where V_s is the stator voltage magnitude, which is assumed to be constant, and g is the slip range. We can rewrite the rotor voltages as follows:

$$\begin{cases} v_{dr} = \sigma L_r \dfrac{di_{dr}}{dt} + R_r i_{dr} + fem_d \\ v_{qr} = \sigma L_r \dfrac{di_{qr}}{dt} + R_r i_{qr} + fem_q \end{cases} \tag{7.27}$$

With fem_d and fem_q, the crossed coupling terms between the d-axis and q-axis are as follows:

$$\begin{cases} fem_d = -\sigma L_r \omega_r i_{qr} \\ fem_q = \sigma L_r \omega_r i_{dr} + s\dfrac{M}{L_s} V_s \end{cases} \tag{7.28}$$

Consequently, regarding Eq. (7.24), the fluxes of Eq. (7.20) are simplified as follows:

$$\begin{cases} \phi_{ds} = L_s i_{ds} + M i_{dr} \\ 0 = L_s i_{qs} + M i_{qr} \end{cases} \tag{7.29}$$

From Eq. (7.29), we can deduce the currents to be

$$\begin{cases} i_{ds} = \dfrac{\phi_{ds} - M i_{dr}}{L_s} \\ i_{qs} = -\dfrac{M}{L_s} i_{qr} \end{cases} \tag{7.30}$$

Using Eqs. (7.21), (7.25), (7.30), the stator active and reactive powers can then be linked to these rotor currents as follows:

$$\begin{cases} P_s = -V_s \cdot \dfrac{M}{L_s} i_{qr} \\ Q_s = -V_s \cdot \dfrac{M}{L_s}\left(i_{dr} - \dfrac{\phi_{ds}}{M}\right) \end{cases} \tag{7.31}$$

This book belongs to Kitab Liaison (ocd1996@gmail.com) Copyright Elsevier 2023

Because of the constant stator voltage, the stator active and reactive powers are controlled via i_{qr} and i_{dr}.

Therefore, field-oriented control of the DFIG can then be performed, with the rotor currents considered as the variables to be controlled. Consequently, by using the precedent block diagram in Fig. 7.8, the proposed control system is presented in Fig. 7.9.

Decoupled control is guaranteed without feed-forward compensation because the FLC inherently eliminates the cross-coupling terms between the two axes (Eq. 7.28). In steady state for a lossless generator, we can use the following energy balance: $P_s + Pr = P_m$, where $P_s = T_{em}\,\omega_s$ and $P_m = T_q\,\omega$.

From the MPPT method, the electromagnetic torque is used to calculate the reference value for the stator's active power, which follows a preadefined turbine power-speed characteristic to track the maximum power point [6, 40].

The turbine shaft speed is then controlled to give the maximum power coefficient. It follows that $P_s = T_{em}\,\omega_s$, where T^*_{em} is the reference electromagnetic torque that is deduced from the MPPT control strategy. The MPPT method significantly increases the efficiency of the wind turbine.

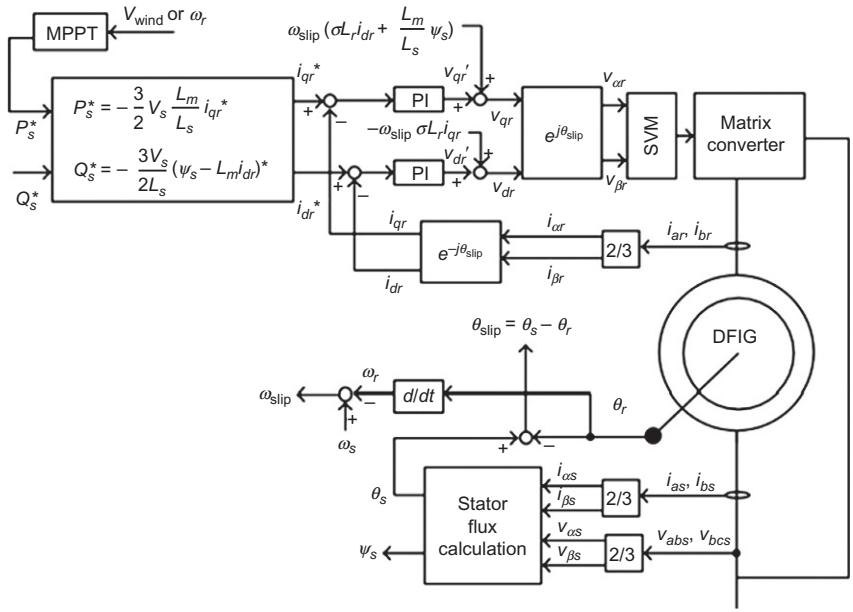

Fig. 7.8 Simplified coupled model of the DFIG rotor current at the operation of the matrix converter when the stator flux is in the MPPT level.

This book belongs to Kitab Liaison (ocd1996@gmail.com)
Copyright Elsevier 2023

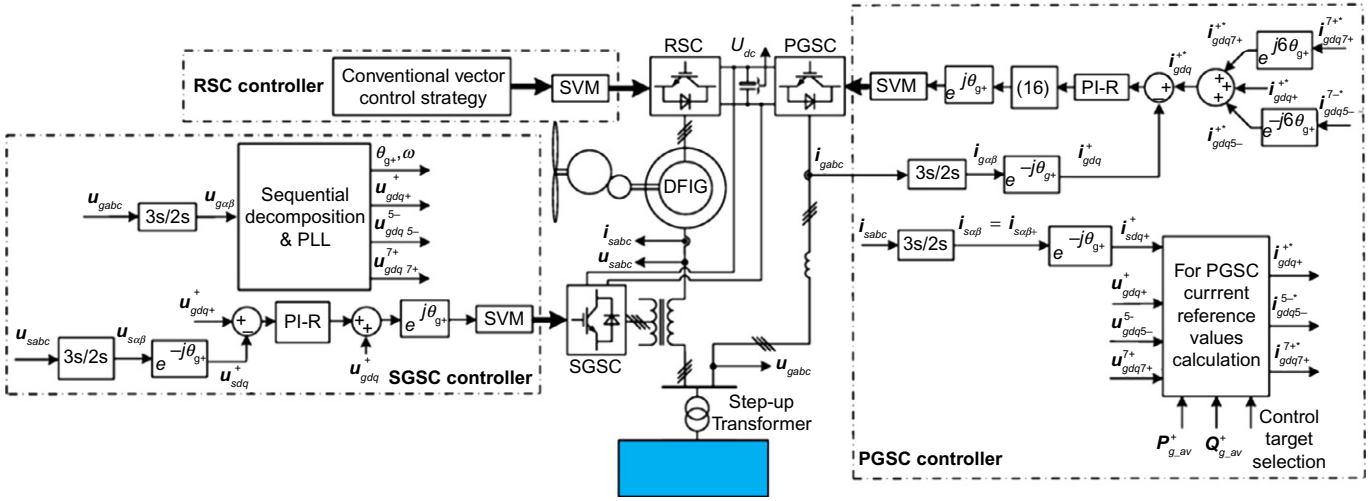

Fig. 7.9 Schematic diagram of the proposed control system of the RSC controller, the SGSC controller, and the PGSC controller.

This book belongs to Kitab Liaison (ocd1996@gmail.com)

Copyright Elsevier 2023

Using Eq. (7.31), we can calculate the rotor current references, which allow setting the desired reference active and reactive powers, as follows:

$$\begin{cases} i_{qr}^{*} = -\dfrac{L_s}{MV_s} P_s^{*} \\ i_{dr}^{*} = -\dfrac{L_s}{MV_s}\left(Q_s^{*} - \dfrac{V_s^2}{\omega_s L_s}\right) \end{cases} \tag{7.32}$$

Controller design

Because of the robustness of the fuzzy logic controller for many nonlinear procedures and characteristics, this paper suggests the design of a fuzzy logic controller (FLC) with a Mamdani fuzzy inference system [41, 42]. The fuzzy logic controller includes three parts: (1) a fuzzification block that determines the input membership values; (2) a fuzzy inference system (FIS) that evaluates which control rules are appropriate at each time by using the fuzzy knowledge-based block [11, 27]; and (3) a defuzzification block that calculates the output of the rules leading to the defuzzification technique [43–45]. Fig. 7.10 shows the block diagram of the fuzzy controller.

For a successful design, proper selection of the gains in the FLC is crucial, and in many cases, this is performed through trial and error to achieve the best possible control performance.

In this section, FLC is used to control the wind turbine subsystem and the DFIG subsystem. For the proposed FLC of a wind turbine, we use the scheme shown in Fig. 7.5. The two input signals to the FLC, the generator shaft speed error and the change of the error, are as follows:

$$\begin{cases} e_{\Omega_g}(n) = \Omega_g^{*}(n) - \Omega_g(n) \\ \Delta e_{\Omega_g}(n) = \Omega_g^{*}(n) - \Omega_g(n-1) \end{cases} \tag{7.33}$$

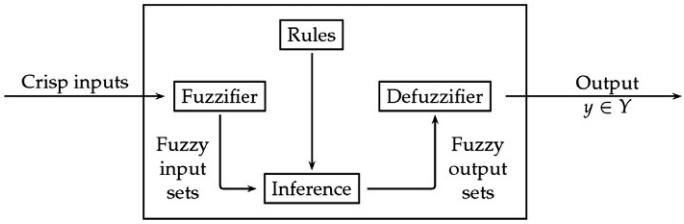

Fig 7.10 Block diagram of the fuzzy controller showing the crisp inputs and outputs through the interference and the defuzzifier.

This book belongs to Kitab Liaison (ocd1996@gmail.com) Copyright Elsevier 2023

The input and output linguistic variables of the fuzzy controller are quantized based on the three fuzzy subsets. The fuzzy sets have been determined to be NG (negative great), EX (zero), and PG (positive great).

The input/output variables used in this paper are fuzzified and evaluated by triangular, trapezoidal, and symmetrical membership functions (MFs). Thus, the input of the generator speed shaft fuzzy controller is T_{em}^{*}. For the proposed FLC of the DFIG, the diagram scheme shown in Fig. 7.9 was used; the inputs of the direct and quadrate axis rotor current fuzzy controllers are the d- and q-axis rotor current errors:

$$\begin{cases} e_{i_{dr}}(n) = i_{dr}^{*}(n) - i_{dr}(n) \\ e_{i_{qr}}(n) = i_{qr}^{*}(n) - i_{qr}(n) \end{cases} \tag{7.34}$$

Their changes in error are

$$\begin{cases} \Delta e_{i_{dr}}(n) = i_{dr}^{*}(n) - i_{dr}(n-1) \\ \Delta e_{i_{qr}}(n) = i_{qr}^{*}(n) - i_{qr}(n-1) \end{cases} \tag{7.35}$$

The input and output linguistic variables of the two fuzzy controllers have been quantized in the following five fuzzy subsets. The fuzzy sets have been defined as NL (negative large), NS (negative small), ZQ (zero), PS (positive small), Pm (positive medium), and PL (positive large).

Short-term fluctuations in the wind speed may result in a change in the output power and a shift in the operating point [46]. Thus, to avoid these undesirable effects, reducing the number of MFs is a solution to smooth the changes in the output power; increasing the number of MFs will produce a delay because of the increased number of computational steps required for some bands [47, 48].

To trade off between accuracy and complexity, rigorous simulation studies found that five MFs are sufficient to produce the desired results in the required bands.

Generator modeling

Either induction or synchronous generators can be used for wind turbine systems [49, 50]. Using a directly driven PMSG not only increases the reliability, but also decreases the weight of the nacelle [51, 52]. The PMSG

This book belongs to Kitab Liaison (ocd1996@gmail.com) Copyright Elsevier 2023

model was designed based on a d-q synchronous reference frame. The PMSG voltage equation is

$$V_q = -R_s i_q - L_q \frac{di_q}{dt} - \omega L_d i_d + \omega \lambda_m \tag{7.36}$$

$$V_d = -R_s i_d - L_d \frac{di_q}{dt} + \omega L_q i_q \tag{7.37}$$

The electronic torque is

$$T_e = 1.5\rho\left[\lambda i_q + \left(L_d - L_q\right) i_d i_q\right] \tag{7.38}$$

where L_q is the q-axis inductance, L_d is the d-axis inductance, i_q is the q-axis current, i_d is the d-axis current, V_q is the q-axis voltage, V_d is the d-axis voltage, ω_r is the angular velocity of the rotor, λ is the amplitude of the flux induced, and p is the number of pairs of poles. In the case of a squirrel cage induction generator (SCIG), the following equation in a stationary d-q frame of reference can be used for dynamical modeling:

$$\begin{bmatrix} V_{qs} \\ V_{ds} \\ V_{qr} \\ V_{dr} \end{bmatrix} = \begin{bmatrix} R_s + pL_s & 0 & pL_m & 0 \\ 0 & R_s + pL_s & 0 & pL_m \\ pL_m & -\omega_r L_m & R_r + pL_r & -\omega_r L_r \\ \omega_r L_m & pL_m & \omega_r L_r & R_r + pL_r \end{bmatrix} \begin{bmatrix} i_{qs} \\ i_{ds} \\ i_{qr} \\ i_{dr} \end{bmatrix} \tag{7.39}$$

From the stator side, the equations are as follows:

$$\begin{aligned} \lambda_{ds} &= L_s i_{ds} + L_m i_{dr} \\ \lambda_{qs} &= L_s i_{qs} + L_m i_{dr} \\ L_s &= L_{is} + L_m \\ L_r &= L_{lr} + L_m \\ V_{ds} &= R_s i_{ds} + \frac{d}{dt}\lambda_{ds} \\ V_{qs} &= R_s i_{qs} + \frac{d}{dt}\lambda_{qs} \end{aligned} \tag{7.40}$$

From the rotor side, the equations are as follows:

$$\begin{aligned} \lambda_{dr} &= L_r i_{dr} + L_m i_{ds} \\ \lambda_{qr} &= L_r i_{qr} + L_m i_{qs} \end{aligned}$$

This book belongs to Kitab Liaison (ocd1996@gmail.com) Copyright Elsevier 2023

$$V_{dr} = R_r i_{dr} + \frac{d}{dt}\lambda_{dr} + \omega_r \lambda_{qr}$$
$$V_{qr} = R_r i_{qr} + \frac{d}{dt}\lambda_{qr} - \omega_r \lambda_{dr} \tag{7.41}$$

For the air gap flux linkage, the equations are as follows:

$$\lambda_{dm} = L_m(i_{ds} + i_{dr})$$
$$\lambda_{qr} = L_m(i_{qr} + i_{qs}) \tag{7.42}$$

where R_s, R_r, L_m, L_{ls}, L_{lr}, ω_r, i_d, i_q, V_d, V_q, λ_d, and λ_q are the stator winding resistance and fluxes of the d-q model, respectively [19]. The output power and torque of the turbine (T_t) in terms of rotational speed can be obtained by substituting Eq. (7.17) into Eq. (7.16):

$$P_w = \frac{1}{2}\rho A C_p(\lambda, \beta)\left(\frac{R\omega_{\text{opt}}}{\lambda_{\text{opt}}}\right)^3 \tag{7.43}$$

$$T_t = \frac{1}{2}\rho A C_p(\lambda, \beta)\left(\frac{R}{\lambda_{\text{opt}}}\right)^3 \omega_{\text{opt}} \tag{7.44}$$

The power coefficient (C_p) is a nonlinear function that is expressed by the fitting equation [51] with the form

$$C_p(\lambda, \beta) = c_1\left(c_2\frac{1}{\lambda_i} - c_3\beta - c_4\right)e^{-c_5\frac{1}{\lambda_i}} + c_6\lambda \tag{7.45}$$

With

$$\frac{1}{\lambda_i} = \frac{1}{\lambda + 0.08\beta} - \frac{0.035}{\beta^3 + 1} \tag{7.46}$$

The values of constants c_1-c_6 are discussed below.

The output of the wind energy generator module is processed by an energy conversion circuit diagram-implemented inverter from the standard Simulink/Sim Power Systems. The resulting MATLAB-Simulink circuit model for the wind generator is a particular case of the more general model of an electrical generator that is presented in Fig. 7.11.

Results and discussion

In this paper, a complete model was presented for a wind turbine generation system based on an induction generator. A cascade control algorithm was

This book belongs to Kitab Liaison (ocd1996@gmail.com) Copyright Elsevier 2023

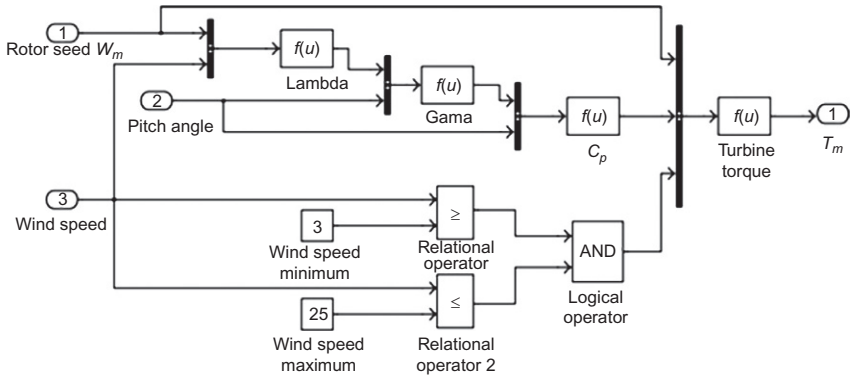

Fig. 7.11 Equivalent circuit diagram of a small wind generator considering all applications of rotor winding resistance and separate generator excitation winding; current through the winding generates a main field, induced voltage, and terminal voltage.

properly designed to ensure optimal operation of the whole system and was based on an FLC with stator flux-orientation and the MPPT technique. Furthermore, the output power is smoothed despite wind fluctuations, which is commonly required in a grid connected to a wind farm. This technique has been successfully applied to generate a reference for tracking the active power by using the rotor-side converter control. Additionally, this strategy can reduce the stress in the pitch control system by adjusting the value of the power coefficient according to wind speed variations to extract the maximum wind power and limit it to its rated value. In simulations, a robustness test was performed by adding a wind speed signal and voltage dips. The simulation results demonstrate the inherent ability of the FLC to address this type of noise while operating under fault conditions at the rated wind speed.

Fig. 7.2 shows that the maximum values of C_p are achieved for the curve associated with $\beta = 2°$. From this curve, the maximum value of C_p ($C_{p,\max} = 0.5$) is obtained for $\lambda_{\text{opt}} = 0.91$. This value ($\lambda_{\text{opt}}$) represents the optimal speed ratio. These conditions permit application of MPPT control. For the DFIG control, we use indirect power control with an FLC. The wind profile was considered to be a wind speed signal with a mean value of 8 m/s and a rated wind speed of 10 m/s; the whole system is tested under standard conditions with a stator voltage of approximately 50% for 0.5 s between 4 and 4.5 s, ~25% between 6 and 6.5 s, and 50% between 8 and 8.5 s [18, 53, 54]. Thus, the machine is considered to be functioning in ideal conditions (no perturbations and no parameter variations). Moreover, to guarantee a unity power factor at the stator side, the reference for the

This book belongs to Kitab Liaison (ocd1996@gmail.com) Copyright Elsevier 2023

reactive power is set to zero. The stator active and reactive powers are controlled according to the MPPT and FLC.

As a result of increasing wind speed, the generator shaft speed achieved maximum angular speed by tracking the maximum power point speed. Thus, the wind turbine always works optimally. Consequently, decoupling among the components of the rotor current was also performed to confirm that the control system worked effectively.

The bidirectional active and reactive power transfer between the rotor and power system is exchanged by the generator according to the super synchronous operation, achieving the nominal stator power. The reactive power can be controlled by the load-side converter to obtain the unit's power factor to generate energy for powering vehicles.

Theoretical experiment on a car

The theoretical assumption of this wind energy is thus modeled on a car as an experimental tool with the aim to ultimately use wind energy for all vehicles. The design of the wind turbines, the materials used in all mechanical and electrical construction of the car, and all related issues have been considered, including all the machine's operational systems, wind strength, wind shears, and the intensity and frequency of turbulence fluctuations [51, 55, 56] (Fig. 7.12).

The turbine speed and mechanical powers are depicted in the following graph with increasing and decreasing rates of wind speed while the car is in

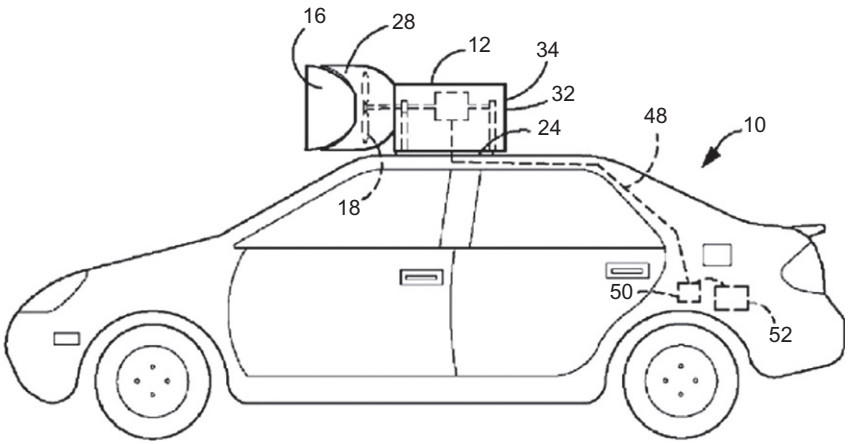

Fig 7.12 A conceptual model of a wind turbine for energy production to power a car while it is in motion.

This book belongs to Kitab Liaison (ocd1996@gmail.com) Copyright Elsevier 2023

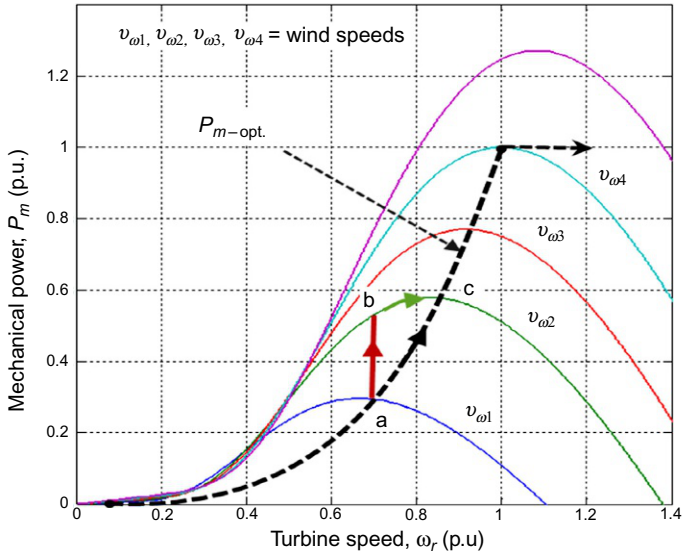

Fig 7.13 Relationship between mechanical power generation and turbine speeds at different wind speeds for implementation in a car.

motion. When the wind is steady, the persistence forecasts yield good results. However, when the wind speed is increased rapidly, sudden "ramps" in power output are generated, which are of tremendous benefit for capturing the energy (Fig. 7.13).

Specifically, the following matrix presents the mathematical calculations for wind energy-capturing strategies when the car is running. S_{r1-b} represents the direct wind energy capture, S_{r2-b} represents the rotation of the generator, S_{r3-b} represents the converting process of wind energy, and S_{r4-b} is the total electricity production to run the car. The matrix calculation shows that 100% of the wind energy is utilized for conversion into electrical energy.

$$S_{f1-b} = \begin{bmatrix} 0 & 0 & 1 \\ \cos(-(90-\varpi)) & \sin(-(90-\varpi)) & 0 \\ -\sin(-(90-\varpi)) & \cos(-(90-\varpi)) & 0 \end{bmatrix}$$

$$= \begin{bmatrix} 0 & 0 & 1 \\ \sin\varpi & -\cos\varpi & 0 \\ \cos\varpi & \sin\varpi & 0 \end{bmatrix} \tag{7.47}$$

This book belongs to Kitab Liaison (ocd1996@gmail.com)
Copyright Elsevier 2023

$$S_{f2-b} = \begin{bmatrix} \cos 120^\circ & \sin 120^\circ & 0 \\ -\sin 120^\circ & \cos 120^\circ & 0 \\ 0 & 0 & 1 \end{bmatrix} \begin{bmatrix} 0 & 0 & 1 \\ \sin\varpi & -\cos\varpi & 0 \\ \cos\varpi & \sin\varpi & 0 \end{bmatrix}$$

$$= \begin{bmatrix} -\frac{1}{2} & \frac{\sqrt{3}}{2}\sin\varpi & -\frac{\sqrt{3}}{2}\cos\varpi \\ -\frac{\sqrt{3}}{2} & -\frac{1}{2}\sin\varpi & \frac{1}{2}\cos\varpi \\ 0 & \cos\varpi & \sin\varpi \end{bmatrix}$$

$$S_{f3-b} = \begin{bmatrix} \cos(-120^\circ) & \sin(-120^\circ) & 0 \\ -\sin(-120^\circ) & \cos(-120^\circ) & 0 \\ 0 & 0 & 1 \end{bmatrix} \begin{bmatrix} 0 & 0 & 1 \\ \sin\varpi & -\cos\varpi & 0 \\ \cos\varpi & \sin\varpi & 0 \end{bmatrix}$$

$$= \begin{bmatrix} -\frac{1}{2} & \frac{\sqrt{3}}{2}\sin\varpi & \frac{\sqrt{3}}{2}\cos\varpi \\ \frac{\sqrt{3}}{2} & \frac{1}{2}\sin\varpi & \frac{1}{2}\cos\varpi \\ 0 & \cos\varpi & \sin\varpi \end{bmatrix}$$

$$S_{f4-b} = S_{f1-b}; S_{f5-b} = S_{f2-b}; S_{f6-b} = S_{f3-b}$$

In a WECS, the accuracy with which the peak power output of electricity is obtained from a point of the maximum power point tracking control system by the controller depends on the track. This experiment thus fed the induction generator stand (DFIG) that is used for extracting the maximum power from the use of a WECS. With the MPPT control method, the MPPT WECS are presented as controllers that are used for extracting the maximum possible energy from wind power generation, which, interestingly, is related to the speed of the car [16, 52].

The analysis was then clarified with the following figure that depicts the relationship between the wind speed (resulting from the motion of the car) in miles per hour (MPH) and kWh power production. Interestingly, it is revealed that at a maximum mean of 8 kWh at an average speed of 10 MPH, energy is produced at a wind speed of 2 MPH immediately after the engine is started by the battery. For a standard car to become fully energized, 20 kWh are required (Fig. 7.14).

This book belongs to Kitab Liaison (ocd1996@gmail.com) Copyright Elsevier 2023

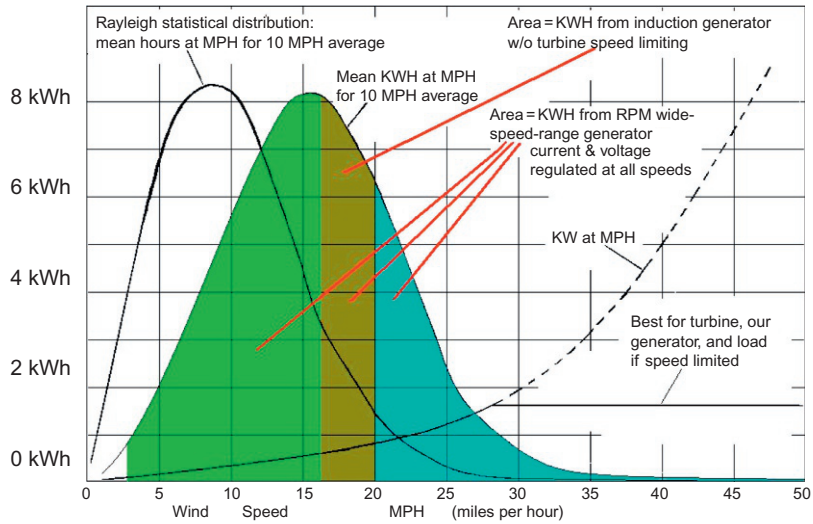

Fig. 7.14 Conversion of wind energy into the car is described in this figure and shows the relationship between the wind speed and energy production considering mean hours (10 MPH average), kWh from the induction generator, and kWh calculated from the revolutions per minute of the speed range generator current and voltage.

Battery modeling

A battery is used as a backup power source to store the power when power production exceeds the demand. For a standard car to become fully energized, 20 kWH are required. Thus, if the car runs at 10 MPH for 2 h, it will fully charge and be able to run for an average of 200 miles; consequently, if the car runs at 60 MPH, it will only take 20 min to fully charge and be able to run for the same number of miles.

In this model, a battery is used as a storage buffer, and all the electricity is supplied through the battery according to Peukert's Law to predict battery discharge considering the nonlinear properties of the battery [57]; this law is stated as follows:

$$t_{\text{discharge}} = H\left(\frac{C}{IH}\right)^{k} \tag{7.48}$$

where t is the battery discharge time, C is the battery capacity (Ampere hour value), I is the current that is drawn, H is the rated discharge time, and k is Peukert's coefficient. Peukert's coefficient is an empirical value that can be determined using the following formula:

$$k = \frac{\log T_2 - \log T_1}{\log I_1 - \log I_2} \tag{7.49}$$

This book belongs to Kitab Liaison (ocd1996@gmail.com) Copyright Elsevier 2023

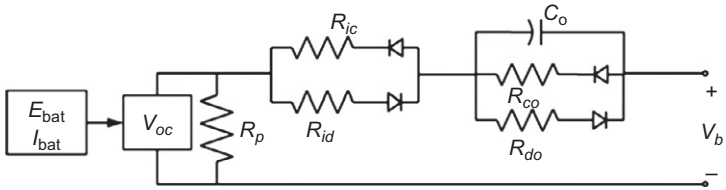

Fig. 7.15 Model of a car with a battery as the backup power source to start the engine and for when the car is not in motion.

where I_1 and I_2 are the two discharge current rates and T_1 and T_2 are the corresponding discharge durations, respectively. The battery capacity decreases with time, that is, the time for charging and discharging will change.

Thus, the value of k should be determined after a certain number of recharge cycles. The value of k for a lead acid battery is 1.3–1.4.

The charging time for a completely discharged battery is given by (Fig. 7.15)

$$t_{\text{charging}} = \frac{\text{Ampere hour of battery}}{\text{Charging current}} \tag{7.50}$$

Conceptual estimate for design and construction of a renewable wind energy-powered car

List of components	Materials cost	Labor cost	Equipment cost	GC & OH cost	Total cost
Wind turbine	$3000	$900	$500	$880	$5280
Instrumentation	$500	$500	$400	$280	$1680
Electrical, and mechanical control	$750	$600	$800	$430	$2580
Supply for 20 years cost is $0.00, but maintenance cost is $200/year					$4000
				Total cost	$13,000

Note: This estimate was prepared using current (March 2016) material costs from top manufacturers and labor costs to install materials per international union labor wages. The equipment purchase was calculated according to current market costs in conjunction with production rates of standard construction practices.

Savings in terms of energy costs

Twenty years of operation of a conventionally powered standard car (15,000 miles/year) requires 750 gallons of gasoline per year at an average

This book belongs to Kitab Liaison (ocd1996@gmail.com) Copyright Elsevier 2023

rate of 20 miles/gallon (750 × 33.70 = 25,275 kWh/year), which is equivalent to 505,500 kWh of energy for 20 years. The cost of this conventional energy is (750 gallons × 20 years × $2.25, or $0.067/kWh for total of 505,500 kh) $33,750. This comparison between conventional energy usage and wind turbine energy production for a car clearly shows cost savings of $20,210 when a wind energy system is used as the energy source for a car.

The energy cost of $13,000 (to furnish and install) for a turbine can be eliminated once the turbine system is commercially installed in cars, and the maintenance costs will be covered by the manufacturer's warranty. Therefore, this estimate suggests that most of the $33,750 cost for running a car for 20 years can be saved once it is powered by wind energy. Subsequently, all other transportation energy costs can also be saved once vehicles are powered by wind energy.

Conclusions

Transportation sectors throughout the world are powered by fossil fuels; these sectors draw on finite resources that are already dwindling, resulting in increased costs. Fossil fuel retrieval is becoming ever more environmentally damaging. It is now generally accepted that meeting the steadily increasing demand for energy in transportation sectors solely on the basis of conventional generation technologies puts unacceptably high stress on the environment. In combination, these factors have led to a major impetus for renewable energy-based power generation during the preceding two to three decades, and the trend is set to continue. Thus, when considering efficiency, WECS have been receiving the most attention among the various renewable energy systems. Extraction of the maximum possible power from available wind power is indeed an innovative source because the development of smaller wind turbines and advanced technology could enable wind energy to serve as a power source for transportation sectors.

Interestingly, this article revealed that natural wind speed is not required because the turbine will start to rotate once the vehicle is in motion. This emergent new technology, together with the favorable framework for renewable energy, can play a prime role in renewable energy utilization for massive use in transportation sectors. The transportation sector needs 5.6×10^{20} J/year (560 EJ/year); currently, this energy is obtained by burning fossil fuel, which accounts for nearly 30% of the total annual global energy demand.

This book belongs to Kitab Liaison (ocd1996@gmail.com) Copyright Elsevier 2023

Therefore, if vehicles could be powered by wind, it would be a new of era of science to utilize wind energy in transportation sectors. Wind energy-powered vehicles would not only eliminate the energy cost for the transportation sector, but also play a vital role in drastically reducing global warming.

Acknowledgments

This research was supported by Green Globe Technology under grant RD-02018-03. Any findings, conclusions, and recommendations expressed in this paper are solely those of the author and do not necessarily reflect those of Green Globe Technology.

References

[1] P. He, F. Wen, G. Ledwich, Y. Xue, Small signal stability analysis of power systems with high penetration of wind power, J. Mod. Power Syst. Clean Energy (2013).
[2] H. Lala, S. Karmakar, Continuous wavelet transform and artificial neural network based fault diagnosis in 52 bus hybrid distributed generation system, in: IEEE Students Conference on Engineering and Systems (SCES), Allahabad, 2015, 2015, pp. 1–6, https://doi.org/10.1109/SCES.2015.7506463.
[3] M. Hossain, N. Fara, Integration of wind into running vehicles to meet its total energy demand, Energy Ecol. Environ. 2 (1) (2016) 35–48.
[4] S. Soedibyo, A. Pradipta, S. Suyanto, M. Ridwan, G. Zulkarnain, M. Ashari, Active and reactive power control in 20 kV grid connected distributed generation system, Int. Rev. Autom. Control 10 (3) (2017) 211.
[5] S. Tamalouzt, T. Rekioua, R. Abdessemed, Direct torque and reactive power control of Grid Connected Doubly Fed Induction Generator for the wind energy conversion, in: International Conference on Electrical Sciences and Technologies in Maghreb (CISTEM), 2014, 2014.
[6] S. Jeong, T. Nguyen, Q. Le, D. Lee, High-performance control of three-phase four-wire DVR systems using feedback linearization, J. Power Electron. 16 (1) (2016) 351–361.
[7] N. Watanakul, An application of wind turbine generator on hybrid power conditioner to improve power quality, Int. Rev. Electr. Eng. 7 (5) (2012) 5487–5495.
[8] T.P. Sheahan, Industrial Superconductivity, a Report to the, Office of Industrial Programs, U.S. Department of Energy, October, 1987.
[9] H. Tien, C. Scherer, J. Scherpen, V. Muller, Linear parameter varying control of doubly fed induction machines, IEEE Trans. Ind. Electron. 63 (1) (2016) 216–224.
[10] K. Kerrouche, A. Mezouar, L. Boumedien, A simple and efficient maximized power control of DFIG variable speed wind turbine. in: 3rd International Conference on Systems and Control, Algiers, 2013, pp. 894–899, https://doi.org/10.1109/ICoSC.2013.6750963.
[11] L. Lu, et al., Investigation on wind power potential on Hong Kong islands—an analysis of wind power and wind turbine characteristics, Renew. Energy 27 (1) (2002) 1–12.
[12] M. Shahidehpour, M. Eremia, Wind power generation, in: Handbook of Electrical Power System Dynamics Modeling Stability and Control, Wiley, 2013, pp. 201–207. ISBN-13: 978-1118497173.
[13] J.G. Slootweg, Reduced order modeling of wind turbines, in: Wind Power in Power Systems, Wiley, New York, 2005, pp. 555–585.S.

This book belongs to Kitab Liaison (ocd1996@gmail.com) Copyright Elsevier 2023

[14] M. Kalantar, G. Mousavi, Dynamic behavior of a stand-alone hybrid power generation system of wind turbine, microturbine, solar array and battery storage, Appl. Energy 87 (10) (2010) 3051–3064.
[15] E. Kamal, M. Oueidat, A. Aitouche, R. Ghorbani, Robust scheduler fuzzy controller of DFIG wind energy systems, IEEE Trans. Sustainable Energy 4 (3) (2013) 706–715.
[16] J.P. Werner, J. Luterbacher, J.E. Smerdon, A pseudoproxy evaluation of Bayesian hierarchical modelling and canonical correlation analysis for climate field reconstructions over Europe, J. Clim. 26 (2012) 851–867.
[17] W.U. Dawei, W.U. Zheng, Z.A.N.G. Landing, H.U. Jizhong, Safety and airworthiness design of ultra-light and very light amphibious aircrafts, in: The 2nd International Symposium on Aircraft Airworthiness (ISAA 2011), Procedia Engineering, vol. 17, 2011, pp. 212–225.
[18] M. Zerikat, S. Chekroun, A. Mechernene, Development and implementation of high-performance variable structure tracking for induction motor using fuzzy-logic controller, Int. Rev. Electr. Eng. 5 (1) (2010) 160–166.
[19] M.V. Kazemi, M. Moradi, R.V. Kazemi, Minimization of powers ripple of direct power controlled DFIG by fuzzy controller and improved discrete space vector modulation, Electr. Power Syst. Res. 89 (2012) 23–30.
[20] J. Khodakarami, P. Ghobadi, Urban pollution and solar radiation impacts, Renew. Sust. Energ. Rev. 57 (2016) 965–976.
[21] L. Wang, D.-N. Truong, Stability enhancement of DFIG-based offshore wind farm fed to a multi-machine system using a STATCOM, IEEE Trans. Power Syst. 28 (3) (2013) 2882–2889.
[22] M. Loucif, A. Boumediene, Modeling and direct power control for a DFIG under wind speed variation, in: 2015 3rd International Conference on Control Engineering & Information Technology (CEIT), 2015.
[23] K.D. Kerrouche, A. Mezouar, L. Boumediene, K. Belgacem, Modeling and optimum power control based DFIG wind energy conversion system, Int. Rev. Electr. Eng. 9 (1) (2014) 32–39.
[24] J. Welsh, Flying car maker offers 'show special' discount, Driver's Seat. Wall St. J. (2012). April 5, Retrieved 2012-07-30.
[25] W. Lin, C. Hong, C. Huang, T. Ou, Hybrid control of a wind induction generator based on Grey–Elman neural network, IEEE Trans. Control Syst. Technol. 21 (6) (2013) 2367–2373.
[26] M.E. Mann, R.S. Bradley, M.K. Hughes, Global-scale temperature patterns and climate forcing over the past six centuries, Nature 392 (1998) 779–787.
[27] M. Boutotbat, L. Mokrani, M. Machmoum, Control of a wind energy conversion system equipped by a DFIG for active power generation and power quality improvement, Renew. Energy 50 (2013) 378–386.
[28] J. De, J.G. de Oliveir, Electric machine topologies in energy storage systems, in: Energy Storage, vol. 1, Intechopen, London, 2010, pp. 1–18.
[29] D.L. Mitchell, D.U. Gubser, "Magnetohydroynaic" ship propulsion with superconducting magnets, J. Supercond. 1 (4) (1988) 349.
[30] M. Dürr, A. Cruden, S. Gair, J.R. McDonald, Dynamic model of a lead acid battery for use in a domestic fuel cell system, J. Power Sources 161 (2) (2006) 1400–1411.
[31] B. Bhandari, S.R. Poudel, K.-T. Lee, S.-H. Ahn, Mathematical modeling of hybrid renewable energy system: a review on small hydro-solar-wind power generation, Int. J. Precis. Eng. Manuf. Green Tech. 1 (2) (2014) 157–173.
[32] S. McBeath, Competition Car Aerodynamics: A Practical Handbook, Haynes Publishing, New York, 2006. ISBN 978-1844252305.

This book belongs to Kitab Liaison (ocd1996@gmail.com) Copyright Elsevier 2023

[33] O.P. Bharti, R.K. Saket and S.K. Nagar, Reliability analysis of DFIG based wind energy conversion system, vol. 67, 2017, pp. 313–317, https://doi.org/10.1145/3057039.3057099
[34] M. Phillips, Flying car takes first flight, The Middle Seat Terminal—WSJ (2009). March 18, Retrieved 2009-03-19.
[35] A. Shaltout, H. Gamal, Power coordination of grid-connected wind turbine doubly fed induction generator augmented with battery storage, in: IEEE International Conference on Smart Energy Grid Engineering (SEGE), 2013, 2013.
[36] K. Sharma, A. Bhargava, K. Gajrani, Stability analysis of DFIG based wind turbines connected to electric grid, Int. Rev.Model. Simul 6 (3) (2013) 879–887.
[37] Terrafugia's Transition street-legal airplane continues flight and drive testing". Terrafugia, 2012. Retrieved 30 July 2012.
[38] T. Yamoto, The "Yamato l," 38 meters long and 10 meters across, is the product of a 6-year, $350 million effort begun in 1985. The vessel will be built at Mitsubishi's Kobe plant, Superconductor Week 4 (5) (1990) 5.
[39] T.K.A. Brekken, N. Mohan, Control of a doubly fed induction wind generator under unbalanced grid voltage conditions, IEEE Trans. Energy Convers. 22 (1) (2007) 129–135.
[40] T.B. Haines, First Roadable Airplane Takes Flight, Aircraft Owners and Pilots Association (AOPA), 2009. 19 March, Retrieved 2009-03-19.
[41] J.P.A. Vieira, A. Nunes, M. Vinicius, U.H. Bezerra, W. Barra Jr., New fuzzy control strategies applied to the DFIG converter in wind generation systems, IEEE Lat. Am. Trans. 5 (3) (2007).
[42] Y.H. Chang, T.H. Liu, D.F. Chen, Design and implementation of a robust controller for a micro permanent magnet synchronous speed control systems, in: Second International Conference on Innovative Computing, Informatio and Control (ICICIC 2007), Kumamoto, 2007, p. 99. https://doi.org/10.1109/ICICIC.2007.245.
[43] A.M. Eltamaly, H.M. Farh, Maximum power extraction from wind energy system based on fuzzy logic control, Electr. Power Syst. Res. 97 (2013) 144–150.
[44] K. Belgacem, A. Mezouar, A. Massoum, Fuzzy logic control of double-fed induction generator wind turbine, Int. Rev. Model. Simul. 6 (2013) 34–41.
[45] B. Robyns, B. Francois, P. Degobert, J.P. Hautier, Vector Control of Induction Machines, Springer-Verlag, London, 2012.
[46] R. Chakib, A. Essadki, M. Cherkaoui, Modeling and control of a wind system based on a DFIG by active disturbance rejection control, Int. Rev.Model. Simul. 7 (4) (2014) 626.
[47] S. Chang, Evaluating disaster mitigations: methodology for urban infrastructure systems, Nat. Hazard. Rev. (2003) 186–196, https://doi.org/10.1061/(ASCE)1527-6988(2003)4:4(186).
[48] E.H. Mamdani, S. Assilina, An experiment in linguistic synthesises with a fuzzy logic controller, Int. J. Man Mach. Stud. (7) (1975) 1–13.
[49] X. Zhang, D. Duan, H. Jing, D. Xu, A strategy of dead-time compensation to DFIG, Int. Rev. Electr. Eng. 7 (3) (2012) 4395–4403.
[50] M. Widyan, Operational performance of synchronous generator hybrid-excited by PMDC and PV generators, Int. Rev. Electr. Eng. 9 (4) (2014) 863.
[51] Wolf-Heinrich Hucho, Chapter 1—introduction to automobile aerodynamics, in: Aerodynamics of Road Vehicles, Elsevier, New York, 1987, pp. 1–46.
[52] Y. Cai, S.S. Chen, Dynamic characteristics of magnetically-levitated vehicle systems, Appl. Mech. Rev. 50 (11) (1997) 647–670.
[53] H. Faida, J. Saadi, Modelling, control strategy of DFIG in a wind energy system and feasibility study of a wind farm in Morocco, Int. Rev.Model. Simul. 3 (6) (2010) 1350–1362.

This book belongs to Kitab Liaison (ocd1996@gmail.com) Copyright Elsevier 2023

[54] G.D. Sams, K. Gurunathan, P. Selvan, V.R.S. Kumar, Conceptual design and analysis of Ferrari F430 flying car, Int. J. Res. Eng. Technol. 1 (6) (2012). ISSN 2277–4378.
[55] X.J. Zheng, J.J. Wu, Y.H. Zhou, Effect of spring non-linearity on dynamic stability of a controlled maglev vehicle and its guideway system, J. Sound Vib. 279 (2005) 201–215.
[56] X.J. Zheng, J.J. Wu, Y.H. Zhou, Numerical analyses on dynamic control of five-degree-of-freedom maglev vehicle moving on flexible guideways, J. Sound Vib. 235 (1997) 43–61.
[57] H.Z. Boroujeni, M.F. Othman, A.H. Shirdel, R. Rahmani, P. Movahedi, E.S. Toosi, Improving waveform quality in direct power control of DFIG using fuzzy controller, Neural Comput. Applic. 32 (2015) 76–84.

This book belongs to Kitab Liaison (ocd1996@gmail.com) Copyright Elsevier 2023

This page intentionally left blank

This book belongs to Kitab Liaison (ocd1996@gmail.com)

Copyright Elsevier 2023

CHAPTER 8

Flying transportation technology

Introduction

Approximately 0.9% of the total planetary surface has been constructed as infrastructure, which equals 1.77 million square miles. This infrastructure leads to roughly 6% of climate change because of the heat reflection back to space; it also costs approximately \$5.575 trillion ($100{,}000{,}000\,\text{mi}^2 \times 5280\,\text{sf} \times 5280\,\text{sf} \times \$200$ per sf cost). Based on research, 1% of infrastructure is added globally each year while 2% of the existing infrastructure is repaired. Therefore, the cost of these two purposes is \$55.75 trillion and \$12 trillion, separately, which is not a small number. Besides, traditional transportation energy usage and traffic jams are not only expensive, but also result in adverse environmental impacts and a loss of time and energy [1–3]. Therefore, to improve this situation, a flying car can be a significant technology. Since the early days of motoring, the flying car concept was studied by several researchers [4–6]. However, the optimized aerodynamic design of the flying car is still a dispiriting but attractive task. These studies showed not only the attempts of the designers to build a flying car for around a century, but also revealed that more effort should be applied to make the flying car a reality.

Recently, computational fluid dynamics (CFD) methods have been integrated into a large scale of engineering discipline. This may attribute to the positive trends in computational power and affordability, and this may also be applied to the flying car design [5–7]. However, the aerodynamic design of a flying car is more sophisticated than a racecar or a traditional aircraft because of the complex prediction of transient unsteady flow features of the wings in the deployment and takeoff phases. Therefore, in this research, a simple propulsive and levitative force model has been introduced with the help of MATLAB software to provide a solution to the drag force, aerodynamics, computational fluid dynamics limitations, and takeoff velocity to realize reliable, safer, and faster flying transportation.

Sustainable Development for Mass Urbanization
https://doi.org/10.1016/B978-0-12-817690-0.00008-7
© 2019 Elsevier Inc.
All rights reserved.

This book belongs to Kitab Liaison (ocd1996@gmail.com)
Copyright Elsevier 2023

Thoughts and methods

To ensure the high performance of the flying car in the air, the major concern is to create an upward force with low takeoff velocity, minimum drag force, and better stability and control [8–10]. Accordingly, the amount of upward force should be considered. It mainly depends on two things: the shape of the wings, including the surface area, aspect ratio, and cross-section composition, and the vehicle's orientation. In this research, first a model will be performed to show the physical mode and the Mach number contours to carry a successful 3D CFD *k-omega* turbulence mode of the flying car (Fig. 8.1). Then, some 3D numerical studies on external flow features of a flying car with different wing positions and deployment history will be conducted to validate the CFD as a preliminary design tool for a reliable flying car [4, 11, 12].

(A)

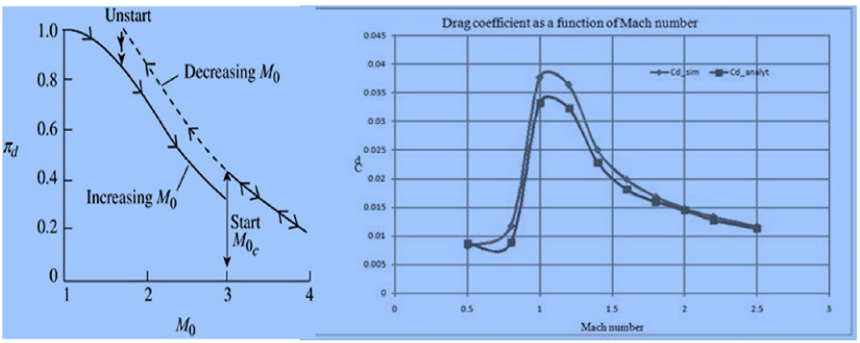

(B)

Fig. 8.1 (A) The conceptual model of a flying car, and (B) demonstration Mach number contours of the proposed flying car.

This book belongs to Kitab Liaison (ocd1996@gmail.com) Copyright Elsevier 2023

Numerical method of solution

As we have mentioned, a 3D standard *k-omega* turbulence model, which is an empirical model based on model transport velocity for the turbulence kinetic energy and a specific dissipation rate, is introduced to deal with the numerical simulations, as shown in the following equations [7, 13, 14].

$$\psi = \left[-\left(\frac{v_\infty r_o^2}{4}\right)\frac{r_o}{r} + \left(\frac{3v_\infty r_o}{4}\right)r - \left(\frac{v_\infty}{2}\right)r^2 \right]\sin^2\theta \tag{8.1}$$

$$v_r = v_\infty \left[1 - \frac{3}{2}\left(\frac{r_o}{r}\right) + \frac{1}{2}\left(\frac{r_o}{r}\right)^3 \right]\cos\theta \tag{8.2}$$

$$v_\theta = -v_\infty \left[1 - \frac{3}{4}\left(\frac{r_o}{r}\right) - \frac{1}{4}\left(\frac{r_o}{r}\right)^3 \right]\sin\theta \tag{8.3}$$

These equations use a coupled second-order implicit unsteady formulation to solve the standard *k-omega* turbulence with shear flow corrections [15–18]. Therefore, this numerical solution will be treated as a fully implicit finite volume scheme of the compressible, Reynolds-averaged, Navier-Stokes forces to neutralize the initial wall temperature and total pressure of the flying car. Being considered about the match number ratio with the velocity calculation, these codes may successfully validate the baseline solutions to design the wings with a NACA series of 9618 airfoils to realize better aerodynamic characteristics (Fig. 8.2).

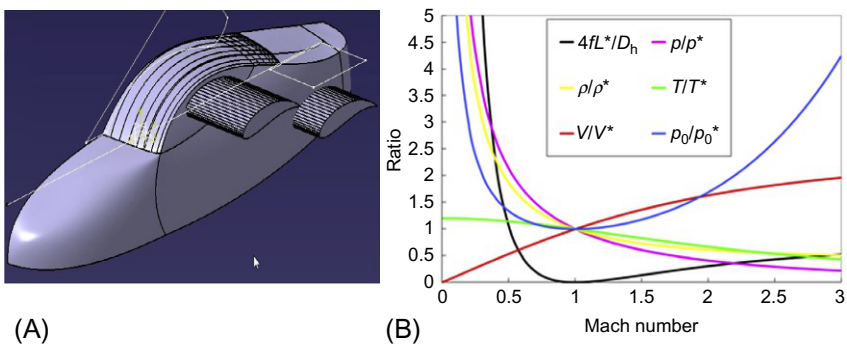

Fig. 8.2 (A) The idealized 3D symmetrical model (half) of a flying car, and (B) the aerodynamic characteristics considering match number ratio considering the velocity of the flying car.

This book belongs to Kitab Liaison (ocd1996@gmail.com)
Copyright Elsevier 2023

Wind energy modeling for flying vehicles

Traditionally, a single wind turbine generator is used for powering vehicles to provide energy. Therefore, to satisfy the higher energy needs for a flying vehicle, a doubly fed induction generator (DFIG) may be used to produce electricity [19–21]. The elementary equation governing the mechanical power of the wind turbine is

$$P_w = \frac{1}{2} C_p(\lambda, \beta) \rho A V^3 \tag{8.4}$$

In this equation, V refers to the average wind speed (m/s), ρ refers to the air density (kg/m^3), C_p refers to the Betz coefficient, which has a theoretical maximum value of 0.593, λ refers to the tip speed ratio, and A refers to the intercepting area of the rotor blades (m^2).

$$\lambda = \frac{R\omega}{V} \tag{8.5}$$

The above equation is used to calculate the tip speed ratio; in this equation, ω is the angular speed (rad/s), V is the average wind speed (m/s), and R is the radius of the turbine (m).

Then, the energy generated by wind can be obtained by

$$Q_w = P \times (\text{Time})[\text{kWh}] \tag{8.6}$$

As the wind velocity cannot be obtained by a direct measurement from any particular motion [22–24], if the velocity is required, a lower motion is needed.

$$v(z)\ \ln\left(\frac{Z_r}{Z_o}\right) = v(Z_r)\ \ln\left(\frac{Z}{Z_0}\right) \tag{8.7}$$

where Z_r is the reference height (m), Z is the height at which the wind speed is to be determined, Z_0 is the measure of surface roughness (0.1–0.25 for cropland), $v(z)$ is wind speed at height z (m/s), and $v(z_r)$ is wind speed at the reference height z (m/s). The power output in terms of the wind speed shall be estimated using the following equation:

$$P_w(v) = \begin{cases} \dfrac{v^k - v_C^k}{v_R^k - v_C^k} \cdot P_R & v_C \le v \le v_R \\ P_R & v_R \le v \le v_F \\ 0 & v \le v_C \text{ and } v \ge v_F \end{cases} \tag{8.8}$$

This book belongs to Kitab Liaison (ocd1996@gmail.com) Copyright Elsevier 2023

where P_R is rated power, v_C is the cut-in wind speed, v_R is the rated wind speed, v_F is the rated cut-out speed, and k is the Weibull shape factor. The angular speed of the generator is to be changed to extract the maximum power, a process known as maximum power point tracking (MPPT). When the blade pitch angle equals zero, the power coefficient will be maximized to get an optimal TSR. The optimal rotor speed is to be calculated by the following equation:

$$\omega_{\text{opt}} = \frac{\lambda_{\text{opt}}}{R} V_{wn} \tag{8.9}$$

which will give

$$V_{wn} = \frac{R\omega_{\text{opt}}}{\lambda_{\text{opt}}} \tag{8.10}$$

where ω_{opt} is the optimal rotor angular speed in rad/s, λ_{opt} is the optimal tip speed ratio, R is the radius of the turbine in meters, and V_{wn} is the wind speed in m/s.

In the following figure, the turbine speed and mechanical powers are described by increasing and decreasing rates of wind speed while the car is working [25–27]. The results can be generated from the figure that when the wind is steady, the persistence forecasts lead to good results, meanwhile, tremendous benefit for capturing the energy can be achieved if the wind speed is increased rapidly (Fig. 8.3).

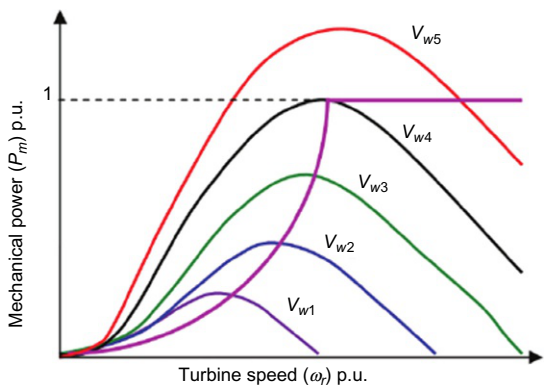

Fig. 8.3 Relationship between mechanical power generation and turbine speeds at different wind speeds for implementation in a car [28–31].

This book belongs to Kitab Liaison (ocd1996@gmail.com) Copyright Elsevier 2023

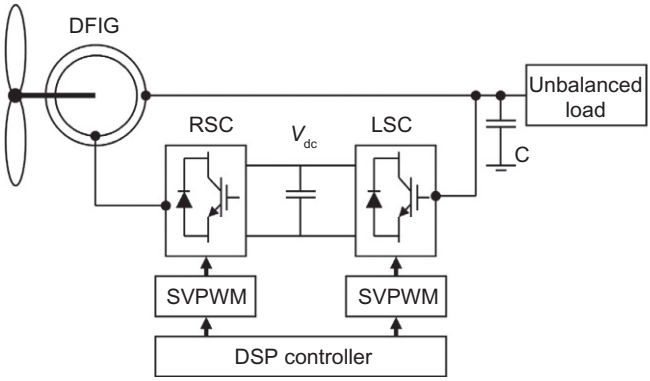

Fig. 8.4 Wind energy conversion chain diagram considering DFIG, RSC, LSC, SVPWM, and DSP controller.

Wind energy conversion

Under the above conditions, the airflow mass has to be controlled at a certain level of kinetic energy, which will be presented by a wind energy conversion system (WECS) that is to be used by DFIG, including the aerodynamic subsystem (wind speed, wind turbine, and gearbox) and the electrical subsystem (DFIG) [23, 24, 32] (Fig. 8.4).

Generator modeling

To provide energy for the wind turbine systems, either synchronous or induction generator models can be used [23, 33, 34]. If being used, the directly driven permanent magnet synchronous generator (PMSG) can not only increase the reliability, but also decrease the weight of the nacelle [35–37]. The following PMSG voltage equations show the principle of the PMSG model designed on the basis of a d-q synchronous reference frame.

$$V_q = -R_s i_q - L_q \frac{di_q}{dt} - \omega L_d i_d + \omega \lambda_m \tag{8.11}$$

$$V_d = -R_s i_d - L_d \frac{di_q}{dt} + \omega L_q i_q \tag{8.12}$$

where the electronic torque is

$$T_e = 1.5\rho\left[\lambda i_q + \left(L_d - L_q\right) i_d i_q\right] \tag{8.13}$$

where L_q is the q-axis inductance, L_d is the d-axis inductance, i_q is the q-axis current, i_d is the d-axis current, V_q is the q-axis voltage, V_d is the d-axis

This book belongs to Kitab Liaison (ocd1996@gmail.com) Copyright Elsevier 2023

voltage, ω_r is the angular velocity of the rotor, λ is the amplitude of the flux induced, and p is the number of pairs of poles.

Another model involves the use of a squirrel cage induction generator (SCIG). For reference, the following equation is used for dynamical modeling under the circumstance of a stationary d-q frame of reference.

$$\begin{bmatrix} V_{qs} \\ V_{ds} \\ V_{qr} \\ V_{dr} \end{bmatrix} = \begin{bmatrix} R_s + pL_s & 0 & pL_m & 0 \\ 0 & R_s + pL_s & 0 & pL_m \\ pL_m & -\omega_r L_m & R_r + pL_r & -\omega_r L_r \\ \omega_r L_m & pL_m & \omega_r L_r & R_r + pL_r \end{bmatrix} \begin{bmatrix} i_{qs} \\ i_{ds} \\ i_{qr} \\ i_{dr} \end{bmatrix} \tag{8.14}$$

From the stator side, the equations shall be as follows:

$$\begin{aligned} \lambda_{ds} &= L_s i_{ds} + L_m i_{dr} \\ \lambda_{qs} &= L_s i_{qs} + L_m i_{dr} \end{aligned}$$

$$\begin{aligned} L_s &= L_{is} + L_m \\ L_r &= L_{lr} + L_m \end{aligned}$$

$$\begin{aligned} V_{ds} &= R_s i_{ds} + \frac{d}{dt}\lambda_{ds} \\ V_{qs} &= R_s i_{qs} + \frac{d}{dt}\lambda_{qs} \end{aligned} \tag{8.15}$$

While from the rotor side, the equations shall be as follows:

$$\begin{aligned} \lambda_{dr} &= L_r i_{dr} + L_m i_{ds} \\ \lambda_{qr} &= L_r i_{qr} + L_m i_{qs} \end{aligned}$$

$$\begin{aligned} V_{dr} &= R_r i_{dr} + \frac{d}{dt}\lambda_{dr} + \omega_r \lambda_{qr} \\ V_{qr} &= R_r i_{qr} + \frac{d}{dt}\lambda_{qr} - \omega_r \lambda_{dr} \end{aligned} \tag{8.16}$$

For the air gap flux linkage, the equations are to be expressed as follows:

$$\begin{aligned} \lambda_{dm} &= L_m\left(i_{ds} + i_{dr}\right) \\ \lambda_{qr} &= L_m\left(i_{qr} + i_{qs}\right) \end{aligned} \tag{8.17}$$

where R_s, R_r, L_m, L_{ls}, L_{lr}, ω_r, i_d, i_q, V_d, V_q, λ_d, and λ_q are the stator winding resistance, and the fluxes of the d-q model, respectively. The output of the wind energy generator modeling is to be prepared by an energy conversion circuit diagram-implemented inverter from the standard Simulink/Sim Power Systems by using the software MATLAB-Simulink to calculate.

This book belongs to Kitab Liaison (ocd1996@gmail.com) Copyright Elsevier 2023

Battery modeling

When the power produced exceeds the demand to start the engine or when the car is not working, a battery modeling is needed to store the power and transfer it into backup power source [26, 38, 39]. In the model introduced in this research, a battery will be used as a storage buffer to supply all the electricity and further predict battery discharge based on the nonlinear properties of the battery considering the Peukert's Law equation below:

$$t_{\text{discharge}} = H\left(\frac{C}{IH}\right)^{k} \tag{8.18}$$

where t is the battery discharge time, C is the battery capacity (Ampere hour value), I is the current that is drawn, H is the rated discharge time, and k is Peukert's coefficient. Peukert's coefficient is an empirical value that shall be determined using the following formula:

$$k = \frac{\log T_2 - \log T_1}{\log I_1 - \log I_2} \tag{8.19}$$

where I_1 and I_2 are the two discharge current rates and T_1 and T_2 are the corresponding discharge durations, respectively. However, after a certain number of recharge cycles, the time for charging and discharging will change because of the decrease in battery capacity. Therefore, the value of k should be redetermined by using 1.3–1.4. Meanwhile, the charging time for a completely discharged battery is to be calculated by the following equation (Fig. 8.5):

$$t_{\text{charging}} = \frac{\text{Ampere hour of battery}}{\text{Charging current}} \tag{8.20}$$

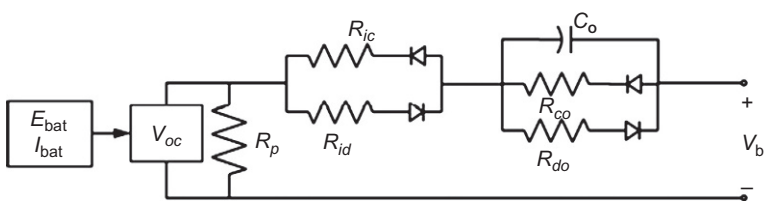

Fig. 8.5 Model of a car with a battery as the backup power source to start the engine and for when the car is not in motion.

This book belongs to Kitab Liaison (ocd1996@gmail.com) Copyright Elsevier 2023

Optimization and discussion

From the models proposed, it is indicated that the flying car can generate desirable lift at a satisfied takeoff velocity with different angles of attack and wing positions [22, 40, 41]. In addition, a detailed parametric analytical study shows that even if at a low takeoff velocity because of the contours of static pressure at various speeds, the flying vehicle can still produce satisfied lift with the help of the deployable high wings (Fig. 8.6). Mathematical analyses imply that at a given range of free stream velocity of a flying car with different geometrical options will generate upward force which indicates that these velocities are deployable and can generate lift higher than the weight of the flying car at the lower take off velocity under different flying conditions, orientations and wing positions.

The analysis of external flow features and aerodynamic characteristics of a flying vehicle indicates that the speed of the flying car can be determined from the results of steady free stream velocity and the aerodynamic characteristics of the flying car can give it the ability to take off, fly, and be controlled properly at various degrees, Cl, Cd, Cm and match numbers (Fig 8.6) has been carried out [42–44]. By using these principles, this paper simulates the condition of the flying vehicle when travelling at takeoff velocity to study the pattern of the car when rising off the ground by creating lift using additional wing force. Answers to this condition include streamlining the car body and using suitable wings to create the desired lift heavier than the weight of the car by installing the rectangular NACA 9816 wings at different positions of the body with different angles of attack (Fig. 8.7).

After satisfying the energy needed by the flying vehicle, a cleaner energy source of the wind turbine generation system should also be considered based on the analysis of an FLC with stator flux-orientation and the MPPT technique. Therefore, a robustness test was introduced in the simulations by adding a wind speed signal and voltage dips. The results of these simulations indicated that the inherent ability of the FLC can handle this issue while operating under fault conditions at rated wind speed. The MPPT control can also be applied into these conditions while for the DFIG control, an FLC is used for indirect power control. In the simulations, the wind profile is considered to be a wind speed signal with a mean value of 8 m/s and a rated wind speed of 10 m/s; the whole system is tested under standard conditions with a stator voltage of approximately 50% for 0.5 s between 4 and 4.5 s,

This book belongs to Kitab Liaison (ocd1996@gmail.com) Copyright Elsevier 2023

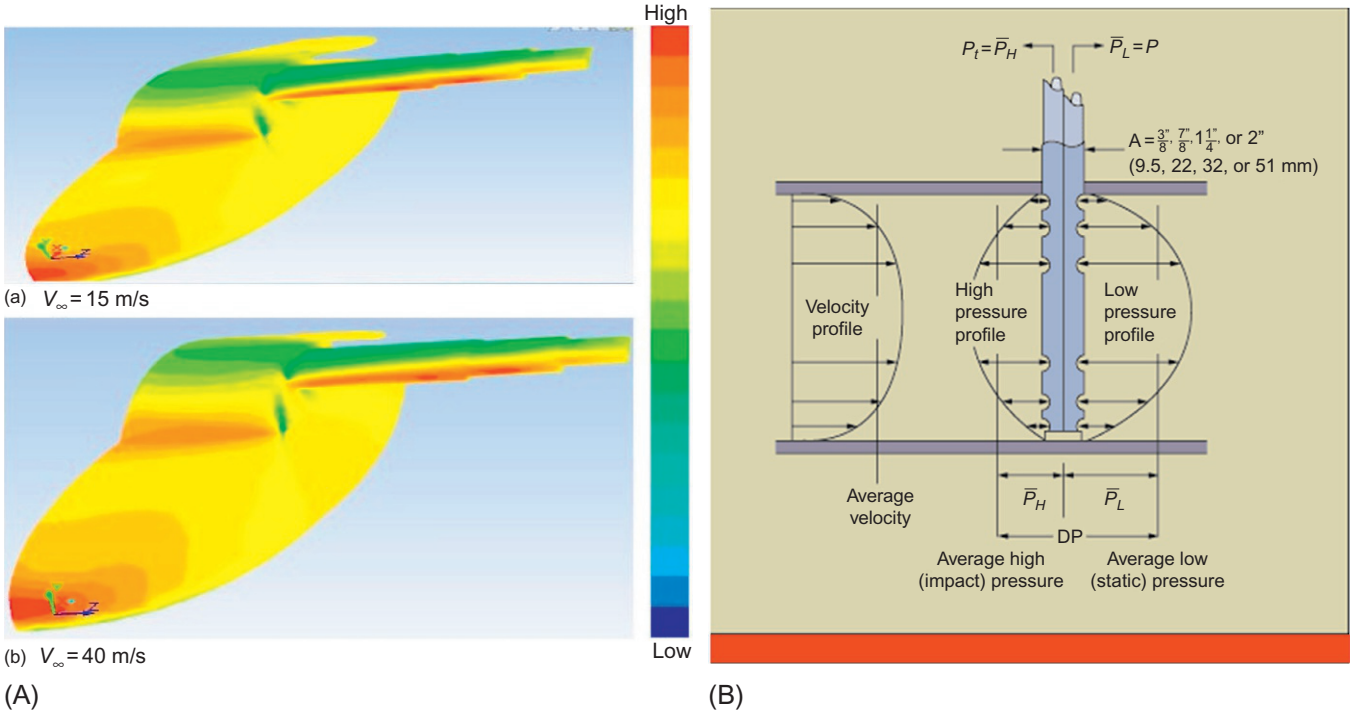

Fig. 8.6 (A) Contours of static pressure at various speeds of a flying car, showing the aerodynamic characteristics of the flying car at two different speeds of lifting the car at (a) 15 and (b) 40 m/s, (B) Contours of the static pressure at various velocities of a car with a short high wing model for getting better aerodynamic efficiency.

This book belongs to Kitab Liaison (ocd1996@gmail.com)

Copyright Elsevier 2023

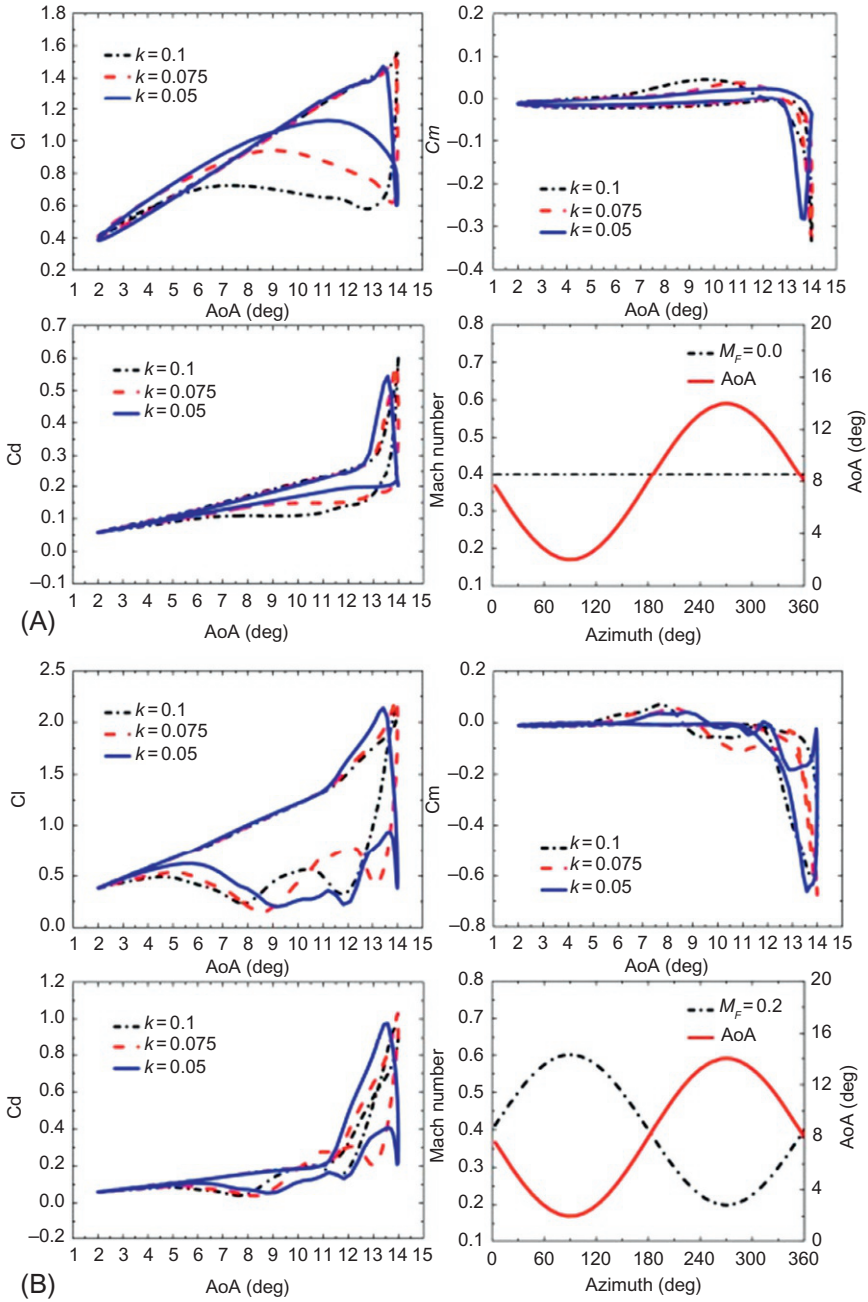

Fig. 8.7 The speed of the flying car determined from (A) steady freestream velocity, and (B) variable freestream velocity considering the aerodynamic characteristics to control the takeoff, flying, and optimization of the velocity.

This book belongs to Kitab Liaison (ocd1996@gmail.com)
Copyright Elsevier 2023

approximately 25% between 6 and 6.5 s, and 50% between 8 and 8.5 s [13, 25, 45, 46], which indicates that under ideal conditions with no perturbations and no parameter variations, the machine is functioning. Besides, the stator active and reactive powers are also controlled by MPPT and FLC; therefore, to ensure a unity power factor at the stator side, the reference for the reactive power needs to be set to zero [21, 40, 47]. Through tracking the maximum power point speed, the generator shaft speed can realize maximum angular speed after the increasing of wind speed [27, 29, 48, 49]. After the tracking, to ensure the efficiency of the control system, a decoupling among the components of the rotor current needs to be conducted. In this process, the bidirectional active and reactive power transfer between the rotor and power system is exchanged by the generator through the super synchronous operation and the realization of the nominal stator power. Meanwhile, the reactive power can be controlled by the load-side converter to obtain the unit's power factor to generate energy for powering vehicles [18, 50–52].

Conclusion

Contemporarily, the conventional transportation infrastructure system worldwide not only wastes large amounts of money each year, but also causes adverse environmental impacts. Therefore, the flying vehicle technology introduced in this research may be an innovative solution to balance the relationship between traffic, cost, energy, and the environment. Considering the higher energy demand and need for a friendlier environment, a wind turbine will be installed into the flying car to produce energy by itself when the vehicle is working. To optimize the use of the turbine, an analyzation with a series of mathematical calculations of the conversion process, the control structure, and generator modeling is conducted in this research. The simulation results of the NACA 9618 model by using MATLAB showed the high extendable nature of commercial use of the flying car by providing the reliability of taking off, flying, safety control of velocity and aerodynamics, and match numbers. Nowadays, infrastructure construction costs trillions of dollars and the transportation sector consumes 5.6×10^{20} J/year (560 EJ/year) fossil fuel each year, respectively. Besides, they also responsible for nearly 34% of the total annual climate change. If developed properly, this technology can be a new era of science to remit severe transportation, infrastructure, and energy problems.

This book belongs to Kitab Liaison (ocd1996@gmail.com) Copyright Elsevier 2023

Acknowledgments

This research was supported by Green Globe Technology under grant RD-02018-03. Any findings, conclusions, and recommendations expressed in this paper are solely those of the author and do not necessarily reflect those of Green Globe Technology.

References

[1] S. Lli, A. Timothy, J.J. Haskew, Integrated power characteristic study of DFIG and its frequency converter in wind power generation, Renew. Energy 35 (2010) 42–51.
[2] G. Sivasankar, V. Suresh Kumar, Improving low voltage ride through capability of wind generators using dynamic voltage restorer, J. Electr. Eng. 65 (4) (2014) 211–219.
[3] T.K.A. Brekken, N. Mohan, Control of a doubly fed induction wind generator under unbalanced grid voltage conditions, IEEE Trans. Energy Convers. 22 (1) (2007) 129–135.
[4] M. Hossain, Solar energy integration into advanced building design for meeting energy demand and environment problem, Int. J. Energy Res. 40 (9) (2016) 1293–1300.
[5] S. Jeong, T. Nguyen, Q. Le, D. Lee, High-performance control of three-phase four-wire DVR systems using feedback linearization, J. Power Electron. 16 (1) (2016) 351–361.
[6] J.G. Slootweg, Reduced order modeling of wind turbines, in: Wind Power in Power Systems, Wiley, New York, 2005, pp. 44–51.
[7] M. Kalantar, G. Mousavi, S., Dynamic behavior of a stand-alone hybrid power generation system of wind turbine, microturbine, solar array and battery storage, Appl. Energy 87 (10) (2010) 3051–3064.
[8] T.B. Haines, First Roadable Airplane Takes Flight, Aircraft Owners and Pilots Association (AOPA), 2009. 19 March. Retrieved 2009-03-19.
[9] P. He, F. Wen, G. Ledwich, Y. Xue, Small signal stability analysis of power systems with high penetration of wind power, J. Mod. Power Syst. Clean Energy 12 (2013) 78–83.
[10] H. Lala, S. Karmakar, Continuous wavelet transform and artificial neural network based fault diagnosis in 52 bus hybrid distributed generation system, in: 2015 IEEE Students Conference on Engineering and Systems (SCES), Allahabad, 2015, pp. 1–6, https://doi.org/10.1109/SCES.2015.7506463.
[11] M. Hossain, N. Fara, Integration of wind into running vehicles to meet its total energy demand, Energy Ecol. Environ. 2 (1) (2016) 35–48.
[12] M. Hossain, Invisible transportation infrastructure technology to mitigate energy and environment, Energy Sustain. Soc. 7 (1) (2017) 27–35.
[13] A.M. Eltamaly, H.M. Farh, Maximum power extraction from wind energy system based on fuzzy logic control, Electr. Power Syst. Res. 97 (2013) 144–150.
[14] P. Santiprapan, K. Areerak, K. Areerak, The enhanced—DQF algorithm and optimal controller design for shunt active power filter, Int. Rev. Electr. Eng. 55 (2015) 32–39.
[15] G.D. Sams, K. Gurunathan, P. Selvan, V.R.S. Kumar, Conceptual design and analysis of Ferrari F430 flying car, Int. J. Res. Eng. Technol. 1 (6) (2012). ISSN 2277–4378.
[16] K. Gopal Sharma, A. Bhargava, K. Gajrani, Stability analysis of DFIG based wind turbines connected to electric grid, Int. Rev. Model. Simul. 6 (3) (2013) 879–887.
[17] G. Tsourakisa, B.M. Nomikosb, C.D. Vournasa, Effect of wind parks with doubly fed asynchronous generators on small-signal stability, Electr. Power Syst. Res. 79 (2009) 190–200.

This book belongs to Kitab Liaison (ocd1996@gmail.com) Copyright Elsevier 2023

[18] N. Gupta, S.P. Singh, S.P. Dubey, D.K. Palwalia, Fuzzy logic controlled three-phase three-wired shunt active power filter for power quality improvement, Int. Rev. Electr. Eng. 6 (3) (2011) 1118–1129.
[19] A. Gaillard, P. Poure, S. Saadate, M. Machmoum, Variable speed DFIG wind energy system for power generation and harmonic current mitigation, Renew. Energy 34 (2009) 1545–1553.
[20] B. Beltran, M. Benbouzid, T. Ahmed-Ali, H. Mangel, DFIG-based wind turbine robust control using high-order sliding modes and a high gain observer, Int. Rev. Model. Simul. 4 (3) (2011) 1148–1155.
[21] C.-H. Tsai, F. Lung-Ming, C.-H. Tai, Y.-L. Huang, J.-C. Leong, Computational aero-acoustic analysis of a passenger car with a rear spoiler, Appl. Math. Model. 33 (9) (2009) 3661–3673.
[22] E.H. Mamdani, S. Assilina, An experiment in linguistic synthesis with a fuzzy logic controller, Int. J. Man Mach. Stud. 7 (1975) 1–13.
[23] E. Kamal, M. Oueidat, A. Aitouch, R. Ghorbani, Robust scheduler fuzzy controller of DFIG wind energy systems, IEEE Trans. Sustain. Energy 4 (3) (2013) 706–715.
[24] A.M. Eltamaly, A.I. Alolah, M.H. Abdel-Rahman, Improved simulation strategy for DFIG in wind energy applications, Int. Rev. Model. Simul. 4 (2) (2011) 525–532.
[25] B. Robyns, B. Francois, P. Degobert, J.P. Hautier, Vector Control of Induction Machines, Springer-Verlag, London, 2012.
[26] H. Xu, X. Ma, D. Sun, Reactive current assignment and control for DFIG based wind turbines during grid voltage sag and swell conditions, J. Power Electron. 3 (2015) 78–83.
[27] W.-H. Hucho, Chapter 1—Introduction to automobile aerodynamics, in: Aerodynamics of Road Vehicles, Elsevier, New York, 1987, pp. 1–46.
[28] S. Engelhardt, J. Kretschmann, J. Fortmann, F. Shewarega, I. Erlich, C. Feltes, Negative sequence control of DFG based wind turbines, in: IEEE Power and Energy Society General Meeting, 2011, IEEE PES, New York, 2011.
[29] H. Faida, J. Saadi, Modelling, control strategy of DFIG in a wind energy system and feasibility study of a wind farm in Morocco, Int. Rev. Model. Simul. 3 (6) (2010) 1350–1362.
[30] A. Gaillard, P. Poure, S. Saadate, FPGA-based reconfigurable control for switch fault tolerant operation of WECS with DFIG without redundancy, Renew. Energy 89 (2013) 33–42.
[31] T. Ghennam, E.M. Berkouk, B. Francois, A vector hysteresis current control applied on three-level inverter. Application to the active and reactive power control of doubly fed induction generator based wind turbine, Int. Rev. Electr. Eng. 2 (2) (2007) 250–259.
[32] O. El-Anwar, J. Ye, W. Orabi, Efficient optimization of post-disaster reconstruction of transportation networks, J. Comput. Civ. Eng. 30 (3) (2016) 04015047.
[33] E. Kamal, A. Aitouche, R. Ghorbani, M. Bayart, Robust fuzzy fault tolerant control of wind energy conversion systems subject to sensor faults, IEEE Trans. Sustain. Energy 3 (2) (2012) 231–241.
[34] E. Kamal, M. Koutb, A.A. Sobaih, B. Abozalam, An intelligent maximum power extraction algorithm for hybrid wind-diesel-storage system, Int. J. Electr. Power Energy Syst. 32 (3) (2010) 170–177.
[35] M. Shahidehpour, M. Eremia, Wind power generation, in: Handbook of Electrical Power System Dynamics Modeling Stability and Control, 12, 2013, pp. 81–85.
[36] X. Zhang, D. Duan, H. Jing, D. Xu, A strategy of dead-time compensation to DFIG, Int. Rev. Electr. Eng. 7 (3) (2012) 4395–4403.
[37] X.J. Zheng, J.J. Wu, Y.H. Zhou, Numerical analyses on dynamic control of five-degree-of-freedom maglev vehicle moving on flexible guideways, J. Sound Vib. 235 (1997) 43–61.

This book belongs to Kitab Liaison (ocd1996@gmail.com) Copyright Elsevier 2023

[38] B. Bhandari, S.R. Poudel, K.-T. Lee, S.-H. Ahn, Mathematical modeling of hybrid renewable energy system: a review on small hydro-solar-wind power generation, Int. J. Precis. Eng. Manuf. Green Tech. 1 (2) (2014) 157–173.
[39] X.J. Zheng, J.J. Wu, Y.H. Zhou, Effect of spring non-linearity on dynamic stability of a controlled maglev vehicle and its guideway system, J. Sound Vib. 279 (2005) 201–215.
[40] Durbin, Dee-Ann, Flying Car Gets Closer to Reality With Test Flight, boston.com. Associated Press, 2012. April 2. Retrieved April 20, 2012.
[41] M. Dürr, A. Cruden, S. Gair, J.R. McDonald, Dynamic model of a lead acid battery for use in a domestic fuel cell system, J. Power Sources 161 (2) (2006) 1400–1411.
[42] B. Bhandari, K.T. Lee, G.Y. Lee, et al., Mathematical modeling of hybrid renewable energy system: a review on small hydro-solar-wind power generation, Int. J. Precis. Eng. Manuf. Green Tech. 2 (2015) 99.
[43] H.Z. Boroujeni, M.F. Othman, A.H. Shirdel, R. Rahmani, P. Movahedi, E.S. Toosi, Improving waveform quality in direct power control of DFIG using fuzzy controller, Neural Comput. Applic. 23 (2015) 78–84.
[44] J. Cardoso, I. Casella, A. Filho, F. Costa, C. Capovilla, SCIG wind turbine wireless controlled using morphological filtering for power quality enhancement, Renew. Energy 92 (2016) 303–311.
[45] I. Casella, C. Capovilla, A. Sguarezi Filho, R. Jacomini, J. Azcue-Puma, E. Ruppert, An ANFIS power control for wind energy generation in smart grid scenario using wireless coded OFDM-16-QAM, J. Control Autom. Electr. Syst. 25 (1) (2013) 22–31.
[46] T. Chikouche, S. Hadjeri, A. Mezouar, T. Terras, A new state-space nonlinear control approach of a doubly fed induction motor using variable gain PI and fuzzy logic controllers, Int. Rev. Model. Simul. 6 (1) (2013) 59–67.
[47] F. Chierchie, E. Paolini, Real-time digital PWM with zero baseband distortion and low switching frequency, IEEE Trans. Circuits Syst. Regul. Pap. 60 (10) (2013) 2752–2762.
[48] S. Chang, Evaluating disaster mitigations: methodology for urban infrastructure systems, Nat. Hazard. Rev. (2003) 186–196, https://doi.org/10.1061/(ASCE)1527-6988(2003)4:4(186).
[49] W.U. Dawei, W.U. Zheng, Z. Landing, H.U. Jizhong, Safety and airworthiness design of ultra-light and very light amphibious aircrafts, in: The 2nd International Symposium on Aircraft Airworthiness (ISAA 2011), Procedia Engineering, vol. 17, 2011, pp. 212–225.
[50] R. Chakib, A. Essadki, M. Cherkaoui, Modeling and control of a wind system based on a DFIG by active disturbance rejection control, Int. Rev. Model. Simul. 7 (4) (2014) 626.
[51] J. De, J.G. de Oliveir, Electric machine topologies in energy storage systems, in: Energy Storage, Springer, New York, 2010.
[52] A. de Sherbinin, M.A. Levy, E. Zell, S. Weber, M. Jaiteh, Using satellite data to develop environmental indicators, Environ. Res. Lett. 7 (2014) 55–59.

This book belongs to Kitab Liaison (ocd1996@gmail.com) Copyright Elsevier 2023

This page intentionally left blank

This book belongs to Kitab Liaison (ocd1996@gmail.com)

Copyright Elsevier 2023

PART 3

Environmental pollution controls

This book belongs to Kitab Liaison (ocd1996@gmail.com)

Copyright Elsevier 2023

This page intentionally left blank

This book belongs to Kitab Liaison (ocd1996@gmail.com)

Copyright Elsevier 2023

CHAPTER 9

Air pollution

Due to the mass urban development since the 1900s, air pollution has occurred through the harmful or excessive quantities of gases, particulates, and biological molecules gathration released into the Earth's atmosphere. This leads to allergies, serious diseases, and death to humans while also adversely affecting other living organisms such as animals and food crops. It could also harm the built environment. Air pollution primarily results from anthropogenic activities where traditional ways of mass urban development play a crucial function in the creation of poor urban air quality. The World Health Organization report of 2014 showed that in 2012, air pollution led to the deaths of approximately 7 million urban people globally, an estimate echoed by the International Energy Agency [1, 2].

Air pollution is material in the air that could have a hostile impact on the ecosystem and humans. For instance, substances released into the atmosphere through human activity contain carbon dioxide (CO_2). Meanwhile, following its function as a greenhouse gas, CO_2 has been labeled as "the leading pollutant" [3, 4]. According to the US Clean Air Act, CO_2 presently forms approximately 410 parts per million (ppm) of the Earth's atmosphere, in relation to around 280 ppm in preindustrial periods [4]. Billions of the annual emission of metric tons of CO_2 through the burning of fossil fuels that build the chemical components of the Earth's atmospheric making them very much unbalanced [5, 6]. Furthermore, sulfur oxides (SOx), mainly sulfur dioxide, from industrial processes produce a chemical compound with the formula SO_2. Often, petroleum and coal have sulfur compounds, and sulfur dioxide is generated from their combustion. Additionally, SO_2 oxidation, typically in the presence of a catalyst such as NO_2, creates H_2SO_4, and hence, results in acid rain. Likewise, nitrogen oxides (NOx), specifically nitrogen dioxide, are produced from combustion at high temperature, and are also released when thunderstorms occur through electric discharge. These particulates, known as fine particles, particulate matter (PM), or atmospheric particulate matter, are tiny particles of liquid or solid suspended in a gas. Aerosol refers to combined gases and particles. Primarily, particulates form through human activities, for example, the combustion of fossil fuels in various industrial processes and

Sustainable Development for Mass Urbanization
https://doi.org/10.1016/B978-0-12-817690-0.00009-9
© 2019 Elsevier Inc.
All rights reserved.

This book belongs to Kitab Liaison (ocd1996@gmail.com)
Copyright Elsevier 2023

power plants also yield significant quantities of aerosols. Averaged globally, anthropogenic aerosols—those created through human activities—are presently responsible for approximately 10% of our atmosphere. High levels of fine particles in the air are connected to health threats, for example, heart disease, lung cancer, and lung malfunctions. Respiratory infections are related to particulates and can be specifically dangerous to those already affected by conditions such as asthma. In addition to the deadly element metals, for instance, chlorofluorocarbons (CFCs) are damaging to the ozone layer. They are released from aerosols sprays, air conditioners, and refrigerators. Here, they interact with other gases and destroy the ozone layer. This permits harmful ultraviolet rays to get to the Earth's surface. This can cause eye disease and skin cancer as well as destroy plants.

Air pollutant production features are reported representative values that try to determine the amount of a pollutant emitted into the ambient air with an activity related to the emission of that pollutant. Usually, these factors are expressed as the pollutant weight divided by a unit volume, weight, duration, or distance of the activity releasing the pollutant (e.g., particulate kilograms emitted for each tonne of coal burned). Such factors enhance the approximation of emissions from numerous sources of air pollution. In the majority of these situations, the features are usually an average of all available information of suitable quality, and in summary it is assumed to be demonstrative of long-term averages. The risk of air pollution is a role of the exposure to that pollutant and its adverse effects. Exposure to air pollution can be represented for certain groups or an individual (e.g., children or neighborhoods cohabiting in a country), or for whole populations. For instance, for a given geographical area, a person may measure the exposure to an unsafe air pollutant that involves different age groups and microenvironments. The analysis can be done as an inhalation exposure. This would be responsible for daily exposure in numerous settings (e.g., varying outdoor locations and indoor microenvironments). The contact requires the inclusion of other demographic groups, particularly infants, children, and pregnant women as well as varying age groups and other sensitive subpopulations. The contact with an air pollutant should incorporate the air pollutant levels of concentrations together with the time taken in each setting and the corresponding rates of inhalation for each subgroup for every single time that the subgroup is available and involved in a specific activity (cooking, playing, reading, spending time in traffic, working etc.). For instance, the inhalation rate of a small child will be lower than that of an adult. A child participating in vigorous activity will have an increased respiration rate than that very child in a sedentary activity. Everyday exposure,

This book belongs to Kitab Liaison (ocd1996@gmail.com) Copyright Elsevier 2023

then, has to reflect the time spent in every microenvironmental setting and the nature of the activities in these settings. The concentration of air pollutants in every microenvironmental/microactivity setting is summarized to show the exposure. Some pollutants such as black carbon, traffic-linked exposures may control the total exposure regardless of a short exposure period for increased concentrations overlap with participation to (motorized) traffic or proximity to main roads. Research has established increased susceptibility to developing asthma with high exposure to traffic-associated air pollution. In addition, according to a joint study by the World Bank and the Institute for Health Metrics and Evaluation (IHME) at the University of Washington, the world economy losses $5 trillion per year to air pollution because of productivity losses and tarnished quality of life. The losses of productivity result from deaths because of diseases due to air pollution. Of every 10 deaths in 2013, one was related to diseases caused by air pollution and the challenge is getting worse. In the developing world, the problem is even more acute. In lower-income countries, children under 5 are more than 60 times (more) susceptable to deaths related to exposure to air pollution as opposed to children in high-income countries. According to the report, additional economic losses resulting from air pollution, including the adverse effect on agriculture, health, and productivity, were not analyzed in the report; hence, the actual costs to the world economy are way more than $5 trillion.

Motor vehicles that use fossil fuels are a key factor in air pollution in urban areas, and can be replaced by electric vehicles. Because a great share of air pollution results from fossil fuel combustion such as oil and coal, this makes the Earth a dangerous place for all living beings. Just because the rate of air pollutant especially CO_2 produced by anthropogenic is active, the natural CO_2 descend is not in a balanced stage. The following research confirmed the fact that the variation between the CO_2 sink through the ocean and the vegetation sink and air pollutant CO_2 by anthropogenic activities primarily in the urban areas, and CO_2 rates had increased annually, hence, causing more CO_2 ppm into the atmosphere and harmful for breathing of any living being on Earth.

Urban air pollution impact on global environment

Introduction

Currently, the annual average concentration of atmospheric CO_2 is 400 ppm [7, 8]. Following the early 1990s industrial revolution, deforestation, fossil fuels, and changes in land use have become the main sources of

This book belongs to Kitab Liaison (ocd1996@gmail.com) Copyright Elsevier 2023

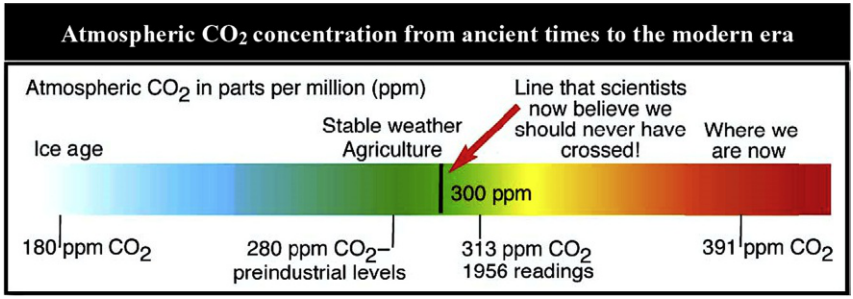

Fig. 9.1 The concentration of CO_2 (ppm) in the atmosphere in ice age in relation to the present (2016) concentration of atmospheric CO_2.

anthropogenic CO_2, which have caused the CO_2 concentration in the atmosphere to increase rapidly (Fig. 9.1). In this article, I have determined the global CO_2 concentration, and the global carbon budget through calculating for the levels of CO_2 being emitted into the atmosphere in relation to the universal CO_2 balance (Eq. 9.1) and the acceleration rates of atmospheric CO_2 emissions per annum.

Moreover, I have prepared comprehensive information sets by MATLAB software and have determined the total emissions of global carbon annually from the preindustrial era (1750) to the modern era (2015). The entire CO_2 emissions from the change in land use and combustion of fossil fuels from 1750 to the era of the Industrial Revolution and from 1870 to the modern era have been discussed in detail. This is through integrating information from the Fifth Assessment Report of the Intergovernmental Panel on Climate Change (IPCC AR5) into MATLAB software so that accurate estimates of CO_2 emissions into the atmosphere could be attained because this gas is the key driver of climate change. The approximate CO_2 emissions from the combustion of fossil fuel are known as E_{FF}; Gt (year^{-1}), and the emissions caused by the change in land use are E_{LUC}; Gt (year^{-1}). The CO_2 absorption and sequestration by the oceans is known as S_{OCEAN}; Gt (year^{-1}), and that by the terrestrial vegetation is known as S_{LAND}; Gt (year^{-1}); they have also been approximated to assess the rate of growth of the concentration of atmospheric CO_2 (G_{ATM}; Gt (year^{-1})) through the subsequent equation relating the balance of CO_2 in the atmosphere, land, and ocean:

$$E_{FF} + E_{LUC} = G_{ATM} + S_{OCEAN} + S_{LAND} \tag{9.1}$$

$$G_{ATM} = E_{FF} + E_{LUC} - S_{OCEAN} - S_{LAND} \tag{9.2}$$

This book belongs to Kitab Liaison (ocd1996@gmail.com) Copyright Elsevier 2023

The atmospheric G_{ATM} is determined in sections per million per annum (ppm/year) that can be converted into the whole mass of carbon per annum (GtC/year).

The evaluation of environmental susceptibility has been carried out worldwide in the last several decades, and many studies have been done [1, 2, 9]. Currently, few studies have been conducted on the hostile effects of toxic quantities of CO_2 in the atmosphere on the Earth's living beings. Therefore, the objective of this report is to determine the annual growth rates of CO_2 concentration in the atmosphere and the effect on the future state of the worldwide environment to establish the survival period of the human race and other living organisms.

Methods

Universal emissions of CO_2, sequestration, and absorption were determined through interpreting reports obtained from numerous organizations (CDIAC, IEA, UNEP, USDoE, ECE, EIA, PBL, NEAA, NEDO, NOAA, and NASA), and the information was integrated into MATLAB software to create the dataset. To correctly calculate the annual global carbon approximations, I considered [7] the entire information up to the year 2015 and the predicted emissions of fossil energy for 2016 [10], and from the predicted the entire carbon approximations for 2016, the yearly rates of growth of the CO_2 atmospheric concentration were determined.

CO_2 emissions from fossil fuel

The annual growth rates of CO_2 emissions were approximated from the variation between two successive years, which was alienated by the first-year emissions per the following equation:

$$\left[\frac{E_{FF\,(t_{0+1})}-E_{FF\,(t_0)}}{E_{FF\,(t_0)}}\right]*100\%\text{year}^{-1} \tag{9.3}$$

In summary, a simple calculation can illustrate the annual CO_2 emission rate of growth. Nevertheless, to determine the rate of growth over multiple decades accurately, I used a leap-year aspect to approve the net annual carbon (E_{FF}) rate of growth through applying its logarithm equivalent in the following equation:

$$\frac{1}{E_{FF}}\frac{d\left(\ln E_{FF}\right)}{dt} \tag{9.4}$$

This book belongs to Kitab Liaison (ocd1996@gmail.com)
Copyright Elsevier 2023

In this section, I determined the pertinent emission growth rates of CO_2, bearing in mind the multidecadal era, through implementing a nonlinear drift into $\ln(E_{FF})$ in Eq. (9.4) and by determining the annual growth percentage. Therefore, I fitted the logarithm of E_{FF} into the equation instead of using E_{FF} directly in order to ensure that the estimates of the growth rate are accurate and satisfy Eq. (9.3) [11, 12].

CO_2 emissions from the land-use change (E_{LUC})

The emissions discussed in this section (E_{LUC}) are comprise of forest degradation, the neglect of agricultural land related to modern civilization, and CO_2 fluxes from deforestation. These were calculated through the implementation of dynamic global vegetation modeling (DGVM) bookkeeping replications in MATLAB [13–15]. The simulation preparations were done using DGVMs, whereby I began by clarifying the historical changes in the use of land and then discussed the concentration of the atmospheric CO_2 [16, 17]. Thus, in the distribution of preindustrial land cover, I employed a time series through allocating the approximated variance into the first simulation and to the prescribed land-cover change [6], including the dynamic evolution of biomass soil carbon [18]. The entire DGVMs in this section feature the whole vegetation processes of growth and decay together with the disintegration of dead organic matter to calculate the response to the rising levels of atmospheric CO_2 [4, 19, 20].

Ocean CO_2 sink

From 1959 to 2015, the CO_2 sequestered via the ocean was determined through incorporating seven global ocean biogeochemical cycle models [1, 21]. The approach is applicable when carrying out a comprehensive analysis of the chemical, biological, and physical processes that are directly influenced by the CO_2 concentration at the ocean surface and the fluxes of air-sea CO_2. Therefore, the sequestration of ocean CO_2 is standardized through correct observational values through partitioning the annual values singularly through the modeled average for 1990–99, followed by multiplying the finding by an observation-based calculation of 2.2 GtC/year [22–24]. Hence, the sequestration oceanic CO_2 per annum (t) in GtC/year is calculated as shown below:

$$S_{OCEAN}(t) = \frac{1}{n}\sum_{m=1}^{m=n} \frac{S^{m}_{OCEAN}(t)}{S^{m}_{OCEAN^{(1990-99)}}} * 2.2 \tag{9.5}$$

This book belongs to Kitab Liaison (ocd1996@gmail.com) Copyright Elsevier 2023

where n is the number of variables, m is the factors, and t is the time period. When the ratio or the sequestration of CO_2 in the 1990s is assumed to be underestimated, the standardization is considered and, in the beginning, it is trigged through diffusion that depends on the gradient of CO_2. Thus, the ratio is considered a naturally suitable method that is responsible for the time dependence of the CO_2 gradient in the oceans [25, 26].

CO_2 absorption by terrestrial vegetation and the Earth

The CO_2 emission variations from land-use changes (E_{LUC}) and fossil fuels (E_{FF}) as well as the rate of growth of the concentration of atmospheric CO_2 (G_{ATM}) and the sequestration of ocean CO_2 (S_{OCEAN}) can be explained to calculate the total ocean CO_2 via terrestrial vegetation (S_{LAND}) by applying Eq. (9.1). Consequently, this form of sequestration can be calculated as the CO_2 remaining from the mass balanced budget that is represented as shown below:

$$S_{LAND} = E_{FF} + E_{LUC} - (G_{ATM} + S_{OCEAN}) \tag{9.6}$$

In this section, S_{LAND} is calculated from the remainder of the approximations and is inclusive of the entire perturbed carbon from land-use changes, the CO_2 atmospheric growth rate, and fossil fuels.

The S_{LAND} computation in Eq. (9.6) together with the budget obtained from the $DGVM_S$ can be applied to determine E_{LUC} through subtracting the effects of land-use changes that will offer an independent result consistent with S_{LAND}. Hence, it can signify a suitable insight on the function of the terrestrial vegetation in calculating the response to climate variability and CO_2 (Fig. 9.2).

Calculation of the growth rate of the atmospheric CO_2 concentration (G_{ATM})

The entire rate of growth of the atmospheric CO_2 concentration was computed for 1956–2016. Implying that, the yearly growth in the atmospheric CO_2 concentration was calculated through relating the records of CO_2 sequestration and emissions from numerous sources (DEP, NASA, NOAA/ESRL, 2015, Scripps, NEDO, and UNDP), bearing in mind that the ocean boundary layers and the air are properly mixed and very much in an operational band with latitude and time period [11, 27]. The rate of growth unit, ppm/year, is then converted from GtC/year to be in with line with other factors.

This book belongs to Kitab Liaison (ocd1996@gmail.com) Copyright Elsevier 2023

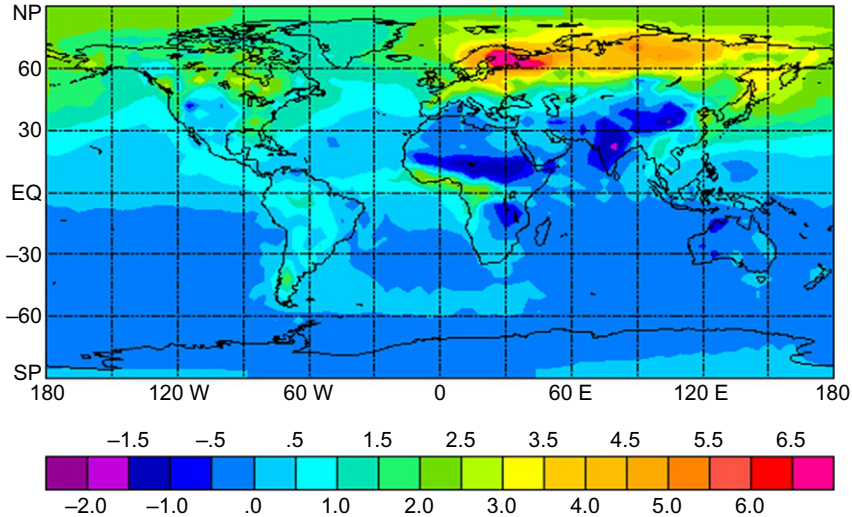

Fig. 9.2 Yearly, as simulated in MATLAB, the mean mixing ratio of CO_2 (ppmv), with respect to the PBL, using terrestrial biosphere surface fluxes. The concentration was reset to be globally uniform, and the model was operated on a course 7.2 × 9 grid with nine levels for 10 years. At the conclusion of this, "*spin up: run" was then applied as the first condition for a further 4-year integration on a 4 × 5 grid with 17 levels. All findings offered here are for the last 3 years of the 4 × 5 run.

Results and discussion

For the period 1875–2016, the average emissions of global carbon have been projected by many scientists from NASA, NOAA, DEP, NASA, NOAA/ESRL, Scripps, NEDO, UNDP, and numerous other agencies (Fig. 9.1). Over this time scale, fossil fuel combustion and other industrial activities were responsible for 91% of the total emissions ($E_{FF} + E_{LUC}$) while 9% were caused by land-use change [3, 28]. These emissions were obtained through sinks within the oceans (26%), the land (30%), and the atmosphere (44%) that account for the yearly growth of the atmospheric CO_2 [4, 11]. In this section, other than the land-use factors, carbon emissions have increased since 1959 with significant interannual variation in the growth rate of atmospheric CO_2 concentration and CO_2 sequestration through terrestrial vegetation [Fig. 9.3 and bearing in mind decadal variances in all terms (Table 9.1)].

CO_2 emissions from fossil fuels and land-use change

In the 1960s, the universal emissions of CO_2 from industrial activities and the combustion of fossil fuels rose at an average of 3.1 ± 0.2 GtC/year

This book belongs to Kitab Liaison (ocd1996@gmail.com) Copyright Elsevier 2023

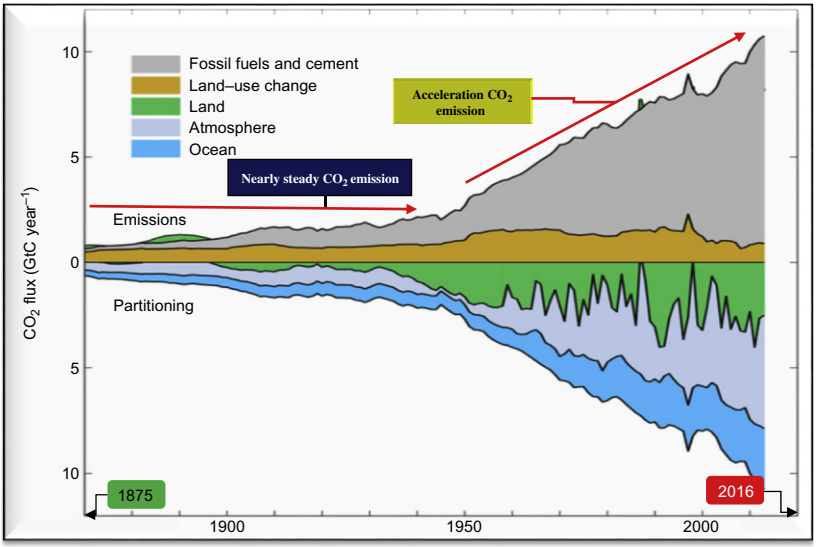

Fig. 9.3 The total global emissions of carbon and separating of the sink budget averaged in the last decades (1875–2016), together with fossil fuel emissions and land-use change along with land, ocean, and atmosphere sinks.

per decade and from 2006 to 2015 through an average of 9.3 ± 0.5 GtC/year (Fig. 9.5). In the 1960s and 1990s, the growth rate of the emissions declined from 4.5% per year in the 1960s (1960–69) to 2.8% per year in the 1970s (1970–79), 1.9% per year in the 1980s (1980–89), and 1.1% per year in the 1990s (1990–99). In the 2000s, growth began to rise again at an average rate of 3.5% per year. However, it has recently decreased to 1.8% per year (2006–15). However, the change in CO_2 emissions from land use have remained about constant at nearly 1.3 ± 0.5 GtC/year during 1960–2015. The decrease in emissions from land conversion proposes that important emissions occurred in the 1990s and 2000s as indicated by DGVM methods in MATLAB software and bookkeeping (Table 9.1). This decrease is not accounted for by the transformation in tropical deforestation, rather by the 1990s flux identical to that in the 2000s, signifying a decline in E_{LUC} from 2011 to 2015 comparable to that from 2001 to 2010 (Fig. 9.4).

Ocean and terrestrial vegetation CO_2 sinks

For 1959–2015, the worldwide CO_2 sequestration via the ocean was projected depending on the mean CO_2 sequestration rate for the 1990s incorporated with the variances in sequestration of ocean CO_2 together with all

This book belongs to Kitab Liaison (ocd1996@gmail.com) Copyright Elsevier 2023

Table 9.1 The findings were employed using budgeted residuals and bookkeeping technology from DGVMs used in MATLAB software, and its inverse calculations for 1960–69, 1970–79, 1980–89, 1990–99, and 2000–09 shown in GtC/year.

Mean (GtC/year)	1960–69	1970–79	1980–89	1990–99	2000–09	2006–15	2016
Carbon emissions from land-use change (E_{LUC})							
Bookkeeping DGVMs	1.5 ± 0.5 1.2 ± 0.3	1.3 ± 0.5 1.2 ± 0.3	1.4 ± 0.5 1.2 ± 0.2	1.6 ± 0.5 1.2 ± 0.2	1.0 ± 0.5 1.1 ± 0.2	1.0 ± 0.5 1.3 ± 0.3	1.3 ± 0.5 1.2 ± 0.4
Residual terrestrial sink (S_{LAND})							
Budget residual DGVMs	1.7 ± 0.7 1.2 ± 0.5	1.7 ± 0.8 2.2 ± 0.5	1.6 ± 0.8 1.7 ± 0.6	2.6 ± 0.8 2.3 ± 0.5	2.6 ± 0.8 2.8 ± 0.6	3.1 ± 0.9 2.8 ± 0.7	1.9 ± 0.9 1.0 ± 1.4
Total land fluxes ($S_{LAND} - E_{Luc}$)							
Budget ($E_{EF} - G_{ATM} - S_{ocean}$) DGVMs Inversions (CTE2016-FT/Jena CarboScope/(CAM)	0.2 ± 0.5 -0.2 ± 0.7 –/–/–	0.4 ± 0.6 1.1 ± 0.5 –/–/–	0.1 ± 0.6 0.4 ± 0.5 –/0.2/0.9	1.0 ± 0.6 1.1 ± 0.3 –/1.0/1.9	1.6 ± 0.6 1.8 ± 0.4 1.5/1.6/2.5	2.2 ± 0.7 1.7 ± 0.5 2.2/2.3/3.4	0.6 ± 0.7 -0.1 ± 1.4 1.9/2.6/2.6

This book belongs to Kitab Liaison (ocd1996@gmail.com)

Copyright Elsevier 2023

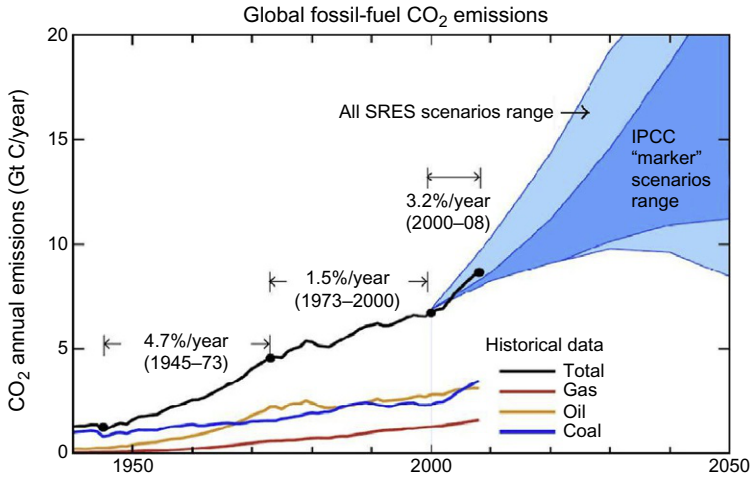

(A)

Global fossil fuel carbon dioxide emissions accelerated after Kyoto Protocol

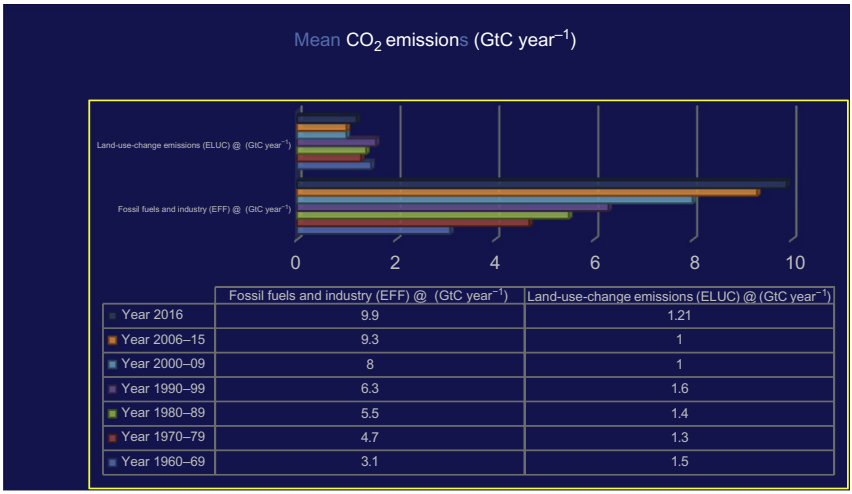

	Fossil fuels and industry (EFF) @ (GtC year^{-1})	Land-use-change emissions (ELUC) @ (GtC year^{-1})
Year 2016	9.9	1.21
Year 2006–15	9.3	1
Year 2000–09	8	1
Year 1990–99	6.3	1.6
Year 1980–89	5.5	1.4
Year 1970–79	4.7	1.3
Year 1960–69	3.1	1.5

(B)

Fig. 9.4 (A) CO_2 budget from combustion of fossil fuels, such as oil, coal, and gas. (B) Total valued CO_2 emissions from both fossil fuels and land-use change from 1960–69 through 2016.

seven global ocean biogeochemical cycles. The average ocean CO_2 sequestration was projected to be around 2.2 ± 0.4 GtC/year for the 1990s, due to indirect IPCC observational data [2, 19] and in view of the time scale for CFC penetration [5, 29]. This CO_2 sequestration score is similar to that of 2.0 ± 0.5 GtC/year determined for the 1990s and 1.9 to 2.5 GtC/year

This book belongs to Kitab Liaison (ocd1996@gmail.com)
Copyright Elsevier 2023

for 1990–2009 [4, 30] with an uncertainty range of ±0.3 to ±0.7 GtC/year. Hence, this technique can correctly calculate observation-based ocean sequestration through applying the sea-air pCO_2, (sea-air pCO_2 variable) * (gas transfer coefficient), and the findings are totally consistent with the observed outcomes [30, 31].

Eventually, the calculation indicated that in the 1960s, the sequestration of residual terrestrial CO_2 rose from 1.7 ± 0.7 GtC/year to 3.1 ± 0.9 GtC/year from 2006 to 2015 with an interannual inconsistency of up to 2 GtC/year. Correspondingly, it shows a decline in land sequestration through El Niño and over accumulation by ocean sequestration that is responsible for the growth rate of atmospheric CO_2 (Fig. 9.5). From 2006 to 2015, the increased sequestration of CO_2 through the land is like that of the 1960s as resolved through DGVMs by including the predicted budget residual in response to the growth in cumulative atmospheric CO_2 (Fig. 9.5). This DGVM mean of 2.8 ± 0.7 GtC/year is theoretically the observational average for 2006–2015 that is approximated from the budget residual (Fig. 9.5).

Then, the total CO_2 land flux ($S_{LAND} - E_{LUC}$) that is stretched through the atmospheric inversion is significantly advantageous to the calculation of

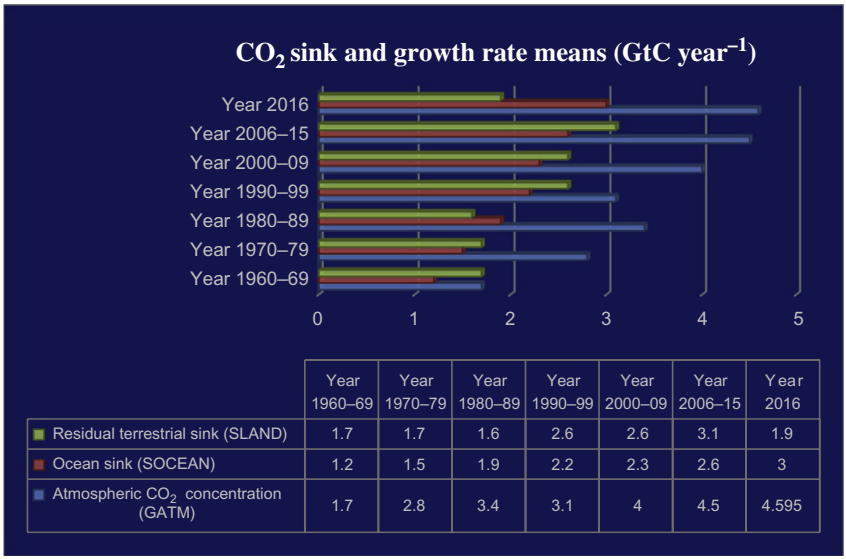

	Year 1960–69	Year 1970–79	Year 1980–89	Year 1990–99	Year 2000–09	Year 2006–15	Year 2016
Residual terrestrial sink (SLAND)	1.7	1.7	1.6	2.6	2.6	3.1	1.9
Ocean sink (SOCEAN)	1.2	1.5	1.9	2.2	2.3	2.6	3
Atmospheric CO_2 concentration (GATM)	1.7	2.8	3.4	3.1	4	4.5	4.595

Fig. 9.5 CO_2 penetrations and yearly growth rate of CO_2 emissions in GtC/year from 1960 to 1969 through 2016. The calculation $\left[\left(\frac{4.595-4.500}{4.500}\right)\times 100\% = 2.11\%\right]$ discovered that atmospheric CO_2 concentration is growing at a rate of 2.11% per annum.

This book belongs to Kitab Liaison (ocd1996@gmail.com)
Copyright Elsevier 2023

the global budget, G_{ATM}, together with the assumption of relative inconsistency in S_{OCEAN} and E_{FF} because of the inversions. The entire land flux has identical magnitude with respect to the decadal mean, which is for 2006–15, computed for three inversions of 2.2, 2.3, and 3.4 GtC/year in comparison to the total flux calculation of 2.1 ± 0.7 GtC/year using Eq. (9.1). The entire sequestrations of land through these inversions are 1.8, 1.8, and 3.0 GtC/year together with the mean of all reverse flux variables, 0.45 GtC/year. Captivatingly, the interannual disparity inside the inversions corresponded to the residual-based S_{LAND} very closely (Fig. 9.5). Thus, the entire land fluxes computed through DGVM supports that the determination of the carbon budget and its inversion in the atmosphere has a decadal average of 1.7 ± 0.5 GtC/year (Table 9.1 and Fig. 9.5).

Cumulative CO_2 emissions and atmospheric impact

In this work, the entire emissions due to fossil fuel burning and land-use change from 1870–2015 were determined as 555 ± 55 GtC. In the atmosphere, the emissions are divided among the atmosphere (235 ± 5 GtC per the atmospheric CO_2 concentrations of 288 ppm in 1870 and 399.1 ppm in 2015 [6, 11]), the ocean (160 ± 20 GtC [1, 22]), and the land (160 ± 60 GtC [11, 22]). The general emissions during the preindustrial development era of 1750–1869 were 3 GtC for E_{FF} and around 45 GtC for E_{LUC} (rounded to the nearest 5), of which 10 GtC were emitted in the 1850–70 period [8, 18] and 30 GtC in the 1750–1850 era for an average of 25 GtC [4, 13, 32], which confirmed that the atmospheric CO_2 concentration growth rate over this era was 25 GtC, that of the ocean sequestration was 20 GtC, and terrestrial land sequestration was 5 GtC.

According to the calculations in this study, in 2016 the increase in the concentration of the atmospheric CO_2 (G_{ATM}) was predicted to rise to 6.7 ± 1.1 GtC (3.15 ± 0.53 ppm). Including the predicted E_{FF} and G_{ATM} shows that adding the sequestration by the ocean and land and subtracting the emissions from land-use change ($S_{LAND} + S_{OCEAN} - E_{LUC}$) only generates around 3 GtC. S_{OCEAN} was calculated for 3.0 GtC in 2015 and is anticipated to grow in 2016 [11, 21], and E_{LUC} was calculated for 1.3 GtC in 2015 with a decadal mean of 1.0 GtC/year. In this part, the terrestrial sequestration remaining, $S_{LAND,}$ for 2016 is, as projected, far less than the average balance of E_{LUC} for 2006–15. Thus, to account for the accumulation of the entire carbon and its decree of increase in the atmosphere from 1750 or 2016, I have applied the concentrations of atmospheric CO_2 of 288 ± 3 or 399 ± 3 ppm, respectively. The difference of ± 3 ppm (converted

This book belongs to Kitab Liaison (ocd1996@gmail.com) Copyright Elsevier 2023

to $\pm 1\sigma$) was attained from IPCC data [1, 33], and the level of growth of the atmospheric CO_2 concentration was determined through MATLAB software by relating the individual annual and decadal scores for the last 10 years. The CO_2 concentration in the atmosphere was confirmed to be growing at a rate of 2.11% ppm yearly. In 2006, the atmospheric concentration of CO_2 was 399.4 ± 0.1 ppm [10, 11], and it has been increasing at a rate of 2.11% annually. As such, a dangerous CO_2 concentration of 60,000 ppm will result in 121,017,712 years.

Conclusion

Emissions and redistributions of global CO_2 within the atmosphere, terrestrial biosphere, and ocean by absorption were determined for the last several decades to establish the atmospheric CO_2 concentration in the future. The yearly rates of growth of the global atmospheric CO_2 concentration (G_{ATM}) (ppm) were determined with respect to the global carbon budget of the land, atmosphere, and the ocean during the past several years; this was indicated to presently be 2.11% per annum. If we fail to lower the present quantities (400 ppm) of yearly CO_2 increases in a timely way, the concentration of atmospheric CO_2 will ultimately reach a dangerous level (60,000 ppm). By that time, the human race and all other living things on the planet will be wiped out in 30 min in 121,017,712 years (i.e., $\int_{400(2.11\%)}^{600}(2017) = 121{,}017{,}712$). This will mark the end of human civilization on Earth.

Urban air pollution control technology

Introduction

In the mid-1990s, numerous processes that emitted greenhouse gases, specifically CO_2, were analyzed, Right before the industrial revolution, there was a CO_2 concentration in the atmosphere estimated as 280 ppm that was almost twice that, 560 ppm, in 2015 [4, 8]. Earth possesses a natural effect whereby greenhouse gases in the atmosphere permit the sunlight to reach it, but absorb the heat radiation. Because of this, the heat is absorbed by the gases, and they ensure that the surface temperature on Earth is near 14°C on average, whereas in its absence the Earth's average surface temperature would have been almost 0°C. Because the human combustion of fossil fuel and human activities have heightened the levels of gases that absorb heat, the atmosphere is retaining more heat; hence, a rise in global average surface temperatures and the outcome is a change in climate. Research associated

This book belongs to Kitab Liaison (ocd1996@gmail.com) Copyright Elsevier 2023

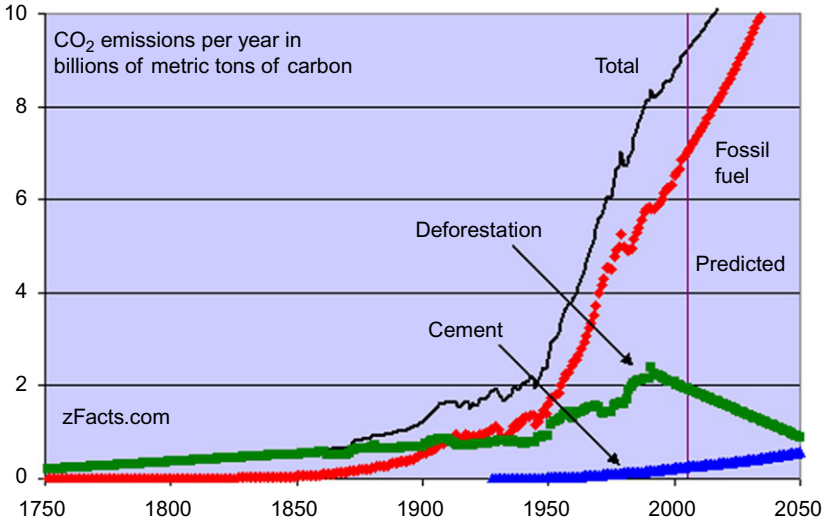

Fig. 9.6 Fossil fuel data are from the US Department of Energy, including an estimate that fossil fuel emissions will increase 1.2% per year until 2030.

with global climate change should explicitly counter the uncertainty about future climate effects [19, 28]. Even when the emissions of global carbon (C) from use of fossil fuel were 9.795 gigatonnes (Gt) in 2015 or 35.9 Gt CO_2 of carbon dioxide [28] that is explained, around 91% of the entire emissions of CO_2 emanate from coal (42%), oil (33%), gas (19%), cement (6%), and gas flaring (1%) by burning the conventional energy supply that threatens the Earth (Fig. 9.6).

Because of the negligence of land-use changes (e.g., excessive development, cutting down forests to allow farming, etc.) changes in the levels of sunlight reflected from the ground back into space (the surface albedo) have resulted [6]. The nature of these changes is projected to be about one-fifth of the compelling on the global climate because of alterations in emissions of greenhouse gases. The significant impact of deforestation is approximated to be at high latitudes whereby the albedo of snow-covered land, formerly forested, has risen. The snow on trees shows only about half of the sunlight is reaching it while snow-covered open ground indicated a level of about two-thirds. Other substantial transformations in the land surface originating from human activities are tropical deforestation that alters the rates of evapotranspiration (the level of water vapor put into the atmosphere through transpiration and evaporation from trees); desertification that builds a surface albedo; and the overall agricultural effects on soil moisture characteristics.

This book belongs to Kitab Liaison (ocd1996@gmail.com) Copyright Elsevier 2023

To counter this fatal effect, an innovative procedure has been suggested through explaining sophisticated chemical reactions to break down the greenhouse gases and a sequence of mathematical calculations for theoretical resolution for global climate change. The suggested technique will offers us practical information and may cause us to apply this suggested theory practically for application.

Global warming

The speed of unexpected global warming together with its complexity of mechanism affects ecosystems, the health of humans, and economies [7]. The definition of hazardous global warming cannot be advanced without developing a reliable mechanism to scientifically resolve this problem [2, 9]. Generally, this is the effective temperature (variation of flux in and out) that the climate change created because of the effect of CO_2 gases in the atmosphere (Fig. 9.7).

The emissivity (ϵ) is associated with the CO_2 concentration in the atmosphere; if the concentration of CO_2 is increased in the atmosphere, ϵ would be larger because of the longwave radiation absorbance and emitting ability of the atmosphere increasing, leading to global warming.

The predictions portray an increasing ecological transformation and stress in Earth's biosphere, with numerous animal and plant species encountering high competition for survival and a substantial species turnover

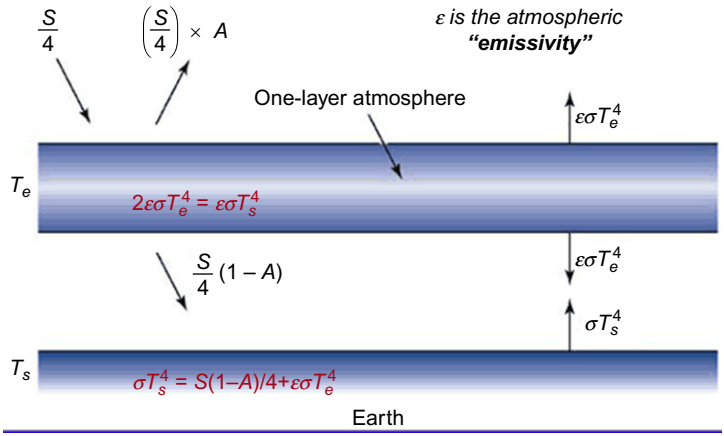

Fig. 9.7 Temperature balance of the Earth with the output and input from space, atmosphere, and surface represented by transparent to solar radiation and with an infrared emissivity ϵ.

This book belongs to Kitab Liaison (ocd1996@gmail.com) Copyright Elsevier 2023

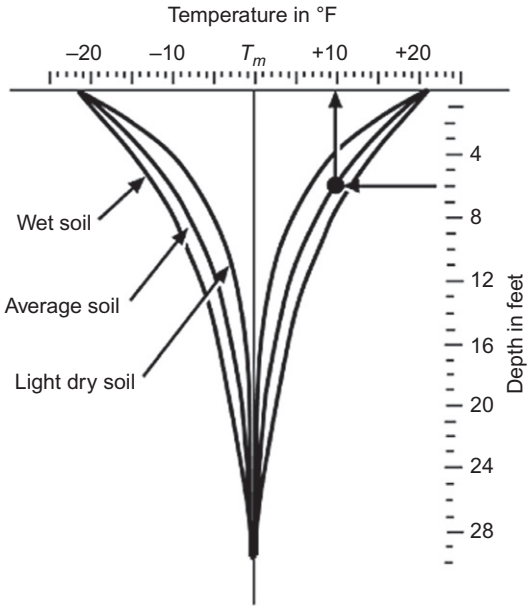

Fig. 9.8 Temperature variation effect the Earth's subsurface considering the depth in between 0 to 30 ft which shows that wet soil, average soils, and light dry soils has severe impact by absorbed temperature within the 6 ft deep.

because some species enter areas occupied by other species [3]. Furthermore, changes in plant communities, it was projected climate change will interfere the ecological equilibrium between often endangered and interdependent animal and plant species, minimize biodiversity and negatively impact on energy, Earth's water, carbon and other element cycles [3, 28]. For more than two decades, scientists have warned of the risks of climate change leading to melting glaciers, increasing sea levels, and other environmental changes and ecological effects. So balancing concentrations of CO_2 would indeed lessen the severe damage to at least one unique ecosystem, the atmospheric chemical cycle, and global warming [29, 30] (Fig. 9.8).

Solution of global warming

Because CO_2 molecules are very stable, a tool has therefore been suggested that can submerge the industrial CO_2 to yield helpful products through a heat-releasing reaction between lithium nitride (Li_3N) and CO_2 through reacting lithium with nitrogen at room temperature. Reacting lithium nitride with carbon dioxide produces an amorphous carbon nitride ($C_3N_4 = C + N_2$), a semiconductor, and lithium cyanamide (Li_2CN_2), a

This book belongs to Kitab Liaison (ocd1996@gmail.com) Copyright Elsevier 2023

predecessor to fertilizers. Other than the fertilizer production, the most beneficial products of this reaction are O_2 and N_2, which will balance the atmospheric chemical cycle through the application of a low energy effect chemical reaction as follows:

$$CO_2 \rightarrow Li3N\,C_3N_4 + O_2 + Li_2CN_{2(\text{Byproduct, a fertilizer})}$$

$$C_3N_4 = C + N_2$$

Through the implementation of a chemical reaction via engineering application at the industry, CO_2 can be seized and stored in a sophisticated tool for permitting reactions to occur as discussed above to produce C, N_2, O_2, and Li_2CN_2. Thus, this reaction shall dramatically lower the emissions of carbon, taking full advantage of CO_2-derived chemical products, so-called carbon capture, and conversion into helpful commodities.

After the CO_2 is controlled as per the technology discussed above, then it was estimated that the atmosphere would be quite clean to balance a chemical configuration. Therefore, the estimation has been done initially with a temperature calculation considering the clean atmosphere in the planet as stated in the equation below:

$$\hat{T} = T_e$$

where $\hat{T}$ is the planet's equilibrium surface temperature, flux in and flux out, and T_e is the planet's actual temperature. The assumption was that our planet revolves within a period of P, and we have a clean atmosphere so that the energy to move from one hemisphere (for example, the one experiencing day) to the other, should conduct through the material composition in the surface. This process is adequately slow, so it can be assumed that every hemisphere is separated from the other. Another assumption was that day and night has $P/2$ amount of time, that is, day and night have the same lengths. They also continued to assume that flux out$=\sigma T^4$, but flux in $= a\Omega/4$. Hence, the actual temperature would be $a\Omega/4 = \sigma T^4$ thus, $T_e = (a\Omega/4\sigma)^{1/4}$, that is, about 261 W/m^2. The real temperature is the temperature that controls the diurnal and surface temperature at Earth previously identified through an estimation of global annual temperature provable analysis of spatiotemporal climate change in the past patterns of 500 years, and an experimental technique to approximate the connection between global temperature changes [4]. The solar constant, denoted as flux in $a\Omega/4$, indicates that the entire power that enters the planet for each square meter of surface area on the planet is $\Omega = 1052\,\text{W/m}^2$ [5]. From the point of view of the sun, the Earth is a circle, rather than a sphere, so the solar flux is

This book belongs to Kitab Liaison (ocd1996@gmail.com) Copyright Elsevier 2023

received via a circle with area r^2 whereby r is the Earth radius. If we obtained the mean of solar energy received via that disk ($\pi r^2 \Omega$) over the whole Earth surface ($4\pi r^2$), the average solar energy received via the Earth per unit area of the Earth surface is $\pi r^2 \Omega / 4\pi r^2 = \Omega/4$ ad flux in, is equivalent to $a\Omega/4$. Because there is a flux in, indeed there should be a flux out. The flux out assumes that the Earth acts like a *blackbody* that can be utilized as the *Stefan-Boltzmann Law* to present an expression for flux out $= \sigma T^4$, whereby σ is the *Stefan-Boltzmann constant* ($\sigma = 5.67 \times 10^{-8}$ W/m^{2}K^4) and T is the blackbody temperature. The *effective temperature* of our Earth, T_e, is what its temperature can be described as flux in = flux out whereby flux in $= a\Omega/4$ and flux out $= \sigma T^4$. Thus, the effective temperature would be $a\Omega/4 = \sigma T^4$; hence, $T_e = (a\Omega/4\sigma)^{1/4}$, equivalent to 261 W/m^2 yielding to deadly global warming (Fig. 9.9).

Basically, we are required to neutralize this 261 W/m^2 effective temperature to ensure that our Earth is cool. To minimize this effective temperature requires for the approach to be computed its new equilibrium with respect to reduction of CO_2 by 91%, which can be done once the above discussed technology is used to the entire emissions of CO_2 from industries. Hence, the remaining 9% CO_2 emission which form the effective temperate 23.49 W/m^2 that is almost 0.74 Celsius/m^2 closer to zero (0) degree Celsius. It is proved that once CO_2 is captured and transformed into helpful commodities, it shall indeed play a dramatic role to ensure that the planet is cool.

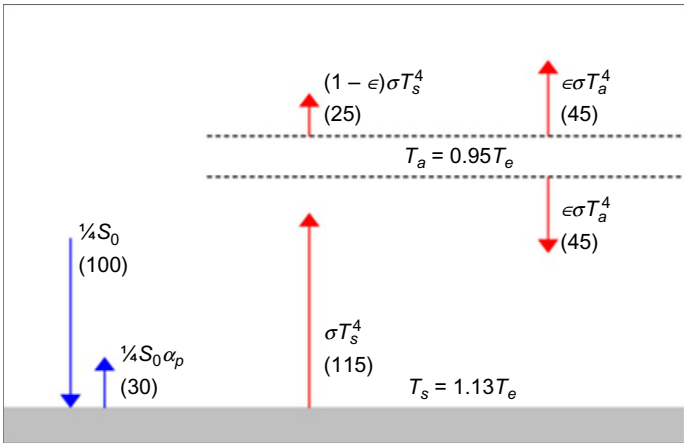

Fig. 9.9 Idealized flux in and flux out to influence diurnal temperature indicates the connection of the influence of radiation with regard to effective temperature, The *blue arrows (dark gray in print version)* represent disperse density awhile the *red arrow (light gray in print version)* denotes longwave (terrestrial) radiative flux out and shortwave (solar) radiative flux in density.

This book belongs to Kitab Liaison (ocd1996@gmail.com) Copyright Elsevier 2023

Conclusion

Following climate change, the credit of trends in current warming alter the atmospheric gases that comes from the analysis of global patterns, not from the comprehensive data of the stations and/or individual weather researchers, even though it is an integrated effort been already described [31]. It is well confirmed that the function of greenhouse gases, precisely CO_2, and their absorption ability and emissivity of the atmosphere have a hazardous warming impact on the surface temperature balance of the Earth because of the combustion of fossil fuels. Moreover, human activities, for example, urbanization and agriculture, are damaging the biosphere balance and atmospheric chemistry resulting in increasing sea levels, sea surface warming, and rising frequency and intensity of severe weather events it makes the long-term capacity of human beings to live in peace [1, 3]. Accordingly, the global warming concept is influencing several biological and physical processes of the health and terrestrial ecosystems composition [11]. Definitely, for any discussion about the advantages of the management of greenhouse gases (GHGs) must be considered seriously as well as the implication continue to be highly uncertain, as amazements of the Earth [22]. Hence, we indeed require sophisticated techniques to create a clean Earth for our future generations. Thus, a time has come to transform these poisonous greenhouses gases into valuable products through a simple chemical reaction that can seize the CO_2 from industries and transform it into Li_2CN_2 as a helpful fertilizer. Then, C, N_2, and O_2 will play a crucial function to balance the chemical cycle at the biosphere and atmosphere to ensure that the Earth is cool.

Acknowledgments

This study has been endorsed by Green Globe Technology, Inc., under grant RD-02018-04 for creating a better environment. The author retains all the rights for the study findings, suggestions, and conclusions, and it can be confirmed that the article doesn't conflict in any way with other publications relating to this field of study.

References

[1] P. Ciais, C. Sabine, Chapter 6: carbon and other biogeochemical cycles, in: T. Stocker, D. Qin, G.K. Platner (Eds.), Climate Change 2013 The Physical Science Basis, Cambridge University Press, London, 2013.

[2] K.L. Denman, et al., Couplings Between Changes in the Climate System and Biogeochemistry, Cambridge University Press, London, 2007.

This book belongs to Kitab Liaison (ocd1996@gmail.com) Copyright Elsevier 2023

[3] J. Prietzel, L. Zimmermann, A. Schubert, D. Christophel, Organic matter losses in German Alps forest soils because the 1970s most likely caused by warming, Nat. Geosci. 9 (2016) 543–548.
[4] W. Li, et al., Reducing uncertainties in decadal variability of the global carbon budget with multiple datasets, Proc. Natl. Acad. Sci. USA 113 (2016) 13104–13108.
[5] B. Gonzalez-Gaya, et al., High atmosphere-ocean exchange of semivolatile aromatic hydrocarbons, Nat. Geosci. 9 (2016) 438–442.
[6] E. Dietzenbacher, J. Pei, C. Yang, Trade, production fragmentation, and China's carbon dioxide emissions, J. Environ. Econ. Manag. 64 (2012) 88–101.
[7] F. Achard, et al., Determination of tropical deforestation rates and related carbon losses from 1990 to 2010, Glob. Chang. Biol. 20 (2014) 2540–2554.
[8] J.E. Bauer, et al., The changing carbon cycle of the coastal ocean, Nature 504 (2013) 61–70.
[9] G.R. van der Werf, et al., Climate regulation of fire emissions and deforestation in equatorial Asia, Proc. Natl. Acad. Sci. USA 105 (2008) 20350–20355.
[10] R.J. Andres, T.A. Boden, D. Higdon, A new evaluation of the uncertainty associated with CDIAC estimates of fossil fuel carbon dioxide emission, Tellus Ser. B Chem. Phys. Meteorol. 66 (2014) 23616.
[11] C. Le Quéré, et al., Global carbon budget 2016, Earth Syst. Sci. Data 8 (2016) 605–649.
[12] C. Vörösmarty, B. Fekete, M. Meybeck, R. Lammers, Global system of rivers: its role in organizing continental land mass and defining land to ocean linkages, Glob. Biogeochem. Cycles 14 (2000) 599–621.
[13] S.J. Davis, K. Caldeira, Consumption-based accounting of CO_2 emissions, Proc. Natl. Acad. Sci. USA 107 (2010) 5687–5692.
[14] J.C. van Dam, Impacts of Climate Change and Climate Variability on Hydrological Regimes, Cambridge University Press, New York, 1999.
[15] J. Milliman, R. Mei-e, D. Eisma (Ed.), Climate Change: Impact on Coastal Habitation, CRC Press, Boca Raton, FL, 1995, pp. 57–83.
[16] J. Mason Earles, S. Yeh, K.E. Skog, Timing of carbon emissions from global forest clearance, Nat. Clim. Chang. 2 (2012) 682–685.
[17] K.-H. Erb, et al., Bias in the attribution of forest carbon sinks, Nat. Clim. Chang. 3 (2013) 854–856.
[18] E. Dlugokencky, P. Tans, Trends in Atmospheric Carbon Dioxide. National Oceanic & Atmospheric Administration, Earth System Research Laboratory (NOAA/ESRL), Available from 2015. Available from: http://www.esrl.noaa.gov/gmd/ccgg/trends/global.
[19] R.A. Duce, et al., Impacts of atmospheric anthropogenic nitrogen on the open ocean, Science 320 (2008) 893–897.
[20] B.B. Stephens, et al., Weak northern and strong tropical land carbon uptake from vertical profiles of atmospheric CO_2 science, Science 316 (2007) 1732.
[21] N. Arnell, et al., R.T. Watson, M.C. Zinyowera, R.H. Moss (Eds.), Climate Change 1995: Impacts, Adaptations, and Mitigation of Climate Change, Cambridge University Press, London, 1996, pp. 325–363.
[22] F. Chevallier, On the statistical optimality of CO_2 atmospheric inversions assimilating CO_2 column retrievals, Atmos. Chem. Phys. 15 (2015) 11133–11145.
[23] T.A. Boden, R.J. Andres, Global regional, and national fossil-fuel CO_2 emissions, Oak Ridge National Laboratory, US Department of Energy, 2016. http://cdiac.ornl.gov/trends/emis/overview_2013.html.
[24] D.M. Karl, M.J. Church, Microbial oceanography and the Hawaii Ocean Time-series programme, Nat. Rev. Microbiol. 12 (2014) 699–713.

This book belongs to Kitab Liaison (ocd1996@gmail.com) Copyright Elsevier 2023

[25] Z. Liu, et al., Reduced carbon emission estimates from fossil fuel combustion and cement production in China, Nature 524 (2015) 335–338.
[26] S. Schwietzke, et al., Upward revision of global fossil fuel methane emissions based on isotope database, Nature 538 (2016) 88–91.
[27] Y. Yin, et al., Variability of fire carbon emissions in equatorial Asia and its nonlinear sensitivity to El Niño, Geophys. Res. Lett. 43 (2016) 10,472–410,479.
[28] A.P. Ballantyne, C.B. Alden, J.B. Miller, P.P. Tans, J.W.C. White, Increase in observed net carbon dioxide uptake by land and oceans during the past 50 years, Nature 488 (2012) 70–72.
[29] R. Houghton, Balancing the global carbon budget, Annu. Rev. Earth Planet. Sci. 35 (2007) 313–347.
[30] A.P. Ballantyne, et al., Audit of the global carbon budget: estimate errors and their impact on uptake uncertainty, Biogeosciences 12 (2015) 2565–2584.
[31] S.L. Postel, G.C. Daily, P.R. Ehrlich, Human appropriation of renewable fresh water, Science 271 (1996) 785.
[32] R.A. Betts, C.D. Jones, J.R. Knight, R.F. Keeling, J.J. Kennedy, El Nino and a record CO_2 rise, Nat. Clim. Chang. 6 (2016) 806–810.
[33] J.G. Canadell, et al., Contributions to accelerating atmospheric CO_2 growth from economic activity, carbon intensity, and efficiency of natural sinks, Proc. Natl. Acad. Sci. USA 104 (2007) 18866–18870.

This book belongs to Kitab Liaison (ocd1996@gmail.com) Copyright Elsevier 2023

CHAPTER 10

Water pollution

Water is a necessary resource. Natural water resources are water sources that are applied for agricultural, domestic, environmental, industrial, and recreational activities. For survival, all living beings need water, leading to the statement that water means life and life means water. The Earth's surface is comprised of 25% land and 75% water, and to survive all creatures require water. Of the surface water, 97% is saline and only 3% is freshwater. Even more interesting, more than two-thirds of the freshwater is present in the form of ice caps or glaciers. Nevertheless, the majority of the rest of the freshwater that is unfrozen is groundwater, and the remainder is in the air or above ground. Freshwater is a reusable resource. Still, the supply of the world's groundwater is declining steadily, with depletion occurring most obviously in whole world which endangers our survival near future (Fig. 10.1).

H_2O is a polar inorganic compound portrayed as a liquid with characteristics of near colorlessness, tastelessness, and odorless, although under normal conditions it is a tiny bit blue. It is the modest hydrogen chalcogenide that is discussed as a universal solvent for its capability to dissolve numerous substances, for example, many sugars, salts, proteins, simple alcohols, polysaccharides, DNA, carbon dioxide, and oxygen. The water molecule is a polar molecule that has a dipole due to the oxygen atom has an advanced electronegativity than hydrogen atoms, which implies that the oxygen atom has a slight negative charge, whereas hydrogen atoms are a little positive. In addition, each water molecule comprises one oxygen atom and two hydrogen atoms linked through covalent bonds (Fig. 10.2).

Outstandingly, it is the only common substance that is present as a gas, solid, and liquid, in usual terrestrial circumstances that is being dangerously polluted. Water implication to the liquid state of a substance present at ordinary ambient pressure and temperature, its solid state (ice), or its gaseous state (steam or water vapor). It also occurs in the forms of icebergs or ice packs, glaciers, fog, aquifers, dew, and atmospheric humidity, which are the key factors of Earth's streams located in varying locations. Under dissimilar conditions, water will have diverse attributes. When the normal pressure is 1 atm, water is in the form of liquid between 0°C (32°F) and 100°C (212°F).

Sustainable Development for Mass Urbanization
https://doi.org/10.1016/B978-0-12-817690-0.00010-5
© 2019 Elsevier Inc.
All rights reserved.

This book belongs to Kitab Liaison (ocd1996@gmail.com)
Copyright Elsevier 2023

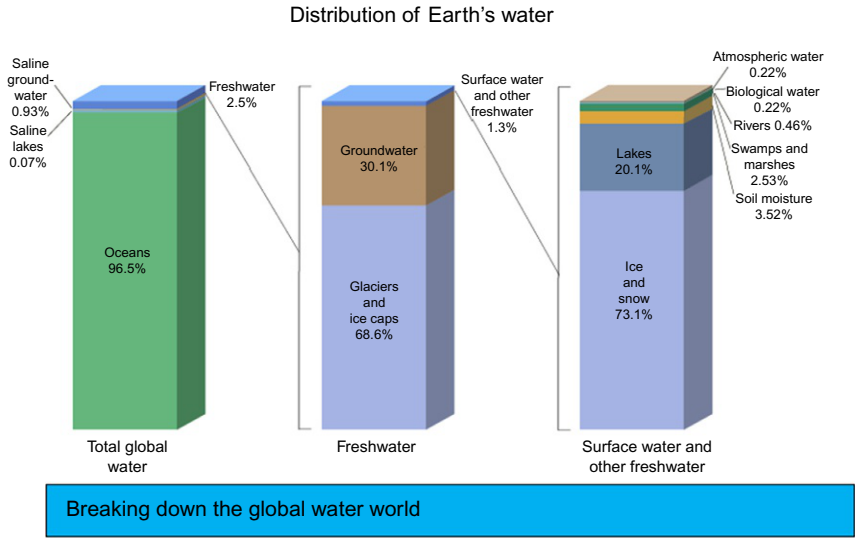

Fig. 10.1 A graphical distribution of the locations of water on Earth. Only 3% of the Earth's water is freshwater. Most of it is in icecaps and glaciers (69%) and groundwater (30%), with all swamps, lakes, and rivers put together to account for a small fraction (0.3%) of the Earth's total freshwater reserves.

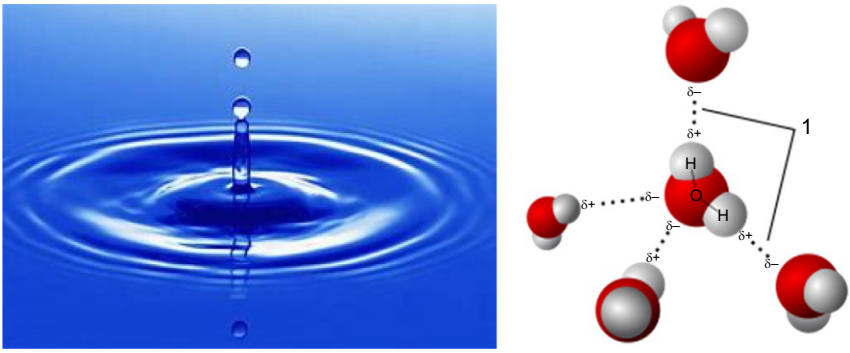

Fig. 10.2 Model of hydrogen bonds (1) between molecules of water prove that the oxygen atom has more advanced electronegativity than hydrogen atom.

Nevertheless, the melting point will change to −5°C at 600 atm and −22°C at 2100 atm, which is applied as the principle to describe the movement of ice skating, glaciers, and buried lakes of Antarctica. Even more interesting, the melting point will hastily rise again, yielding to numerous exotic types of ice that are not present at lower pressures when the pressure is higher than 2100 atm. When the pressure changes, the boiling point will also change.

This book belongs to Kitab Liaison (ocd1996@gmail.com) Copyright Elsevier 2023

For example, the point is 374°C at 220 atm instead of 68°C (154°F) at the top of Mount Everest with an atmospheric pressure of 0.34 atm. The impact of this change is used on steam engine design, deep-sea hydrothermal vents, pressure cooking etc.

Due to mass urban development, under extreme conditions water's attributes change. Water cannot exist in the liquid form and changes directly from solid to gas through sublimation when the pressure is very low (lower than 0.006 atm); this aspect is applied when freeze drying food. The gas and liquid states are no longer distinct when the pressure is extremely high (higher than 221 atm), and a new form known as supercritical steam replaces it.

Another feature of water pollution is that as it freezes, compared to most liquids it becomes less dense. In liquid state, the maximum density of water (at 1 atm) is 1000 kg/m^3 (62.43 lb/cu ft), form at 3.98°C (39.16°F) whereas the density of ice is 917 kg/m^3 (57.25 lb/cu ft). Therefore, by calculation, water increases 9% in volume as it freezes, which confirms the fact that ice floats on liquid water and gets polluted very quickly.

Surface water is the water located in lakes, freshwater wetlands, and rivers. Naturally, it is refilled and lost through discharge and precipitation to evapotranspiration, evaporation, oceans, and groundwater recharge, and it gets polluted mostly from other water deposits because of mass urban consumption. Although precipitation is the only natural input to any surface water system, other numerous aspects also affect the entire quantity of water available at any given period and the proportions of water loss in the system. For instance, artificial and wetland reservoirs, the runoff features of the land in the watershed, the timing of the precipitation, the permeability of the soil beneath these storage bodies, local evaporation rates, and storage capacity in lakes. Basically, mass urban development shall have a big or even damaging influence on these aspects. Through draining wetlands or constructing reservoirs, humans can manage the storage size of surface water systems. Additionally, through paving areas and channelizing the stream flow, humans can intensify the runoff quantities and velocities.

The entire water quantity available at any given period is a significant aspect to consider. Some water users have a bleary requirement for water; farms, for instance, only require water when planting crops, which may only be one season per year. To meet the farm's water requirements, a surface water system may need a large storage capacity to collect water during an entire year, then release it within a short period of time. For other beneficiaries who require a continuous supply of water such as a power plant,

This book belongs to Kitab Liaison (ocd1996@gmail.com) Copyright Elsevier 2023

the storage capacity of the surface water system must meet the minimum condition of the average stream flow.

The total volume of water transported downstream usually contains a visible free water flow and the flow across rocks and sediments that underly the river. This floodplain is known as the hyporheic zone, which is also influenced by mass urbanization during the flow process of a river. For rivers in large valleys, the latter flow may substantially surpass the visible flow. Often, the hyporheic zone plays the function of creating a dynamic interface between surface water and groundwater from aquifers and exchanging flow, which may be beyond capacity or depleted between rivers and aquifers, that are predominantly important in karst areas where pot-holes and underground rivers are common and get polluted quickly.

Groundwater can represent the freshwater situated in the subsurface pore space of soil and rocks and the water flows in the aquifers. The critical distinction between groundwater and surface water is that, in relation to input, the volume of groundwater storage is bigger than that of surface water due to the former's slow turnover rates. This disparity lets human unsustainably use groundwater for a long time where a serious issue does not arise, although the average rate of seepage above a groundwater source constitutes the upper bound for average water consumption from that source in the long term. The natural output and input of groundwater is the seepage from surface water and springs or seepage to the oceans, respectively. Thus, when the surface water source is exposed to significant evaporation, the groundwater source below may become saline. This condition may occur artificially through irrigated farmland or naturally through endorheic bodies of water. Soil salinization may also occur in coastal areas due to the reverse direction of seepage to the ocean caused by human use. Even more, the pollution originates from rapid urbanization because of the loss of groundwater, which could be prevented through constructing reservoirs or detention ponds.

Alternatively, the water consumption in urban areas is estimated at 8% for domestic functions that include laundry, cooking, toilet flushing, drinking water, gardening, cleaning, and bathing [1]. In low-density communities, small private wells and septic tanks are commonly used to provide water, which are not as essential in high-density urban areas. To deliver water to individuals and concentrate wastewater, urbanization needs a large investment from individuals and businesses in water infrastructure. In 60% of European cities with more than 100,000 people, the reloading rate of groundwater is lower than the consumption rate [2, 3]. Though some water can be utilized, a large cost will be required to seize it.

This book belongs to Kitab Liaison (ocd1996@gmail.com) Copyright Elsevier 2023

The basic domestic water requirement is approximately 50 L per person each day according to estimation; an exception is for gardening [4, 5]. Among all the uses of water, the most special is drinking water, which refers to water that is of adequately high quality for consumption or use without any risk that can also be called clean water. Water provided for domestic, commerce, or industry in the majority of developed countries is at the drinking water standard, but only a small proportion is used for the preparation of food and water get polluted.

Another key water polluter is urban industrial consumption, which occupies 22% of global water use [1, 6]. The chief application of industrial water use is thermoelectric power plants, manufacturing plants, ore and oil refineries, and hydroelectric dams. In these processes, water can play the function of coolant, solvent, and chemical reagent. In some industries the water withdrawal may be high, but this consumption is still much less than that of agriculture. Industrial water consumption can also consist of renewable power generation. Hydroelectric power obtains energy from the force of water flowing downhill, driving a turbine linked to a generator; it is a low-cost, nonpolluting source of reusable energy. It can be applied for load following and can offer unlimited power. Another alternative to produce hydroelectricity is the sun. First, heat from the sun evaporates water, then the vapor condenses as rain in higher altitudes and flows downhill, thus generating electricity. As for the two plants above, pumped-storage hydroelectric plants employ grid electricity to pump water uphill if the energy demand is low, then apply the stored water to generate electricity if the demand is high.

The creation of an artificial lake is required in hydroelectric power plants. Because of the larger surface area in contact with the elements, evaporation from this lake is higher in relation to a natural river, and the consumption of water. The process of driving water via the turbine and tunnels or pipes briefly eliminates the water from the natural environment, developing water withdrawal that is the pollutant whose effect on wildlife differs greatly based on the design of the plant.

Pressurized water is another industrial use of water that is often utilized in water blasting, water jet cutters, and high-pressure water guns. These applications not only function safe and well, but also do not pose any danger to the environment. Another industrial use of water is cooling of machinery from overheating, which only occupies a small proportion of water consumption. In numerous large-scale industrial processes such as oil refining, fertilizer production, other chemical plant applications, thermoelectric

This book belongs to Kitab Liaison (ocd1996@gmail.com) Copyright Elsevier 2023

power production, and natural gas extraction from shale rock water is also applied. The discharge of untreated water originating from these processes is pollution, which is comprised of discharged solutes (chemical pollution) and high water temperature (thermal pollution). These industrial water applications usually need pure water and use several purification methods both in water supply and discharge. The majority of the pure water is generated onsite from natural freshwater or municipal grey water. Industrial water consumption is basically much less than withdrawal because of regulations, which require industrial grey water to be treated and disposed to the environment. One exclusion is the thermoelectric power plant applying cooling towers with high water consumption is equivalent to their withdrawal because majority of the withdrawn water is evaporated as a section of the cooling process and lead to water pollution.

Environmental water application is also minimal, although it is increasing as a percentage of the entire water consumption in urban areas. The environmental water sources comprise water stored in retention tanks and freed for environmental functions or water retained in waterways through regulatory limits of abstraction that is polluted. Then, the usages of environmental water are fish ladders, water releasing from reservoirs timed to help fish spawn, restoration of more natural flow regimes, watering of natural or artificial wetlands, and creation of wildlife habitats that are significantly influenced by this polluted water.

Fifty years ago, people once considered that water was an infinite resource. It may be because during that time, less than half of the present number of people on the planet used fewer resources and did not require much water to produce these resources. Nevertheless, currently the water resources are much more serious due to the explosive rise in the number of people and the food they require. In the future, even more water will be required, considering that the global population is predicted to increase to 9 billion by 2050. In 2007, the International Water Management Institute in Sri Lanka carried out a study on the management of water in the agriculture sector to investigate whether the world had offered adequate water for the present population [7, 8]. It evaluated the present accessibility of water for agriculture on a worldwide scale and mapped out areas experiencing water scarcity. This evaluation showed that one-third of the world's population cannot access clean drinking water, and a fifth of the world's people, more than 1.2 billion, live in areas of physical water scarcity, which implies the absence of water to meet all demands. On the other hand, 1.6 billion people live in areas of economic water scarcity, which indicates that the

This book belongs to Kitab Liaison (ocd1996@gmail.com) Copyright Elsevier 2023

authorities have failed to offer adequate water to people due to the absence of investment or human capacity in water. The research confirmed that it may be possible to meet the water requirement for people in the future, but the continuation of today's food production and environmental trends would create a crisis in numerous areas of the world. To prevent this from occurring, farmers have to work harder to build their productivity while the governments identify techniques to use water more effectively (Fig. 10.3).

To grow and increase crop productivity, irrigation is necessary. Numerous irrigation techniques include different links between consumption of water, the capital cost of equipment and structures, and crop yield. Some irrigation techniques that are simple, cheap, and less effective involve furrows and overhead sprinklers, where in the process, much water evaporates, runs off, or drains below the root zone. There are other irrigation methods that are more expensive and more effective that comprise surge irrigation, either trickle or drip irrigation, and some types of sprinkler systems through the sprinklers function near ground level. Matters often inadequately considered when implementing irrigation methods are the salinization of groundwater and the accumulation of contaminant accumulation, resulting in declines in water quality; that is why there is a sharp increase in water scarcity.

As mentioned, there has been a rapid increase in urban areas. According to UN, that growth chiefly originates from developing countries affected by

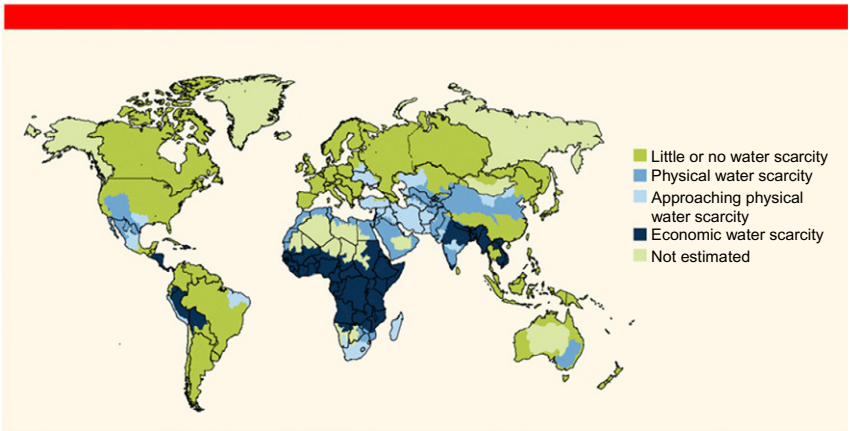

Fig. 10.3 There is already water scarcity that impacts each continent where nearly 1.2 billion people, or almost one-fifth of the world's population, live in areas of physical scarcity while 500 million more people are approaching this condition.

This book belongs to Kitab Liaison (ocd1996@gmail.com) Copyright Elsevier 2023

water stress; by 2050, the world population was 6.2 billion in 2000. This number is anticipated to rise to 9.7 billion [9, 10]. Thus, the demand for water will also rise unless water conservation or recycling increases [9, 11]. The World Bank discussed the findings of the UN's research that showed, in the near future, that access to water for producing food will be one of the main problems [12, 13]. It will require considering the influence of climate change and other environmental and social variables when attempting to increase access to water that is becoming seriously polluted.

In 2025, water shortage difficulties will obviously be greater among poorer regions with rapid population growth and limited resources, for example, the Middle East, parts of Asia, and Africa. Additionally, during that time, to access clean water and acceptable sanitation, large urban and periurban areas will require the construction of new infrastructure that may result in increasing conflicts between government and agricultural water users, who presently use the majority of the water. In relation to these poorer regions, more developed areas of Russia, North America, and Europe will not face the same threat, not just due to their relative wealth, but rather due to their better population that aligns with available water resources.

Basically, today's main concern is water pollution, and numerous countries have attempted to find solutions to solve this challenge. Of all pollutants endangering the water supplies, the most prevalent one is the release of raw sewage, sludge, garbage, or even toxic pollutants into natural water. This is very common in underdeveloped countries and some quasideveloped countries such as China, India, Nepal, and Iran. Treated sewage creates sludge that could be placed in landfills, incinerated, dumped at sea, or spread out on land. Also, in some countries, nonpoint source pollution, for instance, agricultural runoff, chemical wastes, and urban stormwater runoff, is also a key source of pollution. Water pollution is because of toxic chemicals and biological agents that are beyond what is naturally found in the water; these pose a danger to human health and/or the environment. The contamination of water bodies is known as water pollution, usually because of human activities. Water bodies comprise aquifers, ground water, lakes, rivers, and oceans. When contaminants are introduced into the natural environment, for instance, through discharging inadequately treated wastewater into natural water bodies, aquatic ecosystems can be degraded. Consequently, this can result in public health challenges for people living downstream and urban areas because, for daily consumption in various functions, they utilize the same polluted water. Therefore, water pollution is becoming

This book belongs to Kitab Liaison (ocd1996@gmail.com) Copyright Elsevier 2023

a global cause of death and disease, for example due to water-borne diseases [14–16]. Either point sources or nonpoint sources are the sources of water. Point sources contain one recognizable cause of pollution, for example, a storm drain, wastewater treatment plant, or stream. Nonpoint sources are more diffuse, for example agricultural runoff [17]. Pollution is because of the cumulative impact over time. All organisms and plants living in or in contact with polluted water bodies can be influenced. The impact can destroy a single species and affect the natural biological communities they cohabit. The reasons for water pollution comprise a wide range of chemicals, pathogens, and physical parameters. Contaminants may either be organic or inorganic substances. Increased temperatures can also pollute water sources. A common reason for thermal pollution is the utilization of water as a coolant in power plants and industrial manufacturers. Raised water temperatures lessen the levels of oxygen, which can kill fish and change the composition of the food chain and lower species biodiversity as well as create an invasion through new thermophilic species [7, 16]. Water pollution is determined through the analyses of water samples. Physical, biological, and chemical tests can be done. Management of water pollution calls for proper infrastructure and management plans. The infrastructure may consist of wastewater treatment plants. Sewage treatment plants and industrial wastewater treatment plants are normally needed to guard water bodies from untreated wastewater. Agricultural wastewater treatment for farms and erosion control from construction sites can also assist in lowering water pollution. Nature-based solutions are another approach to managing water pollution. Efficient control of urban runoff entails lowering the speed and quantity of flow. In the United States, the best management practices for water pollution consist of methods to lower the levels of water while enhancing its quality [18]. Hence, the following technologies (I. 9.1 Application of Nanotechnology to Control Water Pollution, II. 9.2 Photocatalytic water treatment technology, III. 9.3) are described to control water pollution for mass urban development in order to secure an improved daily life.

Application of nanotechnology to control urban water pollution

Introduction

Water is the most crucial substance for life on earth as well as a valuable resource for human civilization. For the 21st century, achieving dependable access to clean and affordable water is viewed as one of the most basic

This book belongs to Kitab Liaison (ocd1996@gmail.com) Copyright Elsevier 2023

humanitarian objectives, yet it still continues to be a chief global challenge. Our current water supply encounters enormous barriers, both new and old. Universally, some 780 million people continue to lack access to better drinking water sources [19, 20]. In the influenced areas, it is crucial in the implementation of basic water treatment (mainly in developing countries) in which water and wastewater infrastructure are regularly not present. In both industrialized and developing countries, human activities constantly aggravate water shortages through contaminating natural water sources. The increasingly stringent water quality standards, compounded through emerging contaminants, have created new scrutiny for existing water treatment and distribution systems that have been largely established in developed countries. The rapidly growing global population and the development of living standards limitlessly drives up the demand. Furthermore, global climate change highlights the already irregular distribution of fresh water, undermining the supply. Growing pressure on water supplies makes using unconventional water sources (e.g., stormwater, contaminated fresh water, brackish water, wastewater, and seawater) a new model, particularly in historically water-stressed regions. Additionally, the current water and wastewater treatment technologies and infrastructure are at their limit for ensuring suitable water quality to cater for environmental and human requirements. Recent nanotechnology developments offer catapulting opportunities to establish next-generation water supply systems. Our present water treatment, discharge, and distribution practices, which heavily depend on centralized conveyance systems, are not sustainable anymore. The highly efficient, modular, and multifunctional processes enhanced through nanotechnology are envisaged to create increased performance, affordable water, and wastewater treatment solutions that depend on large infrastructures [21, 22]. Nanotechnology-enhanced water and wastewater treatment promises to not just defeat the main problems encountered through present treatment technologies, but also offer new treatment capabilities to grow the water supply through the economic utilization of unconventional water sources. In this case, we offer an outline of recent developments in nanotechnology for water and wastewater treatment. The main uses of nanomaterials are critically analyzed regarding their roles in unit operation processes. The barriers are in their full-scale application and the research overcoming these barriers is also described. The potential influence of nanomaterials on the ecosystem and human health and any possible interference with treatment processes exceed the scope of this review, and hence will not be addressed in detail.

This book belongs to Kitab Liaison (ocd1996@gmail.com) Copyright Elsevier 2023

Methods

Basically, nanomaterials are defined as materials smaller than 100 nm in at least one dimension. At this range, materials often have novel size-dependent properties different from their large counterparts, the majority of which have been explored for applications in water and wastewater treatment. Some of these uses utilize the smoothly scalable size-dependent features of nanomaterials that compare to the high specific surface area, for instance, fast dissolution, high reactivity, and strong sorption. Others take advantage of their irregular properties, for example, super paramagnetism, quantum confinement impact, and localized surface plasmon resonance. These uses are analyzed below, depending on nanomaterial roles in unit operation processes (Table 10.1). The majority of the applications described below are still in the stage of laboratory research. In the text, the pilot-tested or field-tested exceptions will be noted.

Adsorption

Adsorption is commonly implemented as a polishing procedure to eliminate organic and inorganic contaminants in water and wastewater treatment. The effectiveness of conventional adsorbents is normally restricted through the surface area or active sites, the absence of selectivity, and the adsorption kinetics. Nanoadsorbents provide substantial enhancement with their extremely high precise surface area and associated sorption sites, short intraparticle diffusion distance, and tunable pore size and surface chemistry.

Carbon based nanoadsorbents

Organic removal of CNTs has indicated that a higher efficiency than activated carbon on absorption of numerous organic chemicals [23, 24]. Its increased absorption capacity especially originates from the great specific surface area and the varied contaminant-CNT relations. The accessible surface area for adsorption on single CNTs is the external surface [25, 26]. In the aqueous phase, CNTs create loose bundles/aggregates because of the hydrophobicity of their graphitic surface, lowering the effective surface area. Alternatively, CNT aggregates have interstitial spaces and grooves that are high adsorption energy sites for organic molecules [27, 28]. However, activated carbon has an equivalent measured precise surface area as CNT bundles, and it has an important number of micropores unreachable to massive organic molecules, for example, numerous antibiotics and pharmaceuticals [29, 30]. Therefore, CNTs have a greater absorption capacity for

This book belongs to Kitab Liaison (ocd1996@gmail.com) Copyright Elsevier 2023

Table 10.1 Current and potential applications of nanotechnology in water and wastewater treatment

Applications	Representative nanomaterials	Desirable nanomaterial properties	Enabled technologies
Adsorption	Carbon nanotubes	High specific surface area, highly assessable adsorption sites, diverse contaminant-CNT interactions, tunable surface chemistry, easy reuse	Contaminant preconcentration/detection, adsorption of recalcitrant contaminants
	Nanoscale metal oxide	High specific surface area, short intraparticle diffusion distance, more adsorption sites, compressible without significant surface area reduction, easy reuse, some are superparamagnetic	Adsorptive media filters, slurry reactors
	Nanofibers with core shell structure	Tailored shell surface chemistry for selective adsorption, reactive core for degradation, short internal diffusion distance	Reactive nanoadsorbents
Membranes and membrane processes	Nanozeolites	Molecular sieve, hydrophilicity	High permeability thin film nanocomposite membranes
	Nano-Ag	Strong and wide-spectrum antimicrobial activity, low toxicity to humans	Antibiofouling membranes
	Carbon nanotubes	Antimicrobial activity (unaligned carbon nanotubes)	Antibiofouling membranes
		Small diameter, atomic smoothness of inner surface, tunable opening chemistry, high mechanical and chemical stability	Aligned carbon nanotube membranes
	Aquaporin	High permeability and selectivity	Aquaporin membranes
	Nano-TiO_2	Photocatalytic activity, hydrophilicity, high chemical stability	Reactive membranes, high performance thin film nanocomposite membranes
	Nanomagnetite	Tunable surface chemistry, superparamagnetic	Forward osmosis

This book belongs to Kitab Liaison (ocd1996@gmail.com)

Copyright Elsevier 2023

Photocatalysis	Nano-TiO_2	Photocatalytic activity in UV and possibly visible light range, low human toxicity, high stability, low cost	Photocatalytic reactors, solar disinfection systems
	Fullerene derivatives	Photocatalytic activity in solar spectrum, high selectivity	Photocatalytic reactors, solar disinfection systems
Disinfection and microbial control	Nano-Ag	Strong and wide-spectrum antimicrobial activity, low toxicity to humans, ease of use	POU water disinfection, antibiofouling surface
	Carbon nanotubes	Antimicrobial activity, fiber shape, conductivity	POU water disinfection, antibiofouling surface
	Nano-TiO_2	Photocatalytic ROS generation, high chemical stability, low human toxicity and cost	POU to full-scale disinfection and decontamination
Sensing and monitoring	Quantum dots	Broad absorption spectrum, narrow, bright and stable emission that scales with the particle size and chemical component	Optical detection
	Noble metal nanoparticles	Enhanced localized surface plasmon resonances, high conductivity	Optical and electrochemical detection
	Dye-doped silica nanoparticles	High sensitivity and stability, rich silica chemistry for easy conjugation	Optical detection
	Carbon nanotubes	Large surface area, high mechanical strength and chemical stability, excellent electronic properties	Electrochemical detection, sample preconcentration
	Magnetic nanoparticles	Tunable surface chemistry, superparamagnetism	Sample preconcentration and purification

This book belongs to Kitab Liaison (ocd1996@gmail.com)

Copyright Elsevier 2023

some bulky organic molecules due to their larger pores in bundles and more available absorption sites.

A key drawback of activated carbon is its minimal absorption attraction for minimum molecular weight polar organic compounds. CNTs powerfully absorbed a number of these polar organic compounds because of the diverse contaminant-CNT relationship inclusive of the hydrophobic impact, π-π connections, covalent bonding, hydrogen bonding, and electrostatic interactions [26, 31]. The π electron-rich CNT surface permits π-π connections with organic molecules with C—C bonds or benzene rings, for example, polycyclic aromatic hydrocarbons (PAHs) and polar aromatic compounds [32, 33]. Organic compounds that have —COOH, —OH, and —NH2 functional groups could also form hydrogen bonds with the graphitic CNT surface that donates electrons [34, 35]. Electrostatic affinity enhances the adsorption of positively charged organic chemicals, for example, some antibiotics at appropriate pH [30, 36].

Heavy metal removal. Oxidized CNTs have high adsorption capacity for metal ions with rapid kinetics. The surface functional groups (e.g., carboxyl, hydroxyl, and phenol) of CNTs are the key adsorption sites for metal ions, especially by electrostatic affinity and chemical bonding [37, 38]. Consequently, surface oxidation can improve the adsorption capacity of CNTs significantly. Many studies indicate that CNTs are improved adsorbents than activated carbon for heavy metals (e.g., Cu^{2+} fl, Pb^{2+}, Cd^{2+}, and Zn^{2+}) and that the adsorption kinetics are rapid on CNTs due to the increased accessible adsorption sites and the short intraparticle diffusion distance [34, 39].

Generally, CNTs may not be a better alternative for activated carbon as wide-spectrum adsorbents. Relatively, as their surface chemistry can be altered to target explicit contaminants, they may have unique uses in polishing steps to eliminate recalcitrant compounds or in preconcentration of trace organic contaminants for analytical functions. These applications need a small quantity of materials; they are less sensitive to the material cost.

Produced through exfoliating graphite with strong acids and oxidizers, graphite oxide is a potentially low-cost adsorbent. Which sand granules coated with graphite oxide were efficient in eliminating Hg^{2+} and a large dye molecule (Rhodamine B) has been reported; its performance was in relation to commercial activated carbon [40, 41].

Regeneration and reuse. Regeneration is a crucial aspect that regulates the cost efficiency of adsorbents. Adsorption of metal ions on CNTs can be easily reversed by lowering the solution pH. The metal recovery rate is normally above 90% and often close to 100% at pH < 2 [34, 42].

This book belongs to Kitab Liaison (ocd1996@gmail.com) Copyright Elsevier 2023

Furthermore, the adsorption capacity continues to be relatively stable after regeneration. Lu et al. reported that the Zn^{2+} adsorption capacity of SWNT and MWNT was lowered less than 25% after 10 regeneration and reuse cycles while that of activated carbon was decreased by more than 50% after one regeneration [34, 43]. A statistical analysis depends on the best-fit regression of Zn^{2+} adsorption capacity, and the number of regeneration and reuse cycles suggested that CNT nanoadsorbents can be regenerated and reused many hundreds of times for Zn^{2+} removal while upholding reasonable adsorption capacity [44, 45].

Metal-based nanoadsorbent metal oxides, for example, iron oxide, titanium dioxide, and alumina, are effective and reduce the cost of adsorbents for heavy metals and radionuclides. The sorption is majorly controlled by complexation between dissolved metals and the oxygen in metal oxides [46, 47]. It is a two-step process: fast adsorption of metal ions on the external surface, followed by the rate-limiting intraparticle diffusion end to end with the micropore walls [48, 49]. Their nanoscale counterparts have increased adsorption capacity and rapid kinetics due to the higher exact surface area, shorter intraparticle diffusion distance, and larger number of surface reaction sites (i.e., corners, edges, vacancies). For example, as the particle size of nanomagnetite declined from 300 to 11 nm, its arsenic adsorption capacity increased more than 100 times [50, 51]. Most of this observed increase in adsorption was attributed to the increase in specific surface area as the 300- and 20-nm magnetite particles have an identical surface area standardized arsenic adsorption capacity ($\sim$6 μmol/m^2 or 3.6 atoms/nm^2). Nevertheless, when the particle size was lowered to below 20 nm, the specific surface area standardized adsorption capacity heightened, with 11-nm magnetite nanoparticles absorbing three times more arsenic ($\sim$18 μmol/m^2 or 11 atoms/nm^2), proposing a "nanoscale effect." This "nanoscale effect" was associated with the change of magnetite surface structure that formed new adsorption site vacancies [52, 53].

Furthermore, high adsorption capacity, some iron oxide nanoparticles such as nanomaghemite and nanomagnetite, can be superparamagnetic. Magnetism is increasingly volume dependent as it originates from the collective interaction of atomic magnetic dipoles. If the size of a ferro- or ferrimagnet lowers to the critical value ($\sim$40 nm), the magnet transforms from multiple domains to a single domain with higher magnetic availability [35, 54]. As the size decreases further, magnetic particles develop superparamagnetic, losing permanent magnetic moments while responding to an external magnetic field that allows easy separation and recovery by a low-gradient

This book belongs to Kitab Liaison (ocd1996@gmail.com) Copyright Elsevier 2023

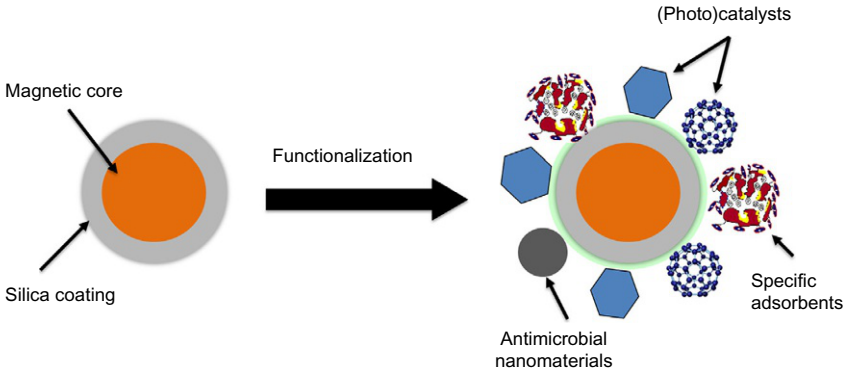

Fig. 10.4 Multifunctional magnetic nanoparticles. Magnetic nanoparticles are applied as the central material in a core-shell nanoparticle structure whereby the shells offer the anticipated function while the magnetic core achieves magnetic separation. A silica coating enhances functionalization because of the rich silica chemistry.

magnetic field. These magnetic nanoparticles can be either applied directly as adsorbents or as the core material in a core-shell nanoparticle structure whereby the shell offers the desired roles while the magnetic core comprehends magnetic separation (Fig. 10.4).

Metal oxide nanocrystals can be compressed to form porous pellets without necessarily conceding their surface area if moderate pressure is used [34, 55]. The pore volume and pore size can be managed through adjusting the consolidation pressure. Therefore, they can be used in forms of both fine powders and porous pellets, which are the potential forms to be applied in industry.

Metal nanomaterials have been investigated for the elimination of several heavy metals, for example arsenic, lead, mercury, copper, cadmium, chromium, and nickel, and have indicated significant possibility to overwhelm the activated carbon [56, 57]. Among them, the elimination of arsenic has attracted great consideration. However, although a good adsorbent for numerous organic and inorganic contaminants, activated carbon has restricted capacity for arsenic, particularly for As (V). Many metal oxide nanomaterials inclusive of nanosized magnetite and TiO_2 have confirmed a superior performance of arsenic adsorption to activated carbon [10, 58, 59]. Additionally, metal (hydr)oxide nanoparticles can be impregnated onto the configuration of other porous materials and activated carbon to attain concurrent elimination of organic cocontaminants and arsenic that favors point-of-use (POU) usages [60, 61].

This book belongs to Kitab Liaison (ocd1996@gmail.com) Copyright Elsevier 2023

Regeneration and recycling. Metal oxide nanoadsorbents can simply be regenerated through changing the pH solution [57, 62]. In several cases, the adsorption capacity of metal oxide nanoadsorbents is well managed after numerous regeneration and recycling cycles [63, 64]. However, lowered adsorption capacity after regeneration has also been reported [65, 66].

Metal-based nanoadsorbents can be generated at a relatively low cost. The increased adsorption capacity, reduced cost, and easy separation and regeneration ensure that metal-based nanoadsorbents are technologically and economically beneficial.

Polymeric nanoadsorbents

Dendrimers are personalized adsorbents that could eliminate both organics and heavy metals. Their interior shells can be hydrophobic for the sorption of organic compounds, whereas the exterior branches can be personalized (e.g., hydroxyl- or amine-terminated) for adsorption of heavy metals. The sorption relies on complexation, electrostatic interactions, hydrophobic impacts, and hydrogen bonding [67, 68]. A dendrimer-ultrafiltration system was made to recover metal ions from aqueous solutions [13, 69]. The system attained nearly complete elimination of Cu^{2+} ions with the first concentration of 10 ppm and Cu^{2+} to the PAMAM dendrimer-NH_2 ratio of 0.2. Next, the metal ion-laden dendrimers were recovered through ultrafiltration and regenerated through lowering the pH to 4.

Potential application in water treatment

Nanoadsorbents can be easily incorporated into the current treatment processes in slurry reactors or adsorbers. Applied in the powder form, nanoadsorbents in slurry reactors can be highly effective because the entire surfaces of the adsorbents are applied and the mixing substantially facilitates the mass transfer. Nonetheless, an extra separation unit is needed to recover the nanoparticles. Nanoadsorbents can also be applied in fixed or fluidized adsorbers in the form of pellets/beads or porous granules loaded with nanoadsorbents. A fixed-bed reactor is normally linked with mass transfer challenges and head loss, although it does not require a separation process in the future. Usages of nanoadsorbents for arsenic elimination have been commercialized, and their functions and cost have been related to other commercial adsorbents in pilot tests [70]. ArsenXnp is a commercial hybrid ion exchange medium consisting of iron oxide nanoparticles and polymers. ADSORBSIATM is a nanocrystalline titanium dioxide medium in the form of beads from

This book belongs to Kitab Liaison (ocd1996@gmail.com) Copyright Elsevier 2023

0.25–1.2 mm in diameter. Both nanoadsorbents were increasingly effective in the elimination of arsenic, and ArsenXnp needed little backwash [70, 71]. The projected cost of treatment for ArsenXnp is \$0.25∼\$0.35/1000 gal if the medium is regenerated, identical to the cost of \$0.37/1000 gal of Bayoxide E33, a high-performance granular iron oxide adsorbent [70, 72]. ArsenXnp and ADSORBSIATM have been used in small- to medium-scale drinking water treatment systems and were proven to be cost-competitive.

Membranes and membrane processes

The basic objective of water treatment is to eliminate undesired components from water. Membranes offer a physical challenge for such composition, depending on their size, permitting the application of unconventional water sources. As the major constituent of water treatment and reuse, they offer increased automation, require less land and chemical use, and the modular configuration permits flexible design [22]. A key problem of the membrane technology is the integral tradeoff between membrane selectivity and permeability. The high consumption of energy is a crucial obstacle to the wide application of pressure-driven membrane processes. Membrane fouling increases the energy consumption and the complexity of the process design and operation. Additionally, it lowers the lifetime of membranes and membrane modules.

The function of membrane systems is greatly selected through the membrane material. Incorporation of operational nanomaterials into membranes provides a significant opportunity to enhance the membrane permeability, mechanical and thermal stability, and fouling resistance, not forgetting to create new operations for contaminant self-cleaning and degradation.

Nanofiber membranes

Electrospinning is an easy, efficient, and inexpensive method of making ultrafine fibers that apply to numerous materials (e.g., polymers, ceramics, or even metals) [73, 74]. The subsequent nanofibers have increased specific surface area and porosity and create nanofiber mats with complex pore structures. The diameter, morphology, composition, secondary structure, and spatial alignment of electrospun nanofibers can simply be controlled for application [74]. However, although nanofiber membranes have been commercially applied for air filtration usage, their potential in water treatment is yet to be exploited. Nanofiber membranes can eliminate micron-sized particles from the aqueous phase at a high rejection rate with no substantial fouling [75]. Therefore, they have been suggested to be utilized as pretreatment

This book belongs to Kitab Liaison (ocd1996@gmail.com) Copyright Elsevier 2023

before the ultrafiltration or reverse osmosis (RO). Functional nanomaterials can simply be doped into the spinning solutions to fabricate nanoparticle-impregnated nanofibers or create in situ [74]. The outstanding characteristics and tunable properties make electrospun nanofibers an ideal platform for building multifunctional media/membrane filters through either directly applying intrinsically multifunctional materials such as TiO_2 or through initializing functional materials on the nanofibers. For instance, through particularly seize agents on the nanofiber scaffold, integrating ceramic nanomaterials, affinity nanofiber membranes can be created to eliminate organic pollutants and heavy metals during filtration.

Nanocomposite membranes

Many studies on membrane nanotechnology have focused on forming synergism or multifunction by increasing nanomaterials into polymeric or inorganic membranes. Nanomaterials applied for such usages include hydrophilic metal oxide nanoparticles (e.g., Al_2O_3, TiO_2, and zeolite), antimicrobial nanoparticles (e.g., nano-Ag and CNTs), and (photo)catalytic nanomaterials (e.g., bimetallic nanoparticles, TiO_2).

The main objective of increasing hydrophilic metal oxide nanoparticles is to lower fouling through adding membrane hydrophilicity. The extra metal oxide nanoparticles inclusive of alumina, silica, zeolite, and TiO_2 to polymeric ultrafiltration membranes has been indicated to growth membrane surface hydrophilicity, water permeability, or fouling resistance [76–79]. These inorganic nanoparticles also improve the mechanical and thermal stability of polymeric membranes, lowering the negative effect of compaction and heat on membrane permeability [79, 80].

Antimicrobial nanomaterials such as nano-Ag and CNTs can lower membrane biofouling. Nano-Ag has been doped or surface-grafted onto polymeric membranes to prevent bacterial attachment and biofilm creation of the membrane surface and inactivate viruses [81–83]. Nonetheless, its long-term efficiency against membrane biofouling has not been recorded. Suitable replacement of nano-Ag needs to be addressed for the application of this technology. CNTs inactivate bacteria upon direct contact [84]. Increased bacterial inactivation ($>90\%$) has been attained applying a polyvinyl-*N*-carbazole-SWNT nanocomposite at a level of 3 wt.% of SWNT [15]. There is no urge for replenishment as CNTs are insoluble in water and not used. Although, as direct contact is needed for inactivation, long-term filtration experiments are required to identify the effect of fouling on the antimicrobial activity of CNTs. The addition of oxidized MWNT at

This book belongs to Kitab Liaison (ocd1996@gmail.com) Copyright Elsevier 2023

a low weight percentage (up to 1.5 wt.%) also increases the hydrophilicity and permeability of polysulfone membranes [85].

Photocatalytic nanoparticle integrated membranes (i.e., reactive membranes) combine their physical separation function and the reactivity of a catalyst toward contaminant degradation. Much effort has been devoted to develop photocatalytic inorganic membranes consisting of nanophotocatalysts (normally nano-TiO_2 or modified nano-TiO2) [86]. Metallic/bimetallic catalyst nanoparticles such as nano zero-valent iron (nZVI) and noble metals supported on nZVI have been incorporated into polymeric membranes for reductive degradation of contaminants, particularly chlorinated compounds [87, 88]. nZVI serves as the electron donor and the noble metals catalyze the reaction.

Thin film nanocomposite (TFN) membranes

Development of TFN membranes mostly focuses on incorporating nanomaterials into the active layer of thin film composite (TFC) membranes through doping in the casting solutions or surface modification. Nanomaterials that have been researched for such applications include nanozeolites, nano-Ag, nano-TiO_2, and CNTs. The effect of nanoparticles on membrane permeability and selectivity is based on the type, size, and number of nanoparticles added.

Nanozeolites are the most frequently used dopants in TFN and have indicated potential in improving membrane permeability. The extra nanozeolites yield to more permeable, negatively charged, and thicker polyamide active layers [89]. One study reported that water permeability increased up to 80% over the TFC membrane, with the salt rejection greatly maintained ($93.9 \pm 0.3\%$) [90]. TFN membranes doped with 250 nm nanozeolites at 0.2 wt.% attained moderately increased permeability and better salt rejection (>99.4%) than commercial RO membranes [91]. It was hypothesized that the small hydrophilic pores of nanozeolites form preferential paths for water. Although, water permeability amplified even with pore-filled zeolites, but lower than the pore-open ones, that could be considered to imperfections at the zeolite-polymer interface. Nanozeolites were also applied as carriers for antimicrobial agents such as Agfl that impart antifouling properties to the membrane [92]. The zeolite TFN technology has attained an early stage of commercialization. QuantumFlux, a seawater TFN RO membrane, is now commercially available (www.nanoH2O.com).

This book belongs to Kitab Liaison (ocd1996@gmail.com) Copyright Elsevier 2023

Incorporation of nano-TiO2 (up to 5 wt.%) into the TFC active layer somewhat augmented the membrane rejection while sustaining the permeability [93]. When the concentration of nano-TiO_2 surpassed 5 wt.%, the water flux amplified in the cost of lowering rejection, proposing imperfection development in the active layer. Upon UV irradiation, TiO_2 can degrade organic contaminants and inactivate microorganisms. This aids in the reduction of organic and biological fouling and the elimination of contaminants that are not reserved through the membrane. Nevertheless, the close adjacency between the photocatalyst and the membrane may also yield to detrimental impacts on polymeric membrane materials that requires to be talked for long-term effectiveness [94]. CNTs (unaligned) also create their application in TFN membranes because of their antimicrobial functions. Tiraferri et al. covalently joined SWNTs to a TFC membrane surface [95]. This method is beneficial as it applies a comparatively small quantity of the nanomaterial and diminishes perturbation of the active layer. The subsequent TFN membrane exhibited modest antibacterial properties (60% inactivation of bacteria attached on the membrane surface in 1 h contact time), potentially declining or delaying membrane biofouling.

Biologically inspired membranes

Numerous biological membranes are increasingly permeable and selective. Aquaporins are protein channels that moderate water flux across cell membranes. Their increased selectivity and water permeability makes their application in polymeric membranes an attractive approach to enhance membrane performance. Aquaporin-Z from *Escherichia coli* has been combined into amphiphilic triblock-polymer vesicles that display water permeability of at least an order of magnitude through the original vesicles with whole rejection to glucose, glycerol, salt, and urea [96]. One possible design is to coat aquaporin combined lipid bilayers on commercial nanofiltration membranes. On this front, restricted success was attained [97]. Associated CNTs have been represented both experimentally and theoretically to provide water permeation much faster than what the Hagen-Poiseuille equation indicates, due to the atomic smoothness of the nanosized channel, and the one-dimensional single-file alignment of water molecules while passing by the nanotubes [98, 99]. It was proved that a membrane containing only 0.03% surface area of ordered CNTs will have flux surpassing the present commercial seawater RO membranes [100]. However, increased rejection for salt and small molecules is challenging for ordered CNT membranes

This book belongs to Kitab Liaison (ocd1996@gmail.com) Copyright Elsevier 2023

because of the absence of CNTs with a uniformly subnanometer diameter. Functional group gating at the nanotube opening has been proposed to enhance the choice of ordered CNT membranes [101]. By grafting carboxyl operational groups on sub-2-nm CNT openings, a 98% rejection of $Fe(CN6)^{3-}$ was achieved at lowered ionic intensity through the Donnan exception [36], even though KCl rejection was only 50% at 0.3 mM and declined to nearly zero at 10 mM. Grafting huge functional groups at the tube opening could exclude salts physically, although the steric exception will lower membrane permeability significantly [102]. Therefore, at the current stage, aligned CNT membranes of desalination. To attain dependable salt rejection, the CNT diameter must be uniformly smaller than 0.8 nm [103]. A major obstacle for both aquaporin and ordered CNT membranes is the scale-up of nanomaterial production and membrane fabrication. Large-scale production and purification of aquaporins is problematic. Currently, chemical vapor deposition (CVD) is the most prominent means of making an alignment of nanotubes. A continuous high-yield CVD prototype has been designed for making vertically ordered CNTs, creating the method for large-scale production [65]. A postmanufacturing arrangement method applying a magnetic field was also established [104].

Nanocomposite and TFN membranes have a better scalability as they can be fabricated through current industrial manufacturing processes. The increased water permeability can lower the applied pressure or the required membrane area and consequently reduce the cost. This strategy may significantly enhance the energy effectiveness for water treatment with reduced osmosis pressure, though it may have restricted benefits on seawater RO, whose energy consumption is already near the thermodynamic limit [6]. A recent analysis ranked present membrane nanotechnologies depending on their potential performance improvement and state of commercial readiness [100].

Forward osmosis

Forward osmosis (FO) applies the osmotic gradient to draw water from a low osmotic pressure solution to a high osmotic pressure one (i.e., the draw solution). The diluted draw solution is then treated by reverse osmosis or thermal processes to produce pure water. FO has two major benefits through pressure-driven reverse osmosis: it does not need high pressure and the membrane is not prone to fouling.

The key to FO is to have a draw solute with increased osmolality and simply distinguishable from water. Chemicals presently applied for drawing

This book belongs to Kitab Liaison (ocd1996@gmail.com) Copyright Elsevier 2023

solutions include NaCl and ammonia bicarbonate. Thus, RO or thermal treatment, both energy intensive, is needed to recover water from the draw solution. Magnetic nanoparticles were presently explored as a new form of draw solute for their simple separation and recycling. Hydrophilic coating was applied to facilitate dissolution and enhance osmotic pressure. An FO permeated flux higher than 10 L/m^2/h was attained applying to 0.065 M poly(ethylene glycol) diacid-coated magnetic nanoparticles when deionized water was applied as the feed solution [105]. Magnetic nanoparticles were also employed to recover draw solutes. In a current study, magnetic nanoparticles (Fe_3O_4@SiO_2) were applied to recover $Al_2(SO_4)_3$ (the draw solute) by flocculation [43].

Photocatalysis

Photocatalytic oxidation is an advanced oxidation process that helps to eliminate traces of microbial pathogens and contaminants. It is a beneficial pretreatment for nonbiodegradable and dangerous contaminants to improve their biodegradability. Photocatalysis can also be applied as polishing to treat recalcitrant organic compounds. The key obstacle for its broad application is its slow kinetics because of restricted photocatalytic and light fluence operations. Present research focuses on enhancing photoactivity range photocatalytic reaction kinetics (Table 10.2).

Nanophotocatalyst optimization

TiO_2 is the most broadly applied semiconductor photocatalyst in water/wastewater treatment due to its low toxicity, chemical stability, reduced cost, and large amount of raw material. It produces an electron/hole (e^-/h^+) pair during absorbing a UV photon that either migrates to the surface and creates a reactive oxygen species (ROS) or undertakes an undesired recombination. The photoactivity of nano-TiO_2 can be enhanced through maximizing particle size and shape, lowering e^-/h^+ recombination by noble metal doping, optimizing reactive facets, and surface treatment to improve contaminant adsorption.

The size of TiO_2 plays a crucial function in its solid-phase change, sorption, and e^-/h^+ dynamics. Among the crystalline structures of TiO_2, rutile is the most stable for particles greater than 35 nm, whereas anatase, which is more effectual in generating ROS, is the most stable for particles smaller than 11 nm [106, 107]. A main reason for the lower reaction kinetics of TiO_2 photocatalysis is the fast recombination of e^- and h^+. Declining TiO_2 particle size reduces the volume recombination of e^-/h^+ and

This book belongs to Kitab Liaison (ocd1996@gmail.com) Copyright Elsevier 2023

Table 10.2 TiO_2 photocatalyst optimization

Optimization objectives	Optimization approaches	Optimization mechanisms	Water treatment applications
Enhance photocatalytic reaction kinetics	Size	More surface reactive sites, higher reactant adsorption, lower electron-hole recombination	High-performance UV activated photocatalytic Reactors
	Nanotube morphology	Shorter carrier-diffusion paths in the tube walls, higher reactant mass transfer rate toward tube surface	
	Noble metal doping	Better electron-hole separation, lower electron-hole recombination	
	Reactive crystallographic facets	Higher reactant sorption, better electron-hole separation, lower electron-hole recombination	
Expanded photoactivity range	Metal impurity doping, anion doping, dye sensitizer doping, narrow band-gap, semiconductor doping	Impurity energy levels, band-gap narrowing, electron injection, electron injection	Low energy cost solar/visible light activated photocatalytic reactors

This book belongs to Kitab Liaison (ocd1996@gmail.com)

Copyright Elsevier 2023

improves the interfacial charge carrier transfer [108]. However, when the particle size is lowered to numerous nanometers, surface recombination dominates, lowering photocatalytic activity. Thus, the photocatalytic activity of TiO_2 has a maximum because of the interplay of the mechanism that lies in the nanometer range. TiO_2 nanotubes were proved to be more efficient than TiO_2 nanoparticles in the decomposition of organic compounds [109]. The higher photocatalytic activity was attributed to the reduced carrier-diffusion paths in the tube walls and the quicker mass movement of reactants toward the nanotube surface.

Noble metal doping can lower the e^-/h^+ recombination due to the tendency of photo-excited electrons to move to the noble metals with fewer Fermi quantities, whereas the holes stay in TiO_2 [110]. The photocatalytic activity of TiO_2 can also be enhanced through formation of advanced reactive crystallographic facets. Because high-energy {001} facets decline rapidly during crystal growth, anatase TiO_2 is normally dominated through the reduced-energy {101} facets. Applying a precise capping agent (usually fluoride), the percentage of {001} facets can be increased from lower than 10% to up to 89%, significantly improving hydroxyl radical production and organic compound disintegration [111, 112]. The improved activity originated from the strong adsorption of reactants on high-energy facets and the spatial separation of electrons and holes on crystal facets [112, 113]. The optimal percentage of {001} facets for photocatalysis continues to be debated [113]. Enhancing contaminant adsorption through adjusting the photocatalyst surface is another method of improving photocatalytic activity because of the short lifetime of ROS. However, little has been done in this area.

Another actively followed research area is to grow the excitation spectrum of TiO_2 to include visible light. The overall strategy is doping metal impurities, dye sensitizers, narrow band-gap semiconductors, or anions into nano-TiO_2 to create hybrid nanoparticles or nanocomposites [106, 110]. Metals and anions form impurity energy quantities or narrow the band-gap; upon visible light excitation, dye sensitizers and narrow band-gap semiconductors inject electrons into TiO_2 to start the catalytic reactions. Among these techniques, anion (especially nitrogen) doping was confirmed to be most cost-effective and feasible for industrial application, but their stability and long-term effectiveness has not been tested. Declining nitrogen concentration in photocatalysis has been reported [106, 114].

Other than TiO_2, WO_3 and some fullerene results also have the potential to be applied in photocatalytic water treatment. WO_3 has a narrower band

This book belongs to Kitab Liaison (ocd1996@gmail.com) Copyright Elsevier 2023

gap than TiO_2, permitting it to be activated through visible light (<450 nm) [115]. Pt doping further improves WO_3 reactivity by facilitating the multi-electron reduction of O_2 and enhancing e^-/h^+ separation [64]. Aminofullerenes produce $^1O_2$ under visible light irradiation (<550 nm), and they have been studied to damage pharmaceutical compounds and inactivate viruses [116, 117]. Fullerol and C_{60} encapsulated with poly(*N*-vinylpyrrolidone) can generate $^1O_2$ and superoxide under UVA light [118]. Aminofullerenes are more amenable to immobilization than fullerol and are more efficient for disinfection functions because of their positive charge. $^1O_2$ has decreased oxidation potential than hydroxyl radicals generated by TiO_2, whereas it is a more selective ROS and is less susceptible to quenching by nontarget background organic matter. Fullerenes are presently much more expensive and not as voluntarily available as TiO_2.

Results and discussion

Applications in water treatment

The general effectiveness of a photocatalytic water treatment process relies greatly on the arrangement and function parameters of the photoreactor. Two orders are commonly applied: slurry reactors and reactors using immobilized TiO_2. Numerous dispersion/recoveries or catalyst control techniques are being followed to optimize the efficacy. Thorough investigations on operating parameters have been done with these lab- or pilot-scale systems. A past critical analysis describes the impact of water quality and a broad range of functional parameters inclusive of TiO_2 loading, pH, temperature, dissolved oxygen, contaminant type and concentration, and light wavelength and intensity [119]. Readers often refer to this analysis for its details on process optimization. A commercial product, the Purifics Photo-CatTM system, has a treatment capacity as high as 2 million gallons daily with a small footprint of 678 ft^2. Pilot tests indicated that the Photo-CatTM system is greatly effective for the elimination of organics without generating waste streams. It also functions with a moderately low specific power consumption of about 4 kWh/m^3 [17, 120, 121]. Nano-TiO_2 facilitated solar disinfection (SODIS) has been tested extensively and apparently it is a feasible choice for generating safe drinking water in rural areas of developing countries. The SODIS system can be small scale for a single person or scaled up to medium-sized solar compound parabolic collectors.

Photocatalysis has confirmed significant potential as a low-cost, sustainable, and environmentally friendly water treatment technology. Nonetheless,

This book belongs to Kitab Liaison (ocd1996@gmail.com) Copyright Elsevier 2023

there are many technical barriers for its large-scale application, including (1) catalyst optimization to enhance quantum yield or to maximize visible light; (2) efficient photocatalytic reactor design and catalyst recovery/immobilization techniques; and (3) better reaction selectivity.

Metal oxide nanomaterials such as TiO_2, CeO_2, and carbon nanotubes have been reviewed as catalysts in heterogeneous catalytic ozonation processes that offer rapid and relatively full degradation of organic pollutants. Both radical-mediated and nonradical-mediated reaction pathways have been suggested [122]. The adsorption of ozone and/or pollutants on the catalyst surface plays an important function in both mechanisms. Nanomaterials have a big specific surface area and easily accessible surface, forming catalytic functions. Some nanomaterials were also reported to improve ozone decomposition into hydroxyl radicals, enhancing the degradation process via radical-mediated routes [123]. For the next industrial-scale applications, a clear understanding of the mechanism of nanomaterial-enabled catalytic ozonation is critically required.

Disinfection and microbial control

The dilemma between efficient disinfection and creation of toxic disinfection byproducts (DBPs) poses a big threat to the water industry. It is now well identified that conventional disinfectants, for instance chlorine disinfectants and ozone, can yield to toxic DBPs (e.g., halogenated disinfection byproducts, carcinogenic nitrosamines, bromate, etc.). UV disinfection occurred as other techniques for oxidative disinfection because it generates fewer DBPs, although it needs a high dosage for specific viruses (e.g., adenoviruses). These problems call for the development of substitute techniques that can improve the robustness of disinfection and still prevent DBP formation.

Our past discussion on antimicrobial nanomaterials described the potential of nanotechnology in disinfection and microbial management [124]. Numerous nanomaterials, including nano-Ag, nano-ZnO, nano-TiO_2, nano-Ce_2O_4, CNTs, and fullerenes, portray antimicrobial characteristics in the absence of strong oxidation, and thus have a reduced tendency to form DBPs (Table 10.3). The antimicrobial mechanisms of these nanomaterials, their advantages and disadvantages, their applicability for water treatment, and the critical research require a comprehensive discussion in the review paper [124]. Therefore, only a brief update will be offered here, particularly regarding nano-Ag and carbon-based nanomaterials.

This book belongs to Kitab Liaison (ocd1996@gmail.com) Copyright Elsevier 2023

Table 10.3 Nanomaterial antimicrobial mechanisms

Nanomaterials	Antimicrobial mechanisms
Nano-Ag	Release of silver ions, protein damage, suppression of DNA replication, membrane damage
Nano-TiO_2	Production of ROS
Nano-ZnO	Release of zinc ions, production of H_2O_2, membrane damage
Nano-MgO	Membrane damage
Nano-Ce_2O_4	Membrane damage
nC_{60}	ROS-independent oxidation
Fullerol and aminofullerene	Production of ROS
Carbon nanotubes	Membrane damage, oxidative stress
Graphene-based nanomaterials	Membrane damage, oxidative stress

Antimicrobial mechanisms

Currently, Nano-Ag is the most broadly applied antimicrobial nanomaterial. Its high antimicrobial functions, broad antimicrobial spectrum, less human toxicity, and ease of application make it a suitable option for water disinfection and microbial management. It is now well known that the antimicrobial activity of nanosilver greatly originates from the discharge of silver ions [125, 126]. Silver ions can join to thiol groups in vital proteins, creating damage on an enzyme [127]. It also has been confirmed that silver ions can hinder DNA replication and initiate structural alterations in the cell envelope [40]. Hence, the rate of release and bioavailability of silver ions is essential for the toxicity of nano-Ag. Studies have proposed that the physicochemical characteristics of nano-Ag play an essential function in its antimicrobial activity. However, the effect of the size, shape, coating, and crystallographic facet apparently is majorly related to the varied release kinetics of silver ions. The existence of common ligands lowers the bioavailability of silver ions and prevents toxicity [125]. A previous study proved that reduced concentration (sublethal) of silver ions or nano-Ag enhances *E. coli* growth, proposing a hermetic response that may be counterproductive to its antimicrobial activities [126].

CNTs kill bacteria through forming a physical perturbation of the cell membrane, oxidative stress, or disturbance of an explicit microbial process through disturbing/oxidizing a vital cellular structure/constituent upon direct interaction with bacterial cells. Graphene and graphite materials portray antimicrobial characteristics via the same mechanisms [128, 129].

This book belongs to Kitab Liaison (ocd1996@gmail.com) Copyright Elsevier 2023

The cytotoxicity of CNTs relies heavily on their physicochemical characteristics. Dispersed, metallic, and short CNTs with small diameters are very toxic [129–131].

Potential applications in water treatment

Antimicrobial nanomaterials are envisaged to identify their usages in three critical barriers in water/wastewater systems: disinfection, membrane biofouling control, and biofilm control on other applicable surfaces. Nano-Ag has great potential for use in POU treatment. It can enhance the water quality for high-end application or offer another challenge against waterborne pathogens for susceptible populations. Commercial devices maximizing nano-Ag are already accessible, for example, the MARATHON and Aquapure systems. Nano-Ag has also been integrated into ceramic microfilters as a restriction for pathogens that can be used in remote areas in developing countries [132].

The antimicrobial properties, fibrous shape, and high conductivity of CNTs ensure novel CNT filters for both bacteria and virus elimination. The thin layer of CNTs efficiently eliminates bacteria via size exclusion and viruses via depth filtration; within hours, the remaining bacteria are greatly inactivated by CNTs [133]. With a little intermittent voltage (2–3 V), MWNTs can directly oxidize bound bacteria and viruses and yield to inactivation in seconds [134, 135]. The used electric potential also improves viral transport to the anodic CNTs [134]. Such CNT filters can be applied as increased performance POU devices for water disinfection with minimal to no power requirement.

The application of nanomaterials in membrane biofouling management is extensive. They can also be applied in other water treatment-related surfaces such as storage tanks and distribution pipes to manage pathogen contamination, biofilm formation, and microbial-influenced corrosion. Cheap coating methods that can economize nanomaterial application and optimize its efficiency while permitting reproduction are critically required. An alternative technique is to use nanoscale biofouling resistant surface structures, a strategy applied in marine organisms (dolphins and sharks) and plants (lotus leafs). A common disadvantage of many nanomaterial-enabled disinfection methods in the absence of disinfection residue, that is important for managing the microbial growth in water storage and distribution. However, nanotechnology-enhanced disinfection can lower DBP formation as chlorine or another chemical disinfectant is only required as a secondary disinfectant. Long-term efficacy is another main inconsistency for all the

This book belongs to Kitab Liaison (ocd1996@gmail.com) Copyright Elsevier 2023

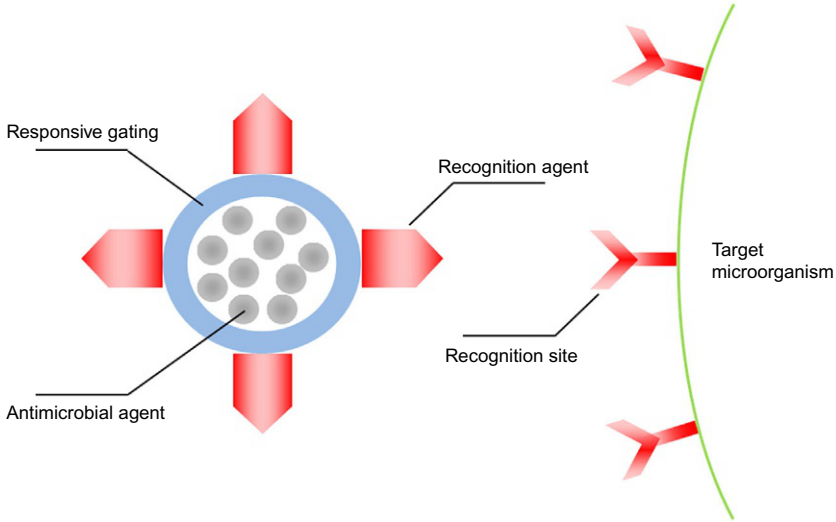

Fig. 10.5 Schematic mechanism for "on-demand" microbial control. "On-demand" microbial control can be attained through the application of recognition agents aimed at specific microorganisms. The responsive gating material is made such that it releases the antimicrobial agent after recognition.

technologies. Antimicrobial nanomaterials that depend on the release of biocidal ions will be depleted eventually. Hence, managed release and replenishment strategies are needed. A potential "on-demand" release strategy is to encapsulate antimicrobial agents into a matrix gated through materials responsive to the existence of microorganisms or biofilms. This "on-demand" mechanism can be further paired with acknowledgment mechanisms for targeted release (Fig. 10.5). For nanomaterials depending on direct interactions, fouling could significantly suppress or even remove their antimicrobial functions.

Sensing and monitoring

A great obstacle to water/wastewater treatment is monitoring of water quality because of the very low concentration of certain contaminants, the absence of fast pathogen detection, and the increased complexity of the water/wastewater matrices. Innovative sensors with great sensitivity and selectivity as well as fast response are greatly needed.

Pathogen detection

Pathogen detection is critical as it is directly associated with public health. Conventional indicator systems such as coliform bacteria are slow and do

This book belongs to Kitab Liaison (ocd1996@gmail.com) Copyright Elsevier 2023

not monitor the existence of some essential or emerging pathogens, especially viruses (hepatitis A and E, coxsackieviruses, echoviruses, adenoviruses, and Norwalk viruses), bacteria (*Legionella* and *Helicobacter*), and protozoa (*Cryptosporidium* and *Giardia*) [136]. A number of these pathogens are etiologic agents in outbreaks associated with drinking water. Furthermore, pathogen detection is the major element of the diagnosis-based water disinfection method in which disinfection is initiated by the detection of aimed microorganisms. Active research is going onto establish nanomaterial-enhanced pathogen sensors. These sensors usually consist of three major components: recognition agents, nanomaterials, and a signal transduction mechanism [137]. The acknowledgement of agents that exactly interact with antigens or other epitopes on the pathogen surface forms the selectivity. Sensitivity and fast response are attained through the nanomaterial associated with signal transduction upon the acknowledgement event. A broad range of recognition agents has been applied, including antibodies, aptamers, carbohydrates, and antimicrobial peptides [137]. Nanomaterials enhance the sensitivity and speed of detection and attain multiplex target detection respecting their unique physicochemical characteristics, particularly electrochemical, optical, and magnetic characteristics. These sensors can be applied to detect an entire cell as well as biomolecules [136, 137].

The most frequently applied nanomaterials in pathogen detection are magnetic nanoparticles, quantum dots (QDs), noble metals, dye-doped nanoparticles, and CNTs. Magnetic nanoparticles and CNTs have been thoroughly studied for sample concentration and purification. A commercial magnetic nanocomposite, Dynabead, is accessible for creating numerous pathogen-detection kits.

QDs are fluorescent nanocrystals of semiconducting materials (e.g., CdSe) whose electronic features rely on the size and shape of the individual crystals. QD particles with smaller sizes have broad band-gaps and hence require extra energy to excite and produce light with a shorter wavelength. QDs have broad absorption spectra though narrow and stable fluorescent emission spectra. Hence, QDs are specifically appropriate for multiplex detection employing a single excitation light source. The emission spectrum of QDs is $w^{10}e^{20}$ times brighter than an organic fluorophore and up to thousands of times more stable than conventional dyes [48, 138].

Noble metal nanomaterials have been greatly applied in sensors, especially because of their advanced localized surface plasmon resonance (LSPR) that relies on the size, shape, composition, and separation distance of nanoparticles, and the dielectric environment of the surrounding medium [139]. The increased conductivity of noble metal nanoparticles also

This book belongs to Kitab Liaison (ocd1996@gmail.com) Copyright Elsevier 2023

facilitates electron movement between the electrode surface and the analyst [140]. The existence of advanced LSPR yields to an increased molar extinction coefficient and Rayleigh scattering, and advanced local electromagnetic fields near the nanoparticle surface. Depending on theoretical calculation, nano-Au spheres of w40 nm in diameter have an absorption cross-section five orders of magnitude higher than conventional dyes while 80-nm nano-Au spheres scatter light five orders of magnitude more than fluorescence dyes [141]. Nobel metals were mainly applied in colorimetric and surface-enhanced Raman spectroscopy (SERS) sensing. Colorimetric assays are rapid and simple. The signal transduction depends on the color transformation of the nanoparticle suspension because of the varied interparticle distance or aggregation state [142]. It has been studied for DNA detection, diagnosis of pathogen infection, and pathogen control in water samples. However, the aggregation state of nanoparticles is sensitive to solution chemistry and is challenging to regulate. The coexisting water/wastewater constitutes will majorly influence results, lowering the reproducibility. The SERS phenomenon is associated with both electromagnetic impact and chemical mechanisms associated with the charge transfer between the noble metals and the target molecules [143]. Consequently, the efficacy of Raman scattering can be developed to more than 1014-fold, which is even able to detect a single molecule [144].

Silica nanoparticles doped with either organic or inorganic luminescent dyes have been advanced for ultrasensitive sensors. The huge number of dye molecules limited to a single silica particle guarantees great enhancement in sensitivity. Furthermore, the silica matrix guards the dye molecules from the external environment, greatly suppressing photobleaching and photodegradation. The renowned photostability develops dye-doped silica nanoparticles specifically beneficial for applications that need increased intensity or lengthy excitations [138]. The rich silica chemistry (e.g., silane chemistry) also facilitates modification and conjugation of future surfaces.

The increased conductivity along the length makes CNTs outstanding electrode materials. Consequently, CNTs can significantly enhance electrochemical detection through promoting electron movement and electrode-analysts relationship [145]. They have been integrated into electrodes through rough-random or associated coating, or applied as a single CNT electrode [146]. Semiconducting CNTs can be applied in a nanoscale field effect transistor [147]. In addition, their exceptional electronic characteristics and the increased adsorption capacity of CNTs heighten detection sensitivity [67]. The major barrier for CNT depended on sensors is the

This book belongs to Kitab Liaison (ocd1996@gmail.com) Copyright Elsevier 2023

heterogeneity of CNTs. Separation of metallic and semiconducting SWNTs has been extensively studied, although it is far from perfect. The production and purification processes of CNTs often introduce impurities, contaminants, and even deprivation of the CNT structure. Thus, better synthesis, purification, and separation are needed to generate more homogeneous CNTs. However, most of these nanosensors have excellent photostability and sensitivity; nonspecific binding continues to be a main challenge for usages in water and wastewater. Strategies to lower nonspecific binding and avoid undesired nanoparticle aggregation are sorely needed.

Trace contaminant detection

In trace organic or inorganic contaminant detection, nanomaterials can be applied for both concentration and detection. CNTs have a large potential for environmental review of trace metals or organic pollutants as they provide increased adsorption capacity and recovery rate, along with the rapid kinetics as described above. The preconcentration aspects for metal ions were found to be between 20 and 300 with rapid adsorption kinetics [148]. CNTs have also been broadly studied for preconcentrating most organic compounds, several of which were done in real water samples [149]. Adsorption of charged species to CNTs yields changes of conductance, offering the foundation for the association between analyte concentration and present fluctuation [101]. Other nanomaterials such as nano-Au and QDs have also been utilized. Nano-Au was applied in the detection of pesticides at ppb quantities in a colorimetric assay; modified nano-Au was confirmed to detect Hg_2fl and CH_3Hgfl rapidly with increased sensitivity and selectivity [44, 150]. QD-modified TiO_2 nanotubes lowered the detection limits of PAHs to the level of a pica-mole per liter based on fluorescence resonance energy transfer [151]. A nanosensor depending on CoTe QDs immobilized on a glassy carbon electrode surface was reported to detect Bisphenol A in water at concentrations as low as w10 nM within 5 s [152].

Multifunctional devices

The development of functional nanomaterials and their convergence with conventional technologies create opportunities to design a new family of nanotechnology-enabled multifunctional water treatment devices that could perform multiple tasks in one device. Such multifunctional systems can improve the overall performance and prevent excessive dismissal, miniaturizing the footprint. Thus, the multifunctional concept is particularly beneficiary in dispersed and small-scale applications. Varied

This book belongs to Kitab Liaison (ocd1996@gmail.com) Copyright Elsevier 2023

functional nanomaterials can be incorporated onto a common platform depending on treatment need. Though magnetic nanoparticles, membranes are a better and broadly studied platform to concept multifunctional devices. Particularly, electrospun nanofibers have drawn much attention as an exceptional nanomaterial carrier. Owing to the increased performance, small footprint, and modular design of nanotechnology-enhanced devices, it is envisaged that varied functionalities can be assembled in layers of cartridges or as modules aligned in series, allowing the optimization/regeneration of every functionality separately [22]. The capacity and functionality of such nanotechnology-enhanced systems can be manipulated easily through plugging in or pulling out modules.

Retention and reuse of nanomaterials

The retention and reuse of nanomaterials is a major component of advanced nanotechnology device design because of both cost and public health considerations. It can be usually attained through the application of a separation device or immobilizing nanomaterials in the treatment system. A reliable separation process is membrane filtration that permits continuous operation with a small footprint and chemical application. Ceramic membranes are more beneficial than polymeric membranes in photocatalytic or catalytic ozonation usages as they are more resistant to UV and chemical oxidants [94]. The suspended particles in the receiving water are damaging to reactor-membrane hybrid systems, as they can be restricted through the membrane and substantially diminish the reaction efficiency. Therefore, raw water pretreatment is normally needed to lower the turbidity. Nanomaterials also can be immobilized on various platforms such as resins and membranes to prevent further separation. Nonetheless, current immobilization methods normally yield a substantial loss of treatment efficacy. Research is required to establish a simple, low-cost technique to immobilize nanomaterials in absence significantly affecting performance. For magnetic nanoparticles/nanocomposites, low-field magnetic separation is a potential energy-efficient option.

Little is known about the release of nanomaterials from nanotechnology-enhanced devices, although the potential release is anticipated to be greatly based on the immobilization method and the separation process applied. If no downstream separation is utilized, nanomaterials coated on treatment system surfaces are most likely to be discharged in a comparatively rapidly and complete mechanism, but nanomaterials embedded in a solid matrix will have least release until they are predisposed of. For nanomaterials that discharge metal ions, their dissolution must be carefully managed (e.g., by

This book belongs to Kitab Liaison (ocd1996@gmail.com) Copyright Elsevier 2023

coating or optimizing size and shape). The detection of nanomaterial release is a key technical hurdle for danger evaluation and remains an obstacle. Details related to detection techniques are beyond the scope of this paper, and readers are referred to numerous recent analyses on this topic [153, 154]. Few methods can detect nanomaterials in complex aqueous matrices and they are normally sophisticated, expensive, and have numerous challenges. Fast, sensitive, and selective nanomaterial analytical techniques are sorely needed.

Barriers and research needs

Although nanotechnology-improved water/wastewater treatment processes have indicated great promise in laboratory studies, their readiness for commercialization varies widely. Some are already on the market while others require significant research before they can be considered for full-scale application. Their future establishment and commercialization face several challenges including technical hurdles, cost-effectiveness, and potential environmental and human risks. There are two main research needs for full-scale application of nanotechnology in water/wastewater treatment. First, the performance of numerous nanotechnologies in treating natural and wastewaters must be tested. Future studies must be done under more realistic situations to assess the applicability and efficiency of varied nanotechnologies as well as to authenticate nanomaterial-enhanced sensing technologies. Second, the long-term efficiency of these nanotechnologies is greatly unknown, as most lab studies were conducted for a relatively short period of time. Research addressing the long-term performance of water and wastewater treatment nanotechnologies is largely needed. Consequently, the side-by-side comparison of nanotechnology enhanced systems and present technologies is problematic.

Despite the superior performance, the adoption of innovative technologies powerfully based on the cost effectiveness and the possible risk involved. The present cost of nanomaterials is prohibitively increased with a few exceptions such as nano-TiO_2, nanoscale ion oxide, and polymeric nanofibers. There are presently two approaches to address the cost issue. One suggested method is to apply low-purity nanomaterials without compromising efficiency significantly, as much of the production cost is associated with separation and purification [22]. On the other hand, the cost effectiveness can be enhanced through retaining and recycling nanomaterials. Nanomaterials possess exceptional problems for risk evaluation and management as they are small particles rather than molecules or ions for

This book belongs to Kitab Liaison (ocd1996@gmail.com) Copyright Elsevier 2023

which danger evaluation frameworks and protocols are already in place. Improved understanding and mitigating potential risks related to the use of nanomaterials in water and wastewater treatment will yield to wider public acceptance, which is crucial for new technology adoption. The compatibility between nanotechnologies and current water and wastewater treatment processes and infrastructure also must be addressed. The majority of the treatment plants and distribution systems in established countries are anticipated to remain in place for decades to come. Considerably, it is crucial to be able to employ nanotechnology with the least infrastructure transformation in the near term. In the meantime, nanotechnology-enhanced treatment processes can be implemented in places where water treatment infrastructure is not present or is in POU devices.

Basically, this nanotechnology for water and wastewater treatment is acquisition of momentum globally. The precise properties of nanomaterials and their convergence with the present treatment technologies present substantial opportunities to revolutionize water and wastewater treatment. Although numerous nanotechnologies discussed in this analysis are still in the laboratory research stage, some have made their way to pilot testing or even commercialization. Among them, three categories indicate most reliable in full scale application soon depended on their stages in research and development, commercial availability and cost of nanomaterials included, and compatibility with the existing infrastructure: nanoadsorbents, nanotechnology enabled membranes, and nanophotocatalysts. All three categories have commercial products, but they have not been used in large-scale water or wastewater treatment. Several other water-treatment nanotechnologies have found their niche usages in POU systems.

The challenges encountered through water/wastewater treatment nanotechnology are crucial, although the majority of these problems are perhaps just temporary, such as technical hurdles, high cost, and potential environmental and human risks. To counter these challenges, collaboration between research institutions, industry, government, and other stakeholders is essential. It is our proposal that advancing nanotechnology by carefully steering its direction while avoiding unintended consequences can cautiously offer robust solutions to our water/wastewater treatment barriers, both developmental and revolutionary.

This book belongs to Kitab Liaison (ocd1996@gmail.com) Copyright Elsevier 2023

Photocatalytic water treatment technology

Semiconductor photocatalytic technology has recently demonstrated a high efficiency as a sustainable, environmentally friendly, and low-cost treatment process to support the "zero" waste arrangement in water/wastewater management. This advanced oxidation technology's potential has been greatly proven to eliminate stubborn microorganisms and organic compounds in water. In recent years, postreclamation of the catalyst elements after water treatment has remained the key technical obstacle that hinders its commercialization. The objective of this paper is to review the present R&D advancements of photoreactor systems, planned photocatalysts, and the optimizations of the process and the photooxidation procedures prototyping for water treatment. Some possible and viable photocatalytic reactor structures are deliberated, particularly the reactors of the photocatalytic membrane. Critical assessment is conducted on the impacts of essential photoreactor activity limits and the quality of water on the photoprocess efficiencies based on disinfection and mineralization. We detailed, for the first time, the procedure of utilizing a multivariable optimization method to measure the finest operation configurations in order to improve photooxidation efficiency and process performance. Not only photomineralization, but also photodisinfection kinetics alongside their modelings related to the photocatalytic process of water treatment are described. This paper briefly describes the life cycle examination for retrofitting the photocatalytic process as an unconventional waste treatment technology. The aim of this article is to provide a technical and scientific outline and important facts to engineers and scientists relevant to this field.

Introduction

Rapid population growth, industrial development, and persistent droughts have led to an increased demand for and scarcity of clean water sources; this has the makings of a global disaster. Such a growing demand for clean water sped up the adoption of different practical approaches and solutions to provide more sustainable water resources. Increasing the catchment capacity for storm water and storing rainwater for daily needs are just some instances that can momentarily solve these difficulties. Water organization and management in a number of arid regions with intense sunlight, minimum rain, and persistent drought face a lot of challenges in finding sustainable water resources. It has been established that about four billion people globally have access to little or no clean or treated water supply while millions of people

This book belongs to Kitab Liaison (ocd1996@gmail.com) Copyright Elsevier 2023

have died annually due to chronic waterborne diseases [155]. The ever-increasing contamination of water as a result of the devastating discharge of contaminants and micropollutants into the existing water cycle is expected to raise these statistical figures in the near future [156–158]. To suppress the deteriorating clean water shortage, there is a need to develop advanced, low-cost, and high efficiency water treatment systems to treat the wastewater. Among the few fascinating options is the potential recycling of onsite country wastewater or the sanitized community wastewater from treatment plants for industrial and agricultural activities [159, 160]. This wastewater can be recycled for a cleaner water supply, as it makes up one of the biggest possible water resources. Wastewater recycling is typically linked to the occurrence of soluble refractory organic compounds, health-threat coliforms, and suspended solids that are tedious as well as expensive to remove [161]. The water treatment technologies that are presently established, including coagulation or adsorption, simply suppress the pollutants in water by transforming them into the next stages, but they still persist and are not totally removed or abolished [162]. The remaining ordinary water treatment processes comprising membrane technology sedimentation, chemicals, and filtration are very expensive to operate and could release poisonous minor pollutants into the environment [163]. Such highly toxic chemicals are very redundant and have become a global concern because of growing environmental responsiveness and regulations. The most widely and commonly used disinfection process is chlorination. However, the byproducts generated due to disinfection in the chlorination process are carcinogenic and mutagenic to people's health [164–166]. As a result, rapid R&D has emerged in the area of advanced oxidation processes (AOPs), as new water treatment methods. The logic behind these AOPs is founded on the in situ production of very reactive transient elements (such as OH, H_2O_2, O_2^-, O_3) for disinfection byproducts, water pathogens, and refractory organic compound mineralization [11, 167]. Heterogeneous photocatalysis using semiconductor catalysts (ZnS, GaP, CdS, Fe_2O_3, TiO_2, and ZnO) is one of the AOPs that has shown its performance in transforming different indistinct refractory elements into simple decomposable materials, and ultimately mineralizing them to harmless water and carbon dioxide. One of the semiconductor catalysts that has received the highest attention in R&D of the photocatalysis process is titanium dioxide (TiO_2). The GaP or Cds are completely degraded to yield toxic residues while TiO_2 is the most dynamic photocatalyst under $300\,\text{nm} < l < 390\,\text{nm}$ photon energy and can be stable after a series of catalytic cycles [155]. Apart from these, the

This book belongs to Kitab Liaison (ocd1996@gmail.com) Copyright Elsevier 2023

complex functional abilities of the TiO_2 catalyst, including the thermal or chemical resistance or stability against chemical disintegration and the tough mechanical qualities, have boosted its diverse application in photocatalytic water management. Some imperative aspects for heterogeneous photocatalysis have protracted their practical applications in water treatment, which involves: (1) cheap operating expenses, (2) thorough mineralization of parents and their transitional compounds with no secondary contamination, and (3) ambient functional temperature and pressure. A detailed documentation exists regarding the fact that the ROS (reactive oxygen species) produced due to the photo-induced charge separation on TiO_2 faces for microbial deactivation and organic mineralization with no creation of secondary contamination. Presently, the use of these TiO_2 catalysts in the water treatment process still experiences a range of technical issues. The main impediment toward its practicality as an industrial technique is the postseparation of the semiconductor TiO_2 catalyst after water treatment. The fact that the TiO_2 is made of small particles and that it has a large surface area-to-volume ratio and surface energy leads to a strong possibility for catalyst accumulation in the operational process. This particle accumulation is very harmful in terms of its recyclable lifespan, reduction of surface area, and particle size conservation. More practical difficulties are involved in catalyst creation with a wider photoactivity series and its incorporation with a reasonable photocatalytic reactor arrangement. Furthermore, the knowledge of the concept behind the conventional reactor functional factors and their connections is as well insufficient and gives a hard assignment for process optimization. Many frequently committed mistakes in researching kinetic modeling on either the photodisinfection or photomineralization have also been considered for many years.

The aim of this review paper is to provide a summary of the knowledge and invention of photocatalytic water treatment processes, from the basics of photoreactor development and catalysts to kinetic modeling and process optimization to the water variables that influence the process performance. A brief review of the practicable utilization of photocatalytic water technology through life cycle understanding and the potential upcoming difficulties is also proposed.

Fundamentals and mechanism of TiO_2 photocatalysis

Heterogeneous TiO_2 photocatalysis

In much of the literature, photochemistry and the photophysics essentials that underlie heterogeneous photocatalysis and use the semiconductor

This book belongs to Kitab Liaison (ocd1996@gmail.com) Copyright Elsevier 2023

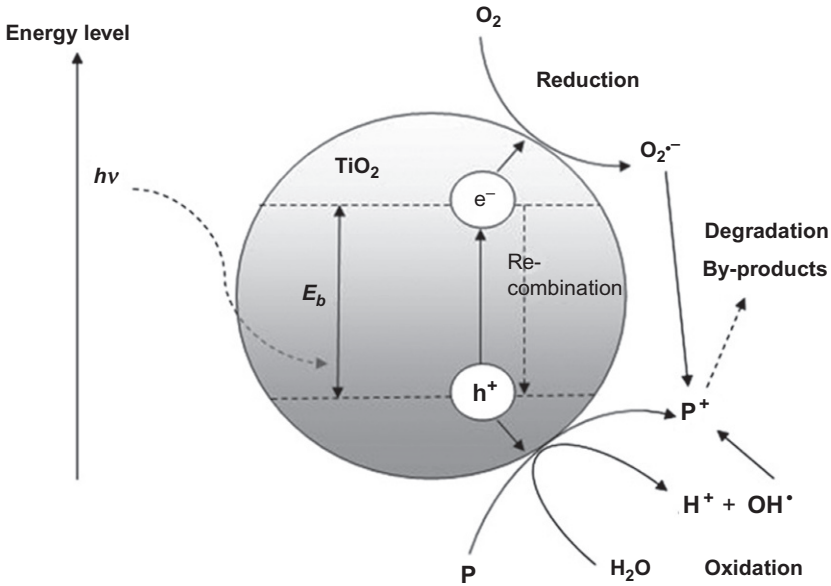

Fig. 10.6 Electron-hole pair's photo-induced formation mechanism in a semiconductor TiO_2 particle with the existence of a water pollutant (P).

TiO_2 catalyst have been reported intensively [163, 168]. The semiconductor TiO_2 has been used broadly as a photocatalyst for inducing on its surface sequences of oxidative and reductive reactions. This is specially backed by the characteristic of a discrete single electron in its outer orbital. When photon energy (*hν*) is equal to or greater than the band-gap, TiO_2's energy is illuminated onto its surface, normally 3.0 eV (rutile) or 3.2 eV (anatase), in femtoseconds, with the sole electron going to be photoexcited to the conduction band that is empty. Fig. 10.6 illustrates the electron-hole pair formation's mechanism whenever the TiO_2 particle is irradiated using sufficient hv. Normally, the light wavelength for this kind of photon energy matches up to $l < 400$ nm. The photonic excitation leaves behind a valence band that is unfilled, and therefore the electron-hole pair is generated ($e^- h^+$). The chain sequences of oxidative-reductive reactions (Eqs. 10.1–10.11) that take place at the photon-activated surface were postulated extensively, as shown below:

$$\text{Photoexcitation}: TiO_2 + h\nu \rightarrow e^- + h^+ \tag{10.1}$$

$$\text{Charge} - \text{carrier trapping of } e^- : e^-_{CB} \rightarrow e^-_{TR} \tag{10.2}$$

This book belongs to Kitab Liaison (ocd1996@gmail.com) Copyright Elsevier 2023

$$\text{Charge} - \text{carrier trapping of } h + h^{+}_{VB} \rightarrow h^{+}_{TR}: \tag{10.3}$$

$$\text{Electron} - \text{hole recombination}: e^{-}_{TR} + h^{+}_{VB}\left(h^{+}_{TR}\right) \rightarrow e^{-}_{CB} + \text{heat} \tag{10.4}$$

$$\text{Photoexcited } e^{-} \text{scavenging}: (O_2)_{ads} + e^{-} \rightarrow O_2^{\bullet -} \tag{10.5}$$

$$\text{Oxidation of hydroxyls}: OH^{-} + h^{+} \rightarrow OH^{\bullet} \tag{10.6}$$

$$\text{Photodegradation by } OH^{\bullet}: R - H + OH^{\bullet} \rightarrow R'^{\bullet} + H_2O \tag{10.7}$$

Direct photoholes:

$$R + h^{+} \rightarrow R^{+\bullet} \rightarrow \text{Intermediate(s)/Final degradation products} \tag{10.8}$$

$$\text{Protonation of superoxides}: O_2^{\bullet -} + OH^{\bullet} \rightarrow HOO^{\bullet} \tag{10.9}$$

$$\text{Coscavenging of } e^{-}: HOO^{\bullet} + e^{-} \rightarrow HO_2^{-} \tag{10.10}$$

$$H_2O_2 \text{ formation}: HOO^{-} + H^{+} \rightarrow H_2O_2 \tag{10.11}$$

The h^{+}_{TR} and e^{-}_{TR} in Eq. (10.4) exemplify the conduction-band hole and the surface-trapped valence band electron correspondingly. It was stated that these trapped carriers are typically TiO_2 surface bounded and do not immediately recombine when photon excitation takes place [169] When electron scavengers are not there (Eq. 10.4), the photoexcited electron combines again with the valence band hole in nanoseconds with heat energy dissipation that is concurrent. Thus, the presence of electron scavengers is therefore very vital for successful functioning of photocatalysis as well as in prolonging the recombination. Eq. (10.5) depicts the way the existence of oxygen averts the electron-hole pair recombination, as it allows the formation of a superoxide radical ($O_2^{\bullet -}$). This $O_2^{\bullet -}$ radical could be protonated more so that it can form the hydroperoxyl radical ($HO_2^{\bullet}$) and consequently H_2O_2, as illustrated in Eqs. (10.9), (10.10), correspondingly. In addition, the $HO_2^{\bullet}$ radical formed was recounted to have a scavenging property and therefore, these radical species' coexistence could particularly extend the recombination time of the h^{+}_{TR} in the whole reaction of photocatalysis. It should, however, be noted that all these phenomena in photocatalysis were accredited to the existence of both water molecules and dissolved oxygen (DO). Short of the existence of water molecules, the hydroxyl radicals ($OH^{\bullet}$) that are highly reactive might not be shaped and could encumber the liquid phase organics' photodegradation. This was demonstrated from some reports that the photocatalysis reaction did not go on without water molecules. Some simple organic compounds (e.g., formic acid and oxalate) could be mineralized with the use of direct electrochemical oxidation where the e^{-}_{TR} is scavenged

This book belongs to Kitab Liaison (ocd1996@gmail.com) Copyright Elsevier 2023

using metal ions in the system devoid of water [170]. Despite the fact that the h^{+}_{TR} has been regarded extensively for its capacity to directly oxidize organic species, this probability is still not conclusive. The h^{+}_{TR} refers to oxidants that are powerful (+1.0 to +3.5 V against NHE), whereas are good redundant is e^{-}_{TR} (+0.5 to −1.5 V in contrast to NHE), the kind determined by the oxidation and catalysts conditions.

Lots of elementary mechanistic studies on diverse surrogate organic compounds (for instance, oxalic acid, phenol, and chlorophenol) have been studied widely over TiO_2 surfaces in photodegradation. The $OH^{\bullet}$ radical that is reactive could hydroxylate aromatic compounds that bring about successive addition/oxidation and finally ring opening. The subsequent intermediates, typically carboxylic acids and aldehydes, are going to be carboxylated further to create water and innocuous carbon dioxide. While the photocatalysis reaction takes place on the photon-activated TiO_2 surface, understanding the reaction steps that comprise organic photodegradation is very important in kinetic expression formulation. The liquid phase organic compounds are ruined to its conforming intermediates and more mineralized to water and carbon dioxide, in a situation where the irradiation time is extended for heterogeneous photocatalysis (Eq. 10.12).

$$\text{Organic contaminants} \xrightarrow{TiO_2/h\nu} \text{Intermediate(s)} \rightarrow CO_2 + H_2O \qquad (10.12)$$

As depicted by Eq. (10.12), the general photocatalysis reaction could be divided into five steps that are independent, as illustrated in Fig. 10.7 [13, 171].

1. The organic contaminant(s)' mass transfer (for instance, A), in the liquid phase to the surface of TiO_2.
2. The organic contaminant(s)' adsorption onto the photon-activated surface of TiO_2 (for instance, surface activation by photon energy takes place instantaneously in this step).
3. Photocatalysis reaction for the adsorbed phase on the surface of TiO_2 (for instance, A → B).
4. The intermediate(s)' desorption (for instance, B) from the surface of TiO_2.
5. The intermediate(s)' mass transfer (for instance, B) to the bulk fluid from the interface region.

The overall reaction rate is equivalent to the step that is slowest when it comes to rate determination. When the steps of mass transfer (1 and 5) are faster than the steps of reaction (2, 3, and 4), the organic concentrations

This book belongs to Kitab Liaison (ocd1996@gmail.com) Copyright Elsevier 2023

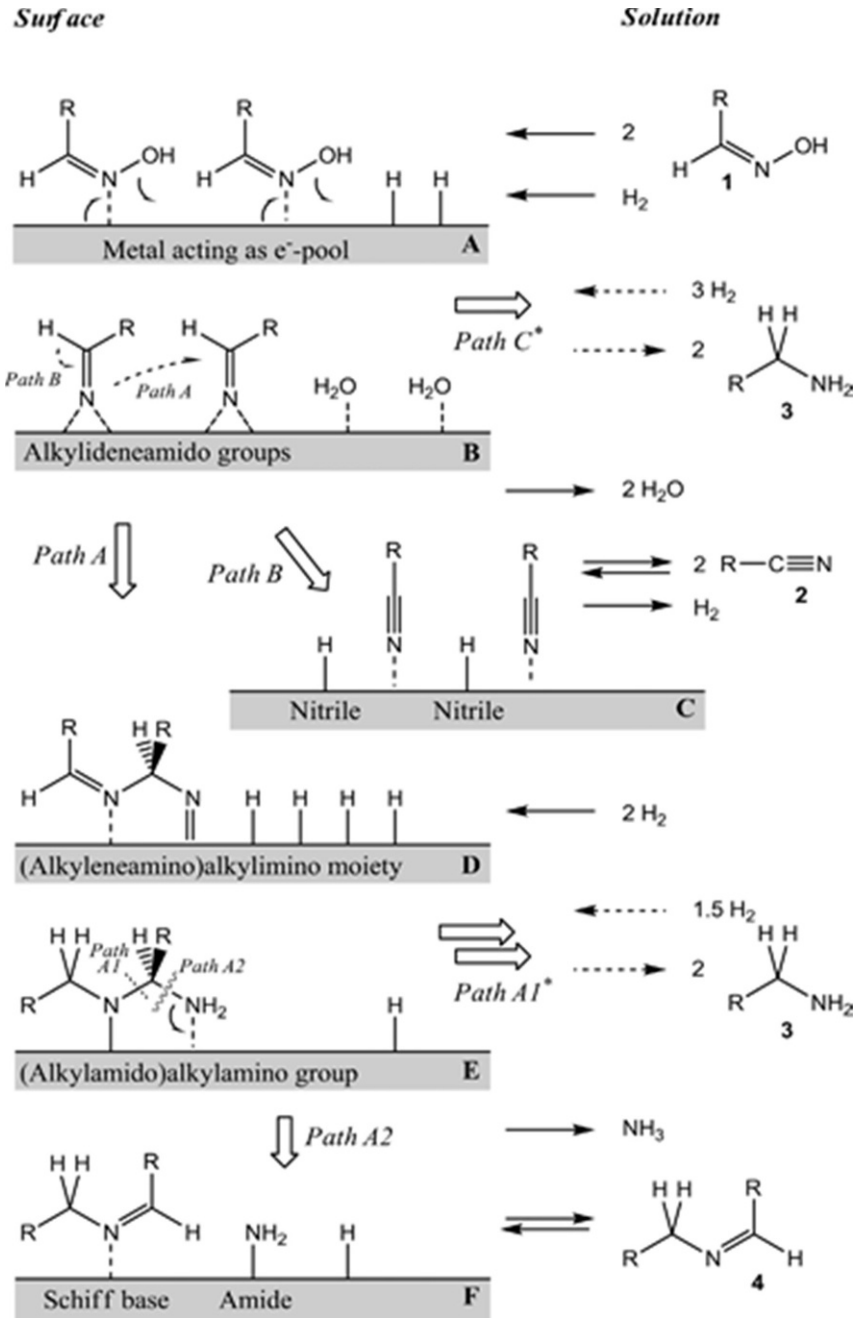

Fig. 10.7 Steps in heterogeneous catalytic reaction.

This book belongs to Kitab Liaison (ocd1996@gmail.com)
Copyright Elsevier 2023

in the instant vicinity of the active locations are not distinguishable from those in the bulk liquid phase. The mass transfer steps in this scene are not rate restrictive and do not have any impact on the general photocatalytic reaction rate. According to Vinodgopal and Kamat [172], the dependence of the photodegradation rate of the organic surrogate on the photocatalysts' surface coverage is applied. This summarizes the significance of surface contact and molecule adsorption with the catalyst in the course of the photocatalytic degradation. When mass transfer steps are rate restrictive, an amendment in the liquid flow or aeration conditions past the TiO_2 photocatalyst could change the general photocatalytic rate of reaction.

Likewise, the microorganisms surface interaction with the catalyst applied in the course of photodisinfection is very important for improving the rate of inactivation. When the ROS that is generated closely contacts the microorganisms, the cell wall is going to be the initial location of attack [173]. The lipopolysaccharide layer of the cell external wall is the original spot that the photo-induced ROS will attack. This is followed by the site attack on the layer of peptidoglycan, the lipid membrane's peroxidation, and the subsequent oxidation on the membrane of proteins. All these are going to bring about a prompt seepage of potassium ions from the bacterial cells, leading to a direct decrease in the viability of a cell. Normally, the reduction in viability of a cell is linked to the peroxidation of polyunsaturated phospholipid of the cell membrane's components (that is, essential cell functions' loss) and in the end brings about cell death. The oxidative stress formation as well as its impacts on the cell membrane could be observed with the use of atomic force microscopy that is advanced or total reflection that is attenuated, Fourier transform infrared spectroscopy. The subsequent photoinactivation together with the adsorption rate is recognized for positively correlating the bactericidal influence of the TiO_2 catalyst. The transfer of the bacterial cell to the close vicinity of the surface-generated ROS site in this instance is still the rate-restricting step in the photodisinfection reaction.

Homogeneous photo-Fenton reaction

In comparison with the heterogeneous TiO_2 photocatalysis reaction, the Fenton reaction refers to a process that does not include any light irradiation while the photo-Fenton does react, even up to a light wavelength of 600 nm. In the 1960s, this was initially discovered and it remains among the most-used AOPs due to its capacity to degrade a high loading of organic compounds in conditions that are highly saline [174–176]. Several studies on

This book belongs to Kitab Liaison (ocd1996@gmail.com) Copyright Elsevier 2023

the photo-Fenton degradation of water pollutants, for instance, pesticides, chlorophenol, and aromatic or phenolic compounds with organic loading that goes up to 25 g/L, have been studied [23, 167, 177–179]. Several studies in the literature have offered an all-inclusive review of the basic clarity and understanding of the principles that underlie the Fenton reaction [176, 180, 181].

Without a source of light, hydrogen peroxide (H_2O_2) is going to decompose by Fe^{2+} ions found in the aqueous phase, leading to the formation of hydroxyl radicals. When there is a source of light, the photo-Fenton reaction is accelerated, bringing about rapid H_2O_2 decomposition through ferric or ferrous ions and resulting in the formation of radicals. All these iron complexes or soluble iron hydroxy could absorb visible light as well as UV radiation. The actual oxidizing species responsible for the photo-Fenton reaction is, however, still under discussion [10, 19]. These photo-Fenton and Fenton reactions could take place concurrently with TiO_2 photocatalysis in the course of UV-Vis irradiation, a stand-alone photo-Fenton process, or the post-TiO_2 photocatalysis period. The Fenton reaction is understood to intensely correlate with the post-TiO_2 photocatalysis reaction and, therefore, is comprehensively described here. Eq. (10.13) illustrates the mechanism for the Fenton reaction:

$$Fe^{2+}(aq) + H_2O_2 \rightarrow Fe^{3+}(aq) + OH^- + HO^\bullet \tag{10.13}$$

The Fe^{2+} can be reverted back to Fe^{3+} via different mechanisms:

$$Fe^{3+}(aq) + H_2O_2 \rightarrow Fe^{2+}(\mathrm{aq}) + HO_2^\bullet + H^+ \tag{10.14}$$

$$Fe^{3+}(\mathrm{aq}) + HO_2^\bullet \rightarrow Fe^{2+}(\mathrm{aq}) + O_2 + H^+ \tag{10.15}$$

In the presence of a light source, the photo-Fenton rate was recounted to be enhanced positively in comparison with the dark condition. This is mostly as a result of the regeneration of $Fe^{2+}(aq)$ from the photochemical influence of light as well as the simultaneous generation of the system's OH radicals. Such a reversion cycle of $Fe^{2+}(aq) \rightarrow Fe^{3+}(aq) \rightarrow Fe^{2+}(aq)$ always generates $HO^\bullet$, so long as the concentration of H_2O_2 in the system is significant. In the catalytic iron cycle, the regeneration of the $Fe^{2+}(aq)$ from $Fe^{3+}(aq)$ is the rate-limiting step in a situation where there is a small amount of iron. This photoassisted reaction is referred to as photo-Fenton reaction, where this kind of reaction might be activated through irradiation wavelengths that go up to 600 nm. It was understood that this reaction functions better under longer wavelengths because it is capable of overcoming

This book belongs to Kitab Liaison (ocd1996@gmail.com) Copyright Elsevier 2023

the inner filter impacts through photolyzing of the ferric iron complexes. The inner filter effects stated the adsorption of photons that are competitive in the water by other species that are light absorbing.

Even in a situation where the photo-Fenton has higher photoactivity as compared to the photocatalysis that is heterogeneous, its viable operation is mainly determined by a number of water quality strictures. The formation of the extremely photoactive iron complexes is mainly dependent on the ion content and the water pH in the photo-Fenton reaction [182]. It was reported that the recurrent optimum pH for the photo-Fenton reaction was pH 2.8 [6, 19]. This is brought about by the fact that at such low pH 2.8, the precipitation does not occur and further promotes the existence of the prevailing iron species in the water of $[Fe(OH)]^{2+}$. Such a low optimum pH 2.8 is, however, expensive for operation because it necessitates high chemical charges for the rectification of pH. The existence of diverse ions, for instance, phosphate (PO_4^{3-}), chlorine (Cl^-), carbonate (CO_3^{2-}), and sulfate (SO_4^{2-}), has an impact on the iron equilibrium in water as well. These ions are capable of raising the water pH as well as effectively lowering the photo-Fenton rate of reaction. Both PO_4^{3-} and CO_3^{2-} have a double harmful impact on the reaction because they precipitate the iron as well as scavenge the OH^- radicals. A higher pH of between 5.0 and 4.0 was determined to be adequate in sustaining the photo-Fenton reaction with 2–6 mM of iron for treatment initiation [178]. So far, the maximal iron loading reported was 450 mg/L [183, 184].

Despite the fact that H_2O_2 may be created using the TiO_2 photocatalysis (Eq. 10.11), its comparative amount in the system could not be sufficient in driving the Fenton reaction. Several researchers have described the adding of H_2O_2 in improving both the TiO_2 photocatalysis and photo-Fenton reactions. The H_2O_2 could hinder the electron-hole pair recombination while further providing more OH^- radicals via the mechanisms below:

$$H_2O_2 + e^- \rightarrow HO^\bullet + HO^- \tag{10.16}$$

$$O_2^{\bullet -} + H_2O_2 \rightarrow O_2 + HO^\bullet + HO^- \tag{10.17}$$

This combined TiO_2 photocatalysis and photo-dark-Fenton reaction is predominantly useful for disinfection [185–187]. The addition of H_2O_2 to the photocatalysis and dark-Fenton system leads to a residual disinfection with the purpose of avoiding microbial regrowth. Rincón and Pulgarin [188] executed trials with the photo-Fenton reaction and TiO_2 photocatalysis for disinfecting water polluted with *Escherichia coli*. They discovered that the rate of bacterial inactivation was higher as compared to the photocatalysis

This book belongs to Kitab Liaison (ocd1996@gmail.com) Copyright Elsevier 2023

only and the reduction in bacterial number was constant in the dark environments devoid of substantial regrowth in the following 60 h. It was, however, discovered that such a residual disinfection impact was extremely reliant on the light intensity applied in the process of the irradiation epoch, together with the comparative concentrations of H_2O_2 and $Fe^{\bullet 3+}$ Further addition of H_2O_2 was discovered to reduce the general rate of reaction in a number of studies as a result of the formation of less penetrative $HO_2^{\bullet}$ radicals, as clearly illustrated by Eq. (10.18):

$$HO^{\bullet} + H_2O_2 \rightarrow HO_2^{\bullet} + H_2O \tag{10.18}$$

More combined procedures of oxidative processes and photo-Fenton have also been recommended in the literature, for instance, ultrasound and ozone [2, 189]. Their significance as compared to the TiO_2/photo-Fenton will, however, not be discussed comprehensively.

Advancements in photocatalyst immobilization and supports

Since the discovery of the photocatalytic impact on water splitting by Fujishima and Honda [190] with the use of a TiO_2 electrode, several studies have progressed to synthesize a TiO_2 catalyst of diverse scale, characterize its physical properties, and determine its photooxidation performances to the surface-oriented photocatalysis reaction nature [31, 190–193]. In nanodimensions, the TiO_2 catalyst permits a large surface area-to-volume ratio and could promote further the resourceful charge trapping and separation at the physical surface [194, 195]. The opaqueness of light in this nanoscale TiO_2 catalyst was described to have an improved oxidation competency than the bulk TiO_2 catalysts [196]. Despite the fact that the nanoscale TiO_2 catalysts exhibit substantial improvement when it comes to their chemical and physical properties, their morphology and particle size are still major problems in large-scale water treatment [197, 198]. The current technical challenges that prevent the application of a slurry TiO_2 photocatalytic system are discussed in this section, along with the conceivable engineering resolutions to deal with the challenge. Under solar irradiation, we are going to have a short discussion on the modified TiO_2 catalyst with dopants for enriched photoactivity.

Challenges in the development of photocatalytic process of water treatment

The Degussa P-25 TiO_2 catalyst is the most commonly used photocatalyst in the research of water treatment so far. It is applied as a standard reference for

This book belongs to Kitab Liaison (ocd1996@gmail.com) Copyright Elsevier 2023

comparisons of photoactivity under diverse conditions of treatment [199]. The Degussa P-25 TiO_2's fine particles have often been used in a slurry form. This is normally related with a high volumetric rate of generation of ROS as compared to the quantity of surface active spots when the TiO_2 catalyst is in suspension [200]. The fixation of catalysts into a large inert substrate, however, decreases the amount of catalyst active spots and at the same time extends the limitations of mass transfer. Catalysts results' immobilization in increasing the operation tension because the photon penetration could not reach each and every single surface site for photonic activation [200]. Therefore, the slurry kind of TiO_2 catalyst application is normally preferred.

With the system of slurry TiO_2, more process steps are needed for the catalysts' postseparation. This process of separation is very important in avoiding the loss of catalyst particles as well as introduction of the fresh pollutant of TiO_2 contamination in the water that is treated [201]. The recovery of the catalyst could be accomplished via process hybridization with various membrane filtrations, conventional sedimentation, or cross-flow filtration [202–205]. Coupled with the pH control strategy near the isoelectric point for prompted coagulation, it was described that the MF (microfiltration) hybridization could recuperate the rest of the 3% of catalyst particles for reclamation [155]. A number of essential operating concerns with slurry TiO_2 are still even with a process of membrane incorporation. These consist of the varieties of fouling, membrane, blockage, and pore size as well as backwashing or regeneration [206–208]. A number of studies have used micron-sized immobilizers for catalyst fixation that increased surface contact with contaminations and barred the pores that block as well as membrane fouling with quick backwashing [208, 209]. These immobilizers comprise catalyst fixation for catalyst fixation, mesoporous clays, onto activated carbon, onto the membrane itself or even fibers [210–213]. The subsections below summarize a few catalyst immobilization policies that are suitable for the use of a membrane reactor, a slurry reactor, or both.

Mesoporous clays

Natural clays have been intensively applied as the support for TiO_2 as a result of their cost effectiveness as well as their high capacity of adsorption. The TiO_2 crystal that is being deposited on a clay material is illustrated in Fig. 10.8 [210]. Diverse kinds of clays have been studied, which comprise kaolinite, bentonite, montmorillonite, sepiolite, and zeolite [210, 214–217]. Despite the fact that these clays are inactive catalytically, their greater

This book belongs to Kitab Liaison (ocd1996@gmail.com) Copyright Elsevier 2023

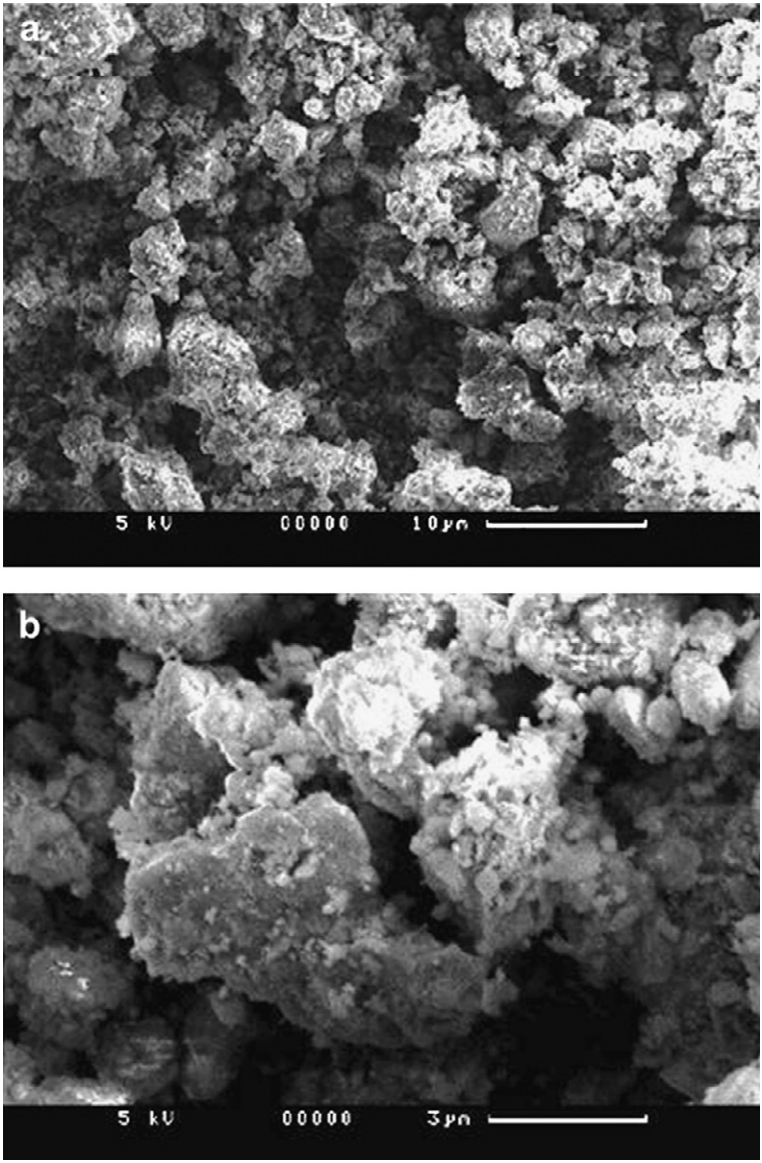

Fig. 10.8 TiO_2 nanocrystal deposited on clay materials by SEM imaging. (A) 10 μm resolution and (B) 3 μm resolution.

adsorption capacity has been eye-catching for increasing the surface contact in the course of the photocatalysis reaction. It was recommended that the natural clays shouldn't be directly used to immobilize TiO_2. This is brought about by the existence of diverse lattice-bounded or surface impurities that

This book belongs to Kitab Liaison (ocd1996@gmail.com) Copyright Elsevier 2023

could diffuse and influence further the efficiency of the TiO_2 immobilized layer [210]. Furthermore, in a situation where these impurities are not eliminated, the polar molecules in the aqueous environment could initiate an inner reaction in the clay structure that brings about clay swelling [210]. In a particular type of clays, the swelling is going to be profound where Van der Waals forces hold the full clay in a turbostatic array. This is objectionable, especially when the photocatalytic reactions occur in a reactor where the hydrodynamics could be strongly influenced and consequently result in photoactivity loss. Other aspects that could need to be considered in case pillared clays are applied as the immobilizer substrate comprise the clays' density, distribution range of particle size, and the complementary photoreactor system applied. The use of mesoporous clays as the nanosized TiO_2 support has been demonstrated successfully in several studies, comprising membrane processes or the slurry [218, 219].

Nanofibers, nanowires, or nanorods

Carbon, glass, woven cloth fibers, optical and titanate have also been studied as support materials in the photooxidation of several organic impurities for water purification [200]. The majority of these fibers have longitudinal or protruded rod-shape morphology. The use of the nanorods, nanowires, or nanofibers, mass transfer limitation could be resolved with the use of their thin longitudinal morphology. Using less durable immobilizer fibers (for instance woven or glass cloths) may, however, result in a low durability as the deposited anatase crystals could wear off, resulting in a loss of photoactivity over reaction time. In addition, immobilizer fibers of this kind in the reactor system upsurge pressure drop. However, a good advantage of nanofibers with commercial accomplishment is that they could be fabricated into MF, UF (ultrafiltration), and PMs (photocatalytic membranes). The MF fiber membrane is of specific interest because it exhibits a high pollutant rate of removal at a low pressure of the transmembrane (<300 kPa). The commercial success of such fabricated MF and UF membranes has been revealed by Zhang and coworkers [204, 220]. More details on the fabricated nanowire and nanofiber MF membranes can be acquired in the literature.

Photocatalytic membrane

Finally, using PMs has been targeted as a result of the photocatalytic reaction that could take place on the membrane surface and the preserved water

This book belongs to Kitab Liaison (ocd1996@gmail.com) Copyright Elsevier 2023

might be unremittingly discharged devoid of the photocatalyst particles loss. The PMs can be prepared from diverse synthesis methods and materials. These comprise the TiO_2/Al_2O_3 composite membranes [62, 221–224]. TiO_2 supported on polymer and metallic membranes or doted polymer membranes containing TiO_2 particles entrapped in the membrane structure in the course of the process of membrane fabrication [12, 29, 225–228]. Furthermore, the potential TiO_2 inorganic and organic ceramic membranes have been studied [211, 226, 229]. Diverse kinds of PMs for water treatment application are demonstrated in Fig. 10.9 [7, 220]. In several studies, PMs may, however, bump into several technical complications such as the loss of a deposited TiO_2 layer over time, membrane structure deterioration, and low photocatalytic activity. In order to avert the problems related to the TiO_2 membrane coating, a methodology of applying membranes devoid of any deposited TiO_2 layer could be instituted into a slurry-membrane hybrid system.

Photocatalyst modification and doping

Whereas TiO_2 photocatalytic reactions occur under ambient functioning conditions, photoactivity is usually reserved by the narrow wavelength spectrum for catalyst photonic activation. The higher end of the UV spectrum needed for catalyst activation is usually accompanied by high operating costs. A nice-looking alternative is to apply the immense abundance of outdoor solar irradiation for catalyst activation in a suitably planned photoreactor system. In order to extend the photoresponse of a TiO_2 catalyst for the solar spectrum, several material engineering resolutions have been formulated, comprising composite photocatalysts with dyed sensitizers, carbon nanotubes, metal ion incorporation or noble metals, nonmetal doping, or transition metals [106, 110, 230–232].

The reason for using these material engineering policies is balancing both the modification of the catalyst structure and the composition or the half-reaction rates of the photocatalytic reaction through the addition of an electron acceptor. The use of diverse mechanisms to boost the catalyst photoactivity is presented in Fig. 10.10. The existence of electron acceptors might rummage the excited electrons and completely avert the electron-hole pair recombination. Contemporary studies have demonstrated that under solar irradiation, modified TiO_2 catalysts have an improved photoactivity [233–235]. TiO_2 coupling with CNTs has revealed a prospective extension of electron-hole pairs through capturing the electron inside their structure.

This book belongs to Kitab Liaison (ocd1996@gmail.com) Copyright Elsevier 2023

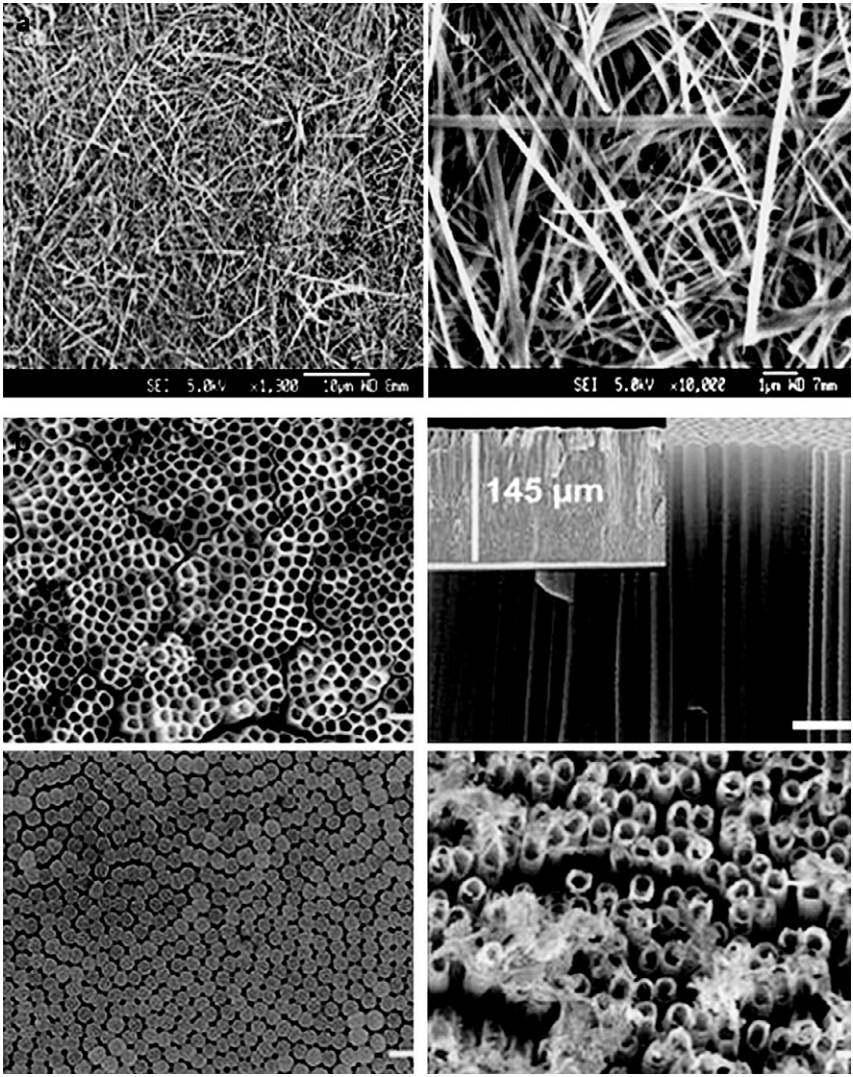

Fig. 10.9 (A) FESEM images of the TiO_2 nanowire membrane; [220] (B) SEM images of TiO_2 nanotube layer that formed a freestanding membrane [7].

When it comes to dye-sensitized coupling, the agitated dye molecules under solar illumination could offer extra electrons to the CB for enhancing the electron-hole pair formation (Fig. 10.10A) [231]. Under solar irradiation, dyes such as crystal violet, methylene blue, rhodamin, azure, and erythosin have been extensively functionalized [231].

This book belongs to Kitab Liaison (ocd1996@gmail.com) Copyright Elsevier 2023

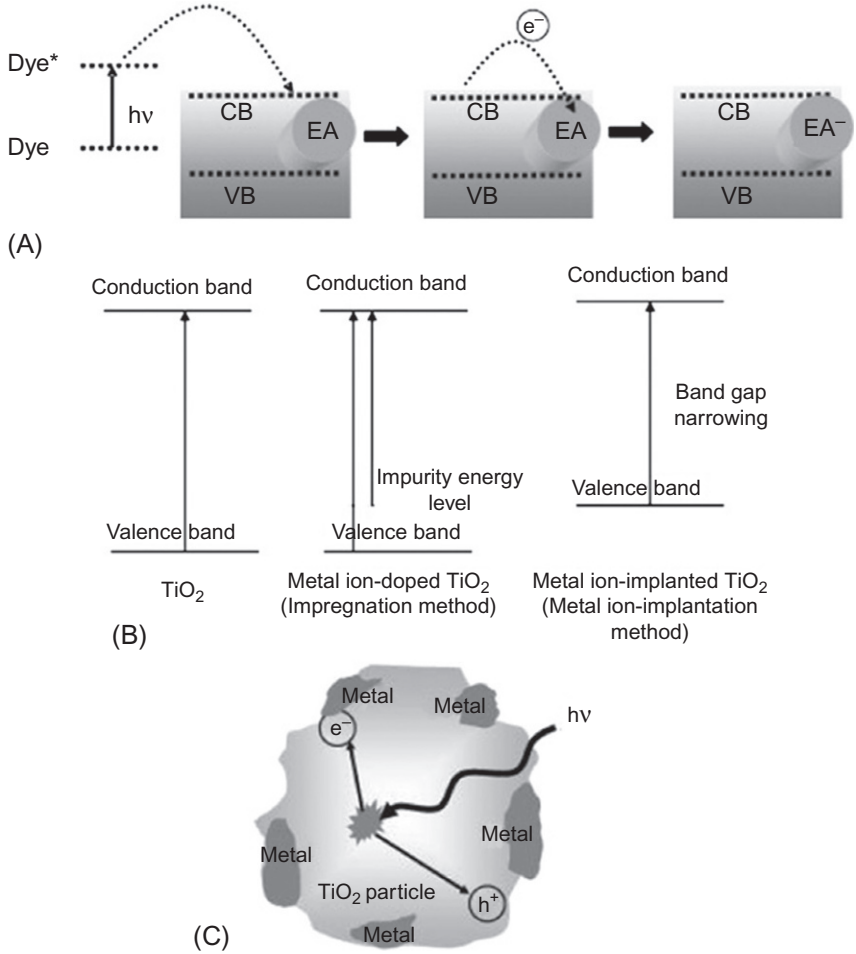

Fig. 10.10 (A) Excitation steps with a sensitizer in the existence of an adsorbed organic EA (electron acceptor); (B) TiO_2 band structures' scheme, physically ion-implanted TiO_2, and chemically ion-doped TiO_2; (C) Electron capture by a metal in contact with a semiconductor surface [155].

Likewise, noble metals (for instance, Cu, Ag, Pt, Ni, Pd, and Rh) with a Fermi level that is lower as compared to the TiO_2 catalyst have as well been put down on the TiO_2 surface for improved charge separation (Fig. 10.10B) [110]. It was stated that these metals enrich electron transfer, although it necessitates upright information concerning the optimal amount of deposit required in the course of the fabrication process. Although noble metal coupling could be efficient in lengthening the separation of the surface charge,

This book belongs to Kitab Liaison (ocd1996@gmail.com) Copyright Elsevier 2023

their cost effectiveness for industrial application is normally substituted by nonmetal doping or a transition that is more economical. This transition and the nonmetal doping mechanism are, however, dissimilar from the noble metal coupling as the TiO_2 is integrated into the TiO_2 crystal lattice [236–238]. This integration presents an impurity in the TiO_2's band-gap, and therefore lessens the requirements of photonic energy (Fig. 10.10C). Of late, the use of nonmetal dopants (for instance, S, N, F, and C) could advance the feasibility and photoactivity of TiO_2 catalysts for industrial use [239, 240]. Extra research efforts could be required in getting a better knowledge of the photoactivity kinetics, with the purpose of improving the water treatment's photooxidation efficiency.

Configuration of photocatalytic reactor

Depending on the applied form of the photocatalysts, photocatalytic reactors for water treatment are mostly categorized into two major configurations: (1) reactors with photocatalyst restrained onto a constant inert carrier, and (2) reactors with suspended photocatalyst elements [241]. Numerous forms of reactors have been employed in photocatalytic water management, such as the downflow contactor reactor, the cascade photoreactor, the annular slurry photoreactor, etc. [218, 242, 243]. The only difference between these two key configurations is that the first one allows for constant operation, whereas the latter necessitates an extra downstream separation unit for the reclamation of photocatalyst elements. Pareek et al. [244] revealed that the useful parameters in designing a photocatalytic reactor are the light dispersal inside the reactor and the overall irradiated catalyst surface area per unit volume. While the fixed-bed photocatalytic structure is frequently linked to mass transfer restriction over the restrained photocatalyst layer, the slurry-type photocatalytic reactor ideally does a higher overall photocatalyst surface area per unit volume. The distribution of light photons via either diffuse or direct paths in the reactors must be definite [19]. Direct photon operation implies that the photocatalysts are directly actuated with light photons, rather than with the help of several parabolic light refractors to transmit the photons. To realize homogeneity in photon flux distribution inside the reactor, the right light source position is important to ensure the greatest and even light distribution transmission. Nowadays, the application of photoreactors with aided parabolic light deflectors has become undesirable because this requires advanced design and high costs of operation. The reactor of this nature must be specially configured to guarantee the

This book belongs to Kitab Liaison (ocd1996@gmail.com) Copyright Elsevier 2023

greatest irradiated reactor volume with the least pressure condition for optimum catalyst mixing and distribution. Over the last decades, the slurry photocatalytic reactor has been the best design because of its high total photocatalyst surface area per unit volume as well as the photocatalysts reactivation affluence. The photocatalyst particles could be separated through an external cross-flow filtration system or settling tanks to allow continuous operation of the slurry reactor. A technically encouraging resolution for explaining the photocatalyst particles' downstream separation following treatment is through the application of processes of a hybrid photocatalysis membrane. Use of such a hybrid system averts the use of sedimentation, coagulation, or flocculation in separating the particles of the catalyst from the well-preserved water stream. More benefits entail more energy savings and size of process installation together with site area needed.

Generally, the hybrid photocatalytic membrane reactor system is referred to as PMRs (photocatalytic membrane reactors). This is brought about by the hybrid system's nature, whereby the membrane filtration unit might be configured into diverse positioning with the photocatalytic reactor. Fu et al. [245] designed a membrane reactor that is submerged (Fig. 10.11), with two diverse zones of reaction: the TiO_2 zone and a UV slurry with a movable baffle, separating the submerged membrane module. These PMRs

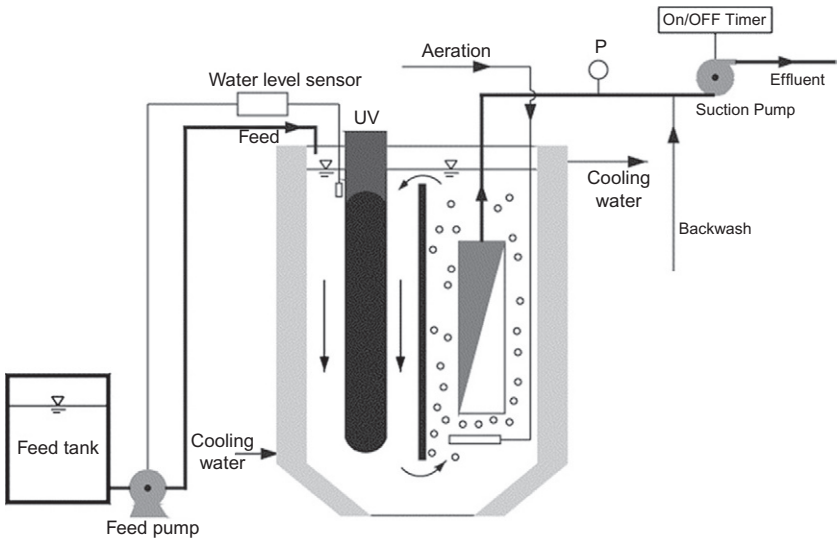

Fig. 10.11 Schematic of a submerged membrane photocatalytic reactor [245].

This book belongs to Kitab Liaison (ocd1996@gmail.com) Copyright Elsevier 2023

could be generalized using: (1) the membrane module irradiation, or (2) the feed tank's irradiation that contains a photocatalyst in suspension [207, 246]. The photocatalyst could be either deposited onto the membrane or suspended in the reaction water for the previous configuration. The PMRs give room for an incessant operation of the slurry-type reactor devoid of any loss of photocatalyst particles as well as controlling the water residence time independently. This enables the treated water to accomplish the predefined level prior to being filtered via the hybrid membrane system. In the PMRs with immobilized PMs, the membrane module is functionalized as the support for the photocatalyst particles and a barrier against the diverse organic molecules in the reaction water. Likewise, the membrane acts as a physical barrier alongside the photocatalyst organic molecules or particles or intermediate compounds in the slurry PMRs to be degraded.

The photocatalytic reaction occurs on the membrane surface or within its pores in the PMRs with immobilized photocatalysts. The PMs applied might be of MF [25, 31, 50, 247–249] UF [207, 219, 240, 250, 251] or NF (nanofiltration) [5, 207, 228, 246, 252], according to the final water quality necessity and the targeted colloidal size. The MF membrane is very important when the colloidal size is in the range of 0.1–5 mm, whereas both NF and UF target smaller particle size ranges. The contaminants' photooxidation effectiveness was described to be higher when an immobilized PM was applied, instead of in the situation of PMRs with catalyst suspended particles [228]. However, it was reported that immobilizing the photocatalyst particles could bring about severe destruction to the membrane structure due to their close contact with both hydroxyl radicals and UV light [94]. In consideration of this, the hybridization configuration of the membrane process with the use of photocatalysts in suspension seems to an arrangement that is more encouraging. In the literature, this PMR configuration has been well defined for water phase degradation of 4-nitrophenol, fulvic and humic acids, phenol, 4-chlorophenol, river water, grey water, dyes, bisphenol A, and para-chlorobenzoate [25, 50, 94, 207, 219, 228, 240, 245, 246, 248–251, 253].

Among the major operational concerns with these PMRs is the transmembrane pressure, which controls operating costs and the rate of filtration. It is well known that the prices of PMR treatment upsurge in a situation where photocatalysts with colloidal size and small particles are applied. Using the UF and MF membrane filtration, the fine photocatalyst particles could bring about membrane fouling and subsequently simplify the membrane permeate flux. Fu et al. [245] used particles that are spherical ball-shaped

This book belongs to Kitab Liaison (ocd1996@gmail.com) Copyright Elsevier 2023

TiO_2, which upholds recovery, separation, and reused whereas prolonging the lifespan of membrane because the particles do not bring about pore blockage. Moreover, the surface charge properties of the photocatalyst particles could as well be deployed with the intention of preventing blockage of the membrane pore. After Xi and Geissen [208] incorporated a thermoplastic membrane module of cross-flow MF, they discovered that the low permeate flux took place when the operating pH differed from the isoelectric point of the TiO_2 particles applied. This is as a result of the pH-induced coagulation-flocculation condition of TiO_2 that deteriorates the permeate flux rate. The resolution of this was through maintaining the operative pH near the isoelectric point of TiO_2 through the addition of particular electrolytes to the TiO_2 slurry. Despite such control policies, the permeate value is low as a result of the quick penetration of small molecules via the membrane applied.

Of late, diverse hybridization of PMRs using pervaporation, dialysis, and direct contact MD (membrane distillation) has been applied (Fig. 10.12) [254–256]. Pervaporation refers to a physical process in which typically a selective organophilic membrane was applied to serve as selective obstruction

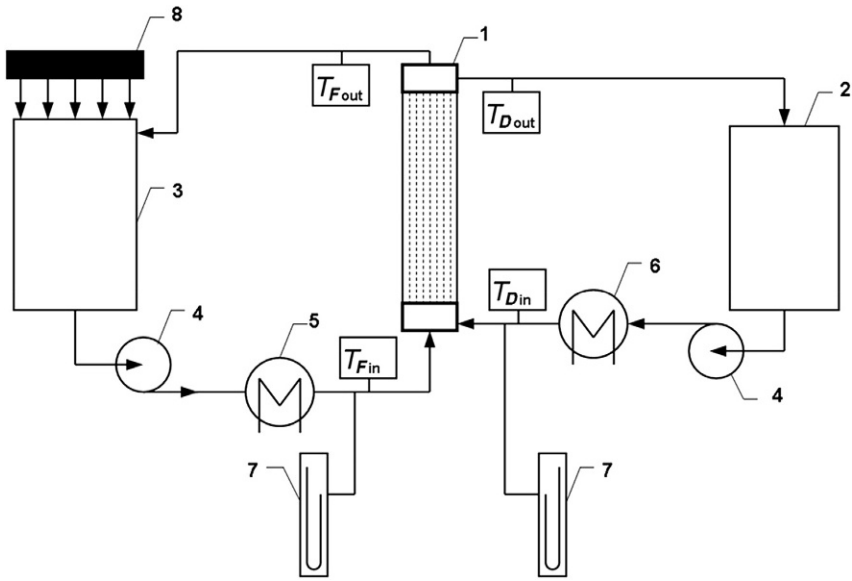

Fig. 10.12 A representation diagram of the apparatus for the process of hybrid photocatalysis-MD is illustrated: (7) manometers; (1) membrane module; (3) feed tank (V 2.9 dm^3); (2) distillate tank; (5) and (6) heat exchangers; (4) pump; (8) UV lamp; T_{Fin}, T_{Din}, T_{Fout}, T_{Dout}—inlet and outlet temperatures of feed and distillate, respectively [254].

This book belongs to Kitab Liaison (ocd1996@gmail.com) Copyright Elsevier 2023

for molecule degradation. In accordance with Augugliaro et al. [257], a synergistic effect takes place when pervaporation was applied, in which the intermediates from the 4-chlorophenol degradation (for instance, benzoquinone, hydroquinone) might be selectively permeable devoid of competition with 4-chlorophenol for photocatalytic reaction. More types of organophilic membranes have also been studied, for instance, polyethersulfonate NF membranes and polymeric UF membranes [76, 258]. A stronger rejection effect on the membrane is normally related to the use of the NF and UF membranes. For efficient hybridization, the choice of membrane is determined by the size of the organic molecular, electrostatic, or pH interaction as well as the Donnan exclusion occurrence [259].

The MD refers to a process in which the feed volatile components in water are evaporated via a porous hydrophobic membrane with the purpose of producing products that are of high-quality distillate [254]. Its major benefit is that when TiO_2 is present, there is no membrane fouling. In the course of the process, the volatile stream is upheld in the pores of the membrane. The vapor pressure difference on the two sides of the porous membrane is still a process driving force. However, this force is mainly reliant on solution composition and the temperatures in the layer that is next to the membrane [260, 261]. It was recounted that in MD, the feeding temperature could range from 303 to 363 K. The same scaling-up operational limitations of high energy demand and low permeate flux have redundant development of its existing full scale. On the other hand, some efforts to make use of other energy sources, for instance solar energy, to give room for MD application were discovered in the literature [8, 262].

Among all the hybrid PMR systems, the pilot Photo-CatTM system (Fig. 10.13) (manufactured by Purifics Inc., Ontario, London) has revealed a prospective application. Benotti et al. [120, 263] has assessed its capacity in estrogenic activity from water, the elimination of 32 pharmaceuticals and endocrine upsetting compounds. They discovered that 29 targeted compounds and estrogenic activity of greater than 70% were eliminated whereas only three compounds eliminated were less than 50% at the maximum number of UV passes. The passage of the water stream is via a prefilter bag as well as a cartridge filter prior to being mixed with a nanoparticle TiO_2 slurry stream in the Photo-CatTM system. Then, the mixed stream passes via the reactor in the 3 mm annulus of the 32 UV lamps lined up in sequence, which could be discretely controlled for the fluctuating quality of water. For the 32 UV, the general hydraulic residence time passes between 1 and 32 s, according to the number of UV lights that have been

This book belongs to Kitab Liaison (ocd1996@gmail.com) Copyright Elsevier 2023

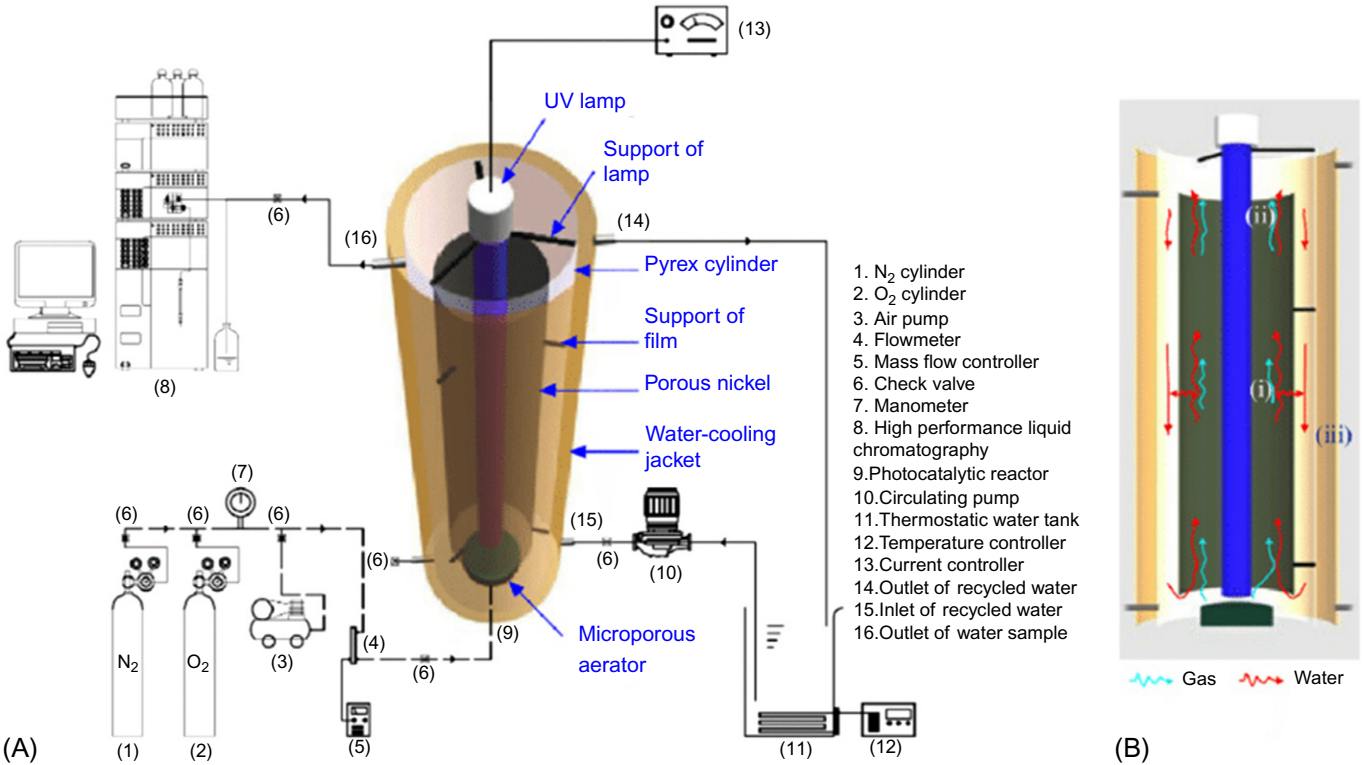

Fig. 10.13 A general representation of a photocatalytic reactor membrane pilot system is illustrated. (A) UV lamp assisted reactor, (B) gas and water separation chamber.

This book belongs to Kitab Liaison (ocd1996@gmail.com)

Copyright Elsevier 2023

turned on. A cross-flow ceramic membrane TiO_2 recovery unit is hybridized downstream of the reactor to eliminate the TiO_2 from the flow stream, as this enables the exit of treated water. Prior to remixing, the retentive TiO_2 stream is reused with the different TiO_2 slurry stream entering the reactor stream.

Operational parameters of the photocatalytic reactor

Following the incorporation of a photoreactor with the semiconductor catalyst, the rates of the photocatalytic system's efficiency and oxidation are greatly reliant on several operation strictures, which administer the photodisinfection and photomineralization kinetics. This sector is going to debate the importance of every operation stricture on the equivalent kinetics as well as a number of the latest techniques to heighten the photocatalytic system through response surface analysis. Below is the summary of a range of photoreactor operating strictures that has an impact on TiO_2 photocatalyst photocatalytic performance in water treatment.

TiO_2 loading

In the photocatalytic water treatment system, the TiO_2 concentration influences the general photocatalysis rate of reaction in a real heterogeneous catalytic regime, in which the amount of TiO_2 is directly proportionate to the general photocatalytic rate of reaction [163]. A linear dependency holds until a particular range when the rate of reaction begins to worsen and is no longer reliant on TiO_2 concentration. This is accredited to the photoreactor's working conditions and the geometry of wherever the surface reaction is instigated upon photon absorption of light [9]. When the TiO_2 amount rises above a saturation level (resulting in a high state of turbidity), the light photon absorption coefficient generally reduces radially. This kind of light attenuation over the radial distance could, however, not be well associated with the Beere-Lambert Law as a result of the sturdy scattering and absorption of the TiO_2 particles' light photons [32]. The extra TiO_2 particles could generate a light screening impact that decreases the TiO_2 surface area, being open to the photocatalytic efficiency and light illumination. Whichever selected photoreactor ought to be operated underneath the level of saturation of TiO_2 photocatalyst applied in avoiding extra catalyst and guarantee effective photons absorption. Both catalyst loading and the light scattering effect in this sense could be deliberated in the reactor as a function of optical path length.

This book belongs to Kitab Liaison (ocd1996@gmail.com) Copyright Elsevier 2023

Several studies have reported the impact of TiO_2 loadings on the efficiency of the process [94, 163, 171, 218, 243, 264]. These outcomes are mainly independent and a direct comparison could not be made because the wavelengths, working geometry, intensity, and radiation fluxes applied were not the same. It was recounted that the photodisinfection and photomineralization's prime catalyst loadings are different, and mostly reliant on the photoreactor's dimension. The diameter of the photoreactor's determination is very important in the water flow hydrodynamics as well as in the effective photon absorption [155]. A constant flow region could make sure that a stable state residence time is acquired, whereas turbulence flow eliminates a reaction dead zone or catalyst deposition [265]. For turbulent flow, reactor diameters less than 20–25 mm were not viable, whereas diameters that exceed 50–60 mm are not practical. This is owing to the fact that, normally, large diameters have less saturated catalyst efficiency and loading. The amount of catalyst in this instance ought to be taken into consideration. Usually, the TiO_2 catalysts could be mixed evenly with the targeted water before being introduced into the reactor system. In the course of the dark homogenization period of the catalyst, organic pollutants' lesser original concentration is witnessed as a result of the strict adsorption of organics onto the surface of catalysts [266]. Likewise, the catalyst-bacteria interaction was recounted in the photodisinfection microorganism's treatment [3].

pH

In a heterogeneous photocatalytic water system, pH is among the most important operating strictures that influences the charge on the catalyst particles, the valence bands and conductance positions, and the size of catalyst aggregates. Owing to the nature of the TiO_2 catalyst applied, whichever variation in the effective pH is famous for affecting the isoelectric point or the applied photocatalyst's surface charge. Several reports have applied the PZC (point of zero charge) of TiO2 in investigating the pH effect on the performance of photocatalytic oxidation [94, 218, 243, 264, 267]. The PZC refers to a state where the TiO_2's surface charge is neutral or zero lying in the pH range of 4.5–7.0, according to the catalysts applied. The interaction between the photocatalyst particles and water contaminants at the PZC of TiO_2 is minimal as a result of the deficiency of whichever electrostatic force. When operating pH $<$ PZC (TiO_2), the catalyst's surface charge becomes positively charged and progressively makes use of an electrostatic attraction force toward the compounds that are negatively charged. These polar attractions between charged anionic organic compounds and TiO_2 could intensify the

This book belongs to Kitab Liaison (ocd1996@gmail.com) Copyright Elsevier 2023

adsorption onto the photon-activated TiO_2 surface for succeeding photocatalytic reactions [3, 266, 268]. This is particularly important in a situation where anionic organic compounds are found in a level of low concentration. The catalyst surface is going to be negatively charged and will rebuff the anionic compounds in water at pH > PZC (TiO_2). Diverse pH is going to affect the TiO_2 catalyst's surface charge density, in line with the water equilibrium equations below (Eqs. 10.19–10.20)

$$\text{At pH} < \text{PZC}: \text{TiOH} + \text{H}^+ \leftrightarrow \text{TiOH}^2_+ \tag{10.19}$$

$$\text{At pH} > \text{PZC}: \text{TiOH} + \text{OH}^- \leftrightarrow \text{TiO}^- + \text{H}_2\text{O} \tag{10.20}$$

The distribution of surface charge density for these TiO_2 catalyst clusters is extremely reliant on the operating pH. It was recounted that at $3 < pH < 10$, the distribution of TiOH is ≥80%; whereas at pH > 10 is TiO^- ≥20% and at pH < 3 is $TiOH_2^+$ ≥20%. At diverse pH, these reactions' equilibrium constants are $pK_{TiOH} = 8.0$ and $pK_{TiOH_2}+ = 2.4$ [269]. In the course of photocatalytic reaction, the original operating pH normally drops slightly from the formation of multitude intermediate byproducts that could sham diverse chemical functional groups and indifferently influence the water pH [270].

The same electrostatic interaction improvement for microorganism photodisinfection was witnessed in the course of the photocatalytic process [3]. All through the photodisinfection, the original photo-induced damage to the microorganisms occurs on the peptidoglycan layer as well as on the external cell wall's lipopolysaccharide layer. Subsequent to this is lipid membrane peroxidation and the succeeding membrane protein's oxidation and polysaccharides. At low pH, an augmented density of $TiOH_2^+$ could form an electrostatic association with the negatively charged surfaces' bacteria, bringing about an increase in the rate of photodisinfection. Herrera Melián et al. [271] discovered that the rate of bacterial inactivation was enriched at pH 5.0. It is worth noting that the enhanced bactericidal activity of TiO_2 at a low pH is exclusively due to the TiO2 interceded photo-killing and not cell's acidification. According to Heyde and Portalier [272], the insignificant *E. coli* reaction to acid conditions was from the existence of an acid tolerance reaction to the bacterium itself, which secreted proteins that are acid-induced for acid-shock fortification. Rincón and Pulgarin [188], on the other hand, did not find any differences in the rates of *E. coli* inactivation when the original pH ranged between 4.0 and 9.0. Up to the present time, several types of microorganisms have been inactivated using TiO_2 photocatalysis, including

This book belongs to Kitab Liaison (ocd1996@gmail.com) Copyright Elsevier 2023

Lactobacillus acidophilus, *E. coli*, *Saccharomyces* successfully with the use of *Aspergillus niger*, *cerevisiae*, *Candida albicans*, *Streptococcus faecalis* and *aureus*, total coliforms, *Chlorella vulgaris*, *Fusarium solami*, *Enterobacter cloacae*, and others [266, 271, 273–275].

Despite the fact that the electrostatic bond between microorganisms and the catalyst particles were recounted to be existent, a subsequent microbial cell adsorption and subsequent penetration of the catalysts via the cell wall are extremely reliant on the mean particle size. Because the comparative sizes between the catalysts and bacteria are considerably different, the charged $TiOH_2^+$ clusters could not come into complete contact with the bacteria. Sichel et al. [276] discovered that the TiO_2 catalyst is really adsorbed onto fungal spores instead of the reverse setting. This is as a result of the large fungal spores (a few order of magnitudes) more than the catalyst particles. A small decrease in microbial loadings was observed in the period of original dark homogenization with particles of the catalyst. This is as a result of the catalyst agglomeration as well as successive agglomerate sedimentation. In this instance, the bacterial adsorption rate was discovered to be directly linked to the applied catalyst's bactericidal activity. In addition, it was reported that the adsorption occurrences all through the dark and irradiated phase are going to act indifferently and therefore, it was not possible to make a strong conclusion.

In addition, there is interaction between the catalyst particles themselves and this is reliant on the operating pH. The particle size of similar catalysts could vary from 300 to 4 mm according to the distance from the TiO_2's PZC [155]. At pH = PZC, the catalyst particles' neutral surface charge is not capable of producing the interactive denial for solid-liquid separation. This therefore prompts catalyst aggregation where the catalyst becomes larger, resulting in catalyst sedimentation [277]. Normally, this physical property is deployed in the hybridized PMR system, whereby the treated wastewater's pH is neutralized to pH 7 for the succeeding retrieval of catalyst particles. The larger TiO_2 clusters settle faster as compared to the smaller ones. It was recounted that with such a policy of neutralization, nearly 97% of the catalysts could be recovered in the settling tank. The rest of the TiO_2 catalysts could be recovered through the system of downstream MF. Likewise, the water pH is going to influence the operational separation in the PMR system where unsuitable control of water pH upholds the electrostatic repulsion, the Donnan exclusion occurrences and therefore, the tendency of denial for the applied membrane [278, 279]. It is worth noting that applicable pH control policies ought to be executed at each diverse

This book belongs to Kitab Liaison (ocd1996@gmail.com) Copyright Elsevier 2023

location of the photocatalytic water treatment process for a proficient photocatalytic reaction to go on.

Temperature

Many studies have been carried out on the photocatalytic reaction's dependence on the reaction temperature [66, 239, 280–282]. Despite the fact that heat energy is not sufficient in triggering the TiO_2 surface, the understanding of such a dependency might be inferred when working the process under the illumination of natural sunlight. The majority of the preceding studies claimed that a rise in temperature of the photocatalytic reaction (>80°C) upholds the charge carriers' recombination and disfavors the organic compounds' adsorption onto the TiO_2 surface [163]. The photocatalytic reaction is interpreted with the Langmuir-Hinshelwood (LeH) mechanism at a reaction temperature above 80°C where the reactants' adsorption is disfavored, leading to KC becoming "1. This is going to decrease the L-H expression (Eq. 10.23) into the rate that is apparent in equation $r = k_{\text{apparent}}C$. All these considerably decrease the TiO_2's photocatalytic activity when the reaction temperature increases. The degraded products' desorption from the TiO_2 surface is a step that is rate-limiting when temperatures increase. However, a low temperature less than 80°C really favors adsorption, an impulsive exothermic occurrence, leading to getting KC of L-H model" 1, improving the final reaction products' adsorption. More reaction in temperature down to 0°C is going to bring about a rise in the seeming energy of activation. The optimum reaction temperature for photomineralization is therefore described as ranging between 20–80°C [155].

The rise in the reaction temperature increased the rate of inactivation in microorganisms for photodisinfection with the use of TiO_2 photocatalysis [282]. Until now, there has been no inclusive investigation carried out to compare the impact of TiO_2 photodisinfection on every microorganism type under diverse operating temperatures. Therefore, photodisinfection with the use of a TiO_2 catalyst is normally performed under an ambient temperature of 80°C with the purpose of averting high water-heating expenses (high heat capacity) [283].

Dissolved oxygen

DO (dissolved oxygen) is very significant in the TiO_2 photocatalysis reaction in that it assures adequate existing electron scavengers to bar the excited electron of the conduction-band from recombining [218]. Because the

This book belongs to Kitab Liaison (ocd1996@gmail.com) Copyright Elsevier 2023

reduction reaction occurs at a dissimilar position from where oxidation takes place, the oxygen does not disturb the adsorption on the TiO_2 surface of the catalyst [155]. DO has some additional roles that include direct photocatalytic reactions, mineralization and creation of other ROSs, and the balance of radical intermediates. Some technical contemplation determines the total quantity of DO in a reactor. The total DO delivered for a photoreactor serves as an electron sink while at the same time giving an essential floating force for absolute suspension of TiO_2 elements. The cost-effectiveness of photoreactor solution sparging with pure oxygen in a TiO_2 slurry reactor is due to the fact that the quantity of DO being retained depends on the photoreactor order. The fact that the transfer of oxygen in mass to the nearby area of the surface is a step that depends on the rate makes the variance between the two sparging air and oxygen media not very pronounced [147]. Henry's Law can generally be considered to provide the best estimate of the quantity of dissolved oxygen under the investigational circumstances, given that the rate of oxygen sparging and the photoreactor gas retention are identified [264]. It is also important, in this law of equilibrium, to explain the drop in oxygen solubility with a rise in reaction temperature. From the previous discussion, it is better to run the photoreactor under an ambient environment to check the elevated cost of air and oxygen sparging for a greater electron sink.

The occurrence of dissolved oxygen can also be linked to the cleavage process for scented rings in organic contaminants that occur in the water media. Wang and Hong [284] suggested that the molecular oxygen follows the cleaving attack of a second hydroxyl radical in scented ring cleavage in the destruction of a dioxyl particle. The oxygen's analogous partial pressure exerted in the reaction for a closed system of a reactor is important as well. A considerably greater partial pressure of oxygen will lead to a greater primary rate of organic photomineralization compared to its physical change [239, 284]. The report indicated that at a minimum oxygen pressure of 0.5 kPa, only 1% of the first 2-CB compounds was mineralized to CO_2 after 5 h of UV irradiation, but 75% of them were changed [284]. Because the photocatalytic liquid phase reaction is polyphasic in nature, it is challenging to measure the precise impact on the surface activity of TiO_2, though higher partial oxygen pressure is vital [171]. Shirayama et al. [285] revealed the negative impact of DO on the photocatalysis reaction. They noted a high rate of chlorinated hydrocarbon photodegradation without DO. This is clearly explainable based on the strong absorption features for UV photons at concentrations of 185 and 254 nm, correspondingly. The DO particles serve as

This book belongs to Kitab Liaison (ocd1996@gmail.com) Copyright Elsevier 2023

an interior filter in this instance and result in a severe weakening of UV light strength, mostly at the UV-C germicidal section. No research has been conducted to define the impact of DO on photocatalysis activity via UV-A and UV-B light supplies. Up to now, the influence of DO on the performance of photodisinfection has been given minimum attention. The creation of different ROSs through a series of redox reactions on the surface of the catalysts was considered to be analogous in not only photomineralization, but also photodisinfection action. When enough nutrients can be found, the continuous sparging of DO will usually stimulate microbial growth and balance the rate of photodisinfection. This incidentally extends the radiation time essential in the achievement of the preferred level of inactivation. It is therefore suggested that the DO influence on the microbial degradation ought to be thoroughly explored in a specific photoreactor process before improvisation of the DO sparging approach.

Pollutants and their loading

From the previous studies, it has been established that the TiO_2 photocatalytic rate of reaction is reliant on the concentration of water pollutants [218, 243, 264, 267]. A difference in the original water contaminant concentration will lead to a dissimilar irradiation time needed to attain thorough disinfection or mineralization under a similar operating state. On account of the photonic characteristics of the photocatalysis activity, extremely high organic substrate concentration instantaneously saturates the TiO_2 surface and lessens the photonic effectiveness, resulting in photocatalyst neutralization [286].

A few organic substrates will profoundly influence the irradiation time, and this likewise is based on the respective chemical condition of the compounds in question for TiO_2 photocatalysis activity. For example, 4-chlorophenol will go through a degradation process with continuous advancement of the intermediate compound (that is benzoquinone and hydroquinone), whereas oxalic acid will go through direct conversion to water and carbon dioxide [287]. In an occasion of 4-chlorophenol, the development of the intermediate will additionally lengthen the irradiation time needed for complete mineralization because of the one-to-one competition over indiscriminate surfaces of TiO_2. When developing a mathematical model representing the kinetics of mineralization based on the necessary TiO_2 loading, the frequently applied parameters of water quality, including DOC (dissolved organic carbon), TOC (total organic carbon),

This book belongs to Kitab Liaison (ocd1996@gmail.com) Copyright Elsevier 2023

and COD (chemical oxygen demand), are more relevant to make up this competitiveness of the intermediate with its preceding particles. Furthermore, organic compounds with electron-receiving characteristics, including nitrobenzene and benzoic acid, were discovered to firmly bond and are more vulnerable to direct oxidation compared to those with electron-donating compounds [288]. A great number of the TiO_2 studies undertaken thus far apply various samples of organic substrates with dissimilar substituent groups, though these hardly express any beneficial information and simply assess the photoeffectiveness of a novel photo catalyst and a cohesive reactor support. A number of field kinetics of the real wastewater photomineralization have also been discussed [289–292]. Owing to the stability of the dissolved organic compounds in the real wastewater, it was reported that deliberate photo mineralization kinetics are achieved with extended irradiation times to realize comprehensive mineralization. Sluggish kinetic throughput of the photocatalytic water treatment as an isolated process implies a higher opening cost on the reactor capacity and site space is necessary. In recent times, biological treatment has been integrated into this assorted photocatalytic technology to boost its industrial viability [293]. This integration facilitates the reduction of the retention time in biological treatment periods, in which the nonbiodegradable chemicals of the wastewater can be converted into biodegradable materials through the help of photocatalytic activity.

In the same way, the assessment on photodisinfection effectiveness of several microorganisms for the potential use of a photocatalytic mechanism in place of the chemical antiseptic techniques has been conducted. The technology applied in microbial sterilization involves the degradation of the microbial protein systems and deactivation of their enzymatic processes [173]. A universal categorization in the microbial resistance to the antiseptic employed has been preferred to the persistency in the photomineralization of organic compounds. The most resistant infectious of all the forms of microorganisms are prions, then *Cryptosporidium* (coccidia), *Bacillus* (bacterial endospores), *M. tuberculosis* (mycobacteria), *poliovirus* (viruses), *Aspergillus* (fungi), *Pseudomonas* (Gram-negative), and finally *Enterococcus* (Gram-positive bacteria) [155]. Their variations in terms of resistance are described by the permeability of their cell wall as well as the complexity and size of the specific microorganisms. Every microorganism is of communicable potential, causing prevalent sicknesses upon their multiplication in water. The majority of bacteria can be easily destroyed with TiO_2 photocatalysis. However, a total inhibition must be guaranteed because they are very

This book belongs to Kitab Liaison (ocd1996@gmail.com) Copyright Elsevier 2023

transferrable. Likewise, this transferrable quality is also common in viruses (rotaviruses, noroviruses, saproviruses, hepatitis A and E viruses, enteroviruses, and adenoviruses) and in protozoa such as *Toxoplasma gondii*, *Naegleria fowleri*, *Giardia intestinalis*, *Entamoeba histolytica*, *Cyclospora cayetanensis*, *Cryptosporidium parvum*, and *Acanthamoeba* spp. [294]. The photocatalytic process must be targeted toward all these protozoa as the surrogate indicators show that these microorganisms are highly communicable in low concentration. Adequate photocatalytic treatment should therefore be performed to prevent the eruption of endemic sicknesses in the treated water, in case photocatalytic treatment is preferred.

Light wavelength

Depending on the forms of photocatalyst applied (crystalline phase, anatase-to-rutile composition, and any state of photocatalyst modifications), the photochemical influences of light supplies with varying wavelength-emitting spectra will result in a notable outcome on the photocatalytic rate of reaction. When a commercial Degussa P-25 TiO2 with an anatase crystalline ratio of 70/80: 20/30 is used, a wavelength of light is $\lambda < 380$ nmis, adequate for photonic initiation [171, 287]. The rutile TiO_2 crystalline phase has an EB ~3.02 eV bandgap energy, which is smaller than the anatase TiO_2 energy of 3.2 eV [31, 163, 191]. This indicates that the activation of rutile TiO_2 can be done using a light wavelength of at most 400 nm, as determined by the band-gap lower limit for the form of rutile TiO_2 applied.

The respective electromagnetic arrays for UV light can be grouped as UV-C, UV-B, and UV-A, based on the emission wavelength. The disinfectant UV-C has a wavelength array that spans from 100–280 nm (4.43–12.4 eV), whereas UV-B is 280–315 nm (3.94–4.43 eV), and the UV-A has its light wavelength range from 315–400 nm (3.10–3.94 eV) [80, 295]. The majority of the previous studies established that the UV-A light yields light photons necessary for catalyst photonic activation [94, 243, 288]. In the case of outdoor solar radiation, the UV-C is commonly absorbed by the space and doesn't get to the Earth's surface. The lamp-compelled photoreactor structure can employ UV-C light dramatically for catalyst photonic activation and a decrease of dynamic microbes. The process of UV-C cell degradation comprises direct stimulation on the pyrimidine, purine, and pyrimidine adducts on the DNA of the cell. But only a few microbes are prone to UV-C emissions and most very-resistant

This book belongs to Kitab Liaison (ocd1996@gmail.com) Copyright Elsevier 2023

microbes may endure the disinfection activity. These are *Cryptosporidium parvum* oocysts and *Legionella pneumonphila* [155].

Both the UV-A and UV-B spectra are usually found in the natural UV radiation that gets to the Earth's surface. The photolysis process for the two UV radiations on cell inhibition is different from the assessed UV-C technology. UV-A and UV-B radiation are absorbable by cellular elements known as intracellular chromophores. The most well-known intracellular chromophore is L-trytophan, which is believed to have unsaturated links including quinines, steroids, and flavins [296]. Of all this UV radiation, UV-A is only poisonous in the oxygen media. The oxidative stress or ROS produced from the light absorption of the chromophore may cause the destruction of cells and cell components, resulting in lipid peroxidation, pyrimidine dimer development, and ultimately DNA lacerations. Nucleic acid modifications and single strand breaks occur as a result of the interaction between the DNA and ROS. These DNA injuries are typically disastrous and mutagenically irretrievable. A high level of cell destructions is evident as the quantity of ROS produced grows correspondingly when the TiO_2 catalyst is used as the light activator. Some microbes that have developed resistance to UV-A photolysis have successfully been inhibited by TiO_2 photocatalysis, specifically *S. typhimurium*, *P. aeruginosa*, *E. coli*, and *E. cloacae* [203].

A longer solar radiation wavelength ($l > 400$ nm) has also been applied in SODIS (solar disinfection study) [274, 276, 297–299]. But the photodestruction process is still indistinct as it encompasses a range of microbes and solar irradiation and a wider assorted scale of UV-A. A similar cell devastation technique to the one preferred for UV-A radiation is believed to occur in this mixed light range. The microorganisms in the drinking water kept in PET bottles, according to SODIS, were discovered to be inhibited in six hours of sunlight. Nevertheless, substantial study and enhancements on decontamination through photocatalytic-based mechanisms must be carried out to develop the photoactivity of the present TiO_2 catalysts applied.

Light intensity

The photocatalysis reaction's photonic nature has defined the overall photocatalytic rate dependency on the source of light applied. Light intensity is among the few strictures that have an impact on the extent of photocatalytic reaction on organic substrates. Fujishima et al. [168] pointed out that the rates of initiation of the TiO_2 photocatalysis reaction are not extremely

This book belongs to Kitab Liaison (ocd1996@gmail.com) Copyright Elsevier 2023

reliant on light intensity, in which a few photons of energy (that is, as low as 1 mW/cm) could adequately prompt the surface reaction. To accomplish a high rate of photocatalytic reaction, specifically in water treatment, a comparatively high light intensity is needed to sufficiently offer every TiO_2 surface lively spots with the adequate photon energy needed. When applying the nominal TiO_2 particles without modifications, however, the surface reaction is limited to photons with wavelengths that are shorter when compared to the absorption edge of about 400 nm. The organic conversion in the existence of UV wavelength ($l < 400$ nm) complies with the linear proportionality correlation in several studies to the incident radiant flux. This was confirmed by Glatzmaier [300] and Glatzmaier et al. [301], in which they witnessed that the destruction of dioxin and polychlorinated biphenyls was considerably boosted by the existence of photons with high intensity. The same result was described in Magrini and Webb [302], in which the rate of organic decomposition was stated to upsurge with the radiation intensity.

It was later discovered that under diverse lighting conditions, the reaction rate dependency on radiant intensity behaves indifferently [27, 303, 304]. The photocatalytic reaction rate of linear dependency on radiant flux ($\varnothing$) reformed to a dependency that is a square root ($\varnothing^{0.5}$) beyond the particular value of the threshold. This shift in the form of dependency was postulated as a consequence of the quantity of photogenerated holes obtainable in the course of the formation of the electron-hole pair. The photo-induced generation of valence band holes is much less compared to the conduction-band electrons available in the TiO_2 catalyst applied. The photogenerated holes in this instance are the rate-limiting step and the detailed derivation of the square-root dependency could be acquired from Malato et al. [155]. The photocatalytic reaction rate's dependency on radiant flux is abridged to zero ($\varnothing^0$) at high intensities. This was explained by the catalyst's saturated surface coverage, leading to a mass transfer limitation in desorption and adsorption and as a result, avert the impact of light intensity to become established. In this case, a rise in the fluid turbulence could help in easing the mass transfer problem on the catalyst's surface. In addition, the desorbed final products could influence the reaction rate's dependency on radiant flux, as they could rummage the electron acceptors and further uphold the recombination of the electron-hole pair.

According to Rincón and Pulgarin [268], the photocatalyst's residual disinfecting ability is highly reliant on the light intensity duration devoid of any progressive disturbances. They studied the impact of light intensities at 400

This book belongs to Kitab Liaison (ocd1996@gmail.com) Copyright Elsevier 2023

and 1000 W/m^2 on bacterial regrowth and lethality, and discovered that the higher intensity devoid of any temporal disruptions could bring about permanent harm to the *E. coli*. The bacteria were seen to regrow in the course of the successive 48 or 24 h in the sporadic light irradiations with persistent interruptions. A number of studies recommended that this regrowth is brought about by the dark-repair mechanism in which the partially damaged cells convalesce in the existence of nutrients [305]. Some have proposed that the cells that are damaged, although not completely inactivated, might recover viability via photorepair under radiation of 300–500 nmor on post-replication of cells or resynthesis [276, 282]. In this case, it should be noted that for photodisinfection with the use of diverse light intensity, an ultimate conclusive point could not be directly made. The disinfection results of 400 W/m^2 at 2.5 h irradiation may not be similar to the outcome that arose from 1000 W/m^2 for 1 h. Therefore, for the prediction of the minimum irradiation needed at constant irradiance, there ought to be introductory studies into both microbial consortia and photoreactor performance (diverse resistance).

Response surface analysis

From the prior discussions on the impact of the operation strictures on the rate of photocatalytic reaction, it could be realized that these strictures are going to indifferently influence the system. In general, it could be understood that an MV (multivariable) optimization methodology is essentially needed in optimizing a photoreactor system because parameter interaction may exist. Parameter interactions are the correlations between operating strictures, for instance, pH on radiant flux or TiO_2 loading on pH. For a photoreactor system's optimization, the conventional one-parameter-at-a-time methodology is typically applied in unveiling the impacts of one stricture after another. Despite the fact that this conventional optimization methodology is broadly acceptable, the stated effects may not be of significance and their predictive power is low in a condition where there is alteration of one operating stricture.

This has brought about the use of DOE (operational design of experiments), response surface analysis, and statistical analysis for photocatalytic studies [306–310]. With the use of this methodology, diverse combinations of experimental designs are incorporated and the operational spans and strictures are established. As compared to the conventional one-parameter-at-a-time approach, the MV optimization approach has predetermined

This book belongs to Kitab Liaison (ocd1996@gmail.com) Copyright Elsevier 2023

experimental points that are uniformly distributed all over the study domain, that is, only a small region in a conventional study's domain is covered. This gives room for optimization to be more time effective and enhances the identification of parameter interactions, where they can be understood with the use of commercial statistical software such as Design Expert.

Chong et al. [210] recommended the use of Taguchi-DOE methodology alongside analysis of variance, statistical regression, and response surface analysis to study the combined effects of four key operation parameters that affect the rate of photocatalytic reaction in an annular photoreactor. They used nine experimental permutations in analyzing the combination of 81 potential strictures. It was stated that the interaction between the aeration rate and TiO_2 loading had a constructive synergistic impact on the general rate of reaction. A response surface model was established with the intention of correlating the reaction rate dependency on the four diverse strictures in line with the statistical regression, as illustrated in (Eq. 10.22)

$$R_o = b_0 + \sum\nolimits_{i=1}^{k} b_i X_i + \sum\nolimits_{i=1}^{k} b_{ij} X_i^2 + \sum_{i_i<j}^{k} \sum_{j}^{k} b_{ij} X_i X_j \tag{10.22}$$

where R_o is the predicted response output of the photomineralization rate, and j and i are quadratic coefficients, linear correspondingly. The strictures of k and b are the number of strictures and regression coefficient investigated in the experiment, respectively, and X_i and X_j ($I = 1, 4; j = 1, 4, i \neq j$) stand for the number of independent variables in the study. This model (Eq. 10.22) is empirical and independent for every photoreactor system. Consequent verification works are needed in controlling the applicability and accuracy of a model of this kind for the prediction of photoreaction rate under the variation of its strictures. In addition, more DOE methodology to photocatalytic reactor optimization has been used over the years, for instance, Plackett-Burman designs, the central composite design, and Bayesian [311–313].

Kinetics and modeling

Mechanistic and kinetics studies on photodisinfection or the photomineralization rate of the water impurities are very important for the scale-up process. The suitable utilization of kinetic models for the interpretation of experimental data allows the optimization and design of a photoreactor system with minimal nonilluminated reactor volume and adequate capacity. The diverse kinetics and rate model for both photodisinfection and

This book belongs to Kitab Liaison (ocd1996@gmail.com) Copyright Elsevier 2023

photomineralization are going be discussed in this section, together with the common misapprehensions in kinetic modeling.

Photomineralization kinetics

In the majority of the photocatalytic studies, mechanistic or kinetic studies over the irradiated TiO_2 surfaces normally involve just a single constituent model organic compound. The diverse organic compounds' kinetics that range from pesticides, dye molecules, phenolic compounds, and herbicides to carboxylic acids, simple alkanes, aliphatic alcohols, and haloalkanes have been studied [155, 163, 171, 287]. The $OH^{\bullet}$ radicals' nonselective nature implies that the rate of disappearance in the studied compound with irradiation time ought not to be referenced as a standard for the purpose of reactor design. This is owing to the fact that several intermediates are molded en route to complete mineralization and disregarding this aspect is a common fault in revealing the photomineralization kinetics. The organic concentrations in this instance could be jointly expressed in TOC or COD with the purpose of producing a detailed understanding concerning the photomineralization kinetics.

Because the L-H model is reliant on a surface area, the rate of reaction is anticipated to rise with irradiation times because less organic substrate is going to remain following increased irradiation times with higher surface availability. A zero rate of degradation is related to the total decomposition accomplished. There are several suppositions for the L-H saturation kinetics type as well as for the applicability in the photomineralization rate, whichever of the four potential circumstances is lawful: (i) reactions occur between two adsorbed components of organics and radicals; (ii) the reactions are between adsorbed organics and the radicals in water; (iii) reactions occur between organics in water and the radical on the surface; and (iv) the reaction occurs with both organics and radicals in water.

A number of researchers discovered that simpler zero- or first-order kinetics are adequate to model the organic compounds' photomineralization. However, this was only appropriate for conditions that are restricted, where the solute concentration is inefficiently low. In the majority of kinetic studies, a plateau-type of kinetic profile is normally seen where the rate of oxidation upsurges with irradiation time up to an extent where the rate becomes zero [314, 315]. Such a kinetics regime's appearance normally fits the scheme of L-H. In line with the L-H model (Eq. 10.23), the rate (r) of the photocatalytic reaction is relative to the surface coverage's fraction

This book belongs to Kitab Liaison (ocd1996@gmail.com) Copyright Elsevier 2023

through the organic substrate (θ_x) and k_r represents the reaction rate constant while C is the organic species' concentration and K represents the Langmuir adsorption constant:

$$r = -\frac{dC}{dt} = k_r = \frac{k_r KC}{1 + KC} \tag{10.23}$$

The Eq. (10.23) applicability is reliant on a number of suppositions, which consist of (i) the dynamic equilibrium's reaction system; (ii) this reaction is surface mediated; and (iii) the competition for the TiO_2 active surface spots by the intermediates as well as other reactive oxygen species is not restrictive [264]. In a situation where these suppositions are lawful, the reactor scheme just consists of adsorption surface sites, the reactive oxygen species, organic molecules as well as their intermediates, and electron-hole pairs. For the majority of the photocatalytic reaction in water, the rate constant (k_r) is normally described to be in the order of 10^6–10^9 $(\mathrm{Ms})^{-1}$ [155]. This value of k_r is the proportionality constant for the photoactivated surfaces' intrinsic reactivity with C. In addition, others have associated that k_r is relative to the power law of the operative radiant flux (that is, $\varnothing_e^n$) in the course of the photomineralization reaction [314, 316]. The K-parameter refers to the dynamic Langmuir adsorption constant (M^{-1}) that stands for the catalysts' adsorption capability. Eq. (10.23) could be explicitly resolved for applying a discrete change in C from the original concentration to a point of reference:

$$\ln\left(\frac{C}{C_0}\right) + K(C - C_0) = k_r K_t \tag{10.24}$$

It is possible to acquire the K-value with the use of a linearized form of Eq. (10.23), whereby $1/r$ is plotted alongside $1/C$:

$$\frac{1}{r_0} = \frac{1}{k_r} + \frac{1}{k_r K C_0} \tag{10.25}$$

It was recounted that the actual K-value acquired from the linearized plot of $1/r$ against $1/C$ is considerably smaller [155]. This was described by the dissimilarities in adsorption-desorption occurrences in the course of illuminated and dark periods. In a situation where the organics concentration is low (in mM), a "seeming" first-order rate constant (Eq. 10.26) might be expressed where k' $(\mathrm{min}^{-1}) = k_r K$:

$$r = -\frac{dC}{dt} = k_r KC = k'C \tag{10.26}$$

This book belongs to Kitab Liaison (ocd1996@gmail.com) Copyright Elsevier 2023

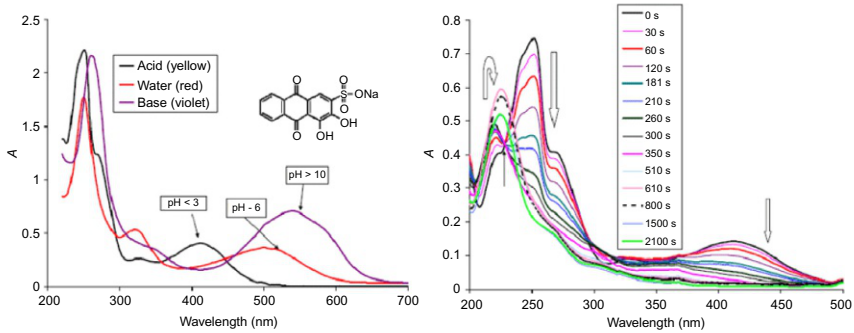

Fig. 10.14 The degradation of organic dye molecules' typical saturation kinetics plot in an annular photoreactor system.

Integration and rearranging of Eq. (10.26) yield the typical pseudo-first-order model as in Eqs. (10.27), (10.28):

$$C = C_o e^{-k't} \tag{10.27}$$

$$\ln\left(\frac{C_0}{C}\right) = -k_r K t = -k' t \tag{10.28}$$

In the reactor system, the seeming rate constant, however, only serves as a description and comparison for the photocatalytic reaction rate. Fig. 10.14 illustrates the degradation of organic dye molecules' classic saturation kinetic plot in an annular photoreactor system in which the rate of reaction rises to a point at which the rate plateaus off. For interpretation of the maximal rate of photomineralization, the tailing rule of the L-H saturation profile ought to be deserted. Only the slope of the tangent to the inflection point must be applied in acquiring the maximal rate of photomineralization. Like the zero-order rate constant, the unit for the slope in this instance has a similar chemical reaction order.

A lump-sum LeH saturation kinetics profile has also been applied in simplifying the estimation for a particular system of photocatalytic reactor [317]. In an empirical lump-sum LeH approach of this kind, the extent of organics mineralization is in fact articulated in terms of TOC (Eq. 10.29):

$$r_{\mathrm{TOC,O}} = \frac{\beta_1[\mathrm{TOC}]}{\beta_2 + \beta_3[\mathrm{TOC}]} \tag{10.29}$$

Eq. (10.29) enables the TOC degradation prediction as a function of irradiation time. The same reciprocal plots of $1/r$ against $1/[\mathrm{TOC}]$ could be

This book belongs to Kitab Liaison (ocd1996@gmail.com) Copyright Elsevier 2023

applied in determining the empirical strictures, β_1, β_2, and β_3 the same way in Eq. (10.25). The irradiation time taken in achieving the TOC's fractional degradation, which could as well be approximated when Eq. (10.29) is, expressed the same way in Eq. (10.24). This empirical lump-sum LeH model has significantly outlined the need for accurate kinetics measurements and made a high estimation for a specific photoreactor system, so long as adequate data are gathered for the determination of rate strictures.

Kinetics of photodisinfection

From the time when Matsunaga et al. [275] made the first use of semiconductor catalysts for decontamination, limited studies have been reported in the literature that deeply investigate the kinetic demonstration of microbe photosterilization in a water-treatment procedure. Experimental kinetic concepts have been used typically for analysis of photodisinfection information, owing to the complexity and variability of the process. Eq. (10.30) demonstrates a broad look for the experimental photodisinfection representations for a demand-free state. In such a situation, a demand-free environments requires that the catalyst concentration is consistent with radiation time.

$$\frac{dN}{dT} = -kmN^x C^n T^{m-1} \tag{10.30}$$

where m, n, and x are the empirical constants; C is the concentration of photocatalyst used; dN/dt is the rate of inactivation; k is the experimental reaction rate; and N is the number of bacterial survivors at irradiation time t. The most frequently used disinfection concept in photodisinfection studies to date, however, is the straightforward automatic C = W (Chick = Watson) concept (Eq. 10.31) [21, 295].

$$\log \frac{N}{N_o} = -k' T \tag{10.31}$$

In the C = W concept, the rate of photodisinfection is stated as a linear function of the known number of microbes and catalyst loading. The joint kinetic limit of CT between irradiation time and the catalyst concentration necessary to realize comprehensive inactivation is extensively applied as a reference for the process outline. Furthermore, this CT-values model is typically applied in comparing the performance of various decontaminators used in the treatment of water [318]. However, this C-W concept is not always relevant because most studies may have gone through a nonlinear

This book belongs to Kitab Liaison (ocd1996@gmail.com) Copyright Elsevier 2023

or curvy photodisinfection system. Hom [319] replicated an important empirical adaptation on the C-W prototype upon making an observation that the plots for disinfection of natural algae-bacterial systems were curvy, instead of the characteristic log-linear form (Eq. 10.32). The microbial inhibition level in the Hom model is foreseen in a nonlinear curve of C and T, according to the practical limits of n and m, correspondingly. The Hom model is a two-parameter model, and it must therefore be emphasized that this model is merely relevant to a photodisinfection system with at most two dissimilar nonlinear parts. The inactivation curve shows the first "shoulder" for the m-value greater than unity, whereas "tailing" is notable when the m-value is less than unity.

$$\log \frac{N}{N_o} = -k' C^n T^m \tag{10.32}$$

Marugán et al. [187] summarized the typical nonlinearity occurring in the kinetics outline of photodisinfection based on a Degussa P-25 TiO_2 catalyst fixed with normal disinfection concepts (Fig. 10.15). Their study revealed that there are three different inactivation sections in the photodisinfection outline, including (a) a delay or original smooth decline, called the "shoulder," (b) a characteristic log-linear inactivation phase, and finally (c) an extended slowing phase at the close of disinfection, referred to as the "tailing." The occurrence of "shoulder" was due to the increasing destructive potential of photodisinfection activity on the cytoplasmic membrane instead of prompt destruction [318]. During photodisinfection, however, the "tailing" is not well comprehended. It was suggested by Benabbou et al. [320] that the "tailing" part is dependent on the struggle for photocatalysis between the remaining intact cells and organic materials released from persistent cell lesions. The rest have suggested that the "tailing" aberrations from the log-linear fall were caused by the existence of disparities in the microbial species resilient to the used disinfectant [321]. However, the application of the Hom concept or the CT model can result in overplanning for a photodisinfection scheme [318]. Any further alteration to the Hom concept was made to compensate for the concurrent manifestation of tailing, log-linear reduction, and shoulder (Eq. 10.33) [187, 322].

$$\log \frac{N}{N_o} = -k_1 [1 - \exp(-k_2 t)]^{k_3} \tag{10.33}$$

Commonly known as the modified Hom model, Eq. (10.33) magnifies the usability of the Hom concept for prolonged tailing, log-linear reduction,

This book belongs to Kitab Liaison (ocd1996@gmail.com) Copyright Elsevier 2023

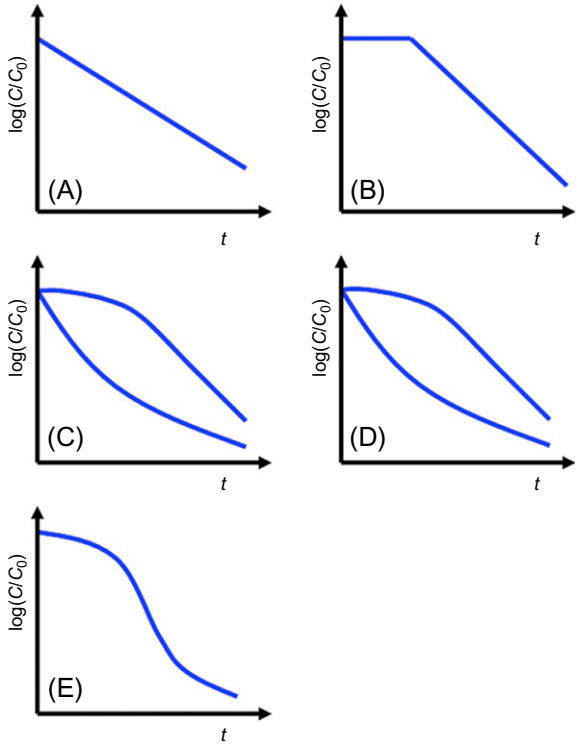

Fig. 10.15 Typical nonlinearity in the kinetics outline of photodisinfection based on a TiO_2 catalyst, together with the suitable disinfection concepts applied [187]: (A) Chick-Watson Eq. (10.22); (B) delayed Chick-Watson Eq. (10.30); (C) Modified Chick-Watson Eq. (10.31); (D) Hom Eq. (10.32); and (E) Modified Hom Eq. (10.33).

and the correct initial shoulder behaviors. The power law expression (Eq. 10.34) is one more comprehensive empirical equation that is able to define the various microbial inactivation parts, when $m = 1$ for the general differential equation (Eq. 10.30) [323].

$$\frac{dN}{dt} = -kN^x C^n \tag{10.34}$$

The rational equation (Eq. 10.35) is produced when Eq. (10.34) is integrated. When $x = 1$, the rational equation can be modified back to the C-W expression. In such a scenario, the rational equation has it that $x \neq 1$;

$$\log \frac{N}{N_o} = -\frac{\log\left[1 + N_o^{x-1}(x-1)kC^n T\right]}{(x-1)} \tag{10.35}$$

This book belongs to Kitab Liaison (ocd1996@gmail.com) Copyright Elsevier 2023

Both "tailing" and "shoulder" behaviors for x greater than or less than unity can be described by the rational expression (Eq. 10.35). In the same way, the Hom expression (Eq. 10.32) can as well be integrated in terms of the rational model with the assumption that both m and $x \neq 1$ produce the home power equation (Eq. 10.36):

$$\log \frac{N}{N_o} = -\frac{\log\left[1 + N_o^{x-1}(x-1)kC^n T^m\right]}{(x-1)} \tag{10.36}$$

According to Anotai [1], this Hom-Power expression can yield a more enhanced fit than either the rational or Hom models. But the presence of four empirical factors in the expression can lead to an undue parameterization with unimportant physical implications for every term in the equation. The Select expression (Eq. 10.37) was suggested to decrease the amount of null terms. The assumption of this equation is that the catalyst concentration is constant throughout the irradiation phase:

$$\frac{dS}{dt} = \frac{kCS}{1 + KCT} \tag{10.37}$$

In which k and K are the rate constants and S represents the survival ratio $= N/N_o$ at irradiation time t. This expression assumes that the "shoulder" occurs as a result of accumulative impacts of the chemical antiseptic on the microorganism in the contact time. A steady decline in the penetrability of *E. coli*'s outer cell membrane as an achievement of the catalysts can be perfected by a sequence of first-order activity stages on one *E. coli* cell that results in lethality. This concept is modifiable to make up the decontamination of coliform microbes in water/wastewater runoff (Eq. 10.38) [323].

$$\log \frac{N}{N_o} = -n \log\left[1 + \frac{CT}{k}\right] \tag{10.38}$$

Even though empirical expressions give a direct association of the photodisinfection information, the mathematical model of their related factors produces unimportant or misinterpreted physical connotations. For example, the m-value > 1 in the Hom expression really proposes that photocatalytic activity rises with ASP irradiation time. If the dynamic supposition of bacterial species resistance dispersal is effective, this essentially points out that the hardiest bacteria are destroyed before the most vulnerable ones [321]. This illustrates that the basis for the effectiveness of the Hom model is inconsistent.

This book belongs to Kitab Liaison (ocd1996@gmail.com) Copyright Elsevier 2023

It was suggested that mechanistic concepts are able to express an improved physical implication in their kinetic positions. From the hypothesis, the photodisinfection process can be considered as an absolute physicochemical occurrence and goes before a chemical reaction in a similar way [321]. A distinctive instance of the mechanistic photodisinfection kinetics concept is the conventional C-W concept. In this concept, the seeming exponential curves of decay for survival probabilities of microbes with irradiation times assume the same decay process of chemical activity, and are therefore effective under the two scenarios. This is evident when the C-W equation is mathematically integrated, with N seeming to be the number of reactant moles to produce the long-linear graph of a first-order activity.

The presence of both "tailing" and "shoulder" sections must be perfectly rationalized to facilitate the development of a mechanistic expression for the kinetics of photodisinfection. The occurrence of "shoulder" can be mechanistically explained by the single-hit numerous marks or successive phenomenon occasions [323]. The injury to the bacterial cell, under the mechanistic hypothesis, is seen as gradually deadly instead of promptly fatal. This shows that many important particles must be denatured before cell inactivation [323]. According to Severin et al. [324], the collective inhibition of one bacterium can be mutually characterized by a succession of numeral phases. Such disinfection phases are believed to convey a bacterium from one stage to another in a first-order activity in regard to the catalyst applied up until a predetermined number of deadly (l) occasions was attained. The microbes that will gather less than the hypothesized number of deadly steps are seen to endure the photodisinfection reaction. With regard to the "tailing" section, most scholars have deduced that it was as a result of the existence of a bacterial subpopulation hardy to thermal disinfection. Najm [325] revealed that "tailing" is caused by the inherent dissemination of microbial resistance to the decontamination technique, rendering the microorganisms more tough, adjusted, and unreachable to heat activity. Marugán et al. [187] revealed that "tailing" has never been a common event in the water-disinfection process. To date, no admissible details have been suggested to explain the incidence of "tailing" in the water-sterilization process with diverse environments and a similarly unaffected cloned bacterial populace. It was discovered that such "tailing" is due to a regular decline in the rate of treatment, and complete inactivation was attainable only upon an adequate holding time. The Poisson probability can express the random bombardments between the bacteria and catalyst, as the number

This book belongs to Kitab Liaison (ocd1996@gmail.com) Copyright Elsevier 2023

of bombardments surpasses before the number of death microbial [323]. If the rate of destruction of the bacteria is believed to be similar for the original and lth mark at the kth microorganisms position, therefore the destruction rate of the bacteria can calculated as;

$$\frac{dN_k}{dt} = kCN_{k-1} - kCN_k \tag{10.39}$$

Calculating for $K = 0$ to $K = l - 1$ yields the log portion of bacterial survival, less than $l - 1$ toward the end of the holding time:

$$\ln \frac{N}{N_o} = -kCT + \ln \left[\sum_{k=0}^{l-1} \frac{(kCT)^K}{K!} \right] \tag{10.40}$$

In the design of each mechanistic model that covers the "shoulder" and "tailing," Lambert and Johnston [321] posit that a transitional population level is typically proposed with diverse rates of disinfection for all microbial states. Characteristically, two dissimilar bacterial conditions for the same injured microbial and uninjured microorganisms (that is $C_{dam} + C_{undam}$) were given to take into account the nonlinearity in survivor curves of bacteria. The same L-H (Langmuire Hinshelwood) form of mechanistic representation (Eqs. 10.41, 10.42) may be used to characterize the photodisinfection kinetics to produce more expressive kinetic factors [10, 71]. Johnston et al. [326] proved that the inoculum dimensions of the microbes largely impact the resistance dissemination, and therefore the blunders related to this factor must be kept in mind throughout the mechanistic demonstration.

$$\frac{dC_{undam}}{dt} = \frac{-k_1 K_{undam} C_{undam}^{\eta_{undam}}}{1 + K_{undam} C_{undam}^{\eta_{undam}} + K_{undam} C_{undam}^{\eta_{undam}}} \tag{10.41}$$

$$\frac{dC_{dam}}{dt} = \frac{k_1 K_{undam} C_{undam}^{\eta_{undam}} - k_2 K_{dam} C_{dam}^{\eta_{dam}}}{1 + K_{undam} C_{undam}^{\eta_{undam}} + K_{dam} C_{dam}^{\eta_{dam}}} \tag{10.42}$$

where k_i is the real log-linear rate of deactivation constant for the reaction between bacteria and generated ROS. The pseudoadsorption constant, K_i, stands for the surface interaction between bacteria and the catalyst. In the conventional L-H model, this constant looks like the adsorption equilibrium constant. As a result of the substantial size dissimilarities between the catalyst agglomerates and *E. coli* cells, these constants do not signify firm adsorption phenomena but a surface interaction that is more general in the course of photodisinfection. In the photodisinfection kinetics data, these adsorption constants give room for the "shoulder" representation. The inhibition

This book belongs to Kitab Liaison (ocd1996@gmail.com) Copyright Elsevier 2023

coefficient η_i is a power coefficient that comprises the "tailing" in the inactivation curve of the bacteria. Marugán et al. [187] recommended that η_i is required in accounting for the inhibition generated by the rising concentrations in the medium of cell oxidation and lysis products contending for the ROS. This is mainly important toward the end of photodisinfection because there are small numbers of viable bacteria and high concentrations of these compounds as well as in the suspension. The η_i in the recommended L-H model in this instance in essence implies that the reaction order regarding the microbial population is above one.

Eqs. (10.41), (10.42) consist of six independent strictures describing rates of photodisinfection. This institutes a high menace of overfitting the experimental data, in which the statistical importance of strictures and the model's plausibility are low. By taking into consideration the ROS attack's intrinsic kinetics and that the inhibition byproducts and catalyst-bacteria interactions are the same for both damaged and undamaged bacteria, the following are presumed:

$$k_1 = k_2 = k \tag{10.43}$$

$$k_{undam} = k_{dam} = K \tag{10.44}$$

$$\eta_{undam} = \eta_{dam} = \eta \tag{10.45}$$

With these, Eqs. (10.41), (10.42) are abridged to Eqs. (10.46), (10.47). The three independent strictures give room for a concurrent fitting of three diverse inactivation regimes of "tailing," "log-linear," and "shoulder." Fitting Eqs. (10.46), (10.47) to the experimental measurements of $(C_{dam} + C_{undam})/C_o$ could be accomplished with the use of a nonlinear regression algorithm together with a fifth-order Runge-Kutta numerical methodology. Marugán et al. [187] indicated a good fitting of such a mechanistic L-H model to the photodisinfection of *E. coli* under a diverse Degussa P25 TiO_2 catalyst's loadings.

$$\frac{dC_{undam}}{dt} = \frac{-kKC_{undam}^{\eta}}{1 + KC_{undam}^{\eta} + KC_{dam}^{\eta}} \tag{10.46}$$

$$\frac{dC_{dam}}{dt} = k\frac{KC_{undam}^{\eta} - KC_{dam}^{\eta}}{1 + KC_{undam}^{\eta} + KC_{dam}^{\eta}} \tag{10.47}$$

Water quality

A number of technical issues have to be redeployed in a full-scale plant for water treatment. With time, the influent water quality in the treatment plant

This book belongs to Kitab Liaison (ocd1996@gmail.com) Copyright Elsevier 2023

could vary. The TiO_2 photocatalytic process implication for treatment of diverse qualities of water sources will be discussed in this section. This gives room for a more complete understanding on the impacts of several key water quality strictures on the appropriateness of using such innovative TiO_2 photocatalytic processes.

Turbidity

Normally, turbidity refers to the insoluble particulates that are found in the targeted water [161]. The existence of such insoluble particulate matter is greatly harmful to the process based on TiO_2 photocatalysis because they could influence the optical properties and further hamper UV light penetration by sturdy absorption and scattering of the rays [327, 328]. This is going to bring about a variation in the foretold application of light intensity, TiO_2 loading, and UV penetration path. In addition, extreme turbidity levels could lessen both the photodisinfection and photomineralization effectiveness of the pollutants found in water as a result of the guarding effects that lessen the light penetration, resulting in those pollutants fleeing from the treatment [327–329]. In addition, target pollutants are going to be safeguarded by solids that are suspended from oxidation reactions. The suspended solids in this instance refer to the nonfilterable residue that is retained on the filter medium following filtration. Ultimately, all these factors lessen the general photocatalytic efficacy for water treatment. To guarantee a quick photocatalytic rate of reaction, the targeted water's turbidity ought to be kept under 5 NTU (nephalometric turbidity units) for photocatalytic reaction and optimum UV light utilization [93, 330]. Rincón and Pulgarin [282] discovered that the water turbidity above 30 NTU is going to adversely influence the photocatalytic disinfection rate. The 5 NTU unit is random and is reliant on the receiving water bodies as well as the treatment levels needed. Because TiO_2 photocatalytic processes are retrofitted to a stage of progressive water treatment, preceding reduction in turbidity might be accomplished through conventional treatment processes such as flocculation, screening, sedimentation, filtration, and coagulation. The standard for 1 NTU is 1.0 mg/L of indicated silica suspension size and could be equipped for laboratory study. The turbidity standard could be standardized with a nephalometry or a photoelectric detector for the scattered light's intensity.

Inorganic ions

In the targeted water for TiO_2 photocatalytic treatment, the existence of inorganic ions is anticipated. The basic understanding of these inorganic ions

This book belongs to Kitab Liaison (ocd1996@gmail.com) Copyright Elsevier 2023

on the photocatalytic performance is essential in order to functionalize a TiO_2 water-treatment process. Crittenden et al. [331] recounted that when a photocatalyst is used in either slurry or fixed-bed configuration for treatment of real waters with diverse inorganic ions, photocatalyst deactivation was typically observed. This brought about a sturdy inhibition from the inorganic ions on the surface of the TiO_2 semiconductor applied. Thus, the presence of these inorganic ions alongside their levels of permissibility on the photocatalytic performance of TiO_2 in water treatment ought to be determined with the intention of making sure that there is no turbulence on the effective operation of the TiO_2-based treatment process. With such data economical fouling preclusion with inorganic ions and photocatalyst regeneration, policies could be tailored.

Several studies have been carried out on the impacts of diverse inorganic cations or anions on both TiO_2 photodisinfection and photomineralization reactions [37, 268, 332–339]. However, it is worth stressing that the majority of these investigations have focused on the way diverse inorganic ions influence the photocatalytic reaction rates with a model surrogate organic compound. The model surrogate organic compound could be biased in the direction of its photocatalytic enactment as a result of its core chemical properties as well as the key constituent groups forming the compound. A case in point is the model compounds with either electron donating or withdrawing groups that are going to underwrite a dissimilar extent of degradation pathways or interactions [171]. As a result of the zwitterionic nature, the TiO_2 particles applied, it is possible as well that the operating pH could have an intense impact on the discerning reticence of inorganic ions on the TiO_2 particles surface [333]. Few discussions have been focused on taking into account the way the chemical nature of the organic model is applied as well as the operating pH in the photocatalytic reactor on the inhibition of diverse inorganic ions in the treatment of photocatalytic water.

So far, the impacts of the inorganic cations (for instance, Al^{3+}, K^+, Na^+, Cu^{2+}, Ca^{2+}, Mn^{2+}, Ni^{2+}, Fe^{2+}, Mg^{2+}, Zn^{2+}) and inorganic anions (for instance, PO_4^{3-}, NO_3^-, Cl^-, HCO_3^-, SO_4^{2-}, ClO_4^-, HPO_4^{2-}) on the treatment of photocatalytic water have been studied [37, 268, 332–338, 340]. An overall consensus from these investigations determines that PO_4^{3-}, Cu^{2+}, Al^{3+}, Fe^{2+}, and Cl^- at particular levels could decrease the rates of photomineralization reaction whereas Zn2+, Mg2+, and Ca^{2+} might have insignificant impacts. This is owing to the fact that Zn^{2+}, Ca^{2+}, and Mg^{2+} are at their supreme states of oxidation resulting in their incapability to hinder the photocatalysis reaction. The existence of Fe^{2+} could catalyze the photo-

This book belongs to Kitab Liaison (ocd1996@gmail.com) Copyright Elsevier 2023

Fenton and Fenton reactions. Choi et al. [341], on the other hand, discovered that Fe^{2+} spoiled the photocatalyst surface through introduction of a rusty orange color change through forming $Fe(OH)_3$, whereas the PO_4^{3-} in the nominal pH range is still sturdily adsorbed onto the surface of TiO_2 and further inhibit s its photoactivity [14, 342]. A number of research groups discovered that HCO_3^-, NO_3^-, ClO_4^-, and SO_4^{2-} hinder the photocatalysts' surface activity, whereas others recommend that there is no such effect. Both SO_4^{2-} and NO_3^- have harmful impacts on the rate of photodisinfection [37]. At its concentration up to 0.1 mM, the Cu^{2+} could enhance the photocatalytic activity whereas further increases in its concentration reduce the rate of reaction [343]. Nitrogen-containing molecules are mineralized into NH_4^+ and mainly NO_3^-. Ammonium ions are moderately stable and their proportion is mainly reliant on the original oxidation degree of nitrogen on the irradiation time. Impurities that contain sulfur atoms are mineralized into sulfate ions, whereas Cl^- does not inhibit the photocatalytic trichloroethylene degradation at a concentration up to 3.0 mM. However, adding oxyanion oxidants, for instance IO_4^-, ClO_2^-, BrO_3^- $S_2O_8^-$, and ClO_3^-, augmented photoreactivity through scavenging of conduction-band electrons as well as lessening the recombination of the charge-carrier [344]. In addition, the existence of salts is known to reduce the colloidal stability as screening impacts become more intense. After this, there was surface charge neutralization and double layer compression, which upsurges the mass transfer restrictions and lessens surface contacts between the catalysts and pollutants. In addition, more inorganic ions influence rates of photodegradation, where the existence of SO_4^{2-} in a TiO_2-coated glass spiral reactor can duple the rate of disappearance in the pesticide monocrotophos [345]. The Mn^{2+} upgraded the photoactivity by increasing simultaneously the electron-hole pairs and averting their recombination [346].

A number of appliances for fouling the impacts of inorganic ions on TiO_2 photoactivity have been recommended [347, 348]. These consist of competitive adsorption to surface active spots, UV screening, surface deposition of precipitates and elemental metals, competition for photons, direct reaction with the photocatalyst, and radical and whole scavenging. The NO_3^- ion was described to UV screening the photocatalyst compared to hindering the TiO_2 surface [347]. The struggle for surface active sites consists of the constant hydroxide ion displacement from the TiO_2 surface. Therefore, this further reduces radical generation. Quantum production is decreased owing to the direct competition of inorganic ions for light photons (dropped number of photons that enter the reactor).

This book belongs to Kitab Liaison (ocd1996@gmail.com) Copyright Elsevier 2023

The same decrease in photonic effectiveness was discovered when precipitates were molded and set down onto the TiO_2 surface, hindering the approachability of organic and photon compounds. The final inorganic anions that were decided to scavenge both the radicals and the hole include HCO_3^-, PO_4^{3-}, Cl^-, and SO_4^{2-} [349]. A Cl^- and HCO_3^- mechanism in hindering photocatalysis through hydroxyl radical and hole scavenging was recommended by [350]; correspondingly:

$$Cl^- + OH^\bullet \longrightarrow Cl^\bullet + OH^- \tag{10.48}$$

$$Cl^- + h^+ \longrightarrow Cl^\bullet \tag{10.49}$$

The Cl^- accounted for its inhibitory effect on TiO_2 photocatalysis through a preferential adsorption displacement mechanism over the surface-bound OH^- ions. This reduces the number of OH^- ions available on the TiO_2 surface, and the substituted Cl^- further increases the recombination of electron-hole pairs. Among other chlorinated molecules, Cl^- ions are readily released in the solution. This effect could be of benefit in a process where photocatalysis is associated with a biological depuration system, which is generally not efficient for chlorinated compounds [171]. Other ions such as PO_4^{3-} are known to avert adsorption of amino acids over the TiO_2 catalysts while CO_3^{2-} and other ionic species react with OH^- radicals to compete with microorganisms and further reduce the efficiency. Thus, the presence of inorganic ions in water subjected to TiO_2 photocatalytic treatment is an important factor in determining its successful implementation.

To resolve the TiO_2 photocatalyst fouling issue, preventative or regenerative strategies can be adopted, depending on the nature of the photocatalyst deactivation in the water matrix. Preventative fouling strategies by means of water pretreatment, complexation, and photocatalyst surface modification can be addressed while rinsing the TiO_2 surface with different chemical solutions constitutes the regenerative strategy. Water pretreatment with ion exchange resins is one of a few techniques that could be used in guaranteeing minimal instabilities via inorganic ions. Burns et al. [347] deliberated that the operational expense of water pretreatment with ion exchange resins could be minimized in a situation where the fouling ions were selectively removed and identified. Other preventative policies such as complexation of fouling agents following "escorting" the ions via the reactor could be used, so long as the strong fouling ions are not easy to eliminate from the feed water

This book belongs to Kitab Liaison (ocd1996@gmail.com) Copyright Elsevier 2023

stream. The TiO_2 surface modifications to increase adsorption capacity and the hydrophobicity are an upstream precautionary means of enhancing the photodegradation rate in the existence of fouling ions. This technique is, however, impractical and not stable as compared to the others, in which the modifications are stated to be moved away with time. When it comes to the regenerative policies, diverse kinds of chemical rinsing were tested to possibly resolubilize reduced metals, surface deposits, and precipitates. Normally, the fouled ions do not form sturdy surface complexes and could be easily moved by an ion exchange rinse. Abdullah et al. [14] stated that TiO_2 fouling with PO_4^{3-} and SO_4^{2-} could be displaced by $NaHCO_3$, NaOH, and KOH whereas Cl^- could be easily rejuvenated with water. More intricate mixtures of inorganic ions ought to be studied to enhance the mimicking of actual water matrices in the treatment of photocatalytic water or following an investigation of water matrices with a known inorganic ion composition at a time.

Heavy and noble metals

Heavy metals that could be present in trace quantities in the wastewater stream are greatly toxic in a number of their valence states [351]. As a result of the malleable nature of biological treatment, these metals could remain and permeate via the treatment process. For the treatment of such metals, the TiO_2 photocatalytic process has been described to convert these metals concurrently into nontoxic ionic states and abridge them further into their corresponding elemental system on the TiO_2 surface for metal recovery. Prairie et al. [352] stated that the metals of Pt(II), Ag(I), Hg(II), and Cr(IV) were treated using TiO_2 of 0.1 wt.% while Cu(II), (II), and Cd(II) could not be eliminated. The degree of conversion of such metals and the process of recovery are extremely reliant on the standard reduction prospective of the metals for the reduction reactions. For an efficient removal of the metals, it was reported that a positive potential higher than 0.4 V or the flat band prospective of TiO_2 was needed [171, 351]. Because the oxidation (organics) and reduction (metals) rates on the TiO_2 surface are naturally interrelated, the presence of abundant organics in the water matrices was discovered to simplify the metal recovery. Below is the process of redox for the metal reduction on the TiO_2 surface:

$$Mn^+ + H_2O \xrightarrow{TiO_2(h\nu)} M^o + nH^+ + \frac{n}{4}O_2 \tag{10.50}$$

This book belongs to Kitab Liaison (ocd1996@gmail.com) Copyright Elsevier 2023

In accordance with Herrmann et al. [353], small silver crystallites (3 and 8 nm) were originally deposited and began agglomerating a few hundreds of nm when the conversion was augmented. A relatively large amount of silver was recovered because the photosensitive surface was not masked, leaving behind a lower concentration as compared to the atomic absorption spectroscopy's detection limits ($\leq$0.01 ppm) in the solution. The impact of numerous aspects on the silver photoreduction on TiO_2 surface was studied further [354]. In addition, Angelidis et al. [18] stated that the photodeposition of metals on the TiO_2 surface from solution was still effectively performed, even at a low concentration of metal ions. They, however, discovered that the photodeposition rate was boosted when Pt-loaded was applied rather than unloaded TiO_2 particles. This metal photodeposition property on the TiO_2 surface is particularly beneficial when the water legislation limit on the metal contents becomes more rigid.

Lifecycle assessment of photocatalytic water treatment processes

In the current development of photocatalytic water/wastewater treatment processes, their possible application for the industry is still being investigated at the pilot-plant scale. A few pilot plants have been established to obtain feasibility data, such as the treatment efficiency, site area requirements for targeted volume, electrical energy consumption, process emissions, and chemical costs. The heterogeneous photocatalysis and photo-Fenton plants located at the INETI (Instituto Nacional de Engenharia, Technologia Industrial e Inovacao, Portugal) and PSA (Plataforma Solar de Almeria, Spain) are two renowned pilot plants that have delivered most of these data for technical analysis. Both plants consist of compound parabolic collectors (4.16 m^2 aperture area) exposed to sunlight, a reservoir tank, a recirculation pump, and connecting tubing; they are also operated in batch mode [355]. Further technical details of these plants can be found in the literature [356, 357].

In order to assess these photocatalytic processes as emerging technologies for large-scale water/wastewater treatment, an LCA (lifecycle assessment) ought to be assessed according to the data that is presently available. An LCA is among the most extensively acknowledged devices that take into consideration the environmental effect of the emergent photocatalytic water treatment as well as its technical costs and feasibility. In addition, Andreozzi et al. [4] indicated that the likely application of ROS-based oxidation

This book belongs to Kitab Liaison (ocd1996@gmail.com) Copyright Elsevier 2023

processes involves high expenses for consumption of reactants and energy. To take into account the photocatalytic water treatment feasibility on the whole, an all-inclusive LCA founded on feasible technical data ought to be performed. Muñoz et al. [358] performed a streamlined LCA founded on small-scale laboratory data of assorted photocatalysis as well as other AOPs. They, however, discovered that the interpretation of small-scale laboratory data in their study of the LCA could result in inconclusive outcomes.

With the use of an LCA, the environmental burdens from an activity, a product, or process through energy and materials balances could be described and reduced besides the waste discharges, its effects on the environmental improvement opportunities, and the environment over the whole lifecycle [359]. This all-inclusive LCA methodology in decision making over other environmental valuation approaches comprises all the impacts and burdens, and emphasizes the generated wastes and emissions [360].

Muñoz et al. [355] perfumed an LCA founded on the two pilot plants of PSA and INETI, which treated 1 m^3 of methyphenylglycerine (MPG) to destroy toxic and nonbiodegradable compounds to a level that attained aquatic ecosystem quality with both heterogeneous photocatalysis and homogeneous photo-Fenton. More technically reasoning suppositions were also made to ease the approximation of materials and energy produced and consumed. Nine effect types of the process of conceivable large-scale photocatalytic water treatment were involved in the analysis: human toxicity potential, ozone depletion potential, freshwater aquatic toxicity potential, global warming potential, nonrenewable energy consumption, photochemical oxidant formation potential, eutrophication potential, and land use and acidification potential (Fig. 10.16).

Future challenges and prospects

Semiconductor photocatalytic technology with the use of either solar or UV light has become more projecting as a result of its advantages of the application of vast additive disinfectants or chemicals and its aspects of mineralization. These are particularly important, as recalcitrant organics are mineralized instead of being transmuted to a different phase. Combined with the process' ambient operation, all these make photocatalytic water treatment technology a feasible choice for commercialization in the near future. Diverse water contaminants ranging from hazardous contaminants of pesticides, herbicides, and detergents to pathogens, viruses, coliforms, and spores are effectively eliminated by this photocatalytic process.

This book belongs to Kitab Liaison (ocd1996@gmail.com) Copyright Elsevier 2023

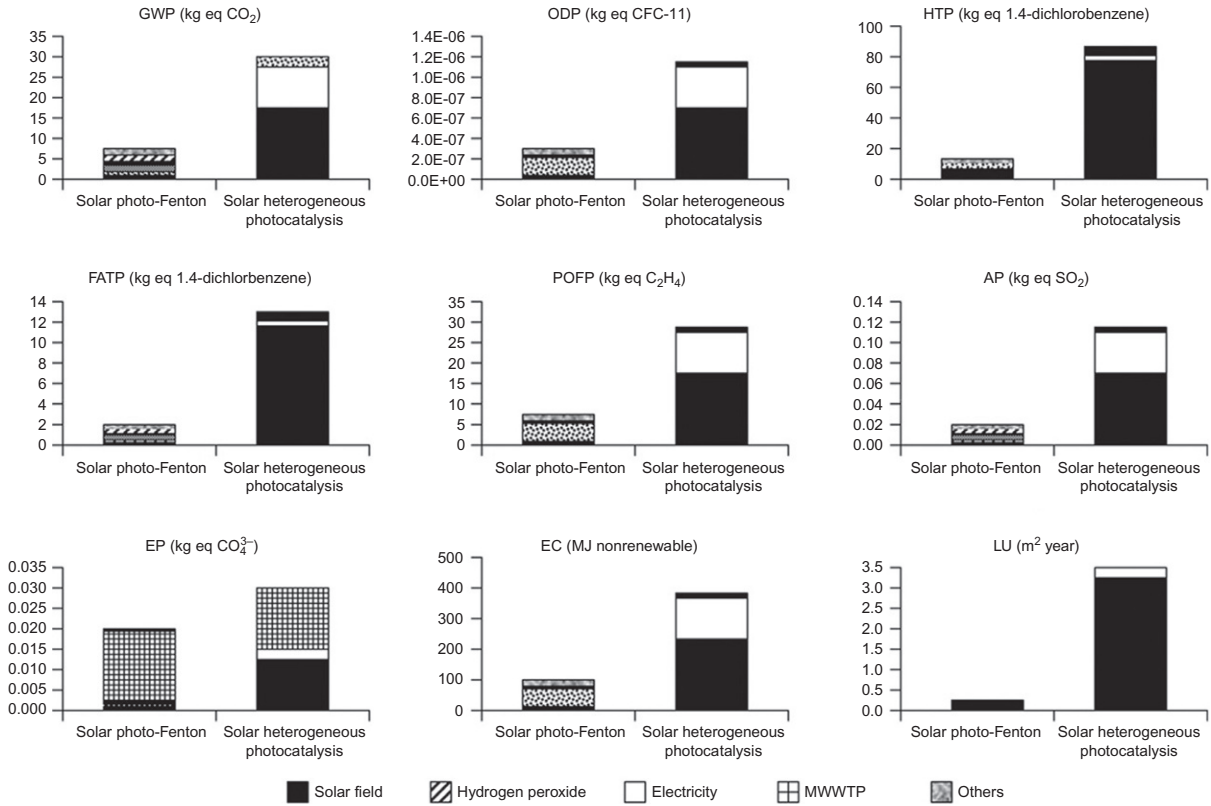

Fig. 10.16 The LCA outcomes for potential large-scale water application with the use of photocatalytic technology. The LCA outcomes demonstrated that retrofitting the heterogeneous photocatalysis process to the current biological wastewater treatment could lower the eutrophication potential, though it necessitates a higher site area prerequisite as well as electricity consumption. These technical limits are a direct outcome from the obligation for the raw materials and large land area for building the parabolic collector infrastructure and the high power required in pumping the wastewater via the system. The outcomes from the effect categories could not be directly compared to each other because they were expressed in diverse measurement units. From an engineering point of view, these constraints mainly arise from the catalyst's low photoactivity applied under solar irradiation. Additional materials engineering studies and solutions ought to be performed to determine such technical matters to allow the technology to be scaled up to a process that is commercially feasible.

This book belongs to Kitab Liaison (ocd1996@gmail.com)
Copyright Elsevier 2023

The heterogeneous photocatalytic technology's applicability for water treatment is controlled by a number of vital technical concerns that ought to be further studied. Whether the photocatalytic process is a pretreatment step or a stand-alone system is the first consideration. The nonselective reactivity on the nonbiodegradable water soluble pollutants implies that the photocatalytic process could be applied efficiently as a step that is the pretreatment in enhancing biodegradation of recalcitrant organic pollutants before biological water treatment. The reaction volume and residence time for the biological treatment might be considerably reduced. In a situation where the photocatalytic process is applied as a stand-alone treatment system, the needed residence time could be prolonged for total bacterial mineralization or inactivation. As deliberated, this is prevented by low photoefficiency, the slow kinetics, and a prerequisite for continuous enlightenment to accomplish the necessary microbial inactivation or total organic carbon elimination. For the stand-alone system, the spot area necessity could be proportionally from any augmented reaction volume needed.

For the feasibility of photocatalytic water treatment technology to be promoted in the near future, a number of crucial technical constraints ranging from catalyst development to process optimization and reactor design have to be dealt with. These entail (i) improvement of the catalyst for a high photoefficiency that could use broader solar spectra; (ii) immobilization policy of the catalyst to offer a lucrative separation of the solid and liquid; (iii) photocatalytic operation improvement for an extensive pH range as well as to reduce the tallying of oxidant additives; (iv) fresh coupling or incorporated system for enhanced photodisinfection or photomineralization kinetics; and (v) parabolic solar collector or effective photocatalytic reactor system's design for higher utilization of solar energy to lessen the electricity expenses. Presently, the use of solar energy is restricted through the photoefficiency of the TiO_2 catalyst band-gap to just 5% of the solar spectrum. The requisite for uninterrupted illumination for effective inactivation of pathogens has distracted solar use to the process of artificial UV lampdriven. The low efficacy design of current solar collecting technology in the water treatment industry (0.04% capture of the initial solar photons) has as well heartened the developmental progress of photocatalytic technology. More pilot-plant studies with diverse reactor configurations are required in making sure that the photocatalytic water technology is ingrained and introduces huge technoeconomic data for LCA investigations. A large-scale photocatalytic treatment process with high efficacy as well as solar-driven and low

This book belongs to Kitab Liaison (ocd1996@gmail.com) Copyright Elsevier 2023

site area requirements could finally be understood in the near future with quick evaluation of diverse potential pilot plant outlines.

Renewable water engineering

The transpiration mechanism has been proposed for rerouting because it is the major cause of groundwater loss, which as well brings about substantial global warming through releasing water vapor into the air. Because electrostatic force has a tendency to tug the water down, therefore, a motionless electricity force created in a plastic tank has been recommended for set up at the bottom of plants to seize the transpiration water vapor and treat it onsite through application of UV technology to help offset everyday water demand all over the world.

Introduction

Plants give O_2 and take CO_2 through photosynthesis to keep the global environment in balance. Plants are simply the heroes for the environment; unfortunately, hero plants are also the villains for the environment that play a significant role in causing global warming. Plants need water for the biochemical metabolism reaction for growth [257]. This water is taken up by the cohesion-tension mechanism of the soil (ground water) through the roots, then transported by osmosis through the xylem to the leaves of the plants [360]. Interestingly, only a mere 0.5%–3% of water is used by plants for their metabolism and the rest is released into the air through stomatal cells by transpiration [5, 53]. This process of transpiration not only causes the largest loss of ground, but is also causing global warming because this water vapor is a notable cause for global warming. Recent studies on the transpiration and ground water relationship have been discussed respectively terrestrial water fluxes where their water models revealed that streamflow getting lower due to the plants transpiration [5, 257]. These are very interesting findings, but no mechanism has been studied yet to trap this transpiration water to meet global water demand. In this research, therefore, a technology has been proposed to eliminate this water loss by collecting this water vapor instead of allowing it to enter the air. We will then transform it into potable water and clean energy. We propose installing plastic tanks that create static electricity near the plants to trap all the water vapor, as the water vapor is attracted by the force of static electricity. Just because water vapor has positive and negative charges and the electrons that ended up on static electrical force has a positive charge, while water molecules have a negative

This book belongs to Kitab Liaison (ocd1996@gmail.com) Copyright Elsevier 2023

charge on one side, the positive charge of static electric force and negative charges of water vapor pull each other closer together, the positive side tug the direction and force the water come down to collect the water in a tank and be treated in site to meet the daily water demand. Calculations reveal that only four standard oak trees could meet the total water demand for a small family throughout the year. Because the ground water strata are getting to lower fast to finite level, and global water and global warming getting dangerous seriously to putting earth on vulnerable condition, thus these two vital needs must be resolved immediately. Interestingly, this new finding offers a total solution to solve the global water and environmental crises for the survival of this planet, and this will indeed open a new door in science.

Methods and simulation

Static electric force generation

To capture the water vapor from air that is released by the stomatal cells of plants during the day, a model been proposed to create the Hossain Static Electric Force ($HsrF = \mathcal{H}$) by implementing the insulator friction into the plastic tank to pull down the water vapor into the plastic tank [14, 16]. To create *HsrF* in the plastic tank, I have implemented an abelian local symmetry calculation by using MATLAB software, considering the gauge field symmetry and the Goldstone scalar with respect to the longitudinal mode of the vector [7, 15]. Thus, for each spontaneously broken particle T^{α} of the local symmetry will be a corresponding gauge field of $A_{\mu}^{\alpha}(x)$ where *HsrF* will start to work at a local U (1) phase symmetry [4, 17]. Therefore, the model will be comprised as a complex scalar field $\Phi(x)$ of static electric charge q coupled to the EM field $A^{\mu}(x)$, which is expressed by $\mathcal{H}$:

$$\mathcal{H} = -\frac{1}{4} F_{\mu\nu} F^{\mu\nu} + D_{\mu}\Phi^{*} D^{\mu}\Phi - V(\Phi^{*}\Phi) \tag{10.51}$$

where

$$D_{\mu}\Phi(x) = \partial_{\mu}\Phi(x) + iqA_{\mu}(x)\Phi(x)$$
$$D_{\mu}\Phi^{*}(x) = \partial_{\mu}\Phi^{*}(x) - iqA_{\mu}(x)\Phi^{*}(x) \tag{10.52}$$

And

$$V(\Phi^{*}\Phi) = \frac{\lambda}{2}(\Phi^{*}\Phi)^{2} + m^{2}(\Phi^{*}\Phi) \tag{10.53}$$

This book belongs to Kitab Liaison (ocd1996@gmail.com) Copyright Elsevier 2023

Suppose $\lambda > 0$ but $m^2 < 0$, so that $\Phi = 0$ is a local maximum of the scalar potential while the minima form a degenerate circle $\Phi = \frac{v}{\sqrt{2}} * e^{i\theta}$,

$$v = \sqrt{\frac{-2m^2}{\lambda}}, \text{any real}\, \theta \tag{10.54}$$

Consequently, the scalar field Φ develops a nonzero vacuum expectation value $\langle \Phi \rangle \neq 0$, which spontaneously creates the U (1) symmetry of the static electric field. The breakdown would lead to a massless Goldstone scalar stemming from the phase of the complex field Φ (x). But for the local U (1) symmetry, the phase of Φ (x)—not just the phase of the expectation value $\langle \Phi \rangle$ but the x-dependent phase of the dynamical Φ (x) field. To analyze this static electricity force mechanism, I have used polar coordinates in the scalar field space, thus

$$\Phi(x) = \frac{1}{\sqrt{2}} \Phi_r(x) * e^{i\Theta(x)}, \text{real}\, \Phi_r(x) > 0, \text{real}\, \Phi(\mathrm{x}) \tag{10.55}$$

This field redefinition is singular when Φ $(x) = 0$, so I never used it for theories with $\langle \Phi \rangle \neq 0$, but it's all right for spontaneously broken theories where I can expect $\Phi \langle x \rangle \neq 0$ almost everywhere. In terms of the real fields $\phi_r(x)$ and $\Theta(x)$, the scalar potential depends only on the radial field ϕ_r,

$$V(\phi) = \frac{\lambda}{8} \left(\phi_r^2 - v^2\right)^2 + \text{const} \tag{10.56}$$

or in terms of the radial field shifted by its VEV, $\Phi_r(x) = v + \sigma(x)$,

$$\phi_r^2 - v^2 = (v + \sigma)^2 - v^2 = 2v\sigma + \sigma^2 \tag{10.57}$$

$$V = \frac{\lambda}{8} \left(2v\sigma - \sigma^2\right)^2 = \frac{\lambda v^2}{2} * \sigma^2 + \frac{\lambda v}{2} * \sigma^3 + \frac{\lambda}{8} * \sigma^4 \tag{10.58}$$

At the same time, the covariant derivative $D_\mu \phi$ becomes

$$D_\mu \phi = \frac{1}{\sqrt{2}} \left(\partial_\mu \left(\phi_r e^{i\Theta}\right) + iqA_\mu * \phi_r e^{i\Theta}\right) = \frac{e^{i\Theta}}{\sqrt{2}} \left(\partial_\mu \phi_r + \phi_r * i\partial_\mu \Theta + \phi_r * iqA_\mu\right) \tag{10.59}$$

$$\begin{aligned} \left|D_\mu \phi\right|^2 &= \frac{1}{2} \left|\partial_\mu \phi_r + \phi_r * i\partial_\mu \Theta + \phi_r * iqA_\mu\right|^2 \\ &= \frac{1}{2} \left(\partial_\mu \phi_r\right) + \frac{\phi_r^2}{2} * \left(\partial_\mu \Theta qA_\mu\right)^2 \\ &= \frac{1}{2} \left(\partial_\mu \sigma\right)^2 + \frac{(v + \sigma)^2}{2} * \left(\partial_\mu \Theta + qA_\mu\right)^2 \end{aligned} \tag{10.60}$$

This book belongs to Kitab Liaison (ocd1996@gmail.com) Copyright Elsevier 2023

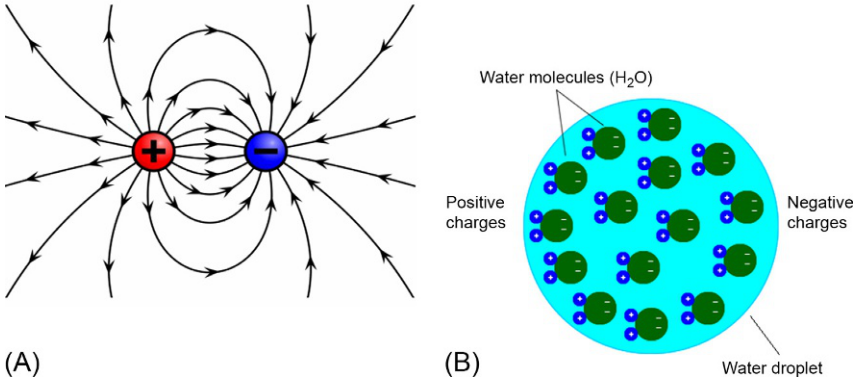

Fig. 10.17 (A) The creating of static electricity force, and (B) its mechanism of conversion of static energy into an electromotive force of positive and negative charges that mobilizes the "static" electricity to tug down the water molecules.

Altogether,

$$\mathfrak{H} = \frac{1}{2}\left(\partial_\mu \sigma\right)^2 - \nu\left(\sigma\right) - \frac{1}{4} F_{\mu\nu} F^{\mu\nu} + \frac{\left(\nu + \sigma\right)^2}{2} * \left(\partial_\mu \Theta + qA_\mu\right)^2 \qquad (10.61)$$

To confirm the creation of this static electric force ($\mathfrak{H}_{\text{sef}}$) into the static electric field properties of this *HsrF*, it has been expanded in powers of the fields (and their derivatives) and focuses on the quadratic part describing the free particles,

$$\mathfrak{H}_{\text{sef}} = \frac{1}{2}\left(\partial_\mu \sigma\right)^2 - \frac{\lambda v^2}{2} * \sigma^2 - \frac{1}{4} F_{\mu\nu} F^{\mu\nu} + \frac{v^2}{2} * \left(qA_\mu + \partial_\mu \Theta\right)^2 \qquad (10.62)$$

Here this HsrF ($\mathfrak{H}_{\text{free}}$) function obviously will suggest a real scalar particle of positive mass $2 = \lambda v^2$ involving the A_μ (x) and the Θ (x) fields to initiate to create a tremendous static electricity force within the electric field of the plastic tank (Fig. 10.17).

Onsite water treatment

Because the collected water in the plastic tank is just nothing but the liquid form of vapor, thus it will not require any sedimentation, coagulation, and or to clean the water. Only mixing physics (UV application) and filtration will be required to treat the water to meet the US National Primary Drinking Water Standard [cc]. It is the simplest way to treat water by using the SODIS system (SOlar DISinfection), where a transparent container is filled with

This book belongs to Kitab Liaison (ocd1996@gmail.com) Copyright Elsevier 2023

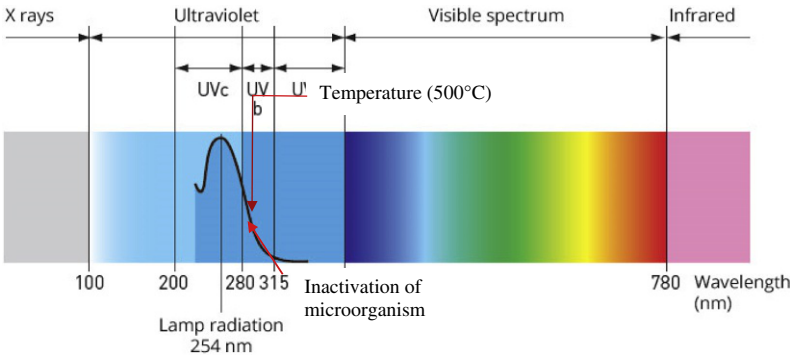

Fig. 10.18 The photo physics radiation application for the purification of water shows that once UV radiation of 320 nm is applied into the water, it starts to disinfect all microorganisms immediately once the temperature reaches at 500°C.

water and exposed to full sunlight for several hours. As soon as the water temperature reaches 50°C with a UV radiation of 320 nm, the inactivation process will be accelerated in order to lead to complete microbiological disinfection immediately and the treated water shall be used to meet the total domestic water demand (Fig. 10.18).

Results and discussion

To mathematically determine the electric static force proliferation around the plastic tank to confirm the tug down of the water, I have initially solved the dynamic photon proliferation by integrating the HSEF electric field to create thus, the local U (1) gauge invariant did allow to add a mass-term for the gauge particle under $\varnothing' \rightarrow e^{i\alpha(x)}\varnothing$ to. In detail, it can be explained by a covariant derivative with a special transformation rule for the scalar field expressing by [52, 236]:

$$\begin{aligned} \partial_\mu \rightarrow D_\mu = \partial_\mu = ieA_\mu \left[\text{covariant derivatives}\right] \\ A'_\mu = A_\mu + \frac{1}{e}\,\partial_\mu \alpha \left[A_\mu \text{derivatives}\right] \end{aligned} \tag{10.63}$$

Where the local U (1) gauge invariant HSEF for a complex scalar field is given by

$$\mathfrak{H} = \left(D^\mu\right)^\dagger \left(D_\mu \varnothing\right) - \frac{1}{4} F_{\mu\nu}F^{\mu\nu} - V(\varnothing) \tag{10.64}$$

The term $\frac{1}{4} F_{\mu\nu}F^{\mu\nu}$ is the kinetic term for the gauge field (heating photon) and $V(\varnothing)$ is the extra term in the HSEF that is $V(\varnothing^*\varnothing) = \mu^2(\varnothing^*\varnothing) + \lambda(\varnothing^*\varnothing)^2$.

This book belongs to Kitab Liaison (ocd1996@gmail.com) Copyright Elsevier 2023

Therefore, the HSEF ($\mathfrak{h}$) under perturbations in the quantum field have initiated with the massive scalar particles $\phi_1$and ϕ_2 along with a mass μ. In this situation, $\mu^2 < 0$ had an infinite number of quantum, each has been satisfied by $\phi_1^2 + \phi_2^2 = -\mu^2/\lambda = v^2$ and the $\mathfrak{h}$ through the covariant derivatives using again the shifted fields η *and* ξ defined the quantum field as $\phi_0 = \frac{1}{\sqrt{2}}\left[(\upsilon + \eta) + i\xi\right]$.

$$\begin{aligned} \text{Kinetic term}: \mathfrak{h}_{(\eta,\,\xi)} &= \left(D^\mu \phi\right)^\dagger \left(D^\mu \phi\right) \\ &= \left(\partial^\mu + ieA^\mu\right)\phi^* \left(\partial_\mu - ieA_\mu\right)\phi \end{aligned} \tag{10.65}$$

Thus, this expanding term in the $\mathfrak{h}$ associated with the scalar field is suggesting that the HSEF electric field is prepared to initiate the proliferation of the static electricity force into its quantum field to tug down the water [1, 225].

To confirm this tug down of water by static electricity, I have implemented the calculation of $\overline{\varphi}[s_0]$ for the confirmation of the expected value of s_0 for capturing water vapor [18, 70]. Thus, the corrective functional asymptotic formulas are being used as follows:

$$\begin{aligned} \overline{\varphi}[s_0] = 2s_0\left(\ln 4s_0 - 2\right) + \ln 4s_0\left(\ln 4s_0 - 2\right) \\ -\frac{\pi^2 - 9}{3} + s_0{}^{-1}\left(\ln 4s_0 + \frac{9}{8}\right) + \ldots (s_0 \gg 1) \end{aligned} \tag{10.66}$$

$$\overline{\varphi}[s_0] = \left(\frac{2}{3}\right)(s_0 - 1)^{\frac{2}{3}} + \left(\frac{5}{3}\right)(s_0 - 1)^{\frac{5}{3}}?\left(\frac{1507}{420}\right)(s_0 - 1)^{\frac{7}{3}} + \ldots (s_0 \gg 1) \tag{10.67}$$

The function $\frac{\overline{\varphi}[s_0]}{(s_0 - 1)}$ is thus described as $1 < s_0 < 10$ for larger s_0, and it contains a natural logarithmic that is s_0 to confirm the tug down of 100% water vapor by the HSEF into the plastic tank.

Then the application of mixing physics (UV application) and filtration for treating this water in the plastic tank as per US National Primary Drinking Water Standard code confirms that this water is potable, and this was analyzed by the SODIS system (SOlar DISinfection).

On average, 100 gallons of water are required per day per person in a standard daily life. [174, 255]. Thus, it will require a total (100 gallons/Day/Person × 4 persons × 365days) of 146,000 gallons of water per year for a small family of four. Because a standard oak tree can transpire 40,000 gallons (151,000 L) per year, thus, a tug down of 100% water vapor by the HSEF described above will require only four standard oak trees to satisfy the total water demand for a small family.

This book belongs to Kitab Liaison (ocd1996@gmail.com) Copyright Elsevier 2023

Conclusions

Water and environmental vulnerability are the top two problems on Earth, where trees play a significant role in creating these problems by the process of transpiration. To mitigate these problems, a transpiration mechanism has been proposed to transform and convert it into clean water to meet the global water demand and reduce global warming by the utilization of electrostatic force to capture this transpiration water vapor and treat it onsite by UV application. This would indeed be a novel, integrated, and innovative field in science to control the global water and global warming crisis.

Acknowledgments

This topic was written by Xiaolei Qu, Pedro J.J. Alvarez, and Qilin Li at the Department of Civil and Environmental Engineering, Rice University, Houston, Texas, United States. I was published as "Applications of nanotechnology in water and wastewater treatment" in Water Research. 47 (2013) 3931-3946.

The writers of this topic are Bo Jin (a, b, c), Christopher W.K. Chow (c), Meng Nan Chong (a, b), Chris Saint (c) at (a) School of Chemical Engineering, The University of Adelaide, 5005 Adelaide, Australia; (b) School of Earth and Environmental Sciences, The University of Adelaide, Adelaide, South Australia 5005, Australia; (c) Australian Water Quality Centre, SA Water Corporation, 5000 Adelaide, South Australia, Australia. It was published as "Recent developments in photocatalytic water treatment technology: A review" in journal "Water Research." 44 (2010); 2997-3027.

This research was supported by Green Globe Technology under grant RD-02018-06 for building a better environment. Any findings, predictions, and conclusions described in this article are solely performed by the authors and we confirm that there is no conflict of interest for publishing in a suitable journal.

References

[1] J. Anotai, Effect of Calcium Ion and Chemistry and Disinfection Efficiency of Free Chlorine at pH 10 (Ph.D dissertation), Drexel University, Philadelphia, 1996.

[2] J. Beltran-Heredia, J. Torregrosa, J.R. Dominguez, J.A. Peres, Comparison of the degradation of p-hydroxybenzoic acid in aqueous solution by several oxidation processes, Chemosphere 42 (2001) 351–359.

[3] G. Gogniat, M. Thyssen, M. Denis, C. Pulgarin, S. Dukan, The bactericidal effect of TiO2 photocatalysis involves adsorption onto catalyst and the loss of membrane integrity, FEMS Microbiol. Lett. 258 (2006) 18–24.

[4] R. Andreozzi, V. Caprio, A. Insola, R. Marotta, Advanced oxidation processes (AOP) for water purification and recovery, Catal. Today 53 (1999) 51–59.

[5] V. Augugliaro, E. García-López, V. Loddo, S. Malato-Rodíguez, I. Maldonado, G. Marcí, R. Molinari, L. Palmisano, Degradation of linomycin in aqueous medium: coupling of solar photocatalysis and membrane separation, Sol. Energy 79 (2005) 402–408.

[6] M. Elimelech, W.A. Phillip, The future of seawater desalination: energy, technology, and the environment, Science 333 (6043) (2011) 712–717.

This book belongs to Kitab Liaison (ocd1996@gmail.com) Copyright Elsevier 2023

[7] S.P. Albu, A. Ghicov, J.M. Macak, R. Hahn, P. Schmuki, Self-organized, free-standing TiO2 nanotube membrane of flow through photocatalytic applications, Nano Lett. 7 (2007) 1286–1289.
[8] S. Bouguecha, B. Hamrouni, M. Dhahbi, Small scale desalination pilots powered by renewable energy sources: case studies, Desalination 183 (2005) 151–165.
[9] D. Bamba, P. Atheba, D. Robert, A. Trokourey, B. Dongui, Photocatalytic degradation of the diuron pesticide, Environ. Chem. Lett. 6 (2008) 163–167.
[10] B. Daus, R. Wennrich, H. Weiss, Sorption materials for arsenic removal from water: a comparative study, Water Res. 38 (12) (2004) 2948–2954.
[11] S. Esplugas, J. Giménez, S. Conteras, E. Pascual, M. Rodríguez, Comparison of different advanced oxidation processes for phenol degradation, Water Res. 36 (2002) 1034–1042.
[12] I.R. Bellobono, F. Morazzoni, R. Bianchi, E.S. Mangone, R. Stanescu, C. Costache, P.M. Tozzi, Solar energy driven photocatalytic membrane modules for water reuse in agricultural and food industries. Pre-industrial experience using s-triazines as model molecules, Int. J. Photoenergy 7 (2005) 87–94.
[13] H.S. Fogler, Elements of Chemical Reaction Engineering: Chapter 10: Catalysis and Catalytic Reactors, Prentice-Hall PTR, New York, 1999, pp. 581–685.
[14] M. Abdullah, G.K.C. Low, R.W. Matthews, Effects of common inorganic anions on rates of photocatalytic oxidation of organic carbon over illuminated titanium dioxide, J. Phys. Chem. 94 (1990) 6820–6825.
[15] F. Ahmed, C.M. Santos, R. Vergara, M.C.R. Tria, R. Advincula, D.F. Rodrigues, Antimicrobial applications of electroactive PVK-SWNT nanocomposites, Environ. Sci. Technol. 46 (3) (2012) 1804–1810.
[16] A. Reinhard, Strongly correlated photons on a chip, in: Nat. Photonics, 23 2011, pp. 4556–4558.
[17] N.M. Al-Bastaki, Performance of advanced methods for treatment of wastewater: UV/TiO2, RO and UF, Chem. Eng. Process. 43 (7) (2004) 935–940.
[18] T.N. Angelidis, M. Koutlemani, I. Poulios, Kinetic study of the photocatalytic recovery of Pt from aqueous solution by TiO2, in a closed-loop reactor, Appl. Catal. B Environ. 16 (1998) 347–357.
[19] A.E. Cassano, O.M. Alfano, Reaction engineering of suspended solid heterogeneous photocatalytic reactors, Catal. Today 58 (2000) 167–197.
[20] WHO, Progress on Drinking Water and Sanitation. 2012 Update, World Heath Organization, Geneva, 2012.
[21] M. Cho, J. Yoon, Measurement of OH radical CT for inactivating Cryptosporidium parvum using photo/ferrioxalate and photo/TiO2 systems, J. Appl. Microbiol. 104 (2008) 759–766.
[22] X.L. Qu, J. Brame, Q. Li, J.J.P. Alvarez, Nanotechnology for a safe and sustainable water supply: enabling integrated water treatment and reuse, Acc. Chem. Res. 46 (3) (2013) 834–843.
[23] W. Gernjak, M.I. Maldonado, S. Malato, J. Cáceres, T. Krutzler, A. Glaser, R. Bauer, Pilot-plant treatment of olive mill wastewater (OMW) by solar TiO2 photocatalysis and solar photo-Fenton, Sol. Energy 77 (2004) 567–572.
[24] B. Pan, B.S. Xing, Adsorption mechanisms of organic chemicals on carbon nanotubes, Environ. Sci. Technol. 42 (24) (2008) 9005–9013.
[25] J. Ryu, W. Choi, K.H. Choo, A pilot-scale photocatalystemembrane hybrid reactor: performance and characterization, Water Sci. Technol. 51 (2005) 491–497.
[26] K. Yang, B.S. Xing, Adsorption of organic compounds by carbon nanomaterials in aqueous phase: Polanyi theory and its application, Chem. Rev. 110 (10) (2010) 5989–6008.
[27] D. Curcó, J. Giménez, A. Addarak, S. Cervera-March, S. Esplugas, Effects of radiation absorption and catalyst concentration on the photocatalytic degradation of pollutants, Catal. Today 76 (2002) 177–188.

This book belongs to Kitab Liaison (ocd1996@gmail.com) Copyright Elsevier 2023

[28] B. Pan, D.H. Lin, H. Mashayekhi, B.S. Xing, Adsorption and hysteresis of bisphenol A and 17 alpha-ethinyl estradiol on carbon nanomaterials, Environ. Sci. Technol. 42 (15) (2008) 5480–5485.
[29] I.R. Bellobono, F. Morazzoni, P.M. Tozzi, Photocatalytic membrane modules for drinking water purification in domestic and community appliances, Int. J. Photoenergy 7 (2005) 109–113.
[30] L.L. Ji, W. Chen, L. Duan, D.Q. Zhu, Mechanisms for strong adsorption of tetracycline to carbon nanotubes: a comparative study using activated carbon and graphite as adsorbents, Environ. Sci. Technol. 43 (7) (2009) 2322–2327.
[31] J. Joo, S.G. Kwon, T. Yu, M. Cho, J. Lee, J. Yoon, T. Hyeon, Large-scale synthesis of TiO2 nanorods via nonhydrolytic solegel ester elimination reaction and their application to photocatalytic inactivation of E. coli, J. Phys. Chem. B 109 (2005) 15297–15302.
[32] C.C. Chen, C.S. Lu, Y.C. Chung, J.L. Jan, UV light induced photodegradation of malachite green on TiO2 nanoparticles, J. Hazard. Mater. 141 (2007) 520–528.
[33] D.H. Lin, B.S. Xing, Adsorption of phenolic compounds by carbon nanotubes: role of aromaticity and substitution of hydroxyl groups, Environ. Sci. Technol. 42 (19) (2008) 7254–7259.
[34] C.S. Lu, H. Chiu, C.T. Liu, Removal of zinc(II) from aqueous solution by purified carbon nanotubes: kinetics and equilibrium studies, Ind. Eng. Chem. Res. 45 (8) (2006) 2850–2855.
[35] K. Yang, W.H. Wu, Q.F. Jing, L.Z. Zhu, Aqueous adsorption of aniline, phenol, and their substitutes by multi-walled carbon manotubes, Environ. Sci. Technol. 42 (21) (2008) 7931–7936.
[36] F. Fornasiero, H.G. Park, J.K. Holt, M. Stadermann, C.P. Grigoropoulos, A. Noy, O. Bakajin, Ion exclusion by sub-2-nm carbon nanotube pores, Proc. Natl. Acad. Sci. USA 105 (45) (2008) 17250–17255.
[37] M.H. Habibi, A. Hassanzadeh, S. Mahdavi, The effect of operational parameters on the photocatalytic degradation of three textile azo dyes in aqueous TiO2 suspensions, J. Photochem. Photobiol. A Chem. 172 (2005) 89–96.
[38] G.P. Rao, C. Lu, F. Su, Sorption of divalent metal ions from aqueous solution by carbon nanotubes: a review, Sep. Purif. Technol. 58 (1) (2007) 224–231.
[39] Y.H. Li, J. Ding, Z.K. Luan, Z.C. Di, Y.F. Zhu, C.L. Xu, D.H. Wu, B.Q. Wei, Competitive adsorption of Pb2+, Cu2+ and Cd2+ ions from aqueous solutions by multiwalled carbon nanotubes, Carbon 41 (14) (2003) 2787–2792.
[40] Q.L. Feng, J. Wu, G.Q. Chen, F.Z. Cui, T.N. Kim, J.O. Kim, A mechanistic study of the antibacterial effect of silver ions on Escherichia coli and Staphylococcus aureus, J. Biomed. Mater. Res. 52 (4) (2000) 662–668.
[41] W. Gao, M. Majumder, L.B. Alemany, T.N. Narayanan, M.A. Ibarra, B.K. Pradhan, P.M. Ajayan, Engineered graphite oxide materials for application in water purification, ACS Appl. Mater. Interfaces 3 (6) (2011) 1821–1826.
[42] Y.H. Li, Z.C. Di, J. Ding, D.H. Wu, Z.K. Luan, Y.Q. Zhu, Adsorption thermodynamic, kinetic and desorption studies of Pb2+ on carbon nanotubes, Water Res. 39 (4) (2005) 605–609.
[43] Z.Y. Liu, H.W. Bai, J. Lee, D.D. Sun, A low-energy forward osmosis process to produce drinking water, Energy Environ. Sci. 4 (7) (2011) 2582–2585.
[44] Y.H. Lin, W.L. Tseng, Ultrasensitive sensing of Hg(2fl) and CH(3)Hg(fl) based on the fluorescence quenching of lysozyme type VI-stabilized gold nanoclusters, Anal. Chem. 82 (22) (2010) 9194–9200.
[45] C. Lu, H. Chiu, H. Bai, Comparisons of adsorbent cost for the removal of zinc (II) from aqueous solution by carbon nanotubes and activated carbon, J. Nanosci. Nanotechnol. 7 (4–5) (2007) 1647–1652.

This book belongs to Kitab Liaison (ocd1996@gmail.com) Copyright Elsevier 2023

[46] J.S. Douglas, H. Habibian, C.-L. Hung, A.V. Gorshkov, H.J. Kimble, D.E. Chang, Quantum many-body models with cold atoms coupled to photonic crystals, Nat. Photonics 12 (2015) 2334–2337.
[47] D. Koeppenkastrop, E.H. Decarlo, Uptake of rare-earth elements from solution by metal-oxides, Environ. Sci. Technol. 27 (9) (1993) 1796–1802.
[48] A. Sukhanova, M. Devy, L. Venteo, H. Kaplan, M. Artemyev, V. Oleinikov, D. Klinov, M. Pluot, J.H.M. Cohen, I. Nabiev, Biocompatible fluorescent nanocrystals for immunolabeling of membrane proteins and cells, Anal. Biochem. 324 (1) (2004) 60–67.
[49] P. Trivedi, L. Axe, Modeling Cd and Zn sorption to hydrous metal oxides, Environ. Sci. Technol. 34 (11) (2000) 2215–2223.
[50] M.J. Rivero, S.A. Parsons, P. Jeffrey, M. Pidou, B. Jefferson, Membrane chemical reactor (MCR) combining photocatalysis and microfiltration for grey water treatment, Water Sci. Technol. 53 (2006) 173–180.
[51] S. Yean, L. Cong, C.T. Yavuz, J.T. Mayo, W.W. Yu, A.T. Kan, V.L. Colvin, M.B. Tomson, Effect of magnetite particle size on adsorption and desorption of arsenite and arsenate, J. Mater. Res. 20 (12) (2005) 3255–3264.
[52] M. Auffan, J. Rose, J.Y. Bottero, G.V. Lowry, J.P. Jolivet, M.R. Wiesner, Towards a definition of inorganic nanoparticles from an environmental, health and safety perspective, Nat. Nanotechnol. 4 (10) (2009) 634–641.
[53] M. Auffan, J. Rose, O. Proux, D. Borschneck, A. Masion, P. Chaurand, J.L. Hazemann, C. Chaneac, J.P. Jolivet, M.R. Wiesner, A. Van Geen, J.Y. Bottero, Enhanced adsorption of arsenic onto maghemites nanoparticles: As(III) as a probe of the surface structure and heterogeneity, Langmuir 24 (7) (2008) 3215–3222.
[54] C.T. Yavuz, J.T. Mayo, W.W. Yu, A. Prakash, J.C. Falkner, S. Yean, L.L. Cong, H.J. Shipley, A. Kan, M. Tomson, D. Natelson, V.L. Colvin, Low-field magnetic separation of monodisperse Fe3O4 nanocrystals, Science 314 (5801) (2006) 964–967.
[55] E. Lucas, S. Decker, A. Khaleel, A. Seitz, S. Fultz, A. Ponce, W.F. Li, C. Carnes, K.J. Klabunde, Nanocrystalline metal oxides as unique chemical reagents/sorbents, Chem Eur J 7 (12) (2001) 2505–2510.
[56] O. Seven, B. Dindar, S. Aydenir, D. Metin, M.A. Ozinel, S. Icli, Solar photocatalytic disinfection of a group of bacteria and fungi aqueous suspensions with TiO2, ZnO and Sahara desert dust, J. Photochem. Photobiol. A Chem. 165 (2004) 103–107.
[57] Y.C. Sharma, V. Srivastava, V.K. Singh, S.N. Kaul, C.H. Weng, Nano-adsorbents for the removal of metallic pollutants from water and wastewater, Environ. Technol. 30 (6) (2009) 583–609.
[58] E.A. Deliyanni, D.N. Bakoyannakis, A.I. Zouboulis, K.A. Matis, Sorption of As(V) ions by akaganeite-type nanocrystals, Chemosphere 50 (1) (2003) 155–163.
[59] J.T. Mayo, C. Yavuz, S. Yean, L. Cong, H. Shipley, W. Yu, J. Falkner, A. Kan, M. Tomson, V.L. Colvin, The effect of nanocrystalline magnetite size on arsenic removal, Sci. Technol. Adv. Mater. 8 (1–2) (2007) 71–75.
[60] M.F. Hossain, Photonic thermal energy control to naturally cool and heat the building, Adv. Therm. Eng. 131 (2018) 576–586.
[61] K.D. Hristovski, P.K. Westerhoff, T. Moller, P. Sylvester, Effect of synthesis conditions on nano-iron (hydr)oxide impregnated granulated activated carbon, Chem. Eng. J. 146 (2) (2009) 237–243.
[62] H. Zhang, X. Quan, S. Chen, H. Zhao, Y. Zhao, Fabrication of photocatalytic membrane and evaluation its efficiency in removal of organic pollutants from water, Sep. Purif. Technol. 50 (2006) 147–155.
[63] J. Hu, G.H. Chen, I.M.C. Lo, Selective removal of heavy metals from industrial wastewater using maghemite nanoparticle: performance and mechanisms, J. Environ. Eng. ASCE 132 (7) (2006) 709–715.

This book belongs to Kitab Liaison (ocd1996@gmail.com) Copyright Elsevier 2023

[64] J. Kim, C.W. Lee, W. Choi, Platinized WO(3) as an environmental photocatalyst that generates OH radicals under visible light, Environ. Sci. Technol. 44 (17) (2010) 6849–6854.
[65] R.G. de Villoria, A.J. Hart, B.L. Wardle, Continuous highyield production of vertically aligned carbon nanotubes on 2D and 3D substrates, ACS Nano 5 (6) (2011) 4850–4857.
[66] E. Evgenidou, K. Fytianos, I. Poulios, Semiconductorsensitized photodegradation of dichlorvos in water using TiO2 and ZnO as catalysts, Appl. Catal. B Environ. 59 (2005) 81–89.
[67] P.G. Collins, K. Bradley, M. Ishigami, A. Zettl, Extreme oxygen sensitivity of electronic properties of carbon nanotubes, Science 287 (5459) (2000) 1801–1804.
[68] R.M. Crooks, M.Q. Zhao, L. Sun, V. Chechik, L.K. Yeung, Dendrimer-encapsulated metal nanoparticles: synthesis, characterization, and applications to catalysis, Acc. Chem. Res. 34 (3) (2001) 181–190.
[69] M.S. Diallo, S. Christie, P. Swaminathan, J.H. Johnson, W.A. Goddard, Dendrimer enhanced ultrafiltration. 1. Recovery of Cu(II) from aqueous solutions using PAMAM dendrimerswithethylenediamine core andterminal NH2 groups, Environ. Sci. Technol. 39 (5) (2005) 1366–1377.
[70] M. Aragon, R. Kottenstette, B. Dwyer, A. Aragon, R. Everett, W. Holub, M. Siegel, J. Wright, Arsenic Pilot Plant Operation and Results, Sandia National Laboratories, Anthony, NM, 2007.
[71] P. Sylvester, P. Westerhoff, T. Mooller, M. Badruzzaman, O. Boyd, A hybrid sorbent utilizing nanoparticles of hydrous iron oxide for arsenic removal from drinking water, Environ. Eng. Sci. 24 (1) (2007) 104–112.
[72] P. Westerhoff, M. De Haan, A. Martindale, M. Badruzzaman, Arsenic adsorptive media technology selection strategies, Water Qual. Res. J. Can. 41 (2) (2006) 171–184.
[73] T.E. Cloete, M.D. Kwaadsteniet, M. Botes, J.M. Lopez-Romero, Nanotechnology in Water Treatment Applications, Caister Academic Press, London, 2010.
[74] D. Li, Y. Xia, Electrospinning of nanofibers: reinventing the wheel? Adv. Mater. 16 (14) (2004) 1151–1170.
[75] S. Ramakrishna, K. Fujihara, W.E. Teo, T. Yong, Z.W. Ma, R. Ramaseshan, Electrospun nanofibers: solving global issues, Mater. Today 9 (3) (2006) 40–50.
[76] T.H. Bae, T.M. Tak, Effect of TiO2 nanoparticles on fouling mitigation of ultrafiltration membranes for activated sludge filtration, J. Membr. Sci. 249 (2005) 1–8.
[77] A. Bottino, G. Capannelli, V. D'Asti, P. Piaggio, Preparation and properties of novel organic-inorganic porous membranes, Sep. Purif. Technol. 22–23 (1–3) (2001) 269–275.
[78] N. Maximous, G. Nakhla, K. Wong, W. Wan, Optimization of Al(2)O(3)/PES membranes for wastewater filtration, Sep. Purif. Technol. 73 (2) (2010) 294–301.
[79] M.T.M. Pendergast, J.M. Nygaard, A.K. Ghosh, E.M.V. Hoek, Using nanocomposite materials technology to understand and control reverse osmosis membrane compaction, Desalination 261 (3) (2010) 255–263.
[80] K. Ebert, D. Fritsch, J. Koll, C. Tjahjawiguna, Influence of inorganic fillers on the compaction behaviour of porous polymer based membranes, J. Membr. Sci. 233 (1-2) (2004) 71–78.
[81] B. De Gusseme, T. Hennebel, E. Christiaens, H. Saveyn, K. Verbeken, J.P. Fitts, N. Boon, W. Verstraete, Virus disinfection in water by biogenic silver immobilized in polyvinylidene fluoride membranes, Water Res. 45 (4) (2011) 1856–1864.
[82] M.S. Mauter, Y. Wang, K.C. Okemgbo, C.O. Osuji, E.P. Giannelis, M. Elimelech, Antifouling ultrafiltration membranes via post-fabrication grafting of biocidal nanomaterials, ACS Appl. Mater. Interfaces 3 (8) (2011) 2861–2868.

This book belongs to Kitab Liaison (ocd1996@gmail.com) Copyright Elsevier 2023

[83] K. Zodrow, L. Brunet, S. Mahendra, D. Li, A. Zhang, Q.L. Li, P.J.J. Alvarez, Polysulfone ultrafiltration membranes impregnated with silver nanoparticles show improved biofouling resistance and virus removal, Water Res. 43 (3) (2009) 715–723.
[84] A.S. Brady-Estevez, S. Kang, M. Elimelech, A single-walledcarbon-nanotube filter for removal of viral and bacterial pathogens, Small 4 (4) (2008) 481–484.
[85] J.H. Choi, J. Jegal, W.N. Kim, Fabrication and characterization of multi-walled carbon nanotubes/polymer blend membranes, J. Membr. Sci. 284 (1–2) (2006) 406–415.
[86] H. Choi, E. Stathatos, D.D. Dionysiou, Sol-gel preparation of mesoporous photocatalytic TiO2 films and TiO2/Al2O3 composite membranes for environmental applications, Appl. Catal. B Environ. 63 (1–2) (2006) 60–67.
[87] L. Wu, M. Shamsuzzoha, S.M.C. Ritchie, Preparation of cellulose acetate supported zero-valent iron nanoparticles for the dechlorination of trichloroethylene in water, J. Nanopart. Res. 7 (4–5) (2005) 469–476.
[88] L.F. Wu, S.M.C. Ritchie, Enhanced dechlorination of trichloroethylene by membrane-supported Pd-coated iron nanoparticles, Environ. Prog. 27 (2) (2008) 218–224.
[89] M.L. Lind, A.K. Ghosh, A. Jawor, X.F. Huang, W. Hou, Y. Yang, E.M.V. Hoek, Influence of zeolite crystal size on zeolitepolyamide thin film nanocomposite membranes, Langmuir 25 (17) (2009) 10139–10145.
[90] B.H. Jeong, E.M.V. Hoek, Y.S. Yan, A. Subramani, X.F. Huang, G. Hurwitz, A.K. Ghosh, A. Jawor, Interfacial polymerization of thin film nanocomposites: a new concept for reverse osmosis membranes, J. Membr. Sci. 294 (1–2) (2007) 1–7.
[91] M.L. Lind, D.E. Suk, T.V. Nguyen, E.M.V. Hoek, Tailoring the structure of thin film nanocomposite membranes to achieve seawater RD membrane performance, Environ. Sci. Technol. 44 (21) (2010) 8230–8235.
[92] M.L. Lind, B.H. Jeong, A. Subramani, X.F. Huang, E.M.V. Hoek, Effect of mobile cation on zeolite-polyamide thin film nanocomposite membranes, J. Mater. Res. 24 (5) (2009) 1624–1631.
[93] P. Fernándezs-Ináñez, C. Sichel, M.I. Poloo López, M. de Cara-Garcia, J.C. Tello, Photocatalytic disinfection of natural well water contaminated by Fusarium solani using TiO2 slurry in solar CPC photo-reactors, Catal. Today 144 (2009) 62–68.
[94] S.S. Chin, K. Chiang, A.G. Fane, The stability of polymeric membranes in TiO2 photocatalysis process, J. Membr. Sci. 275 (2006) 202–211.
[95] A. Tiraferri, C.D. Vecitis, M. Elimelech, Covalent binding of single-walled carbon nanotubes to polyamide membranes for antimicrobial surface properties, ACS Appl. Mater. Interfaces 3 (8) (2011) 2869–2877.
[96] M. Kumar, M. Grzelakowski, J. Zilles, M. Clark, W. Meier, Highly permeable polymeric membranes based on the incorporation of the functional water channel protein Aquaporin Z, Proc. Natl. Acad. Sci. USA 104 (52) (2007) 20719–20724.
[97] Y. Kaufman, A. Berman, V. Freger, Supported lipid bilayer membranes for water purification by reverse osmosis, Langmuir 26 (10) (2010) 7388–7395.
[98] J.K. Holt, H.G. Park, Y.M. Wang, M. Stadermann, A.B. Artyukhin, C.P. Grigoropoulos, A. Noy, O. Bakajin, Fast mass transport through sub-2-nanometer carbon nanotubes, Science 312 (5776) (2006) 1034–1037.
[99] G. Hummer, J.C. Rasaiah, J.P. Noworyta, Water conduction through the hydrophobic channel of a carbon nanotube, Nature 414 (6860) (2001) 188–190.
[100] M.M. Pendergast, E.M.V. Hoek, A review of water treatment membrane nanotechnologies, Energy Environ. Sci. 4 (6) (2011) 1946–1971.
[101] M.S. Mauter, M. Elimelech, Environmental applications of carbon-based nanomaterials, Environ. Sci. Technol. 42 (16) (2008) 5843–5859.
[102] P. Nednoor, N. Chopra, V. Gavalas, L.G. Bachas, B.J. Hinds, Reversible biochemical switching of ionic transport through aligned carbon nanotube membranes, Chem. Mater. 17 (14) (2005) 3595–3599.

This book belongs to Kitab Liaison (ocd1996@gmail.com) Copyright Elsevier 2023

[103] B. Hinds, Dramatic transport properties of carbon nanotube membranes for a robust protein channel mimetic platform, Curr. Opin. Solid State Mater. Sci. 16 (1) (2012) 1–9.
[104] M.S. Mauter, M. Elimelech, C.O. Osuji, Nanocomposites of vertically aligned single-walled carbon nanotubes by magnetic alignment and polymerization of a lyotropic precursor, ACS Nano 4 (11) (2010) 6651–6658.
[105] Q.C. Ge, J.C. Su, T.S. Chung, G. Amy, Hydrophilic superparamagnetic nanoparticles: synthesis, characterization, and performance in forward osmosis processes, Ind. Eng. Chem. Res. 50 (1) (2011) 382–388.
[106] A. Fujishima, X. Zhang, D.A. Tryk, TiO2 photocatalysis and related surface phenomena, Surf. Sci. Rep. 63 (2008) 515–582.
[107] H.Z. Zhang, J.F. Banfield, Understanding polymorphic phase transformation behavior during growth of nanocrystalline aggregates: insights from TiO2, J. Phys. Chem. B 104 (15) (2000) 3481–3487.
[108] Z.B. Zhang, C.C. Wang, R. Zakaria, J.Y. Ying, Role of particle size in nanocrystalline TiO2-based photocatalysts, J. Phys. Chem. B 102 (52) (1998) 10871–10878.
[109] J.M. Macak, M. Zlamal, J. Krysa, P. Schmuki, Selforganized TiO2 nanotube layers as highly efficient photocatalysts, Small 3 (2) (2007) 300–304.
[110] M. Ni, M.K.H. Leung, D.Y.C. Leung, K. Sumathy, A review and recent developments in photocatalytic water-splitting using TiO2 for hydrogen production, Renew. Sust. Energ. Rev. 11 (2007) 401–425.
[111] X.G. Han, Q. Kuang, M.S. Jin, Z.X. Xie, L.S. Zheng, Synthesis of titania nanosheets with a high percentage of exposed (001) facets and related photocatalytic properties, J. Am. Chem. Soc. 131 (9) (2009) 3152.
[112] N. Murakami, Y. Kurihara, T. Tsubota, T. Ohno, Shapecontrolled anatase titanium(IV) oxide particles prepared by hydrothermal treatment of peroxo titanic acid in the presence of polyvinyl alcohol, J. Phys. Chem. C 113 (8) (2009) 3062–3069.
[113] S.W. Liu, J.G. Yu, M. Jaroniec, Anatase TiO(2) with dominant high-energy {001} facets: synthesis, properties, and applications, Chem. Mater. 23 (18) (2011) 4085–4093.
[114] M. Kitano, K. Funatsu, M. Matsuoka, M. Ueshima, M. Anpo, Preparation of nitrogen-substituted TiO(2) thin film photocatalysts by the radio frequency magnetron sputtering deposition method and their photocatalytic reactivity under visible light irradiation, J. Phys. Chem. B 110 (50) (2006) 25266–25272.
[115] H. Kominami, K. Yabutani, T. Yamamoto, Y. Kara, B. Ohtani, Synthesis of highly active tungsten(VI) oxide photocatalysts for oxygen evolution by hydrothermal treatment of aqueous tungstic acid solutions, J. Mater. Chem. 11 (12) (2001) 3222–3227.
[116] J. Lee, Y. Mackeyev, M. Cho, L.J. Wilson, J.H. Kim, P.J.J. Alvarez, C(60) aminofullerene immobilized on silica as a visiblelight-activated photocatalyst, Environ. Sci. Technol. 44 (24) (2010) 9488–9495.
[117] R. Lof, M. Van Veenendaal, H. Jonkman, G. Sawatzky, Band gap, excitons and Coulomb interactions of solid C 60, J. Electron Spectrosc. Relat. Phenom. 72 (1995) 83–87.
[118] L. Brunet, D.Y. Lyon, E.M. Hotze, P.J.J. Alvarez, M.R. Wiesner, Comparative photoactivity and antibacterial properties of C-60 fullerenes and titanium dioxide nanoparticles, Environ. Sci. Technol. 43 (12) (2009) 4355–4360.
[119] M.N. Chong, B. Jin, C.W.K. Chow, C. Saint, Recent developments in photocatalytic water treatment technology: a review, Water Res. 44 (10) (2010) 2997–3027.
[120] M.J. Benotti, B.D. Stanford, E.C. Wert, S.A. Snyder, Evaluation of a photocatalytic reactor membrane pilot system of pharmaceuticals and endocrine disrupting compounds from water, Water Res. 43 (2009) 1513–1522.

This book belongs to Kitab Liaison (ocd1996@gmail.com) Copyright Elsevier 2023

[121] P. Westerhoff, H. Moon, D. Minakata, J. Crittenden, Oxidation of organics in retentates from reverse osmosis wastewater reuse facilities, Water Res. 43 (16) (2009) 3992–3998.
[122] J. Nawrocki, B. Kasprzyk-Hordern, The efficiency and mechanisms of catalytic ozonation, Appl. Catal. B Environ. 99 (1–2) (2010) 27–42.
[123] C.A. Orge, J.J.M. Orfao, M.F.R. Pereira, A.M.D. de Farias, R.C.R. Neto, M.A. Fraga, Ozonation of model organic compounds catalysed by nanostructured cerium oxides, Appl. Catal. B Environ. 103 (1–2) (2011) 190–199.
[124] Q.L. Li, S. Mahendra, D.Y. Lyon, L. Brunet, M.V. Liga, D. Li, P.J.J. Alvarez, Antimicrobial nanomaterials for water disinfection and microbial control: potential applications and implications, Water Res. 42 (18) (2008) 4591–4602.
[125] Z.M. Xiu, J. Ma, P.J.J. Alvarez, Differential effect of common ligands and molecular oxygen on antimicrobial activity of silver nanoparticles versus silver ions, Environ. Sci. Technol. 45 (20) (2011) 9003–9008.
[126] Z.M. Xiu, Q.B. Zhang, H.L. Puppala, V.L. Colvin, J.J.P. Alvarez, Negligible particle-specific antibacterial activity of silver nanoparticles, Nano Lett. 12 (8) (2012) 4271–4275.
[127] S.Y. Liau, D.C. Read, W.J. Pugh, J.R. Furr, A.D. Russell, Interaction of silver nitrate with readily identifiable groups: relationship to the antibacterial action of silver ions, Lett. Appl. Microbiol. 25 (4) (1997) 279–283.
[128] S.B. Liu, T.H. Zeng, M. Hofmann, E. Burcombe, J. Wei, R.R. Jiang, J. Kong, Y. Chen, Antibacterial activity of graphite, graphite oxide, graphene oxide, and reduced graphene oxide: membrane and oxidative stress, ACS Nano 5 (9) (2011) 6971–6980.
[129] C.D. Vecitis, K.R. Zodrow, S. Kang, M. Elimelech, Electronic-structure-dependent bacterial cytotoxicity of single-walled carbon nanotubes, ACS Nano 4 (9) (2010) 5471–5479.
[130] S. Kang, M. Herzberg, D.F. Rodrigues, M. Elimelech, Antibacterial effects of carbon nanotubes: size does matter, Langmuir 24 (13) (2008) 6409–6413.
[131] S. Kang, M.S. Mauter, M. Elimelech, Physicochemical determinants of multiwalled carbon nanotube bacterial cytotoxicity, Environ. Sci. Technol. 42 (19) (2008) 7528–7534.
[132] M. Peter-Varbanets, C. Zurbrugg, C. Swartz, W. Pronk, Decentralized systems for potable water and the potential of membrane technology, Water Res. 43 (2) (2009) 245–265.
[133] A.S. Brady-Estevez, M.H. Schnoor, S. Kang, M. Elimelech, SWNT-MWNT hybrid filter attains high viral removal and bacterial inactivation, Langmuir 26 (24) (2010) 19153–19158.
[134] M.S. Rahaman, C.D. Vecitis, M. Elimelech, Electrochemical carbon-nanotube filter performance toward virus removal and inactivation in the presence of natural organic matter, Environ. Sci. Technol. 46 (3) (2012) 1556–1564.
[135] C.D. Vecitis, M.H. Schnoor, M.S. Rahaman, J.D. Schiffman, M. Elimelech, Electrochemical multiwalled carbon nanotube filter for viral and bacterial removal and inactivation, Environ. Sci. Technol. 45 (8) (2011) 3672–3679.
[136] J. Theron, T.E. Cloete, M. de Kwaadsteniet, Current molecular and emerging nanobiotechnology approaches for the detection of microbial pathogens, Crit. Rev. Microbiol. 36 (4) (2010) 318–339.
[137] P.J. Vikesland, K.R. Wigginton, Nanomaterial enabled biosensors for pathogen monitoring—a review, Environ. Sci. Technol. 44 (10) (2010) 3656–3669.
[138] J.L. Yan, M.C. Estevez, J.E. Smith, K.M. Wang, X.X. He, L. Wang, W.H. Tan, Dye-doped nanoparticles for bioanalysis, Nano Today 2 (3) (2007) 44–50.

This book belongs to Kitab Liaison (ocd1996@gmail.com) Copyright Elsevier 2023

[139] E. Petryayeva, U.J. Krull, Localized surface plasmon resonance: nanostructures, bioassays and biosensing e a review, Anal. Chim. Acta 706 (1) (2011) 8–24.
[140] J.P. Lei, H.X. Ju, Signal amplification using functional nanomaterials for biosensing, Chem. Soc. Rev. 41 (6) (2012) 2122–2134.
[141] P.K. Jain, K.S. Lee, I.H. El-Sayed, M.A. El-Sayed, Calculated absorption and scattering properties of gold nanoparticles of different size, shape, and composition: applications in biological imaging and biomedicine, J. Phys. Chem. B 110 (14) (2006) 7238–7248.
[142] K.L. Kelly, E. Coronado, L.L. Zhao, G.C. Schatz, The optical properties of metal nanoparticles: the influence of size, shape, and dielectric environment, J. Phys. Chem. B 107 (3) (2003) 668–677.
[143] M. Moskovits, Surface-enhanced Raman spectroscopy: a brief retrospective, J. Raman Spectrosc. 36 (6–7) (2005) 485–496.
[144] S.M. Nie, S.R. Emery, Probing single molecules and single nanoparticles by surface-enhanced Raman scattering, Science 275 (5303) (1997) 1102–1106.
[145] R.L. McCreery, Advanced carbon electrode materials for molecular electrochemistry, Chem. Rev. 108 (7) (2008) 2646–2687.
[146] W.R. Yang, K.R. Ratinac, S.P. Ringer, P. Thordarson, J.J. Gooding, F. Braet, Carbon nanomaterials in biosensors: should you use nanotubes or graphene? Angew. Chem. Int. Ed. 49 (12) (2010) 2114–2138.
[147] I. Heller, A.M. Janssens, J. Mannik, E.D. Minot, S.G. Lemay, C. Dekker, Identifying the mechanism of biosensing with carbon nanotube transistors, Nano Lett. 8 (2) (2008) 591–595.
[148] A. Duran, M. Tuzen, M. Soylak, Preconcentration of some trace elements via using multiwalled carbon nanotubes as solid phase extraction adsorbent, J. Hazard. Mater. 169 (1-3) (2009) 466–471.
[149] Y.Q. Cai, G.B. Jiang, J.F. Liu, Q.X. Zhou, Multiwalled carbon nanotubes as a solid-phase extraction adsorbent for the determination of bisphenol a, 4-n-nonylphenol, and 4-tertoctylphenol, Anal. Chem. 75 (10) (2003) 2517–2521.
[150] K.P. Lisha, Anshup, T. Pradeep, Enhanced visual detection of pesticides using gold nanoparticles, J. Environ. Sci. Heal. B 44 (7) (2009) 697–705.
[151] L.X. Yang, B.B. Chen, S.L. Luo, J.X. Li, R.H. Liu, Q.Y. Cai, Sensitive detection of polycyclic aromatic hydrocarbons using CdTe quantum dot-modified TiO(2) nanotube array through fluorescence resonance energy transfer, Environ. Sci. Technol. 44 (20) (2010) 7884–7889.
[152] H.S. Yin, Y.L. Zhou, S.Y. Ai, Q.P. Chen, X.B. Zhu, X.G. Liu, L.S. Zhu, Sensitivity and selectivity determination of BPA in real water samples using PAMAM dendrimer and CoTe quantum dots modified glassy carbon electrode, J. Hazard. Mater. 174 (1–3) (2010) 236–243.
[153] B.F. da Silva, S. Perez, P. Gardinalli, R.K. Singhal, A.A. Mozeto, D. Barcelo, Analytical chemistry of metallic nanoparticles in natural environments, TrAC Trends Anal. Chem. 30 (3) (2011) 528–540.
[154] K. Tiede, A.B.A. Boxall, S.P. Tear, J. Lewis, H. David, M. Hassellov, Detection and characterization of engineered nanoparticles in food and the environment, Food Addit. Contam. 25 (7) (2008) 795–821.
[155] S. Malato, P. Fernández-Ibáñez, M.I. Maldonado, J. Blanco, W. Gernjak, Decontamination and disinfection of water by solar photocatalysis: recent overview and trends, Catal. Today 147 (2009) 1–59.
[156] S.D. Richardson, Environmental mass spectrometry: emerging contaminants and current issues, Anal. Chem. 80 (2008) 4373–4402.
[157] S. Suárez, M. Carballa, F. Omil, J.M. Lema, How are pharmaceutical and personal care products (PPCPs) removed from urban wastewaters? Rev. Environ. Sci. Biotechnol. 7 (2008) 125–138.

This book belongs to Kitab Liaison (ocd1996@gmail.com) Copyright Elsevier 2023

[158] T. Wintgens, F. Salehi, R. Hochstrat, T. Melin, Emerging contaminants and treatment options in water recycling for indirect potable use, Water Sci. Technol. 57 (2008) 99–107.
[159] B.R. Bradley, G.T. Daigger, R. Rubin, G. Tchobanoglous, Evaluation of onsite wastewater treatment technologies using sustainable development criteria, Clean Techn. Environ. Policy 4 (2002) 87–99.
[160] L. Lapña, M. Cerezo, P. Garía-Augustin, Possible reuse of treated municipal wastewater for Citrus spp. plant irrigation, Bull. Environ. Contam. Toxicol. 55 (1995) 697–703.
[161] W. Viessman Jr., M.J. Hammer, Water Supply and Pollution Control, sixth ed., Addison Wesley Longman, California, 1998.
[162] P.V.A. Padmanabhan, K.P. Sreekumar, T.K. Thiyagarajan, R.U. Satpute, K. Bhanumurthy, P. Sengupta, G.K. Dey, K.G.K. Warrier, Nano-crystalline titanium dioxide formed by reactive plasma synthesis, Vacuum 80 (11–12) (2006) 21–26.
[163] U.I. Gaya, A.H. Abdullah, Heterogeneous photocatalytic degradation of organic contaminants over titanium dioxide: a review of fundamentals, progress and problems, J Photochem Photobiol C: Photochem Rev 9 (2008) 1–12.
[164] H.M. Coleman, C.P. Marquis, J.A. Scott, S.S. Chin, R. Amal, Bactericidal effects of titanium dioxide-based photocatalysts, Chem. Eng. J. 113 (2005) 55–63.
[165] J. Lu, T. Zhang, J. Ma, Z. Chen, Evaluation of disinfection by-products formation during chlorination and chloramination of dissolved natural organic matter fractions isolated from a filtered river water, J. Hazard. Mater. 162 (2009) 140–145.
[166] H. Yang, H. Cheng, Controlling nitrite level in drinking water by chlorination and chloramination, Sep. Purif. Technol. 56 (2007) 392–396.
[167] M. Pera-Titus, V. García-Molina, M.A. Baños, J. Giménez, S. Esplugas, Degradation of chlorophenols by means of advanced oxidation processes: a general review, Appl. Catal. B Environ. 47 (2004) 219–256.
[168] A. Fujishima, T.N. Rao, D.A. Tryk, Titanium dioxide photocatalysis, J. Photochem. Photobiol. C: Photochem. Rev. 1 (2000) 1–21.
[169] A. Furube, T. Asahi, H. Masuhara, H. Yamashita, M. Anpo, Direct observation of a picosecond charge separation process in photoexcited platinum-loaded TiO2 particlees by femtosecond diffuse reflectance spectroscopy, Chem. Phys. Lett. 336 (2001) 424–430.
[170] J.A. Byrne, B.R. Eggins, Photoelectrochemistry of oxalate on particulate TiO2 electrodes, J. Electroanal. Chem. 457 (1998) 61–72.
[171] J.M. Herrmann, Heterogeneous photocatalysis: fundamentals and applications to the removal of various types of aqueous pollutants, Catal. Today 53 (1999) 115–129.
[172] K. Vinodgopal, P.V. Kamat, Photochemistry on surfaces: photodegradation of 1, 3-diphenylisobenzofuran over metal oxide particles, J. Phys. Chem. 96 (1992) 5053–5059.
[173] P.C. Maness, S. Smolinski, D.M. Blake, Z. Huang, E.J. Wolfrum, W.A. Jacoby, Bactericidal activity of photocatalytic TiO2 reaction: toward an understanding of its killing mechanism, Appl. Environ. Microbiol. 65 (1999) 4094–4098.
[174] J. Bacardit, J. Stötzner, E. Chamarro, Effect of salinity on the photo-Fenton process, Ind. Eng. Chem. Res. 46 (2007) 7615–7619.
[175] A. Machulek Jr., J.E.F. Moraes, C. Vautier-Giongo, C.A. Silverio, L.C. Friedrich, C. A.O. Nascimento, M.C. Gonzalez, F.H. Quina, Abatement of the inhibitory effect of chloride anions on the photo-Fenton process, Environ. Sci. Technol. 41 (2007) 8459–8463.
[176] E. Neyens, J. Baeyens, A review of classic Fenton's peroxidation as an advanced oxidation technique, Water Res. 98 (2003) 33–50.
[177] H. Fallmann, T. Krutzler, R. Bauer, S. Malato, J. Blanco, Applicability of the photo-Fenton method for treating water containing pesticides, Catal. Today 54 (1999) 309–319.

This book belongs to Kitab Liaison (ocd1996@gmail.com) Copyright Elsevier 2023

[178] W. Gernjak, T. Krutzler, S. Malato, Photo-Fenton treatmentof olive mill wastewater applying a combined Fenton/ flocculation pretreatment, J. Sol. Energy Eng. 129 (2007) 53–59.
[179] P.L. Huston, J.J. Pignatello, Degradation of selected pesticide active ingredients and commercial formulations in water by the photo-assisted Fenton reaction, Water Res. 33 (1999) 1238–1246.
[180] P.R. Gogate, A.B. Pandit, A review of imperative technologies for wastewater treatment II: hybrid methods, Adv. Environ. Res. 8 (2004) 553–597.
[181] J.J. Pignatello, E. Oliveros, A. MacKay, Advanced oxidation processes for organic contaminant destruction based on the Fenton reaction and related chemistry, Crit. Rev. Environ. Sci. Technol. 36 (2006) 1–84.
[182] J. De Laat, G.T. Le, B. Legube, A comparative study of the effects of chloride, sulphate and nitrate ions on the rates of decomposition of H_2O_2 and organic compounds by Fe(II)/H_2O_2 and Fe(III)/H_2O_2, Chemosphere 55 (2004) 715–723.
[183] E. Oliveros, O. Legrini, M. Hohl, T. Müller, A.M. Braun, Industrial wastewater treatment: large scale development of a light-enhanced Fenton reaction, Chem. Eng. Process. 36 (1997) 397–405.
[184] F. Torrades, M. Pérez, H.D. Mansilla, J. Peral, Experimental design of Fenton and photo-Fenton reactions for the treatment of cellulose bleaching effluents, Chemosphere 53 (2003) 1211–1220.
[185] C. Dominguez, J. García, M.A. Pedraz, A. Torres, M.A. Galán, Photocatalytic oxidation of organic pollutants in water, Catal. Today 40 (1998) 85–101.
[186] J. Marugán, M.J. Lopez-Muñoz, W. Gernjak, S. Malato, Fe/ TiO2/pH interactions in solar degradation of imidacloprid with TiO2/SiO2 photocatalysts at pilot-plant scale, Ind. Eng. Chem. Res. 45 (2006) 8900–8908.
[187] J. Marugán, R. van Grieken, C. Sordo, C. Cruz, Kinetics of the photocatalytic disinfection of Escherichia coli suspensions, Appl. Catal. B Environ. 82 (2008) 27–36.
[188] A.G. Rincón, C. Pulgarin, Comparative evaluation of Fe3+ and TiO2 photoassisted processes in solar photocatalytic disinfection of water, Appl. Catal. B Environ. 63 (2006) 222–231.
[189] R.A. Torres, J.I. Nieto, E. Combet, C. Pétrier, C. Pulgarin, Influence of TiO2 concentration on the synergistic effect between photocatalysis and high-frequency ultrasound for organic pollutant mineralization in water, Appl. Catal. B Environ. 80 (2008) 168–175.
[190] A. Fujishima, K. Honda, Electrochemical photolysis of water at a semiconductor electrode, Nature 238 (1972) 37–38.
[191] E. Hosono, S. Fujihara, K. Kakiuchi, H. Imai, Growth of submicrometer-scale reactangular parallelepiped rutile TiO2 films in aqueous TiCl3 solutions under hydrothermal conditions, J. Am. Chem. Soc. 126 (2004) 7790–7791.
[192] Y. Kondo, H. Yoshikawa, K. Awaga, M. Murayama, T. Mori, K. Sunada, S. Bandow, S. Iijima, Preparation, photocatalytic activities, and dye-sensitized solar-cell performance of submicron-scale TiO2 hollow spheres, Langmuir 24 (2008) 547–550.
[193] R. Wang, K. Hashimoto, A. Fujishima, M. Chikuni, E. Kojima, A. Kitamura, M. Shimohigoshi, T. Watanabe, Photogeneration of highly amphiphilic TiO2 surfaces, Adv. Mater. 10 (1999) 135–138.
[194] K. Nagaveni, G. Sivalingam, M.S. Hegde, G. Madras, Solar photocatalytic degradation of dyes. High activity of combustion synthesized nano TiO2, Appl. Catal. B Environ. 48 (2004) 83–93.
[195] K. Nagaveni, G. Sivalingam, M.S. Hegde, G. Madras, Photocatalytic degradation of organic compounds over combustion synthesized nano-TiO2, Environ. Sci. Technol. 38 (2004) 1600–1604.

This book belongs to Kitab Liaison (ocd1996@gmail.com) Copyright Elsevier 2023

[196] I.A. Siddiquey, T. Furusawa, M. Sato, K. Honda, N. Suzuki, Control of the photocatalytic activity of TiO2 nanoparticles by silica coating with polydiethoxysiloxane, Dyes Pigments 76 (2008) 754–759.
[197] J.A. Byrne, B.R. Eggins, N.M.D. Brown, B. McKinley, M. Rouse, Immobilisation of TiO2 powder for the treatment of polluted water, Appl. Catal. B Environ. 17 (1998) 25–36.
[198] J.C. Yu, J. Yu, J. Zhao, Enhanced photocatalytic activity of mesoporous and ordinary TiO2 thin films by sulphuric acid treatment, Appl. Catal. B Environ. 36 (2002) 31–43.
[199] N. Serpone, G. Sauvé, R. Koch, H. Tahiri, P. Pichat, P. Piccinini, E. Pelizetti, H. Hidaka, Standardization protocol of process efficiencies and activation parameters in heterogeneous photocatalysis: relative photonic efficiencies zr, J. Photochem. Photobiol. A Chem. 94 (1996) 191–203.
[200] R.L. Pozzo, M.A. Baltanás, A.E. Cassano, Supported titanium dioxide as photocatalyst in water decontamination: state of the art, Catal. Today 39 (1997) 219–231.
[201] G.C.C. Yang, C.J. Li, Electrofiltration of silica nanoparticlecontaining wastewater using tubular ceramic membranes, Sep. Purif. Technol. 58 (2007) 159–165.
[202] T.E. Doll, F.H. Frimmel, Cross-flow microfiltration with periodical back-washing for photocatalytic degradation of pharmaceutical and diagnostic residues-evaluation of the long-term stability of the photocatalytic activity of TiO2, Water Res. 39 (2005) 847–854.
[203] P. Fernández-Ibáñez, J. Blanco, S. Malato, F.J. de las Nieves, Application of the colloidal stability of TiO2 particles for recovery and reuse in solar photocatalysis, Water Res. 37 (2003) 3180–3188.
[204] X. Zhang, A.J. Du, P. Lee, D.D. Sun, J.O. Leckie, TiO2 nanowire membrane for concurrent filtration and photocatalytic oxidation of humic acid in water, J. Membr. Sci. 313 (2008) 44–51.
[205] Y. Zhao, J. Zhong, H. Li, N. Xu, J. Shi, Fouling and regeneration of ceramic microfiltration membranes in processing acid wastewater containing fine TiO2 particles, J. Membr. Sci. 208 (2002) 331–341.
[206] S.A. Lee, K.H. Choo, C.H. Lee, H.I. Lee, T. Hyeon, W. Choi, H.H. Kwon, Use of ultrafiltration membranes for the separation of TiO2 photocatalysts in drinking water treatment, Ind. Eng. Chem. Res. 40 (2001) 1712–1719.
[207] R. Molinari, L. Palmisano, E. Drioli, M. Schiavello, Studies on various reactor configurations for coupling photocatalysis and membrane processes in water purification, J. Membr. Sci. 206 (2002) 399–415.
[208] W. Xi, S. Geissen, Separation of titanium dioxide from photocatalytically treated water by cross-flow microfiltration, Water Res. 35 (2001) 1256–1262.
[209] X. Zhang, J.H. Pan, A.J. Du, W. Fu, D.D. Sun, J.O. Leckie, Combination of one-dimensional TiO2 nanowire photocatalytic oxidation with microfiltration for water treatment, Water Res. 43 (2009) 1179–1186.
[210] M.N. Chong, V. Vimonses, S. Lei, B. Jin, C. Chow, C. Saint, Synthesis and characterisation of novel titania impregnated kaolinite nano-photocatalyst, Microporus Mesoporus Mater. 117 (2009) 233–242.
[211] S.Y. Kwak, S.H. Kim, Hybrid organic/inorganic reverse osmosis (RO) membrane for bactericidal anti-fouling. 1. Preparation and characterization of TiO2 nanoparticle selfassembled aromatic polyamide thin-film-composite (TFC) membrane, Environ. Sci. Technol. 35 (2001) 2388–2394.
[212] D.K. Lee, S.C. Kim, I.C. Cho, S.J. Kim, S.W. Kim, Photocatalytic oxidation of microcystin-LR in a fluidized bed reactor having TiO2-coated activated carbon, Sep. Purif. Technol. 34 (2004) 59–66.

This book belongs to Kitab Liaison (ocd1996@gmail.com) Copyright Elsevier 2023

[213] H. Zhu, X. Gao, Y. Lan, D. Song, Y. Xi, J. Zhao, Hydrogen titanate nanofibers covered with anatase nanocrystals: a delicate structure achieved by the wet chemistry reaction of the titanate nanofibers, J. Am. Chem. Soc. 126 (2004) 8380–8381.
[214] S. Fukahori, H. Ichiura, T. Kitaoka, H. Tanaka, Capturing of bisphenol A photodecomposition intermediates by composite TiO2ezeolite sheets, Appl. Catal. B Environ. 46 (2003) 453–462.
[215] R. Kun, K. Mogyorósi, I. Dekány, Synthesis and structural and photocatalytic properties of TiO2/montmorillonite nanocomposites, Appl. Clay Sci. 32 (2006) 99–110.
[216] Z. Sun, Y. Chen, Q. Ke, Y. Yang, J. Yuan, Photocatalytic degradation of a cationic azo dye by TiO2/bentonite nanocomposite, J. Photochem. Photobiol. A Chem. 149 (2002) 169–174.
[217] Z.M. Xie, Z. Chen, Y.Z. Dai, Preparation of TiO2/sepiolite photocatalyst and its application to printing and dyeing wastewater treatment, Environ. Sci. Technol. 32 (2009) 123–127.
[218] M.N. Chong, S. Lei, B. Jin, C. Saint, C.W.K. Chow, Optimisation of an annular photoreactor process for degradation of Congo red using a newly synthesized titania impregnated kaolinite nano-photocatalyst, Sep. Purif. Technol. 67 (2009) 355–363.
[219] D. Sun, T.T. Meng, T.H. Loong, T.J. Hwa, Removal of natural organic matter from water using a nano-structured photocatalyst coupled with filtration membrane, Water Sci. Technol. 49 (2004) 103–110.
[220] X. Zhang, A.J. Du, P. Lee, D.D. Sun, J.O. Leckie, Grafted multifunctional titanium dioxide nanotube membrane: separation and photodegradation of aquatic pollutant, Appl. Catal. B Environ. 84 (2008) 262–267.
[221] F. Bosc, A. Ayral, C. Guizard, Mesoporous anatase coatings for coupling membrane separation and photocatalyzed reactions, J. Membr. Sci. 265 (2005) 13–19.
[222] H. Choi, E. Stathatos, D.D. Dionysiou, Solegel preparation of mesoporous photocatalytic TiO2 films and TiO2/Al2O3 composite membranes for environmental applications, Appl. Catal. B Environ. 63 (2005) 60–67.
[223] H. Choi, E. Stathatos, D.D. Dionysiou, Photocatalytic TiO2 films and membranes for the development of efficient wastewater treatment and reuse systems, Desalination 202 (2007) 199–206.
[224] H. Zhang, X. Quan, S. Chen, H. Zhao, Y. Zhao, The removal of sodium dodecylbenzene sulfonate surfactant from water using silica/titania nanorods/nanotubes composite membrane with photocatalytic capability, Appl. Surf. Sci. 252 (2006) 8598–8604.
[225] M.A. Artale, V. Augugliaro, E. Drioli, G. Golemme, C. Grande, V. Loddo, R. Molinari, L. Palmisano, M. Schiavello, Preparation and characterisation of membranes with entrapped TiO2 and preliminary photocatalytic tests, Ann. Chim. 91 (2001) 127–136.
[226] S.H. Kim, S.Y. Kwak, B.H. Sohn, T.H. Park, Design of TiO2 nanoparticle self-assembled aromatic polyamide thin-filmcomposite (TFC) membrane as an approach to solve biofouling problem, J. Membr. Sci. 211 (2003) 157–165.
[227] J. Kleine, K.V. Peinemann, C. Schuster, H.J. Warnecke, Multifunctional system for treatment of wastewaters from adhesive-producing industries: separation of solids and oxidation of dissolved pollutants using doted microfiltration membranes, Chem. Eng. Sci. 57 (2002) 1661–1664.
[228] R. Molinari, F. Pirillo, M. Falco, V. Loddo, L. Palmisano, Photocatalytic degradation of dyes by using a membrane reactor, Chem. Eng. Process. 43 (2004) 1103–1114.
[229] Y. Yang, P. Wang, Preparation and characterizations of a new PS/TiO2 hybrid membrane by solegel process, Polymer 47 (2006) 2683–2688.
[230] M.I. Litter, Heterogeneous photocatalysis: transition metal ions in photocatalytic systems, Appl. Catal. B Environ. 23 (1999) 89–114.

This book belongs to Kitab Liaison (ocd1996@gmail.com) Copyright Elsevier 2023

[231] K. Vinodgopal, D.E. Wynkoop, P.V. Kamat, Environmental photochemistry on semiconductor surfaces: photosensitized degradation of a textile azo dye, Acid Orange 7, on TiO2 particles using visible light, Environ. Sci. Technol. 30 (1996) 1660–1666.
[232] Y. Yu, J.C. Yu, J.G. Yu, Y.C. Kwok, Y.K. Che, J.C. Zhao, L. Ding, W.K. Ge, P.K. Wong, Enhancement of photocatalytic activity of mesoporous TiO2 by using carbon nanotubes, Appl. Catal. A Gen. 289 (2005) 186–196.
[233] Y. Ishibai, J. Sato, T. Nishikawa, S. Miyagishi, Synthesis of visible-light active TiO2 photocatalyst with Pt-modification: role of TiO2 substrate for high photocatalytic activity, Appl. Catal. B Environ. 79 (2008) 117–121.
[234] H. Li, J. Li, Y. Huo, Highly active TiO2N photocatalysts prepared by treating TiO2 precursors in NH3/ethanol fluid under supercritical conditions, J. Phys. Chem. B 110 (2006) 1559–1565.
[235] Y.A. Shaban, S.U.M. Khan, Visible light active carbon modified n-TiO2 for efficient hydrogen production by photoelectrochemical splitting of water, Int. J. Hydrog. Energy 33 (2008) 1118–1126.
[236] R. Asahi, T. Morikawa, T. Ohwaki, K. Aoki, Y. Taga, Visible-light photocatalysis in nitrogen-doped titanium dioxides, Science 293 (2001) 269–271.
[237] T. Ihara, M. Miyoshi, Y. Iriyama, O. Matsumoto, S. Sugihara, Visible-light-active titanium dioxide photocatalyst realized by an oxygen-deficient structure and by nitrogen doping, Appl. Catal. B Environ. 42 (2003) 403–409.
[238] H. Irie, Y. Watanabe, K. Hashimoto, Nitrogenconcentration dependence on photocatalytic activity of TiO2-xNx powders, J. Phys. Chem. B 107 (2003) 5483–5486.
[239] D. Chen, A.K. Ray, Photodegradation kinetics of 4-nitrophenol in TiO2 suspension, Water Res. 32 (1998) 3223–3234.
[240] S.A. Tsarenko, V.M. Kochkodan, A.O. Samsoni-Todorov, V.V. Goncharuk, Removal of humic substances from aqueous solutions with a photocatalytic membrane reactor, Colloid J. 68 (2006) 341–344.
[241] R.L. Pozzo, J.L. Giombi, M.A. Baltanas, A.E. Cassano, The performance in a fluidized bed reactor of photocatalysts immobilized onto inert supports, Catal. Today 62 (2000) 175–187.
[242] A.H.C. Chan, C.K. Chan, J.P. Barford, J.F. Porter, Solar photocatalytic thin film cascade reactor for treatment of benzoic acid containing wastewater, Water Res. 37 (2003) 1125–1135.
[243] I.J. Ochuma, R.P. Fishwick, J. Wood, J.M. Winterbottom, Optimisation of degradation conditions of 1,8-diazabicyclo [5. 4.0] undec-7-ene in water and reaction kinetics analysis using a cocurrent downflow contactor photocatalytic reactor, Appl. Catal. B Environ. 73 (2007) 259–268.
[244] V. Pareek, S. Chong, M. Tadé, A.A. Adesina, Light intensity distribution in heterogeneous photocatalytic reactors, Asia Pac. J. Chem. Eng. 3 (2008) 171–201.
[245] J. Fu, M. Ji, Z. Wang, L. Jin, D. An, A new submerged membrane photocatalysis reactor (SMPR) for fulvic acid removal using a nano-structured photocatalyst, J. Hazard. Mater. 131 (2006) 238–242.
[246] R. Molinari, C. Grande, E. Drioli, L. Palmisano, M. Schiavello, Photocatalytic membrane reactors for degradation of organic pollutants in water, Catal. Today 67 (2001) 273–279.
[247] S.S. Chin, T.M. Lim, K. Chiang, A.G. Fane, Hybrid lowpressure submerged membrane photoreactor for the removal of bisphenol A, Desalination 2002 (2007) 253–261.
[248] X. Huang, Y. Meng, P. Liang, Y. Qian, Operational conditions of a membrane filtration reactor coupled with photocatalytic oxidation, Sep. Purif. Technol. 55 (2007) 165–172.
[249] Y. Meng, X. Huang, Q. Yang, Y. Qian, N. Kubota, S. Fukunaga, Treatment of polluted river water with a photocatalytic slurry reactor using low-pressure mercury lamps coupled with a membrane, Desalination 181 (2005) 121–133.

This book belongs to Kitab Liaison (ocd1996@gmail.com) Copyright Elsevier 2023

[250] K. Sopajaree, S.A. Qasim, S. Basak, K. Rajeshwar, An integrated flow reactor-membrane filtration system for heterogeneous photocatalysis. Part I. Experiments and modelling of a batch-recirculated photoreactor, J. Appl. Electrochem. 29 (1999) 533–539.
[251] K. Sopajaree, S.A. Qasim, S. Basak, K. Rajeshwar, An integrated flow-reactor membrane filtration system for heterogeneous photocatalysis. Part II. Experiments on the ultrafiltration unit and combined operation, J. Appl. Electrochem. 29 (1999) 1111–1118.
[252] R. Molinari, F. Pirilla, V. Loddo, L. Palmisano, Heterogeneous photocatalytic degradation of pharmaceuticals in water by using polycrystalline TiO2 and a nanofiltration membrane reactor, Catal. Today 118 (2006) 205–213.
[253] J.T. Jung, J.O. Kim, W.Y. Choi, Performance of photocatalytic microfiltration with hollow fiber membrane, Mater. Sci. Forum 544 (2007) 95–98.
[254] S. Mozia, A.W. Morawski, M. Toyoda, T. Tsumura, Effect of process parameters on photodegradation of Acid Yellow 36 in a hybrid photocatalysisemembrane distillation system, Chem. Eng. J. 150 (2009) 152–159.
[255] K. Azrague, P. Aimar, F. Benoit-Marqué, M.T. Maurette, A new combination of a membrane and photocatalytic reactor for the depollution of turbid water, Appl. Catal. B Environ. 72 (2006) 197–205.
[256] G. Camera-Roda, F. Santarelli, Intensification of water detoxification by integrating photocatalysis and pervaporation, J. Sol. Energy Eng. 129 (2007) 68–73.
[257] V. Augugliaro, M. Litter, L. Palmisano, J. Soria, The combination of heterogeneous photocatalysis with chemical and physical operations: a tool for improving the photoprocess performance, J Photochem Photobiol C: Photochem Rev 7 (2006) 127–144.
[258] H.S. Lee, S.J. Im, J.H. Kim, H.J. Kim, J.P. Kim, B.R. Min, Polyamide thin-film nanofiltration membranes containing TiO2 nanoparticles, Desalination 219 (2008) 48–56.
[259] P. Meares, Synthetic Membranes: Science, Engineering and Applications, first ed., Springer Publisher, Peidel, Dordrecht, 1986.
[260] M. Gryta, M. Tomaszewska, J. Grzechulska, A.W. Morawski, Membrane distillation of NaCl solution containing natural organic matter, J. Membr. Sci. 181 (2001) 279–287.
[261] M. Tomaszewska, M. Gryta, A.W. Morawski, The influence of salt in solution on hydrochloric acid recovery by membrane distillation, Sep. Purif. Technol. 14 (1998) 183–188.
[262] K.W. Lawson, D.R. Lloyd, Membrane distillation, J. Membr. Sci. 124 (1997) 1–25.
[263] M.J. Benotti, B.D. Stanford, E.C. Wert, S.A. Snyder, Evaluation of a photocatalytic reactor membrane pilot system for the removal of pharmaceuticals and endocrine disrupting compounds from water, Water Res. 43 (6) (2009) 1513–1522.
[264] M.N. Chong, B. Jin, H.Y. Zhu, C.W.K. Chow, C. Saint, Application of H-titanate nanofibers for degradation of Congo red in an annular slurry photoreactor, Chem. Eng. J. 150 (2009) 49–54.
[265] S. Malato, J. Blanco, A. Campos, J. Cáceres, C. Guillard, J.M. Herrmann, A.R. Fernández-Alba, Effect of operating parameters on the testing of new industrial titania catalysts at solar pilot plant scale, Appl. Catal. B Environ. 42 (2003) 349–357.
[266] Y. Xu, C.H. Langford, Variation of Langmuir adsorption constant determined for TiO2-photocatalyzed degradation if acetophenone under different light intensity, J. Photochem. Photobiol. A Chem. 133 (2000) 67–71.
[267] A.P. Toor, A. Verma, C.K. Jotshi, P.K. Bajpai, V. Singh, Photocatalytic degradation of Direct Yellow 12 dye using UV/TiO2 in a shallow pond slurry reactor, Dyes Pigments 68 (2006) 53–60.

This book belongs to Kitab Liaison (ocd1996@gmail.com) Copyright Elsevier 2023

[268] A.G. Rincón, C. Pulgarin, Effect of pH, inorganic ions, organic matter and H2O2 on E. coli K12 photocatalytic inactivation by TiO2-implications in solar water disinfection, Appl. Catal. B Environ. 51 (2004) 283–302.
[269] C. Körmann, D.W. Bahnemann, M.R. Hoffman, Photolysis of chloroform and other organic molecules in aqueous titanium dioxide suspensions, Environ. Sci. Technol. 25 (1991) 494–500.
[270] M. Stylidi, D.I. Kondarides, X.E. Verykios, Pathways of solar light-induced photocatalytic degradation of azo dyes in aqueous TiO2 suspensions, Appl. Catal. B Environ. 40 (2003) 271–286.
[271] J.A. Herrera Melián, J.M. Doña Rodíguez, A. Viera Suárez, C. Valés do Campo, J. Arana, J. Pérez Peña, The photocatalytic disinfection of urban waste waters, Chemosphere 41 (2000) 323–327.
[272] M. Heyde, R. Portalier, Acid shock proteins of Escherichia coli, FEMS Microbiol. Lett. 69 (1990) 19–26.
[273] J.A. Ibáñez, M.I. Litter, R.A. Pizarro, Photocatalytic bactericidal effect of TiO2 on Enterobacter cloacae: comparative study with other Gram (-) bacteria, J. Photochem. Photobiol. A Chem. 157 (2003) 81–85.
[274] J. Lonnen, S. Kilvington, S.C. Kehoe, F. Al-Touati, K.G. McGuigan, Solar and photocatalytic disinfection of protozoan, fungal and bacterial microbes in drinking water, Water Res. 39 (2005) 877–883.
[275] T. Matsunaga, R. Tomoda, T. Nakajima, H. Wake, Photoelectrochemical sterilization of microbial cells by semiconductor powders, FEMS Microbiol. Lett. 29 (1985) 211–214.
[276] C. Sichel, J. Tello, M. de Cara, P. Fernández-Ibáñez, Effect of UV solar intensity and dose on the photocatalytic disinfection of bacteria and fungi, Catal. Today 129 (2007) 152–160.
[277] J. Blanco, S. Malato, J. de las Nieves, P. Fernández, Method of sedimentation of colloidal semiconductor particles, European patent application EP-1-101-737-A1, European Patent Office Bulletin 21, 2001.
[278] R. Molinari, A. Caruso, P. Argurio, T. Poerio, Degradation of the drugs Gemfibrozil and Tamoxifen in pressurized and de-pressurized membrane photoreactors using suspended polycrystalline TiO2 as catalyst, J. Membr. Sci. 319 (2008) 54–63.
[279] N. Seffaj, M. Persin, S. Alami Younssi, A. Albizane, M. Bouhria, H. Loukili, A. Larbot, Removal of salts and dyes by low ZnAl2O4-TiO2 ultrafiltration membrane deposited on support made from raw clay, Sep. Purif. Technol. 47 (2005) 36–42.
[280] X. Fu, L.A. Clark, W.A. Zeltner, M.A. Anderson, Effects of reaction temperature and water vapour content on the heterogeneous photocatalytic oxidation of ethylene, J. Photochem. Photobiol. A Chem. 97 (1996) 181–186.
[281] N.Z. Muradov, A.T. Raissi, D. Muzzey, C.R. Painter, M.R. Kemme, Selective photocatalytic degradation of airborne VOCs, Sol. Energy 56 (1996) 445–453.
[282] A.G. Rincón, C. Pulgarin, Photocatalytical inactivation of E. coli: effect of (continuous-intermittent) light intensity and of (suspended-fixed) TiO2 concentration, Appl. Catal. B Environ. 44 (2003) 263–284.
[283] J.G. Herrmann, Research to protect water infrastructure: EPA's water security research program, Proc. SPIE 5781 (2005) 48.
[284] Y. Wang, C.S. Hong, TiO2-mediated photomineralization of 2-chlorobiphenyl: the role of O2, Water Res. 34 (2000) 2791–2797.
[285] H. Shirayama, Y. Tohezo, S. Taguchi, Photodegradation of chlorinated hydrocarbons in the presence and absence of dissolved oxygen in water, Water Res. 35 (2001) 1941–1950.
[286] M. Saquib, M. Muneer, TiO2-mediated photocatalytic degradation of a triphenylmethane dye (gentian violet), in aqueous suspensions, Dyes Pigments 56 (2003) 37–49.

This book belongs to Kitab Liaison (ocd1996@gmail.com) Copyright Elsevier 2023

[287] D. Bahnemann, Photocatalytic water treatment: solar energy applications, Sol. Energy 77 (2004) 445–459.
[288] D.S. Bhatkhnade, S.P. Kamble, S.B. Sawant, V.G. Pangarkar, Photocatalytic and photochemical degradation of nitrobenzene using artificial ultraviolet light, Chem. Eng. J. 102 (2004) 283–290.
[289] S. Malato-Rodíguez, C. Richter, J.B. Gálvez, M. Vincent, Photocatalytic degradation of industrial residual waters, Sol. Energy 56 (1996) 401–410.
[290] J. Maruán, J. Aguado, W. Gernjak, S. Malato, Solar photocatalytic degradation of dichloroacetic acid with silicasupported titania at pilot-plant scale, Catal. Today 129 (2007) 59–68.
[291] J. Radjenovíc, C. Sirtori, M. Petrovíc, D. Barceló, S. Malato, Solar photocatalytic degradation of persistent pharmaceuticals at pilot-scale: kinetics and characterization of major intermediate products, Appl. Catal. B Environ. 89 (2009) 255–264.
[292] V.J.P. Vilar, M.I. Maldonado, I. Oller, S. Malato, R.A.R. Boaventura, Solar treatment of cork boiling and bleaching wastewaters in a pilot plant, Water Res. 43 (16) (2009) 4050–4062.
[293] S. Parra, S. Malato, C. Pulgarin, New integrated photocatalyticebiological flow system using supported TiO2 and fixed bacteria for the mineralization of isoproturon, Appl. Catal. B Environ. 36 (2002) 131–144.
[294] WHO, Guidelines for Drinking-Water Quality First Addendum to third edition 1 Recommendations, WHO Library Cataloguingin-Publication Data, (2006).
[295] M. Cho, H. Chung, W. Choi, J. Yoon, Linear correlation between inactivation of E. coli and OH radical concentration in TiO2 photocatalytic disinfection, Water Res. 38 (2004) 1069–1077.
[296] R.M. Tyrrell, S.M. Keyse, New trends in photobiology the interaction of UVA radiation with cultured cells, J. Photochem. Photobiol. B Biol. 4 (1990) 349–361.
[297] M. Berney, H.U. Weilenmann, A. Siminetti, T. Egli, Efficacy of solar disinfection of Escherichia coli, Shigella flexneri, Salmonella typhimurium and Vibrio cholera, J. Appl. Microbiol. 101 (2006) 828–836.
[298] S.C. Kehoe, M.R. Barer, L.O. Devlin, K.G. McGuigan, Batch process solar disinfection is an efficient means of disinfecting drinking water contaminated with Shigella dysenteriae type I, Lett. Appl. Microbiol. 38 (2004) 410–414.
[299] K.G. McGuigan, F. Méndez-Hermida, J.A. Castro-Hermida, E. Ares-Mazás, S.C. Kehoe, M. Boyle, C. Sichel, P. Fernández- Ibáñez, B.P. Meyer, S. Ramalingham, E.A. Meyer, Batch solar disinfection inactivates oocysts of Cryptosporidium parvum and cysts of Giardia muris in drinking water, J. Appl. Microbiol. 101 (2006) 453–463.
[300] G.C. Glatzmaier, Innovative solar technologies for treatment of concentrated organic wastes, Sol. Energy Mater. 24 (1991) 672.
[301] G.C. Glatzmaier, R.G. Nix, M.S. Mehos, Solar destruction of hazardous chemicals, J. Environ. Sci. Health A 25 (1990) 571–581.
[302] K.A. Magrini, J.D. Webb, Decomposition of aqueous organic compounds as a function of solar irradiation intensity, in: J.T. Beard, M.A. Ebadian (Eds.), 12th ASME Int. Sol. Energy Conference, ASME, New York, 1990, pp. 159–162.
[303] C. Karunakaran, S. Senthilvelan, Photooxidation of aniline on alumina with sunlight and artificial UV light, Catal. Commun. 6 (2005) 159–165.
[304] M. Qamar, M. Muneer, D. Bahnemann, Heterogeneous photocatalysed degradation of two selected pesticide derivatives, triclopyr and daminozid in aqueous suspensions of titanium dioxide, J. Environ. Manag. 80 (2006) 99–106.
[305] C. Shang, L.M. Cheung, C.M. Ho, M. Zeng, Repression of photoreactivation and dark repair of coliform bacteria by TiO2-modified UV-C disinfection, Appl. Catal. B Environ. 89 (2009) 536–542.

This book belongs to Kitab Liaison (ocd1996@gmail.com) Copyright Elsevier 2023

[306] P. Calza, V.A. Sakkas, C. Medana, C. Baiocchi, A. Dimou, E. Pelizetti, T. Albanis, Photocatalytic degradation study of diclofenac over aqueous TiO2 suspensions, Appl. Catal. B Environ. 67 (2006) 197–205.
[307] M.N. Chong, B. Jin, C.W.K. Chow, C.P. Saint, A new approach to optimise an annular slurry photoreactor system for the degradation of Congo red: statistical analysis and modelling, Chem. Eng. J. 152 (2009) 158–166.
[308] B.K. Korbahti, M.A. Rauf, Application of response surface analysis to the photolytic degradation of Basic Red 2 dye, Chem. Eng. J. 138 (2008) 166–171.
[309] H.L. Liu, Y.R. Chiou, Optimal decolorization efficiency of Reactive Red 239 by UV/TiO2 photocatalytic process coupled with response surface methodology, Chem. Eng. J. 112 (2005) 173–179.
[310] C. Lizama, J. Freer, J. Baeza, H.D. Mansilla, Optimized photodegradation of reactive blue 19 on TiO2 and ZnO suspensions, Catal. Today 76 (2002) 235–246.
[311] I.H. Cho, K.D. Zoh, Photocatalytic degradation of azo dye (Reactive Red 120) in TiO2/UV system: optimization and modelling using a response surface methodology (RSM) based on the central composite design, Dyes Pigments 75 (2007) 533–543.
[312] R. Jaworski, L. Pawlowski, F. Roudet, S. Kozerski, F. Petit, Characterization of mechanical properties of suspension plasma sprayed TiO2 coatings using scratch test, Surf. Coat. Technol. 202 (2008) 2644–2653.
[313] W. De Soto, S.A. Klein, W.A. Beckman, Improvement and validation of a model for photovoltaic array performance, Sol. Energy 80 (1) (2006) 78–88.
[314] J. Cunningham, P. Sedlak, Kinetic studies of depollution process in TiO2 slurries: interdependences of adsorption and UV-intensity, Catal. Today 29 (1996) 209–315.
[315] C. Minero, Kinetic analysis of photoinduced reactions at the water semiconductor interface, Catal. Today 54 (1999) 205–216.
[316] D. Monllor-Satoca, R. ómez, M. González-Hidalgo, P. Salvador, The "Directeindirect" model: an alternative kinetic approach in heterogeneous photocatalysis based on the degree of interaction of dissolved pollutant species with the semiconductor surface, Catal. Today 129 (2007) 247–255.
[317] C. Minero, E. Pelizetti, S. Malato, J. Blanco, Large solar plant photocatalytic water decontamination: effect of operational parameters, Sol. Energy 56 (1996) 421–428.
[318] G.R. Finch, E.K. Black, C.W. Labatiuk, L. Gyürék, M. Belosevic, Comparison of Giardia lamblia and Giardia muris cyst inactivation by ozone, Appl. Environ. Microbiol. 59 (1993) 3674–3680.
[319] L.W. Hom, Kinetics of chlorine disinfection in an ecosystem, J. Sanit. Eng. Div. 98 (1972) 183–194.
[320] A.K. Benabbou, Z. Derriche, C. Felix, P. Lejeune, C. Guillard, Photocatalytic inactivation of Escherischia coli: effect of concentration of TiO2 and microorganism, nature, and intensity of UV irradiation, Appl. Catal. B Environ. 76 (2007) 257–263.
[321] R.J.W. Lambert, M.D. Johnston, The effect of interfering substances on the disinfection process: a mathematical model, J. Appl. Microbiol. 91 (2000) 548–555.
[322] M. Cho, H. Chung, J. Yoon, Disinfection of water containing natural organic matter by using ozoneinitiated radical reactions, Appl. Environ. Microbiol. 69 (2003) 2284–2291.
[323] L.L. Gürék, G.R. Finch, Modelling water treatment chemical disinfection kinetics, J. Environ. Eng. 124 (1998) 783–792.
[324] B.F. Severin, M.T. Suidan, R.S. Engelbrecht, Serieseevent kinetic model for chemical disinfection, J. Environ. Eng. ASCE 110 (1984) 430–439.
[325] I. Najm, An alternative interpretation of disinfection kinetics, J. Am. Water Works Assoc. 98 (2006) 93–101.
[326] M.D. Johnston, E.A. Simons, R.J.W. Lambert, One explanation for the variability of the bacterial suspension test, J. Appl. Microbiol. 88 (2000) 237–242.

This book belongs to Kitab Liaison (ocd1996@gmail.com) Copyright Elsevier 2023

[327] M.L. Chin, A.R. Mohamed, S. Bhatia, Performance of photocatalytic reactors using immobilized TiO2 film for the degradation of phenol and methylene blue dye present in water stream, Chemosphere 57 (2004) 547–554.
[328] C. Tang, V. Chen, The photocatalytic degradation of reactive black 5 using TiO2/UV in an annular photoreactor, Water Res. 38 (2004) 2775–2781.
[329] A.G. Rincón, C. Pulgarin, Use of coaxial photocatalytic reactor (CAPHORE) in the TiO2 photo-assisted treatment of mixed E. coli and Bacillus sp. and bacterial community present in wastewater, Catal. Today 101 (2005) 331–344.
[330] S. Gelover, L.A. Gómez, K. Reyes, M. Teresa Leal, A practical demonstration of water disinfection using TiO2 films and sunlight, Water Res. 40 (2006) 3274–3280.
[331] J.C. Crittenden, Y. Zhang, D.W. Hand, D.L. Perram, E.G. Marchand, Solar detoxification of fuel-contaminated groundwater using fixed-bed photocatalysts, Water Environ. Res. 68 (1996) 270–278.
[332] H.Y. Chen, O. Zahraa, M. Bouchy, Inhibition of the adsorption and photocatalytic degradation of an organic contaminant in an aqueous suspension of TiO2 by inorganic ions, J. Photochem. Photobiol. A Chem. 108 (1997) 37–44.
[333] C. Guillard, H. Lachheb, A. Houas, M. Ksibi, E. Elaloui, J.M. Hermann, Influence of chemical structure of dyes, of pH and of inorganic salts on their photocatalytic degradation by TiO2 comparison of the efficiency of powder and supported TiO2, J. Photochem. Photobiol. A Chem. 158 (2003) 27–36.
[334] W. Leng, H. Liu, S. Cheng, J. Zhang, C. Cao, Kinetics of photocatalytic degradation of aniline in water over TiO2 supported on porous nickel, J. Photochem. Photobiol. A Chem. 131 (2000) 125–132.
[335] A. Özkan, M.H. Özkan, R. Gürkan, M. Akçay, M. Sökmen, Photocatalytic degradation of a textile azo dye, Sirius Gelb GC on TiO2 or Ag-TiO2 particles in the absence and presence of UV irradiation: the effects of some inorganic anions on the photocatalysis, J. Photochem. Photobiol. A Chem. 163 (2004) 29–35.
[336] A. Riga, K. Soutsas, K. Ntampegliotis, V. Karayannis, G. Papapolymerou, Effect of system parameters and of inorganic salts on the decolorization and degradation of Procion H-exl dyes. Comparison of H2O2/UV, Fenton, UV/ Fenton, TiO2/UV and TiO2/UV/H2O2 processes, Desalination 211 (2007) 72–86.
[337] D.C. Schmelling, K.A. Gray, P.V. Vamat, The influence of solution matrix on the photocatalytic degradation of TNT in TiO2 slurries, Water Res. 31 (1997) 1439–1447.
[338] K. Wang, J. Zhang, L. Lou, S. Yang, Y. Chen, UV or visible light induced photodegradation of AO7 on TiO2 particles: the influence of inorganic anions, J. Photochem. Photobiol. A Chem. 165 (2004) 201–207.
[339] C.H. Wu, K.S. Huang, J.M. Chern, Decomposition of acid dye by TiO2 thin films prepared by the solegel method, Ind. Eng. Chem. Res. 45 (2006) 2040–2045.
[340] C.C. Wong, W. Chu, The direct photolysis and photocatalytic degradation of alachlor at different TiO2 and UV sources, Chemosphere 50 (2003) 981–987.
[341] W. Choi, A. Termin, M.R. Hoffman, The role of metal ion dopants in quantum-sized TiO2: correlation between photoreactivity and charge carrier recombination dynamics, J. Phys. Chem. 98 (1994) 13669–13679.
[342] M. Kerzhentsev, C. Guillard, J.M. Herrmann, P. Pichat, Photocatalytic pollutant removal in water at room temperature: case study of the total degradation of the insecticide fenitrothion (phosphorothioic acid O, O-dimethyl- O-(3-methyl-4-nitro-phenyl) ester), Catal. Today 27 (1996) 215–220.
[343] K. Okonomoto, Y. Yamamoto, H. Tanaka, M. Tanaka, A. Itaya, Heterogeneous photocatalytic decomposition of phenol over TiO2 powder, Bull. Chem. Soc. Jpn. 58 (1985) 2015–2022.

This book belongs to Kitab Liaison (ocd1996@gmail.com) Copyright Elsevier 2023

[344] S.T. Martin, A.T. Lee, M.R. Hoffmann, Chemical mechanism of inorganic oxidants in the TiO2/UV process: increased rates of degradation of chlorinated hydrocarbons, Environ. Sci. Technol. 29 (1995) 2567–2573.
[345] H. Zhu, M. Zhang, Z. Xia, G.K.C. Low, Titanium dioxide mediated photocatalytic degradation of monocrotophos, Water Res. 29 (1995) 2681–2688.
[346] Y. Mu, H.Q. Yu, J.C. Zheng, S.J. Zhang, TiO2-mediated photocatalytic degradation of Orange II with the presence of Mn2. in solution, J. Photochem. Photobiol. A Chem. 163 (2004) 311–316.
[347] R. Burns, J.C. Crittenden, D.W. Hand, L.L. Sutter, S.R. Salman, Effect of inorganic ions in heterogeneous photocatalysis, J. Environ. Eng. 125 (1999) 77–85.
[348] L. Rizzo, J. Koch, V. Belgiorno, M.A. Anderson, Removal of methylene blue in a photocatalytic reactor using polymethylmethacrylate supported TiO2 nanofilm, Desalination 211 (2007) 1–9.
[349] U. Diebold, The surface science of titanium dioxide, Surf. Sci. Rep. 48 (2003) 53–229.
[350] R.W. Matthews, S.R. McEnvoy, Photocatalytic degradation of phenol in the presence of near-UV illuminated titanium dioxide, J. Photochem. Photobiol. A Chem. 64 (1992) 231.
[351] K. Kabra, R. Chaudhary, R.L. Sawhney, Treatment of hazardous organic and inorganic compounds through aqueous-phase photocatalysis: a review, Ind. Eng. Chem. Res. 43 (2004) 7683–7696.
[352] M.R. Prairie, L.R. Evans, S.L. Martinez, Destruction of organics and removal of heavymetals inwater via TiO2 photocatalysis, in: W.W. Eckenfelder, J.A. Roth, A.R. Bowers (Eds.), Chemical Oxidation: Technologies for the Nineties, vol. 2, Technomic Publishing Company, Pennsylvania, 1994, pp. 428–441.
[353] J.M. Herrmann, J. Disdier, P. Pichat, Photocatalytic deposition of silver on powder titania: consequences for the recovery of silver, J. Catal. 113 (1988) 72–81.
[354] M. Huang, E. Tso, A.K. Datye, Removal of silver in photographic processing waste by TiO2-based photocatalysis, Environ. Sci. Technol. 30 (1996) 3084–3088.
[355] I. Muñoz, J. Peral, J.A. Ayllón, S. Malato, P. Passarinho, X. Domènech, Life cycle assessment of a coupled solar photocatalyticebiological process for wastewater treatment, Water Res. 40 (2006) 3533–3540.
[356] W. Gernjak, M. Fuerhacker, P. Fernandez-Ibañez, J. Blanco, S. Malato, Solar photo-Fenton treatment process parameters and process control, Appl. Catal. B: Environ. 64 (2006) 121–130.
[357] M. Lapertot, C. Pulgaín, P. Fernandez-Ibáñez, M.I. Maldonado, L. Pérez-Estrada, I. Oller, W. Gernjak, S. Malato, Enhancing biodegradability of priority substances (pesticides) by solar photo-Fenton, Water Res. 40 (2006) 1086–1094.
[358] I. Muñoz, J. Rieradevall, F. Torrades, J. Peral, X. Domenech, Environmental assessment of different solar driven advanced oxidation processess, Sol. Energy 79 (2005) 369–375.
[359] F. Consoli, D. Allen, I. Boustead, N. de Oude, J. Fava, W. Franklin, B. Quay, R. Parrish, R. Perriman, D. Postlethwaite, J. Seguin, B. Vigon, Guidelines for Life-Cycle Assessment: A Code of Practice, Society of Environmental Toxicology and Chemistry, Brussels, 1993.
[360] A. Azapagic, R. Clift, Life cycle assessment and multiobjective optimisation, J. Clean. Prod. 7 (1999) 135–143.

This book belongs to Kitab Liaison (ocd1996@gmail.com) Copyright Elsevier 2023

This page intentionally left blank

This book belongs to Kitab Liaison (ocd1996@gmail.com)

Copyright Elsevier 2023

PART 4

Sustainable buildings

This book belongs to Kitab Liaison (ocd1996@gmail.com)

Copyright Elsevier 2023

This page intentionally left blank

This book belongs to Kitab Liaison (ocd1996@gmail.com)

Copyright Elsevier 2023

CHAPTER 11

Green building technology

Introduction

Climate change depends much on buildings, as nearly 40% of the energy consumption from burning fossil fuel is used by buildings [1–3]. In 2015, the annual global energy consumption was 5.59×10^{20} joules = 559 EJ, in which 2.236×10^{20} EJ was consumed by residential and commercial buildings [4, 5]. Because of this level of energy consumption, buildings have produced nearly 8.01×10^{11} tons of CO_2 (218 gtC by building of global total 545 gtC; 1 gtC = 10^9 ton C = 3.67 gt CO_2). The acceleration in the use of fossil energy by the building sector is still increasing worldwide, and this will not change until a sophisticated renewable technology is developed. Currently, the atmospheric CO_2 level is 400 ppm, which can be reduced to a comfortable level of 300 ppm CO_2 once renewable energy applications are widely used in the building sector [6, 7]. Certainly, a better technology is required for the building sector to ensure a cleaner, greener environment by deploying sustainable technology to alleviate energy and environmental problems. In this paper, thus, a zero-emission building (ZEB) technology that is a combination of the innovative PV system and bioenergy production by the building itself has been proposed. In this concept, a zero-emission building (ZEB) will be an interesting one to balance its energy demand if a certain part of the building skin is designed to be a black body-assisted PV (photovoltaic) panel to capture solar energy, which will reduce nearly 8.01×10^{11} ton CO_2 per year [4, 8, 9]. In addition to the building producing its own energy, the domestic waste, including human feces and wastewater, of the building can be collected into a closed detention tank in the cellar. Then, the waste can be separated as wastewater and human feces with solid waste into two different chambers. Then the *methanogenesis* process would be allowed into the closed detention tank to produce bioenergy in context with domestic solid waste and human feces utilization. It is estimated that a person can produce 0.4–0.5 kg/day and 0.5 kg/day that can form the 0.4 m^3 biogas/day. This amount of biogas (0.4 m^3/day) production is good

Sustainable Development for Mass Urbanization
https://doi.org/10.1016/B978-0-12-817690-0.00011-7
© 2019 Elsevier Inc.
All rights reserved.

This book belongs to Kitab Liaison (ocd1996@gmail.com)
Copyright Elsevier 2023

enough to cook three meals for a family of four persons a day. Subsequently, the wastewater treated *onsite* by applying all primary, secondary, and tertiary processes can be used for gardening and landscaping for a building.

Simulation and method

Model of photovoltaic (PV) array

A mathematical model of a photovoltaic (PV) module has been developed to describe the photovoltaic generator for maximum solar energy, taking into consideration the radiation shield, the thermocouple, and the temperature of the building's exterior skin PV panel (Fig. 11.1A). Naturally, the model of the photovoltaic solar irradiance absorbed by the photovoltaic module can be simplified for the maximum power output connected with the temperature module and the logarithmic with the solar radiation [10–12]. The accurate calculation and the number of parameters of the current-voltage (*I-V*) characteristic are necessarily explain the model in a single-diode equivalent circuit of a PV cell module [13–15]. Then, using a large-scale variation

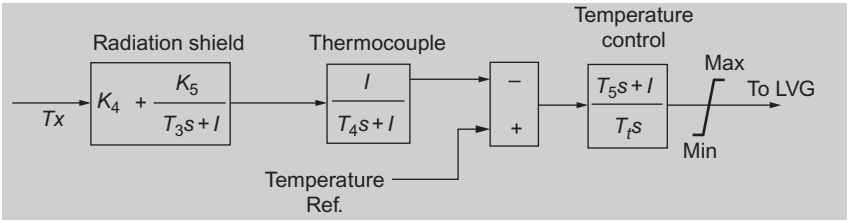

(A)

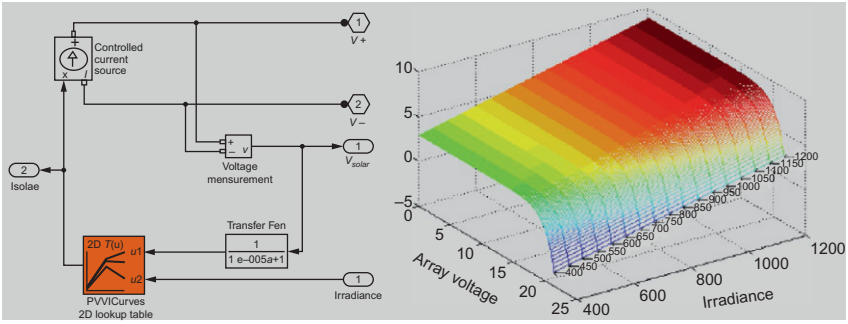

(B)

Fig. 11.1 Diagram of a PV system model, (A) The module flow chart once the photovoltaic solar irradiance on the photovoltaic mode considering radiation shield, thermocouple and temperature to get LVG (localized voltage gain), (B) Simulink block diagram of PV solar array source and the block data of its parameters, respectively.

This book belongs to Kitab Liaison (ocd1996@gmail.com) Copyright Elsevier 2023

of the irradiance collected by the photovoltaic array at various parameters (*voltage proliferation, transformation rate, and PVVI curves*), the least control strategy to be used to realize the active and reactive solar volt (I_{v+}) can be calculated from the model with one diode (Fig. 11.1B).

The next step is to determine the photovoltaic current production by an I_{pv} calculation from the model of one diode (Fig. 11.2A), considering the *I-V-R* relationship (Fig. 11.2B), and using the illumination received by the photovoltaic array to convert from DC to AC and then use for domestic energy and low-voltage current demand (Fig. 11.2C).

The following equation calculates the energy output of a photovoltaic cell, whose basis is solar radiation and ambient temperature:

$$P_{pv} = \eta_{pvg} A_{pvg} G_t \tag{11.1}$$

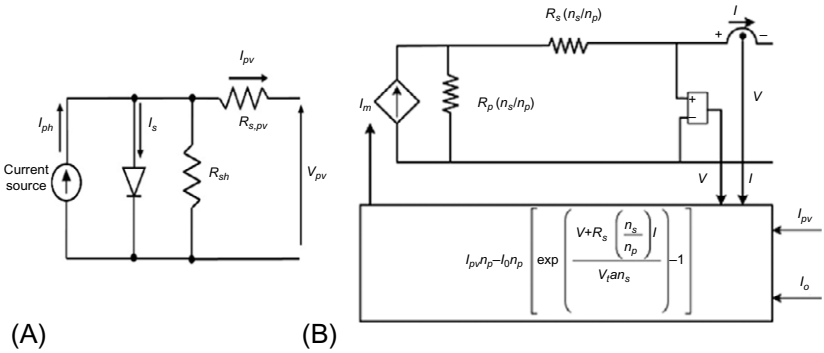

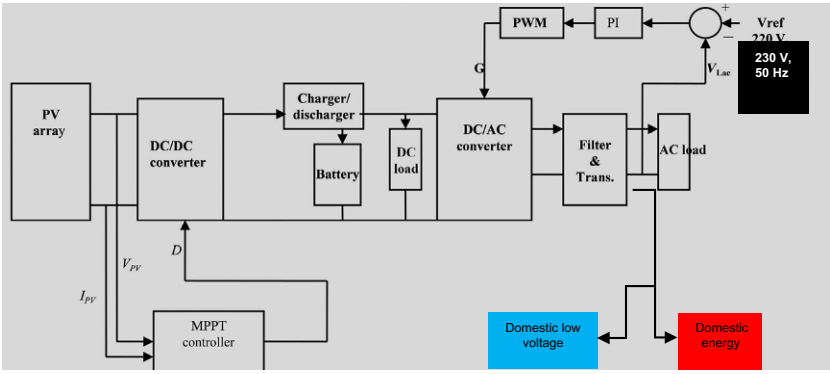

(C)

Fig. 11.2 Single-diode circuit of a photovoltaic (PV) cell modeled by MATLAB simulation, (A) the photovoltaic current production, (B) the model with a diode considering the *I-V-R* relationship (C), the conversion process of DC to AC for domestic energy and a low-voltage current for the building.

This book belongs to Kitab Liaison (ocd1996@gmail.com)
Copyright Elsevier 2023

In this equation, η_{pvg} refers to the PV-generation efficiency, A_{pvg} refers to the PV generator area (m^2), and G_t refers to the solar radiation in a titled module plane (W/m^2). η_{pvg} can be further defined as:

$$\eta_{pvg} = \eta_r \eta_{pc}[1 - \beta(T_c - T_{c\,\mathrm{ref}})] \tag{11.2}$$

η_{pc} refers to the power conditioning efficiency, when MPPT applied, it is equal to 1; β refers to the temperature coefficient (0.004–0.006 per °C); η_r refers to the reference module efficiency; and $T_{c\mathrm{ref}}$ refers to the reference cell temperature in °C. The reference cell temperature ($T_{c\,\mathrm{ref}}$) can be obtained from the relation below:

$$T_c = T_a + \left(\frac{\mathrm{NOCT} - 20}{800}\right) G_t \tag{11.3}$$

T_a refers to the ambient temperature in °C, G_t refers to the solar irradiance in a tilted module plane (W/m^2), and NOCT refers to the standard operating cell temperature in Celsius (°C). The total irradiance in the solar cell, considering both standard and diffuse solar irradiance, can be estimated by the following equation:

$$I_t = I_b R_b + I_d R_d + (I_b + I_d) R_r \tag{11.4}$$

The solar cells, which are essentially a *P-N* junction semiconductor able to produce electricity via the PV effect, are interconnected in a series-parallel configuration to form a photovoltaic cell [10, 16]. Also, to improve the efficiency of the resulting photovoltaic, graphene is integrated into the PV module [12, 17].

Using a standard single diode, as depicted in Fig. 11.2, for a cell with N_s series-connected arrays and N_p parallel-connected arrays, the cell current must be related to the cell voltage as

$$I = N_p \left[I_{ph} - I_{rs} \left[\exp\left(\frac{q(V + IR_s)}{AKTN_s} - 1 \right) \right] \right] \tag{11.5}$$

where

$$I_{rs} = I_{rr} \left(\frac{T}{T_r}\right)^3 \exp\left[\frac{E_G}{AK}\left(\frac{1}{T_r} - \frac{1}{T}\right)\right] \tag{11.6}$$

In Eqs. (11.5), (11.6), q refers to the electron charge (1.6×10^{-19} C), K refers to Boltzmann's constant, A refers to the diode idealist factor, and T refers to the cell temperature (K). I_{rs} refers to the cell reverse saturation current at T, T_r refers to the cell referred temperature, I_{rr} refers to the reverse

This book belongs to Kitab Liaison (ocd1996@gmail.com) Copyright Elsevier 2023

saturation current at T_r, and E_G refers to the band-gap energy of the semiconductor used in the cell. The photo current I_{ph} varies with the cell's temperature and radiation as follows:

$$I_{ph} = \left[I_{SCR} + k_i (T - T_r) \frac{S}{100} \right] \tag{11.7}$$

I_{SCR} refers to the cell short-circuit current at the reference temperature and irradiance, k_i refers to the short-circuit current temperature coefficient, and S refers to the solar irradiance (mW/cm^2). The I-V characteristics of the photovoltaic cell can be derived using a single-diode model that includes an additional shunt resistance concurrent with the optimal shunt diode model as follows:

$$I = I_{ph} - I_D \tag{11.8}$$

$$I = I_{ph} - I_0 \left[\exp\left(\frac{q(V + R_s I)}{AKT} - 1 \right) - \frac{V + R_s I}{R_{sh}} \right] \tag{11.9}$$

I_{ph} refers to the photo current (A), I_D refers to the diode current (A), I_0 refers to the inverse current (A), A refers to the diode constant, q refers to the charge of the electron (1.6×10^{-19} C), K refers to Boltzmann's constant, T refers to the cell temperature (°C), R_s refers to the series resistance (ohm), R_{sh} refers to the shunt resistance (Ohm), I refers to the cell current (A), and V refers to the cell voltage (V). The output current of the PV cell using the diode model can be described as follows:

$$I = I_{PV} - I_{D1} - \left(\frac{V + IR_S}{R_{SH}} \right) \tag{11.10}$$

where

$$I_{D1} = I_{01} \left[\exp\left(\frac{V + IR_s}{a_1 V_{T1}} \right) - 1 \right] \tag{11.11}$$

$$I_{D2} = I_{01} \left[\exp\left(\frac{V + IR_s}{a_2 V_{T2}} \right) - 1 \right] \tag{11.12}$$

I_{01} and I_{02} are the reverse currents of diode 1, respectively, and V_{T1} and V_{T2} are the thermal voltages of the respective diode. The diode idealist constants are represented by a_1 and a_2. The simplified model of the photovoltaic system model is presented below:

$$v_{oc} = \frac{V_{oc}}{cK\,T/q} \tag{11.13}$$

This book belongs to Kitab Liaison (ocd1996@gmail.com) Copyright Elsevier 2023

$$P_{\max} = \frac{\dfrac{V_{oc}}{cK\,T/q} - \ln\left(\dfrac{V_{oc}}{cK\,T/q} + 0.72\right)}{\left(1 + \dfrac{V_{oc}}{K\,T/q}\right)} \left(1 - \frac{V_{oc}}{\dfrac{V_{oc}}{I_{SC}}}\right) \left(\frac{V_{oc0}}{1 + \beta \ln \dfrac{G_0}{G}}\right) \left(\frac{T_o}{T}\right)^{\gamma} I_{sc0} \left(\frac{G}{G_o}\right)^{a} \tag{11.14}$$

where ν_{oc} refers to the normalized value of the open-circuit voltage V_{oc} related to the thermal voltage $V_t = nkT/q$, c refers constant current flow, K refers to Boltzmann's constant, T refers to the temperature of the photovoltaic (PV) module in Kelvin, α refers to the factor responsible for all the nonlinear effects on which the photocurrent depends, q refers to the electron charge, γ refers to the factor representing all the nonlinear temperature-voltage effects, and β refers to a photovoltaic (PV) module technology-specific dimensionless coefficient. Eq. (11.14) only represents the maximum energy output of a single photovoltaic module while a real system consists of several photovoltaic modules connected in series and in parallel. Therefore, the equation of total power output for an array with N_s cells connected in series and N_p cells connected in parallel with power P_M for each module would be

$$P_{\text{array}} = N_s N_p P_M \tag{11.15}$$

Design of PV panel

To ensure the high efficiency of the conversion rate of solar energy as well as the long-lasting ability and other essential abilities of the photovoltaic panel, nanocrystalline materials and films of conductive polymers using the exterior skin of the building wall are introduced as the materials to build up an advanced photovoltaic panel [18, 19]. In addition, load resistant factor design (LRFD), which primarily uniformly distributes the wind load, should also be considered when designing such sophisticated photovoltaic panels to ensure that they are strong enough to protect themselves and operate regularly under storm conditions. To guarantee that the tornado-resistant PV panel is strong enough, it should have the following wind load resistant capacity of wind velocity (F6 tornado level 379 mile/hour) at standard air density 1.2 kg/m^3 and wind pressure and drag coefficient 1.00 considering per meter square (m^2). Because the wind stagnation pressure is half the density of the air times the square of the velocity, the equation for wind pressure can be expressed as

$$p_w = 0.5\rho C_p \nu_r^2 \tag{11.16}$$

This book belongs to Kitab Liaison (ocd1996@gmail.com) Copyright Elsevier 2023

where p_w is the wind pressure (Pa), ρ represents air density (kg/m^3), C_p represents wind pressure coefficient, and v_r^2 represents wind velocity (m/s) at building height.

Therefore, the final calculation of $P_w = 0.5 \times 1.2\,\text{kg/m}^3 \times 379^2\,\text{m/s}$ is 86,185 Pa and the net wind load can be calculated as $F =$ area $\times$ drag coefficient $\times$ stagnation pressure by the following equation.

$$F = 1\,\text{m}^2 \times 1.0 \times 86,185 = 86,185\,\text{N}\,(8788\,\text{kgf}) = 19,375\,\text{ibf} \quad (11.17)$$

Once the sophisticated wind load resistance capacity has been determined, the PV panel needs to be analyzed to capture the maximum sunlight during the whole year based on different directional angles. This can be defined as a spherical coordinate system called a Cartesian coordinate system, as shown in Fig. 11.3, whose x represents horizon conventions, y for east-west, and z for zenith. The position of the celestial body in this system is decided by h, which represents height, and A, which represents the azimuth angle, while the equatorial system uses the protocol that the z axis points to the north pole, the y axis is identical to the system horizon, and the x axis is perpendicular to both. Besides, the δ decline and ω angle hours can also determine the position, and the analysis generally leads to the insertion of vector control strategies to regulate the active and reactive power based on the combination of different controls, which is reproducible and usable for other complex systems [20–22].

The properties of sunlight are considered because of the electromagnetic waves and the movement of photon flux applied to the solar panel because the photophysical relates to photo-induced the charges [1, 23]. The first view is fundamental for all applications of solar thermal energy and antireflective coatings for solar cells while the second view is also basic with respect to solar cells and solar photochemistry. The combination of the two views is represented by quantum electrodynamics, one of the most fruitful and matured technologies in modern physics [24, 25]. All the hot bodies emit radiation while black bodies emit the maximum amount of radiation at a given temperature of approximately 700°C. However, changes in body color to orange, yellow, white, and blue and efficiencies in overlapping loads have been calculated in the band-gap, the sun and the cells, which are supposed to be at temperatures of 6000 and 300°K, respectively [12]. The energy density of the solar radiation considering the photon wave frequency has been modeled by using the classical statistical physics in Fig. 11.4A. Then, the maximum solar energy formation considering a single photon excitation at the rate of 1.4 eV with an energy value of 27.77 MW/m^2 eV has been modeled in Fig. 11.4B.

This book belongs to Kitab Liaison (ocd1996@gmail.com) Copyright Elsevier 2023

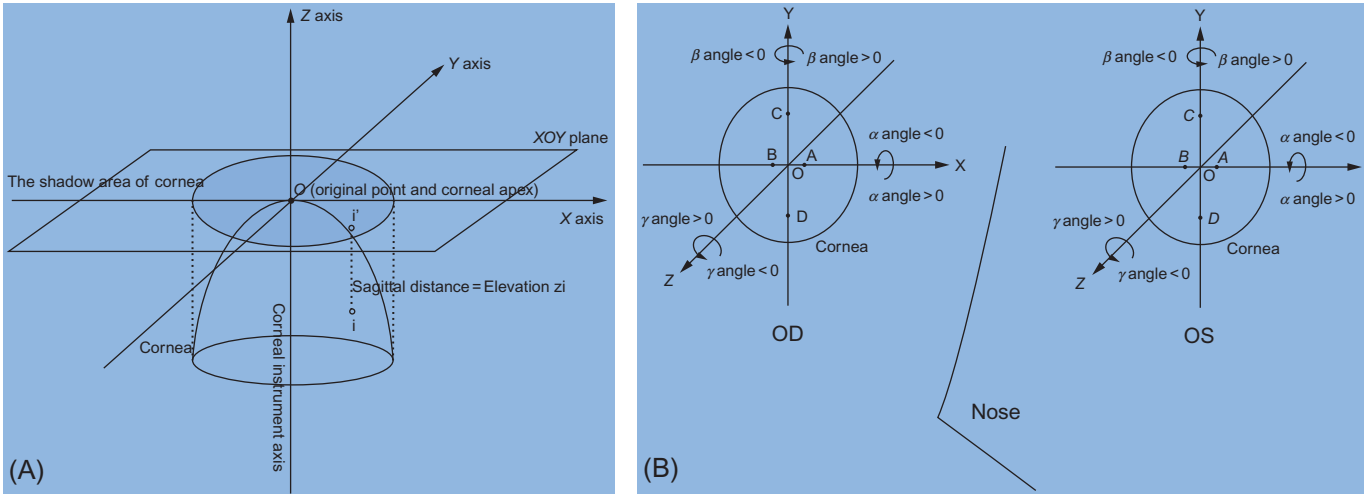

Fig. 11.3 The Cartesian coordinate system. (A) Cartesian coordinate analysis shows the equatorial system, and vector control considering the effect of the placement of solar PV systems, (B) Points *A* to *D* are chosen to test instrument measurement repeatability and analyze interocular symmetry considering the angles α, β, and γ to right the maximum solar irradiance capture.

This book belongs to Kitab Liaison (ocd1996@gmail.com)

Copyright Elsevier 2023

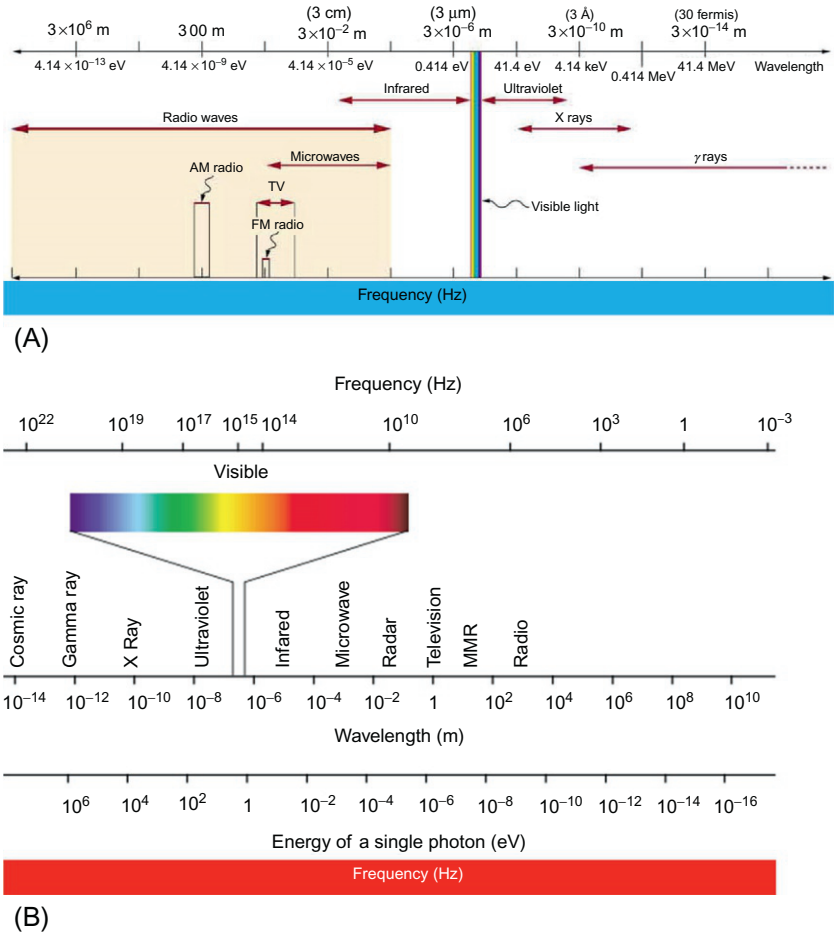

Fig. 11.4 (A) The energy density of the solar radiation frequencies shown by the classical statistical physics, (B) The maximum solar energy formation of a single photon at designated wavelength (ultraviolet to infrared) and frequencies (10^{17} to 10^{14} Hz) at the rate of 1.4 eV with an energy value of 27.77 MW/m^2 eV.

Design of bioreactor

As mentioned earlier, a building's solid waste can be collected in a closed detention tank in the cellar of a building and then be separated into wastewater and human feces, including domestic waste, into two different chambers. During this process, the wastewater needs to be treated by preliminary treatment, primary treatment, secondary treatment, and disinfection. The whole treatment process can remove nearly 100% of the pollutants from the wastewater and disinfect the effluent. Furthermore, the final product can be utilized for local gardening and landscaping (Fig. 11.5).

This book belongs to Kitab Liaison (ocd1996@gmail.com)
Copyright Elsevier 2023

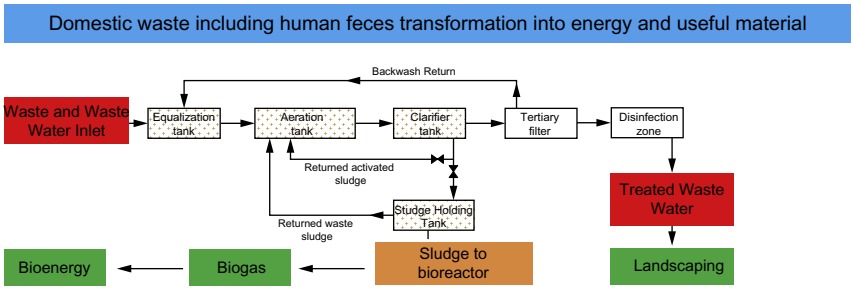

Fig. 11.5 Wastewater treatment process where effluent is used for gardening and sludge is for a further process to produce biogas.

Besides the treated wastewater in situ, the sludge shall undergo in situ anaerobic tank to produce bioenergy. It is a transformation process by performing filters electrochemically active carbon nanotubes (CNT), which can adsorb and oxidize chemicals in the anode effectively [26, 27]. It is a novel system of waste treatment to combine both adsorption and oxidation at the anode CNT. Further oxidation in situ generates hydrogen peroxide (H_2O_2) in the cathode CNT in a small scale. The factors affecting the efficiency of the treatment and the oxidation mechanism of the system are studied systematically. The model of this calculation demonstrates that the H_2O_2 flow may be affected by the electrode material, the cathode potential, the pH, the flow rate, and the oxygen dissolved [17, 28]. The maximum H_2O_2 flow of 1.38 mol/L/m^{2}C is to be achieved by CNT L^{-1}/m^2 with an applied cathodic potential $V-0.4$ (versus Ag/AgCl), a pH of 6.46, a rate flow of 1.5 mL/min, and a DO influent flow of 1.95 mol/L/m^2. Furthermore, phenol can be used as an aromatic compound model for assessing the removal efficiency of the system and its oxidation rate correlates directly with the H_2O_2 flow. The H_2O_2 will probably react with a phenol species anodically activated to itself, which is the reason why the H_2O_2 radical form cannot remove phenol efficiently. In addition, the formation of an electrochemical polymer through chain reactions of phenolic radicals can also contribute to 13% of phenol removal. A stable removal efficiency of 87.0 ± phenol 1.8% to 4 h of continuous operation can be achieved with an average rate of oxidation of 0.059 ± 0.001 mol/h/m^2 [19, 28]. The electrochemical CNT filtering system is thus developed with H_2O_2 generated in situ for a new application of filters in this process, where carbon nanotubes can be used as an effective treatment for removing nearly 100% of organic pollutants (Fig. 11.6).

This book belongs to Kitab Liaison (ocd1996@gmail.com) Copyright Elsevier 2023

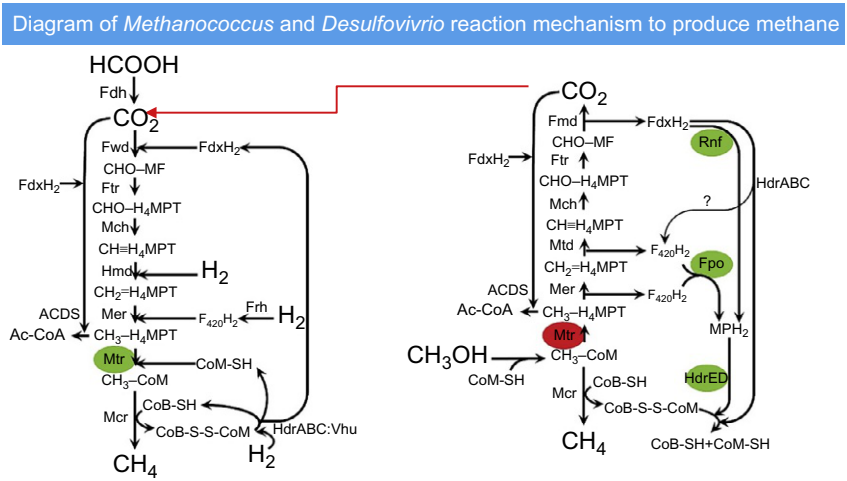

Fig. 11.6 Biochemical path of methanogenesis to a chain reaction for producing methane from domestic waste, including human feces, where *Methanococcus* and *Desulfovivrio* bacteria are the main catalysts.

After this step, the product can be stored in a closed chamber to allow the thermophilic anaerobic codigestion process to thicken. Then, the sludge is to be placed in free oxygen tanks called digesters and heated to at least 95°F for 10–15 days to stabilize the thickened sludge by converting much of the material into methane gas [8, 29]. It will therefore make it a safer environment for the bioreactor when the waste is being discharged, which will stimulate the growth of anaerobic bacteria of *Desulfovivrio* and *Methanecoccus,* which consumes organic matter in the sludge and thrive in a free anaerobic environment, which is different with bacteria in the aeration tanks (Fig. 11.7).

Results and discussion

Conversion of solar energy

To establish a connection between the number of light quanta by the steady state ' the intensity of solar irradiance is considered as the primary source of energy volts to be converted into electricity by the PV panel [23, 30]. The number of stationary states of the light quanta is a certain type of polarization whose frequency is in the range of ν_r to $\nu_r + d\nu_r$. From there, maximum solar radiation it can be achieved at 1.4 eV with an energy value of 27.77 mW/m^2 eV based on an average of 5 h of solar irradiance harvesting

This book belongs to Kitab Liaison (ocd1996@gmail.com) Copyright Elsevier 2023

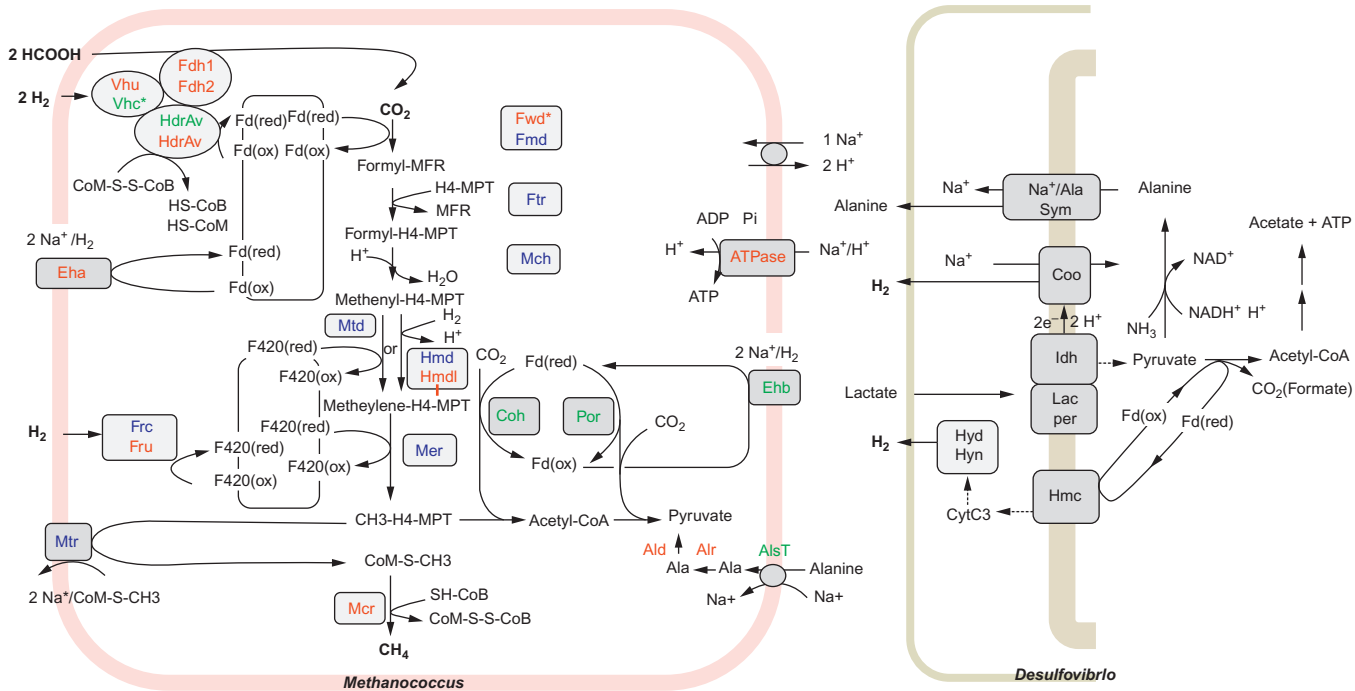

Fig. 11.7 The methanogenesis process shows the detailed biochemical process of *M. maripaludis* and *D. vulgaris* bacterial syntrophic interaction, highlighting the central energy generation and consuming the mechanism to produce methane as a source of bioenergy.

This book belongs to Kitab Liaison (ocd1996@gmail.com)

Copyright Elsevier 2023

in a day at peak levels, which is the equivalent of 27,770 kW/year or 7.6 kW/day energy [13, 31]. Due to physical principles, there are losses in the conversion of solar energy into DC power and converting direct current into alternating current (AC). This ratio of AC to DC is called the "derating factor," which is typically 0.8 [12, 26]. Thus, the surface texture of selective solar metal is excellent in energy conversation [11, 32] because the current net conversion by solar panels is 125% higher level with an efficiency of 80% [1, 30, 33] of solar panels, which means that (27,770 × 1.25 × 0.8) = 27,770 kW/year or 7.6 kW/day. The energy remains equal to the solar energy initially what was before the introduction to the solar panel. Necessarily, the maximum solar irradiance is depicted as 1.4 eV with an energy value of 27.77 mW/m^2 eV in Fig. 11.8 per year in an average of 5 h a day at maximum levels for 365 days referenced by panel Solar and black body [16, 32, 34]. A standard residential house requires an average of 12 kW/day [10, 12, 29]. As the produced energy is equivalent to 27,770 kW/year or 7.6 kW/day, this in fact will meet the energy demand for a residential house requiring 12 kW/day by using only two solar panels of 1 m^2 each. The average monthly energy consumption rate of a commercial office or building is about 10,000 kW/day for a footprint of 32 m × 31 m with 30 m (10 floors), respectively [25, 35, 36]. In the calculation of a building with an average of a 32 m × 31 m footprint with a height of 30 m, the total installation of 1 m^2 PV panels requires 1195 units (945 + 250) with the capacity of 7.6 kW/unit energy production. This can provide total energy × 1195 = 9082 kW/day to meet the daily energy demand of about 10,000 kW/day for a commercial office or building.

Cost comparison

The total cost for 30 years of energy consumption from a conventional source for a standard building (100-person capacity) at 0.12/kwh of 4000 kwh per month is (30 × 12 × 4000 × 0.12) = $172,800. On the other hand, the following data calculated the net cost of solar energy panel installation and energy production and maintenance for 30 years (Table 11.1).

This comparison between conventional energy use and solar panel energy *production* clearly shows a cost savings of $68,400 when solar panels are used as the energy source for a building.

Conversion of biogas

Because the anaerobic *codigestion* of domestic perishable waste and human feces is conducted in the bioreactor, thus, the *methanogenesis* starts in the

This book belongs to Kitab Liaison (ocd1996@gmail.com) Copyright Elsevier 2023

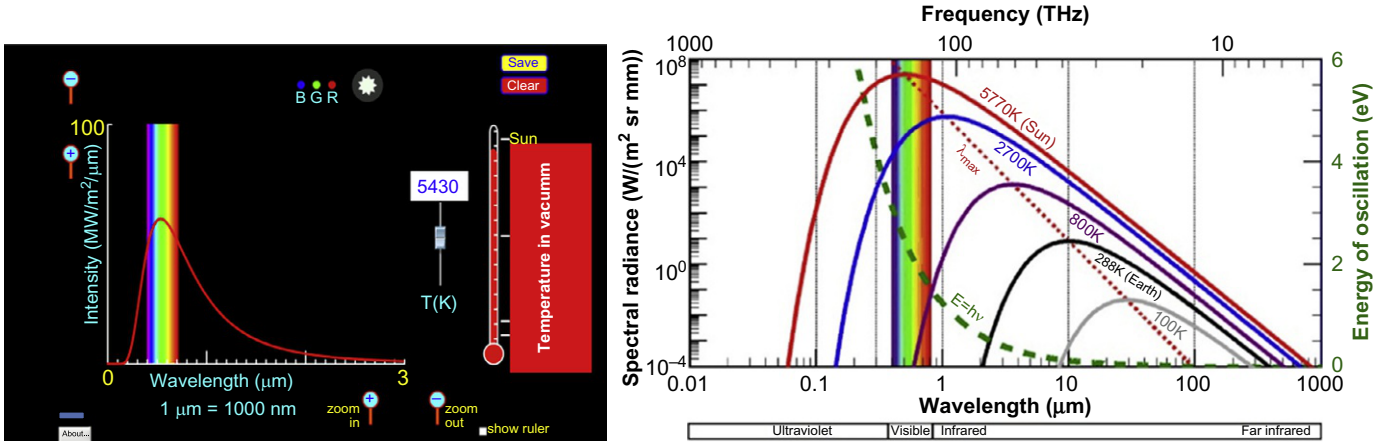

Fig. 11.8 The blackbody radiation in various temperatures at 5770 K power is 6.31 × 107 (W/m^2); Peak E is 1.410 (eV); Peak λ is 0.88 (μm); Peak μ is 2.81 × 107 (W/m^2 eV).

This book belongs to Kitab Liaison (ocd1996@gmail.com)

Copyright Elsevier 2023

Table 11.1 Design and construction cost of the solar panel for energy production of a 10-story building.

List of components	Materials cost	Labor cost	Equipment cost	GC & OH cost	Total cost
Solar panel	$10,000	$5000	$2500	$3500	$21,000
Instrumentation	$2000	$1000	$2000	$1000	$6000
Electrical and mechanical control	$2500	$1000	$1000	$900	$5400
Supply for 30 years cost at $0.05/kwh for monthly 4000 kwh for 100 people					$72,000
				Total cost	$104,400

This estimate is (1 m^2 each solar panel and a total of 1195 panels) prepared by confirming the recent (June 2017) cost of materials from selected manufacturers and a labor rate added in accordance with international unions of specified trade workers considering the location in the United States. The equipment rental cost is calculated as the current rental market in conjunction with the standard practice of construction of the production rate.

bioreactor immediately. Consequently, the inorganic loading rate starts to form a *COD* from the various parameters of *raw thermophilic, raw mesophilic, ground thermophilic, raw mesophilic, sludge thermophilic, and sludge mesophilic* condition of the waste (Fig. 11.9).

The effects of inorganic loading rate are enforced to form anaerobic digestion foaming to produce bioenergy (CH_4), and Fig. 11.10 shows the results of the formation of bioenergy (CH_4), which are examined by computerized gas chromatograph and plotted.

The successful biogas production is practically at a low cost and will have a broad variety of applicable forms to produce heat, steam, electricity, and the utilization of household kitchen gas.

Cost comparison

The total cost for gas supply from a conventional source of a utility company and/or an agency for a standard 10-story building at $100/floors/month is $(1000 \times 50 \times 12 \times 30) = \$1{,}800{,}000$ for 30 years consumption. Similarly,

This book belongs to Kitab Liaison (ocd1996@gmail.com) Copyright Elsevier 2023

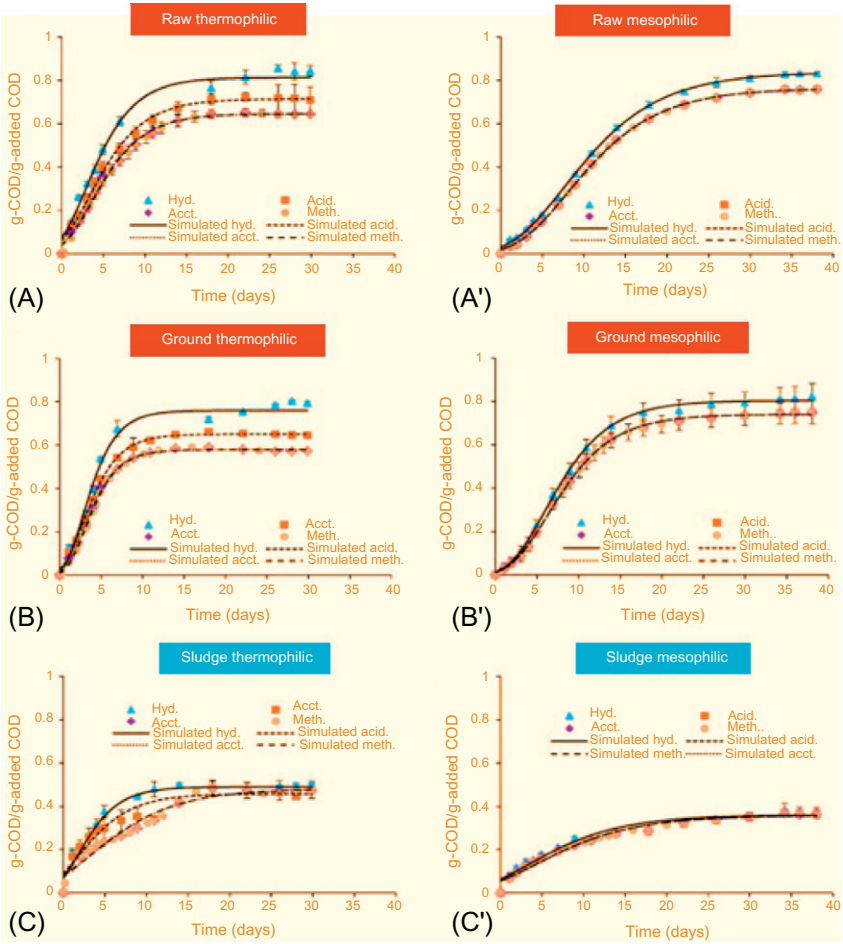

Fig. 11.9 The inorganic (COD) loading rate formation in (A) raw thermophilic and raw mesophilic, (B) ground thermophilic and raw mesophilic, (C) sludge thermophilic and sludge mesophilic condition of the waste.

the comparison between gas use from a conventional utility company and/or an agency and the onsite biogas production revealed a cost savings of $1,400,400 through conducting the following data calculation of bioreactor installation and energy production for 30 years and supply for domestic use (Table 11.2).

This book belongs to Kitab Liaison (ocd1996@gmail.com) Copyright Elsevier 2023

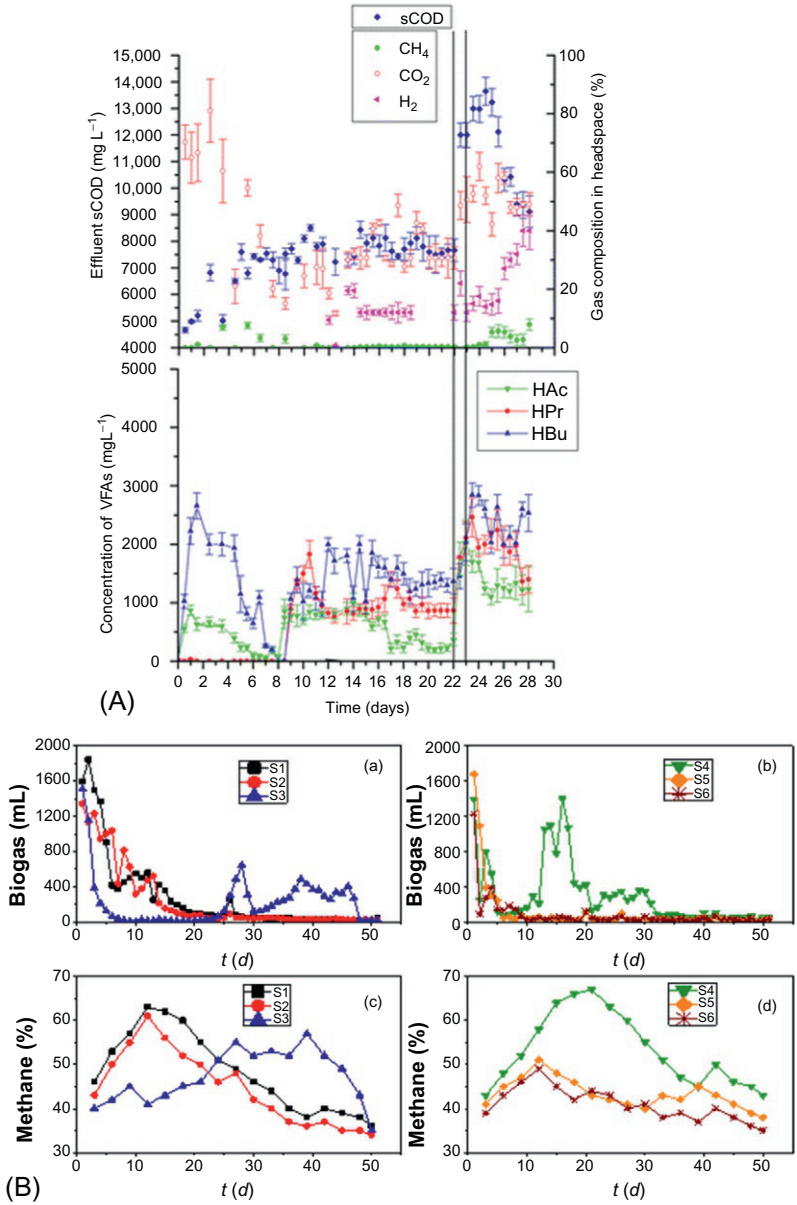

Fig. 11.10 (A) The effects of inorganic loading rate to produce bioenergy (CH_4) and (B) the production of daily biogas levels considering biogas yields; methane contents; and methane yields during the continuous anaerobic digestion of the waste.

This book belongs to Kitab Liaison (ocd1996@gmail.com)
Copyright Elsevier 2023

Table 11.2 Design and construction cost of the biogas production for a 10-story building.

List of components	Materials cost	Labor cost	Equipment cost	GC & OH cost	Total cost
Detention chamber	$10,000	$5000	$2500	$3500	$21,000
Bioreactor	$100,000	$75,000	$50,000	$45,000	$270,000
Electrical and mechanical control	$20,500	$10,000	$10,000	$8100	$48,600
Gas supply and maintenance for 30 years at $2000/year					$60,000
				Total cost	$399,600

This estimate was prepared by confirming recent (June 2017) costs of material from selected manufacturers and the labor rate as added in accordance with international unions of specified trade workers considering the location in the United States. The equipment rental cost is calculated as the current rental market in conjunction with the standard practice of construction of the production rate.

Conclusion

The development of residential and commercial buildings in cities, suburbs, and rural areas around the world has accelerated exponentially over the last few decades. Consequently, climate change is increasing rapidly due to conventional energy consumption by the building sector. In addition, traditional domestic waste and wastewater management are creating severe environmental pollution, causing damage to human health and harm to the flora and fauna in the aquatic environment. Here, with *green science*, an innovative technology could be the cutting-edge science to solve the energy and gas demand for a building. This technology of *green science* that could produce these two vital needs by itself by using the exterior building skin as the PV panel to produce energy and the domestic waste to produce gas would be the most innovative technology for building a sustainable world.

Acknowledgments

This research was supported by Green Globe Technology under grant RD-02018-01 to building a better environment. It is does not have any financial interest by any means. Any findings, conclusions, and recommendations expressed in this paper are solely those of the author, who confirm that the article has no conflicts of interest for publication in a suitable journal.

This book belongs to Kitab Liaison (ocd1996@gmail.com) Copyright Elsevier 2023

References

[1] L. Duan, S. Sun, L. Yue, W. Qu, J. Bian, Study on different zero CO_2 emission IGCC systems with CO_2 capture by integrating OTM, Int. J. Energy Res. 40 (10) (2016) 1410–1427.

[2] M. Hossain, Design and construction of ultra-relativistic collision PV panel and its application into building sector to mitigate total energy demand, J. Build. Eng. 9 (2017) 147–154.

[3] B. Liu, R. Jordan, The interrelationship and characteristic distribution of direct, diffuse and total solar radiation, Sol. Energy 4 (3) (1960) 1–19.

[4] M. Green, J. Zhao, A. Wang, S. Wenham, Progress and outlook for high-efficiency crystalline silicon solar cells, Sol. Energy Mater. Sol. Cells 65 (1–4) (2001) 9–16.

[5] J.C. Maxwell, A Dynamic Theory of the Electromagnetic Field, 1996. Reprinted by Wipf and Stock Publishers 1864 (32).

[6] J. Romero-García, A. Sanchez, G. Rendón-Acosta, J. Martínez-Patiño, E. Ruiz, G. Magaña, E. Castro, An olive tree pruning biorefinery for co-producing high value-added bioproducts and biofuels: economic and energy efficiency analysis, BioEnergy Res. 9 (4) (2016) 1070–1086.

[7] W. Shockley, H. Queisser, Detailed balance limit of efficiency of p-n junction solar cells, J. Appl. Phys. 32 (3) (1961) 510–519.

[8] A. Diniz, L. Neto, C. Camara, P. Morais, C. Cabral, D. Filho, R. Ravinetti, E. França, D. Cassini, M. Souza, J. Santos, M. Amorim, Review of the photovoltaic energy program in the state of Minas Gerais, Brazil, Renew. Sust. Energ. Rev. 15 (6) (2011) 2696–2706.

[9] M. Hossain, Green science: advanced building design technology to mitigate energy and environment, Renew. Sust. Energ. Rev. 81 (2018) 3051–3060.

[10] C. Gopal, M. Mohanraj, P. Chandramohan, P. Chandrasekar, Renewable energy source water pumping systems—a literature review, Renew. Sust. Energ. Rev. 25 (2013) 351–370.

[11] R. Millikan, A direct photoelectric determination of Planck's "h" Phys. Rev. 7 (3) (1916) 355–388.

[12] D. Muhsen, T. Khatib, F. Nagi, A review of photovoltaic water pumping system designing methods, control strategies and field performance, Renew. Sust. Energ. Rev. 68 (2017) 70–86.

[13] B. Bhandari, S. Poudel, K. Lee, S. Ahn, Mathematical modeling of hybrid renewable energy system: a review on small hydro-solar-wind power generation, Int. J. Precis. Eng. Manuf. Green Technol. 1 (2) (2014) 157–173.

[14] C. Chen, Physics of Solar Energy, John Wiley and Sons, Chichester, 2011, pp. 41–100.

[15] A. Mohd Zin, H.A. Mahmoud Pesaran, A. Khairuddin, L. Jahanshaloo, O. Shariati, An overview on doubly fed induction generators′ controls and contributions to wind based electricity generation, Renew. Sustain. Energy Rev. 27 (2013) 692–708.

[16] S. Diaf, G. Notton, M. Belhamel, M. Haddadi, A. Louche, Design and techno-economical optimization for hybrid PV/wind system under various meteorological conditions, Appl. Energy 85 (10) (2008) 968–987.

[17] P. Nema, R. Nema, S. Rangnekar, A current and future state of art development of hybrid energy system using wind and PV-solar: a review, Renew. Sust. Energ. Rev. 13 (8) (2009) 2096–2103.

[18] C. Kennedy, H. Price, Progress in development of high-temperature solar-selective coating, in: ASME 2005 International Solar Energy Conference, 2005, , pp. 749–755.

[19] R. King, D. Law, K. Edmondson, C. Fetzer, G. Kinsey, H. Yoon, R. Sherif, N. Karam, 40% efficient metamorphic GaInP/GaInAs/Ge multijunction solar cells, Appl. Phys. Lett. 90 (18) (2007) 183516.

This book belongs to Kitab Liaison (ocd1996@gmail.com) Copyright Elsevier 2023

[20] C. Brabec, N. Sariciftci, J. Hummelen, Plastic solar cells, Adv. Funct. Mater. 11 (1) (2001) 15–26.
[21] A. Gaillard, P. Poure, S. Saadate, M. Machmoum, Variable speed DFIG wind energy system for power generation and harmonic current mitigation, Renew. Energy 34 (6) (2009) 1545–1553.
[22] I. Gelfand, R. Sahajpal, X. Zhang, R. Izaurralde, K. Gross, G. Robertson, Sustainable bioenergy production from marginal lands in the US Midwest, Nature 493 (7433) (2013) 514–517.
[23] Y. Liu, J. Xie, C. Ong, C. Vecitis, Z. Zhou, Electrochemical wastewater treatment with carbon nanotube filters coupled with in situ generated H_2O_2, Environ. Sci.: Water Res. Technol. 1 (6) (2015) 769–778.
[24] M. Hossain, Photonic thermal control to naturally cool and heat the building, Appl. Therm. Eng. 131 (2018) 576–586.
[25] M. Hossain, Green science: independent building technology to mitigate energy, environment, and climate change, Renew. Sust. Energ. Rev. 73 (2017) 695–705.
[26] J.K. Beatty, C.C. Peterson, A. Chaokin, The Solar System, Cambridge University Press, Cambridge, 1999.
[27] H. Ruiz, A. Martínez, W. Vermerris, Bioenergy potential, energy crops, and biofuel production in Mexico, BioEnergy Res. 9 (4) (2016) 981–984.
[28] J. Rhodes, C. Upshaw, W. Cole, C. Holcomb, M. Webber, A multi-objective assessment of the effect of solar PV array orientation and tilt on energy production and system economics, Sol. Energy 108 (2014) 28–40.
[29] H. Bethe, Energy production in stars, Phys. Rev. 55 (1) (1939) 103.
[30] M. Grätzel, Photoelectrochemical cells, Nature 414 (6861) (2001) 338–344.
[31] J. Zhao, A. Wang, P. Altermatt, S. Wenham, M. Green, 24% efficient perl silicon solar cell: recent improvements in high efficiency silicon cell research, Sol. Energy Mater. Sol. Cells 41–42 (1996) 87–99.
[32] M. Born, E. Wolf, Principles of Optics, seventh ed., Cambridge University Press, Cambridge, 1999 (38).
[33] M. Green, Limits on the open-circuit voltage and efficiency of silicon solar cells imposed by intrinsic Auger processes, IEEE Trans. Energy Convers. 31 (5) (1984) 671–678.
[34] M. Dürr, A. Cruden, S. Gair, J. McDonald, Dynamic model of a lead acid battery for use in a domestic fuel cell system, J. Power Sources 161 (2) (2006) 1400–1411.
[35] N. Izadyar, H. Ong, W. Chong, K. Leong, Resource assessment of the renewable energy potential for a remote area: a review, Renew. Sust. Energ. Rev. 62 (2016) 908–923.
[36] S. Klein, Calculation of flat-plate collector loss coefficients, Sol. Energy 17 (1) (1975) 79–80.

This book belongs to Kitab Liaison (ocd1996@gmail.com) Copyright Elsevier 2023

CHAPTER 12

Green building complexes

Introduction

Conventional heating and cooling systems installed in premises are causing serious environmental and atmospheric problems. Traditional heating technology consumes fossil fuels and releases CO_2, which is a major contributor to climate change. Excessive CO_2 emissions threaten the environment and can potentially trigger catastrophic natural disasters. Conventional cooling technologies also release chlorofluorocarbons, which create holes in the ozone layer. The ozone layer, which lies between 9.3 and 18.6 miles (between 15 and 30 km) above the Earth's surface, is a protective blanket layer that blocks most of the sun's high-frequency ultraviolet rays. Those rays can induce skin cancer in humans and serious reproductive problems in all mammals [1–3]. Although clean-energy technology, climate change, and conventional heating/cooling systems have been extensively researched [4–7], natural cooling and heating systems in the building sector are rarely reported. Therefore, in this study, I propose a natural cooling and heating technology based on the Bose-Einstein photon distribution mechanism and the activation of the Higgs boson ($H \rightarrow \gamma\gamma^{-}$) quantum field. The proposed system decodes photons (solar energy) into cooling and heating states. Cooling photon emission panels consisting of nano-point breaks and waveguides, which install helium in a portion of the exterior curtain wall, have already been proposed [8, 9]. Quantum electrodynamics (QED) waveguides naturally cool the photons emitted by the sun using photon band edges (PBEs) [10, 11]. Mediated by two-diode semiconductors, the cooling-state photon can then be transformed into a heating-state photon through the bremsstrahlung radiation (BR) emitted by quantum Higgs bosons ($H \rightarrow \gamma\gamma^{-}$), creating an electromagnetic field that naturally heats the building [12–14]. This cooling and heating transformation process is a novel approach that mitigates unsustainable energy usage, damage to the environment, and the depletion of the ozone layer.

Sustainable Development for Mass Urbanization
https://doi.org/10.1016/B978-0-12-817690-0.00012-9
© 2019 Elsevier Inc.
All rights reserved.

This book belongs to Kitab Liaison (ocd1996@gmail.com)
Copyright Elsevier 2023

Methods and simulation

Cooling mechanism

Activated photons can be decoded into the cooling state in photon emission networks of nano-point breaks, waveguides, and helium-assisted curtain walls, which create point defects in the photon emission panel [15–17]. In the same way, the arrays of photonic band-gap (PBG) waveguide defects can be incorporated into curtain walls [18–20]. Such point defects and PBG waveguides decode the quantum dynamics of photons under helium cooling conditions, providing a means of cooling solar photons. The present study calculates the formation of the cooling state by the conversion of solar photons in MATLAB (v. 9.0) software. In these calculations, helium waveguides embedded in the curtain wall are treated as photon reservoirs. The electrodynamics of the cooling-state photons can be expressed by the following Hamiltonian [10, 21, 22]:

$$H = \sum \omega_{ci} a_i^{\dagger} a_i + \sum_K \omega_k b_k^{\dagger} b_k + \sum_{ik} \left(V_{ik} a^{\dagger} b_k + V_{ik}^{*} b_k^{\dagger} a_i \right) \tag{12.1}$$

where $a_i(a_i^{\dagger})$ and $b_k(b_k^{\dagger})$ represent the drivers of the nano-point break modes and the photodynamic modes of the photon nanostructure, respectively, and the coefficient, V_{ik}, represents the magnitudes of the photonic modes among the nano-breakpoints and photon nanostructures. Fig. 12.1 displays the transmissivity contours and the spectra of photon plane waves and pulses.

The proposed photon module, which generates HcP^{-} to cool a premise, comprises helium-assisted point breaks, two diodes, and two resistors (see Fig. 12.2). The current in the module is converted from the photon energy.

The current-voltage (I–V) characteristics of the photon cells in the single-diode mode are given by

$$I = I_L - I_o \left\{ \exp\left[\frac{q(V + I_{R_s})}{AkTc} \right] - 1 \right\} - \frac{(V + I_{R_s})}{R_s}. \tag{12.2}$$

where I_L represents the photon generating current, I_o represents the saturated current in the diode, and R_s is the series resistance. A represents the passive function of the diode, k ($= 1.38 \times 10^{-23}$ W/m^{2}K) is the Boltzmann's constant, q ($= 1.6 \times 10^{-19} C$) is the magnitude of the charge of an electron, and T_C represents the functional cell temperature. Subsequently, the I–q relationship in the photon cells varies with the diode and/or saturation current, which is given by [23–25]

This book belongs to Kitab Liaison (ocd1996@gmail.com) Copyright Elsevier 2023

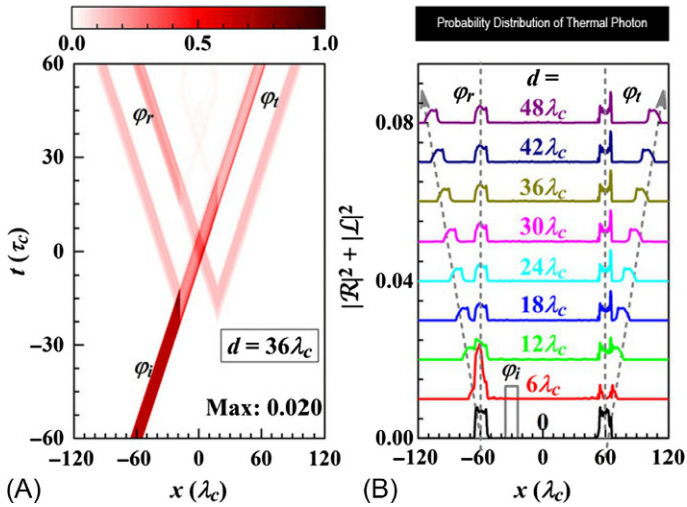

Fig. 12.1 (A) Contour map of the photon probability density (normalized to its maximum value 0.020) as functions of *x* and *t* for an incident square pulse [*gray solid line* in (B)]. (B) Probability distributions of the reflected and transmitted pulses of thermal photons.

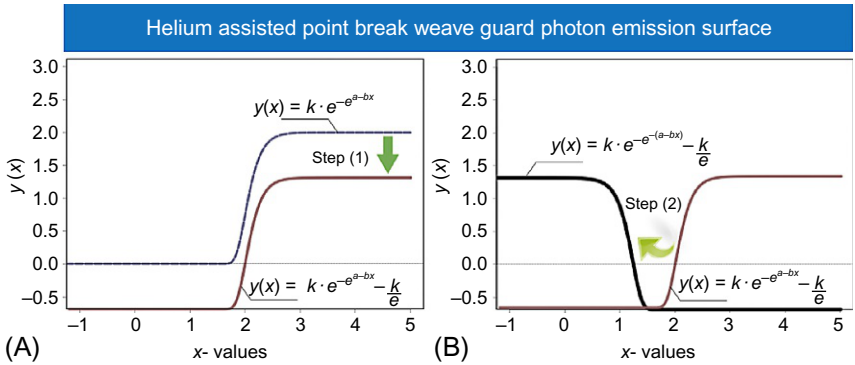

Fig. 12.2 Diagram of the two-diode model of the solar irradiance receptor. Electrons are cooled in the glazing wall skin by photon induction aided by helium-assisted point breaks considering (A) shifting the curve step 1, (B) refection of the symmetry step 2.

$$I_o = I_{R_s}\left(\frac{T_C}{T_{ref}}\right)^3 \exp\left[\frac{qEG\left(\frac{1}{T_{ref}} - \frac{1}{T_C}\right)}{KA}\right] \tag{12.3}$$

In Eq. (12.3), IR_s represents the saturation current, which depends on the functional temperature and solar irradiance speed, and qEG represents

This book belongs to Kitab Liaison (ocd1996@gmail.com) Copyright Elsevier 2023

the band-gap energy of the electrons per unit area of the photon cell. The I–V characteristics of various two-diode models are shown in Fig. 12.3.

In the photon module, the I–V equation integrates the I–V curves of all cells in the photon emission panel. The V–R relationship in the module is given by

$$V = -IR_s + K \log\left[\frac{I_L - I + I_O}{I_O}\right] \tag{12.4}$$

where K is a constant $\left(=\frac{AkT}{q}\right)$ and I_{mo} and V_{mo} are the current and voltage in the PV panel, respectively. Therefore, the relationship between I_{mo} and V_{mo} is the same as the I–V relationship in the PV cell:

$$V_{mo} = -I_{mo}R_{smo} + K_{mo}\log\left(\frac{I_{Lmo} - I_{mo} + I_{omo}}{I_{omo}}\right) \tag{12.5}$$

where I_{Lmo} represents the photon-generated current, I_{omo} represents the saturated current in the diode, R_{smo} is the series resistance, and K_{mo} is a constant. When the resistances of all nonseries (NS) cells are connected in series, the total resistance is $R_{smo} = N_S \times R_s$, and the constant is $K_{mo} = N_S \times K$. The current flowing into the series of connected cells is the same in each component, that is, $I_{omo} = I_o$ and $I_{Lmo} = I_L$. Thus, the I_{mo}–V_{mo} relationship in the N_S connected cells is given by

$$V_{mo} = -I_{mo}N_S R_s + N_S K \log\left(\frac{I_L - I_{mo} + I_o}{I_o}\right) \tag{12.6}$$

Similarly, when all N_p cells are connected in parallel, the I_{mo}–V_{mo} relationship is given by [26, 27]

$$V_{mo} = -I_{mo}\frac{R_s}{N_p} + K\log\left(\frac{N_{sh}I_L - I_{mo} + N_p I_o}{N_p I_o}\right) \tag{12.7}$$

Because the photon-generated current depends primarily on the solar irradiance and relativistic temperature conditions of the photon emission panel, the current can be calculated as follows:

$$I_L = G[I_{SC} + K_I\,(T_{\text{cool}})]\,V_{mo} \tag{12.8}$$

$$T_{\text{cool}} = \left(\frac{I_L}{(G * V_{mo})x(I_{sc} + K_I)}\right)$$

This book belongs to Kitab Liaison (ocd1996@gmail.com) Copyright Elsevier 2023

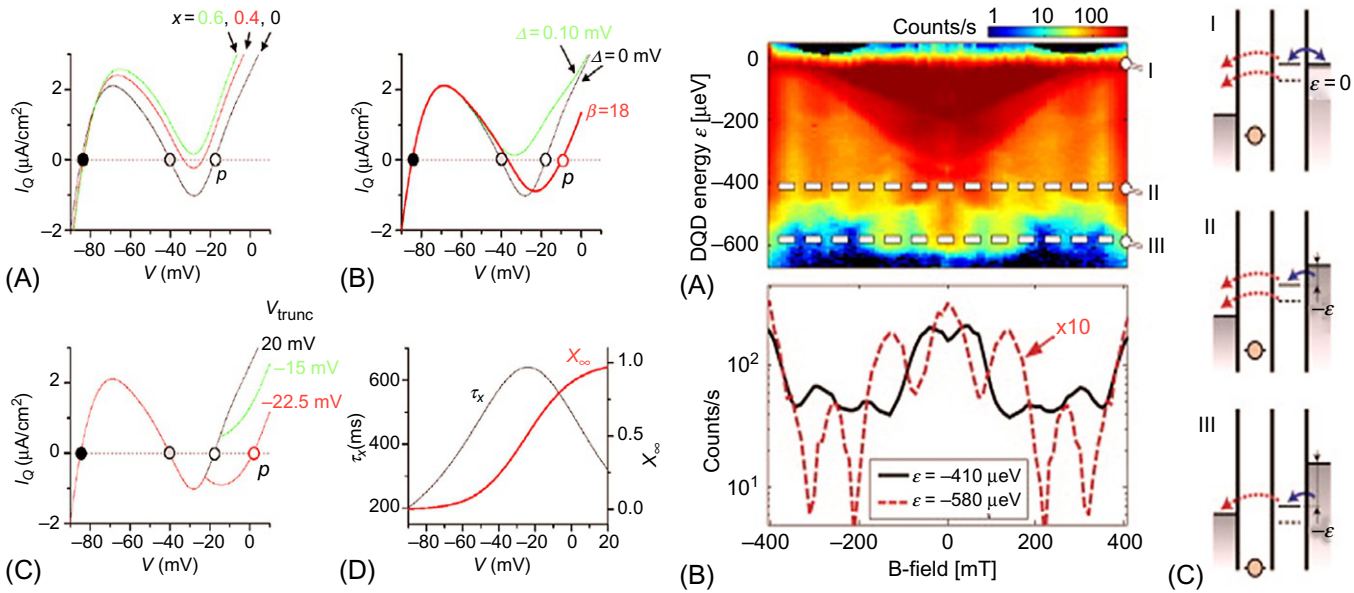

Fig. 12.3 *I–V* characteristics of the two-diode cooling mechanism: (A) glazing wall skin cell in the normal state, (B) glazing wall skin cell under the normalized condition, (C) glazing wall skin cell module in the normal state, and (D) glazing wall skin cell module under the normalized condition.

This book belongs to Kitab Liaison (ocd1996@gmail.com)

Copyright Elsevier 2023

where I_{sc} is the photon current per unit area at 25°C, K_I denotes the relativistic photon panel coefficient, T_{cool} represents the cooling temperature of the photon cell, and G represents the solar energy per unit area [28, 29].

Heating mechanism

To convert cooling photons to heating photons, researchers have exploited the Higgs boson electromagnetic field and determined the accuracy and parameters of the photon-heating relationship [30–32]. Thus, to create a local Higgs quantum field in the curtain wall skin, I simulated abelian local symmetries in MATLAB 9.0 software. The penetration of solar irradiance breaks the gauge field symmetry, and the Goldstone scalar particle becomes the longitudinal mode of the vector boson [27, 33]. In the abelian case, the local symmetry of each spontaneously broken particle T^{α} is the corresponding gauge field of $A_{\mu}^{\alpha}(x)$. The Higgs quantum field begins to operate in local U(1) phase symmetry [26, 34, 35]. Thus, the model can comprise a complex scalar field $\Phi(x)$ of electric charge q coupled to the EM field $A^{\mu}(x)$, which can be expressed by the following Lagrangian function:

$$\mathcal{L} = -\frac{1}{4} F_{\mu\nu} F^{\mu\nu} + D_{\mu}\Phi^{*} D^{\mu}\Phi - V(\Phi^{*}\Phi) \tag{12.9}$$

where

$$\begin{aligned} D_{\mu}\Phi(x) &= \partial_{\mu}\Phi(x) + iqA_{\mu}(x)\Phi(x) \\ D_{\mu}\Phi^{*}(x) &= \partial_{\mu}\Phi^{*}(x) - iqA_{\mu}(x)\Phi^{*}(x) \end{aligned} \tag{12.10}$$

and

$$V(\Phi^{*}\Phi) = \frac{\lambda}{2}(\Phi^{*}\Phi)^{2} + m^{2}(\Phi^{*}\Phi) \tag{12.11}$$

Suppose that $\lambda > 0$ but $m^2 < 0$ so that $\Phi = 0$ is a local maximum of the scalar potential, and the minima form a degenerate circle $\Phi = \frac{v}{\sqrt{2}} * e^{i\theta}$ with

$$v = \sqrt{\frac{-2m^2}{\lambda}} \text{ for any real } \theta \tag{12.12}$$

Consequently, the scalar field Φ develops a nonzero vacuum expectation value $\langle\Phi\rangle \neq 0$, which spontaneously creates the U(1) symmetry of the magnetic field. The breakdown of this symmetry creates a massless Goldstone scalar from the phase of the complex field $\Phi(x)$. However, in local U(1) symmetry, the phase of $\Phi(x)$ is the x-dependent phase of the dynamic $\Phi(x)$ field rather than the phase of the expectation value $\langle\Phi\rangle$.

This book belongs to Kitab Liaison (ocd1996@gmail.com) Copyright Elsevier 2023

To confirm this mechanism, I express the scalar field space in polar coordinates:

$$\Phi(x) = \frac{1}{\sqrt{2}} \Phi_r(x) * e^{i\Theta(x)}, \text{real}\, \Phi_r(x) > 0, \text{real}\, \Phi(x) \tag{12.13}$$

As the field in this formulation is singular at $\Phi(x) = 0$, it is inapplicable to theories with $\langle \Phi \rangle \neq 0$ but is adequate for spontaneously broken theories, where $\Phi\langle x \rangle \neq 0$ is expected almost everywhere. In terms of the real fields $\phi_r(x)$ and $\Theta(x)$, the scalar potential depends only on the radial field ϕ_r,

$$V(\phi) = \frac{\lambda}{8} \left(\phi_r^2 - v^2\right)^2 + \text{const} \tag{12.14}$$

If the radial field shifted by a variable scalar, $\Phi_r(x) = v + \sigma(x)$, we have

$$\phi_r^2 - v^2 = (v + \sigma)^2 - v^2 = 2v\sigma + \sigma^2 \tag{12.15}$$

$$V = \frac{\lambda}{8} \left(2v\sigma - \sigma^2\right)^2 = \frac{\lambda v^2}{2} * \sigma^2 + \frac{\lambda v}{2} * \sigma^3 + \frac{\lambda}{8} * \sigma^4 \tag{12.16}$$

Meanwhile, the covariant derivative $D_\mu \phi$ becomes

$$D_\mu \phi = \frac{1}{\sqrt{2}} \left(\partial_\mu \left(\phi_r e^{i\Theta}\right) + iqA_\mu * \phi_r e^{i\Theta}\right) = \frac{e^{i\Theta}}{\sqrt{2}} \left(\partial_\mu \phi_r + \phi_r * i\partial_\mu \Theta + \phi_r * iqA_\mu\right) \tag{12.17}$$

$$\begin{aligned} \left|D_\mu \phi\right|^2 &= \frac{1}{2} \left|\partial_\mu \phi_r + \phi_r * i\partial_\mu \Theta + \phi_r * iqA_\mu\right|^2 \\ &= \frac{1}{2} \left(\partial_\mu \phi_r\right) + \frac{\phi_r^2}{2} * \left(\partial_\mu \Theta qA_\mu\right)^2 \\ &= \frac{1}{2} \left(\partial_\mu \sigma\right)^2 + \frac{(v + \sigma)^2}{2} * \left(\partial_\mu \Theta + qA_\mu\right)^2 \end{aligned} \tag{12.18}$$

The Lagrangian is then given by

$$\mathcal{L} = \frac{1}{2} \left(\partial_\mu \sigma\right)^2 - v(\sigma) - \frac{1}{4} F_{\mu\nu} F^{\mu\nu} + \frac{(v + \sigma)^2}{2} * \left(\partial_\mu \Theta + qA_\mu\right)^2 \tag{12.19}$$

To incorporate the heating ($\mathcal{L}_{\text{heat}}$) into the magnetic field properties of this Lagrangian, I expand $\mathcal{L}_{\text{heat}}$ as a power series of the fields (and their derivatives) and extract the quadratic part describing the free particles:

$$\mathcal{L}_{\text{heat}} = \frac{1}{2} \left(\partial_\mu \sigma\right)^2 - \frac{\lambda v^2}{2} * \sigma^2 - \frac{1}{4} F_{\mu\nu} F^{\mu\nu} + \frac{v^2}{2} * \left(qA_\mu + \partial_\mu \Theta\right)^2 \tag{12.20}$$

This book belongs to Kitab Liaison (ocd1996@gmail.com)
Copyright Elsevier 2023

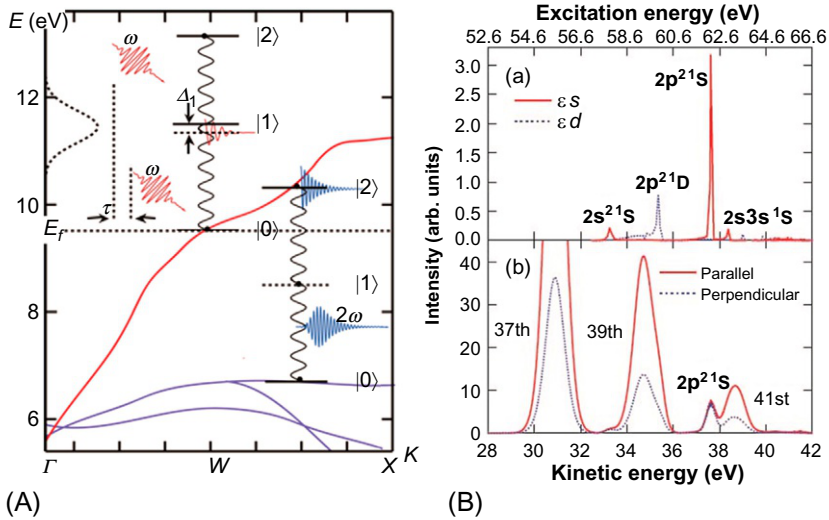

Fig. 12.4 Transformation mechanism of a photon from energy level ω to 2ω (eV) in the two-diode feed semiconductors (A) and quantum field intensity spectra of the electrons (B). The photon excitation energy (eV) is transformed into kinetic energy (eV) by the conversion of the heating state of photons.

Obviously, to initiate high heating within the quantum field of the curtain wall, the free particles (with Lagrangian $\mathcal{L}_{\text{free}}$) must be real scalar particles with positive $m^2 = \lambda v^2$ (where m denotes the particle mass; see Fig. 12.4).

Results and discussion

Cooling mechanism

To mathematically demonstrate the formation of cooling photons by the helium-assisted curtain wall skin, I determined the dynamic photon proliferation by integrating Eqs. (12.15), (12.16). Owing to the cooling unit areal condition $J(\omega)$ and the persistent weak-coupling limit, the curtain wall skin is expected to proliferate photons [10, 26]. Here, $J(\omega)$ is the quantum field area defining the density of states (DOS) field produced in the PV cell by the fine cooling photonic magnitude $V(\omega)$ within the photonic band (PB) and the PV cell [10, 24, 27]. Moreover, photon production should follow the Weisskopf-Winger approximation and/or the Markovian master equation. Consequently, all the proliferated *HcP*s will possess a dynamic state mode [one-dimensional (1D), two-dimensional (2D), and three-dimensional (3D)] in the curtain wall skin, as described in Table 12.1 [36, 37].

This book belongs to Kitab Liaison (ocd1996@gmail.com) Copyright Elsevier 2023

Table 12.1 Photonic structures of the density of states (DOS) in different dimensional modes of the curtain wall skin

Photon	Unit area $J(\omega)$ for different DOS	Reservoir-induced self-energy correction $\Sigma(\omega)$
1D	$\frac{C}{\pi}\frac{1}{\sqrt{\omega-\omega_e}}\Theta(\omega-\omega_e)$	$-\frac{C}{\sqrt{\omega_e-\omega}}$
2D	$-\eta\left[\ln\left\lvert\frac{\omega-\omega_0}{\omega_0}\right\rvert-1\right]\Theta(\omega-\omega_e)\Theta(\Omega_d-\omega)$	$\eta\left[Li_2\left(\frac{\Omega_d-\omega_0}{\omega-\omega_0}\right)-Li_2\left(\frac{\omega_0-\omega_e}{\omega_0-\omega}\right)-\ln\frac{\omega_0-\omega_e}{\Omega_d-\omega_0}\ \ln\frac{\omega_e-\omega}{\omega_0-\omega}\right]$
3D	$\chi\sqrt{\frac{\omega-\omega_e}{\Omega_C}}\exp\left(-\frac{\omega-\omega_e}{\Omega_C}\right)\Theta(\omega-\omega_e)$	$\chi\left[\pi\sqrt{\frac{\omega_e-\omega}{\Omega_C}}\exp\left(-\frac{\omega-\omega_e}{\Omega_C}\right)e_{rfc}\sqrt{\frac{\omega_e-\omega}{\Omega_C}}-\sqrt{\pi}\right]$

The unit area $J(\omega)$ and self-energy induction in the reservoir $\Sigma(\omega)$, determined by the photon dynamics into the extreme relativistic curtain wall skin, differ among the structures. The variables C, η, and χ function as coupled forces between the point break and PV in the curtain wall skin in one, two, and three dimensions [10, 26].

This book belongs to Kitab Liaison (ocd1996@gmail.com)

Copyright Elsevier 2023

In the 3D curtain wall skin, Ω_C is a fine frequency cut-off that avoids the bifurcation of the DOS. Similarly, the 1D and 2D glazing wall skins require a sharp frequency cut-off at Ω_d to avoid negative DOSs (Fig. 12.5). Hence, $Li_2(x)$ and $e_{rfc}(x)$ are di-logarithmic and additive variables, respectively. Subsequently, the DOS of various curtain wall skins, denoted as $\varrho_{PC}(\omega)$, is determined by calculating the photon eigen frequencies and eigen functions of Maxwell's rules in the nanostructures [18, 23, 26]. In a 1D glazing wall skin, the DOS is given by $\varrho_{PC}(\omega) \propto \frac{1}{\sqrt{\omega-\omega_e}}\Theta(\omega-\omega_e)$, where $\Theta(\omega-\omega_e)$ is the Heaviside step function, and ω_e represents the frequency of the PBE at the given DOS.

The DOS is required for accurately predicting the qualitative state of the non-Weisskopf-Winger mode and the photon-cooling state of the photon cell in a 3D isotropic analysis in the curtain wall skin. The DOS and projected DOS (PDOS) are displayed in Fig. 12.6. In a 3D glazing wall skin, the DOS close to the PBE is anisotropic and given by $\varrho_{PC}(\omega) \propto \frac{1}{\sqrt{\omega-\omega_e}}\Theta(\omega-\omega_e)$. This DOS is then clarified with respect to the electromagnetic field vector [1, 10, 26, 35]. In 2D and 1D curtain wall skins, the cooling photon DOS exhibits a pure logarithmic divergence close to the PBE, which is approximated as $\varrho_{PC}(\omega) \propto -[\ln|(\omega-\omega_0)/\omega_0|-1]\Theta(\omega-\omega_e)$, where ω_e represents the central point of the peak in the DOS distribution.

As mentioned above, $J(\omega)$ defines the DOS field produced in the PV cell by the fine cooling photonic magnitude $V(\omega)$ within the PB and the PV cell [10, 24, 27]:

$$J(\omega) = \varrho(\omega)|V(\omega)|^2 \tag{12.21}$$

Hereafter, I consider the PB frequency ω_c and the proliferative photon dynamics $\langle a(t)\rangle = u(t,t_0)\langle a(t_0)\rangle$, where the function $u(t,t_0)$ describes the photon structure. $u(t,t_0)$ is calculated using the dissipative integral differential equation given in Eq. (12.18):

$$u(t,t_0) = \frac{1}{1-\Sigma'(\omega_b)}e^{-i\omega(t-t_0)} + \int_{\omega_e}^{\infty} d\omega \frac{J(\omega)e^{-i\omega(t-t_0)}}{[\omega-\omega_c-\Delta(\omega)]^2+\pi^2 J^2(\omega)} \tag{12.22}$$

where $\Sigma'(\omega_b) = [\partial\Sigma(\omega)/\partial\omega]_{\omega=\omega_b}$ and $\Sigma(\omega)$ represents the PB photon self-energy correction induced in the reservoir,

$$\Sigma(\omega) = \int_{\omega_e}^{\infty} d\omega' \frac{J(\omega')}{\omega-\omega'} \tag{12.23}$$

This book belongs to Kitab Liaison (ocd1996@gmail.com) Copyright Elsevier 2023

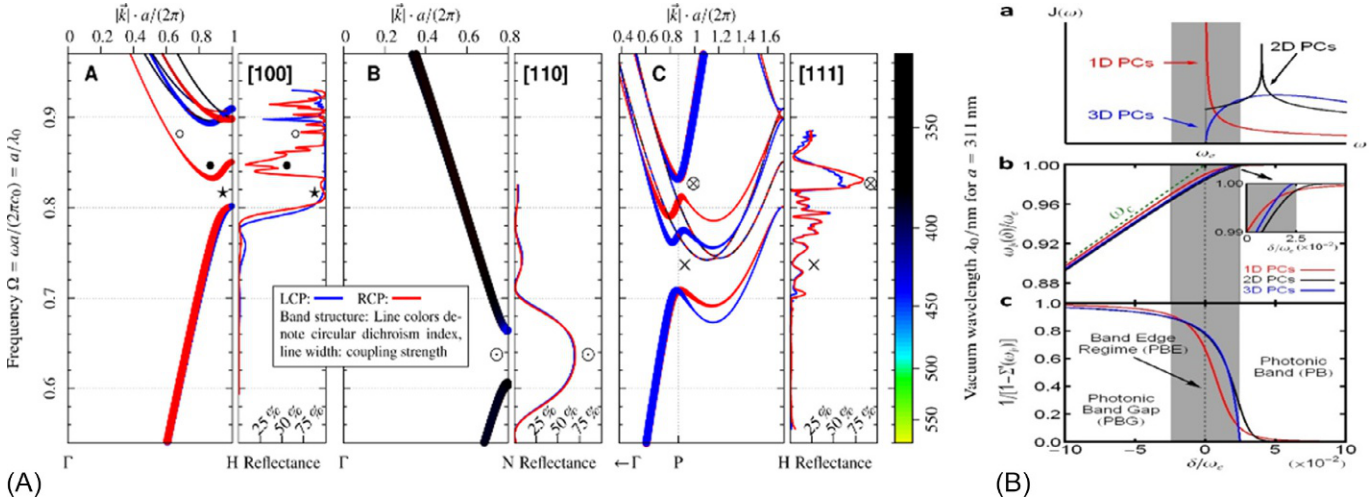

Fig. 12.5 (A) Photonic band structure and energy conversion modes. B—(a) Unit area versus frequency at various DOSs in 1D, 2D, and 3D glazing wall skins. (b) Photonic modes of frequencies for functional tuning. (c) Photonic modes of magnitudes to release the energy calculated by Eq. (12.2). The photonic modes depict the crossover into the glazing wall skin in 1D and 2D. In the complex 3D transitional state, they depict the crossover into the PV cell once the point break frequency *vc* transforms from a PBG area to a photonic band (PB) area [26].

This book belongs to Kitab Liaison (ocd1996@gmail.com)

Copyright Elsevier 2023

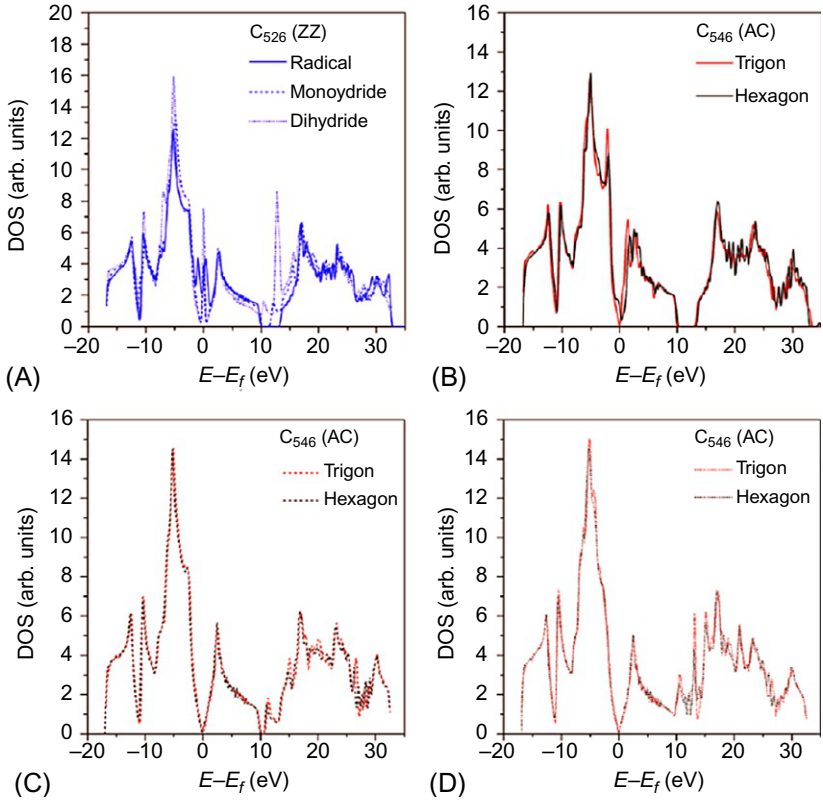

Fig. 12.6 Total density of states (DOS) and the projected density of states (PDOS) of decoded photons for transformation into the cooling state: Panel (A) total DOS (T) and DOS projected onto the s, p, and d orbitals, PDOS of d orbitals on the fourth level of Mo atoms, and PDOS of d orbitals on the third level of Mo atoms; Panel (B) as in Panel (A) but for projected DOS of Mo atoms; Panel (C) as in Panel (A) and PDOS of p orbitals of O atoms. Panel (D) as in Panel (B) and PDOS of *p* orbitals of external S atoms.

Here, the frequency ω_b in Eq. (12.2) represents the cooling photonic frequency mode in the PBG $(0<\omega_b<\omega_e)$,calculated under the pole condition $\omega_b-\omega_c-\Delta(\omega_b)=0$, where $\lesssim\Delta(\omega)=\mathcal{P}\left[\int d\omega'\frac{J(\omega')}{\omega-\omega'}\right]$ is a principal-value integral.

Fig. 12.7A plots the cooling photonic dynamics of the proliferation magnitude $|u(t,t_0)|$, calculated in 1D, 2D, and 3D photon cells for various values of the detuning parameter δ and integrated from the PBG area to the PB area [38–40]. The cooling photonic dynamic rates $\kappa(t)$ are plotted in

This book belongs to Kitab Liaison (ocd1996@gmail.com) Copyright Elsevier 2023

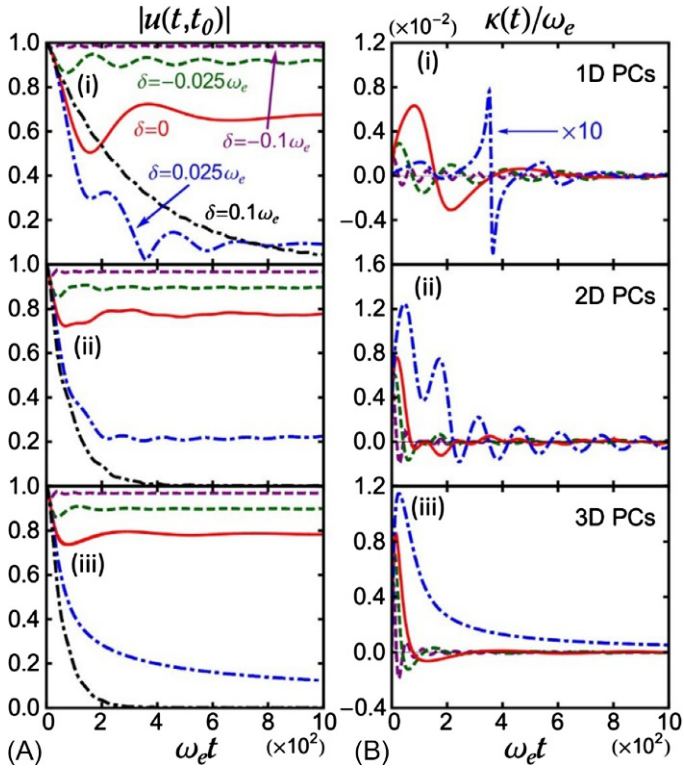

Fig. 12.7 Proliferation of dynamic photons in acted glazing PV cells. (A) PB area $<a(t)> = 5\ u(t,\ t_0)\ <a(t_0)>$ and (B) dynamic photonic rate $k(t)$, plotted for (i) 1D, (ii) 2D, and (iii) 3D acted glazing PV cells [26].

Fig. 12.7B. The results indicate that, once ω_c has crossed from the PBG to the PB area, dynamic photons are produced at a high rate. Because the $u(t, t_0)$ range is $1 \geq |u(t, t_0)| \geq 0$, I have defined the crossover area to satisfy $0.9 \gtrsim |u(t \to \infty, t_0)| \geq 0$. This corresponds to $-0.025\omega_e \lesssim \delta \lesssim 0.025\omega_e$, with a cooling photon induction rate $\kappa(t)$ within the PBG ($\delta < -0.025\omega_e$) and near the PBE($-0.025\omega_e \lesssim \delta \lesssim 0.025\omega_e$).

More specifically, I first consider the PB as the Fock cooling determination n_0, *that is*, $\rho(t_0) = |n_0\rangle\langle n_0|$, which is obtained theoretically through real-time quantum feedback control [2, 26, 41], and then, by solving Eq. (12.1), considering the state of cooling photon induction at time t:

$$\rho(t) = \sum_{n=0}^{\infty} \mathcal{P}_n^{(n_0)}(t)|n_0\rangle\langle n_0| \tag{12.24}$$

This book belongs to Kitab Liaison (ocd1996@gmail.com)
Copyright Elsevier 2023

$$\mathcal{P}_n^{(n_0)}(t) = \frac{[\nu(t,t)]^n}{[1+\nu(t,t)]^{n+1}}[1-\Omega(t)]^{n_0}\, x \sum_{k=0}^{\min\{n_0,\, n\}} \binom{n_0}{k}\binom{n}{k}\left[\frac{1}{\nu(t,t)}\frac{\Omega(t)}{1-\Omega(t)}\right]^k \tag{12.25}$$

where $\Omega(t) = \frac{|u(t,t_0)|^2}{1+\nu(t,t)}$. This result suggests that a Fock state cooling photon is induced into dynamic states $\mathcal{P}_n^{(n_0)}(t)$ of $|n_0\rangle$. In fact, Fig. 12.7 plots the proliferation of photon dissipation $\mathcal{P}_n^{(n_0)}(t)$ in the primary state $|n_0 = 5\rangle$ and in the steady-state limit $\mathcal{P}_n^{(n_0)}(t \to \infty)$. Therefore, the proliferation of the produced cooling photons will ultimately reach a nonequilibrium cooling state that cools the building.

Heating mechanism

In the proposed system, two semiconductors utilize the electromagnetic field created by the Higgs boson quantum field. Therefore, local U(1) gauge-invariant QED allows an additional mass term for the gauge particle under $\varnothing' \to e^{i\alpha(x)}\varnothing$; that is, the cooling photons can be transformed into heating photons. This mechanism can be explained by a covariant derivative with a special transformation rule for the scalar field, given by [42–44]

$$\begin{aligned} \partial_\mu \to D_\mu = \partial_\mu = ieA_\mu \,[\text{covariant derivatives}] \\ A'_\mu = A_\mu + \frac{1}{e}\partial_\mu \alpha \left[A_\mu \text{ derivatives}\right] \end{aligned} \tag{12.26}$$

where the local U(1) gauge-invariant Lagrangian for a complex scalar field is given by

$$\mathcal{L} = (D^\mu)^\dagger \left(D_\mu \varnothing\right) - \frac{1}{4} F_{\mu\nu}F^{\mu\nu} - V(\varnothing) \tag{12.27}$$

The term $\frac{1}{4} F_{\mu\nu}F^{\mu\nu}$ is the kinetic term in the gauge field (heating photons) and $V(\varnothing)$ is an additional term expressed as $V(\varnothing^*\varnothing) = \mu^2(\varnothing^*\varnothing) + \lambda\,(\varnothing^*\varnothing)^2$.

According to the Lagrangian $\mathcal{L}$, perturbations in the quantum field initiate the production of massive scalar particles ϕ_1 and ϕ_2 and a mass μ. In this situation, $\mu^2 < 0$ admits an infinite number of quanta, each satisfying $\phi_1^2 + \phi_2^2 = -\mu^2/\lambda = \nu^2$.In terms of the shifted fields η and ξ, the quantum field is defined as $\phi_0 = \frac{1}{\sqrt{2}}\left[(\upsilon + \eta) + i\xi\right]$, and the covariant derivatives of the Lagrangian become

This book belongs to Kitab Liaison (ocd1996@gmail.com) Copyright Elsevier 2023

$$\begin{aligned}\text{Kinetic term}: \mathcal{L}_{kin}(\eta,\xi) &= (D^{\mu}\phi)^{\dagger}(D^{\mu}\phi) \\ &= (\partial^{\mu} + ieA^{\mu})\phi^{*}\left(\partial_{\mu} - ieA_{\mu}\right)\phi\end{aligned} \tag{12.28}$$

Potential term (to second order): $V(\eta,\xi) = \lambda\, \upsilon^2\eta^2$. Thus, the full Lagrangian can be written as

$$\begin{aligned}\mathcal{L}_{kin}(\eta,\xi) = &\frac{1}{2}\left(\partial_{\mu}\eta\right)^2 - \lambda\upsilon^2\eta^2 + \frac{1}{2}\left(\partial_{\mu}\xi\right)^2 - \frac{1}{4}F_{\mu\nu}F^{\mu\nu} + \frac{1}{2}e^2\upsilon^2A_{\mu}^2 \\ &- e\upsilon A_{\mu}(\partial^{\mu}\xi) + \text{int.terms}\end{aligned} \tag{12.29}$$

Here, η is massive, ξ is massless (as before), μ is the mass term for the quantum, and A_{μ} is fixed up to a term $\partial_{\mu}\alpha$, as is evident in Eq. (12.27). In general, A_{μ} and ϕ change simultaneously, so Eq. (12.28) can be redefined to accommodate the heating photon particle spectrum within the quantum field:

$$\begin{aligned}\mathcal{L}_{\text{scalar}} &= (D^{\mu}\phi)^{\dagger}(D^{\mu}\phi) - V\left(\phi^{\dagger}\phi\right) \\ &= (\partial^{\mu} + ieA^{\mu})\frac{1}{\sqrt{2}}(v+h)\left(\partial_{\mu} - ieA_{\mu}\right)\frac{1}{\sqrt{2}}(v+h) - V\left(\phi^{\dagger}\phi\right)\end{aligned} \tag{12.30}$$

$$\mathcal{L}_{\text{scalar}} = \frac{1}{2}\left(\partial_{\mu}h\right)^2 + \frac{1}{2}e^2A_{\mu}^2(v+h)^2 - \lambda v^2h^2 - \lambda vh^3 - \frac{1}{4}\lambda h^4 + \frac{1}{4}\lambda h^4 \tag{12.31}$$

The expanded term in the Lagrangian of the scalar field suggests that the Higgs boson quantum field can initiate heating photons.

To confirm this heating photon transformation, I calculate the isotropic distribution of movement on the differential cone with respect to the angle θ from the vertical axis. The differential between θ and $\theta + d\theta$ is $\frac{1}{2}\sin\theta\, d\theta$. The differential photon density at energy $\in$ and angle θ is then given by

$$dn = \frac{1}{2}n(\epsilon)\,\sin\theta d_{\in}d\theta \tag{12.32}$$

Consequently, the functional speeds of the high-energy photons were calculated as $c\,(1-\cos\theta)$, and the absorption per unit path length is

$$\frac{d\tau_{abs}}{dx} = \iint\frac{1}{2}\sigma n\,(\epsilon)(1-\cos\theta)\sin\theta d_{\epsilon}d\theta \tag{12.33}$$

Reexpressing these functions as integrals over s instead of θ, by Eqs. (12.31), (12.33), I obtain

This book belongs to Kitab Liaison (ocd1996@gmail.com) Copyright Elsevier 2023

$$\frac{d\tau_{abs}}{dx} = \pi r_0^2 \left(\frac{m^2c^4}{E}\right)^2 \int_{\frac{m^2c^4}{E}}^{\infty} \in^{-2} n(\in)\,\overline{\varphi}\,[s_0(\in)]\,de \tag{12.34}$$

where

$$\overline{\varphi}\,[s_0(\in)] = \int_1^{s_0(\in)} s\overline{\sigma}(s)ds, \overline{\sigma}(s) = \frac{2\sigma(s)}{\pi r_0^2} \tag{12.35}$$

This result defines the dimensional variable $\overline{\varphi}$ and dimensionless cross section $\overline{\sigma}$. The variable $\overline{\varphi}[s_0]$ is calculated based on a detailed graphical frame for $1 < s_0 < 10$. I calculated $\overline{\varphi}$ by a functional asymptotic calculation (Fig. 12.8)

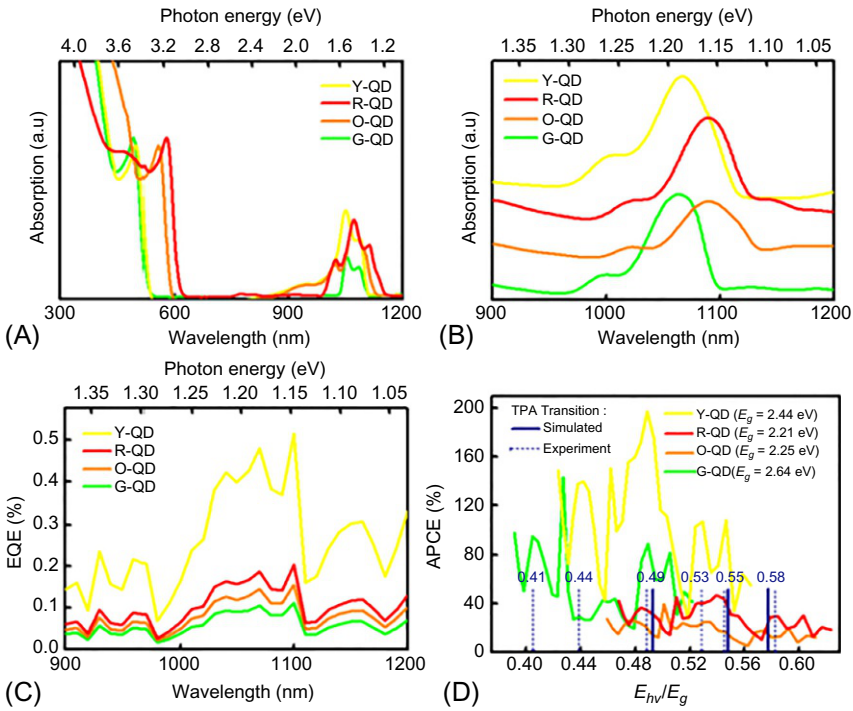

Fig. 12.8 Schematic of the main mechanisms responsible for magnetic-field-induced photon production. (A) Photon heating is simultaneously coupled into the fundamental mode and a higher-order mode of the quantum field. (B) Coincidence rate of the fundamental mode output. (C) Coincidence rate of the higher-order mode output with respect to the detuning parameter. (D) Classical coincidence rates of heating photons with respect to the detuning parameter into the band structure [10, 45, 46].

This book belongs to Kitab Liaison (ocd1996@gmail.com) Copyright Elsevier 2023

$$\overline{\varphi}\,[s_0] = \frac{1+\beta_0^2}{1-\beta_0^2}\ \ln\omega_0 - \beta_0^2\ \ln\omega_0 - \ \ln^2\omega_0 - \frac{4\beta_0}{1-\beta_0^2} - 4\ \ln\omega_0\ \ln(\omega_0+1) - L(\omega_0)$$

where

$$s_0 - 1 \ll 1 \text{ or } s_0 \gg 1$$

$$\beta_0^2 = \frac{1-1}{s_0}, \omega_0 = \frac{(1+\beta_0)}{(1-\beta_0)}$$

and

$$L(\omega_0) = \int_1^{\omega_0} \omega^{-1}\ \ln(\omega_0+1)d\omega \tag{12.36}$$

The last integral can be written as

$$(\omega+1) = \omega\left(\frac{1+1}{\omega}\right), L(\omega_0) = \frac{1}{2}\ \ln^2\omega_0 + L'(\omega_0)$$

where

$$\begin{aligned} L'(\omega_0) &= \int_1^{\omega_0} \omega^{-1}\ \ln\left(1+\frac{1}{\omega}\right)d\omega \\ &= \frac{\pi^2}{12} - \sum_{n=1}^{\infty}(-1)n^{-1}n^{-2}\omega_0^{-n} \end{aligned} \tag{12.37}$$

This accurate representation of the heating photons readily allows the calculation of $\overline{\varphi}[s_0]$ to the desired accuracy for the expected value of s_0. Thus, the corrective functional asymptotic formulas are expressed as follows:

$$\begin{aligned} \overline{\varphi}\,[s_0] &= 2s_0\,(\ln 4s_0 - 2) + \ \ln 4s_0(\ln 4s_0 - 2) \\ &\quad - \frac{(\pi^2-9)}{3} + s_0^{-1}\left(\ln 4s_0 + \frac{9}{8}\right) + \cdots(s_0 \gg 1) \end{aligned} \tag{12.38}$$

$$\begin{aligned} \overline{\varphi}\,[s_0] &= \left(\frac{2}{3}\right)(S_0-1)^{\frac{3}{2}} + \left(\frac{5}{3}\right)(S_0-1)^{\frac{5}{2}} \\ &\quad - \left(\frac{1507}{420}\right)(S_0-1)^{\frac{7}{2}} + \cdots(s_0 - 1 \gg 1) \end{aligned} \tag{12.39}$$

This book belongs to Kitab Liaison (ocd1996@gmail.com)
Copyright Elsevier 2023

The function $\frac{\overline{\varphi}[s_0]}{(s_0-1)}$ is shown in Fig. 12.5 for $1 < s_0 < 10$; at larger s_0, it becomes a natural logarithmic function of s_0. The power-law spectrum of the heating photons is expressed in the form $n(\in) \propto \in^m$ for two systems in a pristine state and for a system with BN in a glazing sheet.

Thus, the light absorption spectrum should feature a high-energy cut-off with $m > 0$. We now derive the heating photon spectrum with a high-energy cut-off.

Consider a spectrum of the form

$$n(\in) = D_{\epsilon}^{\beta}, \epsilon < \epsilon m, \ \beta \leq 0 \tag{12.40}$$

$$n(\in) = 0, \epsilon < \epsilon m \tag{12.41}$$

For this spectrum, I obtained

$$\frac{d\tau_{abs}}{dx} = \pi r_0^2 D \left(\frac{m^2c^4}{E}\right)^{1+\beta} \times \begin{cases} 0, \ E > E_m \\ F_\beta(\sigma_m), \ E > E_m \end{cases} \tag{12.42}$$

where

$$\sigma_m = \frac{E}{E_m} = \frac{\in m^{\cdot E}}{m^2c^4} \tag{12.43}$$

$$F_\beta(\sigma_m) = \int_1^{\sigma m} s_0^{\beta-2} \overline{\varphi}[s_0] ds_0 \tag{12.44}$$

Again, by Eqs. (12.40), (12.41), we can obtain the asymptotic forms

$$\begin{aligned} &\beta = 0 : F_\beta(\sigma_m) \to A_\beta + \ \ln^2\sigma_m - 4\ln\sigma_m + \cdots \\ &\beta \neq 0 : F_\beta(\sigma_m) \to A_\beta + 2\beta^{-1}\left(\ln 4\sigma_m - \beta^{-1} - 2\right) + \cdots, \ \sigma_m > 1 \end{aligned} \tag{12.45}$$

$$\text{all}\,\beta : F_\beta(\sigma_m) \to \left(\frac{4}{15}\right)(\sigma_m - 1)^{\frac{5}{2}} + \left[\frac{2(2\beta+1)}{21}\right](\sigma_m - 1)^{\frac{7}{2}} + \cdots, \sigma_m - 1 \ll 1 \tag{12.46}$$

Fig. 12.6 plots $\sigma_m^{-\beta} F_\beta(\sigma_m)$ for $\beta = 0$–3.0 A_β in $0.5 - A_\beta$ intervals, which contribute to the integral in the region [8, 15]. The values were calculated as $A_\beta = 8.111$ ($\beta = 0$), 13.53 ($\beta = 0.5$), 9.489 ($\beta = 1.0$), 15.675 ($\beta = 1.5$), 34.54 ($\beta = 2.0$), 85.29 ($\beta = 2.5$), and 222.9 ($\beta = 3.0$). Subsequently, I calculated the heating photon terms corresponding to the spectra for both negative and positive indexes:

This book belongs to Kitab Liaison (ocd1996@gmail.com) Copyright Elsevier 2023

$$\begin{aligned} n(\in) &= 0,\ \in < \in_0 \\ &= C_{\in}^{-\alpha} \text{ or } D_{\in}^{\beta},\ \in_0 < \in < \in_m \\ &= 0, \in < \in_0 \end{aligned} \tag{12.47}$$

I then obtain

$$\left(\frac{d\tau_{abs}}{dx}\right)_{\alpha} = \pi r_0^2 C \left(\frac{m^2c^4}{E}\right)^{1-\alpha} \times \begin{cases} 0, E < E_m \\ [F_\alpha(1) - F_\alpha(\sigma_m)], E_m < E < E_0 \\ [F_\alpha(\sigma_0) - F_\alpha(\sigma_m)], E > E_0 \end{cases} \tag{12.48}$$

$$\left(\frac{d\tau_{abs}}{dx}\right)_{\beta} = \pi r_0^2 D \left(\frac{m^2c^4}{E}\right)^{1+\beta} \times \begin{cases} 0, E < E_m \\ \left[F_\beta(\sigma_m)\right], E_m < E < E_0 \\ \left[F_\beta(\sigma_m) - F_\beta(\sigma_0)\right], E > E_0 \end{cases} \tag{12.49}$$

In this case, the heating photon spectrum can be adequately described by asymptotic formulas. The term Γ_γ^{LPM} denotes the photon's contribution to the emitted irradiance per unit volume due to bremsstrahlung processes [47–50]:

$$\Gamma_\gamma \equiv \frac{dn_\gamma}{dVdt} \tag{12.50}$$

After summing the contributions Γ_γ^{LPM}, the irradiance rate of was confirmed as $O(\alpha_{EM}\ \alpha_s)$. Here, I have assumed the following expression for the polarized emission rate Γ_γ^{LPM} at the thermodynamically controlled equilibrium of the plasma surface at temperature T and photophysical reaction μ:

$$\frac{d\Gamma_\gamma^{LPM}}{d^3k} = \frac{d_F q_s^2 \alpha_{EM}}{4\pi^2 k} \int_{-\infty}^{\infty} \frac{dp_\parallel}{2\pi} \int \frac{d^2\mathrm{p}_\perp}{(2\pi)^2} A(p_\parallel, k)\ \mathrm{Re}\left\{2P_\perp \cdot f(p_\perp; p_\parallel, k)\right\} \tag{12.51}$$

where d_F represents the functional strategy of a quark particle [N_c in SU(N_c)], q_s represents the abelian charge of a quark, $k \equiv |k|$, and the kinetic function $A(p_\parallel, k)$ of the emitted particle is given by

$$A(p_\parallel, k) \equiv \begin{cases} \dfrac{n_b(k+p_\parallel)\left[1+n_b(p_\parallel)\right]}{2p_\parallel(p_\parallel+k)}, & \text{scalars} \\ \dfrac{n_f(k+p_\parallel)\left[1-n_f(p_\parallel)\right]}{2\left[p_\parallel(p_\parallel+k)\right]^2}\left[{p_\parallel}^2 + (p_\parallel+k)^2\right], & \text{fermions} \end{cases} \tag{12.52}$$

This book belongs to Kitab Liaison (ocd1996@gmail.com)
Copyright Elsevier 2023

$$\text{with } n_b(p) \equiv \frac{1}{\exp[\beta(p-\mu)]-1},\ n_f(p) \equiv \frac{1}{\exp[\beta(p-\mu)]+1}. \tag{12.53}$$

The function $f(p\perp; p_{||}, k)$ in Eq. (12.51) was introduced to solve the following linear integral equation, which confirms multiple photon production by three-diode scattering [51–53]:

$$2p_\perp = i\delta E f\left(p_\perp; p_{||}, k\right) + \frac{\pi}{2} C_F g_s^2 m_D^2 \int \frac{d^2 q_\perp}{(2\pi)^2} \frac{dq_{||}}{2\pi} \frac{dq^0}{2\pi} 2\pi\delta\left(q^0 - q_{||}\right)$$
$$\times \frac{T}{|q|}\left[\frac{2}{\left|q^2 - \Pi_L(Q)\right|^2} + \frac{\left[1-\left(q^0/\left|q_{||}\right|\right)^2\right]^2}{\left|(q^0)^2 - q^2 - \Pi_T(Q)\right|^2}\right]\left[f\left(p_\perp; p_{||}, k\right) - f\left(q + p_\perp; p_{||}, k\right)\right] \tag{12.54}$$

In Eq. (12.54), C_F is a quadratic quark [$C_F = (N_c^2 - 1)/2N_c = 4/3$ in QCD], m_D is the leading-order Debye mass, and δE is the energy difference between quasiparticles, which considers the photon emission and the state of the thermodynamic temperature equilibrium:

$$\delta E \equiv k^0 + E_p \operatorname{sign}\left(p_{||}\right) - E_{p+k} \operatorname{sign}\left(p_{||} + k\right) \tag{12.55}$$

For an SU(N) gauge theory with N_s complex scalars and N_f Dirac fermions, the Debye mass in the fundamental representation is given by [38]

$$m_D^2 = \frac{1}{6}\left(2N + N_s + N_f\right) g^2 T^2 + \frac{N_f}{2\pi^2} g^2 \mu^2 \tag{12.56}$$

To accurately determine the photon energy emission rate in the region $p|| > 0$, I calculated the distribution of $n(k+p_{||})[1 \pm n(p_{||})]$ in the integral containing $A(p_{||}, k)$ in Eq. (12.51), which determines the distribution of pair annihilations, using the following equation:

$$n_b(-p) = -[1 + \overline{n}_b(p)],\ n_f(-p) = \left[1 - \overline{n}_f(p)\right] \tag{12.57}$$

where $n(p) \equiv 1/[e\beta(p+\mu) \mp 1]$ is the appropriate antiparticle distribution function. Therefore, the factor $A(p'', k)$ in this interval may be rewritten as

$$A\left(p_{||}, k\right) \equiv \begin{cases} \dfrac{n_b\left(k - \left|p_{||}\right|\right)\overline{n}_b\left(\left|p_{||}\right|\right)}{2\left|p_{||}\right|\left(k - \left|p_{||}\right|\right)}, & \text{scalars} \\ \dfrac{n_f\left(k - \left|p_{||}\right|\right)\overline{n}_f\left(\left|p_{||}\right|\right)}{2\left[\left|p_{||}\right|\left(k - \left|p_{||}\right|\right)\right]^2}\left[{p_{||}}^2 + \left(k - \left|p_{||}\right|\right)^2\right], & \text{fermions} \end{cases} \tag{12.58}$$

This book belongs to Kitab Liaison (ocd1996@gmail.com)
Copyright Elsevier 2023

Thus, the energy E_p of a hard quark with momentum $|p|$ is explicitly given by

$$E_p = \sqrt{p^2 + m_\infty^2} \simeq |p| + \frac{m_\infty^2}{2|p|} \simeq |p_\parallel| + \frac{p_\perp^2 + m_\infty^2}{2|p_\parallel|} \tag{12.59}$$

where the asymptotic thermal "mass" is

$$m_\infty^2 = \frac{C_f g^2 T^2}{4} \tag{12.60}$$

Substituting the explicit form of E_p into definition (12.60), we get

$$\delta E = \left[\frac{p_\perp^2 + m_\infty^2}{2}\right]\left[\frac{k}{p_\parallel\left(k + p_\parallel\right)}\right] \tag{12.61}$$

Above, I have derived explicit forms of Eqs. (12.52), (12.55). Fig. 12.9 plots the leading-order heating photoemission rates that maximize the power given the electron time of flight of the photons into the glazing wall plane.

Conclusions

Traditional cooling and heating systems adopted by the building sector are problematic, as they contribute to climate change and threaten the ozone layer. To mitigate these potentially catastrophic effects, the present paper has proposed transforming solar irradiation into cooled photons by implementing the Bose-Einstein (B-E) photon distribution mechanism on helium-assisted glazing walls, which can be installed on the external surfaces of buildings. The cooled photons are then available for cooling the premises. The feasibility of the approach is demonstrated in mathematical tests implemented in MATLAB software. Moreover, the cooling photons can be converted into the heating state by the Higgs boson [BR $(H \to \gamma\bar{\gamma})$] quantum field, which can be created by two thermal semiconductor diodes installed in the helium-assisted glazing wall, providing a natural heat source for buildings. It has been concluded that cooling-state photons (*HcP*) can be extracted from the solar irradiance. Then they can be transformed into heating-state photons (*HtP*), providing a natural cooling and heating system for the premises to reduce global energy consumption, environmental damage, and ozone layer depletion dramatically.

This book belongs to Kitab Liaison (ocd1996@gmail.com) Copyright Elsevier 2023

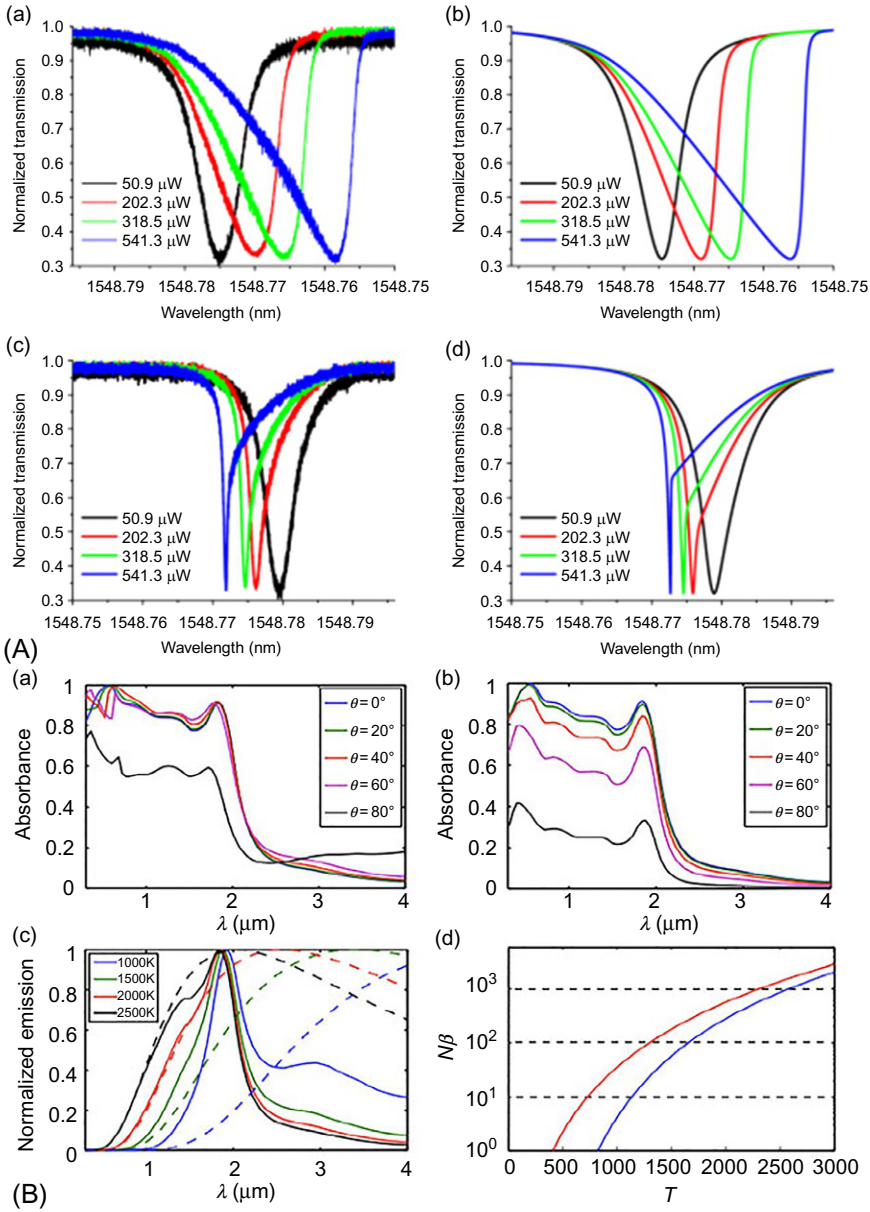

Fig. 12.9 A—(a) Thermal photon transmission versus wavelength at various normalized condition power spectral density of the resonator amplitude as a function of frequency. (b) Quasiparticle recombination time as a function of thermal roll-off frequency. (c) Resonator amplitude as a function of frequency for different bath temperatures. (d) Energy measurements (DQD) incorporating photon excitation into the Higgs boson quantum field. (B)—Numerical demonstration of the wide-angle absorbance thermal spectra into the glazing film for (a) p polarized and (b) s polarized incident radiation for various incidence angles. (c) Normalized thermal emission spectra (per unit frequency) for dashed lines and glazing *(solid lines)* surfaces. The different colors correspond to different emitter temperatures. (d) Solar concentration versus equilibrium temperature for the glazing surface.

This book belongs to Kitab Liaison (ocd1996@gmail.com)
Copyright Elsevier 2023

Acknowledgments

This research was supported by Green Globe Technology under grant RD-02017-05 for building a better environment. Any findings, predictions, and conclusions described in this article are solely performed by the authors and it is confirmed that there is no conflict of interest for publishing this research paper in a suitable journal.

References

[1] F. Hossain, Solar energy integration into advanced building design for meeting energy demand and environment problem, Int. J. Energy Res. 17 (2016) 49–55.
[2] A. Soedibyo, F.A. Pamuji, M. Ashari, Grid quality hybrid power system control of microhydro, wind turbine and fuel cell using fuzzy logic, Int. Rev. Model. Simul. 6 (2013) 1271–1278.
[3] M.F. Hossain, Theory of global cooling, Energy Sustain. Soc. 6 (2016) 1–5. 20166:24.
[4] B. Boukhezzar, H. Siguerdidjane, Nonlinear control with wind estimation of a DFIG variable speed wind turbine for power capture optimization, Energy Convers. Manag. 50 (2009) 885–892.
[5] C. Gopal, M. Mohanraj, P. Chandramohan, P. Chandrasekar, Renewable energy source water pumping systems—a literature review. Renew. Sust. Energ. Rev. 25 (2013) 351–370, https://doi.org/10.1016/j.rser.2013.04.012.
[6] E. Kamal, M. Koutb, A.A. Sobaih, B. Abozalam, An intelligent maximum power extraction algorithm for hybrid wind-diesel-storage system, Int. J. Electr. Power Energy Syst. 32 (2010) 170–177.
[7] N. Gupta, S.P. Singh, S.P. Dubey, D.K. Palwalia, Fuzzy logic controlled three-phase three-wired shunt active power filter for power quality improvement, Int. Rev. Electr. Eng. 6 (2011) 1118–1129.
[8] H. Faida, J. Saadi, Modelling, control strategy of DFIG in a wind energy system and feasibility study of a wind farm in Morocco, Int. Rev. Model. Simul. 3 (2010) 1350–1362.
[9] T. Ghennam, E.M. Berkouk, B. Francois, A vector hysteresis current control applied on three-level inverter. Application to the active and reactive power control of doubly fed induction generator based wind turbine, Int. Rev. Electr. Eng. 2 (2007) 250–259.
[10] L. Langer, S.V. Poltavtsev, I.A. Yugova, M. Salewski, D.R. Yakovlev, G. Karczewski, T. Wojtowicz, I.A. Akimov, M. Bayer, Access to long-term optical memories using photon echoes retrieved from semiconductor spins, Nat. Photonics 8 (2014) 851–857.
[11] N.D. Benavides, P.L. Chapman, Modeling the effect of voltage ripple on the power output of photovoltaic modules, IEEE Trans. Ind. Electron. 55 (2008) 2638–2643.
[12] A. Reinhard, T. Volz, M. Winger, A. Badolato, K.J. Hennessy, E.L. Hu, A. Imamoğlu, Strongly correlated photons on a chip, Nat. Photonics 6 (2012) 93–96.
[13] A. Belkacem, H. Gould, B. Feinberg, R. Bossingham, W.E. Meyerhof, Semiclassical dynamics and relaxation, Phys. Rev. Lett. 71 (1993) 1514–1517.
[14] J.S. Douglas, H. Habibian, C.-L. Hung, A.V. Gorshkov, H.J. Kimble, D.E. Chang, Quantum many-body models with cold atoms coupled to photonic crystals, Nat. Photonics 9 (2015) 326–331.
[15] A.K. Agger, A.H. Sørensen, Atomic and molecular structure and dynamics, Phys. Rev. A 55 (1997) 402–413.
[16] G. Baur, K. Hencken, D. Trautmann, S. Sadovsky, Y. Kharlov, Dense laser-driven electron sheets as relativistic mirrors for coherent production of brilliant X-ray and γ-ray beams, Phys. Rep. 364 (2002) 359–450.
[17] M.F. Hossain, Green science: advanced building design technology to mitigate energy and environment, Renew. Sust. Energ. Rev. 81 (2017) 3051–3060.

This book belongs to Kitab Liaison (ocd1996@gmail.com) Copyright Elsevier 2023

[18] A.N. Celik, N. Acikgoz, Modelling and experimental verification of the operating current of mono-crystalline photovoltaic modules using four- and five-parameter models, Appl. Energy 84 (2007) 1–15.
[19] B. Robyns, B. Francois, P. Degobert, J.P. Hautier, Vector Control of Induction Machines, Springer-Verlag, London, 2012.
[20] M. Faruque Hossain, Design and construction of ultra-relativistic collision pv panel and its application into building sector to mitigate total energy demand, J. Build. Eng. 9 (2017) 147–154.
[21] J. Park, H. Kim, Y. Cho, C. Shin, Simple modeling and simulation of photovoltaic panels using MATLAB/Simulink, Adv. Sci. Technol. Lett. 73 (2014) 147–155.
[22] Y.F. Xiao, M. Li, Y.C. Liu, Y. Li, X. Sun, Q. Gong, Asymmetric Fano resonance analysis in indirectly coupled microresonators, Phys. Rev. A 82 (2010) 065804.
[23] Q. Li, D.Z. Xu, C.Y. Cai, C.P. Sun, Recoil effects of a motional scatterer on single-photon scattering in one dimension, Sci. Rep. 3 (2013) 3445–3449.
[24] B. Najjari, A.B. Voitkiv, A. Artemyev, A. Surzhykov, Simultaneous electron capture and bound-free pair production in relativistic collisions of heavy nuclei with atoms, Phys. Rev. A 80 (2009) 012701.
[25] M.F. Hossain, Green science: independent building technology to mitigate energy, environment, and climate change, Renew. Sust. Energ. Rev. 73 (2017) 695–705.
[26] P.Y. Lo, H.N. Xiong, W.M. Zhang, Breakdown of Bose-Einstein distribution in photonic, crystals, Sci. Rep. 5 (2015) 9423–9429.
[27] M.C. Güçlü, J. Li, A.S. Umar, D.J. Ernst, M.R. Strayer, Electromagnetic lepton pair production in relativistic heavy-ion collisions, Ann. Phys. 272 (1999) 7–48.
[28] G. Baur, K. Hencken, D. Trautmann, Revisiting unitarity corrections for electromagnetic processes in collisions of relativistic nuclei, Phys. Rep. 453 (2007) 1–27.
[29] J. Eichler, T. Stöhlker, Radiative electron capture in relativistic ion-atom collisions and the photoelectric effect in hydrogen-like high-Z systems, Phys. Rep. 439 (2007) 1–99.
[30] J.J. Soon, K.S. Low, Optimizing photovoltaic model parameters for simulation, in: IEEE International Symposium on Industrial Electronics, 2012, pp. 1813–1818.
[31] L. Yang, S. Wang, Q. Zeng, Z. Zhang, T. Pei, Y. Li, L.M. Peng, Efficient photovoltage multiplication in carbon nanotubes, Nat. Photonics 5 (2011) 672–676.
[32] M.F. Hossain, Photonic thermal control to naturally cool and heat the building, Appl. Therm. Eng. 131 (2018) 576–586.
[33] P. Arnold, G.D. Moore, L.G. Yaffe, Photon emission from ultrarelativistic plasmas, J. High Energy Phys. (11) (2001) 057.
[34] K. Hencken, G. Baur, D. Trautmann, Transverse momentum distribution of vector mesons produced in ultraperipheral relativistic heavy ion collisions, Phys. Rev. Lett. 96 (2006) 012303.
[35] N. Artemyev, U.D. Jentschura, V.G. Serbo, A. Surzhykov, Strong electromagnetic field effects in ultra-relativistic heavy-ion collisions, Eur. Phys. J. 72 (2012) 1935.
[36] K.G. Sharma, A. Bhargava, K. Gajrani, Stability analysis of DFIG based wind turbines connected to electric grid, Int. Rev. Model. Simul. 6 (2013) 879–887.
[37] G. Sivasankar, V.S. Kumar, Improving low voltage ride through of wind generators using STATCOM under symmetric and asymmetric fault conditions, Int. Rev. Model. Simul. 6 (2013) 1212–1218.
[38] S.A. Klein, Calculation of flat-plate collector loss coefficients, Sol. Energy 17 (1975) 79–80.
[39] S.R. Valluri, U. Becker, N. Grün, W. Scheid, Relativistic collisions of highly-charged ions, J. Phys. B: At. Mol. Phys. 17 (1984) 4359–4370.
[40] W.M. Zhang, P.Y. Lo, H.N. Xiong, M.W.Y. Tu, F. Nori, General non-Markovian dynamics of open quantum systems, Phys. Rev. Lett. 109 (2012) 170402.

This book belongs to Kitab Liaison (ocd1996@gmail.com) Copyright Elsevier 2023

[41] R.J. Gould, G.P. Schréder, Pair production in photon-photon collisions, Phys. Rev. 155 (1967) 1404–1407.
[42] T. Pregnolato, E.H. Lee, J.D. Song, S. Stobbe, P. Lodahl, Single-photon non-linear optics with a quantum dot in a waveguide, Nat. Commun. 6 (2015) 8655.
[43] W. Xiao, W.G. Dunford, A. Capal, A novel modeling method for photovoltaic cells, in: 35th Annula IEEE Power Electronics Specialists Conference, Aachen, Germany, 2004, pp. 1950–1956.
[44] W.B. Yan, H. Fan, Single-photon quantum router with multiple output ports, Sci. Rep. 4 (2014) 4820.
[45] R. Szafron, A. Czarnecki, High-energy electrons from the muon decay in orbit: radiative corrections, Phys. Lett. B. 6 (2016) 36–41.
[46] A.H. Sørensen, The pairproduction channel in atomic processes, Radiat. Phys. Chem. 23 (2006) 32–38.
[47] M.S. Tame, K.R. McEnery, Ş.K. Özdemir, J. Lee, S.A. Maier, M.S. Kim, Quantum plasmonics, Nat. Phys. 8 (2013) 362–369.
[48] W. De Soto, S.A. Klein, W.A. Beckman, Improvement and validation of a model for photovoltaic array performance, Sol. Energy 80 (2006) 78–88.
[49] Y. Zhu, X. Hu, H. Yang, Q. Gong, On-chip plasmon-induced transparency based on plasmonic coupled nanocavities, Sci. Rep. 9 (2014) 6772–6779.
[50] C. Wu, Metamaterial-based integrated plasmonic absorber/emitter for solar thermo-photovoltaic systems, J. Opt. 23 (2012) 56–63.
[51] M.W.Y. Tu, W.M. Zhang, Non-Markovian decoherence theory for a double-dot charge qubit, Phys. Rev. B 78 (2008) 235311.
[52] U. Becker, N. Grün, W. Scheid, K-shell ionisation in relativistic heavy-ion collisions, J. Phys. B: At. Mol. Phys. 20 (1987) 2075.
[53] Y.T. Tan, D.S. Kirschen, N. Jenkins, A model of PV generation suitable for stability analysis, IEEE Trans. Energy Convers. 19 (2004) 748–755.

This book belongs to Kitab Liaison (ocd1996@gmail.com) Copyright Elsevier 2023

This page intentionally left blank

This book belongs to Kitab Liaison (ocd1996@gmail.com)

Copyright Elsevier 2023

CHAPTER 13

Applied energy technology

Introduction

Solar irradiance is plentiful and contains enormous energy. However, that harvested solar energy is not meeting global energy needs because of the low conversion rate of solar energy by conventional PV systems. Therefore, a better scientific approach has been implied in this paper that a single photon can be scattered into numerous photons, which conversely could be applied to significantly improve the energy-harvesting rate compared with traditional PV panels. In this process, a single photon is allowed to be scattered by a two-feed semiconductor and then a three-diode superconductor into the heavy duty silicon panel by applying the Higgs boson BR ($H \rightarrow \gamma\gamma^{-}$) quantum field under high-temperature conditions. In the past, several researchers, such as Eichler and Stöhlker [1], Najjari et al. [2], and Li et al. [3], have proposed some ultrarelativistic reaction models, and the core theory of those models revealed that a single photon could generate a pair of photons under thermally unequilibrium conditions by the ultrarelativistic collision between two bare ions (Fig. 13.1). Several other studies by Liao and Law [4] have worked on breaking down the Bose-Einstein dormant photon distribution mechanism to create a pair of photons from a single one. Even though their pair of photons production theory is interesting, the knowledge gap between this pair of photons and multiple photon production is yet unknown because no one has yet proved that a pair of photons can further be transformed into a huge number of photons via a triple-layer silicon superconductor under high temperature to produce multiple photons [5–7].

Therefore, the objective of this research is to produce a tremendous amount of photons from a single photon by implementing a Higgs boson quantum field in a high-temperature condition to generate electrons to form a photon-photon intersection to design a micro PV panel. To achieve this multiple photon production, the Higgs boson quantum field has been initiated for photon particles to release electron energy where, in general, each electron carries a unit negative charge that causes electron interaction by electromagnetic force. For this process, electron and positron pairs shall

Sustainable Development for Mass Urbanization
https://doi.org/10.1016/B978-0-12-817690-0.00013-0
© 2019 Elsevier Inc.
All rights reserved.

This book belongs to Kitab Liaison (ocd1996@gmail.com)
Copyright Elsevier 2023

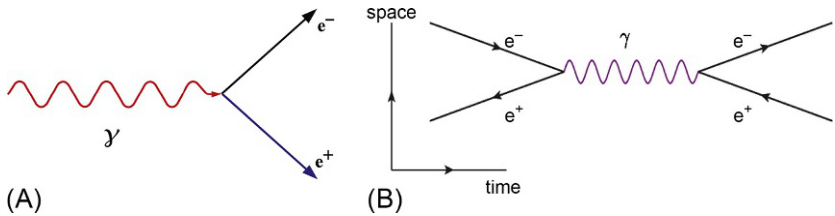

Fig. 13.1 (A) Demonstrates the process that a single photon converts into a pair of photons (e^+e^-), and (B) shows that the pair of photons (e^+e^-) further transforms into four photons in the Higgs boson quantum field under high temperature.

be produced from a single collision by high frequency of the Higgs boson electromagnetic force in the PV panel [8, 9]. Then, the photon pair e^+e^- is to be introduced into a two-feed semiconductor and then a three-diode superconductor for scattering the pair of photons [10–12]. Essentially, the energy production rate has also been calculated, which revealed that if only a $1\,cm^2$ PV panel is used to capture solar energy, it will produce 1590.9 MW/h, which indeed will open a new door of science to create 100% clean energy to dramatically meet global energy demand [13, 14].

Methods and materials

Higgs boson quantum field

To conduct Higgs boson quantum field activation into the silicon surface, abelian local symmetries have been implemented by introducing MATLAB in order to break the photon particle T^{α} into the local symmetry with respect to a gauge field of $A_{\mu}^{\alpha}(x)$ and the Higgs quantum field of U (1) [15, 16]. Therefore, consisted of an intricate scalar area $\Phi(x)$ containing electrical charge q shall couple to $A^{\mu}(x)$ that shall be calculated by *Lagrangian* by the following equation:

$$\mathcal{L} = -\frac{1}{4} F_{\mu\nu}F^{\mu\nu} + D_{\mu}\Phi^{*} D^{\mu}\Phi - V(\Phi^{*}\Phi) \tag{13.1}$$

where

$$\begin{aligned} D_{\mu}\Phi(x) &= \partial_{\mu}\Phi(x) + iqA_{\mu}(x)\Phi(x) \\ D_{\mu}\Phi^{*}(x) &= \partial_{\mu}\Phi^{*}(x) - iqA_{\mu}(x)\Phi^{*}(x) \end{aligned} \tag{13.2}$$

And

$$V(\Phi^{*}\Phi) = \frac{\lambda}{2}(\Phi^{*}\Phi)^2 + m^2(\Phi^{*}\Phi) \tag{13.3}$$

This book belongs to Kitab Liaison (ocd1996@gmail.com) Copyright Elsevier 2023

Suppose $\lambda > 0$ but $m^2 < 0$, thus $\Phi = 0$ is the localized max scalar quantity degenerated from the equation $\Phi = \frac{v}{\sqrt{2}} * e^{i\theta}$,

$$v = \sqrt{\frac{-2m^2}{\lambda}}, \text{ any real } \theta \tag{13.4}$$

Hence, the value $\langle \Phi \rangle \neq 0$ is evolved by the scalar field Φ, which produces the U (1) the magnetic field. Subsequently, a massless scalar Φ (x) shall initiate the breakdown process of the photon particle. Here the local U (1) symmetry, the phase of Φ (x) is the phase of the expectant value of $\langle \Phi \rangle$ that is the x-dependent phase of the dynamical of Φ (x) field. By applying the scalar field in this surface, this mechanism can be written as follows

$$\Phi(x) = \frac{1}{\sqrt{2}} \Phi_r(x) * e^{i\Theta(x)}, \text{real } \Phi_r(x) > 0, \text{real } \Phi(x) \tag{13.5}$$

where Φ $(x) = 0$, this field is to be redefined as singular so that this could be used with $\langle \Phi \rangle \neq 0$ in theory. However, it could be implied in spontaneously broken theories under the assumption that $\Phi \langle x \rangle \neq 0$ is universal. In the real fields $\phi_r(x)$ and $\Theta(x)$, the radial field ϕ_r is the only determining factor to calculate the scalar potential

$$V(\phi) = \frac{\lambda}{8} \left(\phi_r^2 - v^2\right)^2 + \text{const} \tag{13.6}$$

or in the radial field substituted by its VEV, $\Phi_r(x) = v + \sigma(x)$,

$$\phi_r^2 - v^2 = (v + \sigma)^2 - v^2 = 2v\sigma + \sigma^2 \tag{13.7}$$

$$V = \frac{\lambda}{8} \left(2v\sigma - \sigma^2\right)^2 = \frac{\lambda v^2}{2} * \sigma^2 + \frac{\lambda v}{2} * \sigma^3 + \frac{\lambda}{8} * \sigma^4 \tag{13.8}$$

Consequently,

$$\mathcal{L} = \frac{1}{2} \left(\partial_\mu \sigma\right)^2 - v(\sigma) - \frac{1}{4} F_{\mu\nu} F^{\mu\nu} + \frac{(v + \sigma)^2}{2} * \left(\partial_\mu \Theta + qA_\mu\right)^2 \tag{13.9}$$

To define the magnetic field characteristics of this *Lagrangian*, the determined scope has been explained to the powers of the quantum field by describing the quadratic part of the free particles and expressed as follows

$$\mathcal{L}_{\text{free}} = \frac{1}{2} \left(\partial_\mu \sigma\right)^2 - \frac{\lambda v^2}{2} * \sigma^2 - \frac{1}{4} F_{\mu\nu} F^{\mu\nu} + \frac{v^2}{2} * \left(qA_\mu + \partial_\mu \Theta\right)^2 \tag{13.10}$$

Therefore, this equation, *Lagrangian* ($\mathcal{L}_{\text{free}}$), confirms the creation of scalar particles of positive $mass^2 = \lambda v^2$ containing the fields $A_\mu(x)$, which

This book belongs to Kitab Liaison (ocd1996@gmail.com) Copyright Elsevier 2023

suggests that the production of high temperatures in the quantum field is indeed doable.

Pair photon production

Once the quantum field get a high-temperature condition because of the penetration of solar radiance, then the photon energy will be excited and collide with its bare ions within the quantum field into the semiconductor panel (Fig. 13.2). Subsequently, high-energy photon collision theory has been employed to confirm that a pair of photons is created from a single photon, which is sufficient enough to isolate the electrons into the two-feed semiconductors [4, 7].

Consequently, the production of a pair of photons from a single one is verified by the accuracy and parameters of the current-voltage relationship through a detailed mathematical calculation considering solar electromagnetic radiation [15, 17, 18]. Therefore, the momentum of the photovoltaic radiation mechanism is calculated as $2mc^2$, where m represents the mass of an electron [19–21], and the production of a pair of photons in the quantum field is expressed as:

$$\sigma = \frac{1}{2}\pi r_2^0 \left(1-\beta^2\right)\left[\left(3-\beta^4\right)\ln\frac{1+\beta}{1-\beta} - 2\beta\left(2-\beta^2\right)\right] \tag{13.11}$$

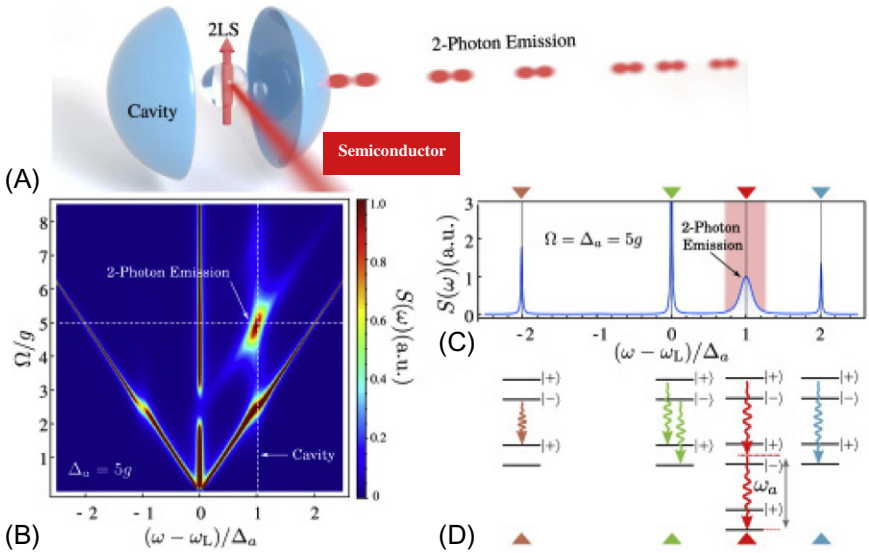

Fig. 13.2 (A) The mechanism of photon emission into the Higgs boson quantum field. (B) Shows the feasibility of the emission of a pair of photons in the point break of the semiconductor of the PV panel. (C) Represents the pair photon dynamics. (D) Pair photon formation mechanism in to the PV cell.

This book belongs to Kitab Liaison (ocd1996@gmail.com) Copyright Elsevier 2023

where $r_0 = \frac{e^2}{mc^2}$ represents the classical radius and β_c indicates the momentum velocity of electrons. Hence, recognizing two photon momentum vectors, the equation between β and E *(high-energy photon)*, $\in$ (*low-energy photon*), and θ (*angle with respect to the x axis*) can be represented as:

$$2 \in E(1 - \cos t) = 4E_e^2 \tag{13.12}$$

where E_{el} represents the electron momentum in the PV panel, which can develop as

$$s = \left(\frac{E_e}{mc^2}\right)^2 = \left(\frac{\in E}{2m^2c^4}\right)(1 - \cos\theta) \tag{13.13}$$

so

$$\beta = |p_e|\frac{c}{E_e} = \left(1 - \frac{1}{s}\right)^{\frac{1}{2}} \tag{13.14}$$

Furthermore,

$$\begin{aligned} s &= s_0 z \\ s_0 &= \frac{\in E}{m^2c^4}, z = (1 - \cos\theta) \end{aligned} \tag{13.15}$$

It clearly reveals that under the relativistic condition, the generation of a pair of photons ($\sigma_{\gamma\gamma}$) does occur, $s > 1$ in the relativistic condition where the threshold condition for a head-on ($\theta = \pi$, $z = 1$) photon collision is $\in E = m^2c^4$, and the photon pair production is expressed as

$$\sigma_{\gamma\gamma} \approx \frac{3}{8}\sigma T\left(\frac{mc^2}{hw}\right)^2\left(\ln\frac{2hw}{mc^2} - 1\right) \tag{13.16}$$

Three-diode photon scattering

To verify the generation process from the photon pair to the multiple photons, the calculation of energy densities has been performed considering the Higgs boson quantum field in different flux dynamics [1, 22]. Hence, particle collision shall cause the physical interaction between a pair of photons, which further results in the production of thousands of photons ($2 \leftrightarrow 16 \leftrightarrow \sum 4092$) via photo-dissociation by three-diode scattering (Fig. 13.3).

Naturally, a three-diode scattering process is used to define the photon dynamics, which occur in a superconductor circuit. Hence, in consideration of the contour map, the purely electron dynamics of continuous photon production in the atomic spectra will be satisfied by the point break in the PV panel (Fig. 13.4).

This book belongs to Kitab Liaison (ocd1996@gmail.com) Copyright Elsevier 2023

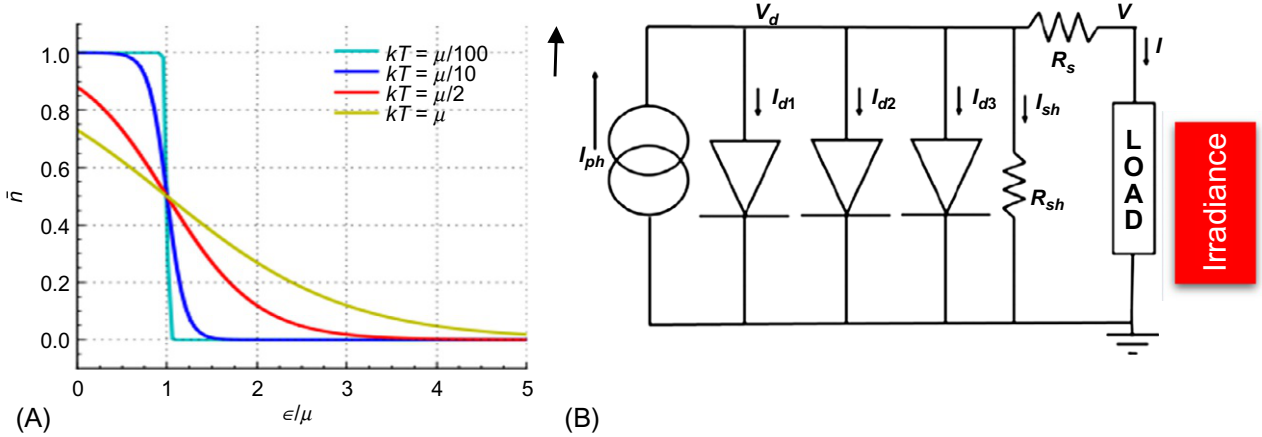

Fig. 13.3 Three-diode photon scattering mechanism: (A) three diode circuits are modeled, with *light blue (dark gray in print version)* being the standard parameter for magnetic flux density (*KTs-kT*), *dark blue (black in print version)* for I_{d1}, *red (dark gray in print version)* for I_{d2}, and *light green (light gray in print version)* for I_{d3}, and (B) shows that the three (I_{d1}, I_{d2}, I_{d3}) diodes are modeled and combined into a quantum field, resulting in a large amount of current I_{ph}.

This book belongs to Kitab Liaison (ocd1996@gmail.com)

Copyright Elsevier 2023

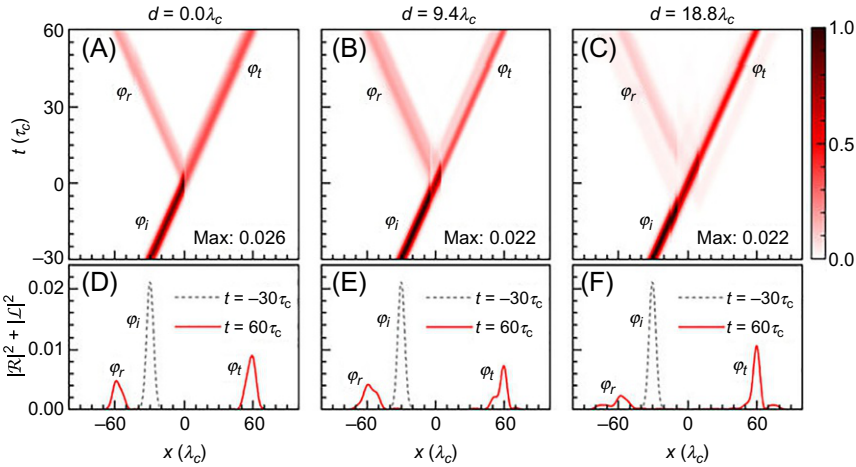

Fig. 13.4 (A–C) Contour maps of the photonic density (standardized to optimum value) as functions of x and t. (D–F) Probability distributions of the incident (φ_i), reflected (φ_r), and transmitted (φ_t) pulses. The figure refers to $V_+(x)$ using $\sigma = 0.4\lambda_c$, $\varepsilon_I = 1.05\,\omega_c$, $L = 12\lambda_c$ and otherwise the parameters of this figure.

The entire photonic reservoir structure will be integrated into the PV semiconductor, when considering that the original photonic structure is balanced, and it can be expressed as [13, 21, 23]

$$\begin{aligned}\rho(t) = -i\left[H_c'(t), \rho(t)\right] + \sum_{ij}\Big\{ & k_{ij}(t)\left[2a_j\rho(t)a_i^\dagger - a_i^\dagger a_j\rho(t), -\rho(t)a_i^\dagger a_j\right] \\ & + k_{ij}(t)\left[a_i^\dagger\rho(t)a_j + a_j\rho(t)a_i^\dagger - a_i^\dagger a_j\rho(t) - \rho(t)a_j a_i^\dagger\right]\Big\}\end{aligned} \tag{13.17}$$

where $\rho(t)$ represents the photon attenuated density in point break states, $H_c'(t) = \sum_{ij}\omega_{cij}'(t)a_i^\dagger a_j$ indicates recalibration related to the point break frequency $\omega_{cii}'(t) = \omega_{ci}'(t)$, and the function between the point break $\omega_{cij}'(t)$ initiates the coupling of photons. Moreover, the factors $\kappa_{ij}(t)$ and $\widetilde{\kappa}_{ij}(t)$ are depicted as photonic dynamics. Not only the recalibration frequency ω_{cij}', but also the time-dependent factor, $\kappa_{ij}(t)$ and $\widetilde{\kappa}_{ij}(t)$, are solved merely by nonperturbing principles. Furthermore, the Hamiltonian in the photon reservoir is expressed as $H_I = \sum_k \lambda_k x q_k$, where x and q_k represent the position of the point break reservoir. In order to affirm the magnitude of the photonic dynamics within the point break, the entire reservoir point break of the Hamiltonian can be further developed as $H_I = \sum_k V_k(a^\dagger b_k + b_k^\dagger a + a^\dagger b_k^\dagger + ab_k)$ in the consideration of a photon's quantum dynamics. Thus, the scattering

This book belongs to Kitab Liaison (ocd1996@gmail.com) Copyright Elsevier 2023

photon factors $\kappa\ (t)$ and $\widetilde{\kappa}\ (t)$ (the subindices (i, j) in Eq. (13.20) is the most significant symbolization of photonic dynamics and they can be expressed as [24, 25]

$$\omega_c'\ (t) = -Im[u\ (t, t_0)/u\ (t, t_0)] \tag{13.18}$$

$$k\ (t) = -Re\ [u\ (t, t_0)/u\ (t, t_0)] \tag{13.19}$$

$$\hat{k}(t) = \dot{v}\ (t, t) + 2v\ (t, t)\ k(t) \tag{13.20}$$

Hence $u\ (t, t_0)$ is considered the point break photon surface and $v\ (t, t)$ denotes the photonic dynamic caused by the induced reservoir, which can be further interpreted by the following equations [20, 26].

$$\dot{u}\ (t, t_0) = -i\omega_c u\ (t, t_0) - \int_{t_0}^{t} dt' g\ (t - t')\ u\ (t^t, t_0) \tag{13.21}$$

$$v\ (t, t) = \int_{t_0}^{t} dt \int_{0}^{t} dt_2 u^*\ (t_1, t_0)\hat{g}\ (t_1 - t_2)\ u\ (t_2, t_0) \tag{13.22}$$

Here, v_c is the primary frequency at the point break. Thus, the backup function within the point breaks is defined by Eqs. (13.24), (13.25) containing integral functions. Furthermore, the nonequilibrium state triggers the generation of numerous photons, which conveys uniquely per *unit* area $J\ (\varepsilon)$ of the photonic structure as the following relations: $g(t - t') = \int d\omega J(\omega) e^{-i\omega(t-t')}$ and $\widetilde{g}\ (t - t') = \int d\omega J(\omega)\overline{n}(\omega, T) e^{-i\omega(t-t')}$, where $\overline{n}(\omega, T) = 1/\left[e^{\hbar\omega/k_B T} - 1\right]$ means the main photon dynamics in the PV panel at temperature T. It is elucidated in the PV panel that the unit area $J(\omega)$ is relevant with the density of states (DOS) $\varrho(\omega)$ photon generation at the magnitude of V_k between the point break and PV circuits,

$$J\ (\omega) = \sum_k |V_k|^2\ \delta\ (\omega - \omega_k) = \varrho\ (\omega)\ |\ V\ (\omega)|^2 = \left[e * n(\gamma + \gamma)^2\right]^3 \tag{13.23}$$

Conversely, the photon-generated diffusion phenomenon in the quantum field is to be summarized so that $V_k \rightarrow V(\omega)$ and i of V_{ik} in Eq. (13.19) can be calculated at the breakpoint in the single-diode mode. Hence, combined with Eq. (13.27), the calculation of the number of generated photons can be simplified as

$$J\ (\omega) = \left[e * n(\gamma + \gamma)^2\right]^3 \tag{13.24}$$

where $n = E = hf$ means the primary photon production, $e = 1$ represents the constant solar irradiance without interruption, γ represents a pair of photons at the electron state, and $J\ (\omega)$ is the amount of photon output.

This book belongs to Kitab Liaison (ocd1996@gmail.com) Copyright Elsevier 2023

Results and discussion

Higgs boson quantum field

The solar irradiance is initiated to heat up the Higgs boson quantum field, which indeed further allows the local U (1) gauge invariant (QED) to add a mass term in the gauge particle under $\varnothing' \rightarrow e^{i\alpha(x)}\varnothing$. It can be expressed with the assistance of a covariant derivative by applying the scalar field as follows

$$\begin{aligned} \partial_\mu \rightarrow D_\mu = \partial_\mu = ieA_\mu \left[\text{covariant derivatives}\right] \\ A'_\mu = A_\mu + \frac{1}{e}\,\partial_\mu \alpha \left[A_\mu \text{ derivatives}\right] \end{aligned} \tag{13.25}$$

For a complex scalar field, the local *Lagrangian* function with local U (1) specifications is expressed as:

$$\mathcal{L} = \left(D^\mu\right)^\dagger \left(D_\mu \varnothing\right) - \frac{1}{4} F_{\mu\nu}F^{\mu\nu} - V(\varnothing) \tag{13.26}$$

$\frac{1}{4} F_{\mu\nu}F^{\mu\nu}$ is the kinetic term for the gauge field (photon) and $V(\varnothing)$ is the extra term in the *Lagrangian* that can be expressed as: $V(\varnothing^*\varnothing) = \mu^2(\varnothing^*\varnothing) + \lambda\,(\varnothing^*\varnothing)^2$.

Thus, beginning with the appearance of massive scalar particles $\phi_1$and ϕ_2 along with a mass μ, the perturbation of *Lagrangian* ($\mathcal{L}$) is in the quantum field. Under this circumstance, even though the quantum number of $\mu^2 < 0$ is infinite, each could fulfill the requirement of $\phi_1^2 + \phi_2^2 = -\mu^2/\lambda = v^2$, and the *Lagrangian* defines the quantum field as $\phi_0 = \frac{1}{\sqrt{2}}\left[(\upsilon + \eta) + i\xi\right]$ by using the covariant derivatives of the again displaced fields η and ξ.

$$\begin{aligned} \text{Kinetic term}: \mathcal{L}_{kin}(\eta, \xi) &= (D^\mu\phi)^\dagger (D^\mu\phi) \\ &= (\partial^\mu + ieA^\mu)\phi^* \left(\partial_\mu - ieA_\mu\right)\phi \end{aligned} \tag{13.27}$$

Potential term: $V(\eta, \xi) = \lambda\ \upsilon^2\eta^2$, which achieves a second order in the fields so that the integral *Lagrangian* can be expressed as:

$$\begin{aligned} \mathcal{L}_{kin}(\eta, \xi) = \frac{1}{2}\left(\partial_\mu\eta\right)^2 - \lambda\upsilon^2\eta^2 + \frac{1}{2}\left(\partial_\mu\xi\right)^2 - \frac{1}{4} F_{\mu\nu}F^{\mu\nu} + \frac{1}{2} e^2\upsilon^2 A_\mu^2 \\ - e\upsilon A_\mu(\partial^\mu\xi) + \text{int.terms} \end{aligned} \tag{13.28}$$

where massive η, massless ξ (as before), a mass quantum term, and A_μ are settled to one term $\partial_\mu\alpha$ that is showed in Eq. (13.28). For the sake of containing the photon particle spectrum within the quantum field, A_μ could be redefined because it alters with the change of ϕ at the same time, which is written as follows

This book belongs to Kitab Liaison (ocd1996@gmail.com) Copyright Elsevier 2023

$$\mathcal{L}_{\text{scalar}} = (D^{\mu}\phi)^{\dagger}(D^{\mu}\phi) - V\left(\phi^{\dagger}\phi\right)$$

$$= (\partial^{\mu} + ieA^{\mu})\frac{1}{\sqrt{2}}(v+h)\left(\partial_{\mu} - ieA_{\mu}\right)\frac{1}{\sqrt{2}}(v+h) - V\left(\phi^{\dagger}\phi\right) \quad (13.29)$$

$$= \frac{1}{2}\left(\partial_{\mu}h\right)^2 + \frac{1}{2}e^2A_{\mu}^2(v+h)^2 - \lambda v^2h^2 - \lambda vh^3 - \frac{1}{4}\lambda h^4 + \frac{1}{4}\lambda h^4 \quad (13.30)$$

Thus, these expanding terms in the *Lagrangian* associated with the scalar field suggest that the Higgs boson quantum field is prepared to initiate photon-photon interaction into its quantum field.

Pair photon production

Because the temperature in the Higgs boson quantum field increases by absorbing solar irradiance, the calculation associate with the harvested solar energy can be applied to verify the generation of the photon pair as per unit time $\frac{d_{\tau_{abs}}}{dx}$. In this equation, τ_{abs} means the optical depth of photonic energy E traveling within the electron spectrum $n\ (\in)$ [4, 27] and $n\ (\in)$ represents the photon yield per unit volume relative to the amount of energy deliverable per unit time. Thus, the angle θ and within θ both need to be considered when calculating the isotropic distribution of the photons' motion on the differential cone and $\theta + d\theta$ is $\frac{1}{2}\sin\theta d\theta$. Then, with the assistance of energy $\in$ and angle θ, the differential photon density is

$$dn = \frac{1}{2}n(\in)\sin\theta d\in d\theta \quad (13.31)$$

As a result, the calculation of the functional speeds of the high-energy photons needs to take the directional form into account, which is $c\ (1-\cos\theta)$, where the absorption per unit path length could be expressed as follows

$$\frac{\tau_{abs}}{dx} = \iint \frac{1}{2}\sigma n(\in)(1-\cos\theta)\sin\theta d\in d\theta \quad (13.32)$$

Replacing the θ by Eqs. (13.3), (13.5) with an integration over s in the functions, the equation could be revised as

$$\frac{\tau_{abs}}{dx} = \pi r_0^2\left(\frac{m^2c^4}{E}\right)^2\int_{\frac{m^2c^4}{E}}^{\infty} \in^{-2} n(\in)\overline{\varphi}[s_0(\in)]de \quad (13.33)$$

where

$$\varphi\left[s_0(\in)\right] = \int_1^{s_0(\in)} s\overline{\sigma}(s)ds, \overline{\sigma}(s) = \frac{2\sigma(s)}{\pi r_0^2} \quad (13.34)$$

This book belongs to Kitab Liaison (ocd1996@gmail.com) Copyright Elsevier 2023

This equation is thus used to calculate the dimensional variable $\overline{\varphi}$ and the dimensionless cross-section $\overline{\sigma}$, where the variable $\overline{\varphi}[s_0]$ is calculated within a detailed graphical frame $1 < s_0 < 10$. When variable $\overline{\varphi}[s_0]$ belongs to the frame $s_0 - 1 \ll 1$ and $s_0 \gg 1$, the specific functional asymptotic calculation can be expressed as

$$\begin{aligned}\overline{\varphi}[s_0] = &\frac{1+\beta_0^2}{1-\beta_0^2}\ \ln\omega_0 - \beta_0^2\ \ln\omega_0 - \ \ln^2\omega_0 \\ &-\frac{4\beta_0}{1-\beta_0^2} + 2\beta_0 + 4\ \ln\omega_0\ \ln(\omega_0+1) - L(\omega_0)\end{aligned} \tag{13.35}$$

where

$$\beta_0^2 = \frac{1-1}{s_0}, \omega_0 = \frac{(1+\beta_0)}{(1-\beta_0)} \tag{13.36}$$

$$L(\omega_0) = \int_1^{\omega_0} \omega^{-1}\ \ln(\omega+1)d\omega$$

The complete equation can be written as

$$(\omega+1) = \omega\left(\frac{1+1}{\omega}\right), L(\omega_0) = \frac{1}{2}\ \ln 2\omega_0 + L'(\omega_0) \tag{13.37}$$

where

$$\begin{aligned}L'(\omega_0) &= \int_1^{\omega_0} \omega^{-1}\ \ln\left(1+\frac{1}{\omega}\right)d\omega \\ &= \frac{\pi^2}{12} - \sum_{n+1}^{\infty}(-1)n^{-1}n^{-2}\omega_0^{-n}\end{aligned} \tag{13.38}$$

The calculation of $\overline{\varphi}[s_0]$ here can meet any accuracy demand regarding the expected value of s_0. Therefore, the detailed functional asymptotic results are written as follows:

$$\begin{aligned}\overline{\varphi}[s_0] = &2s_0(\ \ln 4s_0 - 2) + \ \ln 4s_0(\ \ln 4s_0 - 2) \\ &-\frac{(\pi^2-9)}{3} + s_0^{-1}\left(\ \ln 4s_0 + \frac{9}{8}\right) + \ldots(s_0 \gg 1)\end{aligned} \tag{13.39}$$

$$\overline{\varphi}[s_0] = \left(\frac{2}{3}\right)(s_0-1)^{\frac{3}{2}} + \left(\frac{5}{3}\right)(s_0-1)^{\frac{5}{2}} - \left(\frac{1507}{420}\right)(s_0-1)^{\frac{7}{2}} + \cdots(s_0 - 1 \ll 1) \tag{13.40}$$

This book belongs to Kitab Liaison (ocd1996@gmail.com)
Copyright Elsevier 2023

The function $\frac{\overline{\varphi}[s_0]}{s_0-1}$ is shown in Fig. 13.5 within $1<s_0<10$, and for s_0, which beyond the range contains natural logarithmic dependence on s_0. The calculation related to the number of photon spectra harvested by the power law with assistance of the form $n(\in) \propto \in^m$ needs to take into account that the two systems are in the original state, (b) a system containing BN in the graphene sheet.

As a result, the function of the harvested photon spectrum has similar characteristics with a high-energy cutoff with $m > 0$. In this equation, the photon spectrum resulted in a high-energy cutoff transformation as follows

$$n(\in) = D_{\in^\beta},\ \in < \in_m, \beta \leq 0 \tag{13.41}$$

$$n(\in) = 0,\ \in > \in_m \tag{13.42}$$

This spectrum can be further expressed as

$$\frac{\tau_{abs}}{dx} = \pi r_0^2 D \left(\frac{m^2c^4}{E}\right)^{1+\beta} \times \begin{cases} 0, E < E_m \\ F_\beta(\sigma_m), E > E_m \end{cases} \tag{13.43}$$

where

$$\sigma_m = \frac{E}{E_m} = \frac{\in mE}{m^2c^4} \tag{13.44}$$

$$F_\beta(\sigma_m) = \int_1^{\sigma_m} s_0^{\beta-2}\overline{\varphi}[s_0]ds_0 \tag{13.45}$$

Combined with Eqs. (13.39), (13.40), the asymptotic forms could be expressed as

$$\beta = 0 : F_\beta(\sigma_m) \to A_\beta + \ln^2\sigma_m - 4\ \ln\sigma_m + \ldots,$$

$$\beta \neq 0 : F_\beta(\sigma_m) \to A_\beta + 2\beta^{-1}\sigma_m^\beta\left(\ \ln 4\sigma_m - \beta^{-1} - 2\right) + \ldots, \sigma_m > 1 \tag{13.46}$$

$$\text{all}\,\beta =: F_\beta(\sigma_m) \to \left(\frac{4}{15}\right)(\sigma_m - 1)^{\frac{5}{2}} + \left[\frac{2(2\beta+1)}{21}\right](\sigma_m - 1)^{\frac{7}{2}} + \ldots, \sigma_m - 1 \ll 1 \tag{13.47}$$

$\sigma_m^{-\beta}F_\beta(\sigma_m)$ is shown in Fig. 13.6 regarding $\beta = 0$, 0.5, 1.0, 1.5, 2.0, 2.5, and 3.0 A_β, which impact the entire range [11, 28]. The corresponding value is $A_\beta = 8.111$, 13.53, 9.489, 15.675, 34.54, 85.29, and 222.9 redarding $\beta = 0$, 0.5, 1.0, 1.5, 2.0, 2.5, and 3.0. The coupled terms related to the spectra for both a negative and positive index are applied into the calculation.

This book belongs to Kitab Liaison (ocd1996@gmail.com) Copyright Elsevier 2023

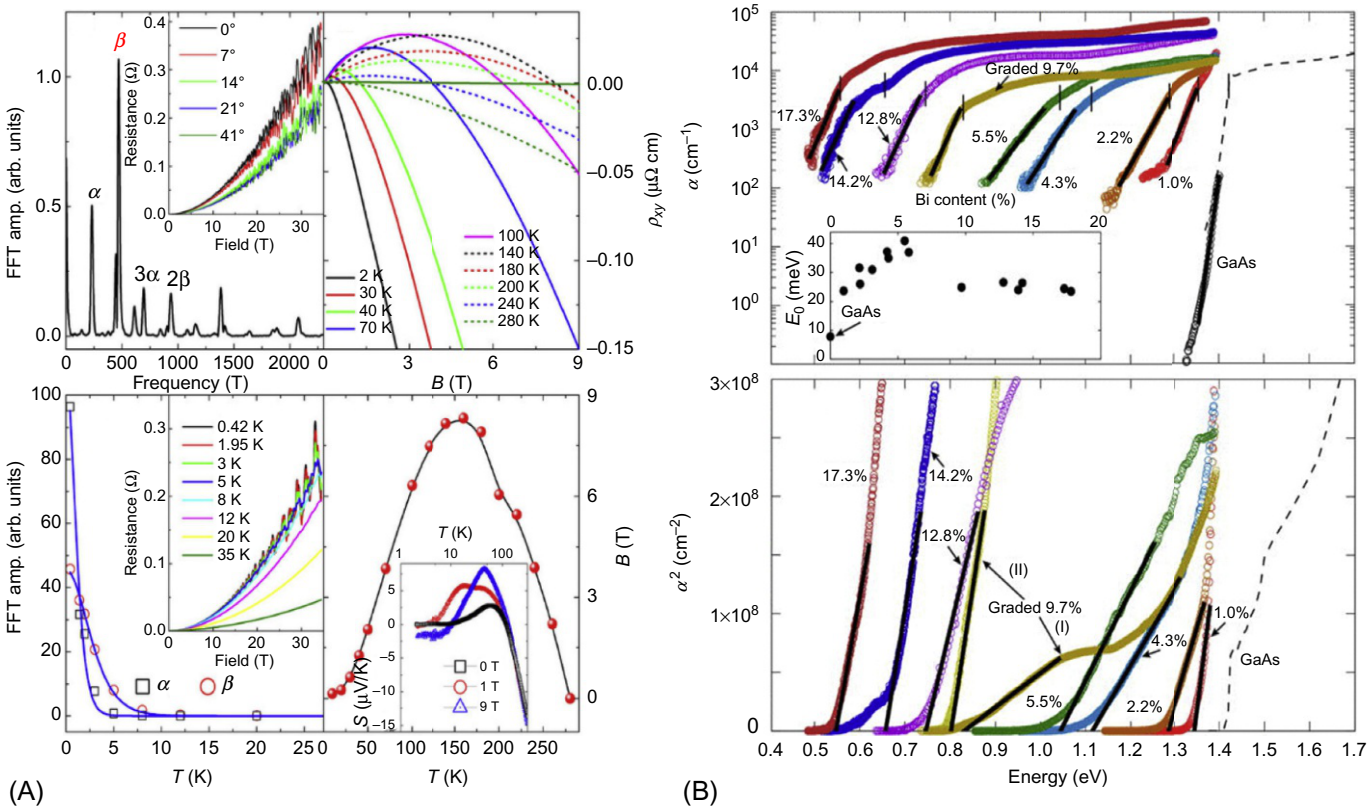

Fig. 13.5 Graph of the function (Eq. 13.42) $\alpha\sigma_0^a Fa(\sigma_0)$ for various values of photon energy in comparison with harvested spectra in the quantum field (A) when it is in the original state, and (B) energy production in the unit area.

This book belongs to Kitab Liaison (ocd1996@gmail.com)

Copyright Elsevier 2023

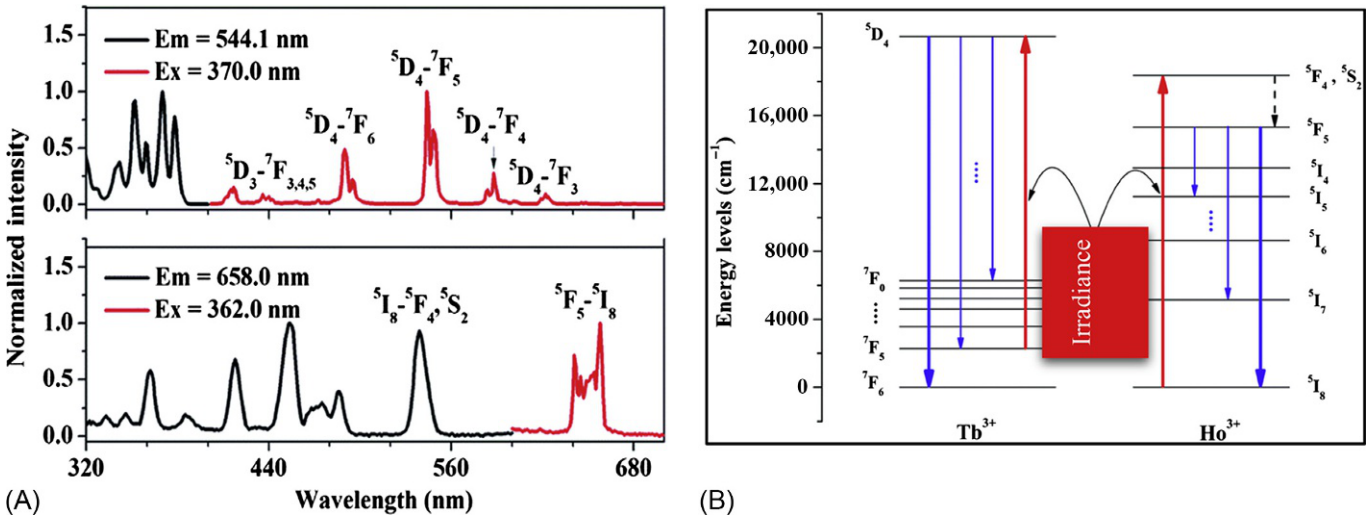

Fig. 13.6 (A) the graph of the function (see Eq. 13.34) $\frac{\overline{\varphi}[s_0]}{(s_0-1)}$, which shows the photon pair coupled to the invariance of normalized intensity into the quantum field wavelength, (B) the coincidence rate of the rapidly distributed higher-order mode output with the assistance of heater power function under the excitation of energy level per unit area.

This book belongs to Kitab Liaison (ocd1996@gmail.com)

Copyright Elsevier 2023

$$\begin{aligned} n(\in) &= 0\ ,\ \in < \in_0 n(\in) \\ C_{\in}^{-\alpha} &= \text{or } D_{\in}^{\beta}, \in_0 < \in < \in_m \\ &= 0,\ \in > \in_m \end{aligned} \tag{13.48}$$

It is a solid and accurate analysis associated with the photon spectrum by using asymptotic formulas, where Γ_{γ}^{LPM} means the rate per unit volume of the photon effect on diverging solar irradiance based on bremsstrahlung and inelastic pair annihilation processes.

$$\Gamma_{\gamma} \equiv \frac{dn_{\gamma}}{dVdt} \tag{13.49}$$

In order to verify the rate of $O(\alpha_{EM}\alpha s)$, the photon effect is added to the results for the $1 \leftarrow 2$ photon production mechanism, which, assuming that under the condition of temperature T and photon physical, the consequence of the divergent surface controlled by thermodynamic is μ, so the equation can be respected as

$$\frac{d\Gamma_{\gamma}^{LPM}}{d^3k} = \frac{d_F q_s^2 \alpha_{EM}}{4\pi^2 k} \int_{-\infty}^{\infty} \frac{dp_{\parallel}}{2\pi} \int \frac{d^2\mathrm{p}_{\perp}}{(2\pi)^2} A\left(p_{\parallel}, k\right) \operatorname{Re}\left\{2P_{\perp} \cdot f\left(p_{\perp}; p_{\parallel}, k\right)\right\} \tag{13.50}$$

where d_F is the quark particle $[N_c$ in $\mathrm{SU}(N_c)]$ function strategy, q_s represents the abelian charge of a quark, $k \equiv |k|$, and the kinetic function $A(p_{||}, k)$ means the emitted particle

$$A\left(p_{\parallel}, k\right) \equiv \begin{cases} \dfrac{n_b\left(k + p_{\parallel}\right)\left[1 + n_b\left(p_{\parallel}\right)\right]}{2p_{\parallel}\left(p_{\parallel} + k\right)}, \text{ scalars} \\ \dfrac{n_f\left(k + p_{\parallel}\right)\left[1 - n_f\left(p_{\parallel}\right)\right]}{2\left[p_{\parallel}\left(p_{\parallel} + k\right)\right]^2}\left[{p_{\parallel}}^2 + \left(p_{\parallel} + k\right)^2\right], \text{ fermions} \end{cases} \tag{13.51}$$

With

$$n_b(p) \equiv \frac{1}{\exp\left[\beta(p - \mu)\right] - 1},\ n_f(p) \equiv \frac{1}{\exp\left[\beta(p - \mu)\right] + 1} \tag{13.52}$$

Further, the calculation of the distribution of $n(k + p_{||})[1 \pm n(p_{||})]$ is used to verify that the photon energy emission rate perfectly matches the range $p_{\parallel} > 0$,which contains $A(p_{||}, k)$ that could affirm the pair annihilation generation by the following equation

$$n_b(-p) = -\left[1 + \overline{n}_b(p)\right],\ n_f(-p) = \left[1 - \overline{n}_f(p)\right] \tag{13.53}$$

This book belongs to Kitab Liaison (ocd1996@gmail.com) Copyright Elsevier 2023

By applying $n(p) \equiv 1/[e\beta(p+\mu) \mp 1]$ as the appropriate antiparticle distribution function, the factor $A(p'', k)$ in this interval may be modified as

$$A(p_{\parallel}, k) \equiv \begin{cases} \dfrac{n_b(k-|p_{\parallel}|)\overline{n}_b(|p_{\parallel}|)}{2|p_{\parallel}|(k-|p_{\parallel}|)}, \text{scalars} \\ \dfrac{n_f(k-|p_{\parallel}|)\overline{n}_f(|p_{\parallel}|)}{2[|p_{\parallel}|(k-|p_{\parallel}|)]^2}\left[{p_{\parallel}}^2 + (k-|p_{\parallel}|)^2\right], \text{fermions} \end{cases} \tag{13.54}$$

Hence, the energy E_p of a hard quark with the assistance of momentum $|p|$ could be elucidated as the following equation

$$E_p = \sqrt{p^2 + m_{\infty}^2} \simeq |p| + \frac{m_{\infty}^2}{2|p|} \simeq |p_{\parallel}| + \frac{p_{\perp}^2 + m_{\infty}^2}{2|p_{\parallel}|} \tag{13.55}$$

Where the mass of the asymptotic thermal is

$$m_{\infty}^2 = \frac{C_f g^2 T^2}{4} \tag{13.56}$$

By replacing the specific form of E_p into Eq. (13.60), the integral result can be written as

$$\delta E = \left[\frac{p_{\perp}^2 + m_{\infty}^2}{2}\right]\left[\frac{k}{p_{\parallel}(k+p_{\parallel})}\right] \tag{13.57}$$

Therefore, the result represents derivation by Eqs. (13.52), (13.55), which is shown in Fig. 13.7 connected with the leading order photoemission rate. Besides, a diagram of power counting analysis related to photon emission during electronic flight time is also demonstrated in Fig. 13.7.

Finally, the calculation related to the number of scalar quarks is added to simplify this result, which is the photodynamic of photon momenta $k = O(T)$ with $|K^2| \leq g^2 T^2$. Therefore, by applying the result of production of multiple photons by the scattering process into the calculation, which related to the emission rate of photon momentum at the scattering rate of $|k| \gg g^4 T \ln g - 1$ per unit volume to the leading order in e^2, this equation could be modified as

$$\sigma = W_{\mu\nu}(K) = \int d^4x e^{-iKx} \langle j_{\mu}(x) j_{\nu}(0) \rangle = (\gamma + \gamma)^2 \tag{13.58}$$

where K refers to the photon 4-momenta with 1-momenta k and positive energy $k^0 = |k| \equiv k$, and $W_{\mu\nu}(K) = \sigma = (\gamma + \gamma)^2$ is the final equation of the photon pair production generated by the two semiconductor parameters $(2+2)^2$, which could be used to affirm the creation of 16 photons.

This book belongs to Kitab Liaison (ocd1996@gmail.com) Copyright Elsevier 2023

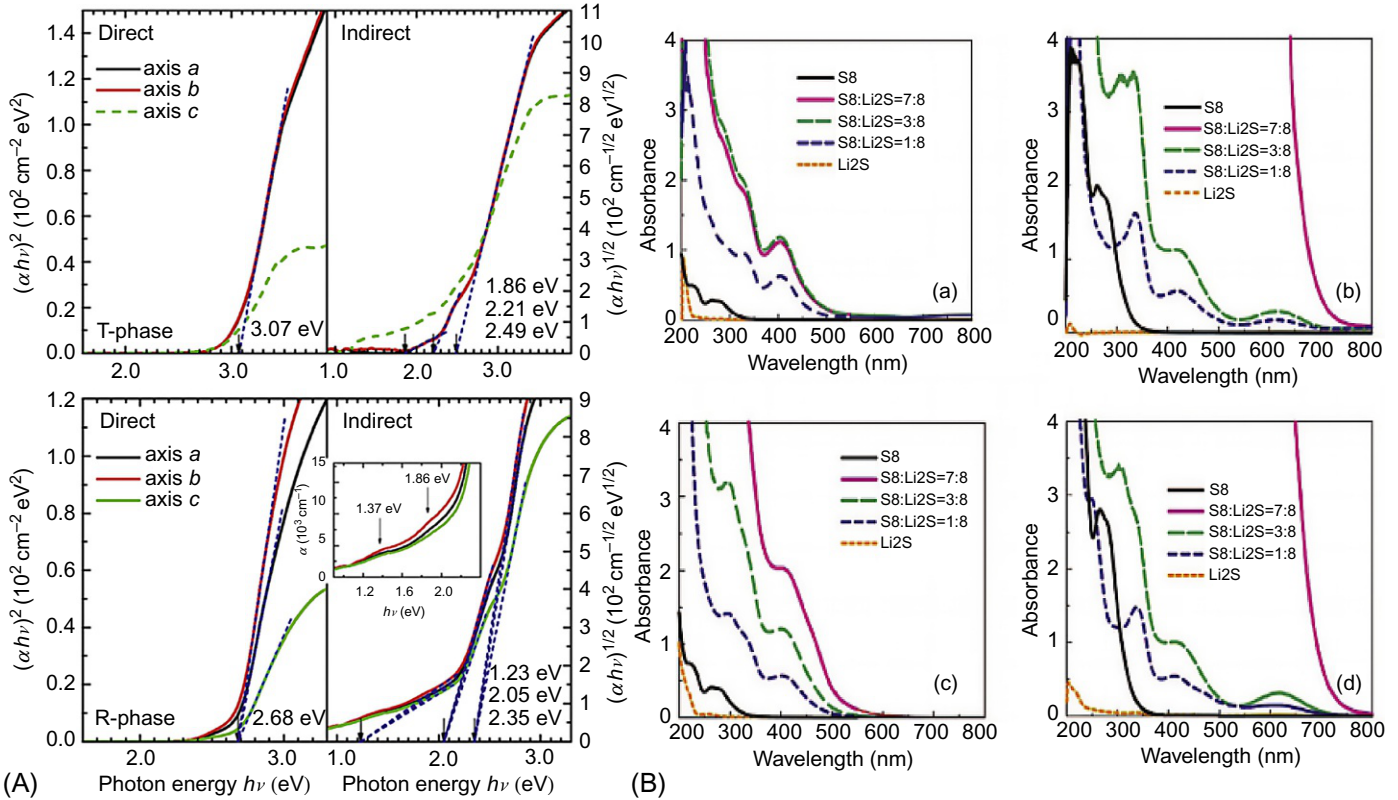

Fig. 13.7 (A) Parts of the dielectric function tensor (εc) and normalized effective carrier number Neff (right) of this work and compared to literature values of photon energy. (B) Plots of ($\alpha h\nu$)2 and ($\alpha h\nu$)1/2 versus photon energy visualizing direct and indirect transitions, respectively. The inset shows the absorption coefficient α versus photon energy highlighting two subtle excitations.

This book belongs to Kitab Liaison (ocd1996@gmail.com)

Copyright Elsevier 2023

Three-diode photon scattering

By integrating Eqs. (13.25), (13.26) into dynamic photon production, the production of thousands of photons in the quantum field has been figured out mathematically. There is no doubt that the unit areal condition $J(\omega)$ is changeable, so that the active quantum field and the areal unit $J(\omega)$ have a definite weak-coupling limitation that is equal to the photon production [4, 29]. Afterward, to prevent divergence of the DOS in a three-dimensional (3D) PV cell, a fine high frequency cut-off Ω_C performed. Likewise, a positive DOS in two-dimensional (2D) and one-dimensional (1D) PV cells is held by a sharpened high frequency cut-off at Ω_d [30]. Therefore, $\mathrm{Li}_2\,(x)$ represents as a dilogarithm variable and $e_{rfc}\,(x)$ acts as an extra variable. Then, the $\varrho_{PC}(\omega)$, which is the DOS of various PV cells, depends on the photon eigenfrequencies and eigenfunctions calculation of Maxwell's rules when taking the PV *nano* structure into account. In terms of a 1D PV cell, the corresponding DOS is calculated as $\varrho_{PC}(\omega) \propto \frac{1}{\sqrt{\omega-\omega_e}}\Theta(\omega-\omega_e)$, where $\Theta(\omega-\omega_e)$ is the Heaviside step function and ω_e means the frequency in the PBE regarding the DOS (Fig. 13.8).

Thus, 3D isotropic analysis in PV cells conducted by the DOS is used for projecting the error-free qualitative state of the non-Weisskopf-Winger mode and the photon-photon collision state in the PV cell [16, 31, 32]. Furthermore, in terms of a 3D PV cell, the DOS adjacent to the PBE is achieved by anisotropic DOS, which is expressed as $\varrho_{PC}(\omega) \propto \frac{1}{\sqrt{\omega-\omega_e}}\Theta(\omega-\omega_e)$ [21, 22], which is further simplified related to the electromagnetic field (EMF) vector. In addition, the photon DOS is similar to the PBE in terms of a pure logarithm divergence in 2D and 1D PV cells, and this relationship can be written as $\varrho_{PC}(\omega) \propto -[\ln|(\omega-\omega_0)/\omega_0|-1]\Theta(\omega-\omega_e)$, where ω_e indicates the central point of the peak logarithm. The unit area $J(\omega)$ refers to the DOS production field in the PV cell connected with the fine photonic magnitude $V(\omega)$ within the PB and PV cell [1, 33]

$$J(\omega) = \varrho(\omega)|V(\omega)|^2 \tag{13.59}$$

Then, it does combine the PB frequency ω_c and the proliferative photon dynamics with the function $u(t, t_0)$ for the photon structure as follows: $\langle a(t)\rangle = u(t, t_0)\langle a(t_0)\rangle$, which employs the dissipative integro-differential equation as

$$u(t, t_0) = \frac{1}{1-\Sigma'(\omega_b)}e^{-i\omega(t-t_0)} + \int_{\omega_e}^{\infty} d\omega \frac{J(\omega)e^{-i\omega(t-t_0)}}{[\omega-\omega_c-\Delta(\omega)]^2+\pi^2 J^2(\omega)} \tag{13.60}$$

This book belongs to Kitab Liaison (ocd1996@gmail.com) Copyright Elsevier 2023

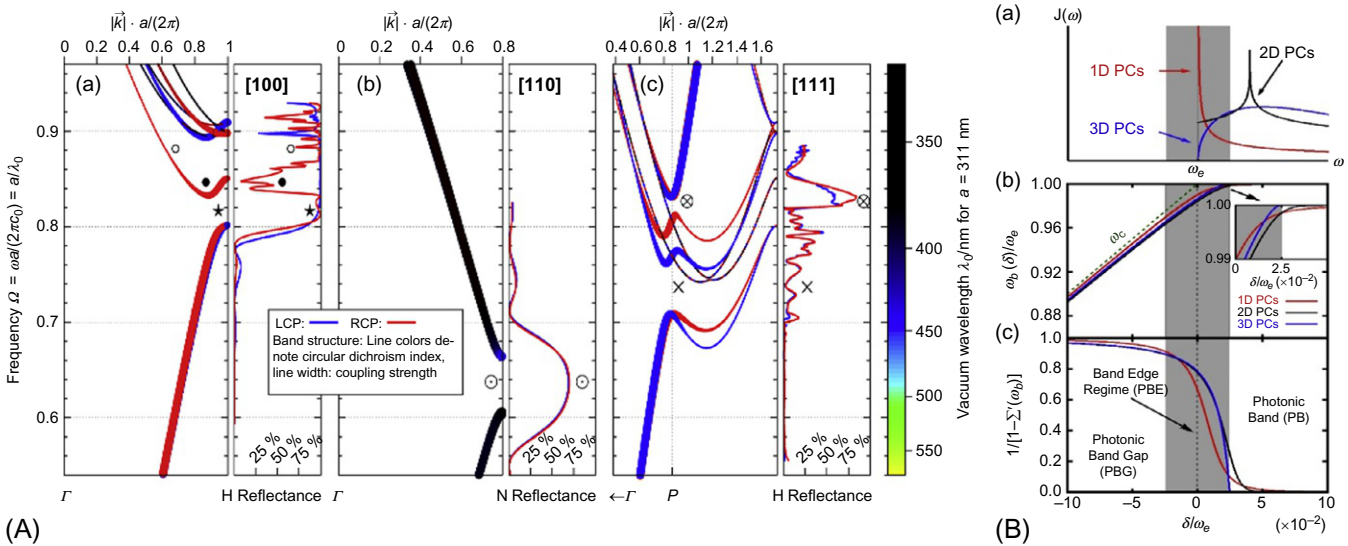

Fig. 13.8 (A) The photon energy conversion modes. (B)—(a) Unit area versus frequency of DOS in 1D, 2D, and 3D glazing wall skins. (b) Photon energy modes of functional tuning. (c) Photon energy modes of magnitudes to release into the PV wall skin in 1D and 2D and in the complex 3D transitional state [3].

This book belongs to Kitab Liaison (ocd1996@gmail.com)

Copyright Elsevier 2023

where $\Sigma'(\omega_b) = [\partial\Sigma(\omega)/\partial\omega]_{\omega=\omega_b}$ and $\Sigma(\omega)$ refers to the reservoir-induced PB photon self-energy correction,

$$\Sigma(\omega) = \int_{\omega_c}^{\infty} d\omega' \frac{J(\omega')}{\omega - \omega'} \tag{13.61}$$

Moreover, the frequency ω_b in Eq. (13.20) is the photonic frequency mode in the PBG $(0 < \omega_b < \omega_e)$ under the pole condition: $\omega_b - \omega_c - \Delta(\omega_b) = 0$, where $\lesssim\Delta(\omega) = \mathcal{P}\left[\int d\omega' \frac{J(\omega')}{\omega-\omega'}\right]$ is a principal-value integral.

Besides, the specific photonic dynamics diagrams are shown in Fig. 13.9A, which is related to the proliferation magnitude $|u(t, t_0)|$ regarding different detuning δ integrated from the PBG area to the PB area [33–35]. Fig. 13.9B shows the photonic dynamic rate $\kappa(t)$, regardless of the function $\delta = 0.1\ \omega_e$. The consequence shows that the production of dynamic photons occurs frequently when ω_c is in the PB area instead of PBG. The crossover area is relevant with the condition $0.9 \gtrsim |ut \to \infty, t_0)| \geq 0$ because $u(t, t_0)$ belongs to $1 \geq |u(t, t_0)| \geq 0$, which is in accord with $-0.025\omega_e \lesssim \delta \lesssim 0.025\omega_e$, with a production rate $\kappa(t)$ within the PBG $(\delta < -0.025\omega_e)$ and in the vicinity of the PBE$(-0.025\omega_e \lesssim \delta \lesssim 0.025\omega_e)$.

Naturally, the dynamic photon output has attained exponential growth in relationship with a Markov factor $\delta \gg 0.025\omega_e$, which is shown as the das-doted curves with $\delta = 0.1\omega_e$ in Fig. 13.9A. Within the crossover area $(-0.025\omega_e \lesssim \delta \lesssim 0.025\omega_e)$ in the mode of dynamic photon production, when in close proximity to the PBE, the PB is in the low-frequent rate, which boosts significantly after that [28, 36, 37]. Hence, the ionic photonic states, where the photons are unstable once in close proximity to the PBG in the PV cell, could be verified by dynamic photon proliferation [19, 24, 38].

Subsequently, considering the change of thermal relative to the photon correlation function $\nu(t, t)$, the dynamics of photon proliferation in the quantum field are elucidated by defining the nonequilibrium photon scattering theorem [39, 40].

$$\nu(t, t) = \int_{t_0}^{t} dt_1 \int_{t_0}^{t} dt_2 u^*(t_1, t_0)\, \tilde{g}\,(t_1, t_2) u(t_2, t_0) \tag{13.62}$$

In this equation, the two time correlation function $\tilde{g}\,(t_1, t_2) = \int d\omega J(\omega)\overline{n}(\omega, T)e^{-i\omega(t-t')}$ represents the photonic dynamic variations under

This book belongs to Kitab Liaison (ocd1996@gmail.com) Copyright Elsevier 2023

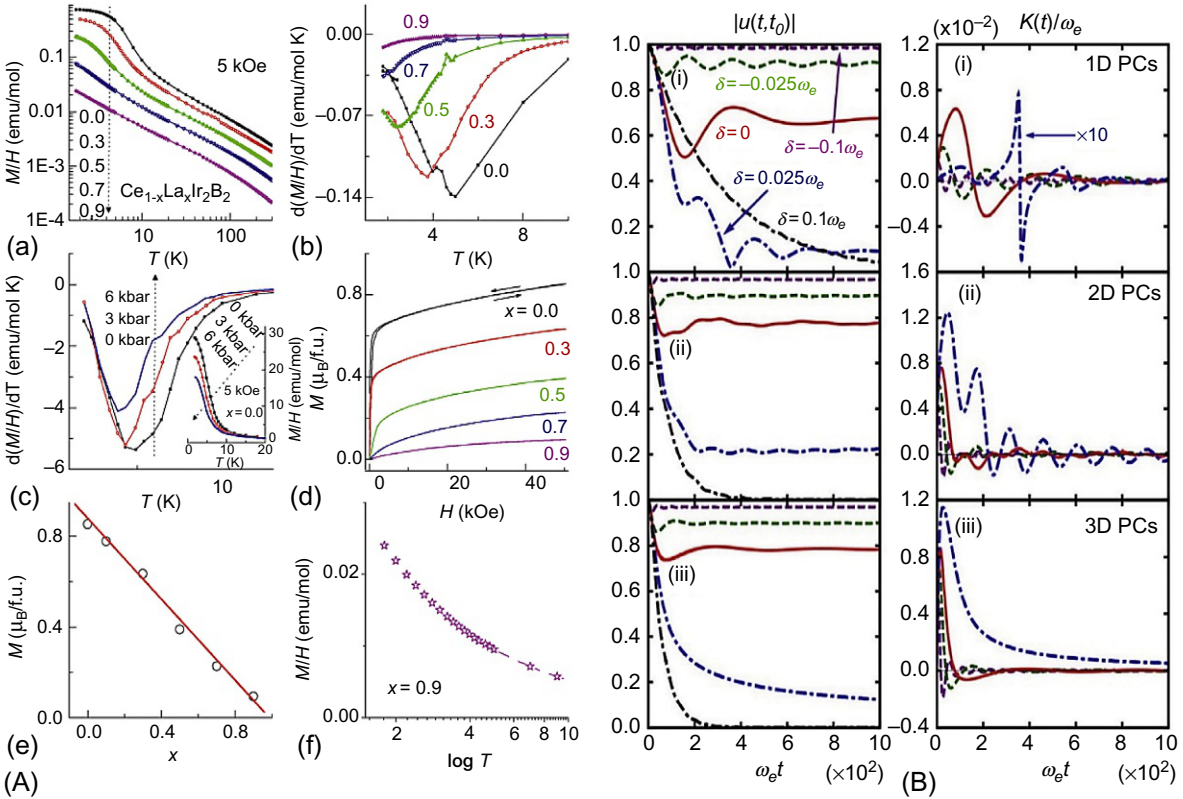

Fig. 13.9 (A) Photon activation mechanism in various PB parameters, (B) Dynamic photon production in PV cells. (a) Shows the generation in the PB area $<a(t)> = 5\ u(t, t_0) < a(t_0)>$, (b) Demonstrates the dynamic photonic rate $k(t)$, plotted for (i) 1D, (ii) 2D and (iii) 3D quantum field into the PV cells [3, 21].

This book belongs to Kitab Liaison (ocd1996@gmail.com)

Copyright Elsevier 2023

the thermal relativistic condition, where $\overline{n}(\omega, T) = 1/\left[e^{\hbar\omega/k_B T} - 1\right]$ means the photon production in the PV cell at relativistic temperature T, which can be written as

$$\nu(t, t \to \infty) = \int_{\omega_e}^{\infty} d\omega \mathcal{V}(\omega)$$

With

$$\mathcal{V}(\omega) = \overline{n}(\omega, T)[\mathcal{D}_l(\omega) + \mathcal{D}_d(\omega)] \tag{13.63}$$

Eq. (13.68) defines the nonequilibrium condition $\mathcal{V}(\omega) = \overline{n}(\omega, T)\mathcal{D}_d(\omega)$. Since Einstein's photon wave motion dissipates on PB is immobile at low-temperature, and thus the connected photonic dormant structures (i.e., the field intensity) [41–43] can be expressed as $n(t) = \langle a^{\dagger}(t)a(t)\rangle = |u(t, t_0)|^2 n(t_0)\nu(t, t)$, where $n(t_0)$ is the primary PB. Thus, the function connecting dynamic photon generation with temperature is shown as the *solid-blue curve (dark gray in print version)* in Fig. 13.9, which is used for the nonequilibrium proliferated photon production conformation. First, the PB as the Fock state photon number n_0, that is, $\rho(t_0) = |n_0\rangle\langle n_0|$, which is obtained via the real-time quantum feedback control in theory [44, 45]. Second, by simplified Eq. (13.67) with the assistance of the state of photon production at time t, the state of photon production at time t could be written as

$$\rho(t) = \sum_{n=0}^{\infty} \mathcal{P}_n^{(n_0)}(t)|n_0\rangle\langle n_0| \tag{13.64}$$

$$\mathcal{P}_n^{(n_0)}(t) = \frac{[\nu(t, t)]^n}{[1 + \nu(t, t)]^{n+1}}[1 - \Omega(t)]^{n_0} \times \sum_{k=0}^{min\{n_0, n\}} \binom{n_0}{k}\binom{n}{k}\left[\frac{1}{\nu(t, t)}\frac{\Omega(t)}{1 - \Omega(t)}\right]^k \tag{13.65}$$

where $\Omega(t) = \frac{|u(t, t_0)|^2}{1 + \nu(t, t)}$. Thus, the result shows that various Fock states of $|n_0\rangle$ is $\mathcal{P}_n^{(n_0)}(t)$ would be developed by a Fock state photon. Besides, the proliferation of photon dissipation $\mathcal{P}_n^{(n_0)}(t)$ has limitation in the primary state $|n_0 = 5\rangle$ and the steady state, which is depicted in Fig. 13.9 as $\mathcal{P}_n^{(n_0)}(t \to \infty)$. Thus, the photon proliferation will achieve the thermal nonequilibrium state of the photonic structure eventually.

$$\mathcal{P}_n^{(n_0)}(t \to \infty) = \frac{[\overline{n}(\omega_c, T)]^n}{[1 + \overline{n}(\omega_c, T)]^{n+1}} \tag{13.66}$$

This book belongs to Kitab Liaison (ocd1996@gmail.com) Copyright Elsevier 2023

In order to confirm this huge photon generation, the calculation of photon distribution in the quantum field at the high temperature of various photon proliferation states is calculated by Eq. (13.72), as below

$$\rho(t) = \mathcal{D}[\alpha(t)]\rho_T[\nu(t,t)]\mathcal{D}^{-1}[\alpha(t)] \tag{13.67}$$

where $\mathcal{D}[\alpha(t)] = \exp\left\{\alpha(t)\alpha^{\dagger} - \alpha^{*}(t)\alpha\right\}$ refers to the displacement driver with $\alpha(t) = u(t,t_0)\alpha_0$ and

$$\rho_T[\nu(t,t)] = \sum_{n=0}^{\infty} \frac{[\nu(t,t)^n]}{[1+\nu(t,t)]^{n+1}} |n\rangle\langle n| \tag{13.68}$$

where ρ_T refers to a thermal state with mean particle number $\nu(t,t)$, and this equation shows that the primary point break cavity state will develop into a displaced thermal state [46, 47], which mixes displaced number states and is written as $\mathcal{D}[\alpha(t)]|n^{37}$. Hence, the photon number could written as below

$$\begin{aligned} m|\,\rho(t)\,|\,n = J(\omega) &= e^{-\Omega(t)|\alpha_0|^2} \frac{[\alpha(t)]^m[\alpha^*(t)]^n}{[1+\nu(t,t)]^{m+n+1}} \\ &= \sum_{k=0}^{min\{m,\,n\}} \frac{\sqrt{m!n!}}{(m-k)!(n-k)!k!} \left[\frac{\nu(t,t)}{\Omega(t)|\alpha_0|^2}\right]^k \end{aligned} \tag{13.69}$$

Where indicates that multiple photon production in the quantum field $(\langle m|\rho(t)|n\rangle)$ does develop into an extreme relativistic thermal state $[1+\nu(t,t)]^{m+n+1}$ and nonequilibrium condition $[\alpha(t)]^m[\alpha^*(t)]^n$. The tremendous photons generated from a PB photon can be further calculated as $J(\omega) = \sum_{k=0}^{min\{m,\,n\}} \frac{\sqrt{m!n!}}{(m-k)!(n-k)!k!} \left[\frac{\nu(t,t)}{\Omega(t)|\alpha_0|^2}\right]^k = \left[e*n(\gamma+\gamma)^2\right]^3 = \left[1*1(2+2)^2\right]^3$, which results in 4092 photons.

Electricity transformation

By using a micro PV module, a solar cell single-diode model that consists of connecting solar cells in series and parallel utilizing photon energy (current), diodes, and two resistors, these thousands of photons can be transformed into electricity. Under the single-diode mode, the PV model can be expressed with the *I-V* equation of PV cells as follows

$$I = I_L - I_0\left\{\exp\left[\frac{q(V+I_{RS})}{AkTc}\right] - 1\right\} - \frac{(V+I_{RS})}{R_{sh}}. \tag{13.70}$$

This book belongs to Kitab Liaison (ocd1996@gmail.com) Copyright Elsevier 2023

where I_L represents the current generated by the photon, IO I_0 refers to the saturated current in the diode, R_s means resistance in a series, A indicates the diode passive function, $k(=1.38 \times 10^{-23}$ W/m^{2}K) its Boltzmann's constant, $q(=1.6 \times 10^{-19}$C) denotes the charge amplitude of an electron, and T_C serves as the functional cell temperature. Afterward, because the diode current and/or saturation current are different, the I-q relationship in the PV cells varies, which can be written as [3, 39]

$$I_0 = I_{RS}\left(\frac{T_C}{T_{\text{ref}}}\right)^3 \exp\left[\frac{qEG\left(\frac{1}{T_{\text{ref}}} - \frac{1}{T_C}\right)}{KA}\right] \tag{13.71}$$

where I_{RS} means the saturation current at the functional temperature, solar irradiance and qEG represents the band-gap energy into the silicon and graphene PV cell with respect to the normal, normalized, and perfect modes (Fig. 13.10).

In a PV module, the I-V equation is a combination of I-V curves across all cells of a PV panel except the I-V curve. Thus, the equation explaining the V-R relationship is represented as

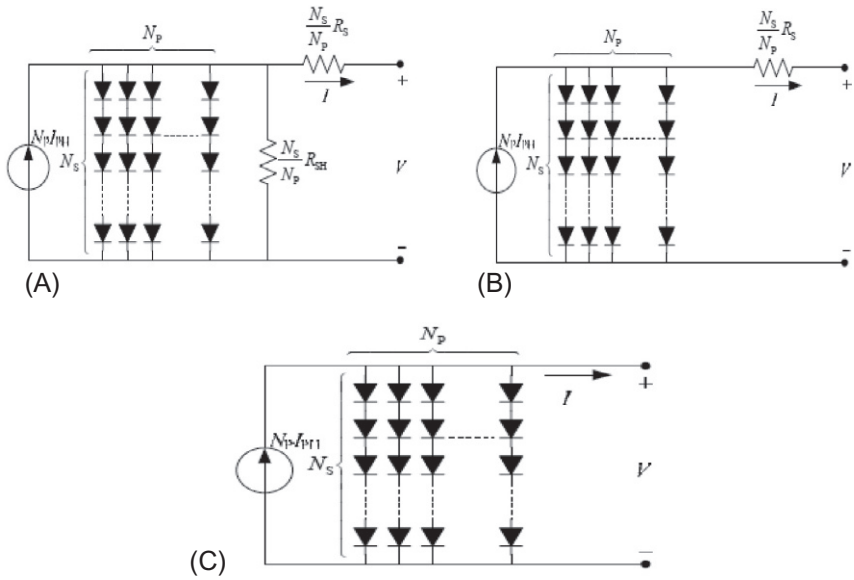

Fig. 13.10 Equivalent circuit models of the PV module (A) normal, (B) normalized, and (C) perfect modes.

This book belongs to Kitab Liaison (ocd1996@gmail.com) Copyright Elsevier 2023

$$V = -IR_s + K \log\left[\frac{I_L - I + I_0}{I_0}\right] \tag{13.72}$$

where K is as a constant $\left(=\frac{AkT}{q}\right)$ and I_{mo} and V_{mo} are the current and voltage in the PV panel. Therefore, the relationship between I_{mo} and V_{mo} is similar with the PV cell I-V relationship and could be written as follow

$$V_{mo} = -I_{mo}\frac{Rs}{N_p} + K \log\left(\frac{N_{sh}I_L - I_{mo} + N_pI_0}{N_pI_0}\right) \tag{13.73}$$

Because the current generated from the photon relates to the solar irradiance and relativistic temperature conditions of the PV panel, the calculation can be written as

$$I_L = G\left[I_{SC} + KI\left(T_C - T_{\text{ref}}\right)\right] \times V_{mo} \tag{13.74}$$

where I_{sc} means PV current at 25°C and KW/m^2, KI represents the relativistic PV panel coefficient factor, T_{ref} is the functional temperature of the PV panel, and G indicates the solar energy in mW/m^2 [25, 48].

Therefore, the total energy would be (1.4 eV = 27.77 mW/m^2 × 4092) = 159,088.78 mW/m^2 eV per hour [49]. If we use just a 1 cm^2 Higgs boson quantum field assisted high temperature PV panel, it will produce 1590.9 mW/h, which is a tremendous source of energy. Consequently, the entire photon generation originating from a single one is calculated as $J(\omega) = [e * n(\gamma + \gamma)^2]^3 = [1 * 1(2+2)^2]^3$, which results in 4092 photons (Eq. 13.27). Then, I performed an estimate to convert these photons into electricity. Because the light quanta of a certain type of polarization has a frequency range of ν_r to $\nu_r + d_{\nu_r}$, thus, the solar energy calculated is as 6728.8 eV [1.4 eV × 4092], where one photon contain 1.4 eV equivalent to 27.77 mW/m^2/h [3, 46]. Thus, the sum of solar energy is (1.4 eV = 27.77 mW/m^2 × 4092) = 159,088.78 mW/m^2 eV per hour. To sum up, a 1 cm^2 Higgs boson quantum field applied with high temperature in a PV panel will produce 1590.9 mW/h energy. Therefore, the solar irradiance would be a source of enormous clean energy that would be widely used in the near future.

Conclusions

The formation of several photons from a single photon was proposed and the photon generation mechanism was calculated through a series of mathematical physics to design a micro PV panel. The proposed research found that a

This book belongs to Kitab Liaison (ocd1996@gmail.com) Copyright Elsevier 2023

photon pair ($e^+ e^-$) can be created from a single photon in the Higgs boson quantum field by initiating a high-temperature state through the photophysical reaction mechanism. Then the photon pair can be transformed by applying the photodissociation of two surfaced semiconductors and scattering by three diodes of superconductors. The processes of *photon-photon collision, photodissociation, and photoscattering* have been tested by mathematical calculations, which confirm that a total of 4092 photons is being generated from a single photon. Further estimates shows that a 1 cm^2 PV panel can produce 1590.9 MW/h energy, which indeed would be a cutting-edge technology to meet the total energy demand for a building itself as well as meet the global energy demand significantly.

Acknowledgments

This research was supported by Green Globe Technology, Inc. under grant RD-02018-04 for building a better environment. Any findings, predictions, and conclusions described in this article are solely those of the authors, who confirm that the article has no conflicts of interest for publication in a suitable journal.

References

[1] J. Eichler, T. Stöhlker, Radiative electron capture in relativistic ion-atom collisions and the photoelectric effect in hydrogen-like high-Z systems, Phys. Rep. 439 (2007) 1.
[2] B. Najjari, A. Voitkiv, A. Artemyev, A. Surzhykov, Simultaneous electron capture and bound-free pair production in relativistic collisions of heavy nuclei with atoms, Phys. Rev. A 80 (2009) 012701.
[3] Q. Li, D.Z. Xu, C.Y. Cai, C.P. Sun, Recoil effects of a motional scatterer on single-photon scattering in one dimension, Sci. Rep. 43 (2013) 3222–3227.
[4] J.Q. Liao, C.K. Law, Correlated two-photon scattering in cavity optomechanics, Phys. Rev. A 87 (2013) 043809.
[5] C.U. Lei, W.M. Zhang, A quantum photonic dissipative transport theory, Ann. Phys. 327 (2012) 1408.
[6] J.Q. Liao, C.K. Law, Correlated two-photon transport in a one-dimensional waveguide side-coupled to a nonlinear cavity, Phys. Rev. A 82 (2010) 053836.
[7] W. Yan, J. Huang, H. Fan, Tunable single-photon frequency conversion in a Sagnac interferometer, Sci. Rep. 67 (2013) 5545–5549.
[8] D.K. Armani, T.J. Kippenberg, S.M. Spillane, K.J. Vahala, Ultra-high-Q toroid microcavity on a chip, Nature 421 (2003) 925.
[9] K.M. Birnbaum, et al., Photon blockade in an optical cavity with one trapped atom, Nature 436 (2005) 87–90.
[10] P. Lo, H. Xiong, W. Zhang, Breakdown of Bose-Einstein distribution in photonic crystals, Sci. Rep. 5 (2015) 9423–9428.
[11] A. Ruiz, Partial recovery of a potential from backscattering data, in: Communications in Partial Differential Equations Springer Tracts in Modern Physics, vol. 5, 2014, pp. 56–59.

This book belongs to Kitab Liaison (ocd1996@gmail.com) Copyright Elsevier 2023

[12] W. Yan, H. Fan, Single-photon quantum router with multiple output ports. Sci. Rep. 6 (2014) 3445–3449.
[13] M.F. Hossain, Green science: independent building technology to mitigate energy, environment, and climate change. Renew. Sust. Energ. Rev. (2017), https://doi.org/10.1016/j.rser.2017.01.136.
[14] A.G. Kofman, G. Kurizki, B. Sherman, Spontaneous and induced atomic decay in photonic band structures, J. Mod. Opt. 41 (1994) 353.
[15] D.E. Chang, A.S. Sørensen, E.A. Demler, M.D. Lukin, A single-photon transistor using nanoscale surface plasmons, Nat. Phys. 3 (2007) 807–812.
[16] M. Cheng, Y. Song, Fano resonance analysis in a pair of semiconductor quantum dots coupling to a metal nanowire, Opt. Lett. 37 (2012) 978–980.
[17] K. Busch, G. von Freymann, S. Linden, S.F. Mingaleev, L. Tkeshelashvili, M. Wegener, Periodic nanostructures for photonics, Phys. Rep. 444 (2007) 101.
[18] C. Sánchez Muñoz, F. Laussy, E. Valle, C. Tejedor, A. González-Tudela, Filtering multiphoton emission from state-of-the-art cavity quantum electrodynamics, Optica 5 (1) (2018) 14–26.
[19] J. Chen, C. Wang, R. Zhang, J. Xiao, Multiple plasmon-induced transparencies in coupled-resonator systems, Opt. Lett. 37 (2012) 5133–5135.
[20] D. Englund, et al., Resonant excitation of a quantum dot strongly coupled to a photonic crystal nanocavity, Phys. Rev. Lett. 104 (2010) 073904.
[21] C. Guerlin, et al., Progressive field-state collapse and quantum non-demolition photon counting, Nature 448 (2007) 889.
[22] J.D. Joannopoulos, P.R. Villeneuve, S. Fan, Photonic crystals: putting a new twist on light, Nature 386 (1997) 143.
[23] N. Gupta, S.P. Singh, S.P. Dubey, D.K. Palwalia, Fuzzy logic controlled three-phase three-wired shunt active power filter for power quality improvement, Int. Rev. Electr. Eng. 6 (3) (2011) 1118–1129.
[24] J.S. Douglas, H. Habibian, C. Hung, A. Gorshkov, H. Kimble, D. Chang, Quantum many-body models with cold atoms coupled to photonic crystals, Nat. Photonics 34 (2015) 6789–6793.
[25] T. Shi, S. Fan, C.P. Sun, Two-photon transport in a waveguide coupled to a cavity in a two-level system, Phys. Rev. A 84 (2011) 063803.
[26] U. Jentschura, K. Hencken, V. Serbo, Revisiting unitarity corrections for electromagnetic processes in collisions of relativistic nuclei, Eur. Phys. J. C 58 (2) (2008) 281–289.
[27] L. Yang, S. Wang, Q. Zeng, Z. Zhang, T. Pei, Y. Li, L. Peng, Efficient photovoltage multiplication in carbon nanotubes, Nat. Photonics (2011) 672–676.
[28] B. Dayan, et al., A photon turnstile dynamically regulated by one atom, Science 319 (2008) 1062–1065.
[29] J.F. Huang, T. Shi, C.P. Sun, F. Nori, Controlling single-photon transport in waveguides with finite cross section, Phys. Rev. A 88 (2013) 013836.
[30] N. Artemyev, U.D. Jentschura, V.G. Serbo, A. Surzhykov, Strong electromagnetic field effects in ultra-relativistic heavy-ion collisions, Eur. Phys. J. C 72 (2012) 1935.
[31] M.F. Hossain, Green science: advanced building design technology to mitigate energy and environment, Renew. Sustain. Energy Rev. 81 (2) (2018) 3051–3060.
[32] M.F. Hossain, Photonic thermal energy control to naturally cool and heat the building, Adv. Therm. Eng. 131 (2018) 576–586.
[33] Y. Huang, C. Min, G. Veronis, Subwavelength slow-light waveguides based on a plasmonic analogue of electromagnetically induced transparency, Appl. Phys. Lett. 99 (2011) 143117.
[34] M.F. Hossain, Transforming dark photon into sustainable energy, Int. J. Energy Environ. Eng. (2018), https://doi.org/10.1007/s40095-017-0257-1.

This book belongs to Kitab Liaison (ocd1996@gmail.com) Copyright Elsevier 2023

[35] D. Roy, Two-photon scattering of a tightly focused weak light beam from a small atomic ensemble: an optical probe to detect atomic level structures, Phys. Rev. A 87 (2013) 063819.
[36] Z. Han, S.I. Bozhevolnyi, Plasmon-induced transparency with detuned ultracompact Fabry-Pérot resonators in integrated plasmonic devices, Opt. Express 19 (2011) 3251–3257.
[37] K. Hencken, Transverse momentum distribution of vector mesons produced in ultra-peripheral relativistic heavy ion collisions, Phys. Rev. Lett. 67 (2006) 345–349.
[38] C. Sayrin, et al., Real-time quantum feedback prepares and stabilizes photon number states, Nature 477 (2011) 73.
[39] M.F. Hossain, Design and construction of ultra-relativistic collision PV panel and its application into building sector to mitigate total energy demand, J. Build. Eng. (2017), https://doi.org/10.1016/j.jobe.2016. 12.005.
[40] P. Longo, P. Schmitteckert, K. Busch, Few-photon transport in low-dimensional systems, Phys. Rev. A 83 (2011) 063828.
[41] P. Kolchin, R.F. Oulton, X. Zhang, Nonlinear quantum optics in a waveguide: Distinct single photons strongly interacting at the single atom level, Phys. Rev. Lett. 106 (2011) 113601.
[42] X. Lü, W. Zhang, S. Ashhab, Y. Wu, F. Nori, Quantum-criticality-induced strong Kerr nonlinearities in optomechanical systems, Sci. Rep. 8 (2013) 5667–5669.
[43] D. O'Shea, C. Junge, J. Volz, A. Rauschenbeutel, Fiber-optical switch controlled by a single atom, Phys. Rev. Lett. 111 (2013) 193601.
[44] R.J. Gould, Pair production in photon-photon collisions, Phys. Rev. 34 (1967) 67–73.
[45] S.R. Valluri, U. Becker, N. Grün, W. Scheid, Relativistic collisions of highly-charged ions, J. Phys. B: At. Mol. Phys. 17 (1984) 4359.
[46] J.T. Shen, S. Fan, Strongly correlated two-photon transport in a one-dimensional waveguide coupled to a two-level system, Phys. Rev. Lett. 98 (2007) 153003.
[47] M.W.Y. Tu, W.M. Zhang, Non-Markovian decoherence theory for a double-dot charge qubit, Phys. Rev. B 78 (2008) 235311.
[48] M.S. Tame, K.R. McEnery, Ş.K. Özdemir, J. Lee, S.A. Maier, M.S. Kim, Quantum plasmonics, Nat. Phys. 23 (2013) 456–459.
[49] S. Gleyzes, et al., Quantum jumps of light recording the birth and death of a photon in a cavity, Nature 446 (2007) 297.

This book belongs to Kitab Liaison (ocd1996@gmail.com) Copyright Elsevier 2023

PART 5

Conclusion

This book belongs to Kitab Liaison (ocd1996@gmail.com)

Copyright Elsevier 2023

This page intentionally left blank

This book belongs to Kitab Liaison (ocd1996@gmail.com)

Copyright Elsevier 2023

CHAPTER 14

Sustainable urbanization

Urban environmental management

Based on current information, urban carbon dioxide discharges have increased more rapidly ever since 2000 than in the course of past years [3–5]. In 2007, the *Intergovernmental Panel on Climate Change* (IPCC) reported that this increase in CO_2 emissions is beyond the worst-scenario case [6–8]. As compared to urban systems in developed countries, developing countries are releasing more carbon dioxide [9–11]. Over the last 50 years, the efficiency of natural sinks such as urban forests, which absorb carbon dioxide, has declined, indicating that human efforts to lessen these emissions from human undertakings will have to be increasingly effective to stabilize the CO_2 level within the urban atmosphere [12–14]. Acquiring a carbon-balance environment requires the implementation of sustainable transport, accommodation, and consumer habits to create a basic, communal alteration in human lifestyles in urban areas.

Because urban air pollution is severely affecting human health and completely damaging the ecosystem, the priority is to clean air quality all living things and the environment [15, 16]. Application of clean technology within every sector, such as proper conservation and recycling of water; where most significantly recycling the industrial, municipal, and domestic waste and converting it into valuable products will be the best decision for environmental management, can manage the practice for reducing air pollution in the urban atmosphere [17, 18]. Considering the environmental and social benefits, the adoption of measures such as low consumption of water, reduction of water sources, more effectual energy systems, and cleaner vehicles will firmly be upheld.

An additional common source of human stress in urban areas is environmental noise [19–21]. Based on research findings, noise pollution results in several health issues, including psychological problems, raised hormone levels, cardiovascular disease, and even untimely death [22, 23]. The levels of noise continue to increase with the increase in demand for mobility, which causes the increased use of planes, trains, and cars [24, 25]. Accordingly, the mobility consequence with urban regions should be controlled,

Sustainable Development for Mass Urbanization
https://doi.org/10.1016/B978-0-12-817690-0.00014-2
© 2019 Elsevier Inc.
All rights reserved.

This book belongs to Kitab Liaison (ocd1996@gmail.com)
Copyright Elsevier 2023

including but not limited to unloading and loading activities, sirens, outdoor activities, and public road works. Moreover, to drastically lessen noise pollution, urban authorities must shift heavy industries to a well-planned new industrial zone that is distant from residential zones. The authorities must put in place noise and vibration regulations to permit maximum noise levels as well as the acoustic measures of all construction, motilities, industries, and their corresponding offices [20, 26]. Furthermore, amid the upcoming mass urban area, a transitional area must be established with a scope to include less pollution and less dense industrial activity. This will enable the urban authorities to carry on with their plans for economic development that certainly will alleviate noise pollution.

Annually, those living within urban areas dispose of more than two billion tons of waste globally globally in an unmannered way [27, 28]. It is necessary for waste management principles such as the "polluter pays" to be practiced, and for a waste framework directive to be set out to control environmental pollution. In order of priorities, the waste management approach must be set with waste prevention as the preferred option, followed by reuse, then recycling, other recovery forms such as energy from waste, and finally, improved final disposal that is followed by strict monitoring. Clearly, it is essential to appropriately manage urban waste so it does not adversely disturb places of spatial interest; be a nuisance via noise or odors; pose risks to animals, plants, soil, or water; cause harm to the environment; or endanger the health of human beings [29–31]. Moreover, development, marketing, usage, and disposal stages should carefully be measured to attain the best environmental management and ultimately secure a sustainable Earth.

Energy management

The urban energy supply involves both renewable and conventional resources that must be appropriately salvaged and reused to avoid waste. To reduce energy demand and acquire environmental and societal benefits for sustainable urbanization, it is necessary to determine and enforce energy efficiency and conservation technologies. Because energy is utilized by urban societies for domestic, commercial, and industrial purposes through heating, air conditioning, illumination, manufacturing, transportation, and communication, the use of energy must be classified as a primary resource with used resources being renewable or nonrenewable [32–34]. While renewable resources are created by continuing processes that are likely to withstand infinite time, nonrenewable resources are considerably

This book belongs to Kitab Liaison (ocd1996@gmail.com) Copyright Elsevier 2023

exhausted by human usage. The conventional urban industries, which include the nuclear industry, the electrical power industry, the natural gas industry, and the petroleum industry, can cause serious ecological disaster. Urban energy management according to VDI-guideline 4602 refers to the proactive prearranged and methodical coordination of energy procurement, distribution, and usage to meet necessities, considering the economic and environmental objectives [35–37]. For urban energy management to be implemented, it is necessary to incorporate energy management within the structure of an organization. The interactions and responsibilities of decision makers must be regularized. The delegation of functions and skills must be spread to the executive worker from top management. Also, task fulfillment can be guaranteed by comprehensive coordination. As a result, within huge or energy-intensive firms, it is recommended to create a distinct organizational unit, that is, the energy management unit, which keeps track and supports management. This relies on the fundamental organizational structure form, where this particular unit is linked. For instance, in the case of a functional institution, the urban energy management unit is situated directly amid the first and the second hierarchical level. Central and numerous sector-particular energy units must exist within a divisional company, so that the individual sectors' needs as well as coordination among the head office and branches can be met [5, 38, 39]. Urban energy management within a matrix company can be incorporated as a matrix function and hence approach a number of functions directly. Accordingly, building constructions in mass urbanization promotes more use of energy for cooling, heating, and lighting through more refined usage of materials, innovative air flow systems, and façade design, all of which must be considered the essential elements of the effort to recycle to attain clean and efficient cities [1, 2]. Correspondingly, buildings in urban areas that proactively integrated lower-carbon energy formation are also capable of making a substantial contribution to the general energy performance of cities. Afterward, the establishment of an incorporated and compatible energy infrastructure on an entire metropolitan basis will create the platform above which smart cities can enhance their energy performance to achieve environmental sustainability [40–42]. Having a strategy for the energy optimization of urban buildings would be most interesting for encouraging the rational use of clean energy where constructed buildings can make sustainable energy such as an exterior curtain wall skin PV panel system as a source of renewable energy.

The application of renewable energy thus encompasses the sustainable energy industry, consisting of sustainable and alternative manufacture, sale,

This book belongs to Kitab Liaison (ocd1996@gmail.com) Copyright Elsevier 2023

and distribution of substitute fuels that would certainly be the finest choice for urban sustainability [43, 44]. Essentially, management of the urban energy supply, including production planning and operation as well as energy consumption, should be set to prudently use logistics, production management, and environmental management for creating a sustainable urban system.

Building management

All urban building management systems (BMS), also known as building automation systems (BAS), refer to a computer-based control system that needs to be installed in all urban buildings to monitor and regulate the building's electrical and mechanical equipment such as power systems, lighting, and ventilation to confirm sustainability [45–47]. Given that the systems connected to a BMS usually represent a building energy use of 40%, this percentage will approach 70% if lighting is included [48, 49]. It is essential for urban building management systems to be set up because they are critical elements to intelligently manage the energy demand of, for example, the electrical system, plumbing, the fire alarm system, heating ventilation, and air conditioning (HVAC), electric power control, and illumination control. As a result, through BMS, urban building management is required to have electronic centralized regulation of a building's air conditioning, ventilation and heating, and lighting as well as other building systems [50, 51]. Bearing in mind the enhanced utilities' lifecycle, a decrease in urban energy operating costs and consumption, a building system's efficient operation, and the comfort of the occupant, the BMS objectives need to be enhanced. Consequently, a distributed control system on the computer networking of automation instruments should be structured to control and monitor the HVAC and humidity ventilation and control systems, lighting, flood and fore safety, security, and mechanical systems within a building [52–54]. Therefore, the core functionality of an urban BAS should be retained within the building climate in a specified range, offering malfunction alarms to a building's maintenance staff, monitoring device failure and performance in all building systems, and supplying lighting to rooms based on an occupancy schedule. Compared to noncontrolled buildings, the BAS reduces energy and maintenance costs, hence most industrial, institutional, and commercial buildings constructed after 2000 include a BMS that should be restructured for a timeworn building [55–57]. Normally, several timeworn urban buildings have been retrofitted with a novel building automation system, financed via

This book belongs to Kitab Liaison (ocd1996@gmail.com) Copyright Elsevier 2023

insurance and energy savings, as well as other savings linked with fault detection and preemptive maintenance. So, an urban building regulated by a building management system is frequently termed an intelligent building a "smart home" in case of a residence or just a "smart building." If proprietary procedures are utilized in homes, industrial and commercial buildings must have in history depended on healthy recognized procedures such as BACnet. Modern urban IEEE standards and groups' efforts or QIVOCON have offered a standard-based ground for different networking of several instruments in several physical networks for varied purposes, and service quality and failover which promises proper support to human safety and health [58, 59].

Designing buildings for mass urbanization must accommodate a building automation system for energy, water, and air preservation characteristics plus appropriate electrical instrument demand response in a typical BAS function. This is fact that the more refined ventilation and moisture monitoring needed of "tight" insulated for achieving urban environmental sustainability.

Water management

Having a sustainable and healthy urban community makes the residents certain of accessing safe water for municipal, industrial, and household use. The significance of acquiring clean drinking water via the urban authorities is the fact that they make sure that the water supplied to residents through water supply systems is nontoxic. It is the duty of the rural and urban authorities to often monitor the water quality supplied at the tap and constantly inform the consumers of the quality. Concerning the quality of water, the rural and urban authorities should always inspire citizens to drink tap water rather than bottled water based on the quality and environmental effect [60, 61]. In order for the water distribution system to feature a greater turnover for a sustainable urban area, there is as well a concentration for clients to "flush through" to raise the drinking water quality and conserve water.

Among the wastewater treatment directive goals that should have to be adapted appropriately is a clean urban environment. The wastewater treatment directive calls for all towns and cities to acquire clean sewage systems onsite and/or treat the sewage water to particular minimum standards prior to discharge into a landfill [56, 62]. Through this approach, urban coastal areas, lakes, and rivers can be cleaned up to meet the health-based minimum standards for fauna, flora, and human health.

This book belongs to Kitab Liaison (ocd1996@gmail.com) Copyright Elsevier 2023

For megacities, if the connection of a sewer system should have to avert leakages, the better option could be the incorporation of density polyethylene pipes. It is necessary to carry out investigations within the catchment area of water, which accounts for 10%–15% of the yearly water distribution [37, 63]. To avert pressure surges, all pipe workers are trained to handle valves as well as other appliances in the right way.

Essentially, the urban wastewater treatment plants are to take good care of the removal of prolonged nitrogen in case it is more than 10 years old. Occasionally, new and strict necessities to deal with the elimination of nitrogen, phosphorus, and organic materials should be integrated. Besides the customary measures to oversee wastewater, urban authorities must also analyze different climate change settings to handle the impacts that this is currently having and will have in the future because of increased storm levels, the water situation, and will have and is water supply. As a result, storm water effective management turns out to be more and more important, and hence, requires working actively to separate storm water from will have and is joint system. This will reduce the overflow risk and provide a smoother flow. This eventually will avert will have and is overflow of sewage system facilities or drainage systems. Afterward, urban authorities must manage rainfall in a more natural way, which will finally play a central role in changes in climate.

Infrastructure and transportation management

Infrastructure, which is a basic facility and system, serves an urban area's movement to facilitate the essential routes to function the economy property and comfort the day to day lives [47, 61]. Usually, urban infrastructure describes technical structures such as telecommunications, electrical grids, tunnels, bridges, and roads. As defined, the interconnected systems' physical components offer goods and services vital to facilitate, sustain, or improve the social condition. On the other hand, urban transportation refers to the movement of goods, animals, and humans from one place to another. Space, pipeline, cable, water, land, and air are the modes of transportation. Because urban transport facilitates trade among people, which is necessary for the development of civilization, it is important. Transport infrastructure is composed of the fixed installations of canals, waterways, airways, railways, roads, and terminals as well as pipelines such as seaports, refueling depots, trucking terminals, warehouses, bus stations, railway stations, and airports. Terminuses can be utilized both for maintenance and exchange of cargo

This book belongs to Kitab Liaison (ocd1996@gmail.com) Copyright Elsevier 2023

and passengers. Aircraft, automobiles, spacecraft, watercraft, people, trucks, trains, buses, and bicycles are the vehicles moving along these networks.

Ownership and operation within the urban transportation industry is either private or public, depending on the country as well mode playing an essential part in globalization and economic growth, though most kinds utilize huge amounts of land and cause air pollution [11, 64]. Essentially, operations cover the way in which vehicles function. To acquire sustainability to preserve biodiversity, the processes set for this particular purpose, including policies, legalities, and financing, should be followed. Besides making cities pleasant, habitable, and green places, biodiversity also provides valued services to urban residents. Therefore, it is essential for infrastructures to be structured, and construction regarding the nontoxic the biodiversity when building infrastructure to operate considering the preservation of biodiversity [14, 23]. Similarly, urban building structures should be constructed considering the public health, relaxation, social activities and nature watching, recreational parks, quiet streets, and green space by given the priority. This will definitely offer building blocks for controlling the ecological crisis and encouraging the quality of life.

Consequently, through the use of enhanced technology, the approach must strongly be applied to build clean urban transport and infrastructure plans. The aim of these plans will include working toward acquiring zero emission vehicles and improving traffic around and within capitals by considering economic interest and encouraging public transport, walking, and cycling within towns and cities, and above all balancing the environmental effects.

General management

General management to achieve a sustainable urban system is based primarily on the overall management system that includes organizational structure, planning activities, responsibilities, practices, procedures, processes, and resources for developing, implementing, achieving, reviewing, and maintaining environmental policy. It is a simple definition of a management tool to help the urban authority to manage the environmental aspects by conducting five principles: (a) commitment and policy, (b) planning, (c) measurement and evaluation, (d) review and improvement, and (e) implementation.

The urban council, therefore, should conform the sustainability commitment to realize the total management, because it has a significant citizen and

This book belongs to Kitab Liaison (ocd1996@gmail.com) Copyright Elsevier 2023

social participation dimension for the rural and urban environment improvement [19, 29]. The use of resources should be characterized by urban councils considering continued thinking on the environment, so as to practice sustainability. Afterward, the city, industry, and residents will find it easier to make sustainable selections concerning waste management, travel, services, and commodities. The following objectives will need to be enforced, precise to its own responsibilities and undertakings, if the above is to be attained: (a) through the increase in the quantities of waste management, waste should be recycled in an operative manner to minimize waste creation. Waste sorting and recycling systems will be more easily reachable; (b) lessen the use of dangerous substances by acquiring information, collaboration, and supervision, which will contribute to staging out the hazardous substances circulation. At the acquiring stage, the urban authorities will require the elimination of commodities with harmful matters, and sustainable substances should be selected within all sectors; and (c) clean procurement, where the city authority will review its purchase and procurement procedures as well the use of resources.

Subsequently, the urban agency should have a representative on the steering committee on green procurement and set up a website on green public procurement, offer criteria documents for green procurement, and hold conferences on green public procurement to inform citizens about green purchases and provide knowledge about the benefit of green products for sustainability of a mass urban system.

Conclusion

To secure sustainable urbanization, the urban public administrations in different areas must be identified in the total range from the management of public administration to individual activities. Because the engagement of the public sector is the driving force securing sustainability, thus, public administration must take a leading role to show the way about urban sustainability. Indeed, the municipal authority shall influence and enforce the management of appropriate sustainable technology for the development of mass urbanization to secure a better urban system. Subsequently, at the local level, municipal authorities should take responsibility for activities ranging from building sectors, energy sectors, land use planning, waste water treatment facilities, transport and mobility, and infrastructure sectors. Within its work, the identification of best management practices must be developed as a sectoral reference document for the best

This book belongs to Kitab Liaison (ocd1996@gmail.com) Copyright Elsevier 2023

environmental management practices by conducting advanced research, planning, application, and management strategy to secure a sustainable urbanization.

Acknowledgments

This research was supported by Green Globe Technology under grant RD-02019-03. Any findings, conclusions, and recommendations expressed in this paper are solely those of the author and do not necessarily reflect those of Green Globe Technology.

References

[1] A.P. Ballantyne, et al., Audit of the global carbon budget: estimate errors and their impact on uptake uncertainty, Biogeosciences 12 (2015) 2565–2584.
[2] P. Box, Spatial units as agents: making the landscape an equal player in agent-based simulations, in: R.H. Gimblett (Ed.), Integrating Geographic Information Systems and Agent-Based Modeling Techniques for Simulating Social and Ecological Processes, Methuen, New York, 2002.
[3] F. Achard, et al., Determination of tropical deforestation rates and related carbon losses from 1990 to 2010, Glob. Chang. Biol. 20 (2014) 2540–2554.
[4] H. Bao, J. Niggemann, L. Luo, T. Dittmar, S.-J. Kao, Aerosols as a source of dissolved black carbon to the ocean, Nat. Commun. 8 (2017) 510.
[5] M.F. Hossain, Green science: independent building technology to mitigate energy, environment, and climate change, Renew. Sust. Energ. Rev. 73 (2017) 695–705.
[6] R.J. Andres, T.A. Boden, D. Higdon, A new evaluation of the uncertainty associated with CDIAC estimates of fossil fuel carbon dioxide emission, Tellus Ser. B Chem. Phys. Meteorol. 66 (2014) 23616.
[7] R.A. Betts, C.D. Jones, J.R. Knight, R.F. Keeling, J.J. Kennedy, El Nino and a record CO2 rise, Nat. Clim. Chang. 6 (2016) 806–810.
[8] P. Ciais, C. Sabine, Chapter 6: carbon and other biogeochemical cycles, in: T. Stocker, D. Qin, G.K. Platner (Eds.), Climate Change 2013: The Physical Science Basis, Cambridge University Press, London, 2013.
[9] R. Andreozzi, V. Caprio, C. Ciniglia, M. De Champdoré, R. Lo Giudice, R. Marotta, E. Zuccato, Antibiotics in the environment: occurrence in Italian STPs, fate, and preliminary assessment on algal toxicity of amoxicillin, Environ. Sci. Technol. 38 (2004) 6832–6838.
[10] E.B. Barbier, The economic determinants of land degradation in developing countries, Phil. Trans. R. Soc. London 352 (1997) 891–899.
[11] A.J. Bebbington, S.P.J. Batterbury, Transnational livelihoods and landscapes: political ecologies of globalization, Ecumene 8 (4) (2001) 369–380.
[12] A.P. Ballantyne, C.B. Alden, J.B. Miller, P.P. Tans, J.W.C. White, Increase in observed net carbon dioxide uptake by land and oceans during the past 50 years, Nature 488 (2012) 70–72.
[13] E.M. Bridges, L.R. Oldeman, Global assessment of human-induced soil degradation, Arid Soil Res. Rehabil. 13 (4) (1999) 319–325.
[14] J.E. Bauer, et al., The changing carbon cycle of the coastal ocean, Nature 504 (2013) 61–70.
[15] F. Chevallier, On the statistical optimality of CO2 atmospheric inversions assimilating CO2 column retrievals, Atmos. Chem. Phys. 15 (2015) 11133–11145.

This book belongs to Kitab Liaison (ocd1996@gmail.com) Copyright Elsevier 2023

[16] C. Le Quéré, R.M. Andrew, P. Friedlingstein, S. Sitch, et al., Global carbon budget 2017, Earth Syst. Sci. Data Discuss. 10 (2017) 405–448.
[17] K. Cleaver, G. Schreiber, Reversing the Spiral: The Population, Agriculture and Environment Nexus in Sub-Saharan Africa, World Bank, Washington, DC, 1994.
[18] K.L. Denman, et al., Couplings Between Changes in the Climate System and Biogeochemistry, Cambridge University Press, London, 2007.
[19] M.F. Hossain, H. Mukai, Importance of Nutrients (N, P, and NO3 + NO2) in Growth of the Surfgrass, Phyllospadix iwatensis Makino, Benthos Res. 55 (2000) 23–35.
[20] R. Houghton, Balancing the global carbon budget, Annu. Rev. Earth Planet. Sci. 35 (2007) 313–347.
[21] W. Li, et al., Reducing uncertainties in decadal variability of the global carbon budget with multiple datasets, Proc. Natl. Acad. Sci. USA 113 (2016) 13104–13108.
[22] M.J. Conroy, Mapping of species richness for conservation of biological diversity: conceptual and methodological issues, Ecol. Appl. 6 (3) (1996) 763–773.
[23] S.J. Davis, K. Caldeira, Consumption-based accounting of CO2 emissions, Proc. Natl. Acad. Sci. USA 107 (2010) 5687–5692.
[24] E. Dietzenbacher, J. Pei, C. Yang, Trade, production fragmentation, and China's carbon dioxide emissions, J. Environ. Econ. Manag. 64 (2012) 88–101.
[25] R.A. Duce, et al., Impacts of atmospheric anthropogenic nitrogen on the open ocean, Science 320 (2008) 893–897.
[26] D.M. Karl, M.J. Church, Microbial oceanography and the Hawaii Ocean Time-series programme, Nat. Rev. Microbiol. 12 (2014) 699–713.
[27] A. de Sherbinin, Land-use and land-cover change, in: A CIESIN Thematic Guide, Center for International Earth Science Information Network of Columbia University, Palisades, NY, 2002.
[28] K.C. Hyland, E.R.V. Dickenson, J.E. Drewes, C.P. Higgins, Sorption of ionized and neutral emerging trace organic compounds onto activated sludge from different wastewater treatment configurations, Water Res. 46 (2012) 1958–1968.
[29] A. Diouf, E.F. Lambin, Monitoring land-cover changes in semi-arid regions: remote sensing data and field observations in the Ferlo, Senegal, J. Arid Environ. 48 (2001) 129–148.
[30] K.C. Ewel, Natural resource management: the need for interdisciplinary collaboration, Ecosystems 4 (2001) 716–722.
[31] J. Fairhead, M. Leach, Misreading the African Landscape: Society and Ecology in a Forest-Savanna Mosaic, Cambridge University Press, Cambridge, 1996.
[32] C.E. Donald, M.R. Elie, B.W. Smith, P.D. Hoffman, K.A. Anderson, Transport stability of pesticides and PAHs sequestered in polyethylene passive sampling devices, Environ. Sci. Pollut. Res. 23 (12) (2016) 12392–12399.
[33] C.C. Gibson, E. Ostrom, T.K. Ahn, The concept of scale and the human dimensions of global change: a survey, Ecol. Econ. 32 (2000) 217–239.
[34] B. Gonzalez-Gaya, et al., High atmosphere-ocean exchange of semivolatile aromatic hydrocarbons, Nat. Geosci. 9 (2016) 438–442.
[35] E. Garcia-Robledo, C.C. Padilla, M. Aldunate, F.J. Stewart, O. Ulloa, A. Paulmier, G. Gregori, N.P. Revsbech, Cryptic oxygen cycling in anoxic marine zones, PNAS 114 (31) (2017) 8319–8324.
[36] K.-H. Erb, et al., Bias in the attribution of forest carbon sinks, Nat. Clim. Chang. 3 (2013) 854–856.
[37] S. Schwietzke, et al., Upward revision of global fossil fuel methane emissions based on isotope database, Nature 538 (2016) 88–91.
[38] D.E. Helbling, J. Hollender, H.-P.E. Kohler, H. Singer, K. Fenner, High-throughput identification of microbial transformation products of organic micropollutants, Environ. Sci. Technol. 44 (2010) 6621–6627.

This book belongs to Kitab Liaison (ocd1996@gmail.com) Copyright Elsevier 2023

[39] A. Tengberg, J. Ellis-Jones, R. Kiome, M. Stocking, Applying the concept of agrodiversity to indigenous soil and water conservation practices in Eastern Kenya, Agric. Ecosyst. Environ. 70 (1998) 259–272.
[40] M.F. Hossain, Green science: advanced building design technology to mitigate energy and environment, Renew. Sust. Energ. Rev. 81 (2) (2018) 3051–3060.
[41] M.F. Hossain, Photonic thermal energy control to naturally cool and heat the building, Adv. Therm. Eng. 131 (2018) 576–586.
[42] M.F. Hossain, Theoretical modeling for hybrid renewable energy: an initiative to meet the global power, J. Sustain. Energy Eng. 4 (2016) 5–36.
[43] M.F. Hossain, Design and construction of ultra-relativistic collision PV panel and its application into building sector to mitigate total energy demand, J. Build. Eng. 9 (2017) 147–154.
[44] M.F. Hossain, Theory of global cooling, Energy Sustain. Soc. 6 (2016) 24.
[45] M.F. Hossain, Application of advanced technology to build a vibrant environment on planet mars, Int. J. Environ. Sci. Technol. 14 (12) (2017) 2709–2720.
[46] M.F. Hossain, Invisible transportation infrastructure technology to mitigate energy and environment, Energy Sustain. Soc. 7 (2017) 27.
[47] K.H. Redford, E. Dinerstein, C. Groves, G. Mace, S. Maginnis, R.A. Mittermeier, R. Noss, D. Olson, J.G. Robinson, A. Vedder, M. Wright, P. Coppolillo, E.W. Sanderson, G.A.B. Da Fonseca, Mapping the conservation landscape, Conserv. Biol. 17 (1) (2003) 116–131.
[48] J. Liu, et al., Contrasting carbon cycle responses of the tropical continents to the 2015–2016 El Niño, Science 8 (2017) 201.
[49] P. Borrelli, D.A. Robinson, L.R. Fleischer, E. Lugato, et al., An assessment of the global impact of 21st century land use change on soil erosion, Nat. Commun. 8 (2017) 2013.
[50] M.F. Hossain, N. Fara, Integration of wind into running vehicles to meet its total energy demand, Energy Ecol. Environ. 2 (1) (2017) 35–48.
[51] M.F. Hossain, Production of clean energy from cyanobacterial biochemical products, Strateg. Plan. Energy Environ. 3 (2016) 6–23.
[52] M.F. Hossain, Solar energy integration into advanced building design for meeting energy demand, Int. J. Energy Res. 40 (2016) 1293–1300.
[53] E.G. Irwin, J. Geoghegan, Theory, data, methods: developing spatially explicit economic models of land use change, Agric. Ecosyst. Environ. 85 (2001) 7–23.
[54] Z. Liu, et al., Reduced carbon emission estimates from fossil fuel combustion and cement production in China, Nature 524 (2015) 335–338.
[55] A.P. Kinzig, Bridging disciplinary divides to address environmental and intellectual challenges, Ecosystems 4 (2001) 709–715.
[56] B.B. Stephens, et al., Weak northern and strong tropical land carbon uptake from vertical profiles of atmospheric CO2 science, Science 316 (2007) 1732.
[57] Y. Yin, et al., Variability of fire carbon emissions in equatorial Asia and its nonlinear sensitivity to El Niño, Geophys. Res. Lett. 43 (2016) 10,472–410,479.
[58] K. Kok, A. Farrow, A. Veldkamp, P.H. Verburg, A method and application of multi-scale validation in spatial land use models, Agric. Ecosyst. Environ. 85 (2001) 223–238.
[59] O.O. Ogunlaja, W.J. Parker, Impact of activated sludge process configuration on removal of micropollutants and estrogenicity, Water Sci. Technol. 72 (2) (2015) 277–283.
[60] J. Mason Earles, S. Yeh, K.E. Skog, Timing of carbon emissions from global forest clearance, Nat. Clim. Chang. 2 (2012) 682–685.
[61] H. Nagendra, D.K. Munroe, J. Southworth, From pattern to process: landscape fragmentation and the analysis of land use/land cover change, Agric. Ecosyst. Environ. 101 (2004) 111–115.

This book belongs to Kitab Liaison (ocd1996@gmail.com) Copyright Elsevier 2023

[62] K.L. Metzger, R.B. Boone, M.B. Coughenour, R.M. Reich, Effects of seasonal grazing on plant species diversity and vegetation structure in a semi-arid ecosystem, J. Arid Environ. 61 (1) (2005) 147–160.
[63] E. Marti, E. Variatza, J.L. Balcazar, The role of aquatic ecosystems as reservoirs of antibiotic resistance, Trends Microbiol. 22 (2014) 36–41.
[64] J.P. Bagnall, L. Malia, A.T. Lubben, B. Kasprzyk-Hordern, Stereoselective biodegradation of amphetamine and methamphetamine in river microcosms, Water Res. 47 (2012) 5708–5718.

This book belongs to Kitab Liaison (ocd1996@gmail.com) Copyright Elsevier 2023

Index

Note: Page numbers followed by *f* indicate figures and *t* indicate tables.

A

AC. *See* Alternating current (AC)
ADSORBSIATM, 167–168
Adsorption, 161
  arsenic, 166
  contaminant, 173, 175
  of charged species, 183
  equilibrium constant, 231–232
  of heavy metals, 167
  Langmuir adsorption constant, 223–224
  of metal ions, 164–165
  of ozone, 177
  of photons, 195–196
Aerosol, 129–130
Agricultural wastewater treatment, 158–159
Air pollution
  aerosol, 129–130
  anthropogenic activities, 129
  carbon dioxide (CO_2), 129–130
  concentration, 130–131
  economic losses, 130–131
  exposure, 130–131
  fossil fuels, 131
  in microenvironmental/microactivity, 130–131
  losses of productivity, 130–131
  mass urban development, 129
  nitrogen oxides (NOx), 129–130
  sulfur oxides (SOx), 129–130
  urban air pollution control technology
    fossil fuel data, 142–143, 143*f*
    global warming, 144–147
  urban air pollution impact
    atmospheric CO_2 concentration, 131–132, 132*f*, 135
    CO_2 absorption by terrestrial vegetation and the Earth, 135, 137–141
    CO_2 emissions from fossil fuel, 132–134, 136–137
    CO_2 emissions from land-use change (ELUC), 132–134, 136–137
    cumulative CO_2 emissions and atmospheric impact, 141–142
    environmental susceptibility, 133
    ocean CO_2 sink, 134–135, 137–141
    total global emissions of carbon, 136, 137*f*, 138*t*
  in urban atmosphere, 347
Air toxicity, 9–10
Alternating current (AC), 26–28, 35–37, 281–283
Aminofullerenes, 175–176
Anaerobic codigestion, 32, 37–38, 281, 283–285
Antimicrobial nanomaterials, 169–170, 177–180
Aquaporins, 171–172
Aromatic compound model, 32, 37, 280
Atmospheric CO_2 concentration, 131–132, 132*f*, 141–142
  growth rate, 132–133, 135–136

B

BAS. *See* Building automation systems (BAS)
Battery modeling, 103–105, 118
Bernoulli-Euler beam equation, 58
Betz's coefficient, 61, 79, 83, 114
Biogas conversion, 283–287, 286–287*f*
Biologically inspired membranes, 171–172
Bioreactor design, 279–281, 281–282*f*
Blackbody radiation, 281–283, 284*f*
Blue Economy, 8
BMS. *See* Building management systems (BMS)
Boltzmann's constant, 28–30, 274–276, 292–293, 339–340
Bose-Einstein (B-E) photon distribution mechanism, 291, 311
BR. *See* Bremsstrahlung radiation (BR)
Bremsstrahlung radiation (BR), 291
Brown Economy, 8

This book belongs to Kitab Liaison (ocd1996@gmail.com)
Copyright Elsevier 2023

Building's exterior skin PV panel, 272–273, 272*f*
Building automation systems (BAS), 350–351
Building management, 350–351
Building management systems (BMS), 350–351
Bioenergy, 25, 32, 37–38, 38*f*, 271–272, 280, 285, 287*f*

C

Carbon based nanoadsorbents, 161–167
Carbon nanotubes (CNT), 161–164, 169–172, 178–179, 182–183, 280
Cartesian coordinate system, 30–31, 31*f*, 277, 278*f*
Catastrophic natural disasters, 291
Ceramic membranes, 184, 200–201
CFCs. *See* Chlorofluorocarbons (CFCs)
CFD. *See* Computational fluid dynamics (CFD)
Chemical pollution, 155–156
Chemical vapor deposition (CVD), 171–172
Chlorofluorocarbons (CFCs), 28–29, 129–130, 291
Climate change, 10–11, 41, 111, 122, 132–133, 142–148, 159–160, 271–272, 291, 352
CNT. *See* Carbon nanotubes (CNT)
CO_2 absorption, 132–133, 135, 137–141
CO_2 emissions, 347
  acceleration rates, 131–132
  and atmospheric impact, 141–142
  catastrophic natural disasters, 291
  from fossil fuel, 132–134, 136–137
  from land-use change (ELUC), 132–134, 136–137
Colorimetric assays, 181–183
Computational fluid dynamics (CFD), 111–112
Cooling photon emission panels, 291
Cooling systems, 291
  cooling photonic dynamics, 302–303, 303*f*
  cooling photonic frequency mode, 302
  cooling-state photons, electrodynamics of, 292
  current-voltage (I–V) characteristics, 292–294, 295*f*
  density of states (DOS)
    bifurcation of, 300
    in PV cell, 300
    non-Weisskopf-Winger mode, 300
    PDOS, 300, 302*f*
    photonic band structure and energy conversion modes, 300, 301*f*
    photonic structures of, 298, 299*t*
    total DOS, 300, 302*f*
  Fock cooling determination, 303–304
  Fock state cooling photon, 304
  helium-assisted curtain wall skin, 298
  helium waveguides, 292
  nonseries (NS) cells, 294
  PB frequency, 300
  PBG waveguide defects, 292
  PB photon self-energy correction, 300
  photon-generated current, 294
  photon probability density, contour map of, 292, 293*f*
  proliferative photon dynamics, 300
  solar irradiance receptor, two-diode model of, 292, 293*f*
  I–q relationship, 292–293
  V–R relationship, 294
Cost savings, 73
Critical infrastructure system
  infrastructure and transportation, 10–11
  power, 9–10
  water, 8–9
CVD. *See* Chemical vapor deposition (CVD)

D

DBPs. *See* Disinfection byproducts (DBPs)
DC. *See* Direct current (DC)
Debye mass, 310
Defuzzification technique, 95
Density of states (DOS)
  bifurcation of, 300
  Fock state cooling photon, 304
  in PV cell, 300
  non-Weisskopf-Winger mode, 300

This book belongs to Kitab Liaison (ocd1996@gmail.com) Copyright Elsevier 2023

PDOS, 300, 302*f*
photonic band structure and energy conversion modes, 300, 301*f*
photonic structures of, 298, 299*t*
total DOS, 300, 302*f*
Derating factor, 35–37, 281–283
Design and construction cost
biogas production, 285–287, 288*t*
solar energy production, 283, 285*t*
Detention tank, 25, 271–272, 279
DFIG. *See* Doubly fed induction generator (DFIG)
DGVM. *See* Dynamic global vegetation modeling (DGVM)
Direct current (DC), 26–28, 35–37, 281–283
Disinfection byproducts (DBPs), 177, 179–180, 187–189
Disposal systems, 25
Dissolved oxygen (DO), 191–192, 214–216
DO. *See* Dissolved oxygen (DO)
DOS. *See* Density of states (DOS)
Doubly fed induction generator (DFIG), 61, 79, 83, 85–86, 88–89, 91–95, 114, 116
Dynamic global vegetation modeling (DGVM), 134–135, 140

E

Earth pressure coefficient, 70
Effective temperature, 144, 146–147
Electrical subsystem, 85–86
Electricity transformation, 339–341
Electromagnetic field (EMF), 334
Electrospinning, 168–169
Electrostatic force, 47–49
analysis, 20–22
generation, 42–47
ELUC, 134
EMF. *See* Electromagnetic field (EMF)
Energy cost savings, 104–105
Energy demand, 10, 45–46, 52–53, 271–272, 281–283, 350–351
Energy-harvesting rate, 317
Energy management, 348–350
Evapotranspiration, 143–144, 153
Environmental pollution control, 11–13

F

FIS. *See* Fuzzy inference system (FIS)
FLC. *See* Fuzzy logic controller (FLC)
Flying car
battery modeling, 118
generator modeling, 116–117
methods, 112
optimization, 119–122
aerodynamic design, 111
WECS, 116
wind energy modeling, 114–115
FO. *See* Forward osmosis (FO)
Forward osmosis (FO), 172–173
Freshwater, 8, 151, 152*f*, 155–156
Fuzzy inference system (FIS), 95
Fuzzy logic controller (FLC), 95–96, 98–100

G

Gas demand, 288
GATM. *See* Growth of the concentration of atmospheric CO2 (GATM)
Gauge field, 17–18, 21, 42, 44, 47
Generator modeling, 96–98, 116–117, 122
GHGs. *See* Greenhouse gases (GHGs)
Gibbs free energy, 50
Glazing wall, 311
Global warming, 57–58, 242–243
ecological transformation and stress, 144–145
emissivity, 144
solution of, 145–147, 147*f*
temperature balance of Earth, 144, 144*f*
temperature variation effect, 144–145, 145*f*
Goldstone scalar, 17–18, 42–43, 243–244, 296
Green building complexes. *See* Natural cooling and heating technology
Green building technology
biogas conversion, 283–287, 286–287*f*
bioreactor design, 279–281, 281–282*f*
black body-assisted PV (photovoltaic) panel, 271–272
methanogenesis process, 271–272
onsite wastewater treatment, 271–272

This book belongs to Kitab Liaison (ocd1996@gmail.com) Copyright Elsevier 2023

Green building technology *(Continued)*
PV system (*see* Photovoltaic (PV) system)
solar energy conversion, 281–283, 285*t*
Greenhouse gases (GHGs), 41–42, 142–144, 148
Green science, 288
Ground thermophilic condition, 283–285, 286*f*
Groundwater, 8–9, 151, 154
Growth of the concentration of atmospheric CO_2 (GATM), 132–133, 135

H

Hagen-Poiseuille equation, 171–172
HCSS software, 68, 71
Heating system
corrective functional asymptotic formulas, 307
covariant derivative, 297, 304–305
Debye mass, 310
differential photon density, 305
gauge field, 304
Higgs boson electromagnetic field, 296
Higgs boson quantum field, 305
Lagrangian, 296–297, 304–305
leading-order heating photoemission rates, 311
light absorption spectrum, 308
magnetic-field-induced photon production, 306–307, 306*f*
negative and positive indexes, 308–309
polarized emission rate, 309
quantum field, 298, 305
radial field, 297
scalar field, 296–297, 304
scalar potential, 296–297
thermodynamic temperature equilibrium, 310
three-diode scattering, 310
transformation mechanism of photon, 298, 298*f*
Helium waveguides, 292
Heterogeneous TiO_2 photocatalysis, 187–194
Higgs boson BR quantum field, 317
displaced fields, 325
Lagrangian, 318–320, 325–326
photon emission mechanism, 320, 320*f*
photon-photon interaction, 326
scalar field, 319, 325
scalar potential, 319
solar irradiance, 325
under high temperature, 317, 318*f*
Higgs boson electromagnetic field, 296
Higgs boson electromagnetic force, 296, 317–318
Higgs boson quantum field, 291, 305
Homogeneous photo-Fenton reaction, 194–197
Hossain cooling photon (HcP^{-}), 292, 311
Hossain static electric force (HSEF), 17–22, 42, 44, 47–49
Hossain thermal photon (HtP^{-}), 311
Hyporheic zone, 154

I

Industrial Revolution, 11–12, 131–132, 142–143
Industrial wastewater treatment plants, 158–159
Infrastructure and transportation management, 352–353
Inorganic loading rate, 283–285, 286–287*f*
Intergovernmental Panel on Climate Change (IPCC), 132–133, 137–142, 347
Invisible infrastructure transportation technology. *See* Maglev transportation infrastructure system
IPCC. *See* Intergovernmental Panel on Climate Change (IPCC)

K

k-omega, 112–113

L

Land-use change, 134, 136–137
Lifecycle assessment (LCA), 238–239, 240*f*
Light wavelength, 218–219
Load resistant factor design (LRFD), 64, 68, 71, 276–277
Localized surface plasmon resonance (LSPR), 181–182

This book belongs to Kitab Liaison (ocd1996@gmail.com) Copyright Elsevier 2023

LRFD. *See* Load resistant factor design (LRFD)
LSPR. *See* Localized surface plasmon resonance (LSPR)

M

Mach number, 112
Maglev transportation infrastructure system
  construction cost estimate comparison, 68–71
  conventional energy utilization, 57
  cost of, 71–72
  cost savings, 73
  global warming, 57–58
  guideway model, 58–59
  MATLAB Simulink software, 57–58
  pedestrian, 63
  simulations and methods, 58
  traditional road infrastructure, cost of, 72–73
  traffic control, design of, 62–63
  uplift levitation and lateral guidance, magnetic forces of, 59–61
  vehicles, wind energy modeling, 61–62
  wind energy storage, battery system, 62
Magnetic levitation (maglev). *See* Maglev transportation infrastructure system
Magnetic nanoparticles, 165–166, 166*f*, 172–173, 181
Massless Goldstone scalar stemming, 18, 42–43, 244, 296
MATLAB simulation, 26–28, 28*f*
MATLAB-Simulink, 57–58, 62, 117
MATLAB-Simulink circuit model, 98
Maximum power efficiency (MPE), 89
Maximum power point tracking (MPPT), 80, 88–89, 89*f*, 93–95, 98–100, 102, 115, 119–122
Megacities, 352
  critical infrastructure system
    infrastructure and transportation, 10–11
    power, 9–10
    water, 8–9
  environmental pollution control, 11–13
  SMU, 7
  sustainable building, 13–14
Membership functions (MFs), 96
Membrane distillation (MD), 207–208, 207*f*
Membrane fouling, 168, 198, 206–207
Mesoporous clays, 198–200, 199*f*
Metal-based nanoadsorbent metal oxides, 165
Metallic/bimetallic catalyst nanoparticles, 170
Metal oxide nanocrystals, 166
Methanogenesis, 32, 34*f*, 37–38, 271–272
MFs. *See* Membership functions (MFs)
Miles per hour (MPH), 102
MPE. *See* Maximum power efficiency (MPE)
MPH. *See* Miles per hour (MPH)
MPPT. *See* Maximum power point tracking (MPPT)
Multifunctional magnetic nanoparticles, 165–166, 166*f*

N

Natural cooling and heating technology
  Bose-Einstein photon distribution mechanism, 291
  cooling mechanism, 292–296, 298–304
  heating mechanism, 296–298, 304–311
  Higgs boson quantum field, 291
Nanoadsorbents, 161, 186
  carbon based nanoadsorbents, 161–167
  polymeric nanoadsorbents, 167
  potential application in water treatment, 167–168
Nanocomposite membranes, 169–170
Nanofiber membranes, 168–169
Nanofiltration (NF), 171–172, 206
Nanomaterials, 169–170, 180–181, 183, 185–186
  antimicrobial, 169–170, 177–180, 178*t*
  application, 179–180
  ceramic, 168–169
  definition, 161
  functional, 168–169, 183–184
  metal depend nanomaterials, 166
  metal oxide nanomaterials, 177

This book belongs to Kitab Liaison (ocd1996@gmail.com)
Copyright Elsevier 2023

Nanomaterials *(Continued)*
operational, 168
potential influence of, 159–160
retention and reuse of, 184–185
Nanoscale effect, 165
Nanotechnology-enhanced water and wastewater treatment. *See* Urban water pollution control, nanotechnology
Nano-TiO_2, 171, 176
Nanozeolites, 170
Nano zero-valent iron (nZVI), 170
Nitrogen oxides (NOx), 129–130
Noble metal nanomaterials, 181–182
Nonrenewable resources, 348–349
Nonseries (NS) cells, 294
NOx. *See* Nitrogen oxides (NOx)
NS cells. *See* Nonseries (NS) cells
Natural water resources, 17, 151

O

Ocean CO_2 sink, 134–135, 137–141
Ozone layer, 129–130, 291, 311

P

PAHs. *See* Polycyclic aromatic hydrocarbons (PAHs)
Pair photon production, 317, 318*f*
bremsstrahlung and inelastic pair annihilation processes, 331
differential photon density, 326
functional asymptotic calculation, 327
electron momentum, 320–321
emission rate of photon momentum, 332
graph of the function, 328–331, 329–330*f*
high-energy cutoff transformation, 328
high-energy photon collision theory, 320
negative and positive index, 328–331
photon effect, 331
photon energy emission rate, 331
photon momentum vectors, 320–321
solar electromagnetic radiation, 320–321
Particulate matter (PM), 129–130, 233
Parts per million (ppm), 129–130
Pathogen detection, 180–183
PB. *See* Photonic band (PB)
PBEs. *See* Photon band edges (PBEs)
PBG. *See* Photonic band-gap (PBG)
PDOS. *See* Projected DOS (PDOS)
PEC. *See* Photoelectrochemical (PEC) device
Permanent magnet synchronous generator (PMSG), 96–97, 116
Peukert's Law, 62, 103, 118
Photocatalysis
dissolved oxygen, 214–216
heterogeneous, 187–189, 238–239
hybrid photocatalysis membrane, 204–205, 207*f*
light intensity, 219–221
metal oxide nanomaterials, 177
nanophotocatalyst optimization, 173–176
photoreactor, 176
Purifics Photo-CatTM system, 176
technical barriers, 176–177
TiO_2 photocatalysis, 189–197, 214–215
TiO_2 photocatalyst optimization, 173–176, 174*t*
Photocatalytic membrane, 187, 200–201
Photocatalytic membrane reactors (PMR)
configuration, 206
diverse hybridization, 207–208
hybrid, 205–206
membrane distillation (MD), 207–208, 207*f*
nanofiltration (NF), 206
pilot Photo-CatTM system, 208–210, 209*f*
submerged, 205–206, 205*f*
TiO_2 zone, 205–206
UF and MF membrane filtration, 206–207
UV slurry with a movable baffle, 205–206
with immobilized photocatalysts, 206
Photocatalytic nanoparticle integrated membranes, 170
Photocatalytic reactor. *See also* Photocatalytic membrane reactors (PMR)
configuration, 204–210
operational parameters, 210

This book belongs to Kitab Liaison (ocd1996@gmail.com) Copyright Elsevier 2023

Photocatalytic water treatment technology, 187–242
challenges
future challenges and prospects, 239–242
in development, 197–198
disinfection byproducts, 187–189
dissolved oxygen (DO), 214–216
heavy and noble metals, 237–238
heterogeneous TiO_2 photocatalysis, 187–194
homogeneous photo-Fenton reaction, 194–197
inorganic ions, 233–237
kinetics and modeling
photodisinfection, 226–232
photomineralization kinetics, 223–226
rate model, 222–223
lifecycle assessment (LCA), 238–239, 240*f*
light intensity, 219–221
light wavelength, 218–219
mesoporous clays, 198–200, 199*f*
nanofibers, 200
nanorods, 200
nanowires, 200
pH, 211–214
photocatalyst immobilization and supports, 197
photocatalyst modification and doping, 201–204
photocatalytic membrane, 200–201
photocatalytic reactor
configuration, 204–210
operational parameters, 210
pollutants and their loading, 216–218
postreclamation, 187
response surface analysis, 221–222
sustainable water resources, 187–189
temperature, 214–216
TiO_2 loading, 210–211
turbidity, 233
wastewater recycling, 187–189
water quality, 232–233
zero waste arrangement, 187
Photodisinfection kinetics, 187, 226–232
Photo-dissociation, 321
Photoelectrochemical (PEC) device, 44–47
Photomineralization kinetics, 210, 223–226
Photon band edges (PBEs), 291
Photonic band (PB), 298, 301*f*
Photonic band-gap (PBG), 292, 302–303, 336
Photon production, 317–318
Photo physics radiation application, 245–246, 246*f*
Photovoltaic (PV), 46–47
current, 49–50
I-V characteristics, 274–276
I-V-R relationship, 273, 273*f*
output current, 274–276
panel design, 276–278
photo current, 274–276
power conditioning efficiency, 274
PV cell module, 272–273
PV-generation efficiency, 26–28, 274
radiation mechanism, 320–321
reference cell temperature, 274
single-diode circuit, 273, 273*f*
solar array source, 272–273, 272*f*
solar cell, 274
solar irradiance, 26, 27*f*, 272–273, 272*f*
solar radiation and ambient temperature, 273
Photovoltaic-generation efficiency, 26–28, 274
Pilot Photo-CatTM system, 208–210
PM. *See* Particulate matter (PM)
PMR. *See* Photocatalytic membrane reactors (PMR)
PMSG. *See* Permanent magnet synchronous generator (PMSG)
Point-of-use (POU), 166
Polycyclic aromatic hydrocarbons (PAHs), 164
Polymeric nanoadsorbents, 167
Postreclamation, 187
Potable water, 242–243
POU. *See* Point-of-use (POU)
Power conditioning efficiency, 26–28, 274
Power system. *See* Urban water vapor
ppm. *See* Parts per million (ppm)
Pressurized water, 155–156
Projected DOS (PDOS), 300, 302*f*
Public transportation systems

This book belongs to Kitab Liaison (ocd1996@gmail.com) Copyright Elsevier 2023

Public transportation systems *(Continued)*
battery modelling, 103–105
car, theoretical experiment on, 100–102
controller design, 95–96
drive train modelling, 77, 80–81
generator modelling, 96–98
induction generator, wind turbine generation system, 98–102
MATLAB Simulink software package, 77–78, 78*f*
methods and simulation, 78–80
one-mass model, 81–82, 81–82*f*
control structure
PWM, 86
DFIG subsystem control, 91–95
wind turbine subsystem control, 86–90
wind energy conversion
electrical subsystem, 85–86
kinetic energy, 83
aerodynamic subsystem, 83–85
wind power technology, 77
wind turbine modeling, 77
Pulse width modulation (PWM), 86
Purifics Photo-CatTM system, 176
PV. *See* Photovoltaic (PV)
PWM. *See* Pulse width modulation (PWM)

Q

QDs. *See* Quantum dots (QDs)
QED. *See* Quantum electrodynamics (QED)
Quantum dots (QDs), 181
Quantum electrodynamics (QED), 35, 277, 291

R

Raw mesophilic condition, 283–285, 286*f*
Raw thermophilic condition, 283–285, 286*f*
Recycling systems, 353–354
Reference module efficiency, 26–28, 274
Renewable energy, 9–10, 105, 348–350
Renewable resources, 13–14, 348–349
Renewable water engineering
cohesion-tension mechanism, 242–243
HSEF electric field, 246–247
onsite water treatment, 245–246
plants transpiration, 242–243
static electric force generation, 243–245
transpiration mechanism, 242
Reverse osmosis (RO), 168–169
RO. *See* Reverse osmosis (RO)
Rotor voltages, 85, 92

S

SEF. *See* Static-electric force (SEF)
Sanitation and waste disposal system
domestic biowaste, 25
environmental pollution, 25
methanogenesis process, 25
simulation and method
solar power implemented bioreactor, 26–31, 35–37
sustainable bioreactor, 31–34, 37–38
Scalar field, 17–18, 20–21, 42–44, 47, 296–297, 304, 319, 325
SCIG. *See* Squirrel cage induction generator (SCIG)
Sequestration of ocean CO_2 (SOCEAN), 135, 137–140
SERS. *See* Surface-enhanced Raman spectroscopy (SERS)
Sewage treatment plants, 158–159
Silica nanoparticles, 182
Simulink/Sim Power Systems, 62, 98, 117
Sludge mesophilic condition, 283–285, 286*f*
Sludge thermophilic condition, 283–285, 286*f*
Smart home, 350–351
SMU. *See* Sustainable mass urbanization (SMU)
SOCEAN. *See* Sequestration of ocean CO_2 (SOCEAN)
SODIS. *See* Solar disinfection (SODIS) system
Soil salinization, 154
Solar disinfection (SODIS) system, 19–20, 176, 219, 245–247
Solar energy, 241–242, 271–272, 276–277, 317, 341
in bioreactor, 26, 37
conversion, 281–283, 285*t*
Solar irradiance, 28, 35–37, 46–47, 49–50, 53, 272–274, 272*f*, 281–283, 294, 317, 325

This book belongs to Kitab Liaison (ocd1996@gmail.com) Copyright Elsevier 2023

Solar photochemistry, 35, 277
Solar power implemented bioreactor, 26–31, 35–37
Solar radiation energy, 35
SOx. *See* Sulfur oxides (SOx)
Squirrel cage induction generator (SCIG), 85, 97, 117
Static-electric force (SEF), 17–19, 41, 44, 53
Static electricity force, 18–19, 20*f*, 21–22, 43, 49, 244–245, 245*f*, 247
Stefan-Boltzmann constant, 146–147
Stefan-Boltzmann law, 146–147
Submerged membrane photocatalytic reactor, 205–206, 205*f*
Sulfur oxides (SOx), 129–130
Supercritical steam, 153
Surface-enhanced Raman spectroscopy (SERS), 181–182
  Surface water, 151, 153–154
Survival period of life on Earth, 133
Sustainable bioreactor, 31–34, 37–38
Sustainable building, 13–14
Sustainable mass urbanization (SMU), 7
Sustainable urbanization, 9–10
  building management, 350–351
  energy management, 348–350
  general management, 353–354
  infrastructure and transportation management, 352–353
  urban environmental management, 347–348
  water management, 351–352

T

Takeoff velocity, 111–112, 119
TCC. *See* Tracking characteristic curve (TCC)
Terminuses, 352–353
TFC. *See* Thin film composite (TFC)
TFN membranes. *See* Thin film nanocomposite (TFN) membranes
Thermal pollution, 155–156, 158–159
Thin film composite (TFC), 170–171
Thin film nanocomposite (TFN) membranes, 170–171
Three-diode photon scattering
  dilogarithm variable, 334
  dissipative integro-differential equation, 334–336
  DOS, 334
  EMF vector, 334
  mechanism, 321, 322*f*
  nonequilibrium condition, 338
  nonequilibrium photon scattering theorem, 336
  photo-dissociation, 321
  photon activation mechanism, 336, 337*f*
  photon energy conversion modes, 335*f*
  photon-generated diffusion phenomenon, 324
  photonic density, contour maps of, 321, 323*f*
  photonic dynamics, 323–324
  photonic structure, 323–324, 338
  photon proliferation, 338
  reservoir-induced PB photon self-energy correction, 334–336
TiO_2 loading, 210–211
TJ. *See* Tunnel junction (TJ)
Trace contaminant detection, 183
Tracking characteristic curve (TCC), 89
Transportation infrastructure system. *See* Maglev transportation infrastructure system
Transport infrastructure, 352–353
TSR, 62, 80, 84, 88, 115
Tunnel junction (TJ), 45–47

U

Urban water vapor
  clean energy, mass urbanization, 41–42
  climate change, 41
  GHGs, 41–42
  material and methods
    electrostatic force generation, 42–44
    photo electrolysis/energy formation, 44–47
  photo-electrochemical-photovoltaic mechanism, 41–42
  photon energy, 41
  results

This book belongs to Kitab Liaison (ocd1996@gmail.com) Copyright Elsevier 2023

Urban water vapor *(Continued)*
conversion of energy into electricity, 50–53
electrostatic force, 47–49
photoelectrolysis/energy formation, 49–50
Ultrarelativistic reaction models, 317
UNEP. *See* United Nations Environment Program (UNEP)
United Nations Environment Program (UNEP), 14
Uplift levitation, 59–60
Urban air pollution, 347
control technology
fossil fuel data, 142–143, 143*f*
global warming, 144–147
impact
atmospheric CO_2 concentration, 131–132, 132*f*, 135
CO_2 absorption by terrestrial vegetation and the Earth, 135, 137–141
CO_2 emissions from fossil fuel, 132–134, 136–137
CO_2 emissions from land-use change (ELUC), 132–134, 136–137
cumulative CO_2 emissions and atmospheric impact, 141–142
environmental susceptibility, 133
ocean CO_2 sink, 134–135, 137–141
total global emissions of carbon, 136, 137*f*, 138*t*
Urban ecosystem, 347
Urban energy management, 348–349
Urban environmental management, 347–348
Urban infrastructure, 10–11, 352–353
Urban system, 11–12, 242, 347, 353
autonomous adaptation, 3–4
definition, 3
environmental vulnerability, 3
resilience, 3–4
Urban transportation industry, 353
Urban wastewater treatment plants, 352
Urban water pollution control, nanotechnology, 159–160
barriers and research needs, 185–186
current and potential applications, 161, 162–163*t*, 167–168, 176–177, 179–180
disinfection and microbial control
nanomaterial antimicrobial mechanisms, 177–179, 178*t*
potential applications in water treatment, 179–180
toxic disinfection byproducts, 177
UV disinfection, 177
methods
adsorption, 161–168
forward osmosis (FO), 172–173
membranes and membrane processes, 168–172
photocatalysis, 173–176, 174*t*
multifunctional devices, 183–184
retention and reuse of nanomaterials, 184–185
sensing and monitoring, 180
pathogen detection, 180–183
trace contaminant detection, 183
UV technology, 242

W

Waste disposal system, 25
Waste management principles, 348
Waste sorting, 353–354
Wastewater treatment (*see also* Urban water pollution control, nanotechnology)
current and potential applications, 162–163*t*
directive goals, 351
process, 33*f*, 280*f*
solutions, 159–160
Wastewater treatment plant (WWTP), 158–159
Water, 17
basic domestic water requirement, 155
critical infrastructure system, 8–11
consumption in urban areas, 154
density, 31–32
drinking water, 155
environmental water application, 156
freshwater, 151, 152*f*
gas, solid, and liquid forms, 151–153

This book belongs to Kitab Liaison (ocd1996@gmail.com) Copyright Elsevier 2023

groundwater, 151, 154
H_2O, 151
hydrogen bonds, 151, 152*f*
hyporheic zone, 154
irrigation, 157
nonpoint sources, 158–159
point sources, 158–159
potable water, 242–243
scarcity, 156–157, 157*f*
supercritical steam, 153
surface water, 153–154
water bodies, 158–159
Water delivery systems
capturing urban cloud, 17–18
electrostatic force analysis, 20–22
material, methods and simulation
in site water treatment, 19–20
static electric force generation, 17–19
plastic tank, 17, 19–22
urban cloud, 17–20
Water management, 351–352
Water pollution
chemical pollution, 155–156
contaminant types, 158–159
garbage, 158–159
industrial wastewater treatment plants, 158–159
nature-based solutions, 158–159
raw sewage, 158–159
sewage treatment plants, 158–159
sludge, 158–159
thermal pollution, 155–156, 158–159
toxic pollutants, 158–159
urban industrial consumption, 155
urban water pollution control, nanotechnology, 159–160
antimicrobial mechanisms, 178–179
barriers and research needs, 185–186
disinfection and microbial control, 177
methods, 161–176
multifunctional devices, 183–184
pathogen detection, 180–183
retention and reuse of nanomaterials, 184–185
sensing and monitoring, 180
trace contaminant detection, 183
water treatment, applications in, 176–177, 179–180
Water quality, 159–160, 176, 179–180, 196, 206, 216–217, 232–233, 351
Water treatment
agricultural wastewater treatment, 158–159
industrial wastewater treatment plants, 158–159
in site water treatment, 19–20
nanotechnology-enhanced water and wastewater treatment (*see* Urban water pollution control, nanotechnology)
onsite water treatment, 245–246
photocatalytic water treatment (*see* Photocatalytic water treatment technology)
sewage treatment plants, 158–159
Water vapor, 22, 41–42, 52–53, 242–243, 247
WECS. *See* Wind energy conversion system (WECS)
Wind energy
on a car, 100
conversion, 83–86, 101–102, 103*f*, 116
modeling, vehicles, 61–62, 114–115
storage, 62
Wind energy conversion system (WECS), 83, 88–89, 91, 102, 116
Wind turbine generation system (WTGS), 83
Wind turbine subsystem control, 86–90
WO_3, 175–176
WTGS. *See* Wind turbine generation system (WTGS)

Z

ZEB. *See* Zero-emission building (ZEB) technology
Zero-emission building (ZEB) technology, 271–272

This book belongs to Kitab Liaison (ocd1996@gmail.com) Copyright Elsevier 2023

This page intentionally left blank

This book belongs to Kitab Liaison (ocd1996@gmail.com)

Copyright Elsevier 2023

Sustainable Development for Mass Urbanization

Md. Faruque Hossain

This book takes an in-depth look at the effects of mass urbanization on critical infrastructural systems in a rapidly changing world

- Covers Infrastructural Systems such as Water Delivery Systems, Sanitation and Waste Disposal Systems, Power Systems, and Public Health Systems
- Scrutinizes the challenges encountered when designing, planning, and constructing sustainable Megacities
- Case studies are presented in each chapter to further illustrate these solutions

Populations are shifting from rural areas to growing cities, creating megacities in the process. Because so many people migrate to cities, more infrastructures must be built to absorb them. *Sustainable Development for Mass Urbanization* scrutinizes the challenges encountered when designing, planning, and constructing sustainable cities. Chapter one briefly explains the role of national and local governments in strategic planning, development, implementation, monitoring, and enforcement for ensuring that the water, air, food, and products used by the community are safe for the public and the environment.

Written by an author who has lived and worked in Mega Cities such as Dhaka, Bangladesh; Kolkata, India; Tokyo, Japan; Sydney, Australia; and New York City, United States, *Sustainable Development for Mass Urbanization* takes an in-depth look at critical infrastructural systems, charting the problems and providing possible solutions for systems such as Water Delivery Systems, Sanitation and Waste Disposal Systems, Power Systems, and Public Health Systems. Chapters 10 through 12 address the new green technologies, practices, and standards predicated by the need for sustainable office building and housing. Case studies are presented in each chapter to further illustrate how these solutions are implemented in existing Megacities around the world.

Related Titles

Kubba / *Handbook of Green Building Design and Construction* / ISBN-13: 978-0123851284

Clark / *Global Sustainable Communities Handbook* 1st Edition / ISBN-13: 978-0123979148

Kubba / *LEED Practices, Certification, and Accreditation Handbook* / ISBN-13: 13: 978-1856176910

Civil Engineering / Construction Management

ISBN 978-0-12-817690-0

9 780128 176900

ELSEVIER elsevier.com/books-and-journals

This book belongs to Kitab Liaison (ocd1996@gmail.com)

Copyright Elsevier 2023